Proceedings of the

9th Patras Workshop

on Axions, WIMPs and WISPs

23-28 June 2013
Mainz, Germany

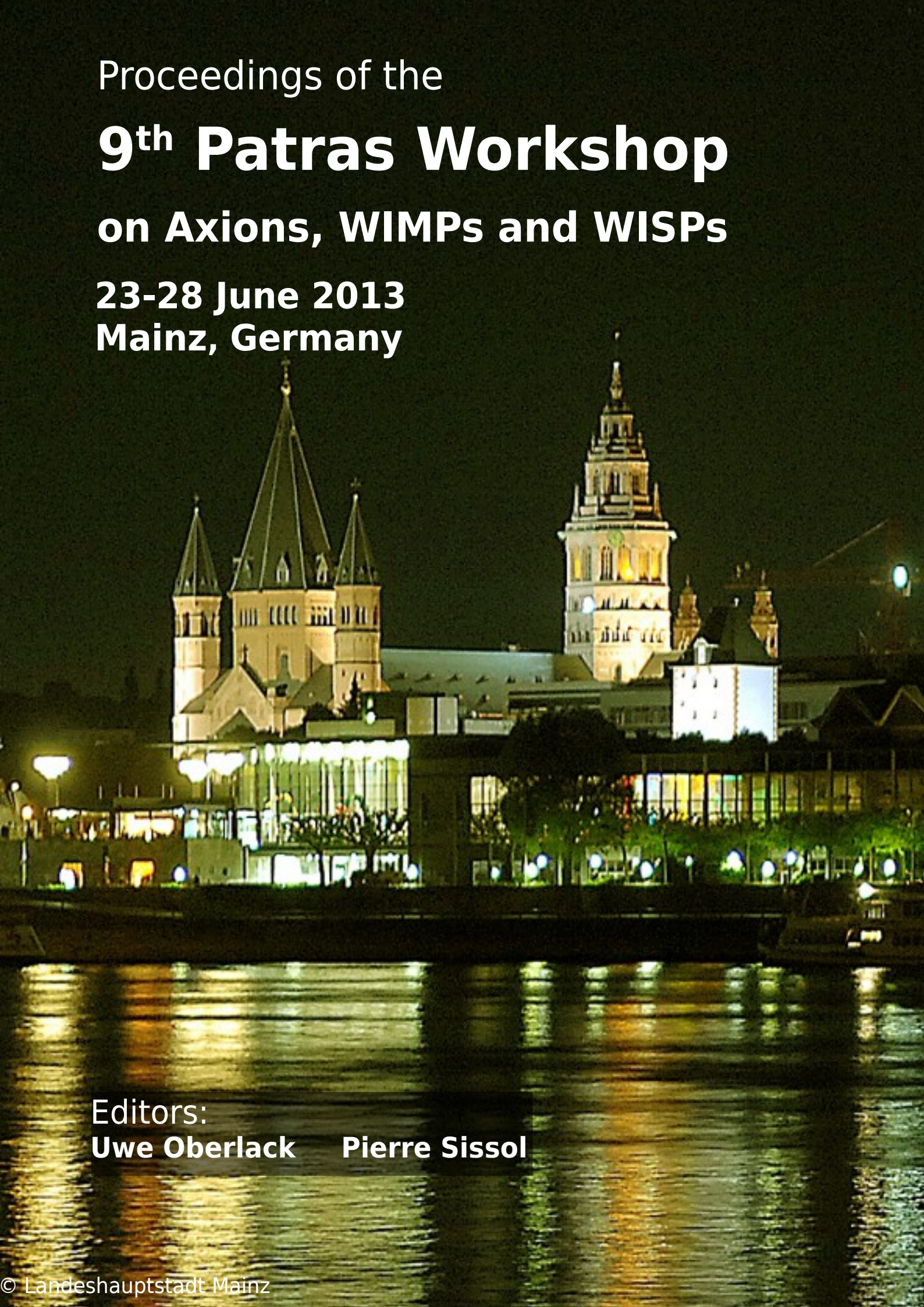

Editors:
Uwe Oberlack **Pierre Sissol**

Impressum

Proceedings of the
9th Patras Workshop on Axions, WIMPs and WISPs 2013
June 24-28, 2013, Mainz, Germany

Conference homepage
`http://axion-wimp2013.desy.de/`

Slides at
`http://axion-wimp2013.desy.de/e201031/`

Online proceedings at
`http://axion-wimp2013.desy.de/e201113/`

Editors:
Uwe Oberlack, Pierre Sissol
November 2013
DESY-PROC-2013-04
ISBN 978-3-935702-83-6
ISSN 1435-8077

Published by
Verlag Deutsches Elektronen-Synchrotron
Notkestraße 85
22607 Hamburg
Germany

Organizing Committee

Uwe Oberlack (Chairman)
Institute of Physics and PRISMA Cluster of Excellence
Johannes Gutenberg University Mainz
Staudingerweg 7
55128 Mainz
Germany

Vassilis Anastassopoulos and Konstantin Zioutas
Department of Physics
University of Patras
26504 Patras
Greece

Laura Baudis
Physik Institut
University of Zurich
Winterthurerstr. 190
8057 Zurich
Switzerland

Jörg Jäckel
Institute for Theoretical Physics
University of Heidelberg
Philosophenweg 16
69120 Heidelberg
Germany

Axel Lindner and Andreas Ringwald
Deutsches Elektronen Synchrotron (DESY)
Notkestr. 85
22607 Hamburg
Germany

Marc Schumann
Albert Einstein Center for Fundamental Physics
University of Bern
Sidlerstrasse 5
3012 Bern
Switzerland

Local Organizers

Uwe Oberlack,

Pierre Sissol,

Silvia Müller,

Rainer Othegraven and

Melanie Scheibelhut
Institute of Physics and PRISMA Cluster of Excellence
Johannes Gutenberg University Mainz
Staudingerweg 7
55128 Mainz
Germany

Barbara Wittmann
Deutsches Elektronen Synchrotron (DESY)
Notkestr. 85
22607 Hamburg
Germany

Preface

Another exciting and lively PATRAS meeting - meanwhile the 9th of this series! With about 90 participants, another increase with respect to the previous year, the meeting shows the continued and still increasing interest in the broad range of theories and experiments related to Dark Matter of all kinds and, maybe with particular emphasis this time, to the hidden side of the universe more broadly. It is a compliment to the initiators of this series that the PATRAS workshop continues to be successful in a field that is not short of competing meetings.

The talks demonstrated the experimental breadth in searches for dark matter, which range from indirect searches with satellites such as Fermi or AMS-02 to solar and astrophysical observations, direct searches in rare event underground experiments, cavity experiments, light shining through wall experiments, to searches at the LHC. Also hidden photons / gauge bosons of various kinds are being searched for with accelerator experiments and solar observations. Theories span even wider breadth, which is evident from merely considering the mass range of hypothetical particles.

At the time of the conference, discussions on low mass WIMPs had just been refueled by the CDMS-II collaboration with a couple of events of low significance. At the same time, XENON100 firmed up the description of their low energy threshold, reaffirming the conflict of their limit with hints of low mass WIMPs. Just recently, at the time of this writing, the LUX experiment with even lower threshold added strong support to the XENON100 exclusion. The Dark Matter interpretation of a 130 GeV line excess at Fermi is being questioned as an instrumental artefact. It appears that the level of excitement in the field, and in the public, is not always matched by the significance of spurious results. The two LHC review talks at the conference were illustrative of a community somewhere in the limbo between the excitement about the Higgs discovery and the worry about not finding any hints of ”new physics” at the LHC yet. A number of talks high-lighted current results and the potential of future experiments in the search for hidden photons at accelerators of lower energy. Various ideas were also presented on new searches with experiments ”off the beaten path”.

The PATRAS workshop took place from June 24-28, 2013 in Schloss Waldthausen, a castle / conference center in the outskirts of Mainz, Germany. In the spirit of this workshop series, discussions were lively and the atmosphere friendly even in scientific controversy. For the local organizers, working with this congenial crowd of scientists made the organizational part very pleasant. We wish to thank all participants and all contributors to these proceedings, who gave their time and effort to an inspiring meeting and to build up this volume. In addition to the proceedings, we would like to point to the slides of the talks that remain available at the PATRAS workshop website: axion-wimp2013.desy.de. As we distribute these proceedings, we already look forward to the 10th PATRAS meeting, which will take place at CERN from June 30th - July 4th, 2014.

Uwe Oberlack and Pierre Sissol

Acknowledgements

The organizers would like to thank the sponsors who supported this meeting, namely the PRISMA Cluster of Excellence at the Johannes Gutenberg University Mainz, CERN, DESY, the University of Heidelberg, the CAST experiment, the University of Patras, the Albert Einstein Center for Fundamental Physics, Bern, and the University of Zurich. Special thanks go to Pierre Sissol who took the time out of his Ph.D. work to do so much of the local organizing including the social event, to Barbara Wittmann (DESY) for creating the online presence of the conference, to Silvia Müller for initiating the connections to Schloss Waldthausen, and to Melanie Scheibelhut and Rainer Othegraven for local support during the conference. We thank the management and staff at Schloss Waldthausen for running a smooth organization and for the pleasant cooperation.

The Organizing Committee

Contents

Chapter 1

Searches for Hidden Photons in the Laboratory

Aharonov-Bohm Effect and Hidden Photons

P. Arias

Pontificia Universidad Catolica de Chile, Casilla 306, Santiago 22, Chile.

DOI: http://dx.doi.org/10.3204/DESY-PROC-2013-04/arias_paola

Signs of hypothetical light gauge bosons from a hidden sector may appear in Aharonov-Bohm-like experiments. The absence of signal in carried on experiments allow us to set a modest constraint to the mass and coupling constant of these particles. Our findings open the possibility to exploit the leaking of *hidden magnetic field* in a different setup of experiments.

1 Introduction

Hidden sectors are on vogue nowadays since they are needed to realize popular extensions of the Standard Model, as Supersymmetry and String Theory. Hidden sectors could be very weakly coupled to our visible sector through heavy messengers, via loop interactions. As a consequence, we are left with effective couplings at low energies, that mix both sectors. Prime candidates, that can emerge from a hidden sector, are hidden photons (HP), i.e., gauge bosons of an extra U(1) gauge group [1]. These particles, if massive, mix kinetically with photons, leading to oscillations between both of them.

Several direct and indirect searches have been performed looking for these particles and many others are being planned for the near future (see ref.[2] and references therein). Even though HPs are very weakly coupled to photons, they do leave an imprint in several physical phenomena, for instance, Coulomb law [3]. In the same way, we want to explore signatures the Aharonov-Bohm (AB) effect [4], can gives us about hidden photons.

2 Aharonov Bohm effect for massive photons

The observable essence of the AB effect is the path-dependent phase, φ, of an electron wave-function, which is shifted in the presence of an electromagnetic potential

$$\exp\left(ie\oint_c \vec{A}\cdot d\vec{x}\right) \equiv \exp(i\Delta\varphi) \quad . \tag{1}$$

Where the phase shift $\Delta\varphi$ is related with the magnetic flux, Φ, enclosed by the path of the electron, $\Delta\varphi = e\Phi$. A theoretical modification of the AB effect under a possible non-zero photon mass was discussed in Boulder and Deser (BD), [5]. They argue that it is not necessary for the vector potential to be a gauge field achieve the AB effect, but to be minimally coupled to matter.

Let us assume a typical AB experiment, with a solenoid of radius a, and a steady current, j. Following BD, for a massive photon, the equation of motion of the system is the Proca equation.

For stationary currents, only the transverse mode survives and the equation of motions becomes

$$\left(-\nabla^2 + M^2\right)\mathbf{A} = e\mathbf{J}. \tag{2}$$

Where M is the photon mass.The current in a magnet solenoid has the form $\mathbf{J} = \hat{\varphi} j\delta(a-\rho)$. Where ρ and φ are cylindrical coordinates.

Imposing a cylindrically symmetric ansatz for the vector potential, of the form $\mathbf{A} = \hat{z} \times \nabla\Pi(\rho)$ we find an equation for $\Pi(\rho)$

$$\left(\partial_\rho^2 + \rho^{-1}\partial_\rho - M^2\right)\Pi(\rho) = ej\Theta(a-\rho). \tag{3}$$

Whose solution is given by

$$\Pi(\rho) = -je\left[-\theta(\rho-a)K_0(m\rho)\int_0^a \rho' d\rho' I_0(m\rho') + \theta(a-\rho)\left(K_0(m\rho)\int_0^\rho \rho' d\rho' I_0(m\rho') + I_0(m\rho)\int_\rho^a \rho' d\rho' K_0(m\rho')\right)\right]. \tag{4}$$

The corresponding magnetic field is given by the expression $\mathbf{B} = \nabla \times \mathbf{A}$. By taking the curl of the vector potential, we get $\mathbf{B} = \hat{z}\, e\, j\Theta(a-\rho) + \hat{z}M^2\Pi(\rho)$.

We note that besides the usual solution – confined to the surface of the solenoid – there is a contribution that leaks out with a range given by M^{-1}. Therefore, the magnetic flux besides its normal value, picks up extra contributions from inside and outside the solenoid, coming from the non-zero mass of the photon.

3 Aharonov Bohm effect for hidden photons

The effective low energy Lagrangian that mixes photons, A_μ, with hidden photons, X_μ, is

$$\mathcal{L} = -\frac{1}{4}F_{\mu\nu}F^{\mu\nu} - \frac{1}{4}G_{\mu\nu}G^{\mu\nu} + \frac{\sin\chi}{2}G_{\mu\nu}F^{\mu\nu} + \frac{\cos^2\chi}{2}m_{\gamma'}^2 X_\mu X^\nu + J_\mu A^\mu \quad , \tag{5}$$

where $F_{\mu\nu}$ is the field strength tensor of photons and $G_{\mu\nu}$ the analogue for hidden photons. The quantity χ accounts for the strength of the coupling between visible and hidden sectors and is predicted to be very small [6]. We have also included a mass term for the hidden photon, $m_{\gamma'}$, arising from a standard Higgs mechanism or Stueckelberg mechanism [7].

Kinetic mixing can be removed from the Lagrangian by rotating the fields to a new basis, with a massless photon and a heavy hidden photon, *i.e.* $\tilde{B}_\mu = B_\mu \cos\chi$, and $\tilde{A}_\mu = A_\mu - \sin\chi B_\mu$

In this new basis the equations of motion for (5) read

$$-\nabla^2\tilde{\mathbf{A}} = e\ \mathbf{J}, \tag{6}$$

$$\left(-\nabla^2 + m_{\gamma'}^2\right)\tilde{\mathbf{X}} = e\tan\chi\mathbf{J}. \tag{7}$$

Where we have chosen a gauge such $\tilde{A}_0 = \tilde{X}_0 = 0$. The equation of motion for the field $\tilde{\mathbf{A}}$ is the usual equation for a massless gauge field, and the equation for the heavy HP is the same as the Proca equation we found for a massive photon, eq. (2). We solve, therefore, in the same way as BD. The magnetic field associated to $\tilde{\mathbf{X}}$, given by $\mathbf{B}_{\tilde{\mathbf{X}}} = \nabla \times \tilde{\mathbf{X}}$, is

$$\mathbf{B}_{\tilde{\mathbf{X}}} = \hat{z}\ e\tan\chi j\Theta(a-\rho) + \hat{z}m_{\gamma'}^2\tan\chi\Pi(\rho), \tag{8}$$

where the function $\Pi(\rho)$ is given again by eq. (4).

Now we can *go back* and find the true magnetic field, $\mathbf{B} = \nabla \times \mathbf{A}$. From eq (**??**) we have, $\mathbf{A} = \tilde{\mathbf{A}} + \tan\chi\tilde{\mathbf{X}}$ and taking the curl to this equation we get

$$\nabla \times \mathbf{A} = \hat{z}\; ej\Theta(a-\rho) + \hat{z}\; e\tan^2\chi j\Theta(a-\rho) + \hat{z}\; m_{\gamma'}^2\tan^2\chi\Pi(\rho). \tag{9}$$

Therefore, we have realize that if a HP mixes with a photon, there is a small component of the magnetic field in a (confined) solenoid that leaks out of it, both inside and outside the solenoid radius. Let us note that therefore the effects stops being topological in nature, since there is actual leaking of magnetic field. This interesting fact opens several detection possibilities, besides Aharonov-Bohm-type experiments [8].

4 Limit from Aharonov-Bohm-type experiments

In this section we will compute the bound that one can get from an AB experiment. Let us recall that the phase shift that an electron beam suffers by surrounding the solenoid is proportional to the magnetic flux enclosed by it

$$\Delta\varphi = e\Phi. \tag{10}$$

Without kinetic mixing, the magnetic flux is given by $\Phi_0 = ej\pi a^2$. Assuming a mixing between photon and HP, Φ can be obtained by taking the surface integral of eq.(9), and reads

$$\Phi = \Phi_0\left(1+\tan^2\chi\right) + m_{\gamma'}^2\tan^2\chi\int_S \Pi(\rho)dS. \tag{11}$$

The above formula is however not final yet, since it is not properly normalized. Note that for $m_{\gamma'} \to 0$, eq. (11) does not recover its natural value, Φ_0. This is because the electric charge gets also renormalized by the mixing photon-HP [9].

This issue has been already addressed by Jaeckel and Roy in [10]. They developed a procedure to get the proper bound from a function, $\mathcal{F}(\chi, m_{\gamma'}, \alpha)$, where there is also a parameter α that depends on χ. The procedure takes as many independent measurements as the number of parameters depend on the kinetic mixing in the function $\mathcal{F}$. In our case, we have χ and the electric charge, which we will write in terms of the fine structure constant $e^2 = 4\pi\alpha$, so we need an extra independent measurement of α (besides the AB experiment). We will consider the electron $g-2$ experiment, worked on [9], since is the most sensitive measurement of α. From ref. [10] we can write the bound on χ as

$$\chi^2 \leq \frac{\frac{|\Delta M_1|}{M_1} + \frac{|\Delta M_2|}{M_2}}{|(n_1 f_1(m_{\gamma'}) - n_2 f_2(m_{\gamma'}))|}, \tag{12}$$

where M_i, $(i=1,2)$, are the two independent measurements of α_i, and have the form $M_i = c_i\alpha^{n_i} + \chi^2 f_i(m_{\gamma'})$. The parameters ΔM_i are the absolute uncertainty in the measurement. The AB experiment provides a measurement on α given by

$$\Delta\varphi = 4\pi\alpha\tilde{\Phi}_0 + 4\pi\alpha\chi^2\tilde{\Phi}_0 f_1(m_{\gamma'}). \tag{13}$$

Where $\tilde{\Phi}_0 = j\pi a^2$ and $f_1(m_{\gamma'}) = 1 + \left(m_{\gamma'}^2/\Phi_0\right)\int_S \Pi(\rho)dS$.

Figure (1) shows our findings. We have considered two scenarios: the green bound considers a magnetic field of $B = 10^{-2}$ T and the red one is the optimistic scenario, considering a magnetic field of $B = 1$ T. Both scenarios assume a sensitivity of the external magnetic field in the solenoid of $\Delta B = 10^{-8}$ T. The dimensions of the set up are a solenoid radius of $a = 0.1$ cm and an electron wavelength range of $\rho = 10$ cm.

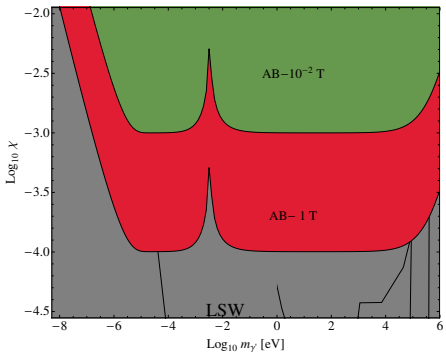

Figure 1: Plot of kinetic mixing parameter (χ) as a function of the HP mass ($m_{\gamma'}$). The gray area corresponds to parameter space that has been already ruled out. For further explanation see text.

5 Outlook

We have explored the phenomenological consequences of mixing photons and hidden photons in the Aharonov-Bohm effect. We found that indeed there is a modification, and therefore the phase acquired by a test electron beam gets an additional shift in the phase. The most attractive feature is to realize there is actual leaking of magnetic field out of the magnetic source. This implies that this AB effect – known to be of topological nature – gets an extra contribution to the phase shift of the electron beam that it has a non-topological nature. We also showed expected constrains from an hypothetical AB experiment. Further development will appear soon in [8].

Acknowledgements

I would like to thank Andreas Ringwald for valuable comments and encouragement, and the DESY Theory Group, for their hospitality. This work has been supported by FONDECYT grant 11123403.

References

[1] S. A. Abel, M. D. Goodsell, J. Jaeckel, V. V. Khoze and A. Ringwald, JHEP **0807** (2008) 124.

[2] A. Ringwald, Phys. Dark Univ. **1** (2012) 116.

[3] D. F. Bartlett and S. Loegl, Phys. Rev. Lett. **61** (1988) 2285.

[4] Y. Aharonov and D. Bohm, Phys. Rev. **115** (1959) 485.

[5] D. G. Boulware and S. Deser, Phys. Rev. Lett. **63** (1989) 2319.

[6] K. R. Dienes, C. F. Kolda and J. March-Russell, Nucl. Phys. B **492** (1997) 104.

[7] M. Ahlers, J. Jaeckel, J. Redondo and A. Ringwald, Phys. Rev. D **78** (2008) 075005.

[8] P. A., J. Jaeckel, B. Koch, J. Redondo, *work in preparation.*

[9] M. Endo, K. Hamaguchi and G. Mishima, Phys. Rev. D **86** (2012) 095029.

[10] J. Jaeckel and S. Roy, Phys. Rev. D **82** (2010) 125020.

Theoretical Framework for the Analysis of Hidden Light Gauge Boson Searches

T. Beranek[1,2]

[1]Institut für Kernphysik, Johannes Gutenberg-Universität Mainz, D-55099 Mainz
[2]PRISMA Cluster of Excellence, Johannes Gutenberg-Universität Mainz, D-55099 Mainz

DOI: will be assigned

Various kinds of physics phenomena can be probed by electron scattering fixed target experiments. Recently, fixed target experiments investigating the reaction $e(A,Z) \to e(A,Z)l^+l^-$, where $(A,\ Z)$ denotes a nucleus of atomic number Z, were utilized to search for physics beyond the Standard Model at modest energies. In these experiments a search for a small, narrow resonance in the invariant mass spectrum of the lepton-antilepton pair, arising from the exchange of a new light gauge boson γ' coupling to the dark sector as well as very weakly to standard model particles, is performed. Such a signal would appear as an enhancement over a smooth QED background, which therefore requires a precise understanding of the background. We present a theoretical analysis of the cross sections describing this process, which are then used to extract exclusion limits on the parameter space of the γ', and compare our results to existing experimental data taken at MAMI.

1 Cross section calculations for exclusion limits

The calculation of an exclusion limit for the kinetic mixing factor ε^2, where the coupling of the γ' to charged particles is given by εe, as function of the γ' mass $m_{\gamma'}$ can be conveniently done by using Eq. (19) of Ref. [3] as approximation of the signal cross section $\Delta\sigma_{\gamma'}$, which relates $\Delta\sigma_{\gamma'}$ to the direct TL cross section $\Delta\sigma_\gamma^{\mathrm{TL}}$ given by the diagrams on the two left panels of Fig. 1. This upper bound for the kinetic mixing factor given in Ref. [3] reads

$$\varepsilon^2 = R\,\frac{\Delta\sigma_\gamma}{\Delta\sigma_\gamma^{\mathrm{TL}}}\,\frac{2\,N\,\alpha}{3\pi}\,\frac{\delta m}{m_{\gamma'}}, \tag{1}$$

where R is the exclusion limit for a possible peak found in experiment, $\Delta\sigma_\gamma/\Delta\sigma_\gamma^{\mathrm{TL}}$ is the ratio of the background cross section $\Delta\sigma_\gamma$, given by sum over all Feynman diagrams of Fig. 1, to $\Delta\sigma_\gamma^{\mathrm{TL}}$, N is a factor accounting for the effective degrees of freedom and δm is the mass resolution. Therefore the understanding of the background for these kind of experiments is essential. The precise knowledge of the ratio $\Delta\sigma_\gamma/\Delta\sigma_\gamma^{\mathrm{TL}}$ from theory is crucial to obtain an accurate exclusion limit. Furthermore, to achieve the best signal to noise ratio, one needs to analyze the kinematic structure of the individual background contributions. The signal cross section is largest when almost all energy is carried by the created lepton pair and in addition, the propagator appearing in the two SL diagrams, $(k-k'-l_+)^{-2}$, is suppressed, if the momentum is distributed nearly equally between the two leptons of the pair [5]. For beam and pair leptons of the same species,

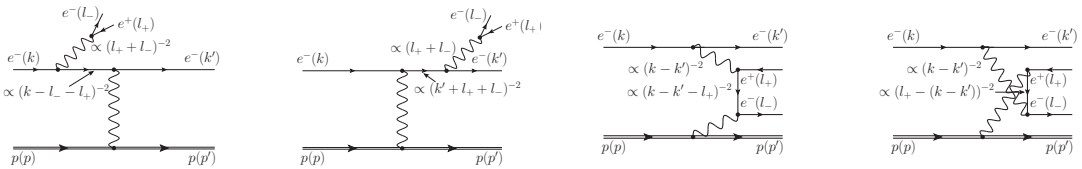

Figure 1: Direct tree level Feynman diagrams contributing to the $ep \to epl^+l^-$ amplitude. Left panels: Exchange of the timelike boson V and a spacelike γ (TL). Right panels: Spacelike boson V and a spacelike γ (SL).

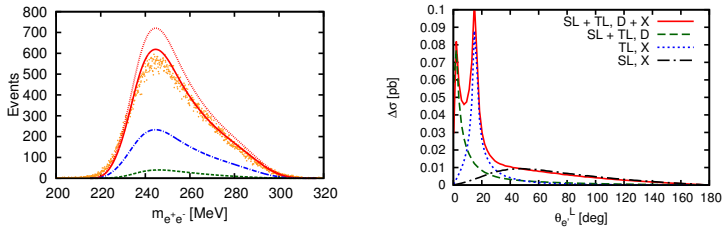

Figure 2: Left panel: Comparison of theory calculations and experimental data for a $m_{e^+e^-}$ bin width of 0.125 MeV. Right panel: Angular distributions per 0.5° with respect to the polar angle of the scattered electron for the MAMI 2010 experiment.

due to the indistinguishability, the amplitude needs to be anti-symmetrized and in addition to the discussed direct contribution the exchange term contributions need to be included in the analysis. Due to these contributions such a clean kinematical separation of signal and background is not possible anymore since the same kinematical structures which enhance the desired cross section are also contributing to the background cross section [10].

2 Comparison with data and predictions for MAMI and MESA

As seen on the left panel of Fig. 2, our calculation (solid curve) of the radiative background and the experimental data (points) [4] are in good agreement. Radiative corrections were estimated by applying those of the corresponding elastic scattering process. The influence of the radiative corrections is displayed by the solid and dotted curve in Fig. 2 which are calculated with and without radiative corrections, respectively. It is obvious from Fig. 2, that the applied radiative corrections lower the result of the theory calculation by an amount in the range of $10 - 20\,\%$. Obviously, our approximate treatment of the radiative corrections already provides a very good description, as theory and data already are in good agreement.
The dashed (dashed-dotted) curve shows the direct TL (SL + TL) cross section. It indicates, that a large contribution to the cross section results from the anti-symmetrization due to the indistinguishability of the scattered beam electron and the pair electron.

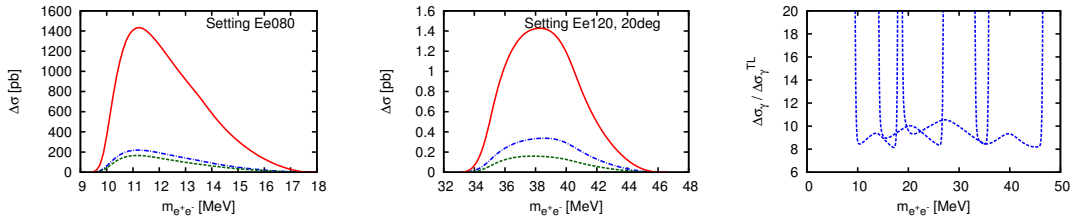

Figure 3: Left and center panel: Invariant mass distributions from the feasibility study for the MESA experiment for selected kinematic settings. Solid curve: SL+TL (direct + exchange term), dashed curve: direct TL, dashed-dotted curve: direct SL+TL. Right panel: Ratio $\Delta\sigma_\gamma/\Delta\sigma_\gamma^{\mathrm{TL}}$ of different settings for the planned MESA experiment.

The angular distribution with respect to the polar angle of the scattered electron presented on the right panel of Fig. 2 shows, that for the 2010 A1 experiment the crossed TL amplitude is responsible for a second peak in the background cross section compared to the direct amplitude (dashed curve) which only peaks at very forward scattering followed by a rapidly dropping tail. The exchange SL term nevertheless enhances the tail of the angular distribution significantly.

In 2012 a γ' search run has been started by the A1 collaboration, in which no signal was found. In this experiment 9 kinematic settings, starting from the one centered around $m_{e^+e^-} = 57\,\mathrm{MeV}$ up to one centered around $m_{e^+e^-} = 218\,\mathrm{MeV}$, are probed. For the chosen kinematical settings, which can be found in Tab. 2 of Ref. [10], we have performed the same calculations as for the 2010 setting. Due to the particular choice of kinematics in that experiment, the ratio $\Delta\sigma_\gamma/\Delta\sigma_\gamma^{\mathrm{TL}}$ has a value between $10-15$ in the probed mass range.
In Figure 4 our predictions for the exclusion limits on ε^2 for this set of kinematics are indicated by the dashed curve for an assumed integrated luminosity of around $10\,\mathrm{fb}^{-1}$.

MESA is aimed to provide a high intensity electron beam up to beam energies of about 160 MeV and thus should be ideally suited to probe the γ' parameter space at low masses. A feasibility study for carrying out this search by using two small spectrometers has been performed, assuming a Xenon target in order to obtain as large cross sections as possible [10]. The results for the obtained invariant mass distributions are shown on the right and central panel of Fig. 3. The kinematical settings we have calculated were chosen in such a way, that the full so-called $(g-2)_\mu$ welcome band is covered together with the MAMI 2012 settings, where the settings were optimized to obtain signal cross sections as large as possible while the QED background is suppressed. The projected limits from this study are shown in Fig. 4.

3 Conclusions

We have performed a detailed study of the underlying process of fixed target γ' searches. A comparison of our calculations with a sample of data taken at MAMI has been performed. We find that, after applying the leading order QED radiative corrections for the corresponding elastic electron-hadron scattering process, our calculations and the data sample are in good agreement. Using the cross sections obtained in our analysis, we are able to provide predictions for the expected exclusion limits for MAMI and MESA. Following our predictions, the exper-

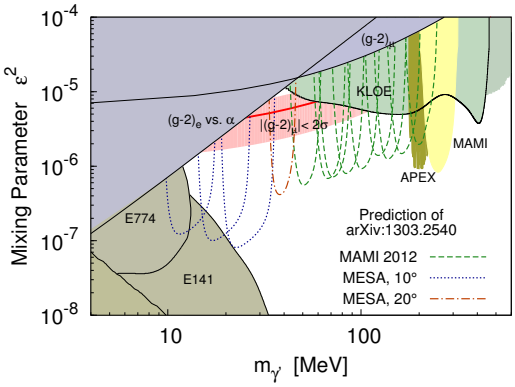

Figure 4: Compilation of existing exclusion limits and our predictions in the parameter space region currently accessible at fixed-target experiments. A detailed discussion of the different limits can be found in literature, e.g. Refs. [3, 4, 6, 10, 11]. The prediction of this work for the exclusion limit expected for the MAMI 2012 experiment is depicted by the dashed curves. The prediction for MESA is indicated by the dotted (dashed-dotted) curve for the setups with a central scattering angle of 10° (20°).

iments at MAMI and MESA will be able to probe the entire $(g-2)_\mu$ welcome band and in addition, increase the existing limits by one order of magnitude.

4 Acknowledgments

This work was supported in part by the Research Centers "Elementarkräfte und Mathematische Grundlagen" at the Johannes Gutenberg University Mainz, in part by the Deutsche Forschungsgemeinschaft DFG through the Collaborative Research Center "The Low-Energy Frontier of the Standard Model" (SFB 1044), and the federal state of Rhineland-Palatinate.

References

[1] B. Holdom, Phys. Lett. B **178**, 65 (1986).
[2] M. Pospelov, Phys. Rev. D **80**, 095002 (2009).
[3] J. D. Bjorken, R. Essig, P. Schuster and N. Toro, Phys. Rev. D **80**, 075018 (2009).
[4] H. Merkel *et al.* [A1 Collaboration], Phys. Rev. Lett. **106**, 251802 (2011).
[5] R. Essig, P. Schuster, N. Toro and B. Wojtsekhowski, JHEP **1102**, 009 (2011).
[6] S. Abrahamyan *et al.* [APEX Collaboration], Phys. Rev. Lett. **107**, 191804 (2011).
[7] The Heavy Photon Search Collaboration (HPS), `https://confluence.slac.stanford.edu/display/hpsg/`
[8] M. Freytsis, G. Ovanesyan and J. Thaler, JHEP **1001**, 111 (2010).
[9] Y. Kahn and J. Thaler, Phys. Rev. D **86**, 115012 (2012).
[10] T. Beranek, H. Merkel and M. Vanderhaeghen, Phys. Rev. D **88**, 015032 (2013), arXiv:1303.2540 [hep-ph].
[11] D. Babusci *et al.* [KLOE-2 Collaboration], arXiv:1210.3927 [hep-ex].

Dark Photon Searches at MAMI and MESA

A. Denig[1]

[1]PRISMA Cluster of Excellence, Institute of Nuclear Physics, University Mainz, Germany

DOI: http://dx.doi.org/10.3204/DDESY-PROC-2013-04/denig_achim

1 Introduction

A hypothetical dark photon, denoted here as γ', is a massive force carrier of an extra U(1) gauge group as predicted in almost all extensions of the Standard Model[1]. In string theory the mass of such a dark photon cannot be predicted and experimental searches are indeed ongoing from very small mass scales, e.g. axion-like scales, to the highest scales at the LHC. More recently, dark photons on the MeV to GeV mass scale are at the focus of interest. This is due to the fact that Arkani-Hamed et al. [1] as well as others have suggested that such a dark photon could couple to dark matter, which would also explain quite a large number of astrophysical observations, such as e.g. the positron excess in the cosmic ray flux. Furthermore, it was realized that the presently seen deviation between the Standard Model prediction and the direct measurement of the anomalous magnetic moment of the muon, $(g-2)_\mu$, on the level of 3 to 4 standard deviations [2] could also be explained by a GeV-scale dark photon. The interaction strength of the dark photon with Standard Model matter is governed by the mechanism of kinetic mixing [3]. The coupling can be subsumed by an effective coupling constant ϵ and a vertex structure of a massive photon.

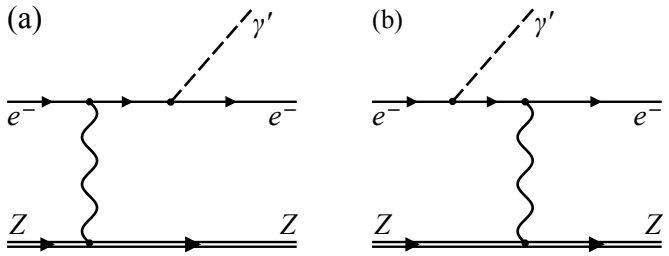

Figure 1: Electromagnetic production of the γ' boson in electron-nucleus scattering.

The above mentioned dark photon explanations of a series of astrophysical as well as particle physics puzzles have motivated searches for a GeV-scale dark photon in a world wide effort. Bjoerken and collaborators [4] have pointed out that low-energy electron accelerators for fixed-target experiments – such as the Mainz Microtron MAMI - in combination with high resolution

[1]In literature the dark photon is also denoted as A', U, or ϕ.

spectrometers – such as the A1 setup in Mainz – are indeed ideally suited for such kind of searches. The production of the dark photon appears as an initial state radiation (final state radiation) process at the vertex of the reaction, see Fig. 1. Since the coupling is small, the cross section for the electromagnetic production of the γ' boson can be enhanced by a factor Z^2 by choosing a heavy nucleus as the target. The subsequent decay of the γ' boson to a lepton pair is the signature of the reaction. Background processes are given by reactions where an ordinatory photon is radiated off the electron rather than a γ'. Also t-channel QED diagrams contribute to the background significantly. A dark photon would appear as a bump on top of the background in the electron-positron invariant mass spectrum. This requires therefore high intensity beams as well as high mass resolution to find a significant signature.

2 MAMI Searches for the Dark Photon

The Mainz Microtron MAMI [5] accelerates electrons in the energy range from 180 MeV to 1604 MeV with intensities up to 140 μA. The search for the γ' boson is carried out by the A1 collaboration with the high-resolution spectrometer setup [6]. The spectrometers feature a very high momentum resolution of approximately 10^{-4} as well as good PID capabilities and an excellent time resolution.

2.1 2010 Pilot Run

In 2010 a pilot run took place at MAMI with the primary goal to investigate up to which extent additional background sources need to be taken into account beyond QED processes. An unpolarized beam with an energy of 855 MeV was incident on a tantalum target. Luminosities in the order of $10^{39}\mathrm{cm}^{-2}\mathrm{s}^{-1}$ were achieved in this experiment. For the detection of the electron-positron pair, two high-resolution spectrometers of the A1 setup were used. The particles were detected by vertical drift chambers for tracking and scintillator detectors for trigger and timing purpose. In addition, a threshold-gas-Čerenkov detector was used in each arm to discriminate between electrons or positrons and pions. The kinematics of the reaction was such, that almost a complete energy transfer of the virtual photon on the potential dark photon was achieved. The two spectrometers were sensitive to decays in electrons and positrons with equal momenta. It was shown in Monte Carlo simulations that such a configuration suppresses background most effectively.

Apart from the well known QED channels no indications for additional background was found. From four days of data taking indeed a competitive exclusion limit could be extracted, which is shown as the yellow area in Fig.2 and which was published in Ref.[7]. The plot shows the hypothetical coupling of the γ' to Standard Model matter ϵ^2 versus its hypothetical mass $m_{\gamma'}$. Recent limits had been obtained by Babar [8] and KLOE [9][2]. Shown are also old exclusion limits from beam dump experiments at SLAC and FNAL. The grey areas are exclusion limits obtained from the $(g-2)_e$ of the electron as well as the $(g-2)_\mu$ of the muon. If one assumes that the presently seen deviation on the level of 3.6σ between the Standard Model prediction and the direct measurement is due to a missing contribution of a dark photon in the $(g-2)_\mu$ calculation, one obtains a prediction for the possible parameter range of the dark photon [11]. As can be seen, a significant progress has been achieved at A1/MAMI compared to the existing Babar exclusion limit at masses from 220 MeV to 290 MeV. The plot demonstrates impressively the

[2] In the meantime a new exclusion limit has obtained also from the WASA collaboration at COSY [10]

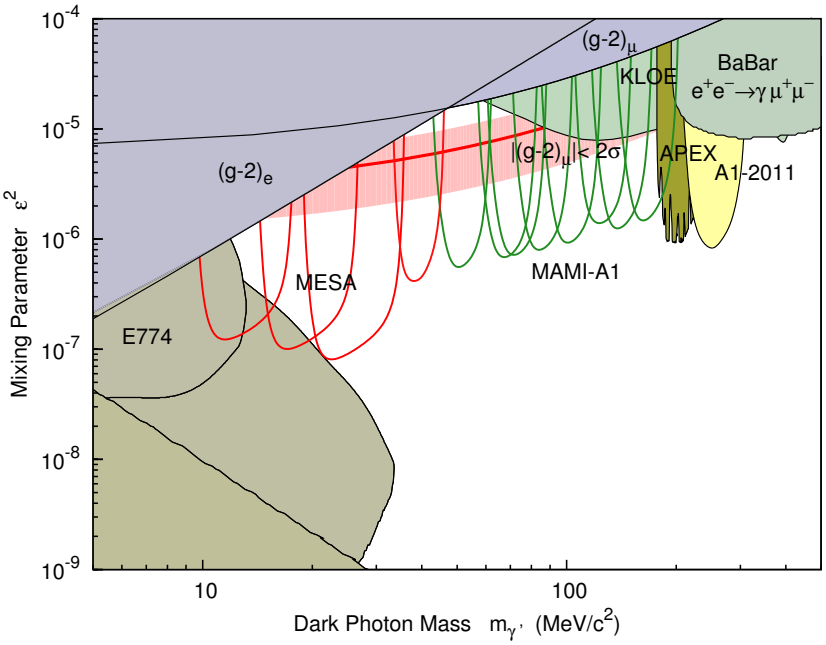

Figure 2: Existing as well as planned exclusion limits for the possible parameter space of the dark photon. Shown is the coupling of the γ' to Standard Model matter ϵ^2 versus its hypothetical mass $m_{\gamma'}$. See text for further explanations.

potential of high-intensity fixed target experiments. After the publication of Ref.[7] a correction of the published MAMI limit has been calculated in Ref.[12]. The correction is related to an issues in the theoretical treatment of the QED background, which in consequence weakens the MAMI limit. The JLab experiment APEX has published a similar exclusion limit at somewhat lower invariant masses [13].

2.2 Data Taking 2012 and 2013

In 2012 and 2013 two data taking periods took place at MAMI with in total nine invariant mass settings of the spectrometers. The analysis of data is in an advanced state. The green exclusion bands in Fig.2 show the sensitivity as expected from simulation. The mass range between approximately 50 MeV and 210 MeV can be covered in these settings with ϵ^2 values in the order 10^{-6} . This allows to test a significant part of the parameter range motivated by $(g-2)_\mu$. With respect to the pilot run the target has been changed from a single Tantalum foil to a stack of 12 strips. This allows to reduce effects of multiple scattering in the target while keeping a very high luminosity. Furthermore, while during the pilot run the beam current was limited due to a relatively high level of radiation in the experimental hall, in 2012 and 2013 the MAMI intensity was limited due to a high rate in the focal plane detectors of the spectrometers.

2.3 Displaced Vertex Technique

In near future a beam time for dark photon searches is planned which will allow to test the low ϵ^2 range around 10^{-10} for dark photon masses from 50 MeV to approximately 140 MeV. This will be possible with a dispaced vertex technique. The primary target will be heavily shielded for this experiment and the geometrical acceptance of the spectrometers will be adjusted such that only dark photons with a mean decay path of several centimeters can be detected. Such a lifetime corresponds to very low ϵ^2 values.

3 Perspectives for Dark Photon Searches at MESA

The construction of the Mainz Energy Recovering Accelerator MESA [14] offers new possibilities for dark photon searches especially at low masses. The existing MAMI accelerator is incapable of studying the mass range below 50 MeV due to the lowest possible beam energy of 180 MeV and the geometrical constraints of the spectrometers. MESA will be operated for dark photon experiments in an ERL (Energy Recovering LINAC) mode with beam intensities of up to 10 mA. The combination of an internal gas target together with the very high beam current provides high luminosities of at least $10^{34}\mathrm{cm}^{-2}\mathrm{s}^{-1}$ while minimizing the effects of multiple scattering. We have performed a feasibility study assuming a setup of high-resolution spectrometers with a similar performance as the A1 setup. Using a Xenon gas target, one achieves sensitivities as the ones shown in in red in Fig.2. Such an experiment in combination with the measurements at MAMI will finally cover the entire parameter range for the dark photon suggested by $(g-2)_\mu$.

4 Acknowledgments

The authors would like to thank the MAMI accelerator group for providing the excellent beam quality and intensity necessary for the dark photon experiment. This work was supported by the Federal State of Rhineland-Palatinate and by the Deutsche Forschungsgemeinschaft within the Collaborative Research Center 1044 *The low-energy frontier of the Standard Model.*

References

[1] N. Arkani-Hamed, D. P. Finkbeiner, T. R. Slatyer and N. Weiner, Phys. Rev. D **79** (2009) 015014.

[2] M. Davier, A. Hoecker, B. Malaescu and Z. Zhang, Eur. Phys. J. C **71** (2011) 1515 [Erratum-ibid. C **72** (2012) 1874].

[3] B. Holdom, Phys. Lett. B **166** (1986) 196.

[4] J. D. Bjorken, R. Essig, P. Schuster and N. Toro, Phys. Rev. D **80** (2009) 075018.

[5] K. H. Kaiser, K. Aulenbacher, O. Chubarov, M. Dehn, H. Euteneuer, F. Hagenbuck, R. Herr and A. Jankowiak *et al.*, Nucl. Instrum. Meth. A **593** (2008) 159.

[6] K. I. Blomqvist, W. U. Boeglin, R. Bohm, M. Distler, R. Edelhoff, J. Friedrich, R. Geiges and P. Jennewein *et al.*, Nucl. Instrum. Meth. A **403** (1998) 263.

[7] H. Merkel *et al.* [A1 Collaboration], Phys. Rev. Lett. **106** (2011) 251802.

[8] B. Aubert *et al.* [BaBar Collaboration], Phys. Rev. Lett. **103** (2009) 081803.

[9] D. Babusci *et al.* [KLOE-2 Collaboration], Phys. Lett. B **720** (2013) 111.

[10] P. Adlarson *et al.* [WASA-at-COSY Collaboration], arXiv:1304.0671 [hep-ex].

[11] M. Pospelov and A. Ritz, Phys. Lett. B **671** (2009) 391.

[12] T. Beranek, H. Merkel and M. Vanderhaeghen, arXiv:1303.2540 [hep-ph].

[13] S. Abrahamyan *et al.* [APEX Collaboration], Phys. Rev. Lett. **107** (2011) 191804.

[14] K. Aulenbacher, M. Dehn, H. -J. Kreidel, R. Heine and R. Eichhorn, ICFA Beam Dyn. Newslett. **58** (2012) 145.

Searching for the Heavy Photon at Jlab.

M. Holtrop[1]

[1]University of New Hampshire, Durham, NH, USA

DOI: http://dx.doi.org/10.3204/DESY-PROC-2013-04/holtrop_maurik

In recent years much interest has been given to new physics models which have hidden sectors with massive, extra, $U(1)$ gauge bosons, so-called heavy photons (or dark photons or A'). Such theories received a lot of attention as a possible dark matter explanation for the larger than expected numbers of cosmic-ray electrons and positrons. The Heavy Photon Search (HPS) and APEX experiments at Jefferson Lab are designed to look for these heavy photons in the mass range 20-1000 MeV that couple to electrons through kinetic mixing with couplings α'/α in the range 10^{-5} to 10^{-10}. The HPS will search for the e^+e^- or $\mu^+\mu^-$ decay of the heavy photon, possibly with a displaced vertex, using a compact forward spectrometer, while the APEX experiment will use the spectrometers of Hall-A at Jefferson lab.

1 Introduction

It is by now well established that the universe consists of approximately 26% Dark Matter (DM), and that there are no candidates for this DM in the Standard Model (SM) of particle interactions [1]. A particle based explanation for DM would thus require extensions of the SM, exhibiting hidden sectors of particles that interact only very weakly with SM particles. Such Beyond the Standard Model (BSM) theories often have additional $U(1)$ gauge symmetries with associated gauge bosons, also known as *heavy photons*, *dark photons*, or A' [2, 3, 4]. As was pointed out some time ago by Holdom [5], this new vector particle will kinematically mix with the SM photon through the interaction with massive fields. This mixing can be recast as a coupling of the A' to electric charge εe, where the expected strength of $\alpha'/\alpha = \varepsilon^2$ is in the range 10^{-5} to 10^{-10}.

Several recent theoretical models have explored the interactions of an A' with dark matter in a hidden sector[6, 7, 8, 9]. These theories favor a mass range range for the A' derived from the weak scale, in the MeV to GeV range, which could be used to explain several observed astrophysical phenomena [10, 11], including the excess of positrons observed by Pamela [12], Fermi-LAT [13] and AMS [14]. Furthermore an A' in the lower part of this mass region could account for the anomalous magnetic moment of the muon [16].

The parameters space of α'/α versus $m_{A'}$ is still only partially constrained by cosmological phenomena and experiment [4], leaving the interesting region in the MeV to GeV mass range largely unexplored. This region can be ideally accessed using high-intensity electron beams, using a high Z fixed-target and either dedicated or existing spectrometers [17]. In such an experiment the heavy photons are produced in a process similar to bremsstrahlung, where the electron looses most of its energy to a radiated A' particle, which will predominantly be

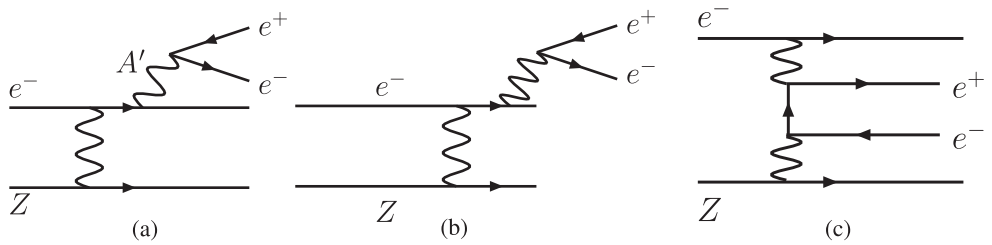

Figure 1: Left (a): Radiative A' production by an incoming electron off a target nucleus with charge Z. The A' subsequently decays to an electron-positron pair. For larger mass A', with $m_{A'} > 2m_\mu$, the decay will also go to a $\mu^+\mu^-$ pair, and for $m_{A'} > 2m_\pi$ to a $\pi^+\pi^-$ pair. Center and Right: Background due to QED trident production, (b) radiative process and (c) Bethe-Heitler process.

produced along the direction of the beam, as is illustrated in Figure 1. This A' will then decay to an e^+e^- pair (or if sufficiently, heavy a $\mu^+\mu^-$ or $\pi^+\pi^-$ pair), which will be highly boosted in the direction of the beam, necessitating detection at very small scattering angles. An experiment will thus require very high luminosity to overcome the small production cross-section, and a very forward, high rate, high resolution spectrometer to detect the produced lepton pair. The A' signal will then be searched for as a small, narrow, peak in the e^+e^- invariant mass on a smooth background. The main background to such an experiment will be QED trident production, the Bethe-Heitler and radiative production of electron-positron pairs. The radiative term of this background is indistinguishable from the main A' production process, but the dominant Bethe-Heitler background can be suppressed using kinematic selection, either in the experimental trigger, or through the spectrometer settings. This works because the radiative tridents, and hence the A' signal, are produced very forward with the electron-positron pair carrying most of the beam energy, while the recoiling electron is soft and scatters at a wide angle. In contrast, the Bethe-Heitler process favors asymmetric configurations with one energetic, forward electron or positron and the other constituent of the pair much softer. See the appendix in [17] for a more detailed explanation. Another way to suppress both backgrounds compared to the A' signal is to look for a displaced vertex for the e^+e^- pair. Since the decay length of the A' is approximately $\gamma c\tau \approx 1 \text{ mm} \left(\frac{\gamma}{10}\right) \left(10^{-8} \frac{\alpha}{\alpha'}\right) \left(\frac{100 \text{ MeV}}{m_{A'}}\right)$, for small coupling constants and moderate to small masses the decay length becomes appreciable. This allows for a cut in the data analysis on the vertex of the e^+e^- pair, reducing the prompt background significantly.

2 The APEX Experiment

The *A-Prime Experiment* (APEX) [18, 19] will search for A' particles in the mass range $50 \text{ MeV/c}^2 < m_{A'} < 550 \text{ MeV/c}^2$ with coupling strengths $\epsilon^2 = \alpha'/\alpha \gtrsim 6 \times 10^{-7}$. This experiment will use the high current continuous electron beam available at Jefferson Laboratory in combination with a special multi foil tungsten target to get to very high luminosities. The existing high resolution spectrometers (HRS) in Hall A [21] will be used to detect the e^+e^- pair. These spectrometers can detect particles down to an angle of 12°. By placing dipole sep-

tum magnets between the target and the spectrometers the particle tracks are bend outwards, making it possible to detect the electron and positron down to angles of about 4° to 5°. This experimental setup is illustrated in Fig. 2.

The Hall-A spectrometers have a momentum acceptance of about $\delta p/p \approx 9\%$ at a momentum resolution of 10^{-4}, a horizontal angular acceptance of ± 30 mrad and a vertical acceptance of ± 60 mrad [21]. This limited acceptance in angle and momentum selects a particular set of kinematics for each spectrometer setting, which can be used to effectively select the signal and radiative tridents and suppress the dominant Bethe-Heitler background.

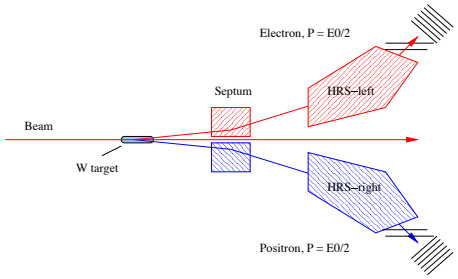

Figure 2: Schematic setup of the APEX experiment, showing the target, septum magnet, main spectrometer magnets and detector packages.

In July of 2010 the APEX experiment ran a one week test run in Hall A at Jefferson Laboratory [20], using a 2.260 ± 0.002 GeV electron beam at currents up to 150 μA on a single tantalum target foil of thickness 22 mg/cm^2. The experiment accumulated a final sample of 770,500 events, consisting almost entirely of true e^+e^- coincidences, with only a small (0.9%) contamination of mesons and 7.4% accidentals. Because the HRS spectrometers have excellent momentum resolution of O(10^{-4}), the invariant mass resolution of the experiment is dominated by the angular resolution. The three dominant contributions to this resolution are the multiple scattering in the target, the track measurement errors by the HRS detectors and the imperfect knowledge of the magnetic optics. For the full experiment, multiple thin target foils will improve the multiple scattering contribution, and a new active sieve slit will improve the measurement of the spectrometer optics.

The results of the test run and the expected full APEX sensitivity are discussed in section 4.

3 The Heavy Photon Search Experiment

The Heavy Photon Search experiment (HPS)[22, 23, 24] will search for A' particles in a mass range of 20 MeV/c^2 $< m_{A'} <$ 1000 MeV/c^2, with coupling strengths $\epsilon^2 = \alpha'/\alpha \gtrsim 10^{-5}$ to 10^{-10}. This experiment will use a new, dedicated, compact forward spectrometer in Hall B at Jefferson Laboratory. The experiment will use the continuous electron beam with energies ranging from 1.1 GeV to 6.6 GeV and currents up to 500 nA on a thin tungsten target of radiation lengths up to 0.25% X_0. An intriguing additional physics signal for the HPS experiment will be the possible discovery of *true muonium*, an $\mu^+\mu^-$ bound state that has so far eluded detection [25, 26]

The HPS experimental setup, shown in Fig. 3, uses a three magnet chicane, with the middle dipole magnet, the Hall-B pair spectrometer dipole, used as the analyzing magnet for the spectrometer. Inside this magnet a vacuum chamber is fitted with the target on a moving target ladder at the upstream edge. This vacuum chamber also houses the Silicon Vertex Tracker (SVT) [27], which consists of six measurement layers, each consisting of two pairs of silicon strip detectors. All the HPS detector elements are split into a top and bottom half with a gap in between, the "dead zone", extending a scattering angle of 15 mrad. This gap, which is only ± 1.5 mm at the location of the first sensor, allows the primary and degraded electron

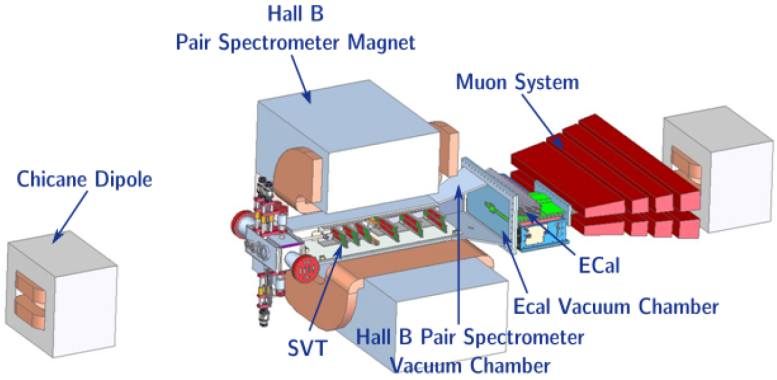

Figure 3: Engineering layout of the full HPS detector, showing the three dipole magnets of the chicane, the Silicon Vertex Tracker (SVT), the Electromagnetic Calorimeter (Ecal) and the Muon System.

beam to pass through without further interaction. The first three tracking layers are optimized for obtaining an excellent vertex determination ($\Delta z \approx 1$ mm), and are placed at 10, 20 and 30 cm from the target, with the second layer at a 100 mrad stereo angle. The next three layers of the tracker are optimized for missing mass resolution ($\delta m/m \approx 1\%$), and are placed at 50, 70 and 90 cm from the target at a 50 mrad stereo angle. The 23,004 channels of the SVT will be continuously readout at 40 MHz using the APV25 readout chip, which will read six data samples per hit, allowing for a timing resolution of ≈ 2 ns and a S/N > 25, resulting in a spacial resolution of ≈ 6 μm.

The tracking volume is followed by an Electromagnetic Calorimeter (Ecal), which is used for particle identification and for triggering the experiment. The Ecal consisting of 442 $PbWO_4$ crystals arranged in 5 layers each for the top and bottom half of the detector. In between the two halves is a vacuum box for the electron beam, which has been carefully designed to minimize interactions of the multiple scattered and degraded electron beam. Each Ecal crystal is read out by an avalanche photodiode, which is connected to a pulse shaping preamplifier whose signal is digitized by a JLab FADC250, a 250 MHz flash ADC. From there the pulse height and timing signals of the individual crystals are combined into clusters in a Field Programmable Gate Array (FPGA), and then passed on to the trigger logic. The trigger logic is also programmed into an FPGA and is capable of using the energy and location of the clusters to select between the signal and radiative events and those caused by accidental coincidences. This trigger logic reduces the trigger rate from close to 2 MHz down to a more manageable 35 kHz.

Behind the Ecal there will be a muon detector, build from alternating layers of iron absorber and plastic scintillator. The design details of this detector are still being optimized.

A simplified version of the full HPS detector was constructed and took data during a test run in May 2012. This was just before the accelerator shutdown and subsequent upgrade from 6 GeV to 12 GeV, and due to scheduling constraints there was no dedicated beam time available with an electron beam. Instead, data was taken parasitically using a photon beam incident on a thin gold converter foil serving as a target upstream of the detector. This test run successfully demonstrated the technical feasibility of the HPS detector concept and confirmed that the Monte Carlo estimates of backgrounds and trigger rates were accurate.

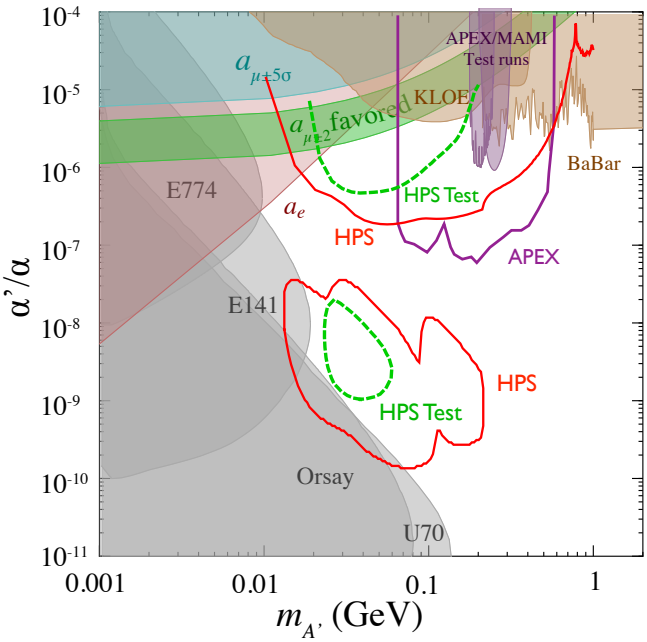

Figure 4: The estimated reach of the HPS and APEX experiments at 2σ significance along with existing constraints (see text). The HPS reach calculations assume running at 1.1 GeV and 2.2 GeV for one week each in 2014/2015, labelled "HPS Test", and running at 2.2 GeV and 6.6 GeV for three weeks each in 2016, labelled "HPS".

4 Experimental Reach

The experimental reach of the HPS and APEX experiments at 2σ significance is shown in the contours of Fig. 4, along with some existing constraints from from previous experiments. The shaded areas show excluded regions from several beam dump experiments with sensitivity for heavy photons, including E141 [28], E774 [29], Orsay [30], and U70 [31], and the reanalysis of collider experiments from BaBar [32] and KLOE [33]. The measurement of the anomalous magnetic moment of the electron [34] also sets a limit. The anomalous magnetic moment of the muon gives both an excluded region and one that would be favored by a heavy photon explanation of the deviation of $g_\mu - 2$ from the expected Standard Model value [16, 35]. The recent test run from APEX [20] and MAMI [36] are also shown as shaded regions. The solid line labelled "APEX" shows the reach for the full APEX experiment. The dashed line labelled "HPS Test" shows the reach of a two week commissioning run expected in 2014/2015, with one week of beam at 1.1 GeV and one week at 2.2 GeV, while the solid line labelled "HPS" is the reach for three weeks of running each at 2.2 GeV and 6.6 GeV, expected in 2016. The top regions are obtained from a "bump hunt" in the data, while the "island" below, at lower coupling strengths, is obtained by using a vertex cut as well. The HPS experiment has a total of 180 days of running approved, so a significant amount of data will still be taken after 2016.

5 Conclusions

Both the APEX and HPS experiments have shown their technical feasibility in recent test runs. The HPS collaboration is now upgrading their test detector, which will be installed in time for a commissioning run in 2014/2015, with additional running in 2016, and APEX is expected to run in a similar time frame. Both these experiments have excellent sensitivity for their search of a heavy photon.

6 Acknowledgments

The work presented here is that of the HPS and APEX Collaborations. The author gratefully acknowledges the support from DOE under contract no. DE-FG02-88ER40410.

7 Bibliography

References

[1] P. A. R. Ade *et al.* [Planck Collaboration], arXiv:1303.5062 [astro-ph.CO].

[2] P. Candelas, G. T. Horowitz, A. Strominger and E. Witten, Nucl. Phys. B **258**, 46 (1985).

[3] S. Andreas, M. D. Goodsell and A. Ringwald, Phys. Rev. D **87**, 025007 (2013) [arXiv:1109.2869 [hep-ph]].

[4] J. Jaeckel and A. Ringwald, Ann. Rev. Nucl. Part. Sci. **60**, 405 (2010) [arXiv:1002.0329 [hep-ph]].

[5] B. Holdom, Phys. Lett. B **166**, 196 (1986).

[6] N. Arkani-Hamed, D. P. Finkbeiner, T. R. Slatyer and N. Weiner, Phys. Rev. D **79**, 015014 (2009) [arXiv:0810.0713 [hep-ph]].

[7] M. Pospelov and A. Ritz, Phys. Lett. B **671**, 391 (2009) [arXiv:0810.1502 [hep-ph]].

[8] N. Arkani-Hamed and N. Weiner, JHEP **0812**, 104 (2008) [arXiv:0810.0714 [hep-ph]].

[9] C. Cheung, J. T. Ruderman, L. -T. Wang and I. Yavin, Phys. Rev. D **80**, 035008 (2009) [arXiv:0902.3246 [hep-ph]].

[10] R. Essig, J. Kaplan, P. Schuster and N. Toro, [arXiv:1004.0691 [hep-ph]].

[11] I. Cholis, D. P. Finkbeiner, L. Goodenough and N. Weiner, JCAP **0912**, 007 (2009) [arXiv:0810.5344 [astro-ph]].

[12] O. Adriani *et al.* [PAMELA Collaboration], Phys. Rev. Lett. **106**, 201101 (2011) [arXiv:1103.2880 [astro-ph.HE]].

[13] M. Ackermann *et al.* [Fermi LAT Collaboration], Phys. Rev. Lett. **108**, 011103 (2012) [arXiv:1109.0521 [astro-ph.HE]].

[14] M. Aguilar *et al.* [AMS Collaboration], Phys. Rev. Lett. **110**, no. 14, 141102 (2013).

[15] M. Davier, A. Hoecker, B. Malaescu and Z. Zhang, Eur. Phys. J. C **71**, 1515 (2011) [Erratum-ibid. C **72**, 1874 (2012)] [arXiv:1010.4180 [hep-ph]].

[16] M. Pospelov, Phys. Rev. D **80**, 095002 (2009) [arXiv:0811.1030 [hep-ph]].

[17] J. D. Bjorken, R. Essig, P. Schuster and N. Toro, Phys. Rev. D **80**, 075018 (2009) [arXiv:0906.0580 [hep-ph]].

[18] R. Essig, P. Schuster, N. Toro and B. Wojtsekhowski, JHEP **1102**, 009 (2011) [arXiv:1001.2557 [hep-ph]].

[19] A New Proposal to Jefferson Lab PAC35: Search for a New Vector Boson A' Decaying to e^+e^- , "http://hallaweb.jlab.org/collab/PAC/PAC35/PR-10- 009-Dark-Matter-Search.pdf".

[20] S. Abrahamyan *et al.* [APEX Collaboration], Phys. Rev. Lett. **107**, 191804 (2011) [arXiv:1108.2750 [hep-ex], arXiv:1108.2750 [hep-ex]].

[21] J. Alcorn, B. D. Anderson, K. A. Aniol, J. R. M. Annand, L. Auerbach, J. Arrington, T. Averett and F. T. Baker *et al.*, Nucl. Instrum. Meth. A **522**, 294 (2004).

[22] The HPS Collaboation, "The Heavy Photon Search Experiment at Jefferson Laboratory", Proposals, https://confluence.slac.stanford.edu/display/hpsg/HPS+Proposals

[23] P. H. Adrian, arXiv:1301.1103 [physics.ins-det].

[24] O. Moreno, arXiv:1310.2060 [physics.ins-det].

[25] S. J. Brodsky and R. F. Lebed, Phys. Rev. Lett. **102**, 213401 (2009) [arXiv:0904.2225 [hep-ph]].

[26] A. Banburski and P. Schuster, Phys. Rev. D **86**, 093007 (2012) [arXiv:1206.3961 [hep-ph]].

[27] T. K. Nelson [HPS Collaboration], PoS Vertex **2012**, 032 (2013).

[28] E. M. Riordan, M. W. Krasny, K. Lang, P. De Barbaro, A. Bodek, S. Dasu, N. Varelas and X. Wang *et al.*, Phys. Rev. Lett. **59**, 755 (1987).

[29] A. Bross, M. Crisler, S. H. Pordes, J. Volk, S. Errede and J. Wrbanek, Phys. Rev. Lett. **67**, 2942 (1991).

[30] S. Andreas, C. Niebuhr and A. Ringwald, Phys. Rev. D **86**, 095019 (2012) [arXiv:1209.6083 [hep-ph]].

[31] J. Blumlein and J. Brunner, Phys. Lett. B **701**, 155 (2011) [arXiv:1104.2747 [hep-ex]].

[32] B. Aubert *et al.* [BaBar Collaboration], Phys. Rev. Lett. **103**, 081803 (2009) [arXiv:0905.4539 [hep-ex]].

[33] D. Babusci *et al.* [KLOE-2 Collaboration], Phys. Lett. B **720**, 111 (2013) [arXiv:1210.3927 [hep-ex]].

[34] M. Endo, K. Hamaguchi and G. Mishima, Phys. Rev. D **86**, 095029 (2012) [arXiv:1209.2558 [hep-ph]].

[35] H. Davoudiasl, H. -S. Lee and W. J. Marciano, Phys. Rev. D **86**, 095009 (2012) [arXiv:1208.2973 [hep-ph]].

[36] H. Merkel *et al.* [A1 Collaboration], Phys. Rev. Lett. **106**, 251802 (2011) [arXiv:1101.4091 [nucl-ex]].

First Result of a Paraphoton Search with Intense X–ray Beams at SPring–8

T. Inada[1], *T. Namba*[2], *S. Asai*[1], *T. Kobayashi*[2],
Y. Tanaka[3], *K. Tamasaku*[3], *K. Sawada*[3], *T. Ishikawa*[3]

[1]Department of Physics, Graduate School of Science, the University of Tokyo, Japan
[2]International Center for Elementary Particle Physics, the University of Tokyo, Japan
[3]Spring-8/RIKEN Harima Institute, Kouto, Sayo-cho, Sayo-gun, Hyogo, Japan

DOI: http://dx.doi.org/10.3204/DESY-PROC-2013-04/inada_toshiaki

We present our first result of a search for paraphotons with *a light shining through a wall* (LSW) method at SPring–8. An intense synchrotron radiation from a long undulator beamline is used to search for paraphotons whose mass is in X–ray region. No excess of events above background is observed, and a stringent constraint is obtained on the photon–paraphoton mixing angle, $\chi < 8.06 \times 10^{-5}$ (95% C.L.) for $0.04\,\mathrm{eV} < m_{\gamma'} < 26\,\mathrm{keV}$. Results as well as plans for the next phase are presented.

1 Introduction

Many extensions of the Standard Model contain extra $U(1)$ symmetries [1]. If SM matter is uncharged in the additional $U(1)$ symmetry, the $U(1)$ gauge bosons are referred to as paraphotons, or hidden sector photons. Paraphotons have tiny mixing with ordinary photons through very massive particles which have both electric and hidden charge [2]. This effective mixing term induces flavor oscillations between paraphotons and ordinary photons [3]. With this oscillation mechanism, a high sensitive search can be done with a method called *a light shinning through a wall* (LSW)[4], in which incident photons oscillate into paraphotons that are able to pass through a wall and oscillate back into photons.

Recently, a detailed theoretical study of the photon and axion-like particle conversion probability has been performed[5]. Since both axion– and paraphoton–conversion are described as the same quantum oscillations, the conversion probability for axions can be interpreted as that of paraphotons by replacing parameters from $\frac{\beta\omega}{m^2}$ to χ in Eq. (29) in [5]. After propagation in vacuum for length L, the probability of converting a paraphoton into a photon (or vice versa) is given by,

$$p_{\gamma\leftrightarrow\gamma'}(L) = \left(\frac{\omega + \sqrt{\omega^2 - m_{\gamma'}^2}}{\sqrt{\omega^2 - m_{\gamma'}^2}}\chi\right)^2 \sin^2\left(\frac{L}{2}\left(\omega - \sqrt{\omega^2 - m_{\gamma'}^2}\right)\right), \tag{1}$$

where χ is the mixing angle, $m_{\gamma'}$ is the mass of the paraphoton, and ω is the energy of photon. For low mass region ($m_{\gamma'} \ll \omega$), it becomes a well-known expression of a neutrino-like oscillation; $p_{\gamma\leftrightarrow\gamma'}(L) = 4\chi^2 \sin^2(m_{\gamma'}^2 L/4\omega)$.

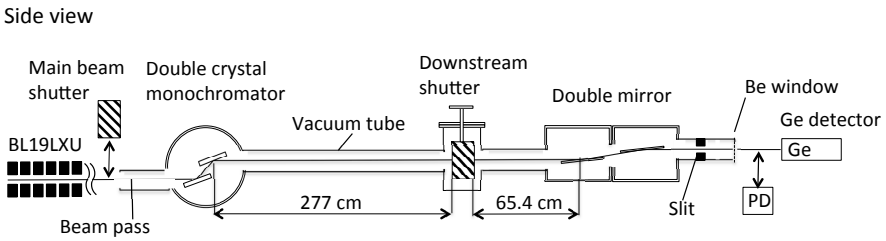

Figure 1: Schematic view of our experimental setup.

Up to now, paraphoton searches with the LSW method have mainly used optical sources [6] or microwave sources [7]. Since the accessible maximum mass of paraphoton is limited to the energy of incident photons, a higher-energy source extends the mass upper limit of LSW experiments. Furthermore, terrestrial sources in an X–ray region provide a new possibility to paraphoton searches since these experiments can be a test of parameter space probed by astrophysics only.

Here, we report a new search for paraphotons with the LSW method. We use an intense X–ray beam created by a long undulator at SPring–8 synchrotron radiation facility to search paraphotons whose mass is in the (10^{-1}–10^{4}) eV region.

2 Experimental Setup

We used BL19LXU [8] beamline at SPring–8 (Fig. 1) as X–ray source. A 30-m long undulator is placed on the electron storage ring as shown in Fig. 1. A bunch length of electrons in the storage ring is 40 ps, and a bunch interval is 23.6 ns. Structure of a X–ray beam represents the bunch structure of electrons, but we regard it as a continuous beam because time resolution of X–ray detector is larger than this structure. An energy of the X–ray beam is tunable between 7.2 and 18 keV by changing a gap width of the undulator. Higher energy of its 3rd harmonics (21.6 $\sim$ 51 keV) is also available. X–ray beam is monochromated with a Si(111) double crystal monochromator to the level of $\Delta\omega/\omega \sim 10^{-4}$. A reflection angle is determined from Bragg condition, and is typically $\sim$ 100 mrad for energies we use. A beam size is about 1 mm, and a vertical profile ($\rho(x)$) is measured with a slit with 10 μm pitch. Shape of $\rho(x)$ is similar to Gaussian whose FWHM is 383 μm.

The X–ray beam from the monochromator is guided through vacuum tubes, whose length is about 3.5 m. Tubes are evacuated better than 4×10^{-5} Pa, and a double mirror is placed at the downstream edge of the tube. These mirrors are adjusted for the total reflection, and their reflection angle is tuned at 3.0 mrad (or 2.0 mrad) during our search (only at 26 keV search). They serve as a beam-pass filter, since only X–ray beams satisfying a severe condition of total reflection are bounced up and the other off-axis background photons are blocked. The X–ray beam changes its path with these mirrors and only the reflected beam is selected with a slit, and guided to the X–ray detector.

There are two beam shutters placed in the beamline. Main Beam Shutter (MBS) is placed just before the monochromator, and DownStream Shutter (DSS) is placed between the monochromator and the mirrors. Photon changes into paraphoton in a vacuum tube between the monochromator and DSS, and then changes back inversely in the region between DSS and

beam energy ω (keV)	livetime (10^4 s)	detector resolution σ (keV)	event rate in $(\omega \pm 2\sigma)$ N (10^{-3} s^{-1})	BG subtracted rate in $(\omega \pm 2\sigma)$ ΔN (10^{-4} s^{-1})	signal upper limit ΔN_{95} (10^{-4} s^{-1})	beam flux I (10^{13} s^{-1})	detector efficiency ϵ (%)	LSW prob. upper limit P_{95} (10^{-16})
7.27	2.5	0.16	7.0 ± 0.5	-0.9 ± 5.7	11.0	7.6	23	0.63
8.00	2.0	0.16	6.5 ± 0.6	-3.8 ± 6.1	10.3	8.9	33	0.35
9.00	3.2	0.17	5.3 ± 0.4	-7.6 ± 4.5	5.5	8.3	46	0.14
15.00	1.9	0.18	4.2 ± 0.5	-3.4 ± 5.0	8.2	4.6	51	0.35
16.00	2.1	0.18	4.2 ± 0.4	-3.1 ± 4.8	7.9	3.7	56	0.38
17.00	2.5	0.18	4.2 ± 0.4	-2.1 ± 4.5	7.8	2.3	61	0.56
21.83	2.5	0.19	4.2 ± 0.4	$+4.2 \pm 4.3$	12.2	0.72	76	2.2
23.00	2.0	0.20	3.9 ± 0.4	$+1.2 \pm 4.7$	10.5	0.43	78	3.1
26.00	2.6	0.21	4.8 ± 0.4	$+7.6 \pm 4.6$	15.6	1.3	83	1.4

Table 1: Summary of 9 measurements of the paraphoton search. Errors are one standard deviation statistical errors.

the mirrors. Each length at the beam center is (277 ± 2) cm and (65.4 ± 0.5) cm, respectively.

We used a germanium detector (Canberra BE2825) to detect X–ray signal. A diameter and thickness of its crystal is 60 mm and 25 mm, respectively. Signal of Ge detector is shaped with an amplifier (ORTEC 572) and recorded by a peak hold ADC (HOSHIN C-011). Energy resolution of the detector is measured with ^{55}Fe, ^{68}Ge, ^{57}Co, and ^{241}Am sources, and typical energy resolution at 10 keV is 0.17 keV (σ: standard deviation). Absolute efficiencies of the X–ray detector (ϵ) are also measured by the same sources. Measured efficiencies are consistent with GEANT4 Monte Carlo results, which includes all attenuations in the air, carbon composite window (thickness= 600 μm) of the detector, and surface dead layer (thickness = (7.7 ± 0.9) μm) of the germanium crystal.

The detector is shielded by lead blocks whose thickness is about 50 mm except for a collimator on the beam axis whose hole diameter is 30 mm, much larger than the X–ray beam size. The position of the collimator and the germanium crystal against the beam is adjusted by using a photosensitive paper which is sensitive to the X–ray.

Absolute flux of the X–ray beam and its stability are monitored by a silicon PIN photodiode (Hamamatsu S3590-09, thickness = 300 μm). This photodiode is inserted in front of the collimator of the lead shield, and DSS is opened for the flux measurement. During this measurement, the collimator hole is closed to avoid the radiation damage to the germanium detector. The energy deposited on the PIN photodiode is calculated using its output current and the W-value of silicon (W = 3.66 eV). Fraction of the X–ray energy deposition in the PIN photodiode is computed with GEANT4 simulation for each energy. To correct the saturation effect of the PIN photodiode, thin aluminum foils are inserted before the photodiode to attenuate X–ray flux. Attenuation coefficient of aluminum is also checked by GEANT4 simulation. The flux can be measured with an accuracy of less than 5%.

3 Measurement and Analysis

A paraphoton search is performed during our beamtime from 14th to 20th June, 2012. 9 measurements are performed with different X–ray energies from 7.27 keV to 26.00 keV. Results are summarized in Tab. 1. Beam intensities (I) are monitored every 3–4 hours by the PIN photodiode as described in the previous section. Energy calibration of the detector is also performed every 3–4 hours with a ^{57}Co source.

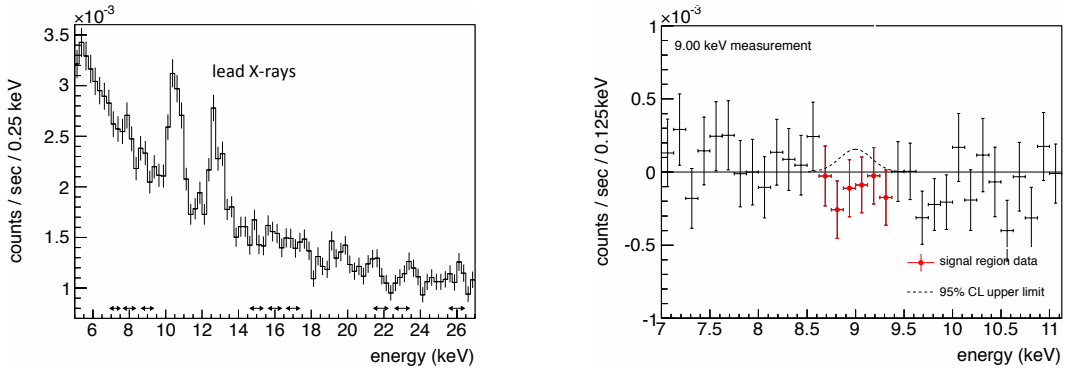

Figure 2: (left) Energy spectrum obtained with MBS closed (BG spectrum). Arrows show regions in which paraphoton searches are performed. (right) Energy spectrum measured at $\omega = 9.00$ keV. Background contributions are subtracted. Signals with statistical errors are shown in cross, and dotted line shows obtained upper limit (95% C.L.) of the signal.

BG spectrum (Fig. 2 (left)) is measured from 16th to 17th June with MBS closed. The other setup including the lead shields are completely the same as in the paraphoton searches. Total livetime of BG measurement is 1.6×10^5 s. The BG rate at 7.00 keV is $(10.9 \pm 0.3) \times 10^{-3}$ s^{-1} keV^{-1} and gradually decreases toward $(4.6 \pm 0.2) \times 10^{-3}$ s^{-1} keV^{-1} at 26.00 keV. No apparent structure is observed in the measured BG spectrum except for 10.6 keV and 12.6 keV, X–rays from the lead shields.

Signal region is defined as inside $\pm 2\sigma$ around the beam energy ω. Since signal regions are not overlapped among all measurements, the BG spectrum is commonly used for all subtractions (Fig. 2 (right)). The subtracted signal rates (ΔN) are also shown in Tab. 1, and no significant excess is observed for all 9 measurements. Using these rates, we set upper limits on signal rates of measurements. Gaussian distributions are assumed from center values and the standard deviations of ΔN, and 95% C.L. positions in the physical (i.e. positive) regions are set as a signal upper limit (ΔN_{95}). Finally, the upper limits on the LSW probability (P_{95}) are obtained by $\Delta N_{95}/\epsilon I$.

Vertical profile of the X–ray beam ($\rho(x)$) has to be taken into account in order to translate P_{95} to the limit on the mixing parameter χ, Since the incident angles of the beam into the second crystal of the monochromator and the first mirror are very shallow, $\rho(x)$ affects the lengths of the oscillation regions. As a result, these lengths are smeared by $\rho(x)$, and the LSW probability is written as,

$$P = \int_x \rho(x)\, p_{\gamma\to\gamma'}\left(L_1\left(x\right)\right)\, p_{\gamma'\to\gamma}\left(L_2\left(x\right)\right)\, \mathrm{d}x. \tag{2}$$

Here, $L_1(x)$ is the length of photon $\rightarrow$ paraphoton oscillation region modified by the vertical position, and $L_2(x)$ is that of the re-oscillation region. The integration is numerically calculated for each ω as a function of $m_{\gamma'}$, and P_{95} is translated to the limit on χ. Figure 3 shows 95% C.L. limit obtained using a data set of 9.00 keV measurement, and upper side of the line is excluded. The limit is smoothed by the smearing effect of $\rho(x)$ and becomes constant for masses from 5 eV up to around 9 keV (labeled as "(b)").

A combined result of 9 measurements rules out the limit oscillations in the region (a), and

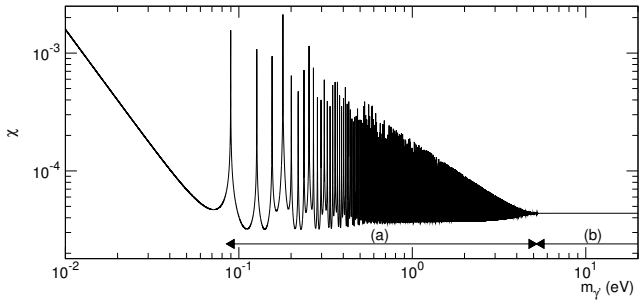

Figure 3: Upper limit (95% C.L.) on χ as a function of paraphoton mass ($m_{\gamma'}$) obtained with only one search at $\omega = 9.00$ keV. Spiky structure is due to the photon–paraphoton oscillation as shown in Formula (1). Spikes are smeared for heavier mass region (labeled as "(b)"), because of the smearing effect in Formula (2).

is shown in Fig. 4 with other results. Conservatively, the worst value around 1.39 eV represents our result (see [11] for details),

$$\chi < 8.06 \times 10^{-5} \quad (95\% \text{ C.L.}). \tag{3}$$

This result is valid for masses up to 26 keV, the maximum beam energy of our search. Our result is the most stringent for masses around eV region as a terrestrial search.

4 Summary and prospects for the next phase

We performed a paraphoton search for the first time with intense X–ray beams at SPring–8 synchrotron radiation facility. A double oscillation process, "photons oscillating into paraphotons and oscillating back into photons", is assumed, and photons passing through a wall are searched. No such photons are observed, and a new limit on the photon–paraphoton mixing angle, $\chi < 8.06 \times 10^{-5}$ (95% C.L.) is obtained for 0.04 eV $< m_{\gamma'} <$ 26 keV. The result provides the most stringent laboratory constrains on paraphotons, and extends the mass region probed with LSW methods up to X–ray region.

Based on this backgrounds obtained from the first phase, a detailed planning for the next-phase paraphoton search has already started. An intense X–ray beam from a *free electron laser* (FEL) is used instead as a pulsed X–ray source. SACLA[12] is one of such FEL facility located next to SPring-8, and started its public use since last year. It provides pulsed beams with 60 Hz and a pulse width of less than 10 fs.

A time window of the detector, which coincides with the pulsed beam is expected to reduce currently observed environmental BGs to zero. Resulting improvement of S/N is about 2 orders of magnitude compared to the first result for one week measurement. An expected limit for the phase 2 is also shown in Fig. 4.

Acknowledgements

The synchrotron radiation experiment is performed at BL19LXU in SPring–8 with the approval of RIKEN (Proposal No. 20120088). Sincere gratitude is also expressed to Dr. Suehara and

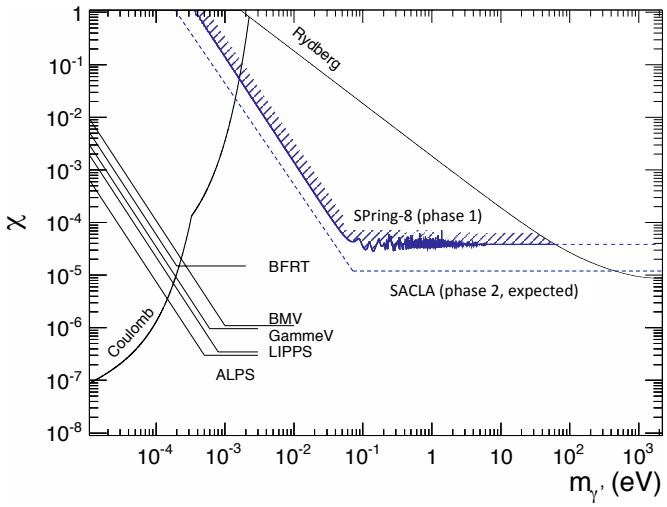

Figure 4: 95% C.L. limit on the paraphoton mixing angle obtained from our first result (SPring-8) compared with other laboratory experiments. Rydberg is a limit from the measurement of Rydberg atoms [9], Coulomb is from the Coulomb low confirmation [10], and BFRT, BMV, GammeV, LIPPS, and ALPS are from LSW experiments using optical laser [6]. An expected limit of our next phase is also shown as SACLA phase 2.

Mr. Ishida for useful discussions. Work of T. Inada is supported in part by Advanced Leading Graduate Course for Photon Science (ALPS) at U. Tokyo.

References

[1] J. Jaeckel and A. Ringwald, Ann. Rev. Nucl. Part. Sci. 60 (2010) 405.

[2] B. Holdom, Phys. Lett. B 166 (1986) 196.

[3] L. B. Okun, JETP 56 (1982) 502.

[4] K. Van Bibber *et al.*, Phys. Rev. Lett. 59 (1987) 759.

[5] S. L. Adler *et al.*, Ann. Phys. 323 (2008) 2851.

[6] BFRT Collaboration, R. Cameron *et al.*, Phys. Rev. D 47 (1993) 3707;
BMV Collaboration, M. Fouche *et al.*, Phys. Rev. D 78 (2008) 032013;
GammeV Collaboration, A. Chou *et al.*, Phys. Rev. Lett. 100 (2008) 080402;
LIPPS Collaboration, A. Afanasev *et al.*, Phys. Lett. B 679 (2009) 317;
ALPS Collaboration, K. Ehret *et al.*, Phys. Lett. B 689 (2010) 149.

[7] ADMX Collaboration, A. Wagner *et al.*, Phys. Rev. Lett. 105 (2010) 171801;
M. Betz and F. Caspers, Conf. Proc. C 1205201 (2012) 3320.

[8] M. Yabashi *et al.*, Nucl. Instrum. Meth. A 467-468 (2001) 678.

[9] R. G. Beausoleil *et al.*, Phys. Rev. A 35 (1987) 4878.

[10] E. R. Williams, J. E. Faller and H. A. Hill. Phys. Rev. Lett. 26 (1971) 721.

[11] T. Inada *et al.*, Phys. Lett. B 722 (2013) 301.

[12] T. Ishikawa *et al.*, Nat. Photonics. 6 (2012) 540.

Dark photon search and the Higgs-strahlung channel at Belle

I. Jaegle[1] *for the Belle Collaboration*

[1]Department of Physics and Astronomy, University of Hawaŕi at Manoa, 2505 Correa Road, Honolulu 96822, Hawaŕi, USA.

DOI: http://dx.doi.org/10.3204/DESY-PROC-2013-04/jaegle_igal

Preliminary individual limits of Belle are reported for the Dark Photon, A, and Dark Higgs, h' searches, for mass ranges, respectively of $0.25 < m_A < 3.5$ GeV/c^2 and $0.5 < m_{h'} < 10.5$ GeV/c^2. The Dark Photon and Dark Higgs were searched for in the Higgs-strahlung channels: $e^+e^- \to Ah'$, with $h' \to AA$ and $A \to l^+l^-$ (with $l = e$ or μ) or $A \to \pi^+\pi^-$.

1 Introduction

Dark gauge bosons are postulated to have low masses; of order MeV to GeV due to astrophysical constraints [1, 2, 3]. These astrophysical observations include: excesses in the cosmic-ray flux of electrons and/or positrons above expected background beyond normal astrophysical processes and the expected flux of protons and/or anti-protons. Dark matter could be charged under the dark $U(1)$ symmetry group and then the observed excess might correspond to dark matter annihilating into a Dark Photon A, which in turn decays into l^+l^- (with $l = e$ or μ or possibly τ if energetically allowed).

The ideal tools to discover such particles are therefore not the highest energy hadron collider experiments, but lower-energy electron-positron high-luminosity collider experiments such as Belle/BelleII and BaBar, or dedicated fixed target experiments, several of which are planned or already under construction at JLAB (Newport News, USA) or at MAMI (Mainz, Germany), for example. In Belle, work on dark gauge boson searches was started only recently, and has focused on the strategies proposed by [4, 5, 6, 7, 8]. The dark $U(1)$ symmetry group could be spontaneously broken, often by a Higgs mechanism, adding a dark Higgs h' (or dark Higgses) to these models. These proceedings will focus on the so-called Higgs-strahlung channel, where the electron-positron annihilation would produce a Dark Photon and a Dark Higgs, $e^+e^- \to Ah'$ and $h' \to AA$; and in particular the prompt decay modes with $3e^+3e^-$, $3\mu^+3\mu^-$, $2\mu^+2\mu^-e^+e^-$ and $2\pi^+2\pi^-e^+e^-$ final states; using the entire data set collected by Belle.

CLOE [9] and BaBar [10] reported their searches on the Dark Photon and the Dark Higgs (see also contribution of W. Gradl to these proceedings). CLOE focused their search on $m_{h'} < m_A$ (where A and h' are not prompt) and BaBar on $m_{h'} > 2m_A$ (where A and h' are prompt), but no signal was found.

2 Experimental setup

The Belle detector is a large-solid-angle magnetic spectrometer, which consists of a silicon vertex detector (SVD), a central drift chamber (CDC), an array of aerogel threshold Cerenkov counters (ACC), a barrel-like arrangement of time-of-flight scintillation counters (TOF), and an electromagnetic calorimeter (ECL) composed of CsI(Tl) crystals located inside a superconducting solenoid that provides a 1.5 T magnetic field. An iron flux-return (KLM) located outside the coil is optimized to detect K_L^0 mesons and to identify muons. A detailed description can be found in [11]. Belle is currently being upgraded to Belle II, an upgraded detector for operation at SuperKEKB, which will have 40 times higher luminosity than KEKB [12]. The KEKB collider [13], located in Tsukuba, Japan, is the world's highest-luminosity electron-position collider. KEKB has produced more than one ab^{-1} of data at center-of-mass energies corresponding to the $\Upsilon(1S)$ to $\Upsilon(5S)$ resonances, and in the nearby continuum.

3 Analysis strategy

Events with six charged tracks final states from $e^+e^- \to Ah' \to AAA$ are reconstructed. Energy and momentum conservation are required. The invariant mass for each combination of leptons is required to be consistent with three distinct $A \to l^+l^-$ (or $\pi^+\pi^-$). Combinations with three "equal" masses eg, (m_{ll}^1, m_{ll}^2 and m_{ll}^3) and $m_{llll} > 2m_{ll}$ are kept. The "equality" is defined as follows: $m_{ll}^{mean} - 3.\sigma(m_{ll}^{mean}) < m_{ll}^{1,2,3} < m_{mean} + 3.\sigma(m_{ll}^{mean})$, with m_{ll}^{mean} the mean mass of the three dark photon candidates and the width (σ) of the signal as function of the Dark Photon mass which is taken from Monte Carlo (MC) simulation. The detection efficiency of Belle was modeled with MC simulations based on the GEANT4 package [14]. Belle can achieve, on average, a detection efficiency of 20 % and 40 % respectively for six electrons and six muons final states and of 15 % and 30 % respectively for 4e2μ and 4π2e.

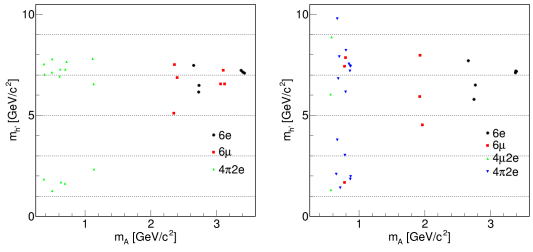

Figure 1: Dark Higgs mass as function of the Dark Photon mass. Left, background estimation. Right, events observed.

4 Results

Figure 1-right shows the preliminary results. Each event observed makes three entries in the plot Dark Higgs mass versus Darh Photon mass since there are three possible combination to form a Dark Higgs from two Dark Photons out of three Dark Photons. The events observed are consistent with the background estimation Figure 1-left. The background estimation is based on a data driven method. In this method, all combinations are combined with their wrong-sign

Table 1: Comparison between predicted Belle background, Belle number of events observed and BaBar number of events observed.

Final state	6e	6μ	$4\mu 2$e	$4\pi 2$e
Belle expected	3.60 ± 1.31	1.64 ± 1.12	0	6.81 ± 3.64
Belle observed	2	2	1	5
BaBar observed	0	0	0	2

partner, eg $(l^-l^-)(l^+l^+)(l^+l^+)$, are kept. Table 1 summarizes the results. Contribution of $\rho \to \pi^+\pi^-$ or $\omega \to \pi^+\pi^-$ decays for $0.7 < m_A < 0.9$ GeV/c^2 is observed;produced most likely by two photon processes.

5 Preliminary individual upper limits

A statistical method based on Bayesian inference with the use of Markov Chain Monte Carlo [16] is used to then calculate preliminary upper limits, 90% Confidence Level (CL), for the full luminosity. Figure 2 (left to right - six electron, right six muons, $4\mu 2e$ and $4\pi 2e$ final states) shows the preliminary individual upper limits for different Dark Higgs mass hypotheses compared to the BaBar upper limits[10]. The preliminary individual upper limits scale nearly linearly with the integrated luminosity as one would expect in presence of almost no background.

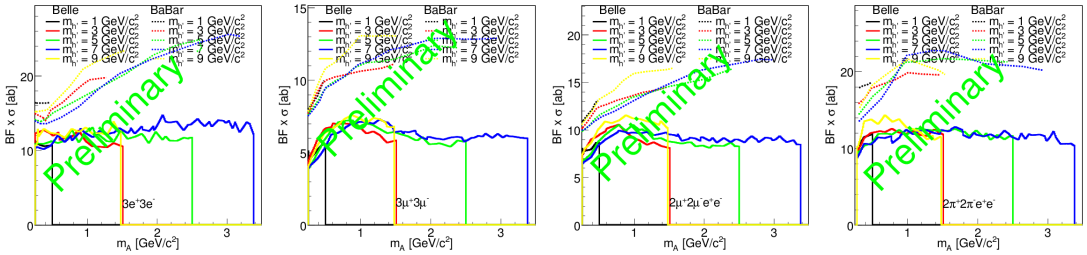

Figure 2: Preliminary individual limits as a function of the Dark Photon mass for different Dark Higgs mass hypotheses. From left to right: $6e$, 6μ, $2\mu^+2\mu^-e^+e^-$ and $2\pi^+2\pi^-e^+e^-$ final states. Full line this Belle analysis. Dashed line BaBar upper limit[10].

6 Conclusions

The Dark Photon and the Dark Higgs are searched for in the mass ranges: $0.25 < m_A < 3.5$ GeV/c^2 and $0.5 < m_{h'} < 10.5$ GeV/c^2. No signal was observed. It was found that the background is small and is consistent with the background estimation. The preliminary individual limits of Belle have been shown. The individual limit scales nearly linearly with the integrated luminosity. In the coming years, Belle2 will take 40 times more statistics. Altough the instantaneous luminosity will be much smaller than for the fixed target experiment instantaneous luminosity, Belle2 can cross-check with no extra cost any fixed target results avobe 20 MeV/c^2 and can extract limit up to 10.5 GeV/c^2.

Acknowledgements

The authors would like to thank the organizers of the 9th PATRAS Workshop on Axions, Wimps, and WISPs for their kind invitation and hospitality and congratulate them for a successful workshop. We acknowledge support from the U.S. Department of Energy under Award Number DE-SC0007852.

7 Bibliography

References

[1] O. Adriani *et al.* [PAMELA Collaboration] Nature **458**, 607-609 (2009).

[2] M. Ackermann *et al.* [Fermi LAT. Collaboration] Phys. Rev. D **82** 092004 (2010).

[3] M. Aguilar *et al.* [AMS Collaboration] Phys. Rev. Lett. **110** 141102 (2013).

[4] M. Reece and L. T. Wang JHEP **0907** 051 (2009).

[5] R. Essig, P. Schuster, and N. Toro arXiv:0903.3941 (2009).

[6] B. Batell, M. Pospelov, and A. Ritz arXiv:0903.0363 (2009).

[7] F. Bossi, arXiv:0904.3815 (2009).

[8] P.-f. Yin, J. Liu, and S.-h. Zhu arXiv:0904.4644 (2009).

[9] Simona Giovannella [CLOE Collaboration] J. Phys. Conf. Ser. **335** 012067 (2011).

[10] J. P. Lees *et al.* [BaBar Collaboration] Phys. Rev. Lett. **108** 211801 (2012).

[11] A. Abashian *et al.* [Belle Collaboration] Nucl. Instrum. Methods Phys. Res. Sect. A **479** 117 (2002).

[12] K. Abe *et al.* [Belle II Collaboration] Belle II Technical Design Report, KEK Report 2010-1, arXiv:1011.0352v1 (2010).

[13] S. Kurokawa *et al.* Nucl. Intr. and Meth. A **499** 1 (2003).

[14] R. Brun *et al.* [GEANT] Cern/DD/ee/84-1 (1986).

[15] R. Essig *et al.* arXiv:1008.0636v1 (2010).

[16] A. Caldwell *et al.* CPC **180** 2197-2209 (2009).

Status of the CASCADE Microwave Cavity Experiment

M. Kalliokoski[1,2], *I. Bailey*[1,2], *P. Williams*[2,3], *N. Woollett*[1,2], *G. Burt*[2,4], *S. Chattopadhay*[2,5,6], *J. Dainton*[2,5], *A. Dexter*[2,4], *P. Goudket*[3], *S. Pattalwar*[3], *T. Thakker*[3]

[1]Department of Physics, Lancaster University, Lancaster, United Kingdom
[2]The Cockcroft Institute, Sci-Tech Daresbury, Warrington, United Kingdom
[3]STFC Daresbury, Sci-Tech Daresbury, Warrington, United Kingdom
[4]Department of Engineering, Lancaster University, Lancaster, United Kingdom
[5]Department of Physics, University of Liverpool, Liverpool, United Kingdom
[6]School of Physics and Astronomy, University of Manchester, Manchester, United Kingdom

DOI: http://dx.doi.org/10.3204/DESY-PROC-2013-04/kalliokoski_matti

The CASCADE experiment is a "light shining through a wall" (LSW) experiment consisting of microwave cavities. It is dedicated to search for photon oscillations into hidden sector photons (HSP). The main measurement setup consists of two normal conducting TM_{010} pillbox cavities at 1.3 GHz. In this paper we present the planned measurement campaign that is divided in four main phases.

1 Introduction

The CASCADE (CAvity Search for Coupling of A Dark sEctor) experiment utilizes microwave cavity technology to search for the new particle interactions. The method that is used is a "light shining through a wall" (LSW), where the detector cavity will be isolated from the emitting cavity and from external RF sources. Since the cavities are identical and tuned to same resonance frequency, the possible signal in the detector cavity could be identified to be originating from photon-HSP-photon oscillations.

2 Measurement Setup

The main parts of the measurement setup are the two pillbox cavities that are used to study the photon HSP oscillations. The cavities are normal conducting copper cavities that are powered in the first transverse magnetic mode (TM_{010}) at 1.3 GHz. With the cavities, the complexity of the measurement setup can be increased in stages with the main goal to replace the measurement setup with two superconducting cavities [1].

A schematic of a CASCADE cavity can be seen in Fig. 1. The cavities were designed using CST Microwave Studio. With the program it was estimated that the cavities can have Q-values of up to 22 000 at the room temperature. The cavities are tunable in the range of 100 MHz and have a bandwidth of 330 kHz.

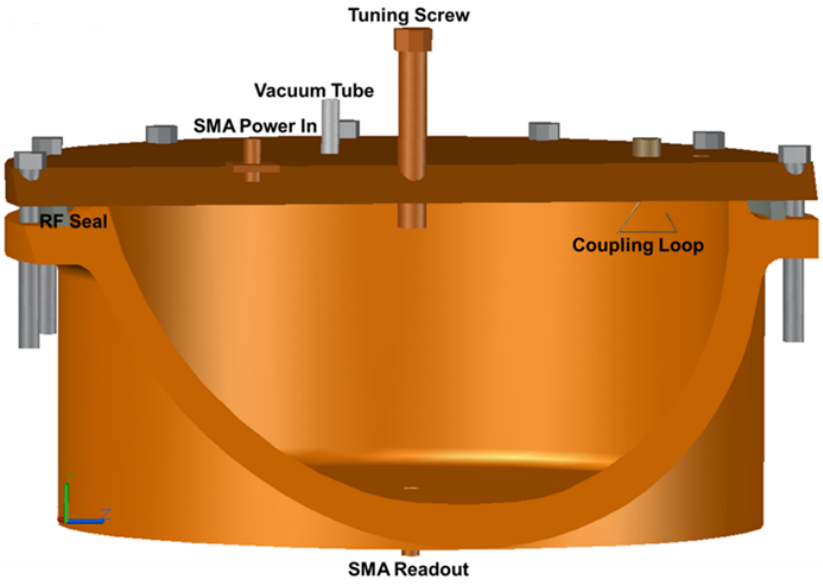

Figure 1: CAD model of the CASCADE pillbox cavity.

The measurement setup is adapted from [2]. A schematic of the setup can be seen in Fig. 2. It consists of a signal generator and a signal analyzer which are frequency locked by 10 MHz reference. The signal generator can produce input power of up to 10 mW which is fed into the source cavity. Both the detector and the source cavities are placed inside a RF shielding box. The required attenuating shielding between the cavities is at least 220 dB. With this shielding, measurements of signal powers of the order of 10^{-25} W can be performed.

The signal analyzer will perform the fast Fourier transformation and the data taking. In the early measurements it was discovered that the signal analyzer produces an internal 1.3 GHz signal which has signal power of the order of -140 dBm. Because of this, the exact 1.3 GHz frequency cannot be used in the measurements, so the cavities were tuned slightly off from this frequency. Test measurements showed that the signal analyzer was already able to make a clear isolation between the peaks, when the off-tuning was only 1 Hz. Since the internal signal has been measured to be stable and almost constant in signal power, it is used as a reference in the measurements.

3 Measurements

The measurements will be divided in four stages, each introducing more sensitivity and complexity to the overall setup. The division in stages is done to better understand the requirements and effects of new elements in the setup.

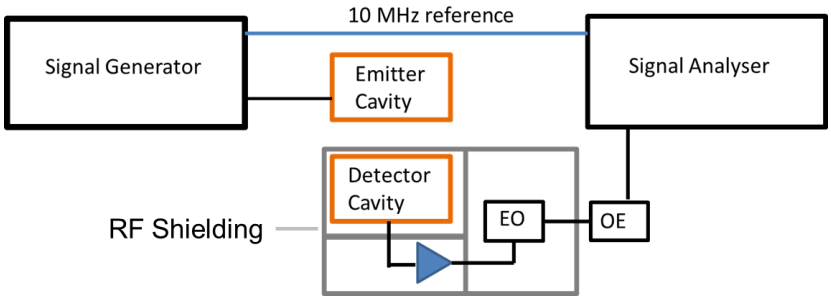

Figure 2: Schema of the measurement setup. The amount of shielding around the detector cavity will be increased according to the requirements of the measurements. Also the optical conversions will not be used in the first measurements but will be developed and implemented when required.

3.1 Stage 1

The first stage of measurements will be at room temperature. In this stage, the cavities are first isolated with a minimal shielding which is then increased gradually. The main focus in this stage is to study the shielding requirements between the cavities. Excluding the components that provide additional shielding such as cryostats, new layers of shielding will not be added in later stages. To monitor the shielding quality, a set of patch antennas will be placed inside the shielding structures to monitor the attenuating power and to locate the possible RF leaks. Since the emitter and the detector cavity will be in room temperature, this stage also allows the studies of effects of varying the distance and positioning of the cavities.

3.2 Stage 2

To increase the overall Q-value of the system, the detector cavity will be placed inside a liquid nitrogen cryostat. This will increase the detecting sensitivity of the of the cavity since the thermal noise is reduced. The flask where the cavity is placed can hold the 77 K temperature for several weeks and allows long duration measurements to be performed.

3.3 Stage 3

The third stage can be seen as an intermediate stage between using plain normal conducting cavities and using superconductive cavities as part of the setup. In this stage, both pillbox cavities will be placed inside the liquid nitrogen cryostat. Since the shielding between the cavities was already optimized in the first stage and since the input power is not increased, the setup will improve the combined Q value of the system. Although there will be some improvements in the overall sensitivity, the detection probability will not improve significantly since there is no changes in the detector cavity. The main goal in this stage is to study the stability and performance of the two cavity system before it is used as combined detector in the next stage.

3.4 Stage 4

In the fourth stage the two pillbox cavity setup will be used as a single detector for superconducting emitter. At the Daresbury Laboratories, a single cell 1.3 GHz superconducting niobium cavities were developed as part of the STFC Industrial Programme Support Scheme [3]. These cavities are operated in $TM_0 10$ mode and can reach Q values of 10^{10}. They also allow input powers over 100 W. By combining the two pillbox cavities as detector for the superconducting emitter, unprecedented regions can be charted in the exclusion plot. Figure 3 shows the expected reach of each planned measurement stage of the CASCADE measurement campaign.

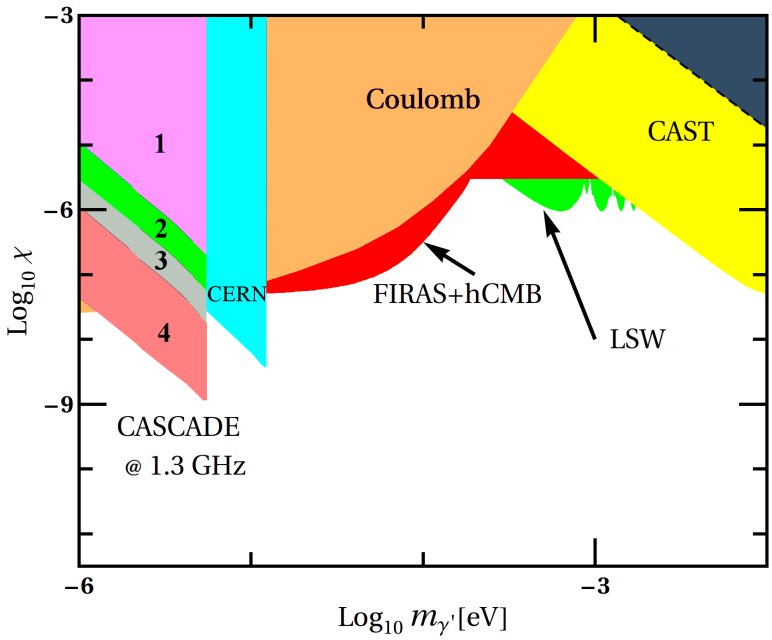

Figure 3: Expected reach of the four measurement stages.

Acknowledgments

The authors would like to thank F. Caspers and M. Betz for discussions and suggestions.

References

[1] P. Williams, "Superconducting RF Cavity Search for a Hidden Sector Photon," In Proc. 6th Patras Workshop, DESY-PROC-2010-03, p.37-40 (2010) [DOI: 10.3204/DESY-PROC-2010-03/williams_peter].

[2] F. Caspers *et al.*, CERN-BE-Note-2009-026.

[3] A.E. Wheelhouse *et al.*, Proc. SRF2011, TUPO038, pp.464 (2011).

Search for Hidden Photons using Microwave Cavities

A. T. Malagon[1], *O. K. Baker*[1], *J. L. Hirshfield*[1], *Y. Jiang*[1], *G. Kazakevitch*[2], *S. Kazakov*[1], *M. A. LaPointe*[1], *A. J. Martin*[1], *S. Shchelkunov*[1], *P. L. Slocum*[1], *A. E. Szymkowiak*[1,3]
[1]Physics Department, Yale University, PO Box 208120, New Haven CT USA 06520
[2]Muons Inc., 552 N. Batavia Avenue, Batavia, IL 60510
[3]Astronomy Department, Yale University, PO Box 208101, New Haven CT 06520

DOI: http://dx.doi.org/10.3204/DESY-PROC-2013-04/malagon_ana

The Yale Microwave Cavity Experiment (YMCE) uses microwave cavities in a "light shining through wall" (LSW) approach to look for hidden photons, hypothesized particles that could exist in many beyond the standard model theories. By cooling one cavity and reducing the bandwidth of our receiver, we increase the sensitivity of our experiment and report first results, excluding hidden photons with a mass of 141.8 μeV for a coupling $\chi > 1.7 \times 10^{-7}$.

1 Introduction

The structure of the Standard Model is SU(3) × SU(2) × U(1); one natural question to ask is, do other symmetries exist? If one adds a local U(1) gauge symmetry then a new gauge boson appears with a wide range of possible couplings and mass (see [1] for a recent review). In the low mass limit, the dominant interaction of the new gauge boson is with the photon via kinetic mixing [2]. This gauge boson, or hidden photon, must have extremely weak couplings in order to have evaded detection. Astrophysical considerations of solar energy loss place strong constraints on possible hidden photon coupling and mass [3, 4]; however, these constraints become weaker in the 1-100 μeV range. Direct searches for hidden photons using the LSW technique nicely complement astrophysical bounds and probe new regions for physics beyond the Standard Model.

The principle behind the LSW method is that a laser shining on a wall will produce photons and via kinetic mixing, hidden photons. The wall will stop the ordinary photons but the hidden photons will pass through unimpeded because they interact very weakly with matter. On the other side of the wall, they can convert to ordinary photons again and be detected. The LSW technique extended to microwaves allows one to probe longer wavelengths and thus smaller masses for the hidden photon, precisely where astrophysical constraints are weakest. Placing resonant cavities on either side of the wall enhances the sensitivity by several orders of magnitude [6] and is the technique used by our group. In this paper we discuss our setup and first results searching for hidden photons at a higher microwave frequency than so far attempted elsewhere.

2 Sensitivity

The experiment consists of a high power microwave source driving a cavity on resonance and a second cavity, electromagnetically shielded from the first, used to look for a power excess at the frequency ω_0 of the microwave source. The expression for the power expected in the second cavity due to photon - hidden photon oscillations is given by [8]:

$$P_{det} = \chi^4 (\frac{m_{\gamma'}}{\omega_0})^8 |G|^2 Q_{drive} Q_{det} P_{drive}$$

where Q_{drive} and Q_{det} are the loaded quality factors of the drive and detection cavities, respectively, P_{drive} is the power of the microwave source, χ is the hidden photon - photon coupling, and $m_{\gamma'}$ is the unknown mass of the hidden photon. $|G|$ is a geometrical form factor that depends on the cavity modes, their separation, and the hidden photon momentum. We use natural units, where $\hbar = c = \epsilon_0 = 1$. Note that the expected power excess P_{det} should appear at one frequency: ω_0. However RF power leaking from the original microwave source will also appear at that frequency, so shielding the detection cavity (and all subsequent electronics) from the microwave source is extremely important to prevent a spurious signal. In order to reduce the background, which is a combination of electronic noise from our amplifiers and thermal noise in the cavity, we cool the detection cavity and our first stage amplifiers to 5 K using liquid helium and use a narrow resolution bandwidth of 6.7 mHz.

3 Experimental Setup

The experiment uses two cylindrical copper cavities resonant at 34.29 GHz in the TE_{011} mode. This mode has a high quality factor, is easily tunable, and has a high geometry factor. The power source used is an Anritsu MG3694C signal generator capable of putting out 22 dBm at our operating frequency. During runs, a spectrum analyzer monitors the reflected power from the driven cavity to ensure the cavity resonance is stable. The detection cavity and cryogenic amplifiers are placed in a cryostat with two waveguide lines; see Figure 1. One waveguide goes to a weakly coupled port on the detection cavity and is used with a network analyzer to determine the resonant frequency, while the second waveguide takes the signal from the strongly coupled port of the cavity and high electron mobility transistor (HEMT) amplifiers [9]. The cavity is tuned to the frequency of the drive cavity by vertically adjusting the top cap, with a slight gap between the cap and the cavity walls to break the degeneracy between the TE_{011} and TM_{111} modes. The waveguides transmit power to a shielded room housing the receiver chain and data acquisition system. The receiver chain is a triple heterodyne mixing scheme [10] that amplifies, filters, and mixes the RF signal down to baseband, where the data is then split into its in-phase (I) and quadrature (Q) components and digitized for further analysis.

The oscillators in the receiver chain, the microwave source, and the digitizer are all frequency locked to a 10 MHz reference - this frequency locking is important to prevent the down mixed signal from smearing out over time from a relative frequency drift of the oscillators and thus degrading the sensitivity of the narrow band measurement. It is also important to know the gain of our system accurately in order to correctly calculate P_{det}; by doing a Y-factor measurement we determined the effective noise temperature of the system to be $T_{\rm noise} = 15 \pm 5$ K and, together with the power levels we observe at the output of the receiver chain inferred the nominal gain to be 86.1 ± 0.5 dB. Shown below in Figure 1 is a schematic of the setup, and Table 1 summarizes the experimental parameters.

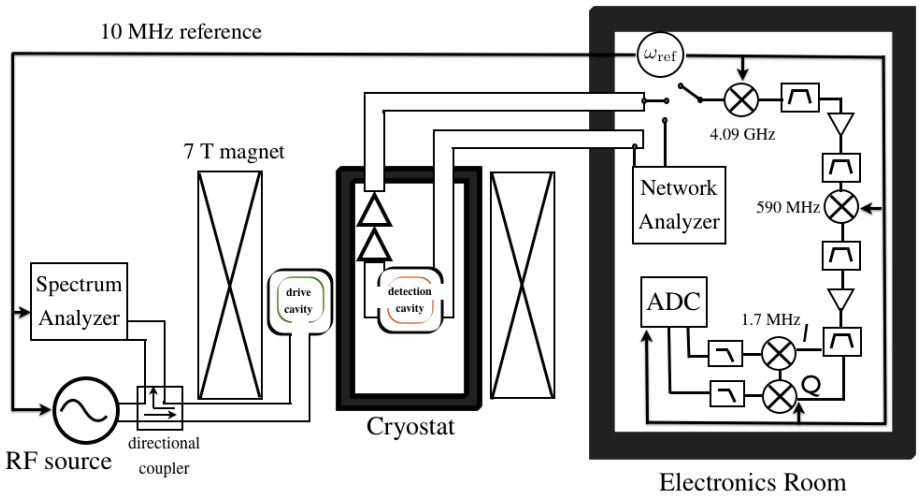

Figure 1: Schematic of the experimental set-up. The intermediate frequency at every stage of the receiver chain is shown, along with the amplifiers and filters.

Table 1: Experimental parameters for May 01 run

Q_{det}	Q_{drive}	ω_0	$\lvert G\rvert$	P_{drive}	$T_{\rm noise}$	Bandwidth	Gain
9000	7000	$2\pi \times 34.29$ GHz	0.1	22 dBm	15 K	6.7 mHz	86.1 dB

Although not needed for this experiment, both the drive and detection cavities are inside the bore of a 7 Tesla superconducting magnet. We will use this magnet later on for a search for primordial axion-like particles [11].

The detection cavity and electronics are each electromagnetically shielded, but even minute levels of RF power leaking into any stage in the setup could cause a fake signal. To reduce this leakage, we covered all waveguide joints and vacuum ports with copper tape, wrapped microwave absorbing foam over the entrance of the 10 MHz cable to the electronics room, powered all the electronics in the shielded room from batteries, and surrounded the drive cavity with aluminum wool. As well, we placed the power supplies for the cryogenic amplifiers behind a wall to shield exposed wiring and reconfigured the grounds of the supplies.

4 First Results

On May 01, 2013, we recorded a two and a half minute trace with no statistically significant excess seen at ω_0, as shown in Figure 3. For comparison, Figure 2 shows a run taken with a visible leak, later attenuated by reconfiguring the grounds of the cryogenic amplifiers. From this data we exclude a hidden photon - photon coupling of $\chi > 1.7 \times 10^{-7}$ for $m_{\gamma'} = 141.8$ μeV. Figure 4 shows the limits of our experiment along with the present best limits set by astrophysical bounds and LSW experiments.

This result is not yet competitive with the bounds placed by astrophysical limits and ana-

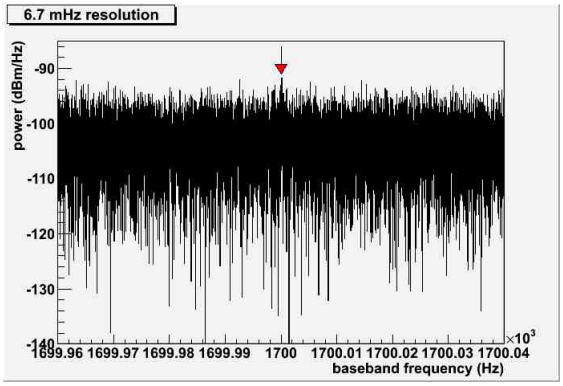

Figure 2: Power related to the signal source can be seen at ω_0. This leak was reduced by reconfiguring the grounds of the cryogenic amplifiers.

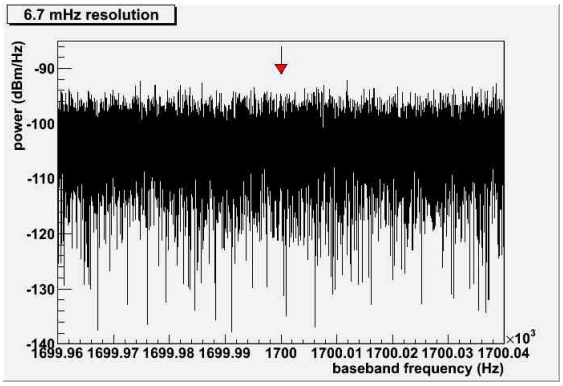

Figure 3: No power is seen at the frequency of the signal source after reconfiguring the grounds of the cryogenic amplifiers.

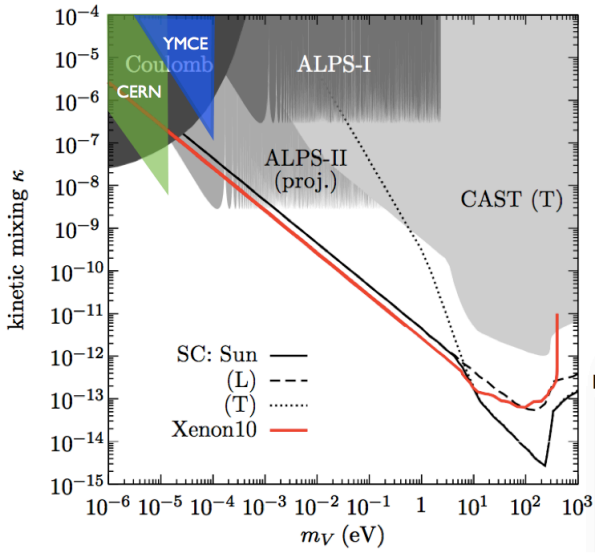

Figure 4: Updated from [13]. The filled in region labeled YMCE denotes the exclusion set by our experiment. This result and the limit from the CERN experiment (Ref. [7]) are the first microwave cavity LSW experiments to surpass the Coulomb limit; the region labeled ALPS-II [5] is the projected sensitivity of future optical LSW experiments.

lyzing XENON10 data [12]; however, in our first run to demonstrate the operation of the experiment, we have placed limits comparable in sensitivity to the first ALPS-I exclusion bound with only a modest amount of data.

5 Outlook

Much work up until this point has gone into calibrating our system, which was non-trivial due to the cryogenic setup, and understanding the various paths for RF leakage. Now that we have established the exact gain of the system and improved the shielding, the exclusion limit reported here can be improved by longer integration times and a more powerful microwave source. We also plan to do a measurement with a microwave cavity operating in the TM_{020} mode; with the strong magnetic field, this cavity will be sensitive to axion-like particles if they form part of the galactic dark matter. Finally, we can use this measurement to simultaneously place constraints on hidden photon dark matter [14, 15].

Acknowledgments

The authors gratefully acknowledge support from Yale University in funding this work and thank K. Zilm for the loan of required equipment.

References

[1] J. Jaeckel, Frascati Phys. Ser. **56**, p. 172-192 (2013) [arXiv:1303.1821].

[2] B. Holdom, Phys. Lett. **B166**, 196 (1986).

[3] H. An, M. Pospelov, and J. Pradler, Phys. Lett. **725** (2013), [arXiv:1302:3884].

[4] J. Redondo, G. Raffelt, JCAP **1308** 034 (2013), [arXiv:1305.2920].

[5] K. Ehret *et al.*, Phys. Lett. **B689**, 149 (2010), [arXiv:1004.1313].

[6] F. Hoogeveen and T. Ziegenhagen, Nucl. Phys. **B358**, 3 (1991).

[7] M. Betz and F. Caspers, Conf.Proc. **C1205201**, 3320 (2012), [arXiv:1207.3275].

[8] J. Jaeckel and A. Ringwald, Phys. Lett. **B659**, 509 (2008), [arXiv:0707.2063].

[9] S. Weinreb, M. W. Pospieszalski, R. Norrod, Proc. IEEE MIT-S International Microwave Symp. (1988), 945

[10] P. L. Slocum *et al.*, (2013) [arXiv:1301.6184]

[11] P. Sikivie, Phys. Rev. Lett. **51**, 1415 (1983).

[12] H. An, M. Pospelov, and J. Pradler, Phys. Rev. Lett. **111**, 041302 (2013), [arXiv:1304.3461]

[13] J. Pradler, talk at Patras 2013 meeting, Mainz, Germany; June 2013.

[14] A. E. Nelson and J. Scholtz, Phys. Rev. **D84**, 103501 (2011), [arXiv:1105.2812].

[15] P. Arias *et al.*, JCAP **1206**, 013 (2012), [arXiv:1201.5902].

Hidden sector photon cavity coupling

S. Parker[1], *G. Rybka*[2] *and M. Tobar*[1]

[1]School of Physics, The University of Western Australia, Perth, Australia
[2]University of Washington, Seattle, USA

DOI: http://dx.doi.org/10.3204/DESY-PROC-2013-04/parker_stephen

Light shining through a wall microwave cavity experiments have traditionally searched for paraphotons via the transmission of power from an actively driven cavity to a passive receiver cavity, with the two cavities separated by a barrier that is impenetrable to photons. We have extended this measurement technique to account for two-way coupling between the cavities. The presence of a paraphoton field can alter the resonance frequencies of the coupled cavity pair and as such measurements of cavity resonance frequencies can be used to constrain the paraphoton kinetic mixing parameter, χ.

1 Introduction

Laboratory based searches for paraphotons have been conducted for several years with some recent tests using microwave frequency resonant cavities [1, 2]. Electromagnetic resonances in otherwise isolated cavities could become coupled in the presence of a paraphoton field. If one resonant cavity is actively driven, this coupling can be seen as photons in the driven cavity mixing with paraphotons, which then cross the boundary between cavities, and then mixing back into photons in the undriven cavity. Resonant regeneration is present even at the subphoton level, and by measuring the power transmitted between the two cavities a bound can be placed on the probability of kinetic mixing between photons and paraphotons. This arrangement is known as a Light Shining through a Wall (LSW) experiment and has been the focus of microwave frequency resonant cavity paraphoton searches [1, 2]. As these searches rely on measuring very low levels of microwave power the fundamental limitation to their sensitivity is imposed by the thermal noise in the detector cavity and amplification system. However, in practice they have been limited by microwave power leakage from the emitter to detector cavity which is indistinguishable from a paraphoton effect [1].

Previous LSW formalism [3] has been focused on the one way flow of paraphotons from a driven emitter cavity to an undriven detection cavity. However, it is also possible to treat the two-way exchange of paraphotons as a weak coupling between the cavities, creating a system analogous to two spring-mass oscillators connected via a third weak spring. When both cavities are actively driven the paraphoton mediated coupling will cause a phase-dependent shift in the resonant frequencies and quality factors of the system. This opens up the possibility of conducting experiments that constrain the strength of photon-paraphoton mixing by observing this coupling induced resonant frequency shift. When given the option it is preferable to make a measurement of frequency rather than power due to the quality and precision of frequency standards, instrumentation and techniques.

Although we focus on the paraphoton, these concepts can be extended and applied to LSW based searches for other hypothetical particles that mix with the photon such as fermionic minicharged particles.

2 Fundamental modes

Following the notation of Jaeckel & Ringwald [3] the renormalizable Lagrangian for low energy photons and paraphotons is given by

$$\mathcal{L} = -\frac{1}{4}F^{\mu\nu}F_{\mu\nu} - \frac{1}{4}B^{\mu\nu}B_{\mu\nu} - \frac{1}{2}\chi F^{\mu\nu}B_{\mu\nu} + \frac{1}{2}m_{\gamma\prime}^2 B_\mu B_\mu, \tag{1}$$

where $F^{\mu\nu}$ is the field strength tensor for the photon field A^μ, $B^{\nu\mu}$ is the field strength tensor for the paraphoton field B^μ, χ is the photon-paraphoton kinetic mixing parameter and $m_{\gamma\prime}$ is the paraphoton mass. From Eq. (1) the equations of motion for the electromagnetic fields in two spatially separated resonant cavities, A_1 and A_2, and the universal paraphoton field B are

$$\left(\partial^\mu\partial_\nu + \chi^2 m_{\gamma\prime}^2\right) A_1 = \chi m_{\gamma\prime}^2 B \tag{2}$$

$$\left(\partial^\mu\partial_\nu + m_{\gamma\prime}^2\right) B = \chi m_{\gamma\prime}^2 \left(A_1 + A_2\right). \tag{3}$$

Due to the infinite nature of the paraphoton field we use the retarded massive Greens function to find the paraphoton field from equation (3),

$$B\left(\mathbf{x},t\right) = \chi m_{\gamma\prime}^2 \left(\int\limits_{V1} d^3\mathbf{y} \frac{\exp\left(ik_b|\mathbf{x}-\mathbf{y}|\right)}{4\pi|\mathbf{x}-\mathbf{y}|} a_1 A_1\left(\mathbf{y}\right) + \int\limits_{V2} d^3\mathbf{y} \frac{\exp\left(ik_b|\mathbf{x}-\mathbf{y}|\right)}{4\pi|\mathbf{x}-\mathbf{y}|} a_2 A_2\left(\mathbf{y}\right) \right). \tag{4}$$

We solve for the photon field in cavity 1 by substituting the paraphoton field of Eq. (4) in to Eq. (2) and we find that:

$$\left(\omega_0^2 - \omega_1^2 - i\frac{\omega_0\omega_1}{Q_1} + \chi^2 m_{\gamma\prime}^2 \left(1 - \frac{m_{\gamma\prime}^2}{\omega_0^2} G_{11}\right)\right) a_1\left(t\right) = \frac{\chi^2 m_{\gamma\prime}^4 G_{12}}{\omega_0^2} a_2\left(t\right) \tag{5}$$

$$G_{11} = \omega_0^2 \int\limits_{V1} d^3\mathbf{x} \int\limits_{V1} d^3\mathbf{y} \frac{\exp\left(ik_b|\mathbf{x}-\mathbf{y}|\right)}{4\pi|\mathbf{x}-\mathbf{y}|} \times A_1\left(\mathbf{y}\right) \cdot A_1\left(\mathbf{x}\right)$$

$$G_{12} = \omega_0^2 \int\limits_{V1} d^3\mathbf{x} \int\limits_{V2} d^3\mathbf{y} \frac{\exp\left(ik_b|\mathbf{x}-\mathbf{y}|\right)}{4\pi|\mathbf{x}-\mathbf{y}|} \times A_2\left(\mathbf{y}\right) \cdot A_1\left(\mathbf{x}\right), \tag{6}$$

where ω_1 is the driving frequency of the cavity and G_{12} is the standard G-function found in the literature [1, 3] that describes the two cavity fields, geometries and relative positions while G_{11} (henceforth G_S) is the G-function for a cavity field overlapped spatially with itself and represents losses in the cavity due to photon to paraphoton conversion. We can now solve for the photon field in cavity 2 and hence relate the fields in the two cavities without using the

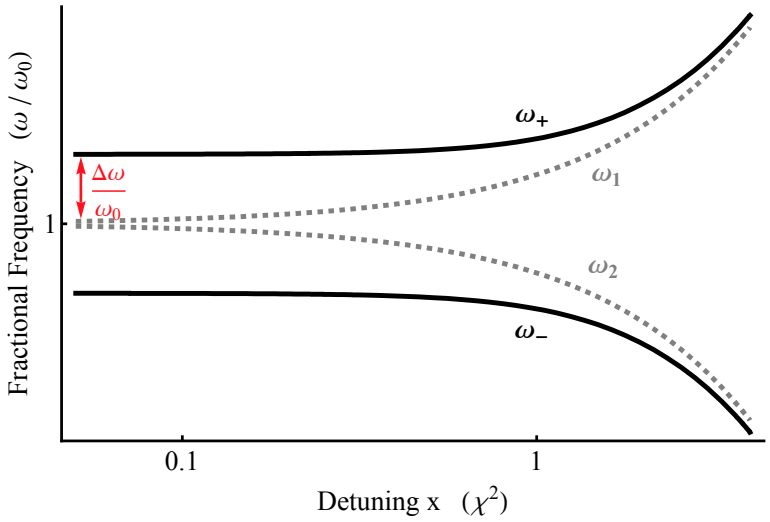

Figure 1: Log-Log plot of resonant frequencies relative to a common central frequency, ω_0, as a function of detuning for a pair of cavities that are coupled (black, full, equation (8)) and uncoupled (gray, dashed, $\omega_{1,2}/\omega_0 = (1 \pm x/2)$). The detuning, x, is given as a factor of the square of the paraphoton kinetic mixing parameter, χ. The magnitude of the fractional frequency shift is proportional to the values of parameters Q_1, Q_2, G, G_S and χ used in Eq. (8).

paraphoton field, $B(\mathbf{x}, t)$. This set of coupled equations can be represented in matrix form as

$$\begin{bmatrix} \omega_0^2 - \omega_1^2 - \frac{i\omega_0\omega_1}{Q_1} + \chi^2 m_{\gamma\prime}^2 \left(1 - \frac{m_{\gamma\prime}^2}{\omega_0^2} G_S\right) & -\frac{\chi^2 m_{\gamma\prime}^4 G}{\omega_0^2} \\ -\frac{\chi^2 m_{\gamma\prime}^4 G}{\omega_0^2} & \omega_0^2 - \omega_2^2 - \frac{i\omega_0\omega_2}{Q_2} + \chi^2 m_{\gamma\prime}^2 \left(1 - \frac{m_{\gamma\prime}^2}{\omega_0^2} G_S\right) \end{bmatrix} \cdot \begin{bmatrix} a_1(t) \\ a_2(t) \end{bmatrix} = \begin{bmatrix} 0 \\ 0 \end{bmatrix}, \tag{7}$$

with $G_{11} = G_{22} = G_S$ and $G_{12} = G_{21} = G$. In an ideal situation both cavities would be driven at the same frequency, ω, however in reality their resonant frequencies are likely to differ by a small amount. We parameterize this detuning by the factor x such that $\omega_1 = \omega\left(1 + \frac{x}{2}\right)$ and $\omega_2 = \omega\left(1 - \frac{x}{2}\right)$. We can find the two fundamental normal mode frequencies of the coupled cavity system by taking the determinant of Eq. (7), equating the real components to zero and solving for ω, yielding

$$\omega_\pm \approx \omega_0 \left(\frac{1}{1 - \frac{x^2}{2}} \left(1 + \frac{1}{2Q_1Q_2} + \frac{x^2}{4} + \frac{m_{\gamma\prime}^2\chi^2}{\omega_0^2} - \frac{m_{\gamma\prime}^4\chi^2 G_S}{\omega_0^4} \pm \left(\frac{1}{Q_1Q_2} + x^2 + \frac{2m_{\gamma\prime}^2 x^2\chi^2}{\omega_0^2} - \frac{2m_{\gamma\prime}^4 x^2\chi^2 G_S}{\omega_0^4} + \frac{m_{\gamma\prime}^8\chi^4 G}{\omega_0^8} \right)^{\frac{1}{2}} \right) \right)^{\frac{1}{2}}, \tag{8}$$

where some insignificant higher order terms have been removed. The coupled resonant modes associated with equation (8) will also have different quality factors (assuming that the initial

uncoupled cavity mode quality factors Q_1 and Q_2 are not identical). Exploiting this effect appears to offer no advantages over existing power based measurements such as LSW [1, 2] experiments, as such we shall focus our attention on frequency effects.

The effect of frequency detuning is demonstrated in figure 1; as the cavities become detuned the strength of the coupling weakens and the resonant frequencies approach their uncoupled values. The fractional frequency shift for a cavity due to the paraphoton coupling is illustrated in red, this is the value that any experiment would seek to measure.

One of the most effective ways to measure the normal mode frequency shift would be to modulate the strength of the coupling between the cavities and look for the induced modulated signal in the beat frequency of a coupled cavity and an uncoupled frequency reference. This allows for a fast rate of data collection and reduces the influence of longterm frequency drift. The strength of the coupling between the cavities can be changed by manipulating the value of the G-factor from equation (6). Changes to the relative field intensity, alignment and separation of the two cavities will in turn alter the dot product of the two cavity fields and hence the G-factor. For example, if one cavity is rotated orthogonally to the other then the dot product of the photon fields will be modulated sinusoidally at twice the rotation frequency, giving a maximum and minimum G-factor every half rotation. Comparing the resonant frequency of one of the cavities to a stable frequency reference would allow χ to be constrained by searching for a modulation in the beat frequency [4]. If the level of frequency detuning between the coupled cavities can be kept sufficiently small (see Fig. 1) then the frequency signal would be proportional to χ^2 whereas traditional LSW power measurements are proportional to χ^4. Although in practice such a level of frequency tuning would be extremely difficult to achieve with high Q cavities.

3 Conclusion

We have derived the fundamental normal mode frequencies for a pair of resonant mode cavities coupled by the exchange of hidden sector photons. These results can be used to bound the paraphoton kinetic mixing parameter χ through cavity resonance frequency measurements.

Acknowledgments

We thank the organizers of the 9th Patras Workshop on Axions, WIMPs and WISPs. This work was partially supported by the Department of Energy and Australian Research Council grants DP1092690, DP130100205, FL0992016 and a University of Western Australia research collaboration award.

References

[1] R. Povey, J. Hartnett and M. Tobar, Phys. Rev. D **82**, 052003 (2010) [arXiv:1003.0964 [hep-ex]].

[2] A. Wagner, G. Rybka, M. Hotz, L. JRosenberg, S. J. Asztalos, G. Carosi, C. Hagmann and D. Kinion *et al.*, Phys. Rev. Lett. **105**, 171801 (2010) [arXiv:1007.3766 [hep-ex]].

[3] J. Jaeckel and A. Ringwald, Phys. Lett. B **659**, 509 (2008) [arXiv:0707.2063 [hep-ph]].

[4] S. R. Parker, G. Rybka and M. E. Tobar, Phys. Rev. D **87**, 115008 (2013) [arXiv:1304.6866 [hep-ph]].

Chapter 2

Searches for WISPs in the Laboratory

Status report of the CERN microwave axion experiment

M. Betz, F. Caspers, M. Gasior

European Organization for Nuclear Research (CERN), Geneve, Switzerland

DOI: will be assigned

"Light Shining Through the Wall" experiments can probe the existence of "axion like particles" through their weak coupling to photons. We have adapted such an experiment to the microwave regime and constructed the table top apparatus. This work presents an overview of the experimental setup and then focuses on our latest measurement run and its results. By operating the apparatus within a superconducting MRI magnet, competitive exclusion limits for axion like particles to the first generation optical light shining through the wall experiments have been achieved.

1 Introduction

The concept of an optical Light Shining Through the Wall (LSW) experiment has been adapted to microwaves as described in [1]. A block diagram of the setup at CERN as it has been used to search for Axion Like Particles (ALPs) with microwaves is shown in Fig. 1a, it consists of two identical microwave cavities with a loaded quality factor of $Q \approx 12000$ and a spacing between them of less than 20 mm. One serves as ALP emitter and is excited by 50 W of RF power on its resonant frequency $f_{\mathrm{sys}} = 1.739990$ GHz. It develops a strong electromagnetic (EM) field, corresponding to a large number of microwave photons γ. These can convert to ALPs by the Primakoff effect [2]. ALPs do not interact with matter and propagate towards the detection cavity, which is connected to a very sensitive microwave receiver. The reciprocal conversion process transforms ALPs back to microwave photons, which can be observed as an excitation of the seemingly empty and well shielded detection cavity. Since there is no energy loss associated with the ALP conversion process, the signal from the detection cavity would be observable at exactly the frequency f_{sys}, making a narrowband receiving concept feasible.

2 Engineering challenges

In this section, we give an overview of the critical engineering challenges, which were encountered during the realization of the microwave based LSW experiment:

Electromagnetic shielding Shielding is required around the detecting cavity and the microwave receiver to eliminate ambient electromagnetic interference (EMI) and to mitigate coupling to the emitting cavity by electromagnetic leakage. This would generate false positive results, as a signal originating from leakage can not be discriminated against an

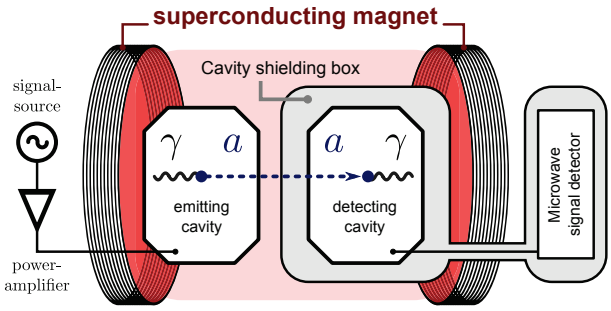

(a) Simplified schematic of the experimental setup

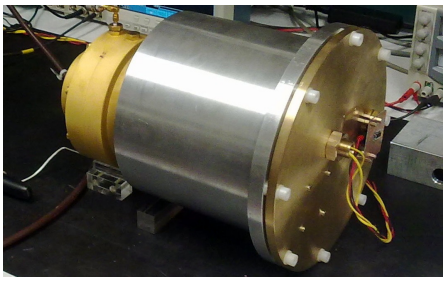

(b) Emitting cavity & detecting cavity in shielding box

Figure 1: Overview of the light shining through the wall experiment in the microwave range configured to search for ALPs

ALP signal. Within 2 cm, the field strength must be reduced by at least a factor of $7.7 \cdot 10^{12} = 258$ dB to obtain meaningful results and avoid degradation of ALP sensitivity. Most microwave components used in the setup like SMA connectors or semi-rigid coaxial cables provide less than 120 dB of shielding, making an external shielding enclosure and strategic use of optical fibres for signal transmission necessary. With the current setup, over 300 dB shielding effectiveness has been achieved [3].

Detection of weak signals The smallest detectable signal power during the ALPs run in June 2013 is $P_{det} = -212$ dBm $= 6.3 \cdot 10^{-25}$ W ≈ 0.5 photons/s. As the experiment is carried out at room temperature, the thermal noise **density** is $P_n \approx -174$ dBm/Hz. A very narrow band filter can be implemented to detect the sinusoidal signal within the background noise. It is realized by a discrete Fourier transformation over the entire recorded time trace of length $\tau =$ 10 h. Each resulting spectral bin will respond to signals within its resolution bandwidth, given by $\mathrm{BW}_{\mathrm{res}} = 1/\tau$. As noise power scales linearly with resolution bandwidth and signal power stays constant, we achieve a signal to noise ratio improvement proportional to measurement time. To keep the filter on the right center frequency, a global 10 MHz reference clock is used to phase lock all oscillators involved in the downmixing chain. This detection method has been successfully demonstrated with resolution bandwidths down to 10 μHz in [4].

Keeping the cavities on tune For an exclusion result, it is necessary to prove that the detector is working and that a potential ALP signal could not have been concealed. Detection sensitivity will be limited if the resonant frequency of any of the cavities does not equal the system frequency f_{sys} within its 3 dB bandwidth. The resonant frequency of the cavities can drift due to thermal expansion. For the emitting cavity, the reflected RF power was monitored to ensure it is on resonance during the whole measurement run. For the detecting cavity, its thermal noise density was measured before and after the recording of experimental data, indicating its resonant frequency.

Compatibility with magnetic fields As the shielding enclosure and the cavities have to be placed in a strong magnetic field for ALP measurements, they need to be constructed from

non-ferromagnetic materials like aluminium or brass. This is to prevent field distortion and to avoid strong attractive forces during insertion of the setup into the magnet. Some electronic components like the low noise amplifier and the analog optical transmitter need to be placed as close as possible to the detection cavity. Therefore special precautions had to be taken to ensure they operate reliably within the magnetic field. For example, ferrite or iron cored inductors or transformers had to be avoided as the material saturates and changes its magnetic properties in strong magnetic fields.

3 Measurement run in June 2013

The most sensitive measurement run for ALPs has been carried out in June 2013 in cooperation with the Brain & Behaviour Laboratory of Geneva University. We were able to operate the setup within the bore of a superconducting magnet, which is part of an MRI scanner. It provides a solenoid-like field of $B = 2.88$ T. Over the course of one weekend, 2 x 10 h of experimental data were recorded. As no ALPs were detected, the corresponding exclusion limits in comparison to other experiments are shown in Fig. 2.

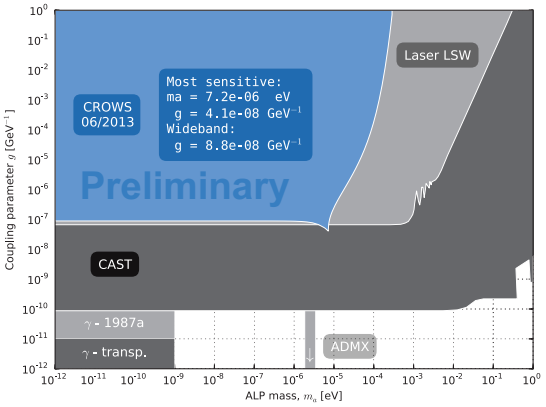

Figure 2: Preliminary exclusion limits for ALPs from the CROWS experiment run in June 2013.

For diagnostic purposes, a sinusoidal signal of known frequency is emitted within the shielding enclosure. This "test tone" of relatively low and constant power (≈ -100 dBm) couples from a $\lambda/4$ antenna to the detection cavity and to the components of the receiver frontend. By identifying the signal in the recorded spectrum, we demonstrate that the entire signal processing chain was operational during the measurement. This also allows to evaluate unwanted frequency offsets, frequency drifts, or phase noise by comparing shape and position of the measured signal peak to the expected one. Furthermore, as long as the test tone signal is observed with constant power during the measurement run, it qualifies that the EM shielding performance has not degraded.

Figure 3 shows the resulting power spectrum from the measurement run. The test tone signal is visible as a single peak, clearly above the noise floor, spanning only one single bin. A frequency window (shaded green) has been defined with a width of $10 \cdot \mathrm{BW}_{\mathrm{res}}$, around the frequency where an ALP signal would be expected. The peaks within this window do not exceed the detection threshold of $\mathrm{P}_{\mathrm{det}} = -212.0$ dBm $= 6.3 \cdot 10^{-25}$ W, allowing us to set an exclusion limit for ALPs.

In order to define the detection threshold, the histogram of $14 \cdot 10^6$ frequency bins – containing exclusively spectral background noise – was evaluated. $\mathrm{P}_{\mathrm{det}}$ was set such, that only in 1% of all measurement runs, a single peak signal above the detection threshold would appear within the WISP window, resulting in a false positive outcome of the experiment.

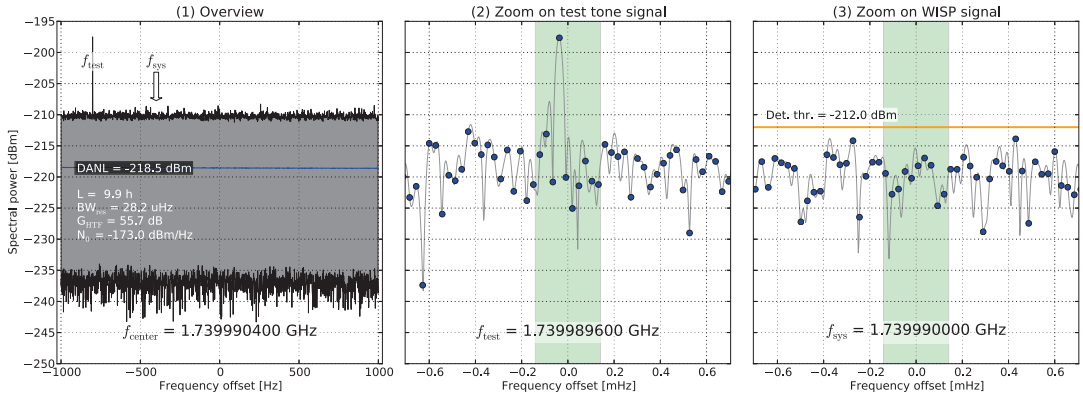

Figure 3: Result of the ALP run in June 2013.(1) Spectrum showing the whole recorded frequency span. (2) Zoom on test tone signal. It is visible within the expected frequency range, marked in green. (3) Zoom on f_{sys}, no ALP signal is visible above the detection threshold.

4 Conclusion and Outlook

Profiting from the high mobility and ruggedness of a microwave based LSW experiment (compared to optical setups), we were able to successfully deploy and operate the apparatus within a 3 T MRI magnet. Over the course of one weekend sufficient experimental data was recorded to achieve comparable sensitivity to first generation optical LSW experiments (e.g., ALPS-1 at DESY).

Sensitivity could be further enhanced with a stronger magnet. There is a recent trend towards 7 T MRI systems in medical research, which might provide us an opportunity for a follow up ALPs measurement. Furthermore, sensitivity can be enhanced with larger and thus lower frequency cavities. One might think of a LSW setup consisting of 200 MHz SPS standing wave cavities [5] within the 3 T M1 magnet [6] at CERN.

Special thanks to S. W. Rieger and the Brain & Behaviour Laboratory of Geneva University, for making the MRI magnet accessible to us on weekends. The authors would like to thank R. Jones, E. Jensen and the BE department management for encouragement and support. Thanks to the organizers of the Patras Workshop for a very enjoyable and inspiring conference. Supported by the Wolfgang-Gentner-Programme of the Bundesministerium für Bildung und Forschung (BMBF).

References

[1] J. Jaeckel, A. Ringwald, *"A Cavity Experiment to Search for Hidden Sector Photons"*, Physics B659 2008

[2] P. Sikivie, *Experimental Tests of the "Invisible" Axion*, Phys. Rev. Lett. 51, 1415 (1983)

[3] M. Betz, F. Caspers, "*A microwave paraphoton and axion detection experiment with 300 dB electromagnetic shielding at 3 GHz*", proc. IPAC 2012, New Orleans, CERN-ATS-2012-089

[4] F. Caspers et al., *Demonstration of* 10^{-22} *W Signal Detection Methods in the Microwave Range at Ambient Temperature*, CERN-BE-Note-2009-026

[5] P.E. Faugeras et al., The new RF system for lepton acceleration in the CERN SPS, proc. of PAC 1987

[6] Private communication: D.L. Lazic, `http://magnet-m1.web.cern.ch/magnet-m1/`

What's new in ALPS-II

B. Döbrich[1]*, for the ALPS-II collaboration*

[1]Deutsches Elektronen-Synchrotron (DESY), Hamburg, Germany

DOI: http://dx.doi.org/10.3204/DESY-PROC-2013-04/doebrich_babette

This proceedings contribution gives a brief experimental update of the 'Any light particle search (ALPS) -II' at DESY which will be sensitive to sub-eV, very weakly coupled particles beyond the Standard Model. First data on hidden sector photon parameter space through photon-hidden photon oscillations in vacuum is expected in 2014. Axion-like particle search (implying the installation of superconducting HERA magnets) could be realized in 2017.

1 ALPS-II setup and goals review

ALPS-II is an experiment of the light-shining-through-a-wall (LSW) type [1], and succeeds the experiment concluded in [2]. In brief, the concept is to keep a large number of $\mathcal{O}$(eV) photons stored in an optical cavity before a 'wall', i.e., a light-proof environment. Measuring photons beyond that wall would indicate beyond-Standard Model (BSM) physics[1]: If the photons are stored in a magnetic field in vacuum, the BSM process could be due to photons oscillating into axion-like or minicharged particles: Axion-like particles have a coupling to photons similarly to the QCD axion, but a relaxed mass-coupling relation; minicharged particles are electrically fractionally charged fermions or bosons, arising typically in hidden-sector models. Even without magnetic field, the photons could have oscillated into hidden photons (kinetically mixed, massive extra U(1) gauge bosons) cf., e.g., [3, 4].

Note that the LSW setup is generically sensitive only to particles with masses lower than the photon energy, i.e., to sub-eV masses in our setup. In addition, for maximum sensitivity, the conversion should be coherent such that the 200m long ALPS-II will be most sensitive below the 10^{-4}eV regime for axion-like particles and minicharged particles and in between 10^{-4}eV and 1.17eV for hidden photons getting mass from a Stückelberg mechanism[2]. For details on the here accessible as well as the physically most interesting parameter space of these light BSM particles, see [6].

ALPS-II will boost its sensitivity to light particles mainly due to the following components: Firstly, the resonator on the 'production-side' before the 'wall' will be complemented by a frequency-locked resonator behind the barrier (in the 'regeneration-region'). This increases the probability of reconversion of the light BSM particle through 'photon-self interference' [7]. Also, the power buildup and the amount of in-coupled light will be enhanced such that one has 150kW circulating power in ALPS-II in comparison to 1kW in ALPS-I. Secondly, the magnetic length is enhanced by the use of 10+10 superconducting HERA dipoles instead of only 1 dipole

[1]The contribution to such a process through a Standard Model background of neutrinos is negligible due to the large mass of the involved mediators.

[2]The situation in the case of mass from a Higgs mechanism is slightly more involved [5].

at ALPS-I. Thirdly, for single-photon detection, a Transition Edge Sensor is employed. Note that ALPS-II is set out to be about three orders of magnitude more sensitive than ALPS-I in the search for axion-like particles and about two orders of magnitude for hidden photons.

The experiment is structured in three phases. In ALPS-IIa (ongoing), meeting the optics and detector experimental challenges at a 10m+10m setup (cavity length before and after the 'wall', respectively) are addressed and a search for hidden photons can be performed. In addition, the magnet straightening-techniques (see below) are studied. ALPS-IIb will show the viability of the setup at 100m+100m length in the HERA tunnel. Finally, ALPS-IIc (still to be approved) will include the HERA dipole magnets, in order to be sensitive to axion-like (ALP) and minicharged particles.

After a thorough review of the ALPS-II Technical Design Report (an excerpt is published in [6]) by appointed, external referees, the DESY management has approved the first two phases of ALPS-II. In addition, an ALPS group has been established in the DESY high energy division. The ALPS-II collaboration comprises DESY, the Albert-Einstein Institute (AEI) in Hanover and the University of Hamburg.

In the following, this proceedings contribution briefly updates the status presented at last year's workshop [8].

2 Experimental status of optics, magnets and detector

Optics:

In brief, the optics challenge is due to the necessity of frequency-locking and aligning the production and regeneration resonators whilst requiring sensitivity to possible single photon-events from BSM physics: To keep both cavities frequency-locked, laser light must also oscillate in the regeneration cavity (to stabilize the cavity, Pound-Drever-Hall locking is employed).

The production cavity is set out to host 35W of *infrared* (1064nm) light at a power build-up of 5000 ($\sim$ number of photons reflections inside the cavity). Thus, to discriminate signal photons (e.g., due to axion-like particles), the regeneration cavity on the other hand is locked with only a few mW of frequency-doubled, *green* light, from the same laser source as the light oscillating in the production resonator. The power build-up for infrared light in the regeneration cavity, however, amounts to 40000 (amplifying the signal photons).

This setting requires great care to avoid that infrared light enters the regeneration region when coupling the green light into the regeneration cavity. In addition, no infrared photons should be created from the green due to down-conversion processes. Both these effects: light-tightness of the production region and down-conversion effects are quantified stepwise with the integration of components to the setup. So far no show-stopper has occurred.

On top of that, the simultaneous locking of both cavities must be shown, this is done at a 1m test-setup at the AEI in Hannover and reported on in [9]. Note that in principle, other locking schemes are conceivable [10], and studying both complementary methods is worthwhile.

In Hamburg, at the ALPS-IIa site (HERA West facility, one floor below ground level), infrastructural measures are mostly completed and successful studies with a low-finesse cavity have been performed throughout this year: As the mirrors of the ALPS-II resonators will be located on different optical tables in the 10m+10m setup, such studies were necessary to assess whether a stable operation with the high-finesse dichroitic mirrors will be possible with available vibration dampening. Our measurements show an integrated RMS noise for the free-running cavity on the order of a few $\times 10^{-9}$m down to 10Hz, allowing to operate the envisaged cavities

in principle. Similar studies to evaluate the conditions in the HERA tunnel (where ALPS-IIb and ALPS-IIc will be located) are in their initial phases.

To facilitate the alignment of the 2+2 cavity mirrors, the plane, rectangular central mirrors will be fixated on a common, very smooth central 'breadboard' [6]. Considering the locking mechanism as described above, we have devised a shutter box which must match the following criteria: Sealing off the regeneration cavity from infrared photons (except for calibration purposes) whilst allowing for an in-coupling of the green light for locking purposes. The light-tightness of the box (through milling of a labyrinth) must be realized without interfering with the planarity of the breadboard surface.

The delivery of the entire set of the set of highly reflective mirrors with 250m ROC is expected soon (choosing this ROC ensures that the mirrors can be used also in the succeeding stages of ALPS-II).

Magnets and vacuum:

As reviewed in detail in [6], achieving the foreseen power-buildups in the optical resonators whilst using a setup with 20 magnets requires reinstating the full aperture of the proton beam tube inside the HERA magnets. For the accelerator-use, the beam pipe was bent such that the free aperture amounts to ∼35mm, instead of ∼55mm. Note that if the aperture would be not reinstated approximately, the envisaged power buildup would only allow for an installation of 4+4 magnets (a high power buildup necessitates to have little clipping losses). However, with 4+4 dipole magnets only, probing couplings beyond the range of CAST [11] and in the physically most interesting parameter region of ALP-photon couplings of $g \lesssim 10^{-10}\mathrm{GeV}^{-1}$ would not be possible.

We have devised a method to reversibly straighten the beam pipe to an effective aperture of ∼50mm by the insertion of 'pressure props' that stabilize the cold mass against the cryostat wall. This was demonstrated first conceptually in a non-functional 'PR'-magnet and subsequently, the deformation 'props' were inserted at the ALPS-I magnet in a dipole test bench. The magnet was quenched on purpose several times to demonstrate the stability of the setup in September 2012. The quench current was higher than during the last runs of ALPS-I.

Note that ALPS-IIc will only require to use *spare* dipole magnets. The dipole magnets in the HERA ring itself will remain in place. Straightening of the 20 dipoles for ALPS–IIc is not foreseen before 2014. Thus, at the moment, the required tools for this procedure are optimized. Fast surveying techniques of the cold and warm dipole bore, respectively, are being studied.

As HERA is equipped with ion getter and titanium sublimation pumps, detailed studies of the light emission in getter pumps have been started this year to asses the possibility fake-signals on our detector, if getter-pumps are used in the regeneration region [12]. In any case, the titanium sublimation pumps will suffice if a problem with light emission is inferred.

Detector:

For detecting photons at ALPS-II, fiber-guiding the photons to a Transition-Edge Sensor detector (TES), is foreseen. In a nutshell, the current-change in a sophisticated multilayer superconductor, operated at the superconducting edge, is picked up by an inductively coupled SQUID at cryogenic temperatures. The cryostat used in ALPS-II to host the TES and the SQUID is an adiabatic demagnetization refrigerator (ADR). Such a setup is perfectly suited for single-photon detection due to its extremely low dark count rate.

Earlier this year, two TE sensors were lent to our collaboration from NIST in the US and AIST in Japan, respectively. In close coordination with the PTB in Berlin, the detection system with these sensors is set up at DESY as reviewed in [13]. Note, that in principle two channels

are available such that two TE sensors can be used in parallel (e.g., one could be used to record solely background events, first background studies have been performed [13]).

In a separate setup, we have studied the in-coupling of an ALPS-II-like photon beam (i.e., diameter as foreseen in experiment but different laser source) into a single-mode fiber. Focusing on a fiber-coupler, an efficiency of more than 80% was achieved. Note that for the overall detector sensitivity, quantifying the coupling of the fiber to the TES inside the ADR is also foreseen.

As a detector fall-back option and for calibration purposes, the Princeton Instruments 'PIXIS CCD' used in ALPS-I has been characterized with respect to the detection of 1064nm photons [14].

3 To take home

With (yet) little stringent indications towards BSM physics in laboratory experiments, it is worthwhile, besides the high-energy frontier, *also* to keep in mind the sub-eV scale as potential host of something undiscovered [15], including Dark Matter [16, 17]. ALPS-II aims at exploring a large parameter space of new sub-eV particle physics by combining idle accelerator infrastructure with pioneering optics and detector techniques. In summary, we hope to report to the next, 10th PATRAS workshop 2014 at CERN with first ALPS-IIa measurement data.

The author would like to thank the workshop organizers for a topical and motivating conference. In addition, the author thanks the Aspen Center for Physics (NSF Grant #1066293) for a lab-timeout to pick up on different unfinished projects and a quiet day to write up this note.

References

[1] J. Redondo and A. Ringwald, Contemp. Phys. **52**, 211 (2011) [arXiv:1011.3741 [hep-ph]].

[2] K. Ehret *et al.*, "New ALPS Results on Hidden-Sector Lightweights," Phys. Lett. B **689**, 149 (2010) [arXiv:1004.1313 [hep-ex]], see also `www.alps.desy.de`

[3] J. Jaeckel and A. Ringwald, Ann. Rev. Nucl. Part. Sci. **60**, 405 (2010) [arXiv:1002.0329 [hep-ph]].

[4] K. Baker *et al.*, Annalen Phys. **525**, A93 (2013) [arXiv:1306.2841 [hep-ph]].

[5] M. Ahlers *et al.*, Phys. Rev. D **78**, 075005 (2008) [arXiv:0807.4143 [hep-ph]].

[6] R. Bähre, B. Döbrich, J. Dreyling-Eschweiler, S. Ghazaryan, R. Hodajerdi, D. Horns, F. Januschek and E. -A. Knabbe *et al.*, JINST **1309**, T09001 (2013) [arXiv:1302.5647 [physics.ins-det]].

[7] F. Hoogeveen and T. Ziegenhagen, Nucl. Phys. B **358**, 3 (1991). J. G. Hartnett, J. Jaeckel, R. G. Povey and M. E. Tobar, Phys. Lett. B **698**, 346 (2011) [arXiv:1101.4089 [quant-ph]].

[8] B. Döbrich, arXiv:1212.2770 [hep-ph]. Contributed to the PATRAS 2012 proceedings

[9] Robin Bähre for the ALPS-II collaboration, these proceedings

[10] G. Mueller *et al.*, Phys. Rev. D **80**, 072004 (2009) [arXiv:0907.5387 [hep-ph]].

[11] E. Ferrer Ribas *et al.* [CAST Collaboration], arXiv:1209.6347 [hep-ex].

[12] Severin Wipf, Bachelor thesis, technical college Jena, 2013

[13] Jan Dreyling-Eschweiler for the ALPS-II collaboration, these proceedings & PhD thesis, Univ. Hamburg, in preparation (2014)

[14] Jan-Eike von Seggern for the ALPS-II collaboration, these proceedings & PhD thesis, Univ. Hamburg, in preparation (2013)

[15] A. Ringwald, Phys. Dark Univ. **1**, 116 (2012) [arXiv:1210.5081 [hep-ph]].

[16] P. Arias *et al.*, JCAP **1206**, 013 (2012) [arXiv:1201.5902 [hep-ph]].

[17] Andrei Lobanov for WISPDMX, these proceedings

Extending axions searches with a spherical TPC

J. Galan[1], *G. Gerbier*[2], *I. Giomataris*[2], *T. Papaevangelou*[2], *I. Savvidis*[3]

[1]University of Zaragoza (Spain)
[2]CEA Saclay
[3]University of Thessaloniki (Greece)

DOI: http://dx.doi.org/10.3204/DESY-PROC-2013-04/galan_javier

We present the prospects for detection of KK-axions using a large volume spherical TPC through natural decay to two gammas. The higher excited mass states of this axion model allows to reach densities which could be detectable by this method. We show the capability of this detector to detect 2-prong events coming from rest-mass axion decays and we provide efficiencies obtained under some gas mixtures and pressure conditions. The sensitivity limit of a future experiment with existing detectors geometry has been estimated for the case of zero background limit.

1 Introduction

The axion is a hypothetical neutral pseudoscalar particle which was already predicted in 1977. This new weakly interacting particle came out as an elegant solution to the CP problem of strong interactions in QCD [1]. We focus on an extension to this model. In superstring theories it turns out to be possible to lower the string scale without lowering the Planck scale [2, 3]. One of the most interesting features of the higher-dimensional axionic theories is that their mass spectrum consists of a tower of Kaluza-Klein (KK) excitations, which have an almost equidistant mass-space related to the compactification radius R [4]. Moreover, the coupling to photons, $g_{a\gamma}$, of the excited states is of the same order as the coupling of the ground state, which is naturally identified with the QCD axion.

As for the case of standard QCD axions, a considerable range of KK-axion mass modes (up to about 20keV) should be produced in the Sun [4]. An immediate consequence of the production of higher axion masses inside the Sun is the capability to produce low momentum axions. A small fraction of the axions produced would have a momentum which is lower than the Sun escape velocity, and these axions would keep gravitationally trapped describing elliptic orbits around the Sun [5]. The accumulation of these axions during the Sun lifetime would allow to reach detectable densities in the Earth's neighborhood (see section 4).

2 Spherical TPC detector

We propose to use a spherical TPC [6] to detect KK-axions through its natural decay to two photons, by studying the topology of 2-prong events. This detector consists of a spherical grounded cavity which is filled with gas. In the center of this cavity is placed a small spherical

sensor (made of metallic or resistive materials) where a high positive voltage is applied. The field produced inside the cavity allows drifting the electrons and ions produced by ionizing interactions in the gas. The field close to the sensor (typically 1 cm diameter) is high enough to produce signal amplification through electron avalanche processes (see Figure 1).

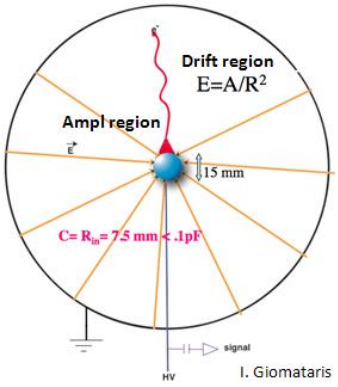

Figure 1: An schematic of the spherical TPC concept and detection principle.

The main advantages of using a spherical TPC reside on its simplicity, single read-out, large volume capability, good energy resolution (11% FWHM at 6keV) and low electronic noise related to the low capacitance of the spherical geometry. The low energy threshold is only limited by the ionization energy of the gas (around 25 eV). The dynamic range of the detector can be adjusted by using different values of the amplification field to scan interactions from few eV to several MeV, as would be produced by alphas or heavy ions.

3 Detection efficiency to 2-prong events

One of the key features of our detector is the capability to detect 2-prong events. In a gaseous detector there are two physical parameters that affect the probability to distinguish two gammas, the attenuation length and the charge diffusion. This two parameters depend on the gas mixture and pressure, providing the detector with certain flexibility to set the efficiency to this kind of events. The field defined by the spherical geometry produces a strong dependence on drift velocity and diffusion as a function of the distance to the sensor (see Figure 2).

In one side, we expect the attenuation length to be as short as possible so that both gammas interact inside the detector, but in the other side, we want that the gammas to be far enough so that they can be differentiated in the detector read-out. In order to evaluate the capability to detect this kind of events in our detector we have produced Montecarlo simulations of rest-mass decays to two gammas at different pressures and gas mixtures. We present efficiencies for two typical mixtures used; argon+2%CH_4, argon+10%CH_4 and neon+2%CH_4 (see Figure 3).

It must be noticed the great flexibility on detection efficiency by using different gas mixtures and pressure, allowing to optimize the detector for this search. Different axion mass ranges can be covered with different efficiencies by varying the pressure, supporting a hypothetical positive signal which could be modulated with the detector pressure.

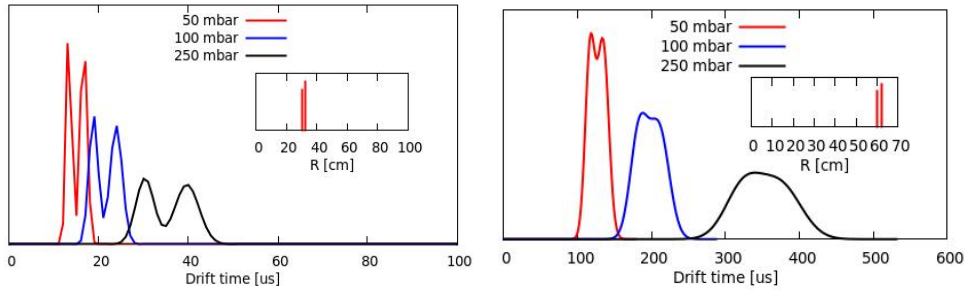

Figure 2: Effect of diffusion for a 2-prong like event at different gas pressures. Inset plots show the distance of the simulated events to the sensor, (left) two close events at about 30 cm, (right) at about 60cm. The different pressures simulated at Argon+10%CH4 show how relevant is the pressure choice in the capability to distinguish such events.

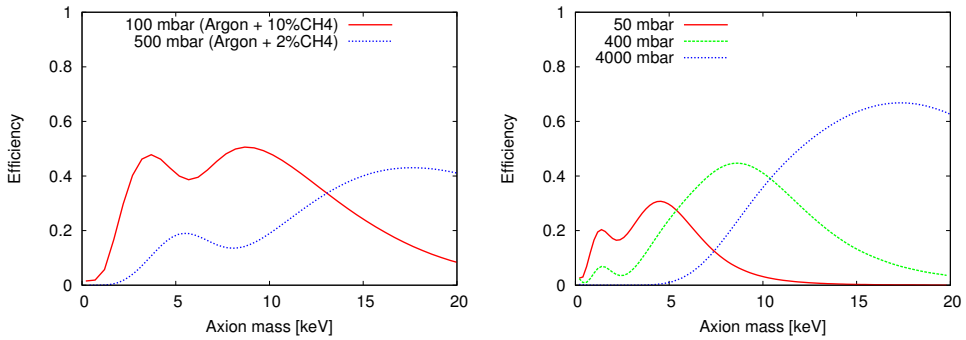

Figure 3: 2-prong events detection efficiency as a function of the axion mass. (left) Gas argon+CH_4 and spherical detector radius 65 cm. (right) Gas neon+2%CH_4 and spherical detector radius 30 cm.

4 Sensitivity prospects to KK-axions

The sensitivity of our experiment for detection of decaying KK-axions will depend on the model described in [5] through the accumulated axion density (ρ_a) and the decay rate, or mean life (τ_a). These quantities depend on the coupling of axion to photon ($g_{a\gamma}$) and the mass of the axion (m_a). Considering the mean life of these particles is few orders of magnitude above the age of the solar system we can express these quantities as follows

$$\rho_a = 1.18 \times 10^{39} \left(\frac{g_{a\gamma}}{\mathrm{GeV}^{-1}}\right)^2 \left[\mathrm{m}^{-3}\right] \qquad \tau_a = 1.35 \times 10^{5} \left(\frac{g_{a\gamma}}{\mathrm{GeV}^{-1}}\right)^{-2} \left(\frac{m_a}{\mathrm{eV}}^{-3}\right) [\mathrm{s}]\,. \tag{1}$$

Our sensitivity will be directly related to the total number of decays observed in a certain amount of time (t_{exp}) in the volume defined by our detector (V_{sph}) and the detection efficiency of 2-prong events (ϵ_{det}). The number of decays observed is then given by the following expression,

$$N_\gamma = \tau_a^{-1} \cdot \rho_a \cdot V_{sph} \cdot t_{exp} \cdot \epsilon_{det} \tag{2}$$

which depends finally on the value of $g_{a\gamma}$ and m_a.

In case no signal is observed we can obtain a limit on the coupling of the axion to photon. For simplicity, here we present the sensitivity limit of such experiment in the case of zero background which provides a rough estimate of the limits achievable (see Figure 4). Further work on this direction should include the measured background level of the detector after necessary optimization.

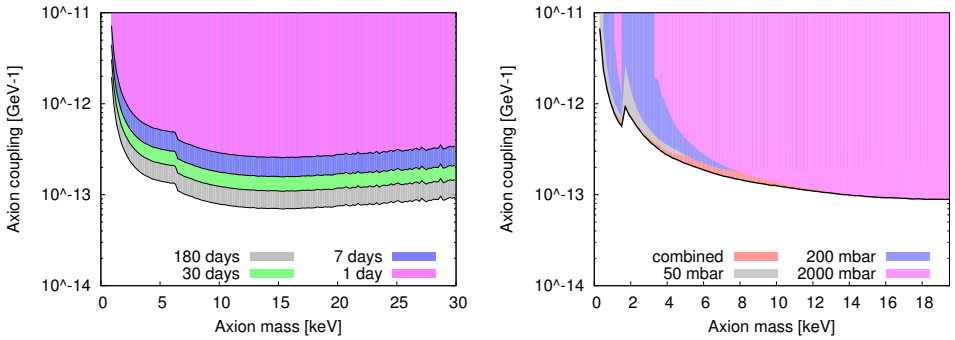

Figure 4: Sensitivity limit estimation for the axion-photon coupling in case of zero background. (left) Coupling limit for different exposure times (sphere radius 65 cm) in an argon+10%CH_4 at 100 mbar. (right) Coupling limit for neon+2%CH_4 gas mixture (sphere radius 30 cm) at different pressures for a 180 days exposure period and the combined result.

5 Discussion

We have shown the sensitivities reachable with a spherical TPC for KK-axions search. The existence of KK-axion implies the existence of the QCD axion, thus the estimated sensitivities for this search correspond to an unexplored region on the QCD axion parameter space. We conclude then that the sensitivities reachable with this type of experiment are competitive enough to prove the existence of KK-axions (and thus QCD axions). In case no signal is found we could set the first experimental limit on this type of axions.

References

[1] R.D. Peccei and H.R. Quinn, Phys. Rev. Lett. **38**, 1440 (1977)

[2] N. Arkani-Hamed, S. Dimopoulos and G. Dvali, Phys. Lett. B **429**, 263 (1998)

[3] K.R. Dienes, E. Dudas and T. Gherghetta, Phys. Lett. B **436**, 55 (1998)

[4] L. Di Lella, A. Pilaftsis, G. Raffelt and K. Zioutas, Phys. Rev. D **62** (2000) 125011.

[5] L. DiLella and K. Zioutas, Astroparticle Physics **Vol 19**, Issue 1, Pages 145-170 (2003)

[6] I. Giomataris *et al.*, Nuclear Physics B, **Vol 150** (2006) Pages 208-213

Axion searches with EDELWEISS Ge bolometers

C. Nones, on behalf of the EDELWEISS collaboration
CEA, Irfu, SPP - Centre de Saclay, F-91191 Gif-sur-Yvette, France

DOI: http://dx.doi.org/10.3204/DESY-PROC-2013-04/nones_claudia

The EDELWEISS experiment aims at the direct detection of dark matter in the form of WIMPs using Ge bolometers operated at 20 mK in a dilution refrigerator installed at the Underground Laboratory of Modane. In addition to this primary search, Ge bolometers are suitable to the study of other phenomena, such as the detection of axions or axion-like particles (ALPs). We will present here results obtained in the framework of the EDELWEISS-II experiment on different ALPs characterized by different coupling mechanisms to ordinary matter and detected exploiting the coherent Bragg diffraction and the axio-electric effect.

1 Introduction to axion detection in EDELWEISS

The hypothetical existance of a new, elusive pseudo-scalar particle, the axion, descends from an elegant solution to the so-called CP problem in QCD [1, 2, 3]. Both the axion mass and coupling strength to ordinary particles are inversely proportional to a symmetry-breaking scale f_A, which plays the role of a free parameter in the modern axion models, such as the popular hadronic axions predicted by the KSVZ (Kim-Shifman-Vainstein-Zakharov) model [4] and the GUT axions foreseen by the DFSZ (Dine-Fischler-Srednicki-Zhitnitskii) model [5]. In both cases, the axion mass, m_A, is related to f_A according to:

$$m_A \simeq 6\,\mathrm{eV} \times \left(\frac{10^6\,\mathrm{GeV}}{f_A}\right) \tag{1}$$

The effective axion couplings to photons ($g_{A\gamma}$), electrons (g_{Ae}) and nucleons (g_{AN}) are model dependent [6, 7] and all proportional to the axion mass. In particular, hadronic axions, unlike GUT axions, do not interact with ordinary quarks and leptons at tree level leading to a strong suppression of g_{Ae}. Experimental searches and astrophysical constraints can be translated to limits on f_A, or equivalently on the axion mass, within a given axion model.

The purpose of this article is to summarize the results – extensively described elsewhere [8] – about the interaction of axions or ALPs produced by different mechanisms in the Sun or constituting the galactic dark matter halo. These results are obtained exploiting the EDELWEISS-II germanium bolometers operated underground to search for WIMPs [9, 10]. Two detection mechanisms in the germanium detectors are exploited: (i) the coherent Bragg diffraction [11], related to $g_{A\gamma}$ and (ii) the axio-electric effect [12, 13, 14], which is the analogue of a photo-electric effect with the absorption of an axion instead of a photon.

2 Results and discussion

First, we will shortly review the possible axion production mechanisms that are relevant for the analysis here described. The Sun could be a major source of axions, due to the following channels:

- Primakoff production: $\gamma \rightarrow$ A in the presence of charged particles (ruled by the coupling constant $g_{A\gamma}$)
- Nuclear magnetic transition of ^{57}Fe nuclei (ruled by the coupling constant g_{AN}): $^{57}\mathrm{Fe}^{*} \rightarrow ^{57}\mathrm{Fe}$ + A
- Compton-like scattering (this and the remaining mechanisms are ruled by the coupling constant g_{Ae}): $\mathrm{e}^{-} + \gamma \rightarrow \mathrm{e}^{-}$ + A
- Axion bremsstrahlung: $\mathrm{e}^{-} \rightarrow \mathrm{e}^{-}$ + A in the presence of charged particles
- Axio-recombination: e^{-} + I $\rightarrow \mathrm{I}^{-}$ + A where I is an ion
- Axio-deexcitation: $\mathrm{I}^{*} \rightarrow$ I + A where I^{*} is an excited state of I

The sum of axio-recombination and axio-deexcitation are often referred as the axio-RD mechanism. The relative intensity of the mechanisms is model-dependent. For example, in the case of non hadronic axions such as those described by the DFSZ model, fluxes related to Compton and bremsstrahlung processes are far more intense than those predicted by hadronic models for the same value of f_A. This is due to the fact that the coupling to electrons arises at the tree level. In this case, the Compton and bremsstrahlung channels for axion production largely prevail over the Primakoff effect. On the contrary, the latter dominates hadronic axion emission. As for the ^{57}Fe axions, whose flux depends only on the isoscalar and isovector coupling constants (which combine to produce an effective coupling constant to nucleons, g_{AN}^{eff}), the axion production rate is similar in hadronic and non hadronic models.

A second possibility leading to axion interactions in terrestrial detectors is that these particles constitute a major fraction of dark matter and are present in the galactic halo. When testing this scenario, we have assumed that axions constitute all of the galactic dark matter. The associated flux does not depend on any axion coupling.

In our search [8] we have used, depending on the production channel, two different mechanisms for axion detection, i.e. the Primakoff effect and the axio-electric effect.

Through the Primakoff effect, axions can be converted into photons in the intense electric field of the germanium crystal [11]. The wavelength of relativistic solar axions, with an energy of a few keV, is of the same order of magnitude as the inter-atomic spacing of the detector. Therefore, depending on the direction of the incoming axion flux with respect to the lattice, the axion signal can be enhanced significantly through Bragg diffraction (EDELWEISS detectors are mono-crystals). The corresponding correlation of the count rate with the position of the Sun in the sky also helps further with an effective background rejection of about two orders of magnitude. Since this effect is used to search for axions assumed to be produced in the Sun through the Primakoff mechanism as well, it is possible to constrain specifically the coupling constant $g_{A\gamma}$.

Axions can also be detected through the aforementioned axio-electric effect: A+e^{-}+Z$\rightarrow$ e^{-}+Z. The axio-electric cross-section, controlled by the parameter g_{Ae}, was computed as a

function of the axion energy in [12, 13, 14]. Through this mechanism, an incoming axion of total energy E (relativistic or not) will generate an electron recoil with the same energy within an EDELWEISS detector. When used to detect solar axions produced via Compton, bremsstrahlung and axio-RD mechanisms, this detection approach allows to constrain solely the parameter g_{Ae}. If instead it is used to search for ^{57}Fe axions, then bounds are set on the product $g_{Ae} \times g_{AN}$. This process is exploited also for the detection of the hypothetical dark matter axions, constraining once again g_{Ae}.

In order to perform our experimental axion searches, we benefit from the quality of the EDELWEISS-II data set: a large exposure corresponding to 14 month data taking with ten 400 g germanium detectors, a good energy resolution and a very low background down to an energy threshold of 2.5 keV. This low background was made possible thanks to both the low-radioactivity underground setup of the experiment and the so-called ID detector design [15] which allows a selection of interactions that take place within a fiducial volume for each detector. For every event in this volume, we exploit also a special feature of the EDELWEISS detectors, which provide a double signal for each particle interaction, corresponding to the energy $E_{\rm ion}$ deposited in the form of charge and to the energy $E_{\rm heat}$ released in the form of heat. Electron recoils are gaussian distributed along the line $E_{\rm ion} = E_{\rm heat}$. We rejected events beyond 3 standard deviations from ! this line.

No axion signal was observed over the energy range $2.5 - 20$ keV, where all the investigated mechanisms have the potential to produce detectable features. This allows to set first of all limits for each detection channel on the respective couplings, summarized in Table 1, where ^{57}Fe stands for 14.4 keV solar axions emitted in ^{57}Fe de-excitation, DM for dark matter axions, C-B-RD for Compton-bremsstrahlung and axio-RD axions, and P for Primakoff axions. The quoted values are in the limit $m_A = 0$, except for the dark matter case, which is given for $m_A = 12.5$ keV, which provides the highest sensitivity in the investigated mass range. All limits are at 90% CL except P (95% CL).

Channel	Limit
^{57}Fe	$g_{Ae} \times g_{AN}^{\rm eff} < 4.82 \times 10^{-17}$
DM	$g_{Ae} < 1.07 \times 10^{-12}$
C-B-RD	$g_{Ae} < 2.59 \times 10^{-11}$
P	$g_{A\gamma} < 2.15 \times 10^{-9}$ GeV^{-1}

Table 1: Summary of the limits on the different axion couplings (see text for channel labels).

Channel	^{57}Fe ($g_{Ae} \times g_{AN}^{\rm eff}$)	C-B-RD (g_{Ae})	P ($g_{A\gamma}$)
KSVZ	$155\,{\rm eV} < m_A < 14.4$ keV	$272\,{\rm eV} < m_A < 40$ keV	$5.78 < m_A \lesssim 200$ eV
DFSZ	$8\,{\rm eV} < m_A < 14.4$ keV	$0.92\,{\rm eV} < m_A < 80$ keV	$15 < m_A \lesssim 200$ eV

Table 2: Excluded ranges of axion masses derived from EDELWEISS-II constraints (see text for channel labels).

Within the framework of a given axion model, such as the two benchmark models KSVZ and DFSZ, the only free parameter is the axion mass, or equivalently the symmetry-breaking scale f_A (see Eq. (1)). Therefore, our limits on the couplings constrain m_A directly. The corresponding bounds are reported in Table 2, where the KSVZ and DFSZ models are considered and the channels are labeled as in Table 1.

In order to show the relevance of our search in an international context, in Figure 1 we compare our limits in terms of axion couplings to ordinary matter with constraints from other

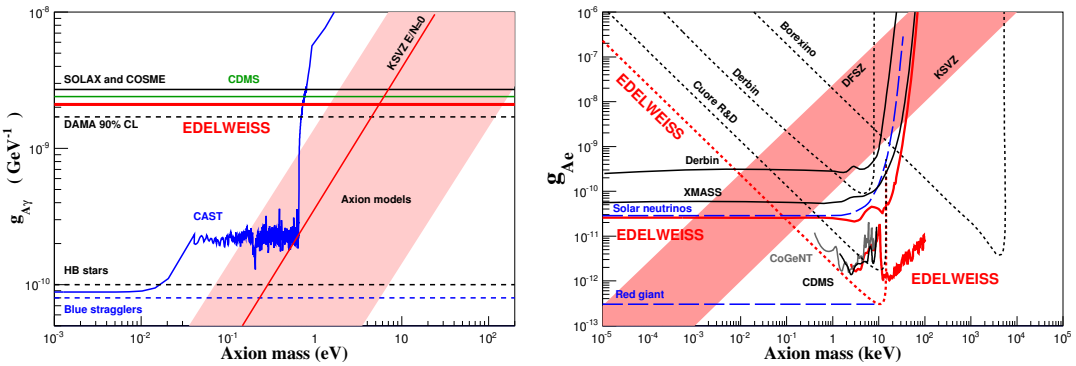

Figure 1: Summary of the constraints obtained by EDELWEISS-II on the $g_{A\gamma}$ and g_{Ae} axion couplings as a function of the axion mass, compared with other searches.

experiments and astrophysical bounds. The references to other searches are detailed in Ref. [8].

3 Conclusions and perspectives

In this paper we have demonstrated the potential of germanium bolometric detectors equipped with the ID design for ALP searches. Improvements are expected with future setups, such as EDELWEISS-III and EURECA, thanks to both better energy resolution and larger exposures.

References

[1] R. D. Peccei and H. R. Quinn, Phys. Rev. D **16**, (1977) 1791.
[2] S. Weinberg, Phys. Rev. Lett. **40**, 223 (1978).
[3] F. Wilczek, Phys. Rev. Lett. **40**, 279 (1978).
[4] J. E. Kim, Phys. Lett. **43**, 103 (1979); M. A. Shifman *et al.*, Nucl. Phys. B **166**, 493 (1980).
[5] A. R. Zhitniskiy, Yad. Fiz. **31**, 497 (1980); M. Dine *et al.*, Phys. Lett. B **104**, 199 (1981).
[6] D. B. Kaplan, Nucl. Phys. B **260**, 215 (1985).
[7] M. Srednicki, Nucl. Phys. B **260**, 689 (1985).
[8] E. Armengaud *et al.*, Accepted for publication in JCAP, arXiv:1307.1488.
[9] E. Armengaud *et al.*, Phys. Lett. B, **687**, 294 (2010).
[10] E. Armengaud *et al.*, Phys. Lett. B **702**, 329 (2011).
[11] R.J. Creswick *et al.*, Phys. Lett. B **427**, 235 (1998).
[12] A. Derevianko *et al.*, Phys. Rev. D **82**, 065006 (2010).
[13] M. Pospelov *et al.*, Phys. Rev. D **78**, 115012 (2008).
[14] F. Alessandria *et al.*, JCAP **05**, 007 (2013).
[15] A. Broniatowski *et al.*, Phys. Lett. B **681**, 305 (2009).

Progress of the Laser-based Experiment OSQAR

M. Sulc[1], *P. Pugnat*[2], *R. Ballou*[3], *G. Deferne*[4], *L. Duvillaret*[5], *M. Finger Jr.*[6], *M. Finger*[6], *J. Hosek*[7], *T. Husek*[6], *R. Jost*[8], *M. Kral*[7], *S. Kunc*[1], *K. Macuchova*[7], *K. A. Meissner*[9], *J. Morville*[10], *D. Romanini*[8], *M. Schott*[4], *A. Siemko*[4], *M. Slunecka*[6], *M. G. Vitrant*[5], *and J. Zicha*[7]

[1]Technical University of Liberec, Czech Republic
[2]LNCMI-G, CNRS-UJF-UPS-INSA, BP 166, 38042 Grenoble Cedex-9, France
[3]Institut Néel, CNRS and Universit Joseph Fourier, BP 166, 38042 Grenoble Cedex-9, France
[4]CERN, CH-1211 Geneva-23, Switzerland
[5]IMEP-LAHC, UMR CNRS 5130, Minatec-INPG, 3 parvis Louis Néel, BP 257, 38016 Grenoble Cedex-1, France
[6]Charles University, Faculty of Mathematics and Physics, Prague, Czech Republic
[7]Czech Technical University, Faculty of Mechanical Engineering, Prague, Czech Republic
[8]LSP, UMR CNRS 5588, Université Joseph Fourier, BP 87, 38402 Saint-Martin d'Hères, France
[9]Institute of Theoretical Physics, University of Warsaw, Poland
[10]LASIM, UMR CNRS 5579, Université Claude Bernard Lyon-1, 69622 Villeurbanne, France

DOI: http://dx.doi.org/10.3204/DESY-PROC-2013-04/sulc_miroslav

OSQAR experiment at CERN is based on two laser methods for search of axions and scalar particles. The light shining through the wall experiment has been using two LHC dipole magnets with an optical barrier, argon laser, and cooled 2D CCD detector for the measuring of expected regenerated photons. The second method wants to measure the Vacuum Magnetic Birefringence. An optical set-up with electro-optical modulator has been proposed, validated and subsequently improved in collaborating institutes. Cotton-Muton effect in nitrogen was measured by this method. Prototype of a one-meter long laser cavity was developed for this experiment.

1 Introduction

The OSQAR (Optical Search for QED vacuum magnetic birefringence, Axions and photon Regeneration) is purely laboratory laser-based experiment, situated at CERN. Its aim is to explore the low energy frontier of particle and astroparticle physics by combining the simultaneous use of high magnetic fields with laser beams in two distinct experiments. In the first one, the photon regeneration effect is looked as a light shining through the wall [1], [2], whereas in the second one, ultra-fine Vacuum Magnetic Birefringence (VMB) predicted by the QED is aimed to be measured for the first time. The OSQAR activities have the preparatory phases at laboratories outside CERN, and measurement at CERN approximately 6 - 8 weeks per year. OSQAR takes advantage of the CERN two state-of-the-art superconducting spare LHC magnets, and vacuum and cooling facilities. The dipole magnets have two apertures of effective length 14.3 m, maximal magnetic field 9.5 T, perpendicular to apertures. Both magnets are placed on the same straight line, so laser beam can pass through both magnets simultaneously.

2 Experimental

2.1 Photon regeneration effect

The theory predicts photon conversion to weakly interacting axion in the magnetic field. This axion can pass through optical barrier, and can convert back to detectable photon at the second magnet field. It looks as light shining though the wall. Argon laser (3.3 W, multi-line mode 488 and 514 nm) has been used as a source of photons. The output light is linearly polarized parallel to magnetic field, so it can be used for the search of new pseudoscalar - axion particles. To look for scalar particles, a half-wave plate, oriented at 45 degrees, is inserted at the laser exit to align the polarization perpendicularly to the magnetic field. The laser beam divergence was reduced by a beam expander. The beam is attenuated and focused by additional lens to liquid nitrogen cooled CCD detector to the spot of radius around 0.1 mm. CCD chip has 1024 x 256 square pixels of 0.026 mm size. The four neighbouring pixels were binned into a 2 x 2 superpixels, so array of 512 x 128 superpixels channels was finally used. The area, where we can expect photon regeneration signal, is about 5 x 5 superpixels. The quantum efficiency of the detector is equal to 30 percent for the argon laser wavelengths, dark current is about 0.5 electrons per pixel per hour, and readout noise is typically 3.4 electrons. The laser was shining with the lower power 1.62 W due to mode stability problems Exposure times for one 2D recorded image were 15 minutes. Total duration of data taking was 22 hours for pseudoscalar search and 24 hours for scalar search.

The analyses were performed to interpret the photon regeneration experimental runs. Cosmic noise, observed as high signal on small area of 1 - 4 superpixels, was cleaned. All data for scalar/pseudoscalar particles were added separately. The data (matrix of intensities - events on CCD superpixels) was divided to the clusters of 4 x 5 superpixels. The integrated signal of each cluster was calculated as the sum of all recorded counts of the corresponding 20 super-pixels. The integrated signal ranges between the lowest and the high signal limits due to random distribution of noise in clusters. The numbers of clusters with the same integrated signals were calculated. Histogram of these numbers was accurately fitted with Gaussian distribution function. No cluster with higher number of events was detected. We can assume from Gaussian fitting parameters that if there is a flux greater than 6.32 photons per hour, we must detect it (conservatively for the 95 percent confidence interval for both scalar/pseudoscalar particles). The values of coupling constants of possible new light scalar and pseudo-scalar particles that can couple to two photons is constrained in the massless limit to be less than $8.0{\cdot}10^{-8}$ GeV^{-1}. It confirms the present reference results obtained by the ALPS collaboration [3].

2.2 Vacuum magnetic birefringence measurement

The predicted VMB [4], [5] effect is very weak so the experiment starts with magnetic-field-induced birefringence measurement at gases (also known as a Cotton-Mouton effect), in air, in nitrogen, diluted nitrogen, helium, with final aim to measure VMB. The optical set-up based on the use of an electro-optical modulator is shown in Figure 1. A laser beam, linearly polarized by a prism (polarizer), is sent through the electro-optical modulator before propagating trough the birefringence sample, where the light acquires the ellipticity to be measured. The polarization of the beam is finally analyzed by a polarizer prism (analyzer), and the modulated light intensity is detected by a photodiode. The electro-optic modulator converts the linearly polarized light into circularly polarized light oscillating between left-handed and right- handed ellipticity at 49.4 kHz

(maximum frequency is limited by second harmonic signal for 100 kHz Lock-in amplifier, which was used for signal detection). The set of possible configurations of polarized elements was investigated. The best orientation of each successive component in the set-up is at 45 degrees rotation to its previous element [6].

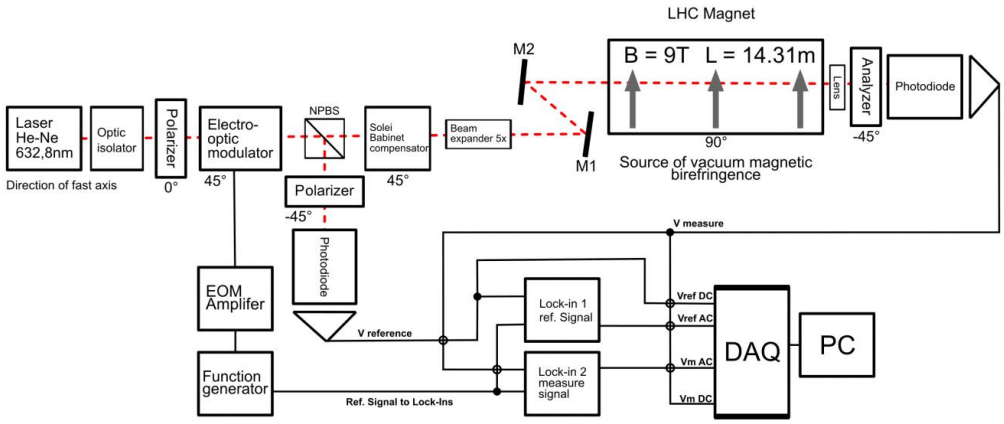

Figure 1: Set-up for the measurement of the Gas Magnetic Birefringence.

Stabilised He-Ne laser 632.8 nm and corresponding optical components were chosen. The optical set-up was installed with one LHC dipole dedicated to OSQAR. The Cotton-Mouton effect was measured in N_2 gas with pressure in the dipole aperture ranging from 1000 to 2000 mbars. The measured optical retardance was found to increase with the square of magnetic field as expected. The constant of the Cotton-Mouton effect for N_2 at 1 bar was found to be equal to - $3.6{\cdot}10^{-7}$ rad $T^{-2}m^{-1}$. The difference in refractive indices for = 632.8 nm, and L = 14.3 m effective LHC dipole magnetic length was n - $2.28{\cdot}10^{-13}$ for N_2 at atmospheric pressure in 1 T field. This result is in good agreement with published values [7].

2.3 Development of high finesse optical cavity

Application of resonant cavities will increase the optical path of the laser beam passing within strong magnetic field and it can increase sensitivity of the both laser experiments. A prototype of an one-meter long plano-concave resonator cavity was built in the laboratory of CTU Prague. The cavity is constructed to be used with He-Ne laser, wavelength 632.8 nm. The optical cavity is build using two circular mirrors: one semi-permeable planar 2 - inch mirror and one highly reflective concave 2 - inch mirror with radius of 1 m. Distance between the mirrors is 980 mm. Mirrors are mounted in kinematic holders. Planar 2-inch mirror is used for locking the cavity resonance frequency. The mount of this mirror has 5 degrees of freedom (two rotations and three translations) tuned by piezoelectric actuators and controled by a close loop controller.

Concave 2-inch mirror has 4 degrees of freedom (two rotations and three translations) and its mount can be also positioned by piezoelectric actuators too.

Obviously all components should be compatible with ultra-high vacuum ($< 10^{-9}$ mbar). The light will be locked inside the cavity using the Pound-Drever-Hall lock-in technique [8]. The prototype was successfully tested at the laboratory. Two full length (19.6 m) cavities are now built on the base of these experiences. The first one for VMB experiment, using 632 nm He-Ne laser, the second one for photon regeneration experiment, using second-harmonic of solid state laser 532 nm used at present. Both with different optics, but with the same mechanics and piezoelectronics control.

3 Conclusion

The results of the photon regeneration experimental runs for pseudoscalar/axion and scalar particle search were deeply analyzed. They confirm the results published by the ALPs collaboration. Progress towardst the measurement of the VMB has been achieved. Cotton-Mouton effect for N_2 at 1 bar was used to confirm sensitivity of apparatus. The constant of the C-M effect was found to be equal to - $3.6{\cdot}10^{-7}$ rad $T^{-2}m^{-1}$. The one-meter long prototype of the cavity was built and tested. New full length cavities for VMB and PR experiments were designed and constructed too.

4 Acknowledgments

This work was supported by the the Grant Agency of the Czech Republic 203/11/1546 and partly supported by SGS 58010 Grant of Technical University of Liberec.

References

[1] P. Sikivie, "Detection rates for invisible-axion searches," Phys. Rev. Lett. **51**, 1415 (1983); Phys. Rev. D **32**, 2988 (1985)

[2] K. van Bibber, *et al.*, "Proposed experiment to produce and detect light pseudoscalars," Phys. Rev. Lett. **59**, 759 (1987)

[3] K. Ehret *et al.*, "New ALPS Results on Hidden-Sector Lightweights," Phys. Lett. B **689**, 149 (2010) [arXiv:1004.1313 [hep-ex]].

[4] W. Heisenberg and H. Euler, Z. Phys. **98**, 714 (1936)

[5] V. S. Weisskopf, Mat.Fys. Medd. Dan Vidensk. Selsk. **14**, 1, (1936)

[6] F.A. Modine, R.W. Major, E. Sonder Applied optics **14**, 3 (1975)

[7] Mei Hsien-Hao *et al.*, "Measurement of the Cotton-Mouton effect in nitrogen, oxygen, carbon dioxide, argon, and krypton with the QandA apparatus," Chem. Phys. Lett. **471**, 216 (2009) [http://arxiv.org/abs/0812.3328]

[8] R. W. P. Drever *et al.*, "Laser phase and frequency stabilization using an optical resonator," Appl. Phys. B **31**, 97 (1983)

Chapter 3

Searches for WISPs in Astrophysics

A new Constraint on the Axion-Photon Coupling

A. Friedland[1], *M. Giannotti*[2], *M. Wise*[2]

[1]Los Alamos National Laboratory, Los Alamos, US
[2]Barry University, Miami Shores, US

DOI: http://dx.doi.org/10.3204/DESY-PROC-2013-04/giannotti_maurizio

We show that the emission of axions coupled to photons with $g_{a\gamma} \geq 0.8 \times 10^{-10}\mathrm{GeV}^{-1}$ would eliminate the blue loop stage for stars in the mass window $\sim 8 - 12\ M_\odot$. This is excluded by observations of the blue sequences and of Cepheid stars.

1 Introduction

Stars are efficient laboratories to study the properties of *light, weakly interacting* particles. Observations require, in fact, that the energy drain cannot be too different from the Standard Model (SM) predictions [1]. This has provided a great deal of understanding in different sectors of particle physics beyond the standard model, including nonstandard neutrino properties [2, 3, 4], majorons [5], novel baryonic or leptonic forces [6], and more recently unparticles [7] and extra-dimensional photons [8].

An interesting example of light, weakly interacting particle is the axion [9, 10, 11, 12] and, more generally, Axion Like Particles (ALPs). These are pseudoscalar particles coupled to photons through the interaction term

$$\mathcal{L}_{a\gamma} = -\frac{g_{a\gamma}}{4} a F \tilde{F}\,. \tag{1}$$

Current experiments are probing the region of $g_{a\gamma} \sim 10^{-10}\mathrm{GeV}^{-1}$ and it is common to measure the coupling strength in terms of the dimensionless parameter $g_{10} = g_{a\gamma}/(10^{-10}\mathrm{GeV}^{-1})$.

Astronomical observations can provide very useful insights in our knowledge of this coupling. In particular, the analysis of globular cluster stars in the Horizontal Brunch (HB) in comparison with the number of stars in the Red Giant (RG) phase leads to the strong bound $g_{10} \leq 1$, valid for masses below a few 10 GeV, that is for axions light enough to be efficiently produced in the stellar core [13, 14].

A slightly stronger bound, valid however in a quite smaller ALP mass range, is derived from the terrestrial experiment CAST (Cern Axion Solar Telescope) [15], which has excluded the region $g_{10} \geq 0.88$ for an ALP mass below 0.02 eV.

The strongest bound to date, however, is derived by the analysis of the evolution of massive stars [16, 17]. These stars, while burning helium in their core, evolve into a stage called the *blue loop* during which they contract and expand again. In the Hertzsprung-Russell (HR) diagram, this appears as a loop which extends toward the left (see Figure 1), in the region of higher surface temperature (*blue*) before turning back in the colder (*red*) region to the right side of the diagram.

The existence of the loop is corroborated by astronomical observations. In particular, the loop is essential to account for the observed Cepheid stars.

In [16] it was shown that the additional cooling induced by axions coupled to photons would eliminate this evolutionary stage for stars of mass between 8 and 12 $M_\odot$, unless $g_{10} < 0.8$.

Here we will discuss this new constraint on the axion-photon coupling and provide some insight on how the blue loop stage can be used as a sensitive probe for exotic processes and weakly interacting particles.

2 Blue loop and particle physics

At the end of the H-burning stage (main sequence) stars expand and cool down. During the following stage the star burns helium in the core and hydrogen in a shell.

Figure 2 (top curve) shows the surface temperature evolution of a $9.5M_\odot$ star from the main sequence to the end of the He-burning stage. The transition from H- to He- burning happens at $t_{\rm MS} \simeq 23.8$ Myr and corresponds to the (relatively fast) migration toward the right of the HR diagram shown in Fig. 1 (pre-blue loop stage).

As shown in Fig. 2, at $t_{\rm BL} \simeq 25.4$ Myr the surface temperature rapidly increases and the star contracts. This is the start of the blue loop stage, a migration toward the left of the HR diagram. Simulations have shown that this happens when the hydrogen has burned enough in the shell and the H fraction has reached an *almost step-like profile* [18, 19, 20].

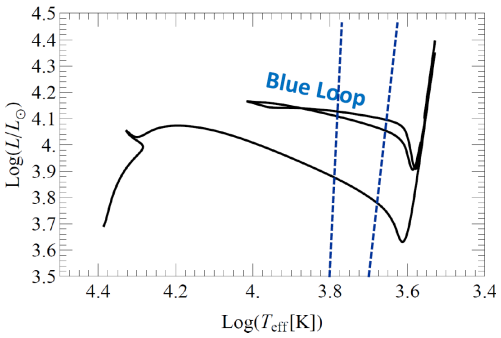

Figure 1: Evolution in the HR diagram of a 9.5 $M_\odot$ star. The region between the two dashed lines is the instability strip, where the Cepheid variables are found.

Finally, after another 1 Myr or so, the surface temperature begins to decrease again and the star starts its journey back to the right of the HR diagram. Physically, the end of the stellar contraction and the *turning back* in the HR diagram, say at $t = t_{\rm back}$, is caused by the dropping of the helium content in the core below some threshold value [18].

It is quite remarkable, for our analysis, that the set and the end of the blue loop stage are determined by the physics of the shell and of the core respectively. Consequently, an exotic process which is efficiently produced in the core but not in the shell would cause a shortening of the blue loop stage without significantly changing $t_{\rm BL}$ (see Fig. 2).

Observationally, the shortening of the blue loop stage corresponds to a reduction of the number of *blue* with respect to *red* stars of a given luminosity (see [21] for a recent analysis of the observations).

More significantly, if the ratio of the time scales of the core and shell burning changes enough, the blue loop stage may disappear altogether [22] and that would have the additional consequence of leaving us without an explanation for the observed Cepheid stars at that particular luminosity. Given the good level at which the Cepheid stars are known, the complete disappearance of the blue loop stage, even for a small range of luminosities, is observationally forbidden.

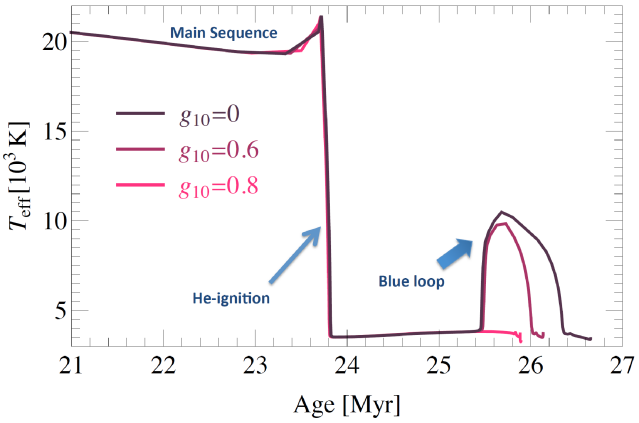

Figure 2: Surface temperature evolution of a 9.5 $M_\odot$ star for three different values of the axion-photon coupling.

This fact can be used to constraint new physics, in particular novel cooling mechanisms which are strongly dependent on the temperature and efficient at relatively low densities.

As a simple criteria, we require that an additional cooling mechanism must always satisfy $t_{\rm back} \geq t_{\rm BL}$ to guaranty the existence of the blue loop. This may be more conveniently restated in terms of the He-burning stage lifetime as follows: an additional cooling is phenomenologically forbidden if

$$t'_{\rm He}/t_{\rm He} \leq (t_{\rm BL} - t_{\rm MS})/(t_{\rm back} - t_{\rm MS})\,. \tag{2}$$

The exact value for the right hand side should be determined by numerical simulations and depends on the star mass and, possibly, other stellar parameters. Our simulations with the publicly available stellar evolution code MESA [23] show that a value of 0.8 is a fairly conservative choice for stars of initial mass around 10 $M_\odot$. A more detailed analysis is in preparation.

3 Discussion and conclusion

The blue loop criteria described above is very efficient in constraining the axion-photon coupling [16].

Axions (and, more generally, ALPs) can be produced in stars through the Primakoff process, $\gamma + Ze \to a + Ze$, which is efficient at relatively low densities and high temperatures, that is, in an environment typical of the core He-burning stars. After being produced, they freely stream out of the star carrying energy away and providing, therefore, a very efficient cooling mechanism. This results in a shortening of the He-burning stage.

In the case of low mass HB stars, it is possible to show that, under reasonable assumptions, $t'_{\rm He}/t_{\rm He} \simeq 1/(1 + 0.4 g_{10}^2)$ [1]. Preliminary simulations indicate that the above scaling formula is reasonably correct also in the case of more massive stars.

From the discussion in the previous section we know that a 20 % reduction of the (central) He-burning time would eliminate the blue loop stage for stars in the 10 $M_\odot$ mass range and

is, therefore, observationally forbidden. This corresponds to the requirement that $g_{10} \geq 0.8$, a result confirmed by the numerical simulation shown in Fig. 2.

This bound is somewhat more stringent than the one from HB stars. In addition, since the core temperature of more massive stars is higher than that in low mass stars, the bound extends to higher ALP masses.

Only recently massive stars have been considered to study particle physics [24]. This work shows that they may be quite efficient laboratories.

References

[1] G. G. Raffelt, Chicago, USA: Univ. Pr. (1996) 664 p.

[2] J. Bernstein, M. Ruderman and G. Feinberg, Phys. Rev. **132**, 1227 (1963).

[3] P. Sutherland, J. N. Ng, E. Flowers, M. Ruderman and C. Inman, Phys. Rev. D **13**, 2700 (1976).

[4] D. A. Dicus and E. W. Kolb, Phys. Rev. D **15**, 977 (1977).

[5] H. M. Georgi, S. L. Glashow and S. Nussinov, Nucl. Phys. B **193** (1981) 297.

[6] J. A. Grifols and E. Masso, Phys. Lett. B **173** (1986) 237.

[7] S. Hannestad, G. Raffelt and Y. Y. Y. Wong, Phys. Rev. D **76**, 121701 (2007) [arXiv:0708.1404 [hep-ph]].

[8] A. Friedland and M. Giannotti, Phys. Rev. Lett. **100**, 031602 (2008) [arXiv:0709.2164 [hep-ph]].

[9] R. D. Peccei and H. R. Quinn, Phys. Rev. Lett. **38**, 1440 (1977).

[10] R. D. Peccei and H. R. Quinn, Phys. Rev. D **16**, 1791 (1977).

[11] S. Weinberg, Phys. Rev. Lett. **40**, 223 (1978).

[12] F. Wilczek, Phys. Rev. Lett. **40**, 279 (1978).

[13] G. G. Raffelt, Phys. Rev. D **33**, 897 (1986).

[14] G. G. Raffelt and D. S. P. Dearborn, Phys. Rev. D **36**, 2211 (1987).

[15] M. Arik, S. Aune, K. Barth, A. Belov, S. Borghi, H. Brauninger, G. Cantatore and J. M. Carmona *et al.*, arXiv:1307.1985 [hep-ex].

[16] A. Friedland, M. Giannotti and M. Wise, Phys. Rev. Lett. **110**, 061101 (2013) [arXiv:1210.1271 [hep-ph]].

[17] G. Raffelt, Physics **6**, 14 (2013).

[18] D. Lauterborn, S. Refsdal and A. Weigert, Astron. Astrophys. **10** (1971) 97.

[19] D. Lauterborn, S. Refsdal and M. L. Roth, Astron. Astrophys. **13** (1971) 119.

[20] R. Kippenhahn and A. Weigert, Berlin: Springer (2012) 668 p.

[21] K. B. W. McQuinn, E. D. Skillman, J. J. Dalcanton, A. E. Dolphin, J. Holtzman, D. R. Weisz and B. F. Williams, Astrophys. J. **740**, 48 (2011) [arXiv:1108.1405 [astro-ph.CO]].

[22] E. Hofmeister, Zeitschrift für Astrophysik. **65** (1967) 164.

[23] B. Paxton, L. Bildsten, A. Dotter, F. Herwig, P. Lesaffre and F. Timmes, Astrophys. J. Suppl. **192**, 3 (2011) [arXiv:1009.1622 [astro-ph.SR]].

[24] A. Heger, A. Friedland, M. Giannotti and V. Cirigliano, Astrophys. J. **696**, 608 (2009) [arXiv:0809.4703 [astro-ph]].

Pair-production opacity at high and very-high gamma-ray energies

D. Horns[1], *M. Meyer*[1,2]

[1]Institut für Experimentalphysik, Universiät Hamburg , Germany
[2]Oskar-Klein Centrum, Stockholm, Sweden

DOI: http://dx.doi.org/10.3204/DESY-PROC-2013-04/horns_dieter

The propagation of high energy (HE, $E_\gamma > 100$ MeV) and very high-energy gamma-rays (VHE, $E_\gamma > 100$ GeV) in the extra-galactic photon field leads to pair-production and consequently energy- and distance-dependent attenuation of the primary intensity. The spectroscopy of an increasing number of extra-galactic objects at HE and VHE energies has demonstrated indeed the presence of such an attenuation which in turn has been used to constrain the photon density in the medium. At large optical depth ($\tau \gtrsim 2$) potential modifications of pair-production due to competing but rare processes (as, e.g., the presence of sub-neV axion-like particle) may be found. Indications for a pair-production anomaly have previously been found with VHE-spectra. Here, we present further indications (at the level of 3.68 σ) for a reduced optical depth at high energies from an analysis of Fermi-LAT data.

1 Introduction

The extra-galactic photon field in the optical/ultraviolet and infra-red is the stellar and dust-reprocessed light (see [7] for a review) accumulated during the cosmological evolution following the era of re-ionization. For sufficiently energetic ($E > 10$ GeV) photons from distant sources, pair-production processes with this background photon field lead to an energy- and distance dependent exponential attenuation, $\exp(-\tau)$, where τ is the optical depth. This effect has recently been detected in the observed HE gamma-ray spectra of 50 Blazars in the redshift range 0.5 to 1.6 [3] as well as independently in the observed VHE gamma-ray spectra of mainly 2 BL Lac type objects at redshifts of 0.116 and 0.186 [1]. Given the measurement uncertainties, the spectral shape of the extra-galactic background light (EBL) has been fixed to a choice of models with normalizations left to vary. The two independent measurements of the redshift dependent EBL level for one particular model [11] is shown in Fig. 1. Given the large uncertainties, variations of the normalization by a factor of two are consistent with the data. Particularly, the VHE data favor a drop of the EBL normalization towards larger redshifts, broadly consistent with the HE measurement.
At large optical depth ($\tau > 2$), modifications of the transparency by non-standard propagation effects may lead to noticable effects in the attenuation. Even though in principle the residuals (Fig. 4 of [1] and Fig. 2 of [3]) do not show obvious deviations from the best-fit, it is difficult to interpret this result given that the normalization of the EBL (and therefore of the optical depth) was varied by more than a factor of two between the different redshift bins.

Several studies of the VHE measurements provided indications for deviations from the expected transparency [4, 5, 9, 12]. The proposed interpretations have either focussed on the assumption that Blazars are powerful accelerators of ultra-high energy protons [8] or additional processes including light pseudo-scalars (a la axion-like particles, for a review see, e.g., [13]) have been invoked [6, 16]. In this contribution, we extend our previous work in the HE energy regime (see also [15] for an update of the original analyses of VHE data [12]) using Fermi-*LAT* observations of distant AGN [14].[1]

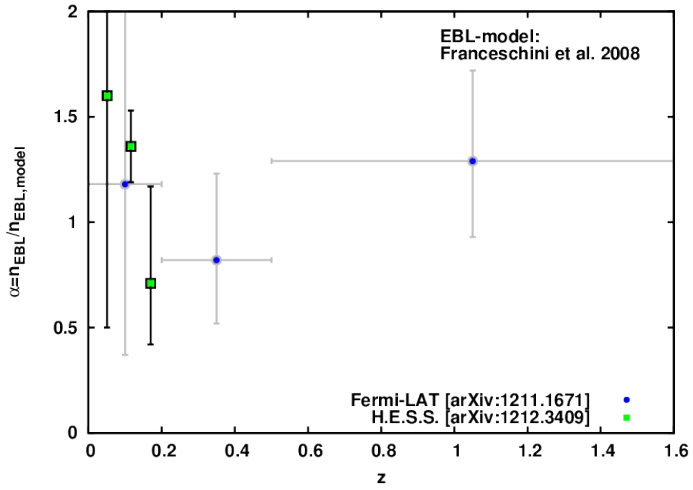

Figure 1: Comparison of the high-energy ($E_\gamma > 100$ MeV) and VHE ($E_\gamma > 100$ GeV) measurements of the normalization factor of the extra-galactic background light (EBL) for different ranges of redshift.

2 Fermi-*LAT* observations

The data-set from the first 4.3 years of operation (until Nov. 29, 2012)[2] of Fermi-*LAT* are searched for the most energetic photons which can be associated with known gamma-ray emitting AGN from the second Fermi-*LAT* catalog [18] as well as from [17]. Each photon-like event detected at energies $E_\gamma > 10$ GeV at high Galactic latitude $|b| > 10°$ of event class `ULTRACLEAN` and zenith angle $Z < 100°$ is matched against the list of AGN with known redshift. An event is considered to be associated with a source, if its angular uncertainty (r_{68} at 68 % c.l. derived from the instrumental response function P7V6_ULTRACLEAN from the in-flight calibration) is larger than the angular distance to the location of the AGN. The resulting list of photons (see Fig. 2) contains 23(9) photons with optical depth $\tau > 1(2)$. Similar to the study carried out with VHE-spectra, we focus on the photons detected from sources at an optical depth $\tau > 2$ (assuming the best-fit level of the extra-galactic background [3]). The two highest-energy photons exceeding the well-calibrated energy range of 500 GeV are excluded from the sample as well as four photons where the probability of association with the source is less than 90 % even in the case of no absorption present[3]. The final sample comprises three photons from GB6J1001+2911

[1] Note, the search for anomalous transparency effects as discussed here is complementary to searches for additional noise induced by photon-axion coupling in AGN spectra as originally proposed for optical QSO spectra [19] and recently extended to a VHE and X-ray spectra [20].

[2] using time-intervals passing the standard cuts

[3] The probability is calculated using the `gtsrcprob` tool.

($\tau(E = 308$ GeV$, z = 0.558) = 2.18$), S4 0218+35 ($\tau(E = 179$ GeV$, z = 0.944) = 2.46$), Ton 599 ($\tau(E = 301$ GeV$, z = 0.725) = 3.1$). For each photon and source, the number of photons predicted from the source for a nominal absorption is calculated ($= \mathcal{O}(10^{-3})$) as well as the number of background events ($= \mathcal{O}(10^{-4})$). The predicted number of source photons is based upon a power-law extrapolation of the energy spectrum fit in the range from 1 GeV to the energy where absorption diminishes the expected flux by 1 %. A power-law was chosen even in the case of significant curvature of the energy spectrum. Given this choice, the predicted number of source photons is an upper limit to the real value.
The resulting probability for detecting the three photons is combined using Fisher's method [10] to be $P_{\mathrm{pre-trial}} = 6.57 \times 10^{-6} (4.36\ \sigma)$ and correcting for trials $P_{\mathrm{post-trial}} = 1.17 \times 10^{-4} (3.68\ \sigma)$, consistent with the result obtained from the VHE data. Systematic effects include changing of the energy within the estimated 68 % c.l. uncertainty ($P_{\mathrm{pre-trial}} = 3.34 \times 10^{-5}$) and assuming a harder intrinsic spectrum ($P_{\mathrm{pre-trial}} = 1.85 \times 10^{-5}$). In both cases, the probabilities increase, but the significance remains larger than 3 σ.

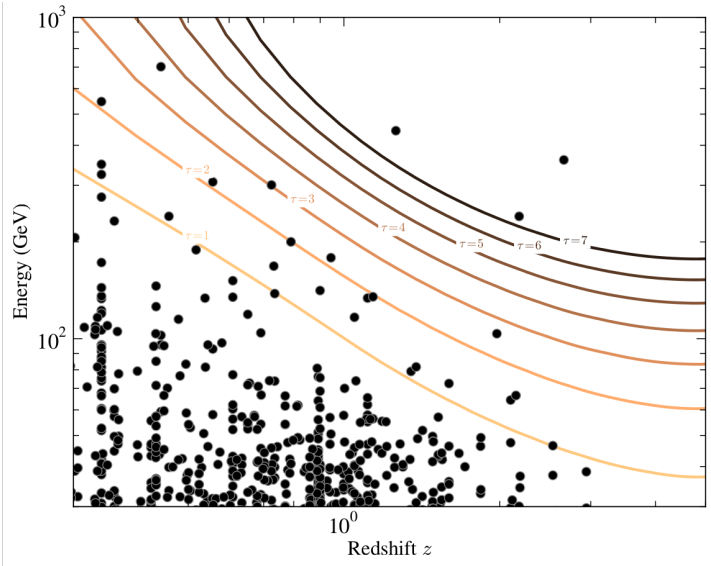

Figure 2: Photons detected at energies $E > 10$ GeV associated with γ-ray emitting AGN with known redshift.

3 Summary and discussion

We have extended our previous work to search for anomalous transparency of the Universe to very-high energy (VHE) γ-rays to the low-energy regime covered with the Fermi-*LAT* instrument. We find three photons from three sources with optical depth $\tau > 2$. The combined probability to detect these photons is (post-trial) 1.17×10^{-4} corresponding to (3.68 σ). The on-going observation as well as improvements of data-analysis will increase the sensitivity to search for deviations from the expected (astrophysical) transparency for gamma-rays. Future observations carried out with the next generation of ground-based air Cherenkov telescopes (Cherenkov telescope array: CTA [2]) will bridge the energy gap between the energy range covered with today's ground based installation and space-based telescopes and therefore will be sensitive to confirm the indications for anomalous transparency.

Acknowledgements

The authors thank the organizers of the Patras workshop. The work of MM has been funded through SFB 676 and the LEXI *Connecting particles with the cosmos*.

References

[1] A. Abramowski et al. Measurement of the extragalactic background light imprint on the spectra of the brightest blazars observed with H.E.S.S. *Astronomy and Astrophysics*, 550:4, 2013.

[2] B.S. Acharya, M. Actis, T. Aghajani, G. Agnetta, J. Aguilar, et al. Introducing the CTA concept. *Astropart.Phys.*, 43:3–18, 2013.

[3] M. Ackermann et al. The Imprint of The Extragalactic Background Light in the Gamma-Ray Spectra of Blazars. *Science*, 338:1190–1192, 2012.

[4] F. Aharonian et al. New constraints on the Mid-IR EBL from the HESS discovery of VHE gamma rays from 1ES 0229+200. *Astron.Astrophys.*, 475:L9–L13, 2007.

[5] E. Aliu et al. Very-High-Energy Gamma Rays from a Distant Quasar: How Transparent Is the Universe? *Science*, 320:1752, 2008.

[6] Alessandro De Angelis, Marco Roncadelli, and Oriana Mansutti. Evidence for a new light spin-zero boson from cosmological gamma-ray propagation? *Phys.Rev.*, D76:121301, 2007.

[7] Eli Dwek and Frank Krennrich. The Extragalactic Background Light and the Gamma-ray Opacity of the Universe. *Astropart.Phys.*, 43:112–133, 2013.

[8] Warren Essey and Alexander Kusenko. A new interpretation of the gamma-ray observations of active galactic nuclei. *Astropart.Phys.*, 33:81–85, 2010.

[9] Warren Essey and Alexander Kusenko. On weak redshift dependence of gamma-ray spectra of distant blazars. *Astrophys.J.*, 751:L11, 2012.

[10] R. Fisher. Theory of Statistical Estimation. *Proceedings of the Cambridge Philosophical Society*, 22:700–725, 1925.

[11] Alberto Franceschini, Giulia Rodighiero, and Mattia Vaccari. The extragalactic optical-infrared background radiations, their time evolution and the cosmic photon-photon opacity. *Astron.Astrophys.*, 487:837, 2008.

[12] D. Horns and M. Meyer. Indications for a pair-production anomaly from the propagation of VHE gamma-rays. *JCAP*, 1202:033, 2012.

[13] Joerg Jaeckel and Andreas Ringwald. The Low-Energy Frontier of Particle Physics. *Ann.Rev.Nucl.Part.Sci.*, 60:405–437, 2010.

[14] M. Meyer. *The Opacity of the Universe for high and very-high energy γ-rays*. PhD thesis, Dep. Physics, Univ. Hamburg, 2013. DESY-THESIS-033/2013.

[15] Manuel Meyer, Dieter Horns, and Martin Raue. Revisiting the Indication for a low opacity Universe for very high energy gamma-rays. 2012.

[16] Manuel Meyer, Dieter Horns, and Martin Raue. First lower limits on the photon-axion-like particle coupling from very high energy gamma-ray observation. *Phys.Rev.*, D87:035027, 2013.

[17] A. Neronov, D.V. Semikoz, A.M. Taylor, and Ie. Vovk. Very-high-energy gamma-ray emission from high-redshift blazars. 2012.

[18] P.L. Nolan et al. Fermi Large Area Telescope Second Source Catalog. *Astrophys.J.Suppl.*, 199:31, 2012.

[19] Linda Ostman and Edvard Mortsell. Limiting the dimming of distant Type Ia supernovae. *JCAP*, 0502:005, 2005.

[20] D. Wouter. Axion-like particles in the high energy universe. *These proceedings*, 2013.

WISPers from the Dark Side: Radio Probes of Axions and Hidden Photons

D. Horns[1], *A. Lindner*[2], *A. Lobanov*[3,1], *A. Ringwald*[2]

[1]Institut für Experimentalphysik, Universität Hamburg, Germany
[2]Deutsches Elektronen-Synchrotron (DESY), Hamburg, Germany
[3]Max-Planck-Institut für Radioastronomie, Bonn, Germany

DOI: http://dx.doi.org/10.3204/DESY-PROC-2013-04/lobanov_andrei

Measurements in the radio regime embrace a number of effective approaches for WISP searches, often covering unique or highly complementary ranges of the parameter space compared to those explored in other research domains. These measurements can be used to search for electromagnetic tracers of the hidden photon and axion oscillations, extending down to $\sim 10^{-19}$ eV the range of the hidden photon mass probed, and closing the last gaps in the strongly favoured 1–5 μeV range for axion dark matter. This provides a strong impetus for several new initiatives in the field, including the WISP Dark Matter eXperiment (WISPDMX) and novel conceptual approaches for broad-band WISP searches in the 0.1–1000 μeV range.

1 WISP in the radio regime

The scope of experimental studies of dark matter (DM) has been expanding steadily towards low energies and to weakly interacting slim particles (WISP) [1, 2, 3] such as axions, axion-like particles (ALP) and hidden photons (HP). Best revealed by their coupling to standard model (SM) photons, the WISP may give rise to dark matter for a broad range of the particle mass and the photon coupling strength [4] as indicated by red lines in Fig. 1. At particle masses above $\sim 10^{-3}$ eV, the existing constraints effectively rule out WISP as DM particles, while there are very few measurements reaching sensible exclusion levels at lower energies. This domain corresponds to the radio regime at frequencies below 240 GHz where highly sensitive measurement techniques are developed for radioastronomical measurements, with typical detection levels of $\lesssim 10^{-22}$ W. Such sensitivity provides excellent opportunities for laboratory [5, 6, 7] and astrophysical [8] searches for WISP of both cosmological (dark matter) and astrophysical origin (photon-WISP conversion). The dependence of the latter signal in HP on the distance to the target object also offers a unique tool for reaching particle masses down to $\lesssim 10^{-18}$ eV [9] (see Fig. 1).

2 Astrophysical measurements

Astrophysical measurements in the radio can broaden substantially the range of parameter space probed for ALP and HP. Analysis of the WMAP CMB measurements in the radio domain at frequencies above 22 GHz has already provided excellent ALP and HP bounds down to masses

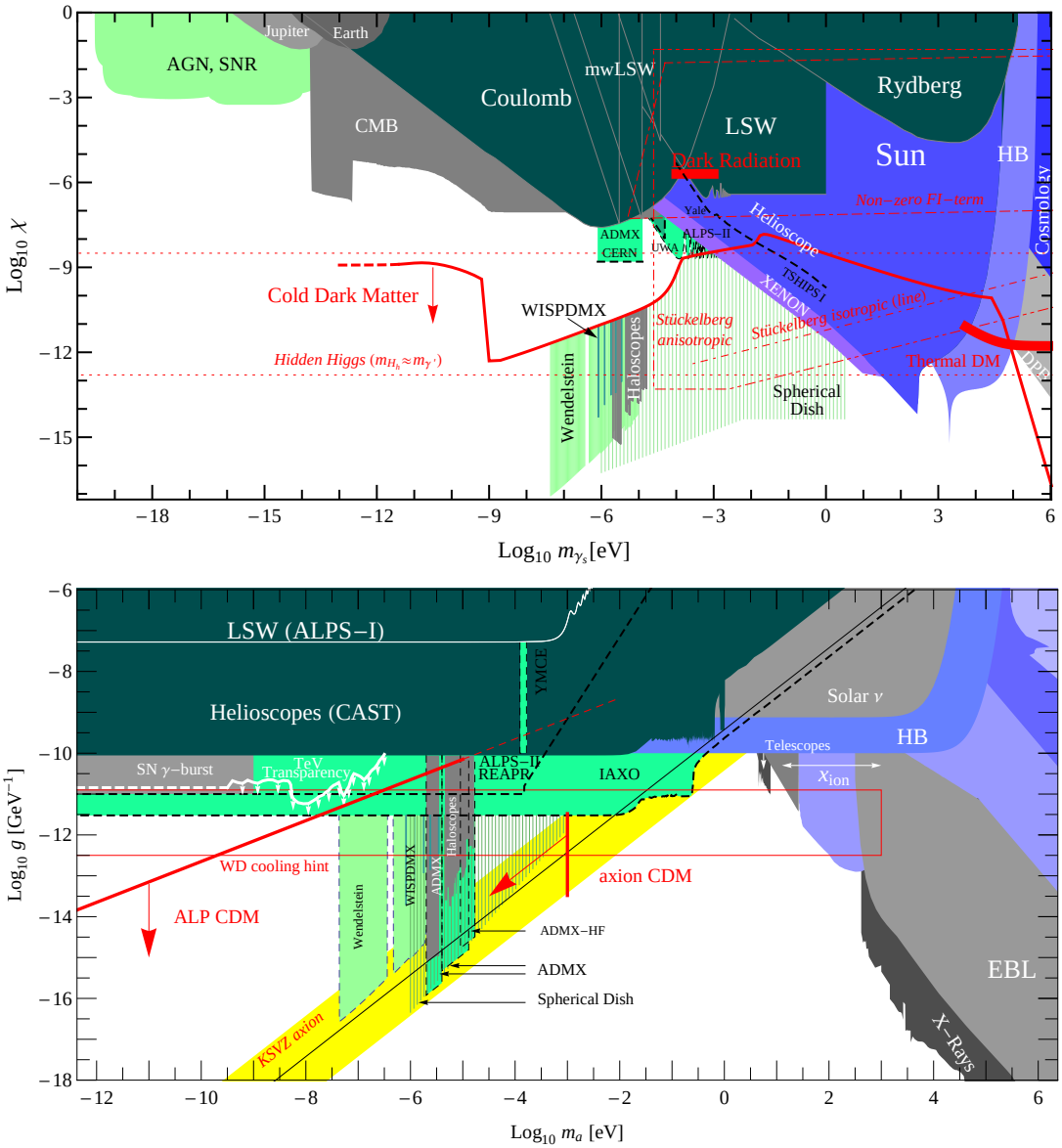

Figure 1: Exclusion limits for hidden photon (top) and ALP (bottom) couplings to SM photons. Existing measurements are indicated with gray/blue/dark green shades and white captions. Expected limits from future measurements are indicated with light green shades and black captions. The yellow band in the axion plot marks properties of the QCD axion. Red color indicates theoretical constrains for hidden photon and axion production and expectations for dark matter and dark radiation (for hidden photons) produced by hidden photons (figures adapted from [3]).

of 2×10^{-14} eV [10, 11]. Dedicated radio astronomical measurements at frequencies below 22 GHz should extend axion searches to masses below 10^{-9} eV and probe coupling constants down to $10^{-14}\,\mathrm{GeV}^{-1}$ [12]. Signals from relic DM axions can be detected in the spectra of isolated neutron stars [8] and possibly also in pulsars.

2.1 Hidden photon signals in compact radio sources

For hidden photons (γ_s), radio observations at frequencies below 22 GHz offer an excellent (if not unique) tool for placing bounds on the mixing angle χ for m_{γ_s} down to $\approx 10^{-18}$ eV [9]. Existing data are sufficiently accurate for detection of kinetic mixing angles χ down to ~ 0.01, yielding presently a weak hint for a possible oscillatory signal with $\chi \approx 0.02$ in the 2–5 $\times\, 10^{-16}$ eV energy range. As adverse systematic effects mimicking the signal cannot be presently excluded, this indication should be verified. Placing better bounds on χ down to $\lesssim 10^{-3}$ can be made by using the expanded capabilities of the next generation radio astronomical facilities [9].

3 Laboratory experiments

Laboratory experiments using resonant microwave cavities at frequencies between 0.5 and 34 GHz have yielded the best sensitivity achieved for HP and ALP dark matter at masses below 10^{-3} eV [13]. While capable of reaching the fundamental sensitivity levels, these experiments are slow in scanning over large ranges of mass. Novel and fast broadband measurement techniques are critically needed here.

3.1 Microwave cavity experiments

Building on the success of the ADMX axion DM searches [5, 6, 13] covering the 2-5 μeV energy range, a WISP Dark Matter eXperiment has been initiated at DESY and the University of Hamburg, aiming at covering the 0.8-2 μeV energy range. The experiment utilizes a 208-MHz resonant cavity used at the DESY HERA accelerator and plans to make use of the H1 solenoid magnet. The cavity has a volume of 460 liters and a resonant amplification factor $Q = 46000$ at the ground TM_{010} mode. The H1 magnet provides $B = 1.15$ T in a volume of 7.2 m^3. The signal is amplified by a broad-band 0.2–1 GHz amplifier with a system temperature of 100 K. Broad-band digitization and FFT analysis of the signal are performed using a commercial 12-bit spectral analyzer, enabling measuring at several resonant modes simultaneously.

Since the bandwidth of a single measurement is $\propto Q^{-1}$, the resonant modes of the cavity must be tuned in order to enable scanning over a sizable range of particle mass. The tuning will be done with a plunger assembly providing a ~ 2 MHz tuning range at the ground mode. The expected exclusion limits are shown in Fig. 1.

3.2 Experimental concepts for broad-band searches

The exceptional sensitivity of microwave cavity experiments comes at the expense of rather low scanning speeds (~ 10 MHz/year for WISPDMX), which makes it difficult to implement this kind of measurements for scanning over large ranges of particle mass. To overcome this difficulty, new experimental concepts are being developed that could relax the necessity of using the resonant enhancement and working in a radiometer mode with an effective $Q = 1$.

The measurement bandwidth of radiometry experiments is limited only by the detector technology, with modern detectors employed in radio astronomy routinely providing bandwidths in excess of 1 GHz and spectral resolutions of better than 10^6.

One possibility for a radiometer experiment is to employ a spherical dish reflector that provides a signal enhancement proportional to the area of the reflector [7]. Another possibility is to use the combination of large chamber volume and strong magnetic field provided by superconducting TOKAMAKs or stellarators such as the Wendelstein 7-X stellarator in Greifswald (providing $B = 3\,T$ in a $30\,\mathrm{m}^3$ volume). The exclusion limits expected to be achievable with the spherical reflector and stellarator experiments are shown in Fig. 1.

Deriving from the stellarator approach, a large chamber can be designed specifically for the radiometer searches, with the inner walls of the chamber covered by fractal antenna elements providing a broad-band receiving response and also enabling directional sensitivity to the incoming photons (through high time resolution enabling phase difference measurements between individual elements).

Further exploration of these approaches should ultimately enable performing definitive searches for hidden photon and axion/ALP dark matter in the 10^{-7}–$10^{-3}\,\mathrm{eV}$ mass range.

Acknowledgments

Andrei Lobanov acknowledges support from the Collaborative Research Center (Sonderforschungsbereich) SFB 676 “Particles, Strings, and the Early Universe” funded by the German Research Society (Deutsche Forschungsgemeinschaft, DFG).

References

[1] J. Jaeckel and A. Ringwald, Ann. Rev. Nucl. Part. Sci. **60** (2010) 405 [arXiv:1002.0329 [hep-ph]].

[2] A. Ringwald, Phys. Dark Univ. **1**, 116 (2012) [arXiv:1210.5081 [hep-ph]].

[3] J.L. Hewett, H. Weerts, R. Brock *et al.*, arXiv:1205.2671 [hep-ex].

[4] P. Arias, D. Cadamuro, M. Goodsell, *et al.*, JCAP **1206**, 013 (2012) [arXiv:1201.5902 [hep-ph]].

[5] [ADMX Collaboration], S. J. Asztalos *et al.*, Phys. Rev. Lett. **104**, 041301 (2010) [arXiv:0910.5914 [hep-ex]].

[6] A. Wagner, G. Rybka, M. Hotz *et al.*, Phys. Rev. Lett. **105**, 171801 (2010) [arXiv:1007.3766 [hep-ex]].

[7] D. Horns, J. Jaeckel, Lindner, A. *et al.*, JCAP **4**, 016 (2013) [arXiv:1212.2970 [hep-ph]].

[8] M.S. Pshirkov, S.B. Popov, JETP **108**, 384 (2009) [arXiv:0711.1264 [astro-ph]].

[9] A.P. Lobanov, H.-S. Zechlin, D. Horns, Phys. Rev. D **87**, 065004 (2013) [arXiv:1211.6268 [astro-ph.co]]

[10] A. Mirizzi, J. Redondo and G. Sigl, JCAP **0908**, 001 (2009) [arXiv:0905.4865 [hep-ph]].

[11] A. Mirizzi, J. Redondo and G. Sigl, JCAP **0903**, 026 (2009) [arXiv:0901.0014 [hep-ph]].

[12] D. Chelouche, R. Rabadán, S.S. Pavlov, F. Castejón, ApJSS **180**, 1 (2009) [arXiv:0806.0411 [astro-ph]].

[13] R. Bradley, J. Clarke, D. Kinion *et al.*, Rev. Mod. Phys. **75**, 777 (2003).

Constraining ALPs with linear and circular Polarisation Measurements of Quasar Light

A. Payez

IFPA group, AGO Dept., University of Liège, Liège, Belgium
Deutsches Elektronen-Synchrotron (DESY), Hamburg, Germany

DOI: http://dx.doi.org/10.3204/DESY-PROC-2013-04/payez_alexandre

We discuss the constraints derived on the mixing of photons with light pseudoscalars using the distributions of good-quality linear and circular polarisation measurements of light from the least polarised classes of quasars. We also provide the dependence of our limit on the average electron density in the local supercluster for nearly massless particles.

1 Introduction

In theoretical extensions of the Standard Model, all the new particles are not necessarily on the heavy side; the prediction of very light (sub-eV) scalar or pseudoscalar particles that are very weakly interacting is actually quite generic. Looking for signatures of such "axion-like particles" (or ALPs) therefore represents another exciting possibility to probe the kind of physics there can be at very high scales, associated with these new degrees of freedom, which is complementary to collider searches. It is thus not surprising that a lot of ongoing effort is made to scan the parameter space of these hypothetical particles, actively searched for mostly via their electromagnetic coupling. Current experimental developments include for instance light-shining-through-a-wall experiments such as ALPS, which is being upgraded [1], or projects of next-generation helioscopes such as the International Axion Observatory [2].

Due to their mixing with photons, these spinless particles are moreover not only of interest in particle physics but also in astrophysics, as their existence would change the properties and the propagation of light emitted from distant sources. A sizeable signal could be expected as the distances involved are huge, even if the ALPs are only coupled very weakly. In this context, various phenomena have in fact already been interpreted as possible astrophysical hints for the existence of ALPs, especially in the low-mass region of the parameter space: namely ALPs with masses $m \lesssim 10^{-9}$ eV and couplings to photons $g \sim 10^{-12}$–10^{-11} GeV^{-1}. For a recent summary of the motivations for these particles from theory and of their implications, see Refs. [3, 4, 5] and references therein.

In this work [6], we consider light coming from quasars. The fact that these high-luminosity active galactic nuclei (AGN) are among the brightest and furthest steady light sources known in the Universe makes them particularly appealing to look for signals of ALPs and to constrain their parameter space. We focus on the window of astrophysical interest and show that constraints can be derived using both linear and circular polarisation data.

2 What polarisation can tell us

Polarimetry is an extremely valuable tool to search for axion-like particles as the interaction of these particles with photons, in external magnetic fields for instance, would change the polarisation of light [7, 8, 9]. Suitable interaction Lagrangians read

$$\begin{aligned} \mathcal{L}_{\phi\gamma\gamma} &= \frac{1}{4}\, g\phi F_{\mu\nu}\widetilde{F}^{\mu\nu} = -g\phi(\vec{E}\cdot\vec{B}) \text{ for pseudoscalar } \phi, \\ \text{and } \mathcal{L}_{\phi\gamma\gamma} &= \frac{1}{4}\, g\phi F_{\mu\nu}F^{\mu\nu} = \frac{1}{2}\, g\phi(\vec{B}^2-\vec{E}^2) \text{ for scalar } \phi, \end{aligned} \tag{1}$$

and lead to similar phenomenological consequences; henceforth we focus on pseudoscalars. In a nutshell, one expects from the mixing that even unpolarised light will develop a non-vanishing degree of linear polarisation and that, in general, linear and circular polarisation will convert at least partially into one another as a consequence of phase-shifts induced by the mixing.[1] As is well-known and readily seen from Eq. (1), this is because, in an external magnetic field, such spinless particles only couple to one direction of polarisation [10].

The mixing can actually be very efficient at modifying polarisation and can therefore be constrained by precise measurements. The limits derived from the absence of rotation of the linear polarisation of UV light from AGN [11] are a recent example of this.

In this work, we follow a different idea, which is to consider the spectroscopically defined quasar classes known to have the smallest intrinsic polarisations in visible light, and to compare the predictions of the mixing with observations. As already discussed by Harari and Sikivie in Ref. [9], light from distant sources should be characterised by at least some amount of polarisation if axion-photon mixing happens along the way. We do this for both linear ($p_{\rm lin}$) and circular ($p_{\rm circ}$) polarisation.

Quasar polarisation measurements at optical wavelengths can be found in the literature with uncertainties below 0.1%. Light from quasars is known to be intrinsically linearly polarised, as differences can be seen in different spectroscopic types, and the polarisation is at the 1%-level for the least polarised ones. If there are many catalogs of linear polarisation measurements, the same cannot be said about circular polarisation: it has rarely been studied, despite being measured in the same way as the linear one by simply adding a quarter-wave retarder plate. Following the predictions of the mixing, new dedicated observations of quasar circular polarisation in visible light have therefore been carried out [12]. For observational reasons, most of the objects are located towards the North Galactic Pole direction, which points to the center of the local supercluster; see *e.g.* [13]. No evidence for non-vanishing circular polarisation could be found at the 3σ-level however [12].[2]

We will not repeat here the discussion leading to our subsample ($p_{\rm lin}$ and $p_{\rm circ}$) or the method used to obtain our limits, as all the necessary details can be found in Ref. [6]. Let us simply emphasise again that we have aimed at being as conservative as possible: taking only into account the influence of the magnetic field in the supercluster, allowing the magnetic field to get a longitudinal component most of the time (and allowing other quantities to fluctuate), as well as considering initially unpolarised light to make sure that the final polarisation due to the mixing is not overestimated for example.

[1] There are different regimes, with distinctive properties; more details can be found for instance in Ref. [3].

[2] That is, except for some highly linearly polarised blazars which could be intrinsically circularly polarised: as for radio waves, their optical emission would mostly be due to beamed synchrotron radiation from ultra-relativistic electrons rather than to the usual thermal emission from the accretion disc; see, *e.g.* Refs. [12, 14].

Using a conservative method leading to robust results, we can safely say that the mixing of light with axion-like particles is strongly constrained by the good-quality measurements of polarisation, and especially of circular polarisation, even when bandwidth effects are taken into account [15]. However this might say something about the magnetic fields or the electron density, and not about ALPs. This is why we provide here the evolution of our limit with the maximum transverse magnetic field strength and with the mean electron density.

The only reported detection available in the literature for the magnetic field in the local supercluster plane favours a collection of ~ 2 μG magnetic field domains that are coherent over ~ 100 kpc [16], averaging to a field 5–10 times weaker at the supercluster scale. If we use this result, the 2σ-limit we obtain is $g < 2.5 \times 10^{-13}$ GeV^{-1} for $m < 4.2 \times 10^{-14}$ eV; as emphasised in our paper [6], this limit can however be easily rescaled for any other value of the magnetic field strength as it always appears together with the coupling constant in the equations.

On the other hand, in order to give the evolution of our limit with the average electron density, we can take advantage of the fact that, for ALP masses much smaller than the plasma frequency

$$\omega_{\rm p} = 3.7 \times 10^{-14}\ {\rm eV} \times \sqrt{\frac{n_{\rm e}}{10^{-6}\ {\rm cm}^{-3}}}, \tag{2}$$

the two dimensionless quantities that determine the evolution of the Stokes parameters then become independent of m, leading to a plateau [6]. Here, we give in Fig. 1 the evolution of this plateau for various values of the average electron density $n_{\rm e,0}$; the case illustrated in the paper [6] is given by $n_{\rm e,0} = 10^{-6}$ cm^{-3}, which is the value usually considered in superclusters. The information is summarised by saying that points in the parameter space are excluded at 1σ, 2σ and 3σ when the average probability that they contradict the observations is respectively 68.3%, 95.5% and 99.7%. As anticipated in the paper, the limits on the coupling constant g for nearly massless pseudoscalars would be more stringent for values of the plasma frequency smaller than the one we have considered, which reflects the fact that the mixing then becomes more efficient. Conversely, if the electron density in the local supercluster were to actually be much higher than that, then no constraint could be put on such particles as the mixing would then simply not take place in that medium.

Acknowledgments

We thank the IFPA group for the financial support received to attend this workshop, and acknowledge useful discussions with Jean-René Cudell and Damien Hutsemékers.

References

[1] R. Bähre, B. Döbrich, J. Dreyling-Eschweiler, S. Ghazaryan, R. Hodajerdi, D. Horns, F. Januschek and E.-A. Knabbe *et al.*, JINST **1308** (2013) T09001 [arXiv:1302.5647 [physics.ins-det]].

[2] J. K. Vogel, F. T. Avignone, G. Cantatore, J. M. Carmona, S. Caspi, S. A. Cetin, F. E. Christensen and A. Dael *et al.*, arXiv:1302.3273 [physics.ins-det].

[3] A. Payez, Ph.D. thesis, arXiv:1308.6608 [astro-ph.CO]. See the Introduction and Chap. 1.

[4] K. Baker, G. Cantatore, S. A. Cetin, M. Davenport, K. Desch, B. Döbrich, H. Gies and I. G. Irastorza *et al.*, Annalen Phys. **525** (2013) A93 [arXiv:1306.2841 [hep-ph]].

[5] A. Ringwald, Phys. Dark Univ. **1** (2012) 116 [arXiv:1210.5081 [hep-ph]].

[6] A. Payez, J.R. Cudell and D. Hutsemékers, JCAP **1207** (2012) 041 [arXiv:1204.6187 [astro-ph.CO]].

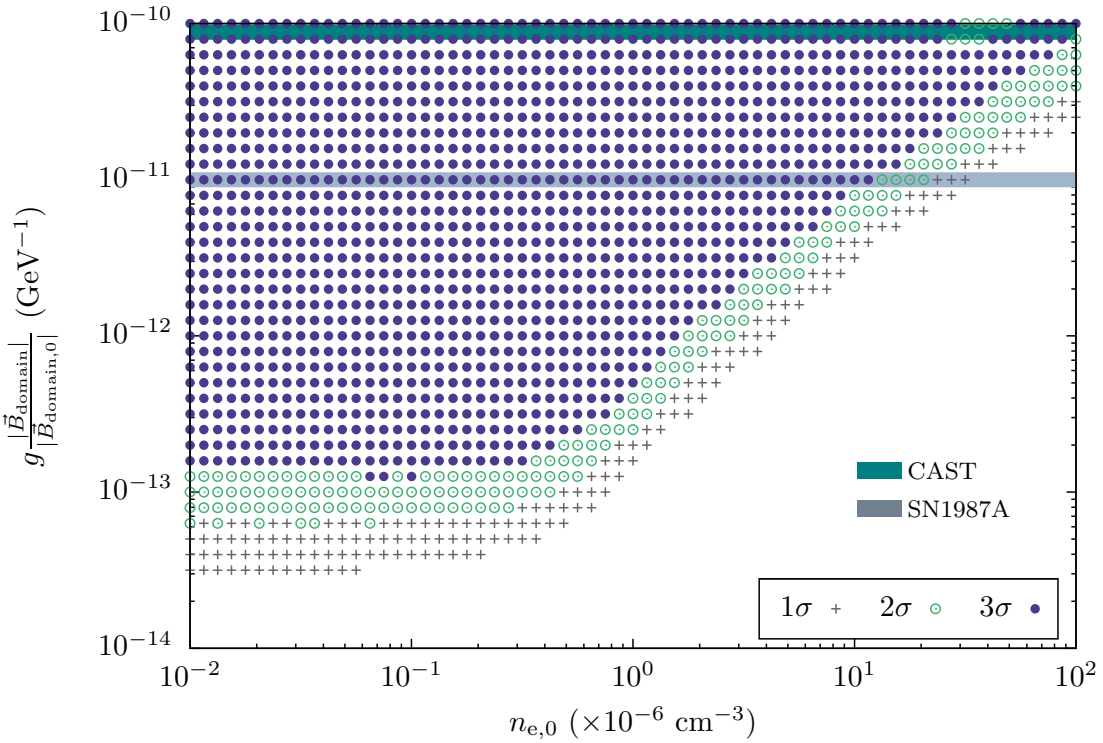

Figure 1: Dependence of the plateau corresponding to $m^2 \lll {\omega_{\rm p}}^2$ on the average electron density. The maximum transverse magnetic strength used here is $|\vec{B}_{\rm domain,0}| = 2\ \mu$G.

[7] L. Maiani, R. Petronzio and E. Zavattini, Phys. Lett. B **175** (1986) 359.

[8] G. Raffelt and L. Stodolsky, Phys. Rev. D **37** (1988) 1237.

[9] D. Harari and P. Sikivie, Phys. Lett. B **289** (1992) 67.

[10] P. Sikivie, Phys. Rev. Lett. **51** (1983) 1415 [Erratum-ibid. **52** (1984) 695].

[11] D. Horns, L. Maccione, A. Mirizzi and M. Roncadelli, Phys. Rev. D **85** (2012) 085021 [arXiv:1203.2184 [astro-ph.HE]]; S. d. S. Alighieri, F. Finelli and M. Galaverni, Astrophys. J. **715** (2010) 33 [arXiv:1003.4823 [astro-ph.CO]].

[12] D. Hutsemékers, B. Borguet, D. Sluse, R. Cabanac and H. Lamy, Astron. Astrophys. **520** (2010) L7 [arXiv:1009.4049 [astro-ph.CO]].

[13] H. M. Courtois, D. Pomarède, R. B. Tully, Y. Hoffman, and D. Courtois, Astron. J. **146** (2013) 69 [arXiv:1306.0091 [astro-ph.CO]].

[14] J. Tinbergen, Astrophys. Space Sci. **288** (2003) 3.

[15] A. Payez, J.R. Cudell and D. Hutsemékers, Phys. Rev. D **84** (2011) 085029 [arXiv:1107.2013 [astro-ph.CO]].

[16] J. P. Vallée, New Astron. Rev. **55** (2011) 91.

Very-high-energy quasars hint at ALPs

M. Roncadelli[1], *G. Galanti*[2], *F. Tavecchio*[3], *G. Bonnoli*[4]

[1]INFN, Pavia, Italy
[2]Università dell'Insubria, Como, Italy
[3]Osservatorio di Brera-INAF, Milano, Italy
[4]Osservatorio di Brera-INAF, Milano, Italy

DOI: http://dx.doi.org/10.3204/DESY-PROC-2013-04/roncadelli_marco

One of the mysteries of very-high-energy (VHE) astrophysics is the observation of flat spectrum radio quasars (FSRQs) above about 30 GeV, because at those energies their broad line region should prevent photons produced by the central engine to escape. Although a few astrophysical explanations have been put forward, they are totally *ad hoc*. We show that a natural explanation emerges within the conventional models of FSRQs provided that photon-ALP oscillations take place inside the source for the model parameters within an allowed range.

1 Why do VHE quasars exist?

With the advent of Imaging Atmospheric Cherenkov Telescopes (IACTs) H.E.S.S., MAGIC, VERITAS and CANGAROO III (the last one is not anymore operative) the VHE astrophysics has undergone a stunning development. Among the many discoveries, a remarkable one is that active galactic nuclei (AGN) emit photons up to energies of a few TeV.

Before proceeding further, let us recall the basic properties of AGN. Basically, they are supermassive black holes (SMBHs) at the centre of elliptical galaxies. While observations have shown that SMBHs are hosted at the centre of both spiral and elliptical galaxies, in the former case they tend to be quiescent while in the latter one they are often active, namely they accrete matter which emits at all frequencies. Observations entail that such an emission is non-thermal, and two possible mechanisms have been envisaged. One is leptonic in nature, and usually called *synchro-self Compton* mechanism (SSC): owing to the presence of a magnetic field, relativistic electrons emit synchrotron radiation, and these photons acquire much larger energies by inverse Compton scattering off the parent electrons. In some cases also external electrons are responsible for the latter process. The resulting spectral energy distribution (SED) $\nu F_\nu \propto E^2\, dN/dE$ has two peaks: the synchrotron one located somewhere from the IR to the X-ray band, while the inverse Compton peak lies in the γ-ray band around 50 GeV. The other emission mechanism is hadronic: the situation is the same for synchrotron emission, but the gamma peak is produced by hadronic collisions so that also neutrinos are emitted. In either case – because the SMBHs is generally rotating – it is surrounded by an accretion disk and the emission is strongly beamed in the direction perpendicular to the disk, which gives rise to two jets. As a consequence, they can be detected only when one of the jets points towards us. It has become customary to call *blazars* the AGN which are in such a configuration. This is

schematically shown in Fig. 1.

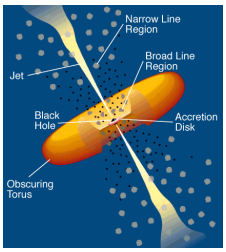

Figure 1: Schematic structure of an AGN.

As a matter of fact, blazars are commonly divided into two classes, depending on whether or not the broads line region (BLR) – at about 1 pc from the centre – is present or not. In the former case the blazar is called *flat spectrum radio quasar* (FSRQ), whereas in the latter case it is named BL LAC (this nomenclature is due to historical reasons). We remark that the BLR gives rise to broad optical lines, which where detected when the first quasars were discovered. Such a difference is very important for VHE astrophysics. In fact, in the BLR there is a huge density of ultraviolet photons so that the very-high-energy (VHE) photons ($E > 30\,\mathrm{GeV}$) produced at the jet base undergo the process $\gamma\gamma \to e^+e^-$, thereby disappearing from the spectrum. As a result, FSRQs should be invisible in the VHE band, as the optical depth depicted in Fig. 2 eloquently shows.

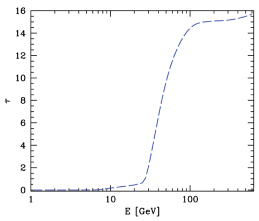

Figure 2: Energy behaviour of the optical depth in the BLR according to conventional models.

However observations tell us that this is *not* true. For, at least 3 FSRQs have been detected by the IACTs in the energy range $100\,\mathrm{GeV} - 1\,\mathrm{TeV}$: PKS 1222+216, 3C 279 and PKS 1510-089. And their fluxes are similar to those of the BL LACs! So, what is going on?

Actually, the most striking case is that of PKS 1222+216 which has been observed simultaneously by *Fermi*/LAT in the band $0.3 - 3\,\mathrm{GeV}$ and by MAGIC in the band $70 - 400\,\mathrm{GeV}$. In addition, MAGIC has detected a flux doubling in about 10 minutes, which implies that the emitting region has size of about 10^{14} cm, but the observed flux is similar to that of a BL LAC. Thus, we have to face *two* problems at once!

Various astrophysical solutions have been proposed, but all of them are totally *ad hoc*, even because one has to suppose that a blob with size 10^{14} cm at a distance of more than 1 pc from the centre exists with the luminosity of a whole BL LAC!

2 Photon-ALP oscillations

Nowadays our understanding of particle physics is based on the Standard Model (SM), which not only explains an enormous amount of data but has turned out to be fully correct with the discovery of the Higgs boson. Yet, it cannot be regarded as the ultimate theory. Apart from leaving the elementary particle masses and mixing angles as free parameters and ignoring gravity, it fails to provide any explanation for cold non-baryonic dark matter needed e.g. to explain cosmic structure formation, as well as for dark energy which presumably triggers the present accelerated cosmic expansion. A generic prediction of many attempts towards the development of a final theory – like supersymmetric models, Kaluza-Klein theories and especially superstring theories – is the existence of very light pseudo-scalar bosons characterized by a two-photon coupling, called *axion-like particles* (ALPs) due to their analogy with the axion.

As far as our analysis is concerned, the ALP Lagrangian has the form

$$\mathcal{L}^0_{\rm ALP} = \frac{1}{2}\,\partial^\mu a\,\partial_\mu a - \frac{1}{2}\,m^2\,a^2 + \frac{1}{M}\,\mathbf{E}\cdot\mathbf{B}\,a + \frac{2\alpha^2}{45m_e^4}\,\left[\left(\mathbf{E}^2-\mathbf{B}^2\right)^2 + 7\,(\mathbf{E}\cdot\mathbf{B})^2\right] \qquad (1)$$

where a is the ALP field, the last term is the Heisenberg-Euler-Weisskopf effective Lagrangian accounting for the photon one-loop vacuum polarization in the presence of an external magnetic field (α is the fine-structure constant and m_e is the electron mass), m is the ALP mass and M is a constant with the dimension of an energy. We stress that the parameters m and M are assumed to be *uncorrelated*, and it is merely supposed that $m < 1\,\text{eV}$ and $M \gg G_F^{-1/2}$ with $G_F^{-1/2} \simeq 250\,\text{GeV}$ denoting the Fermi scale. The only robust available bound on M comes from the CAST experiment and reads $M > 10^{10}\,\text{GeV}$.

In the presence of an external magnetic field, the two-photon coupling produces a mismatch between the interaction eigenstates and the propagation eigenstates, thereby giving rise to the phenomenon of photon-ALP oscillations.

3 A natural ALP-based explanation

Our idea is remarkably simple. We assume that photons are produced by a standard emission model like the SSC at the jet base as in BL LACs, but that ALPs exist. Then photons can become mostly ALPs *before* reaching the BLR in the jet magnetic field. As a result, ALPs can go unimpeded through the BLR – because $\sigma(a\gamma \to e^+e^-) \sim \alpha/M^2 < 10^{-50}\,\text{cm}^2$ – and *outside* it they can reconvert into photons in the outer magnetic field. Because of lack of space, we cannot report the calculations which can be found in our original work [1], but we have found that the best choice to reduce the photon absorption by the BLR is $B = 0.2\,\text{G}$, $M = 7\cdot 10^{10}\,\text{GeV}$ and $m < 10^{-9}\,\text{eV}$. This choice leads to the results exhibited in Fig. 3.

However, this is not enough. For, we have supposed that photons are produced by a standard emission mechanism. Moreover, PKS 1222+216 has been simultaneously observed by *Fermi*/LAT and MAGIC. So, we should pretend that the detected photons have a *standard* SED, namely that both data sets lie on the same inverse Compton peak. This requirement is *a priori* not guaranteed, since in the presence of absorption and one-loop QED effects the photon-ALP conversion probability is *energy-dependent*. Nevertheless, it turns out that a standard two-blob emission model with realistic values for the parameters yields the SED shown in the right panel of Fig. 3. Hence, we see that the *Fermi*/LAT and MAGIC data indeed lie on the same inverse Compton peak.

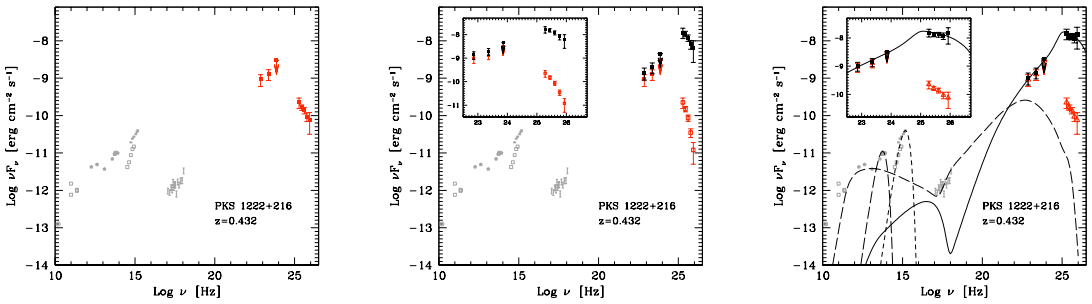

Figure 3: Left panel: red triangles at high and VHE are the spectrum of PKS 1222+216 recorded by *Fermi*/LAT and the one detected by MAGIC but EBL-deabsorbed according to conventional physics. Central panel: red triangles are the same as before, while black squares represent the same data once further corrected for the photon-ALP oscillation effect. Right panel: red triangles and black squares are the same as before, whereas the solid black line is the SED of our model (the other points and broken lines should be presently ignored).

Needless to say, our scenario naturally applies also to the other FSRQs detected at VHE.

It looks tantalizing that just the most favorable choice of the parameters mentioned above corresponds to the most favorable case for a large-scale magnetic field of $B = 0.7\,\mathrm{nG}$ in the DARMA scenario that enlarges the "γ-ray horizon" and provides a natural solution to the cosmic opacity problem (it requires $m < 1.7 \cdot 10^{-10}\,\mathrm{eV}$ which is consistent with the present choice) [2]. Moreover, this kind of ALP is a good candidate for cold dark matter [3].

Obviously the CTA will provide a crucial test of our model, but it is remarkable that a laboratory check will be performed with the planned upgrade of the photon regeneration experiment ALPS at DESY and with the next generation of solar axion detectors like IAXO.

4 Acknowledgments

M. R. acknowledges the INFN grant TAsP (ex FA51).

References

[1] F. Tavecchio, M. Roncadelli, G. Galanti and G. Bonnoli, Phys. Rev. D **86**, 085036 (2012).

[2] A. De Angelis, G. Galanti and M. Roncadelli, Phys. Rev. D **84**, 105030 (2011); Err. D **87**, 109903 (2013).

[3] P. Arias *et al.*, JCAP **06** 013 (2012).

Constraints on axion-like Particles from the high-energy Universe

D. Wouters

CEA, Irfu, Centre de Saclay, F-91191 Gif-sur-Yvette, France

DOI: http://dx.doi.org/10.3204/DESY-PROC-2013-04/wouters_denis

The interaction of axion-like particles (ALPs) with two photons enable the oscillations between photons and ALPs in an external magnetic field. This interaction modify the energy spectrum of astrophysical sources under the form of an irregular behavior in a limited energy range. This signature is searched in the high-energy spectra of active galactic nuclei to put stringent constraints on the ALP coupling to photons.

1 Introduction and phenomenology

Axions are hypothetical new light bosons, theoretically introduced to solve the strong CP problem [1]. Axions generically couple to two photons, with their coupling strength proportional to their mass. More general light particles with the same coupling to photons but their mass and coupling unrelated are also a prediction from some string theories [2] and are considered as a possible constituent of dark matter. Such particles are called axion-like particles (ALPs). Because of the coupling between photons and ALPs, a photon can oscillate into an ALP in an external magnetic field and vice-versa, in a way similar to the neutrino flavor oscillation case. The probability of conversion of a photon into an ALP in an homogeneous magnetic field of strength B over a distance s is [3]:

$$P_{\gamma\to a} = \frac{1}{2}\frac{1}{1+E_c^2/E^2}\sin^2\frac{g_{\gamma a}Bs}{2}\sqrt{1+E_c^2/E^2} \ , \tag{1}$$

where $g_{\gamma a}$ is the coupling strength and $E_c = m^2/2g_{\gamma a}B$ is the energy threshold of the photon/ALP mixing and depends on the mass m of the ALP. For coupling strength close to the current upper limit set by the CAST experiment, $g_{\gamma a} = 5\times10^{-11}\mathrm{GeV}^{-1}$ and a magnetic field strength of 1 μG typical of galaxy clusters magnetic fields, the energy threshold is of the order of 1 TeV for ALP masses close to 1 μeV. In this study, the initial photon beam is assumed to be unpolarized, so that the conversion probability cannot be lower than 0.5.

If the magnetic field is turbulent, as it is generally the case for astrophysical magnetic fields, the conversion probability has a very complex energy behavior around the energy threshold [4]. The stochastic nature of the magnetic field translates to an irregular behavior on the conversion probability that is not predictable and depends on the specific realization of the magnetic field. An example of such modification is shown on Fig. 1 for the same ALP parameters than above and a magnetic field strength of 1 μG. The lower panel shows the same signal smeared by the energy resolution of H.E.S.S., of the order of 12%.

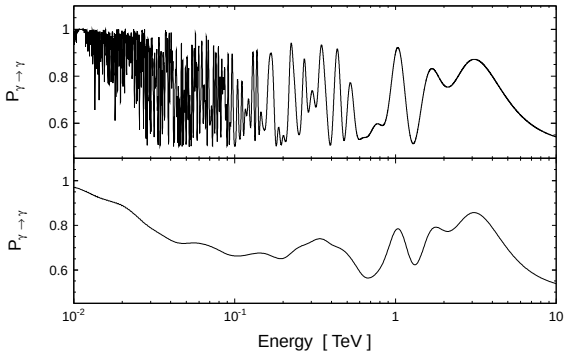

Figure 1: Typical modulation from an ALP signal with $E_c \sim 1$ TeV. Top panel : raw function. Bottom panel : Same function smeared with the energy resolution and bias of H.E.S.S.

2 Constraints from observations with H.E.S.S.

In order to identify possible anomalous deviations in the spectrum, a bright source with a large statistics is required. The brightest extragalactic source observed by H.E.S.S. is the active galactic nuclei PKS 2155-304. A strong flare has been observed in July 2006 where the flux reached levels of 7 time the flux of the Crab Nebula. Because of the high luminosity of the source during the flare the background is negligible.

A crucial point for the search of an ALP signal is a good knowledge of the magnetic field involved in the photon-ALP mixing. In the case of PKS 2155-304 a galaxy cluster of radius 370 kpc is observed. Galaxy cluster are hosts of strong magnetic fields that can be probed by Faraday rotation of the polarization axis in radio. Such measurements show that the magnetic field strength is of order of 1-10 μG [5]. The turbulence power spectrum can also be estimated with Faraday rotation [6]. Studies on the Hydra A cluster obtained a power spectrum compatible with a Kolmogorov spectrum with a maximal turbulence scale of 10 kpc. The magnetic field in the galaxy cluster of PKS 2155-304 cannot be probed via Faraday rotation since the radio lobes are aligned on the line of sight. In the following a minimal value for the magnetic field strength of 1 μG is assumed. The turbulence power spectrum is assumed to follow a Kolmogorov spectrum with a coherence length of 10 kpc. Constraints will be derived with this conservative description of the magnetic field. For the intergalactic magnetic field (IGMF), no measurements have been possible so far. The current upper limit is of 1 nG for coherence scales of order 1 Mpc. Optimistic constraints with this description of the IGMF are also derived. They are independent from the constraints derived with the cluster magnetic field because of the different values of the magnetic field strength.

The spectrum measured by H.E.S.S. during the flare, shown on the Fig. 2 of [7], does not show any evidence of an irregular behavior. Constraints on the ALP coupling are derived on a statistical basis where MC simulations of the spectrum with an ALP signal are produced. To estimate the minimal sensitivity to irregularities, an irregularity estimator is built that measure the fluctuations from bins to bins assuming that the intrinsic spectrum locally follows a power law shape on scales of three bins. The constraints derived with this method are shown on Fig. 2 for conversion in the galaxy cluster magnetic field and in the IGMF. The range of mass probed

by the different conversion domains is determined by the magnetic field strength so that the energy threshold of the mixing lies in the energy range of H.E.S.S.

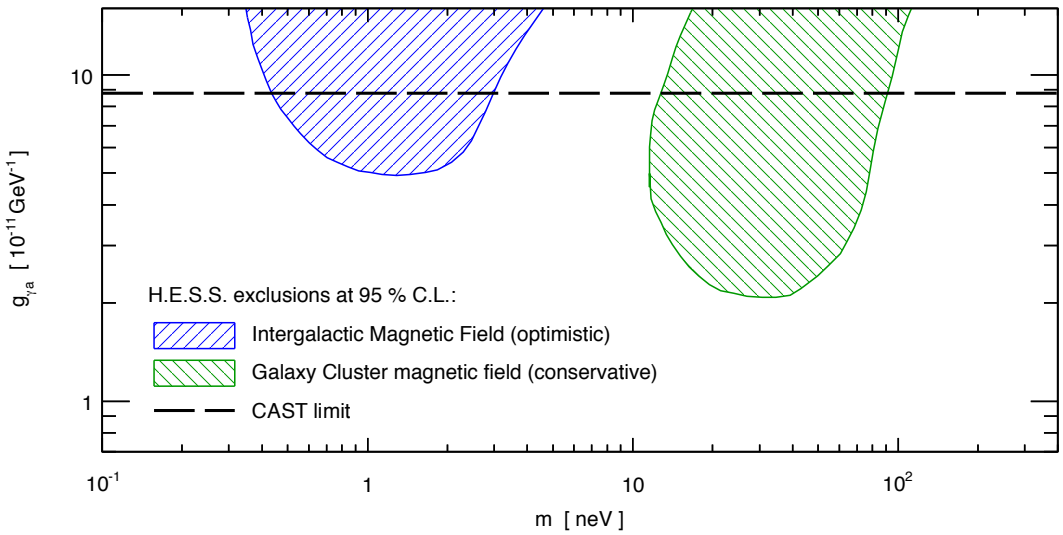

Figure 2: H.E.S.S. exclusion limits on the ALP parameters $g_{\gamma a}$ and m. The blue dashed region on the left is obtained considering γ-ALP mixing in the IGMF with in an optimistic scenario with a 1 nG strength. The green dashed region on the right is obtained considering γ-ALP mixing in the galaxy cluster of PSK 2155-304.

3 Constraints from X-ray observations

If the photon/ALP oscillations occur in an astrophysical plasma, the energy threshold of the mixing is modified: $E_c = |m_\gamma^2 - m^2|/2g_{\gamma a}B$ by taking into account the effective mass of the photon in the plasma, $m_\gamma^2 = 4\pi\alpha n_e/m_e$. Typically, the electron density of the plasma n_e in a galaxy cluster is of order of 0.01 cm^{-3}. The corresponding effective mass of the photon is $m_\gamma \sim 10^{-12}$ eV. In the case of the H.E.S.S. analysis, the range of mass probed is orders of magnitudes higher so that the effect of the plasma is negligible. For $m < m_\gamma$, the energy threshold is independent of m and is around a few keV for electron density typical of galaxy clusters. Observations in X-rays are therefore sensitive to irregularities caused by the energy threshold set by the effective mass of the photons propagating in the galaxy cluster plasma.

A good candidate source for this analysis is a bright point-like source embedded in a galaxy cluster. In order to minimize uncertainties from the lack of knowledge on the magnetic field, the magnetic field in the galaxy cluster should be measured. The magnetic field of the Hydra A galaxy cluster has been extensively measured by Faraday rotation and a good knowledge of the electron density profile and turbulence power spectrum is available. A Fanaroff-Riley I radio galaxy lies at the center of the cluster and has been observed by *Chandra* with a low angular resolution enabling the collection of a large statistics on the source. A conservative description for the magnetic field of the galaxy cluster is assumed, following the results of [6] for a jet

viewing angle of 30°. In this model, the magnetic field strength at the centre of the cluster is 21 μG and the electron density is 0.056 cm^{-3}.

The spectrum of the central source observed by *Chandra* is reconstructed with observations in 1999 and 2003. Because of an important absorption system in Hydra A, the central source is only visible above 1 keV. The spectrum, shown on Fig. 1 of [8] is well fitted by a power-law moduled by the absorption system and does not show any anomalous irregularities. The exclusion is obtained by fitting simulated ALP signal on the spectrum. When the coupling strength is high enough, the spectrum with ALP signal significantly (95% C.L.) deteriorate the fit whatever the realization of the magnetic field is. The 95% C.L. exclusion is shown on Fig. 3. It extends to arbitrary small ALP masses because the energy threshold is in this case independent of the mass. When ALP masses higher than the effective photon mass are considered, the energy threshold is shifted towards higher energies and the sensitivity decreases. For ALP masses equal to the effective photon mass, the conversion is resonant and energy independent so that the sensitivity decreases.

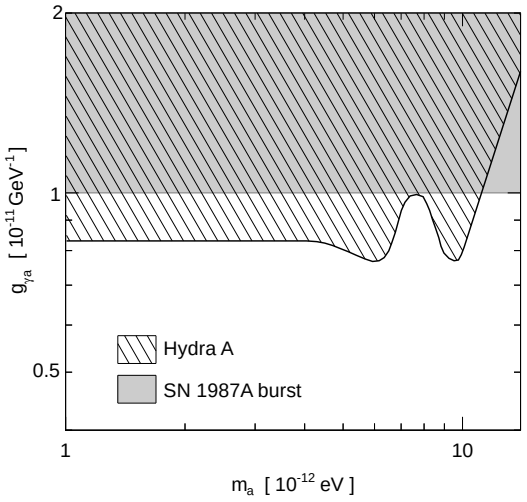

Figure 3: Exclusion limits on the ALP parameters $g_{\gamma a}$ and m from *Chandra* observations of the Hydra galaxy cluster.

References

[1] R. D. Peccei and H. R. Quinn, Phys. Rev. Lett. **38** (1977) 1440.

[2] A. Ringwald, Phys. Dark Univ. **1** (2012) 116 [arXiv:1210.5081 [hep-ph]].

[3] K. A. Hochmuth and G. Sigl, Phys. Rev. D **76** (2007) 123011 [arXiv:0708.1144 [astro-ph]].

[4] D. Wouters and P. Brun, Phys. Rev. D **86** (2012) 043005 [arXiv:1205.6428 [astro-ph.HE]].

[5] C. L. Carilli and G. B. Taylor, Ann. Rev. Astron. Astrophys. **40** (2002) 319 [astro-ph/0110655].

[6] C. Vogt and T. A. Ensslin, Astron. Astrophys. **434** (2005) 67 [astro-ph/0501211].

[7] D. Wouters *et al.* [HESS Collaboration], arXiv:1304.0700 [astro-ph.HE].

[8] D. Wouters and P. Brun, Astrophys. J. **772** (2013) 44 [arXiv:1304.0989 [astro-ph.HE]].

Chapter 4

Searches for Solar WISPs

Point-contact detectors in searches for bremsstrahlung production of axions from the Sun.

F.T. Avignone III and R.J. Creswick
Department of Physics and Astronomy, University of South Carolina, Columbia, SC 29208, USA

DOI: http://dx.doi.org/10.3204/DESY-PROC-2012-04/avignone_frank

The low-energy portion of the published spectrum of the COGENT experiment has been reanalyzed to search for evidence of low-energy bremsstrahlung-generated solar axions. In the case of the DFSZ model, an upper bound of $g_{ae} \leq 3.0 \times 10^{-11}$ (90% C.L.) is placed on the direct coupling of axions to electrons.

1 Introduction

The strong-CP problem has been with us for many years. The strong force described by QCD has a CP-violating term in the Lagrangian, the strength of which is fixed by a parameter θ. This parameter must be less than 10^{-10} for QCD to be consistent with the experimental bound,$|d_n| \leq 2.9 \times 10^{-26}$ e-cm for the electric dipole moment of the neutron[1]. The fact that the strong-interaction parameter, θ, must have such a small value is indeed unnatural. To address this problem, Roberto Peccei and Helen Quinn postulated a new global symmetry that is spontaneously broken at a high-energy scale[2]. This mechanism produces a term that cancels the problematic one. The properties of the Goldstone boson (the axion) resulting from this symmetry breaking were discussed in the context of the standard model in 1978 in independent articles by Weinberg[3] and by Wilczek[4].

The standard-model axion was ruled out by early experiments. However, to explain the lack of experimental observation, a model for the "invisible hadronic axion" was introduced by Kim[5], and also by Shifman, Vainstein and Zakharov[6], the KSVZ model. In this model, the axion couples directly to hadrons and photons but does not couple to electrons at the tree level. In the KSVZ model the axion and electron couple radiatively at the one-loop level.

Another model for an "*invisible axion*" was introduced by Zhitnitskii[7], and independently by Dine, Fischler and Srednicki[8], the DFSZ model. In this model the axion couples to hadrons and photons, and also to electrons at the tree level. In this paper we present a reanalysis of a previously published spectrum from the COGENT experiment[9] in order to place bounds on the coupling of DFSZ axions to electrons. We assume that the axions in question are produced by a bremsstrahlung-like process in the Sun and are detected with the axioelectric effect in the point-contact COGENT germanium detector. In this way the predicted rate depends only on the coupling of axions and electrons since both production and detection depend on the same coupling. The COGENT experiment was a search for cold dark matter with a well-shielded, ultra-low-background, point-contact germanium detector operated in an underground facility. All details can be found in reference[9] and references therein, and will not be discussed here.

2 Axion Phenomenology

The mass of the axion, m_a, (in eV) is connected to the Peccei-Quinn symmetry breaking scale, f_a, in both the DFSZ and KSVZ models by

$$m_a = \frac{f_\pi m_\pi}{f_a}\Big(\frac{z}{(1+z+w)(1+z)}\Big)^{1/2} \simeq 6.0(\text{eV})\frac{10^6(\text{Gev})}{f_a(\text{GeV})} \tag{1}$$

where, $f_\pi = 93$MeV is the pion decay constant,$z = m_u/m_d \simeq 0.56$ is the ratio of the masses of up and down quarks, and $w = m_u/m_s \simeq 0.029$ is the ratio of up and strange quark masses.

In this analysis we choose to use the form for the axion flux produced by a bremsstrahlung-like process in the Sun derived in a recent paper by Derbin et al.[10]. This expression differs somewhat from that derived by Kekez et al.[11]. The differential flux is

$$\frac{d\Phi}{dE} = 4.14\times10^{35} g_{ae}^2 E_a^{0.89} e^{-0.7E_a - 1.26\sqrt{E_a}} \text{cm}^{-2}\text{s}^{-1}\text{keV}^{-1} \tag{2}$$

where g_{ae} is the dimensionless coupling constant of axions to electrons, and E_a is the axion energy in keV. The cross section for the axioelectric absorption of very light, relativistic axions on electrons is also driven by g_{ae}. This expression was rederived by Pospelov, Ritz and Voloshin[12], and is a factor of two larger than the originally published expression[13, 14]. It can be conveniently expressed in terms of the photoelectric cross section,σ_{pe}, as follows:

$$\sigma_{ae} = \frac{\omega_a^2}{2\pi\alpha f_a^2}\sigma_{pe} \tag{3}$$

In the DFSZ model, the axion-electron coupling constant, g_{ae}, is related to the axion mass, m_a by[8]

$$g_{ae} = \frac{m_e}{3f_a}\cos^2\beta \tag{4}$$

where $\cos\beta$ is the ratio of Higgs expectation values[8], and it is customary to set $\cos^2\beta = 1$[10]. Combining equations (1) and (4) the relation between g_{ae} and f_a can be expressed $1/f_a = 5.87\times10^3 g_{ae}\text{MeV}^{-1}$. Equation (3) becomes

$$\sigma_{ae} = 7.72\times10^{-4} g_{ae}^2 E_a^2 \sigma_{pe} \tag{5}$$

Integrating the product of the axion flux, (2), with the cross section (5) over an energy interval between 0.45 keV $\leq E_a \leq$ 1.0 keV gives the rate

$$\int_{0.45}^{1.0}\frac{d\Phi}{dE_a}\sigma_{ae}dE_a = 2.505\times10^{-20}\text{axions/sec} \tag{6}$$

3 Data Analysis

We consider the low-energy portion of the COGENT spectrum published by Hooper et al.[9]. This spectrum was collected over 56 days with a point-contact, high-purity germanium detector with a fiducial mass of 0.33 kg. The energy range of the present analysis is from 0.45keV $\leq E_a \leq$ 1.0keV. A fit to the data including the x-ray peaks up to 3 keV is shown in Figure (3) of reference [9] and justifies the subtraction of 2 background counts from each 0.05 keV

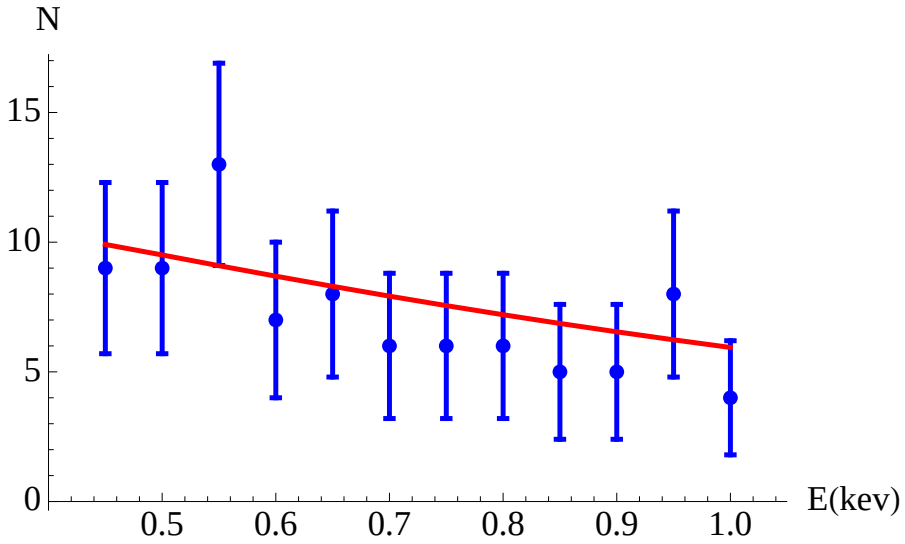

Figure 1: The experimental data with a constant 2 counts per 0.05 keV subtracted across the energy range 0.45 keV to 1.0 keV. This is justified from the fit to the data above the x-ray peaks shown in Figure 3 of ref. [9]. The red curve is a plot of the theoretical prediction for $g_{ae} = 2 \times 10^{-11}$.

bin. The portion of interest of the corrected spectrum is shown in Figure 1. The number of Ge atoms in the fiducial mass is $N = 2.74 \times 10^{24}$ and $t = 56$ days $= 4.84 \times 10^6$s which gives $Nt = 1.33 \times 10^{31}$ atom-s.

If we arbitrarily choose $g_{ae} = 10^{-10}$ and calculate the predicted axio-electric absorption rate of solar axions in the COGENT detector, we find $R = 7.95 \times 10^{28}$/atom-s.

The total number of predicted events in this scenario is 10595. There were only 85 candidate events in the experimental data, or less than 100 events with 90% C.L. If we make the conservative assumption that all the events in the energy interval 0.45keV $\leq E_a \leq$ 1.0keV are caused by axions we can place an upper limit

$$g_{ae} \leq 3.0 \times 10^{-11} \text{ 90\% C.L.} \tag{7}$$

This is similar the limit $g_{ae} \leq 5.4 \times 10^{-11}$ 90% C.L. obtained by the XMASS Collaboration with their 835-kg xenon detector running for 6 days[16]. It should also be pointed out that the data used in the present analysis are vastly lower in background at 0.5-keV than the data of XMASS[16], or from the that of reference[11]. The present 95% C.L. bound is similar to the 95% solar bound of Gondolo and Raffelt[17].

In the present case, the experimental spectrum and the predicted bremsstrahlung-like solar-axion spectrum are very similar. Therefore, it is appropriate to assume that all the counts in the spectrum above the flat 2 counts/0.05 keV from fitting the background at higher energy could be candidate events. For this reason, in searches for the continuous solar-axion spectra, it is most important to have the lowest background possible.

For experiments of this type to have discovery potential, it would be ideal to use the model-independent annual modulation in the sun-earth distance. The solar- axion flux is proportional

to $1/r^2$, which is 6.68% larger in January than in July. The analysis of the data from the MAJORANA Broad-Energy Detector at Kimallton, MALBEK, is being analyzed in this way by the MAJORANA Collaboration.[19]

Acknowledgments

The authors are supported by the National Science Foundation under Grants PHY-0855314 and PHY-1202950

References

[1] C.A. Baker et al., Phys. Rev. Lett. 97, 131801 (2006).

[2] R.D. Peccei and H.R. Quinn, Phys. Rev. Lett. 38, 1440 (1977).

[3] S. Weinberg, Phys. Rev. Lett. 40, 223 (1978).

[4] F. Wilczek, Phys. Rev. Lett. 40, 279 (1978).

[5] J.E. Kim, Phys. Rev. Lett. 43, 103 (1979).

[6] M.A. Shifman, A.I. Vainstein, and V.I. Zakharov, Nucl. Phys. B166, 493 (1980).

[7] A.R. Zhitnitskii, Yad. Fiz. 31, 497 (1980) [Sov. J. Nucl. Phys. 31, 260 (1980).

[8] M. Dine, F. Fischler, and M. Srednicki, Phys. Lett. 104B, 199 (1981)

[9] D. Hooper et al., Phys. Rev. D 82, 123509 (2010)

[10] A.V. Derbin et al., Phys. Rev. D 83, 023505 (2011)

[11] D. Kekez, et al., Physics Letters B 671, 345 (2009)

[12] M. Pospelov, A. Ritz, and M. Voloshin, Phys. Rev. D 78, 115012 (2008)

[13] F.T. Avignone III, et al., Phys. Rev. D 35, 2752 (1987)

[14] S. Dimopoulos, G.D. Starkman, and B.W. Lynn, Phys. Rev. Lett. 168B, 146 (1986)

[15] M.A. Howe et al., IEEE Trans. Nucl. Sci. NS-51, 878 (2004).

[16] K. Abe et al., (The XMASS Collaboration), arXiv:1212.6153 [astro-ph CO] 26 December 2012.

[17] P. Gondolo and G.G. Raffelt, Phys. Rev. D 79, 107301 (2009).

[18] A.G. Schubert et al., AIP Conf. Proc. 1441, 480 (2012); arXiv:1109.1567; J. F. Wilkerson et al., J. Phys. Conf. Ser. 375, 042010 (2012). E. Aguayo et al., AIP. Conf. Proc. 417, 95 (2011).

[19] P. Finnerty et al., Nucl. Instrum. and Meth. 642, 65 (2011)

Search for solar axions produced by Compton process and bremsstrahlung using the resonant absorption and axioelectric effect

A.V. Derbin, I.S. Dratchnev, A.S. Kayunov, V.N. Muratova, D.A. Semenov, E.V. Unzhakov

St.Petersburg Nuclear Physics Institute, Gatchina, Russia 188300

DOI: http://dx.doi.org/10.3204/DESY-PROC-2013-04/derbin_alexander

The search for resonant absorption of Compton and bremsstrahlung solar axions by ^{169}Tm nuclei have been performed. Such an absorption should lead to the excitation of low-lying nuclear energy level: $A+^{169}\mathrm{Tm} \rightarrow ^{169}\mathrm{Tm}^* \rightarrow ^{169}\mathrm{Tm} + \gamma$ (8.41 keV). Additionally the axioelectric effect in silicon atoms is sought. The axions are detected using a Si(Li) detectors placed in a low-background setup. As a result, a new model independent restrictions on the axion-electron and the axion-nucleon coupling: $g_{Ae} \times |g^0_{AN} + g^3_{AN}| \leq 2.1 \times 10^{-14}$ and the axion-electron coupling constant: $|g_{Ae}| \leq 2.2 \times 10^{-10}$ has been obtained. The limits leads to the bounds $m_A \leq 7.9$ eV and $m_A \leq 1.3$ keV for the mass of the axion in the DFSZ and KSVZ models, respectively (90% C.L.).

1 The axions spectra and the rate of axions resonant absorbtion by ^{169}Tm nucleus

If the axions or other axion-like pseudoscalar particles couple with electrons then they are emitted from Sun by the Compton process and by bremsstrahlung [1]-[6]. The expected spectrum of axions was calculated using theoretical predictions for the Compton cross section given in [7, 8] and the axion bremsstrahlung due to electron-nucleus collisions given in [9]. The axion flux is determined for radial distribution of the temperature, density of electrons and nuclei given by BS05(OP) Standard Solar Model [10] based on high-Z abundances [11]. The results of our calculations presented in Fig.1 [12].

As a pseudoscalar particle, the axion should be subject to resonant absorption and emission in the nuclear transitions of a magnetic type. In our experiment we have chosen the ^{169}Tm nucleus as a target. The energy of the first nuclear level ($3/2^+$) is equal to 8.41 keV, the total axion flux at this energy is $g^2_{Ae} \times 1.34 \times 10^{33}\mathrm{cm}^{-2}\mathrm{s}^{-1}\mathrm{keV}^{-1}$. The 8.41 keV nuclear level discharges through $M1$-type transition with $E2$-transition admixture value of δ^2=0.11% and the relative probability of γ-ray emission is $\eta = 3.79 \times 10^{-3}$ [13].

The cross-section for the resonant absorption of the axions with energy E_A is given by the expression that is similar to the one for γ-ray resonant absorption, but the ratio of the nuclear transition probability with the emission of an axion (ω_A) to the probability of magnetic type transition (ω_γ) has to be taken into account [12]. The ω_A/ω_γ ratio calculated in the long-wave approximation, depends on isoscalar g^0_{AN} and isovector g^3_{AN} coupling constants and parameters

depending on the particular nuclear matrix elements [14, 15, 16].

As a result the rate of axion absorption by ^{169}Tm nucleus dependent only on the coupling constants is (the model-independent view) [12]:

$$R_A = 1.55 \times 10^5 g_{Ae}^2 (g_{AN}^0 + g_{AN}^3)^2 (p_A/p_\gamma)^3, \mathrm{s}^{-1}. \quad (1)$$

Using the relations between g_{AN}^0, g_{AN}^3 and axion mass given by KSVZ model, the absorption rate can be presented as a function of g_{Ae} and axion mass m_A (m_A in eV units):

$$R_A = 5.79 \times 10^{-10} g_{Ae}^2 m_A^2 (p_A/p_\gamma)^3, \mathrm{s}^{-1}. \quad (2)$$

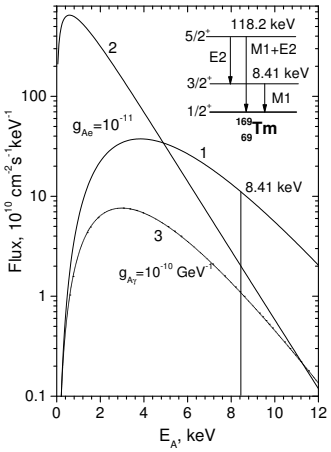

Figure 1: 1,2 - the spectra of the axions produced by the Compton process and the bremsstrahlung, correspondingly ($g_{Ae} = 10^{-11}$, $m_A = 0$) [12]. 3 - spectrum of the axions produced by Primakoff effect ($g_{A\gamma} = 10^{-10}\mathrm{GeV}^{-1}$). The level scheme of ^{169}Tm nucleus is shown in the inset [12].

2 Spectra of massive solar axions and a cross section for the axioelectric effect

If the mass of the axion is several keV, the expected solar axion spectra changes significantly and depends on the particular m_A value [19]. To calculate spectra we used the procedure similar described above. The spectra of solar axions were determined for different values of m_A [19].

An axion interacting with an electron should undergo axio-electric absorption, which is an analog of the photoelectric effect. Silicon atoms entering into the composition of a Si(Li) detector were used in our experiment as targets for the axio-electric effect. The cross section of the axioelectric absorption was calculated by the formula

$$\sigma_{abs}(E_A) = \sigma_{pe}(E_A) \frac{g_{Ae}^2}{\beta} \frac{3E_A^2}{16\pi\alpha m_e^2} \left(1 - \frac{\beta}{3}\right) \quad (3)$$

where σ_{pe} is the cross section for the photoelectric effect and $\beta = v/c = p_A/E_A$ is the velocity of the axion. At $\beta \to 1$ and $\beta \to 0$, this formula coincides with the cross sections for relativistic and nonrelativistic axions obtained in [17, 18] and provides an extrapolation approximately linear in β, which ensures a sufficient accuracy for the case under consideration.

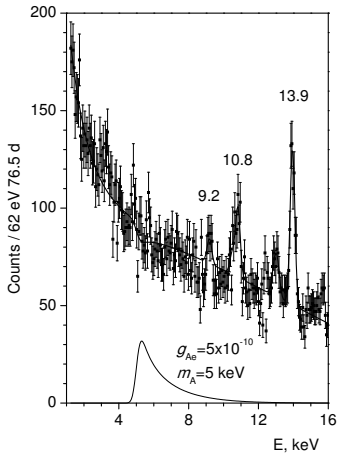

Figure 2: Spectrum of the signals of the Si(Li) detector in the range of (1–16) keV with the optimal fit for $m_A = 5$ keV. The energies of the Gaussian peaks are given near them. The expected spectrum is shown for the case of the detection of axions with $m_A = 5$ keV and $g_{Ae} = 5 \times 10^{-10}$.

The expected signal from 5 keV axions undergouing axioelctric effect in Si-detector is shown in Fig.2.

3 Experimental setups

To search for quanta with an energy of 8.41keV due to axion resonant absorption, the planar Si(Li) detector with a sensitive area diameter of 66 mm and a thickness of 5 mm was used. The detector was mounted on 5 cm thick copper plate that protected the detector from the external radioactivity. The detector and the holder were placed in a vacuum cryostat and cooled to liquid nitrogen temperatures. A Tm_2O_3 target of 2 g mass was uniformly deposited on a plexiglas substrate 70 mm in diameter at a distance of 1.5 mm from the detector surface. External passive shielding composed of copper, iron and lead layers was adjusted to the cryostat and eliminated external radioactivity background by a factor of about 500.

To search for axioelectric effect we used a Si(Li) detector with a sensitive-region diameter of 17 mm and a thickness of 2.5 mm. The detector was placed in a vacuum cryostat with the input beryllium window 20 μm thick. The window was used for energy calibration and determination of the detection efficiency of gamma-ray photons in order to find the sensitive volume of the detector. The detector was surrounded by 12.5 cm of copper and 2.5 cm of lead, which reduced the background of the detector at an energy of 14 keV by a factor of 110 as compared to the unshielded detector.

The experimental setups were located on the ground surface. Events produced by cosmic rays and fast neutrons were registered by an active shielding consisting of five plastic scintillators $50 \times 50 \times 12$ cm in size. The rate of 50 μs veto signals was 600 counts/s, that lead to $\approx 3\%$ dead time. More details of experiments one can find in [12, 19].

4 Results

The upper limit on axions absorption rate by ^{169}Tm nucleus $R_A \leq 5.43 \times 10^{-23}\mathrm{s}^{-1}$ set by our experiment limits the possible values of coupling constants g_{Ae}, g_{AN} and axion mass m_A. According to (1) and (2) and taking into account the approximate equality of the axion and γ-quantum momenta $(p_A/p_\gamma)^3 \simeq 1$ for $m_A \leq 2$ keV we obtain (at 90% c.l.):

$$g_{Ae} \times |(g^0_{AN} + g^3_{AN})| \leq 2.1 \times 10^{-14} \tag{4}$$

$$g_{Ae} \times m_A \leq 3.1 \times 10^{-7}\ \mathrm{eV} \tag{5}$$

The restriction (4) is a model independent one on axion (or any other pseudoscalar particle) couplings with electron and nucleons. The result (5) presented as a restriction on the range of possible values of g_{Ae} and m_A (KSVZ relations between g_{AN} and m_A are used) allows one to compare our result (Fig.3, line 9) with results of other experiments restricting g_{Ae} (Fig.3). The limits on $g_{Ae} \times m_A$ for DFSZ axion lie in the range $(0.33 - 1.32)$ of the restriction. As we mention in [20, 12] the sensitivity of experiment with ^{169}Tm can be increased significantly (in $\sim 10^6$ times) by introducing the Tm target inside the sensitive volume of detector having high energy resolution, at present, cryogenic detector have the best option.

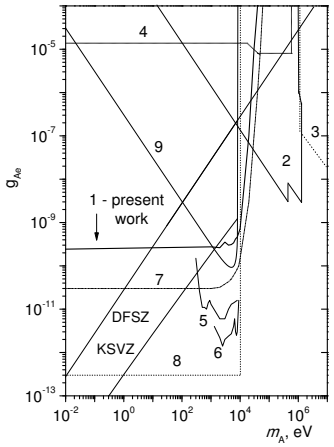

Figure 3: Bounds for the axion-electron coupling constant: (1) Si-axioelectrical effect [19], (2) reactor experiments and solar axions with energies of 0.478 and 5.5 MeV,(3) beam dump experiments, (4) decay of orthopositronium, (5) CoGeNT, (6) CDMS, (7) bound for the axion luminosity of the Sun, (8) red giants and (9) experiment with ^{169}Tm. The regions of excluded values lie above the corresponding lines. The inclined lines show the g_{Ae} values in the DFSZ and KSVZ ($E/N = 8/3$) models.

When looking for the axioelectric effect the measured spectrum is fitted by the sum of an exponential function, describing the smooth background and the response function for axions $S(E, m_A)$:

$$N(E) = a + b\exp(cE) + g_{Ae}^4 S(E, m_A) N_{Si} T \quad (6)$$

Here, N_{Si} is the number of silicon atoms in the sensitive volume of the detector and $T = 6.61 \times 10^6$ is the live time of measurement. The upper bound for $|g_{Ae}|$ at m_A=0 is

$$|g_{Ae}| \leq 2.2 \times 10^{-10} \quad (7)$$

at 90% C.L. Limit (7) is a model independent bound for the coupling constant of the axion or any other pseudoscalar relativistic particle with the electron.

For nonrelativistic axions the fitting range was expanded to 16 keV. To describe the experimental spectrum in a wide range, function 6 was supplemented by a linear term for describing the continuous background and six Gaussians for describing the peaks of the characteristic Np X rays manifested in the measurements [20, 21]. The fit results and $S(E, m_A)$ for $m_A = 5$ keV are shown in Fig.2.

The maximum deviation of g_{Ae}^4 from zero for all tested (from 1 to 10 keV with a step of 1 keV) m_A values is 2.5σ. The upper bounds obtained for $|g_{Ae}|$ at various m_A values are shown in Fig.3 (line 1) in comparison with the other experimental results.

5 Acknowledgments

This work was supported by RFBR grants 13-02-01199-a and 13-02-12140-ofi-m.

References

[1] K. Kato, H. Sato, Prog. Theor. Phys. **54**, 1564 (1975)
[2] M.I. Vysotsskii, Ya.B. Zeldovich, M.Yu. Khlopov, V.M. Chechetkin, JETP Lett. **27**, 502 (1978)
[3] D.A. Dicus, E.W. Colb, V.L.Teplitz, R.V. Wagover, Phys. Rev. D **18**, 1829 (1978), D **22**, 839 (1980)
[4] M. Fukugita, S. Watamura, M. Yoshimura, Phys. Rev. Lett. **48**, 1522 (1982)
[5] L.M. Krauss, J.E. Moody, F. Wilczek, Phys. Lett. B **144**, 391 (1984)
[6] G.G. Raffelt, Phys. Rev. D **33**, 897 (1986)
[7] M. Pospelov, A. Ritz and M.B. Voloshin, Phys. Rev. D **78**, 115012 (2008) [arXiv:0807.3279]
[8] P. Gondolo and G.G. Raffelt Phys.Rev. D **79**, 107301 (2009) [arXiv:0807.2926]
[9] A.R. Zhitnitsky, Yu.I. Skovpen, Sov. J. Nucl. Phys. **29**, 513 (1979)
[10] J.N. Bahcall, A.M. Serenelli, and S. Basu, Astrophys. J. **621**, L85 (2005)
[11] M. Asplund, N. Grevesse, and J. Sauval, Nucl. Phys. A **777**, 1 (2006)
[12] A.V. Derbin *et al.* Phys. Rev. D **83**, 023505 (2011) [arXiv:1101.2290]
[13] C.M. Baglin, Nucl. Data Sheets, **109**, 2033 (2008)
[14] T.W. Donnelly *et al.* Phys. Rev. D **18**, 1607 (1978)
[15] F.T. Avignone III *et al.* Phys. Rev. D **37**, 618 (1988)
[16] W.C. Haxton and K.Y. Lee, Phys. Rev. Lett. **66**, 2557 (1991)
[17] M. Pospelov, A. Ritz, and M.B. Voloshin, Phys. Rev. D **78**, 115012 (2008)
[18] A. Derevianko *et al.* Phys. Rev. D **82**,065006 (2010)
[19] A.V. Derbin, I.S. Drachnev, A.S. Kayunov, V.N. Muratova, JETP Lett. **95**, 379 (2012) [arXiv:1206.4142]
[20] A.V. Derbin *et al.* Phys. Lett. B **678**, 181 (2009) [arXiv:0904.3443]
[21] A.V. Derbin *et al.* Eur. Phys. J. C **62**, 755 (2009) [arXiv:0906.0256]

Search for Hidden photons with Sumico

Y. Inoue[1], *T. Mizumoto*[2], *R. Ohta*[1], *T. Horie*[1], *J. Suzuki*[1], *M. Minowa*[1]
(the Sumico collaboration)

[1]The University of Tokyo, Japan
[2]Kyoto University, Japan

DOI: http://dx.doi.org/10.3204/DESY-PROC-2013-04/inoue_yoshizumi

We searched for solar hidden photons in the visible photon energy range using a hidden photon detector add-on attached to Sumico. It consists of a parabolic mirror of $\phi 0.5\,\mathrm{m}$ and $f = 1\,\mathrm{m}$ installed in a vacuum chamber, and a low noise photomultiplier tube at the focal point. No evidence for the existence of hidden photons was found in the latest measurement giving a new limit on the photon-hidden photon mixing parameter in the hidden photon mass range 0.001–1 eV.

1 Introduction

The sun can be a powerful source of weakly interacting light particles, such as the axions [1, 2]. The Tokyo axion helioscope, aka. Sumico [3, 4, 5, 6], was built aiming at the direct detection of the solar axions in the mass range up to a few eV. It is equipped with a dedicated cryogen-free superconducting magnet which can produce a transverse magnetic field of 4 T over 2.3 m, a container to hold cold ^{4}He gas, a PIN-photodiode-array X-ray detector, and a telescope mount mechanism to track the sun. The transverse magnetic field is essential in the axion helioscope, where the solar axions oscillate into X-ray photons. In the past measurements, the axion mass ranges 0–0.27 eV and 0.84–1 eV have been scanned. We were striving to push up the sensitive mass range to higher masses. Unfortunately, however, axion search activity is currently suspended due to a trouble in the cryogenic system which is preventing the magnet from exciting. Meanwhile, we searched for solar hidden photons using Sumico.

The hidden photon is the gauge boson of a hypothetical hidden local U(1) symmetry. Many extensions of the standard model, in particular those based on string theory, predict such symmetries [7]. The hidden photon can couple to the ordinary photons via a so-called *kinetic mixing*, and it can be massive as described by the following Lagrangian [8, 9, 10],

$$\mathcal{L} = -\frac{1}{4}F_{\mu\nu}F^{\mu\nu} - \frac{1}{4}B_{\mu\nu}B^{\mu\nu} - \frac{\chi}{2}F_{\mu\nu}B^{\mu\nu} + \frac{m_{\gamma'}}{2}B_{\mu}B^{\mu},$$

where $F_{\mu\nu}$ and $B_{\mu\nu}$ represent the ordinary- and hidden- photon field strengths, respectively, χ is the kinetic mixing parameter, and $m_{\gamma'}$ is the hidden photon mass. When the hidden photon has a small mass, it leads to photon–hidden-photon vacuum oscillations. In vacuum, hidden photon to photon transition probability for photons of energy ω after traveling ℓ is given by:

$$P_{\gamma'\to\gamma} = 4\chi^2 \sin^2\left(\frac{m_{\gamma'}^2 \ell}{4\omega}\right)$$

assuming $m_{\gamma'} \ll \omega$. Since the refractive index for visible light in the matter is normally larger than 1, the matter in the conversion path always affects the transition probability negatively.

The emission of hidden photons from the sun was discussed by J. Redondo [11]. The transverse hidden photon flux at the earth is given by:

$$\frac{\mathrm{d}\Phi_{\mathrm{T}}}{\mathrm{d}\omega} = \int_0^{R_\odot} \frac{r^2 dr}{(1\,\mathrm{AU})^2} \frac{\omega^2}{\pi^2} \frac{\Gamma}{e^{\omega/T}-1} \frac{\chi^2 m_{\gamma'}^4}{(m_\gamma^2 - m_{\gamma'}^2)^2 + (\omega\Gamma)^2},$$

where $R_\odot$ is the solar radius, T is the temperature, Γ is the damping rate of photons, and m_γ is the effective photon mass in plasma. For $m_{\gamma'} \ll 1\,\mathrm{eV}$, one can use the following conservative estimate for the bulk component of the hidden photon flux [11]:

$$\frac{\mathrm{d}\Phi_{\mathrm{T}}}{\mathrm{d}\omega} \gtrsim \chi^2 \left(\frac{m_{\gamma'}}{\mathrm{eV}}\right)^4 10^{32} \frac{1}{\mathrm{eV\,cm^2\,s}} \qquad \text{for} \quad \omega = 1\text{–}5\,\mathrm{eV}.$$

Recently, a refined estimation including the contribution from a thin resonant region below the photosphere is given [12, 13] for four typical cases $m_{\gamma'} = 0, 0.01, 0.1$ and $1\,\mathrm{eV}$. They claim that the resonant production dominates over the emission from the rest of the sun.

In more recent studies [14, 15], the estimated emission rate of longitudinal hidden photons was revised and it turned out that the resonant longitudinal-mode production is dominating the total solar hidden photon emission in the low mass case $m_{\gamma'} < 1\,\mathrm{eV}$. This result has nothing to do with the analysis of our experiment since longitudinal hidden photons do not oscillate into photons in vacuum. However, it has a strong impact on the hidden photon searches by providing stringent constraints on the hidden photon parameters along with their another work [16] in which they re-analyzed the published data of the XENON10 dark matter experiment.

Various constraints on the hidden photon parameters are summarized in Ref. [17].

In this paper, we report on a direct experimental search for the flux of solar hidden photons.

2 Experimental apparatus

Our solar hidden photon detector was built as an add-on unit mounted on Sumico, the Tokyo axion helioscope, as shown in Fig. 1. Sumico can track the sun with a driving range from $-28°$ to $28°$ in altitudinal direction and $360°$ in azimuth. The overall tracking accuracy is better than 0.5 mrad in both directions, which is negligibly small for this measurement.

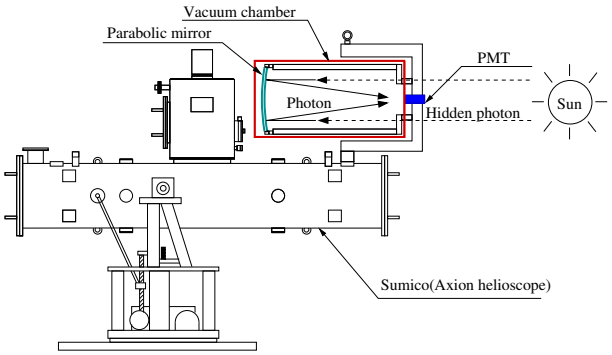

Figure 1: The schematic view of Sumico and the solar hidden photon detector.

The solar hidden photon detector consists of a vacuum chamber, a parabolic mirror and a photomultiplier tube (PMT). The vacuum chamber holds the conversion region in vacuum to keep the hidden photon to photon conversion probability high enough. It is a cylinder made of 1.5-mm thick stainless steel plates with wrinkles on its side for the mechanical reinforcement. The inner diameter of the vacuum chamber is 567mm and its length is 1200mm. The parabolic mirror was used to collect the conversion photons to the PMT. It is made of aluminium deposited soda glass. Its diameter is 500 mm, the focal length is 1007 mm and the focal

spot diameter is 1.5 mm. The reflectance measured by the manufacturer is higher than 80% over the wavelength range 300–650 nm. The mirror and its supporting structure is constructed inside the vacuum chamber.

A low noise head-on type 25-mm diameter photon counting PMT, Hamamatsu Photonics R3550P, was used as the photon detector at the focal point. It is sensitive to photons of wavelength range 300–650 nm with a peak quantum efficiency of 17 %. It is set at the atmospheric pressure side and is viewing the reflected photons through a quartz glass window. Single- and multi photon events detected by the PMT make current pulses which enter a charge-sensitive preamplifier (ORTEC 113) and a shaping amplifier (ORTEC 572). The signal is then digitized by an ADC (Laboratory Equipment Corp. 2201A) and pulse height spectra are taken by a multichannel analyser (MCA).

The temperatures of the PMT and the vacuum chamber are measured by Pt100 thermometers. The inner pressure of the vacuum chamber is measured by a vacuum gauge (Balzers PKR250). During the solar tracking- and background measurements, the inner pressure of the vacuum chamber was lower than $(5 \pm 2) \times 10^{-3}$ Pa. The effect of this residual gas on the conversion probability is negligible.

3 Measurement and analysis

If a hidden photon is converted into a photon in the vacuum chamber, it would be detected by the PMT as a single photon event. Before starting the measurement, the shape of a single photon spectrum in the MCA was measured by illuminating the PMT with a blue LED with sufficiently low current pulses. It was fitted by a Gaussian function which was later used as the template for the single photon analysis.

Measurements were done from October 26, 2010 till November 16, 2010. The solar tracking measurements were done around the time of sunrise and sunset with tracking time of about 5 hours each. Background was measured while the detector was directed away from the sun.

To find out the possible evidence of solar hidden photons, the background spectrum was subtracted from the solar tracking spectrum. We must eliminate some systematic effects which have nothing to do with the solar hidden photons. It is well known that the dark count rate gets lower as time passes after an operating voltage is applied. We, therefore, waited for four

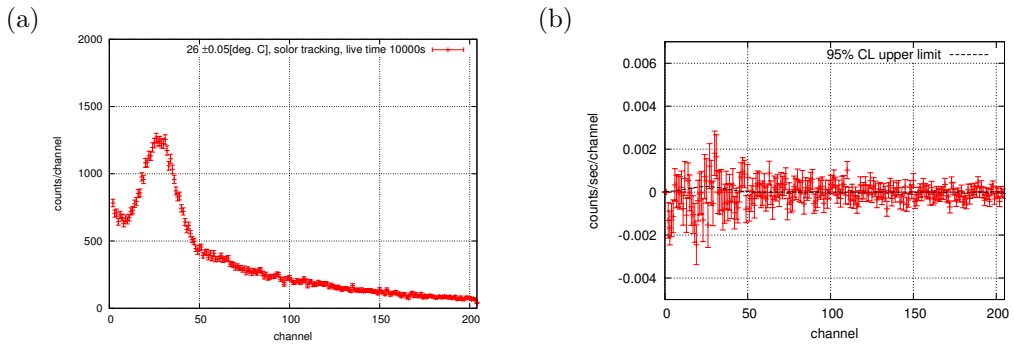

Figure 2: (a) An example of a pulse height spectrum (PMT temperature 26.0 ± 0.05°C, solar tracking data). (b) Total residual spectrum and the 95% confidence level upper limit.

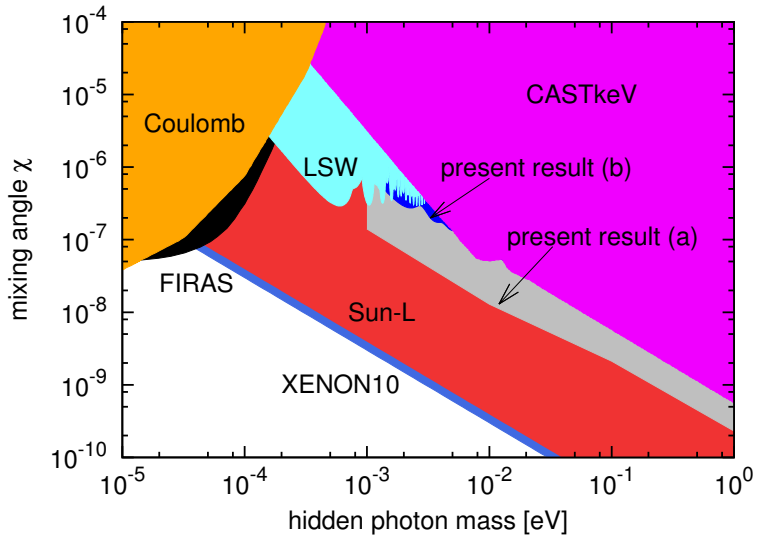

Figure 3: 95 % Confidence level upper limits to the mixing parameter χ set by this experiment. Present result (a) is obtained based on the the newer solar hidden photon flux calculation [12, 13] and (b) on the older conservative estimation [11]. Excluded area by other experiments are; Coulomb: tests of Coulomb's law [18, 19], LSW: Light Shining through Walls experiments [20, 21, 22, 23], CAST keV: the CAST experiment [11], FIRAS: FIRAS CMB spectrum [24], Sun-L: the solar luminosity constraints in the longitudinal channel [14, 15], and XENON10: interpretation of the XENON10 result in view of the longitudinal solar hidden photons [16].

days until the time dependence on the dark count rate became negligible.

To avoid the systematic effect from a temperature dependence of the dark count rate, we subtracted background isothermally. First, we grouped the solar tracking- and background-spectra each with 100 s of live time into 21 temperature bins of 0.1°C interval whose central values ranging 25.9–27.9°C. Then, we apply the background subtraction within every temperature bin and obtained 21 residual spectra. Finally, the total residual spectrum was obtained by combining them.

In the above procedure, we used only the data during the holidays when the air conditioning system was switched off, because we observed abrupt room temperature changes on weekdays due to automatic switching of the air conditioning system of the building.

Figure 2 (a) shows the pulse height spectrum from solar tracking data in the temperature bin 26.0 ± 0.05°C, as an example. Figure 2 (b) shows the total residual spectrum. It is worth noting that the peak from single photon events is already evident in the background spectrum and it vanished away after the background subtraction.

We then estimated how many single photons could there be in the total residual spectrum by fitting the magnitude of the Gaussian template function to it. The best fit was obtained with

$$N_{\rm fit} = (-7.9 \pm 6.5(\text{stat.}) \pm 3.4(\text{sys.})) \times 10^{-3}[\text{s}^{-1}].$$

The systematic errors considered include an effect of Cherenkov light emitted in the quartz

glass vacuum window and the PMT window by cosmic muons, the finite bin width of the PMT temperatures, and the residual drift of the dark count rate after four days.

As we observed no excess of the single photon events, the 95% confidence level upper limit to the hidden photon counting rate was estimated taking the statistical and systematic errors into account:

$$N_{\mathrm{UL95}} = 1.02 \times 10^{-2}\mathrm{s}^{-1}.$$

The upper limit N_{UL95} is now compared with the count rate expected by the hidden photon model with given parameters. The 95% confidence level upper limit to the mixing parameter χ as a function of the hidden photon mass $m_{\gamma'}$ is calculated as shown in Fig. 3. For the solar hidden photon flux $\frac{\mathrm{d}\Phi_{\mathrm{T}}}{\mathrm{d}\omega}$, two cases were assumed. One is based on the conservative estimation [11] which is indicated by 'present result (b)' in Fig. 3. The other is based on the newer estimation [12, 13] including the contribution from a thin resonant region below the photosphere, which is indicated by (a). Limits set by other experiments are also shown.

4 Conclusion and prospects

We have searched for solar hidden photons in the visible photon energy range using a dedicated detector for the first time. The detector was attached to the Tokyo axion helioscope, Sumico which has a mechanism to track the sun. No evidence of the existence of hidden photons is observed in the measurement and we set a limit on photon–hidden-photon mixing parameter χ depending on the hidden photon mass $m_{\gamma'}$. The present result improved the existing limits given by the LSW experiments and the CAST experiment in the hidden photon mass region between 10^{-3} and 1 eV. With recent new calculations of the longitudinal-mode hidden photon, more stringent limits came out by the solar luminosity consideration and also by the re-analysis of the XENON10 data. This result is already published in Ref. [25].

If solar tracking- and background measurements could be switched in less than 10 minutes, the effect of the dark-count-rate drift including that caused by the temperature changes would become negligible. This can be achieved by slightly switching the helioscope axis as much as 2 degrees while Sumico is tracking the sun. A test has demonstrated that Sumico can switch between the on-axis solar tracking and off-axis tracking within 20 seconds with enough direction accuracy. Use of a parabolic mirror of larger area and a photodetector with lower noise and higher quantum efficiency will also improve the sensitivity. However, such upgrades would not improve the sensitivity in terms of χ by orders of magnitude.

Acknowledgements

This research is supported by the Grant-in-Aid for challenging Exploratory Research by MEXT, Japan, and by the Research Center for the Early Universe, School of Science, the University of Tokyo.

References

[1] R. Peccei, H. Quinn, Phys. Rev. Lett. **38**, 1440 (1977).

[2] R. Peccei, H. Quinn, Phys. Rev. D **16**, 1791 (1977).

[3] R. Ohta, *et al.*, Nucl. Instr. Meth. A **670**, 73 (2012).

[4] S. Moriyama, *et al.*, Phys. Lett. B **434**, 147 (1998).

[5] Y. Inoue, *et al.*, Phys. Lett. B **536**, 18 (2002).

[6] Y. Inoue, *et al.*, Phys. Lett. B **668** 93 (2008).

[7] M. Goodsell and A. Ringwald, Fortsch. Phys. **58**, 716 (2010).

[8] L. Okun, Sov. Phys. JETP **56**, 502 (1982).

[9] B. Holdom, Phys. Lett. B **166**, 196 (1986).

[10] R. Foot, X. He, Phys. Lett. B **267**, 509 (1991).

[11] J. Redondo, JCAP **07**, 008 (2008) [arXiv:0801.1527 [hep-ph]], S. N. Gninenko and J. Redondo, Phys. Lett. B **664**, 180 (2008) [arXiv:0804.3736v1 [hep-ex]].

[12] D. Cadamuro and J. Redondo, arXiv:1010.4689v1 [hep-ph].

[13] J. Redondo, arXiv:1202.4932v1 [hep-ph].

[14] H. An, M. Pospelov, J. Pradler, arXiv:1302.3884 [hep-ph].

[15] J. Redondo, G. Raffelt, arXiv:1305.2920 [hep-ph].

[16] H. An, M. Pospelov, J. Pradler, arXiv:1304.3461 [hep-ph].

[17] J. Jaeckel, A. Ringwald, Annu. Rev. Nucl. Part. Sci. 2010.60:405 [arXiv:1002.0329v1 [hep-ph]].

[18] E. Williams, J. Faller, H. A. Hill, Phys. Rev. Lett. **26**, 721 (1971).

[19] D. F. Bartlett and S. Loegl, Phys. Rev. Lett. **61**, 2285 (1988).

[20] K. Ehret *et al.* [ALPS Collaboration], Phys. Lett. B **689**, 149 (2010) [arXiv:1004 .1313v1 [hep-ex]].

[21] M. Fouche *et al.* [BMV Collaboration], Phys. Rev. D **78**, 032013 (2008) [arXiv:0808.2800v1 [hep-ex]].

[22] M. Ahlers *et al.*, Phys. Rev. D **77**, 095001 (2008) [arXiv:0711.4991v1 [hep-ph]], A. S. Chou *et al.* [GammeV Collaboration], Phys. Rev. Lett. **100**, 080402 (2008) [arXiv:0710.3783 [hep-ex]].

[23] A. Afanasev *et al.* [LIPSS Collaboration], Phys. Lett. B **679**, 317 (2009) [arXiv:0810.4189v1 [hep-ex]].

[24] A. Mirizzi, J. Redondo and G. Sigl, JCAP **03**, 026 (2009) [arXiv:0901.0014[hep-ph]].

[25] T. Mizumoto *et al.*, JCAP **07**, 013 (2013) [arXiv:1302.1000v3 [astro-ph.SR]].

IAXO-the Future Axion Helioscope

B. Lakić[1], *F. T. Avignone*[2], *M. Betz*[3], *P. Brax*[4], *P. Brun*[5], *G. Cantatore*[6], *J. M. Carmona*[7], *G. P. Carosi*[8], *F. Caspers*[3], *S. Caspi*[9], *S. A. Cetin*[10], *D. Chelouche*[11], *F. E. Christensen*[12], *A. Dael*[5], *T. Dafni*[7], *M. Davenport*[3], *A. V. Derbin*[13], *K. Desch*[14], *A. Diago*[7], *B. Döbrich*[15], *I. Dratchnev*[13], *A. Dudarev*[3], *C. Eleftheriadis*[16], *G. Fanourakis*[17], *E. Ferrer-Ribas*[5], *J. Galán*[5], *J. A. García*[7], *J. G. Garza*[7], *T. Geralis*[17], *B. Gimeno*[18], *I. Giomataris*[5], *S. Gninenko*[19], *H. Gómez*[7], *D. González-Díaz*[7], *E. Guendelman*[20], *C. J. Hailey*[21], *T. Hiramatsu*[22], *D. H. H. Hoffmann*[23], *D. Horns*[24], *F. J. Iguaz*[7], *I. G. Irastorza*[7], *J. Isern*[25], *K. Imai*[26], *A. C. Jakobsen*[12], *J. Jaeckel*[27], *K. Jakovčić*[1], *J. Kaminski*[14], *M. Kawasaki*[28], *M. Karuza*[29], *M. Krčmar*[1], *K. Kousouris*[3], *C. Krieger*[14], *O. Limousin*[5], *A. Lindner*[15], *A. Liolios*[16], *G. Luzón*[7], *S. Matsuki*[30], *V. N. Muratova*[13], *C. Nones*[5], *I. Ortega*[7], *T. Papaevangelou*[5], *M. J. Pivovaroff*[8], *G. Raffelt*[31], *J. Redondo*[31], *A. Ringwald*[15], *S. Russenschuck*[3], *J. Ruz*[8], *K. Saikawa*[32], *I. Savvidis*[16], *T. Sekiguchi*[28], *Y. K. Semertzidis*[33], *I. Shilon*[3], *P. Sikivie*[34], *H. Silva*[3], *H. ten Kate*[3], *A. Tomas*[7], *S. Troitsky*[19], *T. Vafeiadis*[3], *K. van Bibber*[35], *P. Vedrine*[5], *J. A. Villar*[7], *J. K. Vogel*[8], *L. Walckiers*[3], *A. Weltman*[36], *W. Wester*[37], *S. C. Yildiz*[10], *K. Zioutas*[38] *(IAXO Collaboration)*

[1]Rudjer Bošković Institute, Zagreb, Croatia
[2]Physics Department, University of South Carolina, Columbia, SC, USA
[3]European Organization for Nuclear Research (CERN), Genève, Switzerland
[4]IPHT, Centre d'Études de Saclay (CEA-Saclay), Gif-sur-Yvette, France
[5]CEA Irfu, Centre de Saclay, Gif-sur-Yvette, France
[6]INFN, Sezione di Trieste and Università di Trieste, Trieste, Italy
[7]Laboratorio de Física Nuclear y Altas Energías, Universidad de Zaragoza, Zaragoza, Spain
[8]Lawrence Livermore National Laboratory, Livermore, CA, USA
[9]Lawrence Berkley National Laboratory, USA
[10]Dogus University, Istanbul, Turkey
[11]Physics Department, University of Haifa, Haifa, Israel
[12]Technical University of Denmark, DTU Space Kgs. Lyngby, Denmark
[13]St. Petersburg Nuclear Physics Institute, St. Petersburg, Russia
[14]Physikalisches Institut der Universität Bonn, Bonn, Germany
[15]Deutsches Elektronen-Synchrotron DESY, Hamburg, Germany
[16]Aristotle University of Thessaloniki, Thessaloniki, Greece
[17]National Center for Scientific Research *Demokritos*, Athens, Greece
[18]Instituto de Ciencias de las Materiales, Universidad de Valencia, Valencia, Spain
[19]Institute for Nuclear Research (INR), Russian Academy of Sciences, Moscow, Russia
[20]Physics department, Ben Gurion University, Beer Sheva, Israel
[21]Columbia Astrophysics Laboratory, New York, USA
[22]Yukawa Institute for Theoretical Physics, Kyoto University, Kyoto, Japan
[23]Technische Universität Darmstadt, IKP, Darmstadt, Germany
[24]Institut für Experimentalphysik, Universität Hamburg, Hamburg, Germany
[25]Institut de Ciències de l'Espai (CSIC-IEEC), Facultat de Ciències, Bellaterra, Spain
[26]Advanced Sci. Research Center, Japan Atomic En. Agency, Tokai-mura, Ibaraki-ken, Japan
[27]Institut für theoretische Physik, Universität Heidelberg, Heidelberg, Germany

[28]Institute for Cosmic Ray Research, University of Tokyo, Tokyo, Japan
[29]University of Rijeka, Rijeka, Croatia
[30]Research Center for Low Temperature and Material Sciences, Kyoto University, Kyoto, Japan
[31]Max-Planck-Institut für Physik, Munich, Germany
[32]Department of Physics, Tokyo Institute of Technology, Tokyo, Japan
[33]Physics Department, Brookhaven National Lab, Upton, NY, USA
[34]Department of Physics, University of Florida, Gainesville, FL, USA
[35]Department of Nuclear Engineering, University of California Berkley, Berkley, CA, USA
[36]ACGC, Department of Math. and Applied Math., University of Cape Town, South Africa
[37]Fermi National Accelerator Laboratory, Batavia, IL, USA
[38]Physics Department, University of Patras, Patras, Greece

DOI: http://dx.doi.org/10.3204/DESY-PROC-2013-04/lakic_biljana_IAXO

International Axion Observatory (IAXO) is a new generation axion helioscope aiming to search for axions and axion-like particles with a sensitivity to the axion-photon coupling that is 1 to 1.5 orders of magnitude beyond the one achieved by currently the most sensitive axion helioscope, CAST. IAXO relies on large improvements in magnetic field volume, X-ray focusing optics and detector backgrounds with respect to CAST. Additional IAXO searches would include electron-coupled axions, relic axions, and other more generic axion-like particles.

1 Introduction

Axions are neutral pseudoscalar particles that may solve the strong CP problem. They arise as pseudo-Nambu-Goldstone bosons of the $U(1)$ Peccei-Quinn symmetry [1] which is spontaneously broken at a large energy scale. The spontaneous breaking of other global symmetries is predicted in many extensions of the standard model (including string theory) and can give rise to light axion-like scalar or pseudoscalar particles, called ALPs. Axions and ALPs are candidates for the dark matter (DM) of the universe and can explain a variety of astrophysical observations.

Most of the axion experimental searches are based on the axion interaction with two photons. As a consequence of this interaction, axions could transform into photons and vice versa in external electric and magnetic fields. A promising experimental approach is based on the axion helioscope technique [2] where a dipole magnet is oriented towards the Sun. Axions could be produced in the solar plasma by converting thermal photons in the Coulomb fields of nuclei and electrons - the Primakoff process, and back-converted into photons in a laboratory transverse magnetic field.

Currently the most sensitive heliscope experiment CAST [3, 4, 5, 6] has been taking data since 2003. No signal over background has been observed so far and CAST set the best experimental limit on the axion-photon coupling constant $g_{a\gamma}$ over a broad range of axion masses. IAXO (International AXion Observatory) is a new generation axion helioscope [7], currently at the level of the Conceptual Design. IAXO relies on known technologies, there is no need for development. It will also benefit from the expertise and knowledge gained from the successful operation of CAST.

2 Experimental setup

IAXO concept relies on a dedicated magnet capable to track the Sun for about 12 hours each day, focusing X-ray optics to minimize detector area, and low background X-ray detectors optimized for operation in $0.5 - 10$ keV energy range.

The magnet, inspired by the toroidal ATLAS-like magnet geometry, is being designed at CERN [8]. The new toroid will have eight, 60 cm diameter and 21 m long, magnet bores at room temperature. It is designed to realize a peak magnetic field of 5.4 T. The magnet system will be decoupled from the optical system, which greatly simplifies the system integration. The magnet design opens the way for the sensitivity improvement, with respect to CAST, mainly through a large cross-sectional area.

Each of the eight magnet bores will be equipped with X-ray optics. CAST has successfully used optics, but only for one magnet bore of area ~ 15 cm^2. IAXO relies on focusing from much larger bore areas of $\sim$ m^2 down to spot of ~ 0.2 cm^2. The challenge is the availability of cost-effective X-ray optics of the required size. For IAXO, the baseline fabrication approach is segmented, slumped glass optics. This technology has been successfully used, most recently for the NuSTAR satellite mission.

The baseline technology for the low background detectors are small gaseous detectors with a pixelated Micromegas readout, manufactured with the microbulk technique. This kind of detector has already been used in CAST. The latest generation of Micromegas detecors in CAST are acheiving background levels of around 10^{-6} counts keV^{-1} cm^{-2} s^{-1}, a factor of more than 100 better than the levels at the beginning of CAST data taking. The goal for IAXO is to reduce the background level down to 10^{-7} counts keV^{-1} cm^{-2} s^{-1} or even lower.

3 Expected sensitivity

The primary physics goal of IAXO will be to search for axions and ALPs produced in the solar core via the Primakoff conversion of the solar plasma photons. The goal is to achieve 5 orders of magnitude better sensitivity than CAST, which translates into a factor of about 20 in terms of the axion-photon coupling constant $g_{a\gamma}$. That is, IAXO will reach the few $\times 10^{-12}$ GeV^{-1} level for a wide range of axion masses up to about 0.25 eV. Since IAXO will cover a big part of the unexplored parameter space, it has potential for the discovery of axions and ALPs. At high masses, the experiment would explore a range of realistic axion models related to the Peccei-Quinn solution to the strong CP problem. At low masses (below 10^{-7} eV), IAXO would test the hypothesis in which ALPs explain the transparency of the universe to very high energy photons [9]. Most of the region at reach by IAXO contains possible DM candidates. Figure 1 shows the expected IAXO sensitivity on $g_{a\gamma}$ as a function of the axion mass.

Another important physics goal for IAXO will be to search for solar axions produced in the processes based on the axion-electron coupling g_{ae}. An astrophysical observation shows that axions with g_{ae} of few $\times 10^{-13}$ could solve the anomalous cooling observed in white dwarfs [11]. IAXO is the first axion helioscope with sufficient sensitivity to g_{ae} to test this hypothesis.

Additional physics cases include searches for other proposed particles at the low energy frontier, like hidden photons or chameleons [12]. Also, the IAXO magnet has been designed to easily accomodate new equipment (e.g., microwave cavities or antennas). This provides an intriguing possibility to search in parallel for solar axions and also for relic axions in the galactic halo that could have been produced in the early universe.

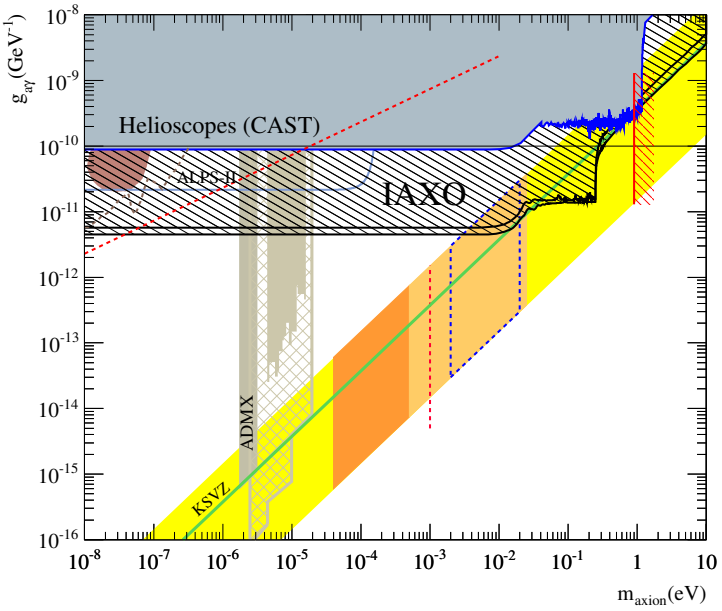

Figure 1: Expected IAXO sensitivity on $g_{a\gamma}$ as a function of m_a, compared with current bounds (solid) and future prospects (dashed) of other experiments (CAST, ADMX, ALPS-II). The region below the red dashed line is viable ALP DM parameter space. The region at low m_a above the dashed grey line is the one invoked in the context of the transparency of the universe while the solid brown region is excluded by H.E.S.S. data [10]. The yellow band represents the range of realistic axion models where the green line refers to the benchmark KSVZ model.

Acknowledgments

We acknowledge support from MSES (Croatia) under grant no. 098-0982887-2872.

References

[1] R. D. Peccei, Lect. Notes Phys. **741**, 3 (2008) [hep-ph/0607268].
[2] P. Sikivie, Phys. Rev. Lett. **51**, 1415 (1983) [Erratum-ibid. **52**, 695 (1984)].
[3] K. Zioutas *et al.* [CAST Collaboration], Phys. Rev. Lett. **94**, 121301 (2005) [hep-ex/0411033].
[4] S. Andriamonje *et al.* [CAST Collaboration], JCAP **0704**, 010 (2007) [hep-ex/0702006].
[5] E. Arik *et al.* [CAST Collaboration], JCAP **0902**, 008 (2009) [arXiv:0810.4482 [hep-ex]].
[6] M. Arik *et al.* [CAST Collaboration], Phys. Rev. Lett. **107**, 261302 (2011) [arXiv:1106.3919 [hep-ex]].
[7] I. G. Irastorza *et al.*, JCAP **1106**, 013 (2011) [arXiv:1103.5334 [hep-ex]].
[8] I. Shilon, A. Dudarev, H. Silva, U. Wagner and H. H. J. t. Kate, arXiv:1308.2526 [physics.ins-det].
[9] M. Meyer, D. Horns and M. Raue, Phys. Rev. D **87**, 035027 (2013) [arXiv:1302.1208 [astro-ph.HE]].
[10] P. Brun, D. Wouters (for the H.E.S.S. collaboration), proceedings of the 33rd ICRC, 2013, Rio de Janeiro
[11] J. Isern *et al.*, Astronomy and Astrophysics **512**, A86 (2010) [arXiv:1001.5248 [astro-ph.SR]].
[12] J. Jaeckel and A. Ringwald, Ann. Rev. Nucl. Part. Sci. **60**, 405 (2010) [arXiv:1002.0329 [hep-ph]].

Status and Perspectives of the CAST Experiment

B. Lakić[1], *M. Arik*[2], *S. Aune*[3], *K. Barth*[4], *A. Belov*[5], *S. Borghi*[4], *H. Bräuninger*[6], *G. Cantatore*[7], *J. M. Carmona*[8], *S. A. Cetin*[2], *J. I. Collar*[9], *E. Da Riva*[4], *T. Dafni*[8], *M. Davenport*[4], *C. Eleftheriadis*[10], *N. Elias*[4], *G. Fanourakis*[11], *E. Ferrer-Ribas*[3], *P. Friedrich*[6], *J. Galán*[8,3], *J. A. García*[8], *A. Gardikiotis*[12], *J. G. Garza*[8], *E. N. Gazis*[13], *T. Geralis*[11], *E. Georgiopoulou*[12], *I. Giomataris*[3], *S. Gninenko*[5], *H. Gómez*[8], *M. Gómez Marzoa*[4], *E. Gruber*[14], *T. Guthörl*[14], *R. Hartmann*[15], *S. Hauf*[16], *F. Haug*[4], *M. D. Hasinoff*[17], *D. H. H. Hoffmann*[16], *F. J. Iguaz*[8,3], *I. G. Irastorza*[8], *J. Jacoby*[18], *K. Jakovčić*[1], *M. Karuza*[7], *K. Königsmann*[14], *R. Kotthaus*[19], *M. Krčmar*[1], *M. Kuster*[6,16], *P. M. Lang*[16], *J. M. Laurent*[4], *A. Liolios*[10], *A. Ljubičić*[1], *V. Lozza*[7], *G. Luzón*[8], *S. Neff*[16], *T. Niinikoski*[4], *A. Nordt*[6,16], *T. Papaevangelou*[3], *M. J. Pivovaroff*[20], *G. Raffelt*[19], *H. Riege*[16], *A. Rodríguez*[8], *M. Rosu*[16], *J. Ruz*[4,20], *I. Savvidis*[10], *I. Shilon*[8,4], *P. S. Silva*[4], *S. K. Solanki*[21], *L. Stewart*[4], *A. Tomás*[8], *M. Tsagri*[12,4], *K. van Bibber*[20], *T. Vafeiadis*[4,10,12], *J. Villar*[8], *J. K. Vogel*[14,20], *S. C. Yildiz*[2], *K. Zioutas*[4,12]

[1]Rudjer Bošković Institute, Zagreb, Croatia
[2]Dogus University, Istanbul, Turkey
[3]IRFU, Centre d'Études Nucléaires de Saclay (CEA-Saclay), Gif-sur-Yvette, France
[4]European Organization for Nuclear Research (CERN), Genève, Switzerland
[5]Institute for Nuclear Research (INR), Russian Academy of Sciences, Moscow, Russia
[6]Max-Planck-Institut für Extraterrestrische Physik, Garching, Germany
[7]INFN, Sezione di Trieste and Università di Trieste, Trieste, Italy
[8]Instituto de Física Nuclear y Altas Energías, Universidad de Zaragoza, Zaragoza, Spain
[9]Enrico Fermi Institute and KICP, University of Chicago, Chicago, IL, USA
[10]Aristotle University of Thessaloniki, Thessaloniki, Greece
[11]National Center for Scientific Research *Demokritos*, Athens, Greece
[12]Physics Department, University of Patras, Patras, Greece
[13]National Technical University of Athens, Athens, Greece
[14]Albert-Ludwigs-Universität Freiburg, Freiburg, Germany
[15]MPI Halbleiterlabor, München, Germany
[16]Technische Universität Darmstadt, IKP, Darmstadt, Germany
[17]Department of Physics and Astronomy, University of British Columbia, Vancouver, Canada
[18]J. W. Goethe-Universität, Institut für Angewandte Physik, Frankfurt am Main, Germany
[19]Max-Planck-Institut für Physik (Werner-Heisenberg-Institut), München, Germany
[20]Lawrence Livermore National Laboratory, Livermore, CA, USA
[21]Max-Planck-Institut für Sonnensystemforschung, Katlenburg-Lindau, Germany

DOI: http://dx.doi.org/10.3204/DESY-PROC-2013-04/lakic_biljana_CAST

CERN Axion Solar Telescope (CAST) is currently the most sensitive axion helioscope designed to search for axions and axion-like particles produced in the Sun. CAST is using a Large Hadron Collider prototype magnet where axions could be converted into X-rays. So far, no evidence of signal has been found and CAST set the best experimental limit on the axion-photon coupling constant over a broad range of axion masses up to ~ 1 eV.

1 Introduction

Axions are hypothetical particles arising in models which may solve the CP problem of strong interactions. The underlying Peccei-Quinn (PQ) mechanism [1] introduces a new global U(1) symmetry that is spontaneously broken at a large energy scale f_a. Axions are neutral pseudoscalars with phenomenology determined by the scale f_a. They generically couple to gluons and mix with neutral pions. The axion mass can be expressed in the form $m_a = m_\pi f_\pi / f_a = 6\ \text{eV}(10^6\ \text{GeV}/f_a)$, where m_π and f_π are the pion mass and decay constant, respectively. Axions couple to photons, nucleons and electrons. Most of the axion experimental searches rely on the axion interaction with two photons, allowing for axion-photon conversion in external electric or magnetic fields.

The CAST experiment is based on the axion helioscope technique [2] where a dipole magnet is oriented towards the Sun. Axions could be produced in the solar plasma via the Primakoff process, and back-converted into photons in a laboratory magnetic field. The expected solar axion flux at the Earth would have a continuous energy spectrum peaked near the mean energy $\langle E_a \rangle = 4.2$ keV and dying off above 10 keV. The expected number of photons (X-rays) reaching a detector is $N_\gamma = \int (d\Phi_a/dE_a) P_{a\to\gamma} S\, t\, dE_a$ where $(d\Phi_a/dE_a)$ is the differential axion flux at the Earth, $P_{a\to\gamma}$ the axion-photon conversion probablilty, S the effective area and t the measurement time. The axion-photon conversion probability in vacuum can be written as $P_{a\to\gamma} = (g_{a\gamma} B/q)^2 \sin^2(qL)$ where L is the magnet length, B the magnetic field and $q = m_a^2/2E_a$ the axion-photon momentum difference. The probability is maximal if the axion and photon remain in phase over the magnet length, i.e. when the coherence condition $qL < \pi$ is satisfied. As a consequence, the experimental sensitivity is restricted to a range of axion masses. In order to extend the sensitivity to higher axion masses, the conversion region has to be filled with a buffer gas which provides an effective photon mass.

The first implementation of the axion helioscope technique was performed in Brookhaven [3] and later a more sensitive search in Tokyo [4, 5, 6]. The most sensitive heliscope experiment CAST has been taking data since 2003, both with vacuum and gas (helium) inside the conversion region.

2 Experimental setup

CAST utilizes a Large Hadron Collider (LHC) prototype dipole magnet as the source of external magnetic field ($B = 9$ T). Inside the magnet there are two paralell pipes with the length $L = 9.26$ m and cross-sectional area $S = 2\times 14.5$ cm^2. The magnet is mounted on a rotating platform with $\pm 40°$ horizontal and $\pm 8°$ vertical movement. As a result, the Sun can be followed for about 1.5 hours both at sunrise and sunset during the whole year. At both ends of the magnet, different detectors are searching for X-rays coming from axion conversion inside the magnet when it is pointing to the Sun. The time the Sun is not reachable is used for background measurements. Two different X-ray detectors are used presently. Three Micromegas detectors [7, 8, 9] cover two bores on the sunset side and one of the bores of the sunrise side. A Charged Coupled Device (CCD) [10] is covering the other bore on the sunrise side. The CCD is working in combination with an X-ray telescope which can focus the photons to a few mm^2 spot, thus significantly improving the experimental sensitivity.

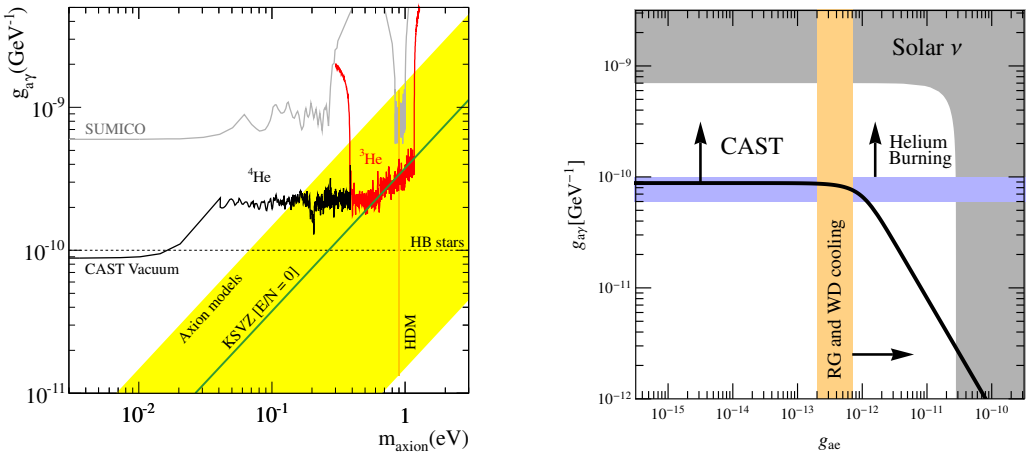

Figure 1: *Left*: Exclusion regions in the $m_a - g_{a\gamma}$ plane achieved by CAST in the vacuum, ^{4}He, first part of the ^{3}He phase and our new preliminary results (all in red). We also show constraints from the Tokyo helioscope (Sumico), horizontal branch (HB) stars, and the hot dark matter (HDM) bound. The yellow band represents typical theoretical models while the green solid line corresponds to the KSVZ model. *Right*: CAST constraints on g_{ae} and $g_{a\gamma}$ for $m_a \lesssim 10$ meV. The region above the thick black line is excluded by CAST. The gray region is excluded by solar neutrino measurements. In the vertical orange band, axion emission strongly affects white dwarf cooling and the evolution of low-mass red giants; the region to the right of this band is excluded. Likewise, helium-burning stars would be affected in the horizontal blue band; parameters above it are excluded.

3 CAST operation, results and prospects

The CAST experiment has been taking data since 2003. During 2003 and 2004 the experiment operated with vacuum inside the magnet bores, and set the best experimental limit on the axion-photon coupling constant for the axion mass range up to 0.02 eV [11, 12]. In order to extend the sensitivity to higher axion masses, the conversion region had to be filled with a buffer gas. By changing the pressure of the buffer gas in steps, one can scan an entire range of axion mass values. During 2005 and 2006 the magnet bores were filled with ^{4}He, and the range of axion masses up to 0.39 eV was scanned. For the first time, the obtained limit [13] entered the QCD axion model band in the electroweak range. From 2008 to 2011, with ^{3}He as the buffer gas, CAST covered the range of axion masses up to 1.18 eV. The results of the first part of ^{3}He data, with the sensitivity up to 0.64 eV, were published in [14]. Figure 1 (left) shows the CAST published limits on the axion-photon coupling constant for axion masses up to 0.64 eV, as well as the preliminary limit for masses up to 1.18 eV.

Apart from the main line of research, CAST has also performed searches from M1 nuclear transitions [15, 16] and low energy axions [17]. The most recent search investigated non-hadronic axion models, which have a tree-level axion-electron interaction. In these models, axions would be abundantly produced in the Sun via bremsstrahlung, Compton scattering, and axio-recombination. Figure 1 (right) shows the obtained constraints [18] on the axion-electron (g_{ae}) and axion-photon coupling constant ($g_{a\gamma}$) for the range of axion masses up to 0.01 eV.

In the immediate future, CAST is planning to revisit the vacuum phase with significantly improved low-background Micromegas detectors and new X-ray optics for the sunrise Micromegas. With the improved sensitivity, CAST will be able to scan a new region of the parameter space searching for axion-like particles. These particles appear in many extensions of the standard model (including string theory) and are viable candidates for the dark matter of the universe. In parallel, CAST will be able to search for other proposed particles at the low energy frontier, like hidden photons or chameleons.

The challenge for the long-term future is to move down in the $m_a - g_{a\gamma}$ parameter space. This goal could be achieved with significant improvements of magnet and detector properties, and extensive use of X-ray optics [19]. A new generation of axion helioscope, IAXO (International AXion Observatory), is currently at the level of the Conceptual Design.

Acknowledgments

We acknowledge support from MSES (Croatia) under grant no. 098-0982887-2872.

References

[1] R. D. Peccei, Lect. Notes Phys. **741**, 3 (2008) [hep-ph/0607268].
[2] P. Sikivie, Phys. Rev. Lett. **51**, 1415 (1983) [Erratum-ibid. **52**, 695 (1984)].
[3] D. M. Lazarus *et al.*, Phys. Rev. Lett. **69**, 2333 (1992).
[4] S. Moriyama *et al.*, Phys. Lett. B **434**, 147 (1998) [hep-ex/9805026].
[5] Y. Inoue *et al.*, Phys. Lett. B **536**, 18 (2002) [astro-ph/0204388].
[6] Y. Inoue *et al.*, Phys. Lett. B **668**, 93 (2008) [arXiv:0806.2230 [astro-ph]].
[7] P. Abbon *et al.*, New J. Phys. **9**, 170 (2007) [physics/0702190].
[8] S. Aune *et al.*, J. Phys. Conf. Ser. **179**, 012015 (2009).
[9] T. Dafni *et al.*, Nucl. Instrum. Meth. A **628**, 172 (2011).
[10] M. Kuster *et al.*, New J. Phys. **9**, 169 (2007) [physics/0702188].
[11] K. Zioutas *et al.* [CAST Collaboration], Phys. Rev. Lett. **94**, 121301 (2005) [hep-ex/0411033].
[12] S. Andriamonje *et al.* [CAST Collaboration], JCAP **0704**, 010 (2007) [hep-ex/0702006].
[13] E. Arik *et al.* [CAST Collaboration], JCAP **0902**, 008 (2009) [arXiv:0810.4482 [hep-ex]].
[14] M. Arik *et al.* [CAST Collaboration], Phys. Rev. Lett. **107**, 261302 (2011) [arXiv:1106.3919 [hep-ex]].
[15] S. Andriamonje *et al.* [CAST Collaboration], JCAP **0912**, 002 (2009) [arXiv:0906.4488 [hep-ex]].
[16] S. Andriamonje *et al.* [CAST Collaboration], JCAP **1003**, 032 (2010) [arXiv:0904.2103 [hep-ex]].
[17] G. Cantatore *et al.* [CAST Collaboration], arXiv:0809.4581 [hep-ex].
[18] K. Barth *et al.*, JCAP **1305**, 010 (2013) [arXiv:1302.6283 [astro-ph.SR]].
[19] I. G. Irastorza *et al.*, JCAP **1106**, 013 (2011) [arXiv:1103.5334 [hep-ex]].

Search for axioelectric effect of 5.5 MeV solar axions using BGO detectors

V.N. Muratova, A.V. Derbin, S.V. Bakhlanov, I.S. Dratchnev, A.S. Kayunov,

St.Petersburg Nuclear Physics Institute, Gatchina, Russia 188300

DOI: http://dx.doi.org/10.3204/DESY-PROC-2013-04/muratova_valentina

A search for axioelectric absorption of solar axions produced in $p+d \rightarrow {}^3\mathrm{He}+\gamma$ (5.5 MeV) reactions has been performed with a BGO detector placed in a low-background setup. A model-independent limit on an axion-nucleon and axion-electron coupling constant has been obtained: $|g_{Ae} \times g^3_{AN}| < 2.9 \times 10^{-9}$ for 90% confidence level. The constrains of the axion-electron coupling have been obtained for hadronic axion with masses in (0.1 - 1) MeV range: $|g_{Ae}| \leq (1.4 - 9.7) \times 10^{-7}$.

1 Introduction

New possibilities for solving a strong CP problem are based on the concept of the existence of the mirror particles [1] and supersymmetry [2]. These models suppose the existence of axions with the mass of about 1 MeV, and this existence is forbidden by neither laboratory experiments nor astrophysical data.

Recently, the high energy solar axions and axions from a nuclear reactor have been sought by the Borexino [3, 4], the CAST [5] and the Texono [6] collaborations. We have previously published a search for 5.5 MeV axions with BGO detectors [7, 8].

2 Axion production in nuclear magnetic transitions and the axioelectric effect

The reactions of the main solar chain and CNO cycle can produce axions with higher energies. The most intensive flux is expected as a result of the reaction: $p + d \rightarrow {}^3\mathrm{He} + \gamma$ when 5.5 MeV axion is emitted instead $\gamma-$quantum. The expected solar axion flux can thus be expressed in terms of the pp-neutrino flux, which is $\Phi_{\nu pp} = 6.0 \times 10^{10}\mathrm{cm}^{-2}\mathrm{s}^{-1}$ [9].

In the $p(d,{}^3\mathrm{He})\gamma$ reaction, the M1-type transition corresponds to the capture of a proton with a zero orbital momentum. The probability of proton capture from the S state at proton energies below 80 keV has been measured in [10]; at the proton energy of ~ 1 keV, M1 fraction of the total $p(d,{}^3\mathrm{He})\gamma$ cross section is $\chi = 0.55$. The proton capture from the S state corresponds to the isovector transition, and the ratio of the probability of a nuclear transition with the axion

production (ω_A) to the probability of a magnetic transition (ω_γ) depends only on g_{AN}^3 [8, 11]:

$$\frac{\omega_A}{\omega_\gamma} = \frac{\chi}{2\pi\alpha}\left[\frac{g_{AN}^3}{\mu_3}\right]^2\left(\frac{p_A}{p_\gamma}\right)^3 = 0.54(g_{AN}^3)^2\left(\frac{p_A}{p_\gamma}\right)^3. \quad (1)$$

where p_γ and p_A are, respectively, the photon and axion momenta; α is the fine-structure constant; and μ_3 is isovector nuclear magnetic momenta.

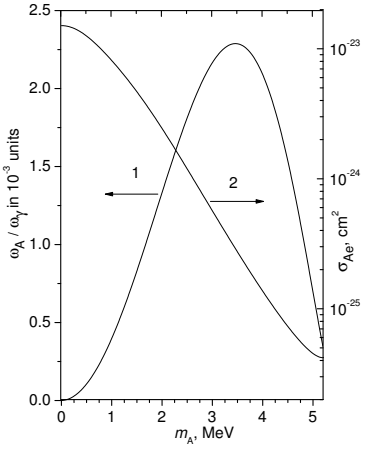

Figure 1: The ratio of the emission probabilities for axions and γ quanta (ω_A/ω_γ) in the $p + d \to {}^3\mathrm{He} + \gamma$ reaction (curve 1, left-hand scale); the cross section of the axioelectric effect for 5.5-MeV axions on bismuth atoms for $g_{Ae} = 1$ (curve 2, right-hand scale).

The calculated values of the ω_A/ω_γ ratio as a function of the axion mass are shown in Fig.1. The axion flux on the Earth's surface is $\Phi_A = \Phi_{\nu pp}(\omega_A/\omega_\gamma)$.

To detect 5.5 MeV axions, we chose the reaction of axioelectric effect $A+Z+e \to Z+e$ which is caused by the axion-electron interaction. The cross section of the axioelectric effect depends on the nuclear charge according to the Z^5 law, and therefore, it is reasonable to search for this process using detectors with a large Z. The detection efficiency for the produced electron is close to 1 and the background level at 5.5 MeV is much lower than in the range of natural radioactivity. As a result, the sensitivity to constants g_{Ae} and g_{AN} can be high even in an experiment using a relatively small target mass.

The axioelectric effect cross section for K-shell electrons has been calculated (on the assumption that $E_A \gg E_b$ and $Z \ll 137$) in [12]. The dependence of the cross section on the axion mass for the coupling constant $g_{Ae} = 1$ is shown in Fig.1.

3 Experimental setup

We used a 2.46 kg BGO crystal, manufactured from bismuth orthogermanate $Bi_4Ge_3O_{12}$ (1.65 kg of Bi), to search for the 5.5 MeV axions. The BGO crystal was grown at the Nikolaev Institute of Inorganic Chemistry and it was shaped as a cylinder, 76 mm in diameter and 76 mm in height. The detector signal was measured by an R2887 photoelectron multiplier, which had an optical contact with a crystal end surface.

The external γ activity was suppressed using a passive shield that consisted of successive layers of lead (90 mm) and bismuth (15 mm Bi_2O_3). The total thickness of the passive shield was ≈ 110 g cm^{-2}. The setup was located on the Earth's surface. In order to suppress the cosmic-ray background we used an active veto, which consisted of five $50 \times 50 \times 12$ cm plastic scintillators.

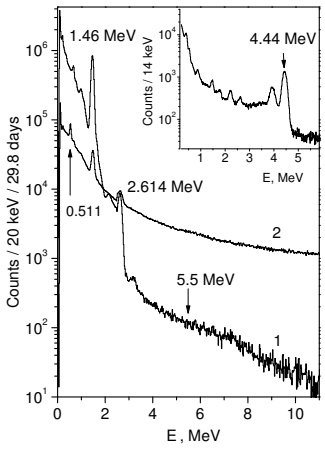

Figure 2: The energy spectrum of the BGO detector measured (1) in anticoincidence and (2) in coincidence with the active shielding signal. The location of the expected 5.5 MeV axion peak is denoted by an arrow. In inset the spectrum measured with Pu-Be neutron source is shown.

4 Results

The measurements were performed over 29.8 days in live time. The energy spectrum of the BGO detector in the range of (0–11) MeV is shown in Fig.2. The spectrum of the BGO signals that were not accompanied by the active shielding signal is designated as 1.

The positions and dispersion of the 1.46 MeV and 2.614 MeV peaks determined during the measurements were used to find the energy scale and resolution of the BGO detector. For higher energies the energy calibration was checked with a ^{239}Am-^{9}Be neutron source. (Fig.2, inset).

Figure 3 shows the energy range of $(4.5 - 6.5)$ MeV, in which the axion peak was expected. The spectrum measured was fitted by a sum of exponential and two Gaussian functions. The intensity of the 5.49 MeV peak was found to be $S_1 = -18 \pm 58$, this corresponds to the upper limit on the number of counts in the peak, $S_{lim} = 85$ at a 90% confidence level.

The expected number of axioelectric absorption events are:

$$S_{abs} = \varepsilon N_{Bi} T \Phi_A \sigma_{Ae} \tag{2}$$

where σ_{Ae} is the axioelectric effect cross section; Φ_A is the axion flux; $N_{Bi} = 4.76 \times 10^{24}$ is the number of Bi atoms; $T = 2.57 \times 10^6$ s is the measurement time; and $\varepsilon = 0.67$ is the detection efficiency for 5.5 MeV electrons. The axion flux Φ_A is proportional to the constant $(g_{AN}^3)^2$, and

the cross section σ_{Ae} is proportional to the constant g_{Ae}^2. As a result, the S_{abs} value depends on the product of the axion-electron and axion-nucleon coupling constants: $(g_{Ae})^2 \times (g_{AN}^3)^2$.

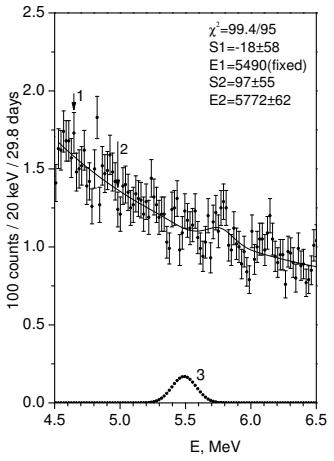

Figure 3: The fitted BGO spectrum in the $(4.5 - 6.5)$ MeV range. Curve 3 is the detector response function for $E_0 = 5.49$ MeV and $\sigma = 0.093$ MeV.

The experimentally found condition $S_{abs} \leq S_{lim}$ imposes some constraints on the range of possible $|g_{Ae} \times g_{AN}^3|$ and m_A values. The range of excluded $|g_{Ae} \times g_{AN}^3|$ values is shown in Fig. 4, at $m_A \to 0$ the limit is

$$|g_{Ae} \times g_{AN}^3| \leq 2.9 \times 10^{-9}. \quad (3)$$

The dependence of $|g_{Ae} \times g_{AN}^3|$ on m_A is related only to the kinematic factor in axio-electric cross section. These constraints are completely model-independent and valid for any pseudoscalar particle with coupling $|g_{Ae}|$ less than $10^{-6(4)}$ [8].

Within the hadronic axion model, g_{AN}^3 and m_A quantities are related to the known relation, which can be used to obtain a constraint on the g_{Ae} constant, depending on the axion mass (Fig.4). For $m_A = 1$ MeV, this constraint corresponds to $|g_{Ae}| \leq 1.4 \times 10^{-7}$.

Figure 4 also shows the constraints on the constant $|g_{Ae}|$ that were obtained in the Borexino experiment for 478-keV ^{7}Li solar axions [3] and in the Texono reactor experiment for 2.2-MeV axions produced in the $n + p \to d + A$ reaction [6]. Recently, Borexino coll. reported new more stringent limits on g_{Ae} coupling for 5.5 MeV solar axions [4]. Unlike our work, these limits on g_{Ae} were obtained in assumption that the axion interacts with electron through the Compton conversion process.

5 Acknowledgments

This work was supported by RFBR grants 13-02-01199-a and 13-02-12140-ofi-m.

References

[1] Z. Berezhiani *et al.* Phys. Lett. B **500**, 286 (2001)

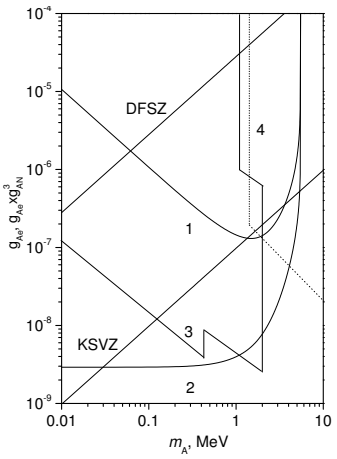

Figure 4: The limits on the g_{Ae} coupling constant obtained by 1- present work, 2 - present work for $|g_{Ae} \times g_{AN}^3|$, 3- solar [3] and reactor experiments [6, 13], 4- beam dump experiments [14, 15]. The allowed $|g_{Ae}|$ and $|g_{Ae} \times g_{AN}^3|$ values lie below the corresponding curves. The relations between g_{Ae} and m_A for DFSZ- and KSVZ-models are also shown .

[2] L.J. Hall and T. Watari, Phys. Rev. D **70**, 115001 (2004)

[3] G. Bellini *et al.* [Borexino coll.] EPJ, C **54**, 61 (2008)

[4] G. Bellini *et al.* [Borexino Coll.], Phys. Rev. D **85**, 092003 (2012)

[5] S. Andriamonje *et al.* [CAST coll.] JCAP 1003, 032, (2010) [arXiv:0904.2103]

[6] H.M. Chang *et al.* [Texono Coll.] Phys. Rev. D **75**, 052004 (2007)

[7] A.V. Derbin *et al.* Bull.Rus.Acad.Sci. Phys. 74, 805 (2010) [arXiv:1007.3387]

[8] A.V. Derbin *et al.* EPJ, C **73**, 2490 (2013)[arXiv:1306.4574]

[9] A.M. Serenelli, W.C. Haxton and C. Peña-Garay, [arXiv:1104.1639]

[10] G.J. Schmid *et al.* Phys. Rev. C **56**, 2565 (1997)

[11] G. Raffelt, L. Stodolsky, Phys. Lett. B **119**, 323 (1982)

[12] A.R. Zhitnitskii and Yu.I. Skovpen, Yad. Fiz., 29, 995 (1979)

[13] M. Altmann *et al.* Z. Phys. C **68**, 221 (1995)

[14] A. Konaka *et al.* Phys. Rev. Lett. 57, 659 (1986)

[15] J.D. Bjorken *et al.* Phys. Rev. D **38**, 3375 (1988)

New Light on Dark Photons

H. An[1], *M. Pospelov*[1,2], *J. Pradler*[3*]

[1]Perimeter Institute for Theoretical Physics, Waterloo, ON N2L 2Y5, Canada
[2]Department of Physics and Astronomy, University of Victoria, Victoria, BC V8P 5C2, Canada
[3]Department of Physics and Astronomy, Johns Hopkins University, Baltimore, MD 21218, USA

DOI: http://dx.doi.org/10.3204/DESY-PROC-2013-04/pradler_josef

"Dark Photons", light new vector particles V_μ kinetically mixed with the photon, are a frequently considered extension of the Standard Model. For masses below 10 keV they are emitted from the solar interior. In the limit of small mass m_V the dark photon flux is strongly peaked at low energies and we demonstrate that the constraint on the atomic ionization rate imposed by the results of the XENON10 Dark Matter experiment sets the to-date most stringent limit on the kinetic mixing parameter of this model: $\kappa \times m_V < 3 \times 10^{-12}\,\mathrm{eV}$. The result significantly improves previous experimental bounds and surpasses even the most stringent astrophysical and cosmological limits in a seven-decade-wide interval of m_V.

1 Introduction

In the recent years, the model of light vector particles with kinetic mixing to the Standard Model photon has received tremendous attention, theoretically as well as experimentally. Whereas $m_V \gtrsim 1\,\mathrm{MeV}$ is mainly being probed in medium-to-high energy collider experiments, masses in the sub-MeV regime are subject to severe astrophysical and cosmological constraints. Below $m_V < 10$ eV, those limits are complemented by direct laboratory searches for dark photons in non-accelerator type experiments. Among the most prominent are the "light-shining-through-wall" experiments (LSW) [1] and the conversion experiments from the solar dark photon flux, "helioscopes" [2]; a collection of low-energy constraints on dark photons can *e.g.* be found in the recent review [3]. Helioscopes derive their sensitivity from the fact that such light vectors are easily produced in astrophysical environments, such as in the solar interior, covering a wide range of masses up to $m_V \sim$ few keV. In general, stellar astrophysics provides stringent constraints on any type of light, weakly-interacting particles once the state becomes kinematically accessible [4]. Only in a handful of examples does the sensitivity of terrestrial experiments match the stellar energy loss constraints.

Here we review our works [5, 6] in which we have identified a new stellar energy loss mechanism originating from the resonant production of longitudinally polarized dark photons and derived ensuing constraints from underground rare event searches. Limits on dark photons were improved to the extent that previously derived constraints from all LSW and helioscope experiments are now superseded by the revised astrophysical and new experimental limits.

*Speaker. 9th Patras Workshop on Axions, WIMPs and WISPs.

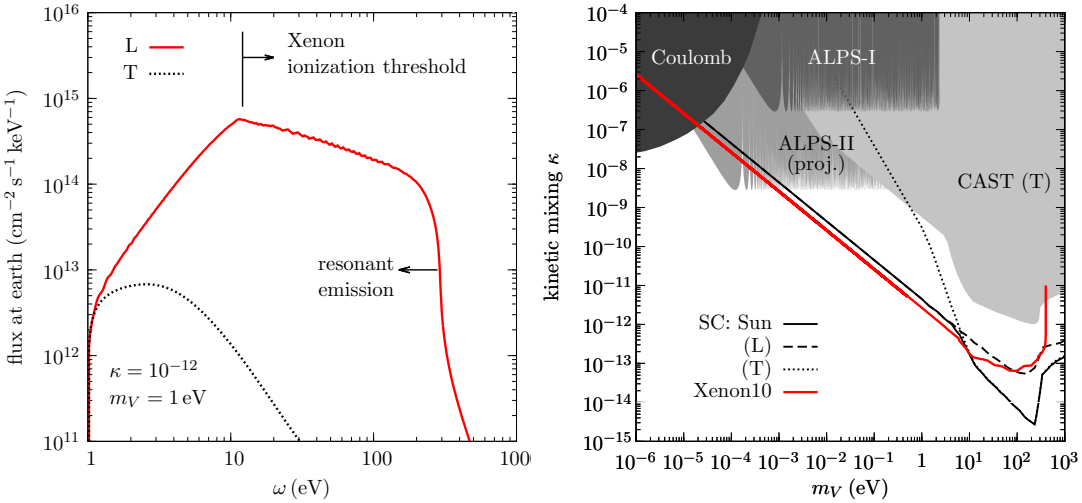

Figure 1: *Left:* Energy differential solar dark photon flux at Earth for $\kappa = 10^{-12}$ and $m_V = 1\,\mathrm{eV}$. The solid/dotted line shows the longitudinal(L)/transverse(T) contribution. *Right:* Constraints on κ as a function of m_V. The black solid/dashed/dotted curves show the total/longitudinal/transverse energy loss limit of the Sun by requiring that the dark photon luminosity does not exceed 10% of the standard solar luminosity [7]. The red line shows the constraint derived from the XENON10 data. Previous and future (="proj.") experimental bounds/sensitivities are shown by the shaded regions. From light to dark shading these are from the CAST experiment [8] considering the contributions from only the transverse modes [2], from the ALPS collaboration [9], and from tests of the inverse square law of the Coulomb interaction [10].

2 Dark Photons from the sun: flux and detection

The minimal extension of the SM gauge group by an additional $\mathrm{U}(1)_V$ gauge factor yields the following effective Lagrangian well below the electroweak scale,

$$\mathcal{L} = -\frac{1}{4}F_{\mu\nu}^2 - \frac{1}{4}V_{\mu\nu}^2 - \frac{\kappa}{2}F_{\mu\nu}V^{\mu\nu} + \frac{m_V^2}{2}V_\mu V^\mu + eJ_{\mathrm{em}}^\mu A_\mu, \tag{1}$$

where V_μ is the vector field associated with the Abelian factor $\mathrm{U}(1)_V$. The field strengths of the photon $F_{\mu\nu}$ and of the dark photon $V_{\mu\nu}$ are connected via the kinetic mixing parameter κ where a dependence on the weak mixing angle was absorbed; J_{em}^μ is the usual electromagnetic current with electric charge e.

Because of the U(1) nature of (1), we must distinguish two cases for the origin of m_V: the Stueckelberg case (SC) with non-dynamical mass, and the Higgs case (HC), where m_V originates through the spontaneous breaking of $\mathrm{U}(1)_V$ by a new Higgs field h'. The crucial difference between the two cases comes in the small m_V limit: while all processes of production or absorption of V in SC are suppressed, $\Gamma_{\mathrm{SC}} \sim O(m_V^2)$, in HC there is no decoupling, and $\Gamma_{\mathrm{HC}} \sim O(m_V^0)$. Indeed, in the limit $m_{V,h'} \to 0$ the interaction resembles one of a mini-charged scalar with the effective EM charge of $e_{\mathrm{eff}} = \kappa e'$ [11, 12, 13, 14]. In the following we discuss the SC and refer the reader to our work [6] as well as to [15] and references therein for HC.

Solar flux The solar flux of dark photons in the SC is thoroughly calculated in Ref. [5]; for further discussion see also [16]. In the small mass region, $m_V \ll \omega_p$ where ω_p is the plasma frequency, the emission of longitudinal modes of V dominates the total flux, and the emission power of dark photons per volume can be approximated as

$$\frac{dP_L}{dV} \approx \frac{1}{4\pi} \frac{\kappa^2 m_V^2 \omega_p^3}{e^{\omega_p/T} - 1}. \tag{2}$$

This formula is most readily obtained by noting that a resonant conversion of longitudinal plasmons into dark photons is possible whenever $\omega^2 = \omega_p^2$. The energy-differential flux of dark photons at the location of the Earth is shown in the left panel of Fig. 1. Resonant emission stops for $\omega \gtrsim 300\,\mathrm{eV}$ since ω_p is limited by the temperature in the sun's core.

Absorption of dark photons In the SC, the ionization of an atom A in the detector can then be schematically described as $V + A \to A^+ + e^-$. The total dark photon absorption rate is given by,

$$\Gamma_{T,L} = -\frac{\kappa_{T,L}^2 \,\mathrm{Im}\,\Pi_{T,L}}{\omega}, \qquad \kappa_{T,L}^2 = \frac{\kappa^2 m_V^4}{(m_V^2 - \mathrm{Re}\,\Pi_{T,L})^2 + (\mathrm{Im}\,\Pi_{T,L})^2}. \tag{3}$$

$\kappa_{T,L}$ are the effective mixings for the transverse (T) and longitudinal (L) modes respectively. The polarization functions $\Pi_{T,L}$ are found from the in-medium polarization tensor $\Pi^{\mu\nu}$,

$$\Pi^{\mu\nu}(q) = ie^2 \int d^4x\, e^{iq\cdot x} \langle \Omega | T J_{em}^\mu(x) J_{em}^\nu(0) | \Omega \rangle = -\Pi_T \sum_{i=1,2} \varepsilon_i^{T\mu} \varepsilon_i^{T\nu} - \Pi_L \varepsilon^{L\mu} \varepsilon^{L\nu}, \tag{4}$$

where $q = (\omega, \vec{q})$ is the dark photon four momentum and $\epsilon_\mu^{T,L}$ are the polarization vectors for the transverse and longitudinal modes of the dark photon, $\epsilon_\mu^2 = -1$. The first relation (3) is a manifestation of the optical theorem.

The polarization functions $\Pi_{T,L}$ are related to the complex index of refraction, n_{refr} or, equivalently, to the permittivity of the medium $\varepsilon = n_{\mathrm{refr}}^2$. For an isotropic, non-magnetic medium $\Pi_L = (\omega^2 - \vec{q}^2)(1 - n_{\mathrm{refr}}^2)$, and $\Pi_T = \omega^2(1 - n_{\mathrm{refr}}^2)$, so that for an incoming on-shell dark photon with $q^2 = m_V^2$, $\Gamma_L \propto \kappa^2 m_V^2$ indeed holds. We obtain n_{refr} from its relation to the forward scattering amplitude $f(0) = f_1 + i f_2$ where the atomic scattering factors $f_{1,2}$ are *e.g.* tabulated in [17]. Close to the ionization threshold we make use of the Kramers-Kronig dispersion relations to relate f_1 and f_2 for estimating n_{refr}. Alternatively, one can solve an integral equation relating $\mathrm{Im}\,\varepsilon$ and $\mathrm{Re}\,\varepsilon$ in a self-consistent manner, an approach taken in [6].

Limits from direct detection With flux $d\Phi_{T,L}/d\omega$ and absorption rate $\Gamma_{T,L}$ at hand, the expected number of signal events in a given experiment reads

$$N_{\mathrm{exp}} = VT \int_{\omega_{\mathrm{min}}}^{\omega_{\mathrm{max}}} \frac{\omega d\omega}{|\vec{q}|} \left(\frac{d\Phi_T}{d\omega} \Gamma_T + \frac{d\Phi_L}{d\omega} \Gamma_L \right) \mathrm{Br}, \tag{5}$$

where V and T are the fiducial volume and live time of the experiment, respectively, and Br is the branching ratio of photoionization rate to total absorption rate.

Given the significant infrared enhancement of the solar dark photon spectrum, left panel of Fig. 1, the low-energy ionization signals measured in the XENON10 [18] dark matter experiment

have the best sensitivity to constrain a dark photon flux that is also supported by the Sun. With ∼12 eV ionization energy in xenon, the absorption of a dark photon with 300 eV energy can produce about 25 electrons. From [18] we estimate a 90% C.L upper limit on the detecting rate to be $r < 19.3$ events $\mathrm{kg}^{-1}\mathrm{day}^{-1}$ (similar to limits deduced in Ref. [19]). In the region $12\ \mathrm{eV} < \omega < 300\ \mathrm{eV}$ the ionization process dominates the absorption, and therefore Br in this region can be set to unity. The 90% C.L. upper limit on κ as a function of m_V is shown by the thick red curve in Fig. 1. As can be seen it surpasses other current experimental limits as well as the solar energy loss bound in a mass interval from $10^{-5}\,\mathrm{eV} < m_V \lesssim 10\,\mathrm{eV}$.

Given the enormous amount of experimental progress in the field of direct Dark Matter detection, one can be optimistic that future sensitivity to dark photons, and other light particles is bound to be further improved.

3 Acknowledgments

The speaker would like to thank the conference organizers for financial support.

References

[1] M. Ahlers, H. Gies, J. Jaeckel, J. Redondo and A. Ringwald, Phys. Rev. D **77**, 095001 (2008) [arXiv:0711.4991 [hep-ph]].

[2] J. Redondo, JCAP **0807**, 008 (2008) [arXiv:0801.1527 [hep-ph]].

[3] J. Jaeckel and A. Ringwald, Ann. Rev. Nucl. Part. Sci. **60**, 405 (2010) [arXiv:1002.0329 [hep-ph]].

[4] G. G. Raffelt, Chicago, USA: Univ. Pr. (1996) 664 p

[5] H. An, M. Pospelov and J. Pradler, Phys. Lett. B **725**, 190 (2013) [arXiv:1302.3884 [hep-ph]].

[6] H. An, M. Pospelov and J. Pradler, Phys. Rev. Lett. 111, **041302** (2013) [arXiv:1304.3461 [hep-ph]].

[7] P. Gondolo and G. Raffelt, Phys. Rev. D **79**, 107301 (2009) [arXiv:0807.2926 [astro-ph]].

[8] S. Andriamonje *et al.* [CAST Collaboration], JCAP **0704**, 010 (2007) [hep-ex/0702006].

[9] K. Ehret, M. Frede, S. Ghazaryan, M. Hildebrandt, E. -A. Knabbe, D. Kracht, A. Lindner and J. List *et al.*, Phys. Lett. B **689**, 149 (2010) [arXiv:1004.1313 [hep-ex]].

[10] D. F. Bartlett and S. Loegl, Phys. Rev. Lett. **61**, 2285 (1988).

[11] B. Holdom, Phys. Lett. B **166**, 196 (1986).

[12] L. B. Okun, Sov. Phys. JETP **56**, 502 (1982) [Zh. Eksp. Teor. Fiz. **83**, 892 (1982)].

[13] S. Davidson, B. Campbell and D. C. Bailey, Phys. Rev. D **43**, 2314 (1991).

[14] S. Davidson, S. Hannestad and G. Raffelt, JHEP **0005**, 003 (2000) [hep-ph/0001179].

[15] M. Ahlers, J. Jaeckel, J. Redondo and A. Ringwald, Phys. Rev. D **78**, 075005 (2008) [arXiv:0807.4143 [hep-ph]].

[16] J. Redondo and G. Raffelt, JCAP **1308**, 034 (2013) [arXiv:1305.2920 [hep-ph]].

[17] B. L. Henke, E. M. Gullikson and J. C. Davis, Atom. Data Nucl. Data Tabl. **54**, no. 2, 181 (1993).

[18] J. Angle *et al.* [XENON10 Collaboration], Phys. Rev. Lett. **107**, 051301 (2011) [arXiv:1104.3088 [astro-ph.CO]].

[19] R. Essig, A. Manalaysay, J. Mardon, P. Sorensen and T. Volansky, Phys. Rev. Lett. **109**, 021301 (2012) [arXiv:1206.2644 [astro-ph.CO]].

The 11-years solar cycle as the manifestation of the dark Universe

K. Zioutas[1,2]*, *M. Tsagri*[3]†, *Y.K. Semertzidis*[4], *T. Papaevangelou*[5], *D.H.H. Hoffmann*[6], *V. Anastassopoulos*[1]

[1]University of Patras, 26504 Patras, Greece
[2]CERN, 1211 Geneva 23, Switzerland
[3]Nikhef - University of Amsterdam, Amsterdam, The Netherlands
[4]Brookhaven National Lab, Physics Deptment, Upton, NY 11973-5000, USA
[5]IRFU, Centre d'Études Nuclaires de Saclay, Gif-sur-Yvette, France
[6]Institut für Kernphysik, TU-Darmstadt, Schlossgartenstr. 9, 64289 Darmstadt, Germany

DOI: http://dx.doi.org/10.3204/DESY-PROC-2013-04/zioutas_konstantin

Sun's luminosity in the visible changes at the 10^{-3} level, following an 11 years period. In X-rays, which should not be there, the amplitude varies even $\sim 10^5$ times stronger, making their mysterious origin since the discovery in 1938 even more puzzling, and inspiring. We suggest that the multifaceted mysterious solar cycle is due to some kind of dark matter streams hitting the Sun. Planetary gravitational lensing enhances (occasionally) slow moving flows of dark constituents towards the Sun, giving rise to the periodic behaviour. Jupiter provides the driving oscillatory force, though its 11.8 years orbital period appears slightly decreased, just as 11 years, if the lensing impact of other planets is included. Then, the 11 years solar clock may help to decipher (overlooked) signatures from the dark sector in laboratory experiments or observations in space.

1 Introduction

The nearby Sun is full of large and small mysteries, with its unnatural hot outer atmosphere being the mostly impressive one, with an anomalous strong temperature rise being quasi step-like. The biggest of all mysteries, which is almost ubiquitous in solar phenomena, remains however the celebrated 11 years Schwabe solar cycle. The working of the underlying clock is still unknown. R. Wolf already in 1859 [1] was the first to bring-up the possible planetary origin of the 11 years periodic behaviour of the sunspots, because of Jupiter's close orbital period (11.8 yr). In fact, various investigations could establish a clear correlation between the Suns cyclic dynamical behaviour and the planetary orbiting periods [2]. As the most obvious and promising potential mechanism behind such a planetary impact on the Sun, it has been considered gravitational tidal forces acting on the Sun, mainly by Jupiter; their periodicity drifts towards the solar cycle, if a few other inner solar planets are also included when summing up their periodic tidal impact. However, it was realized that the estimated planetary tidal

*email: zioutas@cern.ch
†present address: University of Geneva, Switzerland

impact was extremely small to cause any significant change of the dynamic Sun [2], or even less to justify the origin of the enigmatic 11 years cycle. For this reason the planetary - Sun connection has been ignored for long time, while such a claim was also seen not only within astronomy, but rather instead within the frame of astrology [3]. Though, the significance of the correlation was high, since planetary tides follow a temporal pattern with a conspicuous correlation with the solar activity cycle, and therefore this challenging observation was not set *ad acta* [4, 5]. Hence, the many faces of the 11 years solar cycle may hold many important clues as to how the solar clock is working. To constrain the underlying mechanism(s), we discuss here an alternative scenario, which couples the dynamic Sun with the planets via the already introduced streams of dark constituents [6]. Further, dark disk configurations which co-rotate with the galaxy may contribute to the local dark matter flows [7]. Actually, this seems to be the only procedure left-over, in which the precise planetary periods can enter into the suggested 11 years scenario, explaining thus how the apparent 'communication' between the planets and the Sun is settled.

2 The new mechanism

In this work we suggest a new physical mechanism aiming to explain the solar cycle, which is cosmic in origin. It is based not on planetary torque, but on the gravitational lensing effect by the planets as they revolve with a constant orbital period around the Sun, entailing all the striking planetary periodic changes. In fact, they can focus gravitationally at the Sun's position slow moving incident dark matter (or any other exotic) constituents [6]. The flux enhancement and its duration depend on the relative alignment between the Sun, the planet(s) and the otherwise as yet invisible cosmic irradiation [8]. For a flux enhancement to occur, the incident irradiation of the solar system by any kind of feebly interacting particles must not be isotropic, arriving preferentially along the ecliptic plane. In this way, the planets may still leave somehow their imprints as the Sun's 11 years enigmatic activity rhythm. The bulk of the celebrated dark matter halo in our neighbourhood is not further considered here, since its origin goes back to the early Universe, and therefore it is isotropic. By contrast, for example, non-relativistic particles from point-like sources along / near the ecliptic plane like the celebrated "constellations", or, incident slow moving streams of dark matter or the like, can be gravitationally lensed towards the Sun by one or more planet(s), when a stream is properly co-aligned with the Sun and the planet(s). This can happen, because of the v^{-2} - dependence of the lensing (=deflection) angle [8]. For example, the planets Jupiter and Earth can focus at the Sun's position incoming particles with speeds $v \leq 10^{-2}c$ and $v \leq 3 \cdot 10^{-3}c$, respectively, provided such particles propagate near the ecliptic, since most planets move coplanar (within a few degrees). We recall that relativistic particles ($v \approx c$) have focal lengths substantially larger than the orbital radius of Jupiter, even if the Sun is taken as the gravitational lens. But, over the last ~ 150 years, Jupiter's 11.8 years orbital revolution around the Sun was considered as the possible cause of the strikingly close ~ 11 years solar cycle, despite the rejected tidal mechanism (see e.g. [2]).

We note that the mentioned speeds of non-relativistic particles, resemble that of dark matter, but also dark constituents produced possibly in stars. Therefore, their direction of propagation can be influenced noticeably by the planetary gravitational fields. We mention, as a generic example, massive solar axions of the Kaluza-Klein (KK) type [10], which escape from the Sun with a mean velocity of about $0.6c$. For the purpose of this work, it is reasonable to assume that

a percentage of the solar KK axions (or the like) of about 1‰ leave the Sun with speeds below about $0.01c$ (see Figure 5 in ref. [10]). However, the fraction of such or other slowly moving exotica is not negligible, and it might be much more from other stars like pulsars, because of the much stronger gravity ($v_{escape} \leq 0.3c$).

It is of particular interest, the actual flux enhancement which can be expected by planetary gravitational focusing. Thus, it was shown recently [9] that Jupiter can cause, in the ideal case, a flux increase at its focal plane of as much as by a factor of 10^6, assuming incident streaming particle candidates from the dark sector with the aforementioned speeds. As it was pointed out for KK-axions, it is not unreasonable to assume that such or other slow moving dark fluxes do exist; they may reach the solar system either as some sort of streaming dark matter, or, they may come from some point-like sources in the sky. Then, they can get (temporally) focused, by one or more planets, towards and interfere with the Sun. Apparently, similar gravitational lensing can take place between the planets, and other celestial bodies. Thus, the sporadic planetary co-alignment repeats in precisely predictable time intervals. Coincidentally, the various planetary configurations elaborated for the tidal scenario can be taken over for this work, as it also gives the time-variable influx of focused directional dark constituents. Of course, this additional influx must interact with the Sun and cause a considerable influence, whatever the underlying process is at the end (see below).

2.1 Some numerics

The possible existence of dark matter particle streams in the galactic halo has been already considered [6, 7]. The Sagittarius Dwarf Elliptical Galaxy is a well studied case. The expected stream density at the Sun's position is a few % of the local dark halo, with stream velocities around $10^{-3}c$ [6, 7]. Here we assume that streaming dark constituents make about 1% of the local $\sim 0.3 GeV/cm^3$ relic dark matter. With velocities around $10^{-2} - 10^{-3}c$, the integrated energy flux reaching the Sun can be as much as $10^{30\pm1} erg/s$, if (temporarily / periodically) a $\sim 10^6$ times flux enhancement due to planetary gravitational focusing takes place. Such an external energy influx (up to $\sim 10^{-2} L_{\odot}$) is possibly not negligible. We mention, for comparison reasons, that the much less radiant energy emitted in X-rays by the solar corona ($\sim 10^{24\pm2} erg/s$) cannot be overlooked, while known physics failed to explain its origin since several decades [12]. Keeping in mind the behaviour of axion(-like) particles [12, 13], the energy deposit by a directional external dark irradiation of the Sun may take place spatiotemporally only at certain solar magnetized layers of specific density, etc. Though, the magnetic field is for particles like paraphotons redundant due to the kinetic mixing of the photon-to-paraphoton oscillation [13]. In addition, incident dark matter particles may be gravitationally captured and accumulated with time inside the Sun. Such or other processes may bring the Sun out of equilibrium short and/or long term, giving rise to the otherwise puzzling and unpredictable (local / global) solar activity. Some of the diverse exotica from the dark sector, like axions, paraphotons, WISPs, WIMPs, etc., may interact 'preferably' with the Sun, since its huge dynamic range of properties none Earth-bound detector can actually mimic. For example, if the additional energy deposit goes, e.g., via the Primakoff - effect [12, 13], a fine-tuned spatiotemporal resonance between the rest mass of the dark constituents, the local solar plasma frequency (=energy), and/or eventually the local solar magnetic field, may occur somewhere inside the Sun or its atmosphere. Such an interaction occurring only with the Sun, it does not necessarily contradict Earth bound dark matter experiments. After all, they could not unravel a signature, because they have failed

to pin down those necessary conditions within their very limited detector parameter values. Finally, in order to recuperate an 11 years solar cycle from the since ever suggestive 11.8 years Jupiter's orbital period, it suffices to consider the combined gravitational lensing effect with few more inner ones. Figure 1 shows actually an outstanding agreement between Schwabe's solar cycle periods and the planetary tides [11, 2], which are used here as proxy for gravitational lensing.

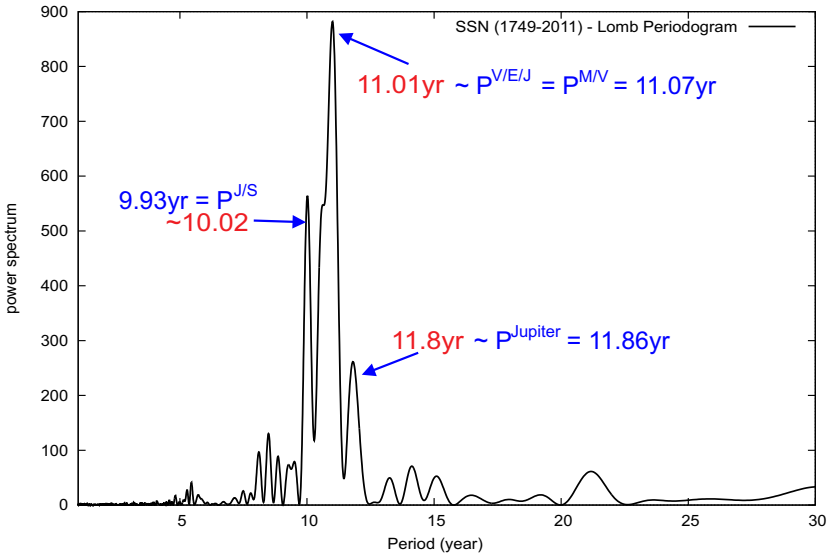

Figure 1: The monthly average sunspot number reveals the existence of three peaks around 11 years (red) [11], which are all associated to planetary tides (blue). Tidal periods (P) of single and combined planets by Jupiter, Saturn, Venus, Earth, Mercury fit to planetary frequencies around 11 years. Note, in this work tidal timing reflects also gravitational lensing by the same planet(s). Courtesy, Nicola Scafetta (2013).

3 Discussion

The suggested planetary gravitational lensing scenario fits the characteristic timing of the as yet enigmatic solar cycle, which follows impressively the combined orbital rhythm of the inner planets; the Jupiter's period (11.8 years) is the most strikingly one close to the 11 years. The earlier suggestion, based on the tidal forces acting on the Sun by the various planetary configurations, failed to explain any reasonable impact on the Sun's workings. But, interestingly, most derived findings there, e.g., the planetary alignment(s) and period(s) of appearance, can be borrowed actually unmodified to corroborate the alternative scenario based on gravitational focusing of streaming constituents from the dark sector. The plethora of candidates like slow moving massive exotica, from axions and axion-like particles [12, 13, 14, 15] to D-particles defects [16], which have been already discussed, are inspiring and may provide the energy input for the present solution of the 11 years solar clock.

Then, Wolf's suggestion was advanced for his time, since both, gravitational lensing and dark matter, were unknown. In fact, Jupiter provides the main driving force of the solar cycle, while the synergy with the other planets shifts slightly the 11.8 years period to the 11 years solar master clock. Actually, there is nothing else one could imagine beyond the assumed flows of dark particles, which may settle such an oscillatory behaviour for the Sun being identical with the combined planetary orbital rhythm. Then, it is not unreasonable to assume that the main as yet unidentified piece of the whole puzzle, i.e., some kind of dark streams do exist, showering the Sun, thanks to the intervening planets, periodically and probably also irregularly, in large quantities. Moreover, the mystery of the 11 years solar cycle might be pointing at the properties of the assumed dark streams towards the Sun near the ecliptic, whose intensity reaching the Sun gets occasionally enhanced by the planetary gravitational lenses. The same holds also for Earth-bound or some experiments in space, since they may profit from introducing in the data analysis the aforementioned period(s), or, the predicted time intervals with increased signal-to-noise ratio due to flux enhancement. This might allow to unravel an otherwise hidden signature.

4 Conclusions

It is suggested, that the mysterious 11 years solar cycle could be explained by incident particle streams (from the widely discussed dark sector) towards the Sun. More specifically, the flux of expected streaming dark matter component(s) beyond the isotropic local dark matter halo ($\sim 0.3 GeV/cm^3$) with velocities around $10^{-3} - 10^{-2} c$ can be temporarily increased by the gravitational lensing potential of a single or more planets. For a constant influx of dark particles near the ecliptic, the combined planetary focusing efficiency shows surprisingly a periodicity of 11 years. In addition, dark streams varying with time could explain the fluctuations of the 11 years period in length and in amplitude. The same might hold for the unpredictable nature of puzzling, irregularly occurring solar events, which could also be another manifestation of the suggested scheme. Moreover, the expected external energy input to the Sun due to periodic flux enhancement is not negligible. This is true when a comparison is made with the total solar luminosity, but it is more suggestive, if such an additional external irradiation is compared with the several orders of magnitude weaker corona energy emission in X-rays, which is unexpected.

Interestingly, the coronal emission shows also an 11 years cycle, though with a change in intensity by a factor of about 10^2. This is to be compared with the corresponding amplitude variation of the bulk of the solar luminosity, which is only at the 10^{-3} level! The impressive 11 years coronal modulation must be seen on top of the already enigmatic origin of the coronal heating mechanism. Obviously, the 75 years old corona riddle becomes even more intriguing, as one has to explain, not only the puzzling temperature inversion occurring close to the photosphere, but also why the Sun emits in X-rays at all (and even more above quiet magnetized regions), and, why its X-ray brightness changes with time following the mysterious 11 years clock. These mysteries may be interrelated, and they may or may not be of common origin. Therefore, in dark matter research the anyhow experimentally challenging detection in the (sub−) keV energy range, seems even more promising to pursue, as it might become the window to the (multifaceted?) dark sector. The energy overlap with the mysterious X-ray luminous Sun is certainly motivating.

In summary, the efficient planetary gravitational lensing of slow dark streams towards the Sun is suggested as the underlying mechanism, which drives the 11 years cycle. Actually, one may ask, since tidal effects have been excluded from further consideration, what else could fit to the striking 11 years solar rhythm reminiscent of the identical combined orbital period of Sun's inner planets? Following this scenario, the 11 years solar cycle with its many faces is the overlooked manifestation of streaming constituents from the dark sector. Hence, dark matter exotica show up not only on cosmic scales due to their prevailing gravitational force, but also on sizes like the solar system, or even much smaller. Then, there exists a preferred spatial direction in our neighbourhood, which is given by the flow of new exotica. Moreover, if (directional) dark matter constituents cause the mysterious and multifaceted 11 years cycle, this could provide the tool to design accordingly future direct dark matter searches, while aiming to unravel overlooked signatures by re-evaluating previous experiments / observations.

References

[1] R. Wolf, "Extract of a letter to Mr. Carrington." M.N.R.A.S. **19** (1859) 85.

[2] N. Scafetta, J. Atm. & Sol.-Terr. Phys. 81-82 (2012) 27, and ref's therein; http://www.sciencedirect.com/science/article/pii/S1364682612001034

[3] P. Charbonneau, Nature 493 (2013) 613; http://www.nature.com/nature/journal/v493/n7434/pdf/493613a.pdf See also J.A. Abreu, J. Beer, A. Ferriz-Mas, K.G. McCracken, F. Steinhilber, Astron. Astrophys. **548** (2012) A88; http://www.aanda.org/articles/aa/pdf/2012/12/aa19997-12.pdf.

[4] I. Seker, Solar Phys. **286** (2013) 303; http://link.springer.com/article/10.1007\%2Fs11207-013-0288-6.

[5] K.D. Wood, Nature 240 (1972) 91;

[6] R. Bernabei et al., Eur. Phys. J. C47 (2006) 263; [arXiv:astro-ph/0604303] See also: M. Lisanti, D.N. Spergel / Dark Universe 1 (2012) 155 and ref's therein: http://www.sciencedirect.com/science/journal/22126864/1/1-2; On caustics: F.S. Ling, P. Sikivie, S. Wick, Phys. Rev. D 70 (2004) 123503; http://prd.aps.org/abstract/PRD/v70/i12/e123503.

[7] S.K. Lee, M. Lisanti, A.H.G. Peter, B.R. Safdi, arXiv:1308.1953 [astro-ph]. See also: C. W. Purcell, J. S. Bullock, and M. Kaplinghat, ApJ. 703 (2009) 2275; arXiv:0906.5348 [astro-ph], and, T. Bruch, J. Read, L. Baudis, G. Lake, ApJ. 696 (2009) 920; arXiv:0804.2896 [astro-ph].

[8] D.H.H. Hoffmann, J. Jacoby, K. Zioutas, Astroparticle Phys. 20 (2003) 73; http://www.sciencedirect.com/science/article/pii/S0927650503001385.

[9] B.R. Patla, R.J. Nemiroff, D.H.H. Hoffmann, K. Zioutas, [arXiv:1305.2454 [astro-ph]].

[10] L. Di Lella, K. Zioutas, Astroparticle Phys. 19 (2003) 145; http://adsabs.harvard.edu//abs/2003APh....19..145D.

[11] N. Scafetta, J. Atm. & Sol.-Terr. Phys. 80 (2012) 296; http://www.sciencedirect.com/science/article/pii/S1364682612000648.

[12] K. Zioutas, M. Tsagri, Y. Semertzidis, T. Papaevangelou, T. Dafni, V. Anastassopoulos, New J. Phys.**11** (2009) 105020; [arXiv:0903.1807 [astro-ph]].

[13] K. Baker, G. Cantatore, S. A. Cetin, M. Davenport, K. Desch, B. Döbrich, H. Gies, I. G. Irastorza, J. Jaeckel, A. Lindner, T. Papaevangelou, M. Pivovaroff, G. Raffelt, J. Redondo, A. Ringwald, Y. Semertzidis, A. Siemko, M. Sulc, A. Upadhye, K. Zioutas, Ann. Phys. (Berlin) **525** (2013) A93; [arXiv:1306.2841 [hep-ph]].

[14] M. Cicoli, M. Goodsell, A. Ringwald, JHEP 1210 (2012) 146 [arXiv:1206.0819].

[15] K. Arisaka, P. Beltrame, C. Ghag, J. Kaidi, K. Lung, A. Lyashenko, R.D. Peccei, P. Smith, K. Ye, Astroparticle Phys. **44** (2013) 59 [arXiv:1209.3810].

[16] N.E. Mavromatos, V.A. Mitsou, S. Sarkar, A. Vergou, Eur. Phys. J. **C72** (2012) 1956; [arXiv:1012.4094 [hep-ph]].

Chapter 5

Dark Matter WISPs

Axion, axino and neutralino dark matter in minimal supergravity

C. Balázs[1,2,3,4] *and S. K. Gupta*[1,2]

[1]School of Physics, Monash University, Victoria 3800, Australia
[2]ARC Centre of Excellence for Particle Physics, Monash University, Victoria 3800 Australia
[3]Monash Centre for Astrophysics, Monash University, Victoria 3800 Australia
[4]Australian Collaboration for Accelerator Science, Monash University, Victoria 3800 Australia

DOI: http://dx.doi.org/10.3204/DESY-PROC-2013-XX/balazs_csaba

Dark matter can be a mixture of axions, axinos and neutralinos in a Peccei-Quinn extension of supergravity. To find out which dark matter candidate is preferred by data we perform a Bayesian statistical analysis on four such scenarios. The main experimental constraints on these models come from the Planck satellite and from the Large Hadron Collider. Weaker constrains arise from other astrophysical, collider and low energy measurements. Our study reveals that the Peccei-Quinn scenario featuring axino dark matter is clearly preferred over the minimal supegravity model with neutralino dark matter.

1 Introduction

The 7 and 8 TeV center of mass runs of the Large Hadron Collider strongly constrained the simplest supersymmetric models. The ATLAS and CMS collaborations discovered a Higgs boson with a mass close to 126 GeV [1, 2]. Assuming this is the lightest Higgs, in the framework of the Minimal Supersymmetric Standard Model (MSSM) this implies substantial radiative corrections within the Higgs sector. These radiative corrections enter in the MSSM electroweak symmetry breaking condition, which gives the electroweak scale as the difference of Higgs sector masses and the Higgsino mass parameter, and leads to a fine tuning [3].

This unnatural situation is escalated by dark matter fine tuning in the R-parity conserving constrained versions of the MSSM. The minimal supergravity motivated model, the constrained MSSM (CMSSM), is one of these models. The CMSSM is spanned at the Grand Unification Theory (GUT) scale by four parameters: M_0 a common mass for all spin 0 superpartners, $M_{1/2}$ the mass of all spin 1/2 superpartners, A_0 the coefficient in front of all tri-linear terms in the supersymmetry breaking Lagrangian, and $\tan\beta$ the ratio of the vacuum expectation values of the two Higgs doublets.

In the CMSSM dark matter is the lightest neutralino. The abundance of the lightest neutralino, however, only satisfies the Planck implied relic density observation in very narrow slices of the parameter space. This leads to a serious tension between the CMSSM and observation. It is very hard to satisfy the Higgs mass, the dark matter density, and other low energy constraints (such as the anomalous magnetic moment of the muon) simultaneously in the CMSSM. Even if one makes a reasonable compromise, electroweak naturalness will be sacrificed.

Naturalness, thus, suggests extending the MSSM. There are, however, numerous possible ways to extend the MSSM, ranging from modifying its symmetries to introducing new fields. In this brief submission we consider a Peccei-Quinn extension of the CMSSM. Although this scenario does not improve the electroweak naturalness, we show that the dark matter fine tuning is vastly improved. In our case dark matter is an combination of axions, axinos and neutralinos. We show that in the Peccei-Quinn extension of the of the CMSSM the axino is the preferred dark matter candidate when compared to the CMSSM.

2 Peccei-Quinn extended MSSM

To solve the strong CP problem Peccei and Quinn (PQ) extended the Standard Model with a global $U(1)$ symmetry [4, 5]. The $U(1)_{PQ}$ symmetry is spontaneously broken at a scale Λ_{PQ} and the pseudo-Goldstone boson induced by this breaking is the axion. The axion mass is related to the symmetry breaking scale as [6]

$$m_a \simeq 6 \, \frac{10^6 \, \text{GeV}}{\Lambda_{PQ}} \, \text{eV}. \tag{1}$$

Supersymmetric Peccei-Quinn models feature the chiral superfield

$$\hat{\Phi}_a = \frac{s + ia}{\sqrt{2}} + i\sqrt{2}\bar{\theta}\tilde{a} + i\bar{\theta}\theta F_a, \tag{2}$$

where s is the scalar axion or saxion, a is the the pseudo-scalar axion, $\tilde{a}$ is the axino, and F_a is an auxiliary field [6]. The masses of these field depend on the supersymmetry breaking mechanism. In most cases the saxion is ultra heavy with a mass of about Λ_{PQ}. For the supergravity inspired model the axino mass takes the following form [7],

$$m_{\tilde{a}} \simeq \left(\frac{\Lambda_{PQ}}{M_{Pl}} \right)^{\kappa} M_{Pl} \qquad \text{with} \qquad \kappa \gtrsim 2. \tag{3}$$

A broken Peccei-Quinn symmetry contributes to the neutron electric-dipole moment (nEDM) at tree level [8]. The current experimental limit on the nEDM is $d_n < \left|1.9 \times 10^{-26}\right| \, e\,\text{cm}$ at 90% CL [9]. This translates into a lower bound on the PQ breaking scale. A model dependent upper bound has also been obtained for the supergravity case [10], leading to

$$1 \times 10^9 \text{ GeV} < \Lambda_{PQ} < 5 \times 10^{11} \text{ GeV}. \tag{4}$$

Due to the bounds on the Peccei-Quinn breaking scale in Eq.(4), the axion mass is always restricted in the range between about 10^{-5} eV and about 6×10^{-3} eV. The axino mass can take values between 2 GeV and 1 TeV for the case $\kappa = 2$, and about 1 eV and 7 keV for $\kappa = 3$. Thus the axion is always the lightest of the three and it also serves as a good hot dark matter candidate. The axino, covering a wide range of masses between a few eV to about a TeV, can be lighter, degenerate or heavier than the lightest neutralino. This makes the PQ violating supergravity (PQSuGra) scenario very interesting since both the axino and the neutralino can contribute to the cold matter abundance.

For $\kappa = 2$, for example, three qualitatively different PQSuGra scenarios are possible depending on the relation between the lightest neutralino mass, $m_{\tilde{\chi}_1}$ and the axino mass, $m_{\tilde{a}}$. These are

- **PQ-1** (neutralino LSP): $m_{\widetilde{\chi}_1^0} < m_{\tilde{a}}$,
- **PQ-2** (axino-neutarlino co-LSPs): $m_{\tilde{a}} \simeq m_{\widetilde{\chi}_1^0}$,
- **PQ-3** (axino LSP): $m_{\tilde{a}} < m_{\widetilde{\chi}_1^0}$.

In the first (third) case the lightest neutralino $\tilde{\chi}_1^0$ (axino $\tilde{a}$) is the dark matter candidate. In the second case they are both cold dark matter candidates.

For $\kappa > 2$ the axino is always the lightest superpartner. However, scenarios with $\kappa > 3$ are unable to generate sufficient dark matter relic density and hence are less interesting. Therefore in the current work we will only analyze the PQSuGra scenarios with $\kappa = 2$ (**PQ-1, PQ-2** and **PQ-3** as defined above) and $\kappa = 3$ (**PQ-3′**).

Following Ref.s [10, 11], we calculate the relic densities for the axions and axinos using

$$\Omega_a h^2 \simeq \frac{1}{4}\left(\frac{6\times 10^{-6}\ \text{eV}}{m_a}\right)^{7/6}, \qquad \Omega_{\tilde{a}}^{NTP} h^2 = \frac{m_{\tilde{a}}}{m_{\widetilde{\chi}_1^0}}\Omega_{\widetilde{\chi}_1^0} h^2, \tag{5}$$

$$\Omega_{\tilde{a}}^{TP} h^2 \simeq 5.5 g_s^6 \ln\left(\frac{1.211}{g_s}\right)\left(\frac{10^{11}\ \text{GeV}}{\Lambda_{PQ}/N}\right)^2\left(\frac{m_{\tilde{a}}}{0.1\ \text{GeV}}\right)\left(\frac{T_R}{10^4\ \text{GeV}}\right). \tag{6}$$

Here, $\Omega_a h^2$ is the axion relic density, $\Omega_{\tilde{a}}^{NTP} h^2$ is the relic abundance of non-thermally produced axinos from neutralino decay and $\Omega_{\tilde{a}}^{TP} h^2$ is the relic abundance of thermal produced axinos.

Axino dark matter lends the PQSuGra model considerably more flexibility compared to the minimal SuGra model. The properties of axino dark matter, such as its abundance and couplings to standard matter, are governed by its mass and Λ_{PQ} which are independent from the CMSSM parameters. Thus, obtaining a Higgs mass of about 126 GeV, a neutralino abundance of 0.22 ρ_C and low fine tuning is impossible in CMSSM. The PQSuGra model not only accommodates these requirements much easier but its Bayesian evidence suggests that, despite of its extra parameters, it is more viable.

3 Statistical analysis of the PQSuGra model

The Peccei-Quinn extended supergravity model is parametrized by

$$\mathcal{P} = \left\{M_0, M_{1/2}, A_0, \tan\beta, sgn(\mu), \Lambda_{PQ}\right\}. \tag{7}$$

We use a modified version of `SUSY-HIT` [12] to calculate sparticle masses and decay rates, and `MicrOmegas 2.4.5` [13] to calculate the relic density of the lightest neutralinos. The calculation of Bayesian evidences involves the sampling of the likelihood function over the parameter space of the model. Motivated by naturalness, this scan is done over the following parameter ranges:

$$\begin{aligned} M_0 \in [10, 2000]\,\text{GeV}, \qquad M_{1/2} \in [10, 2000]\,\text{GeV}, \qquad A_0 \in [-3000, 4000]\,\text{GeV}, \\ \tan\beta \in [0, 62]\,, \qquad \Lambda_{PQ} \in \left[1\times 10^9, 5\times 10^{11}\right]\,\text{GeV}. \end{aligned} \tag{8}$$

The likelihood function includes the following observables:

- LHC Higgs searches: $m_h, \mathcal{R}_{gg\gamma\gamma}, \mathcal{R}_{gg2l2\nu}, \mathcal{R}_{gg4l}$,
- Precision observables (POs): $\delta\rho, (g-2)_\mu^{SUSY}, BR(b\to s\gamma)$,
- LEP-2/Tevatron: $m_{\widetilde{\chi}_1^0}, m_{\widetilde{\chi}_1^\pm}, m_{\tilde{l}}$,

- Planck dark matter abundance: Ω_{DM}.

Here $\mathcal{R}_{gg\gamma\gamma}, \mathcal{R}_{gg2l2\nu}$, and, $\mathcal{R}_{gg4l}$ are ratios of diphoton, $2l2\nu$, and $4l$ event rates in PQSuGra relative to the Standard Model. We calculate posterior probabilities for the SuGra and PQ-SuGra models for two choices of priors: (a) the flat (uniform) prior which is constant in a finite parameter region; and (b) the log prior $\propto (M_0 M_{1/2})^{-1}$.

The calculation of the Bayesian evidences is described in detail in Ref. [14]. The ratio of the evidences allows us to calculate the Bayes factors presented in Table 1. This table shows that the PQSuGra scenario is somewhat preferred over the CMSSM when only constraints from Higgs and precision observables (POs) are imposed. However, scenarios where the axino is dark matter are strongly preferred over the CMSSM. This is because in the latter it is hard to satisfy the LHC Higgs mass constraint, Planck and $g_{mu} - 2$ simultaneously. In contrast, the $PQ-3$ (and $PQ-3'$) models satisfy Planck in a wider range of the PQSuGra parameter space.

Observables	**PQ-1**	**PQ-2**	**PQ-3**	**PQ-3′**
LHC Higgs	0.244	0.305	0.663	0.506
+ POs & LEP	0.238	0.322	0.724	0.626
+ Planck	0.181	0.231	1.693	2.466

Table 1: Bayes factors for various Peccei-Quinn extended supergravity scenarios against the CMSSM. These factors should be interpreted according to Jeffreys: $0-0.5$ "no preference", $0.5-1$ "moderate preference", $1-2$ "strong preference", >2 "decisive evidence".

In conclusion, in the framework of the Peccei-Quinn extended simplest supergravity model a wide variety of experimental data clearly prefers axino over axion or neutralino dark matter.

4 Acknowledgments

This work was supported by the *ARC Centre of Excellence for Particle Physics*. The use of Monash University Sun Grid, a high-performance computing facility, is gratefully acknowledged.

References

[1] G. Aad *et al.* [ATLAS Collaboration], Phys. Lett. B **716**, 1 (2012) [arXiv:1207.7214 [hep-ex]].

[2] S. Chatrchyan *et al.* [CMS Collaboration], Phys. Lett. B **716**, 30 (2012) [arXiv:1207.7235 [hep-ex]].

[3] G. F. Giudice, arXiv:1307.7879 [hep-ph].

[4] R. D. Peccei and H. R. Quinn, Phys. Rev. Lett. **38**, 1440 (1977).

[5] R. D. Peccei and H. R. Quinn, Phys. Rev. D **16**, 1791 (1977).

[6] H. Baer, M. Haider, S. Kraml, S. Sekmen and H. Summy, JCAP **0902**, 002 (2009) [arXiv:0812.2693 [hep-ph]].

[7] E. J. Chun and A. Lukas, Phys. Lett. B **357** (1995) 43 [hep-ph/9503233];

[8] J. E. Kim and G. Carosi, Rev. Mod. Phys. **82**, 557 (2010) [arXiv:0807.3125 [hep-ph]];

[9] M. Burghoff, A. Schnabel, G. Ban, T. Lefort, Y. Lemiere, O. Naviliat-Cuncic, E. Pierre and G. Quemener *et al.*, arXiv:1110.1505 [nucl-ex];

[10] H. Baer and A. Lessa, JHEP **1106**, 027 (2011) [arXiv:1104.4807 [hep-ph]];

[11] H. Baer, A. D. Box and H. Summy, JHEP **0908**, 080 (2009) [arXiv:0906.2595 [hep-ph]].

[12] A. Djouadi, M. M. Muhlleitner and M. Spira, Acta Phys. Polon. B **38**, 635 (2007) [hep-ph/0609292].

[13] G. Belanger, F. Boudjema, A. Pukhov and A. Semenov, Comput. Phys. Commun. **149**, 103 (2002) [hep-ph/0112278].

[14] C. Balazs and S. K. Gupta, Phys. Rev. D **87**, no. 3, 035023 (2013) [arXiv:1212.1708 [hep-ph]].

Photon propagation in a cold axion condensate

D. Espriu and A. Renau

Departament d'Estructura i Constituents de la Matèria and Institut de Ciències del Cosmos (ICCUB), Universitat de Barcelona, Martí i Franquès 1, 08028 Barcelona, Catalonia, Spain

DOI: http://dx.doi.org/10.3204/DESY-PROC-2013-04/espriu_domenec

We discuss some striking properties of photons propagating in a cold axion condensate oscillating coherently in time with a frequency $1/m_a$. Three effects are discussed in this contribution: (a) due to the time dependence of the background, photons moving in the cold axion background have no definite energies and some momenta are not accessible to them. (b) we investigate the combined influence of a magnetic field and the cold axion background and propose a possible interferometric experiment to detect the latter. (c) if the axion condensate has a space dependence, the photon refraction index is modified in the medium, possibly leading to total reflection at the interface with the ordinary vacuum.

1 Introduction

Cold relic axions resulting from vacuum misalignment in the early universe are good candidates for dark matter[1, 2]. A coherent spatially constant axion field (it may be a genuine Peccei-Quinn axion[3] or a similar field) acquires a mass m_a once instanton effects set in and oscillates

$$a(t) = a_0 \cos m_a t. \tag{1}$$

The energy density stored in these oscillations $\rho \simeq a_0^2 m_a^2$ contributes to the energy-matter budget of the universe. This constitutes the cold axion background, or CAB for short.

As it is well known, the coupling of axions to photons is universal

$$\mathcal{L}_{a\gamma\gamma} = g_{a\gamma\gamma} \frac{\alpha}{2\pi} \frac{a}{f_a} F_{\mu\nu} \tilde{F}^{\mu\nu}. \tag{2}$$

The only arbitrariness lies in the coefficient $g_{a\gamma\gamma}$ but most models [4] give $g_{a\gamma\gamma} \simeq 1$. Using (1)

$$\mathcal{L}_{a\gamma\gamma} = -g_{a\gamma\gamma} \frac{\alpha}{\pi} \frac{a_0}{f_a} \cos(m_a t)\, \epsilon^{ijk} A_i F_{jk}. \tag{3}$$

Cosmology considerations place the axion mass in a range $10^{-2} - 10^{-6}$ eV[2]. For Peccei-Quinn axions an approximate relation of the form $f_a m_a \simeq f_\pi m_\pi$ holds, thus forcing the axion decay constant to be at least $f_a > 10^9$ GeV. From astrophysics the limit $f_a > 10^7$ GeV seems now well established. This makes the axion extremely long-lived and very weakly coupled.

In addition to the axion-photon coupling, as indicated above, axions can also couple to matter in specific models. However, the smallness of the coupling makes their detection extremely

challenging. Nevertheless, some of the best bounds on axion masses and couplings do come from the study of abnormal cooling in white dwarfs due to axion emission[5].

In fact there are two separate questions we have to address. The first one is whether axions exist at all. This is what experiments such as CAST, AMDX, AMDXII, IAXO or ALPS try to address. If its mass turns out to be in the relevant range for cosmology we would indeed have a strong hint that axions may provide the elusive dark matter.

However, we would eventually like to verify or falsify the CAB hypothesis and determine to what extent cold axions contribute to the dark matter budget. Finding the axion particle with the appropriate properties is not enough. Unfortunately a direct experimental confirmation of the CAB is extremely difficult and it could possibly be accomplished only via some collective effect on the propagation of particles. Looking for the effect of the CAB on photon propagation is the most natural possibility.

In a previous Patras meeting we reported on three effects that the presence of a CAB induces on photon propagation[6]. The CAB modifies the photon dispersion relation introducing a Lorentz non-invariant term, which makes Bremsstrahlung from cosmic rays possible. The amount of energy radiated by this process was computed and found to be non-negligible[7], but normal synchrotron radiation background is a tough enemy for its detection. The second effect discussed was the presence of an additional rotation in the polarization plane of light (on top of the familiar one[8], see [9] for a detailed discussion). The third effect discussed is that some photon wave-lengths are actually forbidden in a universe filled with cold axions oscillating coherently[9]. In this talk we will continue our discussion on the last two points, and also speculate very briefly on possible consequences of having a CAB with some spatial dependence.

In order to determine the properties of photons in a CAB we need to solve the equation of motion in momentum space. For the time being let us ignore the magnetic field.

$$\left[g^{\,\lambda\nu}\left(k^2-m_\gamma^2\right)+i\,\varepsilon^{\,\lambda\nu\alpha\beta}\,\eta_\alpha\,k_\beta\right]\tilde{A}_\lambda(k)=0. \tag{4}$$

where $\eta_\alpha \sim \partial_\alpha a = \delta_{\alpha 0}\dot{a}$. We shall approximate the sinusoidal variation with of the axion background by a piecewise linear function (see figure). The astrophysical and observational bounds on $|\eta_0| = \pm 2 g_{a\gamma\gamma}\frac{\alpha}{\pi}\frac{a_0 m_a}{f_a}$ range from $|\eta_0| < 10^{-24}$ to $\eta_0 < 10^{-20}$ eV. The quantity η_0 changes alternatively from positive to negative with a period $2\pi/m_a$. Within each period of oscillation two complex and space-like chiral polarization vectors $\varepsilon^\mu_\pm(k)$ can be defined (see [10]). The two polarization vectors are solutions of the vector field equations if and only if

$$k^\mu_\pm = (\omega_\pm, \vec{k}) \qquad \omega_\pm = \sqrt{\vec{k}^2 + m_\gamma^2 \pm \eta_0 k}, \qquad k = |\vec{k}|. \tag{5}$$

2 Forbidden wavelengths

Using this approximation of replacing the CAB oscillation by a piecewise-linear function, as shown in the figure, we can solve exactly for the propagating modes. The equation for $\hat{A}_\nu(t,\vec{k})$

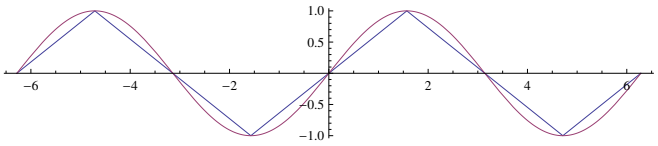

is

$$\left[g^{\mu\nu}(\partial_t^2+\vec{k}^2)-i\epsilon^{\mu\nu\alpha\beta}\eta_\alpha k_\beta\right]\hat{A}_\nu(t,\vec{k})=0. \qquad \hat{A}_\nu(t,\vec{k})=\sum_{\lambda=+,-} f_\lambda(t)\varepsilon_\nu(\vec{k},\lambda). \tag{6}$$

We write $f(t)=e^{-i\omega t}g(t)$ and demand that $g(t)$ have the same periodicity as $\eta(t)=\eta_0\sin(m_a t)$. This requires the fulfillment of the condition

$$\cos(2\omega T)=\cos(\alpha T)\cos(\beta T)-\frac{\alpha^2+\beta^2}{2\alpha\beta}\sin(\alpha T)\sin(\beta T), \quad T=\frac{\pi}{m_a}, \tag{7}$$

where α,β coincide with the two frequencies $\omega_\pm$.

A close inspection of the solutions to the previous equation reveals the existence of momentum gaps: some values of k admit no solution for ω. The phenomenon is visible for large values of the dimensionless ratio η_0/m_a. In a universe filled with cold axions oscillating with a period

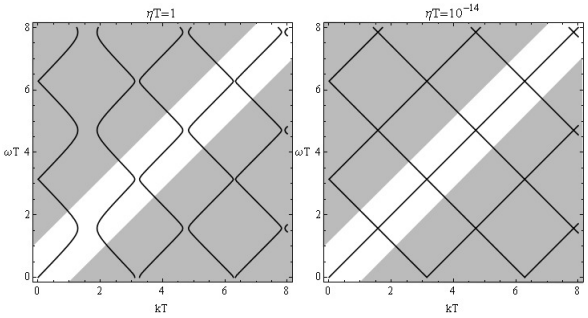

$2\pi/m_a$ some wavelengths are forbidden by a mechanism that is similar to the one preventing some energies from existing in a semiconductor. See [9] for more details. Unfortunately, for realistic values of η_0 the gaps are probably far too small to be seen. Their width is actually proportional to η_0^2/m_a

3 Adding a magnetic field

If $\eta_0=0$ the theoretical technology is well known. It amounts to resumming the Feynman diagrams shown below. Interaction with the cold axion background implies that we need to

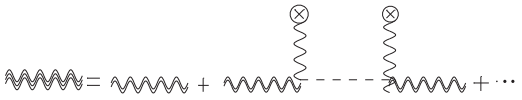

take into account also the diagrams that include interaction with the CAB This can be done

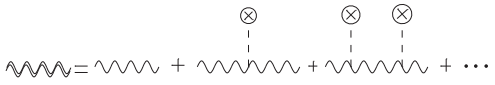

and the resulting resummed propagator can fe found in [9], where we examined the evolution of the polarization plane under the joint influence of the magnetic field and the CAB.

The relevant parameters are $b = 2g_{a\gamma\gamma}\frac{\alpha}{\pi}\frac{B}{f_a}$ and η_0, where B is the magnetic field. Taking as a reference value (just to set an approximate range of variation for b) $f_a > 10^7$ GeV (this would correspond for PQ axions to $m_a \simeq 1$ eV) and $B = 10$ T then $b \leq 10^{-15}$ eV and $\eta_0 \leq 10^{-20}$ eV. However, we shall consider m_a and f_a (and obviously b) to be free parameters.

The relevant evolution equations are

$$\begin{pmatrix} \partial_t^2 + k^2 + m_a^2 & -ib\partial_t & 0 \\ -ib\partial_t & \partial_t^2 + k^2 & \eta_0 k \\ 0 & \eta_0 k & \partial_t^2 + k^2 \end{pmatrix} \begin{pmatrix} \hat{a} \\ i\hat{A}_1 \\ \hat{A}_2 \end{pmatrix} = \begin{pmatrix} 0 \\ 0 \\ 0 \end{pmatrix} \tag{8}$$

We try a solution of the form: $(\hat{a}, i\hat{A}_1, \hat{A}_2) = e^{-i\omega t}(x, X_1, X_2)$:

$$\begin{pmatrix} -\omega^2 + k^2 + m_a^2 & \omega b & 0 \\ \omega b & -\omega^2 + k^2 & \eta_0 k \\ 0 & \eta_0 k & -\omega^2 + k^2 \end{pmatrix} \begin{pmatrix} x \\ X_1 \\ X_2 \end{pmatrix} = \begin{pmatrix} 0 \\ 0 \\ 0 \end{pmatrix} \tag{9}$$

Within each period of oscillation the proper frequencies are in the limit $\eta_0 \ll b \ll \{m_a, k\}$

$$\omega_a^2 \approx k^2 + m_a^2 + b^2 + \frac{b^2k^2}{m_a^2} + \frac{b^2\eta_0^2k^4}{m_a^6} + \frac{b^2\eta_0^2k^2}{m_a^4} \tag{10}$$

$$\omega_1^2 \approx k^2 - \frac{b^2\eta_0^2k^4}{m_a^6} - \frac{b^2\eta_0^2k^2}{m_a^4} - \frac{b^2k^2}{m_a^2} - \frac{\eta_0^2m_a^2}{b^2} \tag{11}$$

$$\omega_2^2 \approx k^2 + \frac{\eta_0^2m_a^2}{b^2} \tag{12}$$

To be compared with the proper modes without magnetic field

$$\omega_\pm^2 = k^2 \pm \eta_0 k. \tag{13}$$

Note that one should not attempt to take the $b \to 0$ limit above because we assume $\eta_0 \ll b$. The natural basis is now parallel and perpendicular (to the magnetic field) rather than left or right polarization. Notice that the proper frequencies in this natural basis and in this limit contain only even powers of η_0 and hence do not change when η_0 changes sign. Unlike the $b = 0$ case both modes are in an eigenstate of energy. We do not expect momentum gaps.

Numerically for $b = 10^{-15}$ eV (a magnetic field of 10 T for $f_a = 10^7$ GeV), $\eta_0 = 10^{-24}$ eV and $k = 1$ keV, the relevant terms are

$$\begin{aligned} \omega_a^2 &\approx k^2 + m_a^2 + \frac{b^2k^2}{m_a^2} \\ \omega_1^2 &\approx k^2 - \frac{b^2k^2}{m_a^2} - \frac{\eta_0^2m_a^2}{b^2} \qquad (14) \\ \omega_2^2 &\approx k^2 + \frac{\eta_0^2m_a^2}{b^2}. \qquad (15) \end{aligned}$$

The splitting between the two polarizations goes as

$$\omega_2^2 - \omega_1^2 \approx \frac{b^2k^2}{m_a^2} + 2\frac{\eta_0^2m_a^2}{b^2}. \tag{16}$$

The relevance of the CAB is somehow enhanced by the magnetic field and dominates for

$$b < m_a \sqrt{\frac{\eta_0}{k}} \simeq 10^{-14} m_a. \tag{17}$$

The difference (16) is very small; typically it could be as "large" as 10^{-9}eV^2. Small as this number is, it should be remembered that Michelson-Morley type experiments can detect differences in frequencies with 17 significant figures[11]. If so, by tuning the magnetic field one should be able to switch in and out the effect of the CAB and perhaps "seeing" it.

There is also a change in the plane of polarization with an angle

$$\sim \frac{\eta_0 m_a^2}{b^2 k} \tag{18}$$

(for "large" axion masses, the actual result is more complicated). This angle could be be as large as 10^{-3}. What this means is that the plane of polarization changes from period to period. Of course the change is not instantaneous and a more complete description of the evolution can be found with the help of the photon correlator derived in [9]. The evolution of the plane of polarization with respect to the $b = 0$ case has a new component due to the CAB.

The rotation survives even without magnetic field and the effect is independent of the frequency. Note that the previous result holds only for table-top experiments when the photon can approximately be considered an eigenstate of energy, i.e. when the time-of-flight of the photon, $|x|$, is smaller than $2\pi/m_a$. This means $|x| < 2\pi/m_a$ and the method could perhaps be useful for very small axion masses.

Due to the smallness of the numbers involved it is somewhat dangerous to rely on approximate formulae - many scales play in the game. In a forthcoming paper[12] a detailed numerical analysis will be performed.

4 Crossing the boundary

Let us finish with a few words on the third topic that was discussed in our presentation. This is work done in collaboration with A. Andrianov and S. Kolevatov and it will be described very succintly here. We refer the readers to [13] for more details.

We want to explore different possible axion backgrounds (other than the cold background oscillating in time with period $\sim 1/m_a$). Consider the term in the lagrangian

$$-\tfrac{1}{4} F^{\mu\nu}(x) \widetilde{F}_{\mu\nu}(x)\, \zeta_\lambda x^\lambda\, \theta(-\zeta \cdot x) \leftrightarrow \tfrac{1}{2}\, \zeta_\mu A_\nu(x) \widetilde{F}^{\mu\nu}(x)\, \theta(-\zeta \cdot x), \tag{19}$$

This associates a space-like boundary with a space-like vector

$$\zeta_\mu = \zeta \times (0, \vec{a}) \quad |\vec{a}| = 1 \tag{20}$$

The Lorentz invariance violating vector has been renamed from η_μ to ζ_μ to avoid confusion with the CAB case.

Although not totally realistic for astrophysical purposes, this would correspond to a region where a linearly decreasing axion density meets the vacuum. For convenience the "wall" is placed in the $\hat{X}$ direction at $x = 0$. Matching on the boundary $\zeta \cdot x = 0$ leads to

$$\delta(\zeta \cdot x) \left[A^\mu_{\text{vacuum}}(x) - A^\mu_\zeta(x) \right] = 0. \tag{21}$$

Different polarizations have different dispersion relations in the axion phase

$$\left\{\begin{array}{c} k_{1L} = k_{10} = \sqrt{\omega^2 - m_\gamma^2 - k_\perp^2} \\ k_{1+} = \sqrt{\omega^2 - m_\gamma^2 - k_\perp^2 + \zeta\sqrt{\omega^2 - k_\perp^2}} \\ k_{1-} = \sqrt{\omega^2 - m_\gamma^2 - k_\perp^2 - \zeta\sqrt{\omega^2 - k_\perp^2}} \end{array}\right. \tag{22}$$

that have to be matched to the usual dispersion law in the normal phase (m_γ is the photon mass and need not be zero, due to plasma effects)

$$k_1 = \sqrt{\omega^2 - m_\gamma^2 - k_\perp^2}. \tag{23}$$

This actually leads to a non-trivial reflection coefficient (see [13] for details). As a function of the invariant mass of the photon M^2

$$\kappa_{ref}(M^2) = \frac{|\sqrt{\frac{(M^2-m_\gamma^2)^2}{\zeta^2} - M^2} - \sqrt{\frac{(M^2-m_\gamma^2)^2}{\zeta^2} - m_\gamma^2}|}{|\sqrt{\frac{(M^2-m_\gamma^2)^2}{\zeta^2} - M^2} + \sqrt{\frac{(M^2-m_\gamma^2)^2}{\zeta^2} - m_\gamma^2}|} \tag{24}$$

Again, the effect seems to depend crucially on the ratio of two very small numbers: m_γ and η_0.

Acknowledgments

It is a pleasure to thank the organizers of Patras 2013 for an enjoyable conference and encouragement. We acknowledge financial support from projects FPA2010-20807, 2009SGR502 and Consolider CPAN.

References

[1] L.Abbott and P. Sikivie, Phys. Lett. 120B, 133 (1983).

[2] M. Kuster, G. Raffelt and B. Beltran (eds), Lecture Notes in Physics 741 (2008).

[3] R.D. Peccei, H.R. Quinn, Phys. Rev. Lett. 38 (1977) 1440; S. Weinberg, Phys. Rev. Lett. 40 (1978) 223; F. Wilzcek, Phys. Rev. Lett. 40 (1978) 279.

[4] M. Dine, W. Fischler and M. Srednicki, Phys. Lett. B, 104, 199 (1981); A.R. Zhitnitsky, Sov. J. Nucl. Phys. 31, 260 (1980); J. E. Kim, Phys. Rev. Lett. 43, 103 (1979); M. A. Shifman, A. I. Vainshtein and V. I. Zakharov, Nucl. Phys. B 166, 493 (1980).

[5] A.H. Corsico et al, JCAP 1212 (2012) 010.

[6] D. Espriu and A. Renau, in Proceedings, 7th Patras Workshop, PATRAS 2011, Mykonos, Greece [arXiv:1111.3141].

[7] A. Andrianov, D. Espriu, F. Mescia and A. Renau, Phys. Lett. B 684 (2010) 101; D. Espriu, F. Mescia, A. Renau, JCAP 1108 (2011) 002.

[8] G. Raffelt and L. Stodolsky, Phys. Rev. D 37, 1237 (1988).

[9] D. Espriu and A. Renau, Phys. Rev. D85 (2012) 025010.

[10] A.A. Andrianov, D. Espriu, P. Giacconi and R. Soldati, JHEP 0909:057,2009.

[11] S. Herrmann et al., Phys. Rev. D 80 (100): 105011.

[12] D. Espriu and A. Renau, in preparation.

[13] A. Andrianov, S. Kolevatov, Theor.Math.Phys. 175 (2013) 744.

Stronger QCD in the early Universe to suppress axion isocurvature perturbations

K. S. Jeong, F. Takahashi

Department of Physics, Tohoku University, Sendai 980-8578, Japan

DOI: http://dx.doi.org/10.3204/DESY-PROC-2013-04/jeong_kwang_sik

A stronger QCD in the early Universe renders the axion heavy, and thus can suppress the isocurvature perturbations of axion dark matter, relaxing the constraint on the inflation scale. Supersymmetry provides a natural framework for this because there is a flat direction involving Higgs fields. Stabilized at a large value during inflation, the Higgs flat direction leads to that the QCD interaction becomes strong at a high energy scale, making high scale inflation scenarios compatible with axion dark matter.

1 Introduction

The Peccei-Quinn (PQ) extension of the standard model (SM) includes the axion, which provides a natural solution to the strong CP problem through spontaneously broken PQ symmetry [1, 2]. The axion potential is generated by non-perturbative QCD instanton effects, dynamically relaxing the CP phase in QCD. This implies that coherent oscillations of the axion are necessarily induced and contribute to cold dark matter via the misalignment mechanism [2]. The axion can thus explain both a tiny CP violation in QCD and the dark matter of the Universe. However, the axion dark matter generally puts a strong constraint on the inflation scale because its quantum fluctuations during inflation induce isocurvature perturbations in the CMB spectrum. If the axion is the main component of dark matter in the Universe, the observed CMB spectrum constrains the inflation scale to be [3, 4, 5]

$$H_{\rm inf} < 0.87 \times 10^7 {\rm GeV} \left(\frac{f_a}{10^{11} {\rm GeV}} \right)^{0.408}, \quad (1)$$

at 95% CL, where f_a is the axion decay constant. Hence high scale inflation scenarios such as the chaotic inflation [6] are in tension with the axion dark matter.

The isocurvature constraint can be avoided if the PQ symmetry is restored during or after inflation since the axion appears after PQ symmetry breaking [7, 8]. However, in this case, the axion properties are constrained because topological defects such as cosmic strings and domain walls are generated. To avoid overclosure of the Universe, the PQ sector should be such that the domain wall number is equal to one and f_a is less than about 10^{10} GeV. Alternatively one can consider models where the coefficient of the axion kinetic term is larger during inflation than present so that axion quantum fluctuations can be suppressed [7, 9, 10].

In this work, we propose another interesting way to relax the isocurvature constraint on the inflation scale in the axion dark matter scenario. The idea is to make the QCD stronger during

inflation so that the axion becomes heavy enough to have quantum fluctuations significantly suppressed at superhorizon scales. A stronger QCD can be achieved when the Higgs field has a sufficiently large value during inflation because the quarks then decouple at a high energy scale while making the QCD coupling run faster at lower scales.

2 Suppressing axion isocurvature perturbations

The Higgs field can naturally have a large field value during inflation in the supersymmetry SM since they compose flat directions. Let us consider a supersymmetry axion model where the Higgs fields H_u and H_d are neutral under the PQ symmetry. We are interested in the case that the $H_u H_d$ flat direction is stabilized at a large value during inflation so that the QCD confines at a high scale. This is realized when it obtains a tachyonic mass from a Planck-suppressed coupling with the inflaton in the Kähler potential. The Higgs flat direction can then be fixed at a large value through the interplay between the Hubble-induced tachyonic mass and a higher order superpotential term. We will assume that it is stabilized around or above the GUT scale, $M_{\rm GUT} \simeq 2 \times 10^{16}$ GeV.

2.1 Axion potential

Let us first examine how the axion potential is generated in the early Universe. If all the quarks become heavier than the effective QCD scale Λ_h for the flat direction fixed around $M_{\rm GUT}$, they can be integrated out in a supersymmetric way. The low energy theory is a pure supersymmetric SU(3)$_c$ with gauge kinetic function given by [11]

$$f_h = (\text{constant}) - \frac{n}{8\pi^2} \ln S - \frac{N_f}{8\pi^2} \ln \phi, \tag{2}$$

where S is the axion superfield, and ϕ^2 parameterizes the $H_u H_d$ flat direction. The constant n counts the number of PQ charged quarks when the PQ symmetry is linearly realized, and $N_f = 6$ is the flavor number of the SM quarks. For Λ_h larger than $H_{\rm inf}$, the gluino condensate is formed during inflation, and consequently induces the non-perturbative superpotential [12]

$$W_{\rm np} = N_c \Lambda_0^3 \propto e^{-8\pi^2 f_h / N_c}, \tag{3}$$

with $N_c = 3$. Here Λ_0 denotes the condensation scale, which is equal to the QCD scale Λ_h in the present case.

The axion potential is generated from the non-perturbative superpotential $W_{\rm np}$ through supersymmetry breaking with the dominant contribution from the Higgs F-term:

$$V = |\partial_\phi (\Delta W + W_{\rm np})|^2 + \cdots = c N_f H_{\rm inf} \Lambda_0^3 \cos\left(\frac{a}{N_c f_a} + \theta_0 \right) + \cdots, \tag{4}$$

where the constant c determines the overall size of the Hubble-induced mass term for ϕ and is generally order unity, and ΔW is the higher order superpotential term which competes with the Hubble-induced mass term to stabilize the flat direction. The above relation holds when the condensation scale lies in the range

$$H_{\rm inf} < \Lambda_0 < f_a, \tag{5}$$

where the upper bound is needed not to destabilize the saxion, while the lower bound comes from the requirement that the gauge-mediated gluino mass associated with Higgs F-term $F_\phi/\phi \sim cH_{\rm inf}$ should be small since otherwise the gluino would decouple at a scale above Λ_0. Note also that the non-perturbative superpotential does not modify significantly the potential of ϕ if

$$H_{\rm inf}\phi_0^3 \gg \Lambda_0^3. \tag{6}$$

On the other hand, in the case that there are n_f quarks lighter than Λ_h, they form meson fields and are stabilized by their mass term m and the Affleck-Dine-Seiberg superpotential. Integrating out the meson fields leads to the gluino condensation with $\Lambda_0^{3N_c} = \Lambda_h^{3N_c - n_f}\det(m)$. One thus obtains the axion potential given by (4) using Λ_0 defined this way.

From the axion potential (4) induced by the non-perturbative superpotential and supersymmetry breaking, one finds that the axion mass is given by

$$m_a^2 = \frac{\hat{c}H_{\rm inf}\Lambda_0^3}{f_a^2}, \tag{7}$$

during inflation, where $\hat{c} \equiv cN_f/N_c^2$ is generally order unity.

2.2 Stronger QCD

The QCD confines at a higher scale during inflation if the quarks become heavier, which is realized when the Higgs fields are stabilized at a large value. It is obvious that such effect is more efficient if there exist extra colored particles that obtain larger masses during inflation. Let us introduce N_Ψ pairs of PQ-singlet fields that belong to $\mathbf{5} + \bar{\mathbf{5}}$ of SU(5) and obtain masses from

$$W = \left(M_\Psi + \frac{\phi^2}{M}\right)\Psi\Psi^c, \tag{8}$$

where M is an effective cut-off scale. The coupling to H_uH_d $(= \phi^2)$ can make $\Psi + \Psi^c$ heavier during inflation for the flat direction stabilized at a large field value. Using the property that the universal gauge coupling constant at $M_{\rm GUT}$ is $g_{\rm GUT}^2 \simeq 0.5$ in the MSSM, we find that the QCD scale reads

$$\Lambda_h \simeq 1.3 \times 10^7 {\rm GeV}\left(\frac{M_{\rm GUT}}{M_\Psi}\right)^{N_\Psi/9}, \tag{9}$$

for ϕ_0 and M around $M_{\rm GUT}$. Here we have taken into account the hierarchy in the SM quark Yukawa couplings, because of which the condensation scale Λ_0 is slightly smaller than Λ_h if Λ_h is larger than about $10^{-5}M_{\rm GUT}$. One can see that the QCD scale is about 10^7 GeV in the MSSM for $\phi_0 \sim M_{\rm GUT}$, but it is raised higher in the presence of extra colored particles which couple to H_uH_d.

Let us now examine how much the QCD scale can be raised in the supersymmetric axion model. An important constraint comes from the perturbativity condition because the gauge coupling at $M_{\rm GUT}$ increases if one adds extra colored fields:

$$\frac{1}{g_{\rm GUT}^2} \simeq 2 - \sum_{i=\Phi,\Psi}\frac{N_i}{8\pi^2}\ln\left(\frac{M_{\rm GUT}}{M_i}\right) > \frac{1}{4\pi}, \tag{10}$$

where $\Phi + \Phi^c$ are PQ quarks which belong to $\mathbf{5} + \bar{\mathbf{5}}$ and obtain masses $M_\Phi \sim f_a$ from the superpotential term $S\Phi\Phi^c$. The PQ quarks are added to make S couple to the QCD anomaly, which is required to solve the strong CP problem via the PQ mechanism. However, these PQ quarks play no role in raising the QCD scale since their masses are the same during and after inflation. Combined with the relation (9), the above requirement places an upper bound on the QCD scale,

$$\Lambda_h < 2.7 \times 10^{14}\text{GeV} \left(\frac{f_a}{M_{\rm GUT}} \right)^{N_\Phi/9}, \tag{11}$$

which is insensitive to M_Ψ. For instance, taking $f_a \geq 10^9$ GeV and $N_\Phi = 1$, the QCD scale can be as high as 10^{13} GeV.

2.3 Axion isocurvature perturbations

A higher QCD scale and large axion mass during inflation provide a simple way to relax the isocurvature constraint in the axion dark matter scenario. The axion is stabilized at the minimum of the potential (4) during inflation if its mass (7) is heavier than the inflation scale:

$$H_{\rm inf} < 10^{12}\text{GeV} \times \hat{c} \left(\frac{\Lambda_0}{f_a} \right)^3 \left(\frac{f_a}{10^{12}\text{GeV}} \right), \tag{12}$$

and then quantum fluctuations are highly suppressed at superhorizon scales. This shows that a high QCD scale can relax significantly the isocurvature constraint compared to the conventional scenario.

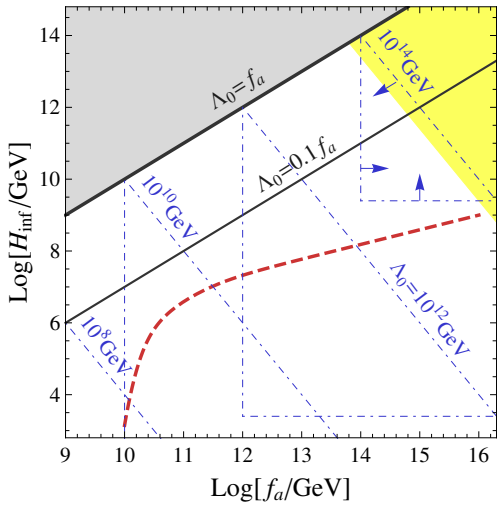

Figure 1: Inflation scale compatible with the axion cold dark matter.

Figure 1 shows the region where the axion isocurvature fluctuations are suppressed by a stronger QCD leading to $m_a > H_{\rm inf}$. Here we have taken $\hat{c} = 1$ and Λ_0 as a free parameter. The upper-right shaded region (yellow) is excluded by the perturbativity limit of the gauge

interactions up to the GUT scale, while the upper-left region (gray) leads to saxion destabilization as $\Lambda_0 < f_a$. The thick (thin) solid line corresponds to the upper bound on $H_{\rm inf}$ for $\Lambda_0 = f_a$ ($\Lambda_0 = 0.1 f_a$). For fixed Λ_0, the suppression mechanism works inside a right-angled triangle, whose base, height, and hypotenuse come from the requirement $\Lambda_0 < f_a$, $H_{\rm inf} > \Lambda^3/\phi_0^2$ with $\phi_0 \sim M_{\rm GUT}$, and $m_a > H_{\rm inf}$, respectively. For instance, the upper-right one with blue dot-dashed sides is obtained for $\Lambda_0 = 10^{14}$ GeV. Other cases with $\Lambda_0 = 10^8$, 10^{10}, 10^{12} GeV are also shown from left to right. For comparison, we present the conventional isocurvature bound in the dashed red line, taking into account the anharmonic effect [13, 14].

We close this section by noting that f_a appearing in the relation (12) is the axion decay constant during inflation, which we have simply assumed to be the same as the present value. One may consider the case where f_a is around 10^{12} GeV at present but it has a larger value during inflation. Then the right amount of axion dark matter is obtained through the misalignment mechanism for an initial misalignment angle of order unity, while allowing high inflation scales around 10^{13-14} GeV.

3 Conclusions

The QCD axion not only provides a natural solution to the strong CP problem, but also can account for the dark matter of the Universe if its isocurvature perturbations are sufficiently suppressed to be consistent with the observation. We have shown that a stronger QCD in the early Universe can significantly relax the isocurvature constraint on the inflation scale, making high scale inflation models compatible with the axion dark matter. This is naturally realized within a supersymmetric axion model. For the Higgs flat direction stabilized at a large value during inflation, the QCD confines at a high energy scale, and consequently the axion becomes heavy and has no sizable quantum fluctuations at superhorizon scales.

Acknowledgments

This work was supported by JSPS KAKENHI Grant Numbers 23540283, 22244030, 21244033, 24740135, MEXT KAKENHI Grant Numbers 24111702, 21111006, 23104008, and Inoue Foundation for Science.

References

[1] R. D. Peccei and H. R. Quinn, "CP Conservation in the Presence of Instantons," Phys. Rev. Lett. **38**, 1440 (1977); "Constraints Imposed by CP Conservation in the Presence of Instantons," Phys. Rev. D **16**, 1791 (1977).

[2] For a review, see J. E. Kim, "Light Pseudoscalars, Particle Physics and Cosmology," Phys. Rept. **150**, 1 (1987); H. Y. Cheng, "The Strong CP Problem Revisited," Phys. Rept. **158**, 1 (1988); J. E. Kim and G. Carosi, "Axions and the Strong CP Problem," Rev. Mod. Phys. **82**, 557 (2010); A. Ringwald, "Exploring the Role of Axions and Other WISPs in the Dark Universe," Phys. Dark Univ. **1** (2012) 116; M. Kawasaki and K. Nakayama, "Axions : Theory and Cosmological Role," arXiv:1301.1123 [hep-ph].

[3] P. A. R. Ade *et al.* [Planck Collaboration], "Planck 2013 results. XXII. Constraints on inflation," arXiv:1303.5082 [astro-ph.CO].

[4] D. Seckel and M. S. Turner, "Isothermal Density Perturbations in an Axion Dominated Inflationary Universe," Phys. Rev. D **32**, 3178 (1985).

[5] D. H. Lyth, "A Limit On The Inflationary Energy Density From Axion Isocurvature Fluctuations," Phys. Lett. B **236**, 408 (1990).

[6] A. D. Linde, "Chaotic Inflation," Phys. Lett. B **129**, 177 (1983); M. Kawasaki, M. Yamaguchi and T. Yanagida, "Natural chaotic inflation in supergravity," Phys. Rev. Lett. **85**, 3572 (2000) [hep-ph/0004243]; R. Kallosh and A. Linde, "New models of chaotic inflation in supergravity," JCAP **1011**, 011 (2010) [arXiv:1008.3375 [hep-th]]; K. Nakayama, F. Takahashi and T. T. Yanagida, "Polynomial Chaotic Inflation in the Planck Era," Phys. Lett. B725, **111** (2013) [arXiv:1303.7315 [hep-ph]].

[7] A. D. Linde and D. H. Lyth, "Axionic domain wall production during inflation," Phys. Lett. B **246**, 353 (1990).

[8] D. H. Lyth and E. D. Stewart, "Constraining the inflationary energy scale from axion cosmology," Phys. Lett. B **283**, 189 (1992).

[9] A. D. Linde, "Axions in inflationary cosmology," Phys. Lett. B **259**, 38 (1991).

[10] S. Folkerts, C. Germani and J. Redondo, "Axion Dark Matter and Planck favor non-minimal couplings to gravity," arXiv:1304.7270 [hep-ph].

[11] G. F. Giudice and R. Rattazzi, "Extracting supersymmetry breaking effects from wave function renormalization," Nucl. Phys. B **511**, 25 (1998) [hep-ph/9706540]; N. Arkani-Hamed, G. F. Giudice, M. A. Luty and R. Rattazzi, "Supersymmetry breaking loops from analytic continuation into superspace," Phys. Rev. D **58**, 115005 (1998) [hep-ph/9803290].

[12] I. Affleck, M. Dine and N. Seiberg, "Dynamical Supersymmetry Breaking in Supersymmetric QCD," Nucl. Phys. B **241**, 493 (1984).

[13] D. H. Lyth, "Axions and inflation: Sitting in the vacuum," Phys. Rev. D **45**, 3394 (1992).

[14] T. Kobayashi, R. Kurematsu and F. Takahashi, "Isocurvature Constraints and Anharmonic Effects on QCD Axion Dark Matter," arXiv:1304.0922 [hep-ph].

Hints of a Cosmic Axion Background

M.C. D. Marsh

Rudolph Peierls Centre for Theoretical Physics, University of Oxford, Oxford, United Kingdom.

DOI: http://dx.doi.org/10.3204/DESY-PROC-2013-04/marsh_david

In models of particle physics and cosmology arising from compactifications of string theory, the reheating of the standard model after inflation generically proceeds through the decay of heavy moduli. Non-vanishing branching ratios for moduli decay into axions generate axionic dark radiation which linger in the present universe as a homogeneous and isotropic background of relativistic axions, hence called the Cosmic Axion Background (CAB). Axion-photon conversion in magnetic fields may render the CAB visible, and we show that the soft X-ray excess observed in galaxy clusters may provide hints for the existence of a CAB.

1 Reheating in String Theory

A salient feature of the four-dimensional effective theories arising from compactifications of string theory is the presence of scalar particles with feeble, Planck-mass suppressed interactions. Such particles, or moduli, parametrize the size and shape of the compactification manifold and determine the values of coupling constants in the four-dimensional effective theory. The scalar potential for the moduli may arise from both perturbative and non-perturbative effects, and to extract predictions from the theory, this potential must be minimised and meta-stable vacua within the regime of computational control identified.

Over the past decade a number of relatively general methods to obtain controlled compactifications have been found and investigated by many authors, see e.g. [1, 2, 3] for compactifications of type IIB, and [4] for G_2 compactifications of M-theory. For compactifications with soft supersymmetry breaking at the TeV-scale, the lightest moduli turn out to have a mass of $m_\Phi \approx 10^6$ GeV in several moduli stabilisation scenarios [5, 6, 7].

Moreover, successful string theory models of our universe must in addition to stabilising moduli also realise realistic particle phenomenology and provide a compelling cosmology, which is typically assumed to include a period of inflation in the early universe. String theory models of inflation generically lead to the displacement of moduli from their final meta-stable minimum, and hence to oscillating moduli at the end of inflation. An oscillating scalar field red-shifts like matter,

$$\rho_{\rm moduli} \sim 1/a(t)^3 \,,$$

where $a(t)$ denotes the Friedmann-Robertson-Walker scale factor. Thus, with time the oscillating moduli field will come to dominate over any initial radiation, which red-shifts like $\rho_{\rm radiation} \sim 1/a(t)^4$.

The massive moduli fields decay with a typical life-time of

$$\tau \sim 8\pi \frac{M_{Pl}^2}{m_\Phi^3} \approx 10^{-4} \text{ s } \left(\frac{10^6 \text{ GeV}}{m_\Phi}\right)^3 ,$$

where m_Φ denotes the modulus mass and M_{Pl} denotes the reduced Planck mass. The decay of the lightest moduli fields into visible sector particles will reheat the Standard Model to a temperature,

$$T_{reheat} \sim \frac{m_\Phi^{3/2}}{M_{Pl}^{1/2}} \sim 0.6 \text{ GeV } \left(\frac{m_\Phi}{10^6 \text{ GeV}}\right)^{3/2} .$$

2 Axionic dark radiation from moduli decay

String compactifications typically give rise to additional light hidden sectors to which the moduli may couple with M_{Pl} suppressed couplings. We here consider the theoretically well-motivated case in which the moduli has an additional decay channel into axion-like particles (hence, axions). Such a decay channel may arise from a Lagrangian coupling,

$$\mathcal{L} \supset \frac{1}{2}\frac{\Phi}{M_{Pl}} \partial_\mu a \partial^\mu a \, ,$$

and gives rise to axions with energy $E_a^{(0)} = m_\Phi/2 \approx (M_{Pl}/m_\Phi)^{1/2} T_{reheat} \gg T_{reheat}$ [9, 10]. These axions contribute to the *dark radiation* of the universe, and affect the CMB spectrum and the BBN abundances through the corresponding increase in the Hubble expansion parameter. The amount of dark radiation is traditionally parametrized in terms of the "effective number of neutrino species", $N_{eff} = 3.046 + \Delta N_{eff}$. For axionic dark radiation arising from the decay $\Phi \to aa$, ΔN_{eff} is given by

$$\Delta N_{eff} = \frac{43}{7}\frac{B_a}{1-B_a}\left(\frac{g_\star(T_{\nu \text{ decoupling}})}{g_\star(T_{reheat})}\right)^{1/3} ,$$

where B_a denotes the branching ratio into axions, and $g_\star(T)$ denotes the number of degrees of freedom in thermal equilibrium at temperature T.

There are tentative observational hints of dark radiation at the $1-2$ σ level both from the determination of light element abundances at BBN and from observations of the CMB, as summarised in table 1. Closely following [8], in this contribution to the *Proceedings of the 9th Patras Workshop on Axions, WIMPs and WISPs*, we will entertain the possibility of axionic dark radiation contributing to the energy density of the universe.

Experiment	N_{eff}
CMB: WMAP9 [11]	3.55 ± 0.60
CMB: Planck [12]	3.30 ± 0.27
CMB+H_0: WMAP9 +H_0 [11]	3.89 ± 0.40
CMB+H_0: Planck +H_0 [12]	3.62 ± 0.25
BBN+CMB: Cook *et al.* [13]	3.28 ± 0.28
BBN: Cook *et al.* [13]	3.57 ± 0.18

Table 1: Observational hints of dark radiation.

2.1 The Cosmic Axion Background

As the universe expands, the axion energies redshift as $E_a(t) = E_a^{(0)} a(t_0)/a(t)$ where $a(t_0)$ denotes scale factor at the time of decay. In the approximation in which all moduli decay simultaneously at $t_0 = \tau$, this results in a mono-energetic population of relativistic axions which will remain a factor of approximately $(M_{Pl}/m_\Phi)^{1/2}$ more energetic than the visible sector radiation (up to small changes in $g_\star$). In reality however, moduli decaying early will result in axions which appear more red-shifted than those arising from subsequent moduli decays, and in [14], the non-thermal spectrum of the present day axions was calculated. For $m_\Phi = 10^6$ GeV, the resulting axion spectrum in our present universe has a mean energy of around $E_a^{(today)} \approx 200$ eV, and is shown in Figure 1. These axions constitute a homogenous and isotropic Cosmic Axion Background (CAB) with a present day number density of $n_a^{(today)} \approx 7 \cdot 10^{-5}$ cm^{-3} and a flux of $\Phi_a^{(today)} \approx 5 \cdot 10^5$ cm^{-2} s^{-1}.

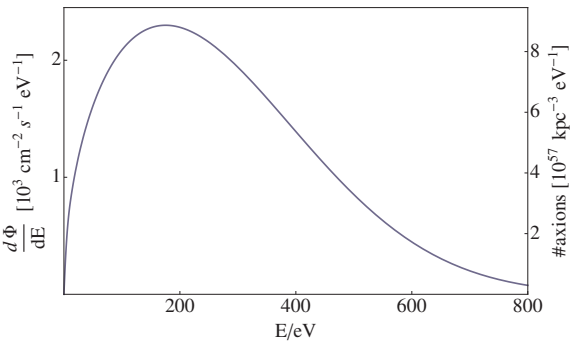

Figure 1: The present day CAB spectrum arising from decay of a modulus with $m_\Phi \sim 10^6$ GeV.

3 Hints of a Cosmic Axion Background

It has long been realised that axions may convert into photons in the presence of a magnetic field [15, 16]. The axion-photon Lagrangian is given by

$$\mathcal{L} = -\frac{1}{4} F_{\mu\nu} F^{\mu\nu} - \frac{a}{4M} F_{\mu\nu} \tilde{F}^{\mu\nu} + \frac{1}{2} \partial_\mu a \partial^\mu a - \frac{1}{2} m_a^2 a^2 \,,$$

where bounds from supernova constrain $M > 10^{11}$ GeV, and we will here consider an axion-like particle with $m_a^2 \approx 0$. The probability for an axion traveling through a perpendicular magnetic field with coherence length L and field strength B to convert into a photon is given by [17],

$$P(a \to \gamma) = \sin^2(2\theta) \sin^2 \left(\frac{\Delta}{\cos 2\theta} \right) \,,$$

where $\tan 2\theta = \frac{2B\omega}{M m_{eff}^2}$, $\Delta = \frac{m_{eff}^2 L}{4\omega}$, $m_{eff}^2 = m_a^2 - \omega_{pl}^2$, ω_{pl} is the plasma frequency,

$$\omega_{pl} = \left(4\pi\alpha \frac{n_e}{m_e} \right)^{1/2} = 1.2 \cdot 10^{-12} \sqrt{\frac{n_e}{10^{-3}\text{cm}^{-3}}} \text{ eV} \,,$$

and ω denotes the photon energy. Though not crucial for our analysis, we note that in the small-angle approximation $\theta \ll 1$ and $\Delta \ll 1$, the conversion probability is simply given by

$$P(a \to \gamma) \approx \frac{1}{4} \left(\frac{BL}{M} \right)^2 \,.$$

Thus, a CAB may possibly be detectable as photons in the extreme ultraviolet (EUV) or soft X-ray spectrum through conversion in a magnetic field. Galaxy clusters support magnetic fields of μG strength which are coherent over several kpc, and thus provide a natural place to search for photons from axion-photon conversion of the CAB.

In fact, a soft X-ray excess above the emission from the hot (~ 8 keV) intracluster medium has been observed by a number of experiments in a large number of galaxy clusters since 1996 [18], for a review see [19]. For example, the observed excess luminosity from the central 0.5 Mpc region of the nearby Coma cluster is $\mathcal{L}_{obs.excess} \approx 10^{42}$ erg s^{-1}.

From observations of Faraday rotation of polarised sources in and behind Coma, it has been argued that the typical size of the cluster magnetic field is $\mathcal{O}(B) = 1 - 10$ μG with coherence lengths ranging from 2 kpc to around 30 kpc [20].

The expected luminosity from axion-photon conversion of the CAB arising from a cylindrical volume of radius 0.5 Mpc and depth 3 Mpc along the line of sight may then easily be estimated as,

$$\mathcal{L}_{a\to\gamma} \approx 1.7 \cdot 10^{42} \times \left(\frac{\Delta N_{eff}}{0.57}\right) \left(\frac{B}{2\ \mu\text{G}} \frac{10^{13}\ \text{GeV}}{M}\right)^2 \left(\frac{L}{1\ \text{kpc}}\right) .$$

Thus, the observed soft X-ray excess appears to easily be accommodated by axion-photon conversion in the cluster magnetic field. This conclusion holds also away from the small-angle approximation, as shown in [8]. A more detailed study of the morphology of the expected excess flux from the Coma cluster will appear in future publications.

This scenario makes several additional predictions. As the CAB is uniformly distributed, the produced luminosity is determined only by the magnetic field and the electron density, and is independent of the cluster temperature or matter distribution. The model predicts that the soft excess should be largest in cluster regions with large magnetic fields and small electron densities, and its spatial extent should be coterminous with the magnetic field. Furthermore, since the production of the soft excess is non-thermal, it should not be possible to associate any thermal emission lines to the soft excess. Moreover, the CAB axions are redshifting, and used to be more energetic by $(1 + z)$ and more dense by $(1 + z)^3$. It is then a prediction that the energy scale of the soft excess should grow as $(1 + z)$ and, if other aspects of cluster physics are identical, the overall energy in the soft excess should grow as $(1 + z)^4$.

In sum, axionic dark radiation constitute a well-motivated extension of standard cosmology, and some of the best studied string theory models predict a present day primordial background of relativistic axions with energies in the $E_a \sim 0.1 - 1$ keV range. This CAB may be detected through axion-photon conversions in magnetic fields, and may in fact already be visible through the long standing soft excess in galaxy clusters.

Acknowledgments

We thank Konstantin Zioutas for informing us about the soft X-ray excess from galaxy clusters. We thank Jo Dunkley and Alexander Schekochihin for discussions.

References

[1] S. B. Giddings, S. Kachru and J. Polchinski, Phys. Rev. D **66**, 106006 (2002) [hep-th/0105097].

[2] S. Kachru, R. Kallosh, A. D. Linde and S. P. Trivedi, Phys. Rev. D **68**, 046005 (2003) [hep-th/0301240].

[3] V. Balasubramanian, P. Berglund, J. P. Conlon and F. Quevedo, JHEP **0503**, 007 (2005) [hep-th/0502058].

[4] B. S. Acharya, K. Bobkov, G. Kane, P. Kumar and D. Vaman, Phys. Rev. Lett. **97**, 191601 (2006) [hep-th/0606262].

[5] K. Choi, A. Falkowski, H. P. Nilles and M. Olechowski, Nucl. Phys. B **718**, 113 (2005) [hep-th/0503216].

[6] R. Blumenhagen, J. P. Conlon, S. Krippendorf, S. Moster and F. Quevedo, JHEP **0909**, 007 (2009) [arXiv:0906.3297 [hep-th]].

[7] B. S. Acharya, P. Kumar, K. Bobkov, G. Kane, J. Shao and S. Watson, JHEP **0806**, 064 (2008) [arXiv:0804.0863 [hep-ph]].

[8] J. P. Conlon and M. C. D. Marsh, arXiv:1305.3603 [astro-ph.CO].

[9] M. Cicoli, J. P. Conlon and F. Quevedo, Phys. Rev. D **87**, no. 4, 043520 (2013) [arXiv:1208.3562 [hep-ph]].

[10] T. Higaki and F. Takahashi, JHEP **1211**, 125 (2012) [arXiv:1208.3563 [hep-ph]].

[11] G. Hinshaw *et al.* [WMAP Collaboration], arXiv:1212.5226 [astro-ph.CO].

[12] P. A. R. Ade *et al.* [Planck Collaboration], arXiv:1303.5076 [astro-ph.CO].

[13] R. Cooke, M. Pettini, R. A. Jorgenson, M. T. Murphy and C. C. Steidel, arXiv:1308.3240 [astro-ph.CO].

[14] J. P. Conlon and M. C. D. Marsh, arXiv:1304.1804 [hep-ph].

[15] P. Sikivie, Phys. Rev. Lett. **51**, 1415 (1983) [Erratum-ibid. **52**, 695 (1984)].

[16] P. Sikivie, Phys. Rev. D **32**, 2988 (1985) [Erratum-ibid. D **36**, 974 (1987)].

[17] G. Raffelt and L. Stodolsky, Phys. Rev. D **37**, 1237 (1988).

[18] R. Lieu et al, *Science*:274, 1335.

[19] F. Durret, J. S. Kaastra, J. Nevalainen, T. Ohashi and N. Werner, Space Science Reviews, **134**, 51 (2008) arXiv:0801.0977 [astro-ph].

[20] A. Bonafede, L. Feretti, M. Murgia, F. Govoni, G. Giovannini, D. Dallacasa, K. Dolag and G. B. Taylor, arXiv:1002.0594 [astro-ph.CO].

Dark Matter – a light move

B. Döbrich[1], *J. Redondo*[2,3]

[1] Deutsches Elektronen-Synchrotron (DESY), Hamburg, Germany
[2] Arnold Sommerfeld Center, Ludwig-Maximilians-Universität, München, Germany
[3] Max-Planck-Institut für Physik, München, Germany

DOI: http://dx.doi.org/10.3204/DESY-PROC-2013-04/redondo_javier

This proceedings contribution reports from the workshop Dark Matter - a light move, held at DESY Hamburg in June 2013. Dark Matter particle candidates span a huge parameter range. In particular, well motivated candidates exist also in the sub-eV mass region, for example the axion. Whilst a plethora of setups searches for rather heavy Dark Matter particles, to this date only very few experiments aimed at direct detection of sub-eV Dark Matter exist. The aim of our workshop was to discuss if and how this could be changed in the near future.

1 Introduction and light Dark Matter theory

The standard model of particle physics (SM) has passed its last test with the recent discovery of the Higgs boson, but it is still incomplete as a full theory of nature. The most urgent claim of physics beyond the SM is the existence of non-baryonic dark matter (DM) in the Universe, most likely new particles whose nature we have failed to unveil so far. Extensions of the SM originally proposed to convert it in a more natural choice among conceivable theories, suggest a few DM candidates: weakly-interacting massive particles (WIMPs) or the axion, among the best motivated. To date, a major part of the community hopes for direct detection of DM in experiments aiming to record the recoil energy of nuclei after scattering with DM particles. This strategy is optimal for WIMPs with masses $\gtrsim$ 100 GeV but leaves out very light DM candidates such as the axion, searched for by just one experiment (of a very different nature): ADMX. While there are great chances of discovering WIMPs in the near future, ADMX can only cover a part of all the viable axion DM parameter space. Moreover, axions are just an example of a broad class of particles, weakly-interacting slim particles (WISPs), that share most of their phenomenology [1]. In particular, WISPs are excellent DM candidates [2]. New experiments have been proposed to search for WISPy DM [3–7], sometimes sensitive to more than one type of DM candidate at a time, e.g. axion-like particles and hidden photons. These novel experiments can explore decades of pristine DM parameter space and pave the road to boost the sensitivity of ADMX-like experiments looking for axions in unexplored parameter regions.

The workshop 'Dark Matter – a light move' took place at DESY Hamburg at June 17th-18th [8] with the purpose of fostering new direct detection experiments looking for axions and other WISPs. The gathering was a blend of theorists and experimentalists expected to team up in selecting the most promising regions of parameter space and realistic set-ups that can cover them. The expertise of the audience was chosen to focus on exploiting the couplings of

WISPs to photons, which present several advantages. At the theoretical level, WISPs appear in well motivated field and string-theory extensions of the SM [9]. Axions and axion-like particles (ALPs) appear as pseudo-Nambu-Goldstone bosons of spontaneously broken global symmetries at high energy scales and as imaginary parts of moduli fields in string-theoretic theories or in general in theories where the sizes of gauge couplings are set by the vacuum expectation value of new fields. Their coupling to photons is of the well-known kind

$$\mathcal{L}_\phi = \frac{\phi}{2\pi f_\phi} F_{\mu\nu} F^{\mu\nu}, \tag{1}$$

where ϕ is the axion(ALP), f_ϕ a symmetry breaking energy scale and $F_{\mu\nu}$ the electromagnetic tensor. The mass of axions(ALPs) depends upon terms that explicitly break the global symmetries. For the axion we have $m_a = 6$ meV$(10^9$ GeV/f$_\mathrm{a})$ while for ALPs such a relation is much more model dependent. Hidden photons (HPs) appear also in field and string-theoretic extensions [10]. Their main interaction with photons is through kinetic mixing

$$\mathcal{L}_\chi = -\frac{\chi}{2} F_{\mu\nu} B^{\mu\nu}, \tag{2}$$

where $B^{\mu\nu}$ the HP field-strength and χ is the kinetic mixing, with typical values in the $10^{-12} \sim 10^{-3}$ range. WISPy cold dark matter can be produced in the early Universe by a variety of mechanisms. The most relevant are the misalignment mechanism and the decay of topological defects. The regions of mass-coupling parameter space where the full DM can be accounted for the different cases were summarized in the workshop and is shown in figs. 1 and 2. The most important constraints on WISPy DM come from: non-observation of WISP DM decay, absorption of WISP DM in the early universe plasma and indirect effects on stellar cooling (non-DM WISP emission), from refs. [10, 11] which we have shadowed in black in the figures. A DM WISP background imprints generically isocurvature anisotropies (generated during inflation) in the cosmic microwave background which have not been observed, imposing strong constraints in WISP DM models and the parameters of inflation [12]. Finally, the WISPy DM paradigm could be particularly well tested because WISPs can form a Bose-Einstein condensate [13] and thus lead to the formation of peculiar caustics in galaxies [14], which could have already been observed [15].

2 Detecting WISPy DM

DM axions(ALPs) mix with photons in a background magnetic field (strength B) with an angle

$$\chi_\phi = \frac{g_{\phi\gamma} B}{m_\phi} \quad \text{(generic ALP)} \quad ; \quad \chi_a = \frac{g_{a\gamma} B}{m_a} \sim 10^{-15} \left(\frac{B}{10\ \mathrm{T}} \right) C_{a\gamma} \quad \text{(axions)}; \tag{3}$$

with $C_{a\gamma} \sim \mathcal{O}(1)$, while for HPs the angle is simply χ. The local density of DM, 0.3 GeV/cm^3 implies an electric field $|E| \sim 2.3 \times \chi$ kV/m and it holds for the DM mass m, and its frequency, $f = 240\mathrm{MHz} \times (m/\mu\mathrm{eV})$. The E-field carried by the DM WISP drives reflected waves from mirrors, emitted perpendicularly to the surface to a large degree due to the spatial coherence of DM waves [6]. The simplest experiment to concentrate this radiation is a spherical dish with a detector at its center, getting a radiated power per dish area $\sim \chi^2 |E|^2 = 1.4 \times 10^4 \chi^2$ W and $\sim 10^{-27} (B/10\ \mathrm{T})^2 C_{a\gamma}^2$ W for axions (note that for axions and HPs, the radiated power is independent of the mass).

The emitted power can be amplified in a resonant cavity up to a factor of 10^6 (the width of the DM energy distribution) but since the WISP mass is unknown, one is forced to scan over frequencies in search for the tiny signal [16]. ADMX [17] is nowadays the only haloscope [18] of this kind. It employs a cylindrical cavity tunable with internal rods inside a 8T solenoid. Its dimensions (1 m long, 0.5 m diameter) set its lowest resonant frequency 0.48 GHz ($m = 2\ \mu eV$). ADMX has already taken data in the $2-3.6\mu$eV mass range with a low-noise SQUID amplifier reaching a system temperature $T_S \sim 3$K. Cooling with a dilution refrigerator is planed to achieve $T_S \sim 200\mu$K, which will be used to scan over masses with unprecedented sensitivity (ADMX-II). The first two cavity harmonics will be scanned in parallel, masses $2-9\mu$eV. R&D is taking place at Yale U. to produce haloscopes sensitive at higher masses (to cover the Scenario-I, see fig. 1 left hand panel) using superconducting hybrid cavities and Josephson parametric amplifiers working below the quantum limit (ADMX-HF). A first setup will take data in the 4-8 GHz range ($17-33\mu$eV) and new designs are being pushed with the ambition to cover up to 20 GHz. These prospects are shown in figs. 1 & 2 as green regions, IAXO is elaborated in the next section.

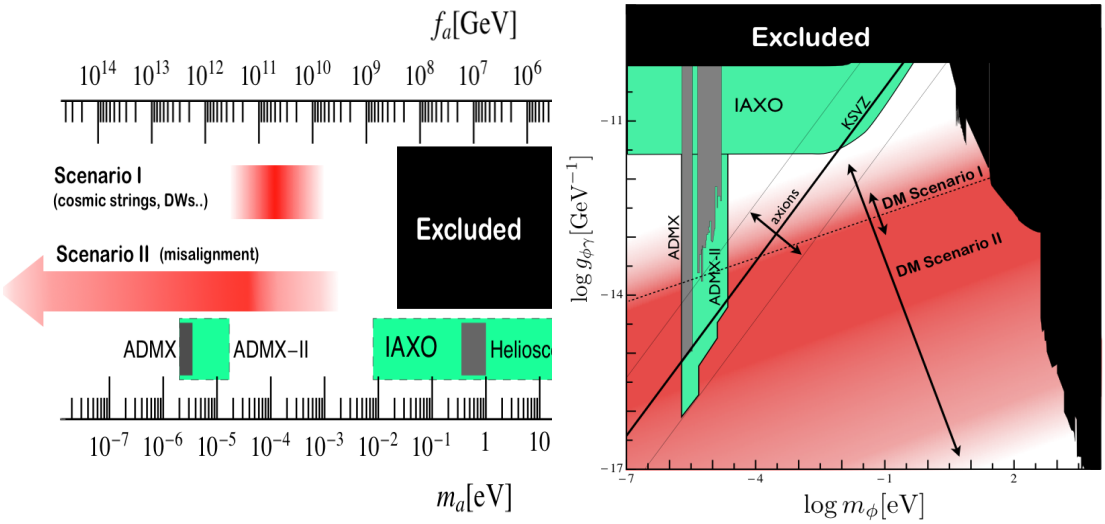

Figure 1: Parameter space for axions (left), ALPs (right) where they can account for the cold DM of the Universe together with excluded regions and the forecasts of ADMX and IAXO [19].

3 New experiments

Listening at the workshop to the future plans of ADMX, it was quickly realized that rather than competing with ADMX in the 2-10 μeV mass range search for axions, the community would benefit of complementing it at different mass ranges and developing new approaches such as the dish-antenna experiment. First efforts in the first direction have started with WISPDMX [20], a cavity experiment [16] based on a HERA proton accelerator cavity. Two modes at 208 and 437.3 MHz ($\sim$ 0.9 and 1.8 μeV mass) will be recorded simultaneously with a tunning range $\sim$ 2% provided by 5 plungers. A HP run is foreseen next year and magnet options for an

axion(ALP) search at DESY or CERN were discussed. At the latter facility, the considerable experience in microwave light-shining through a wall setups [21] could be used to boost the sensitivity and tuning range.

An exciting opportunity to look for WISP DM could also arise with IAXO, see [19]. IAXO's main purpose is detecting the solar axion flux, but the required toroidal magnet could host one or several long-cavity experiments or dish-antenna searches. The intense B-field (up to 5 T), the gigantic volume (8 cylindrical bores 20 m long and 0.6 m diameter) and the already implemented cryogenics are very desirable for DM searches. A long rectangular cavity (up to 20 m long and 0.42 m wide) can be fit into one bore and scan masses above 1.5 μeV in the spirit of ref. [3]. Tuning strategies are under discussion. As a pathfinder experiment, it was proposed to install such a wave-guide in the HERA dipole used by the ALPS experiment for its light-shining-through walls experiment[1], aiming at higher masses ($\sim$ 20 μeV). Such an experiment is under discussion. Among the workshop participants, expertise in cavity construction, tuning, operation and signal detection was quickly put forward.

A good amendment to the cavity option could be a broadband dish search [6], see also the next section. A good deal of the workshop addressed the possible detector options for this undertaking.

4 A little workshop aftermath

In addition to WISPDMX at DESY, a small collaboration has formed from workshop participants to realize the first dish-antenna experiment searching for HP (and eventually ALP) DM. It will be a proof-of principle experiment: quick and cheap but having still an acceptable reach in the WISP Dark Matter parameter space. For this goal, we have successfully applied for additional support from the Helmholtz Alliance for Astroparticle Physics.

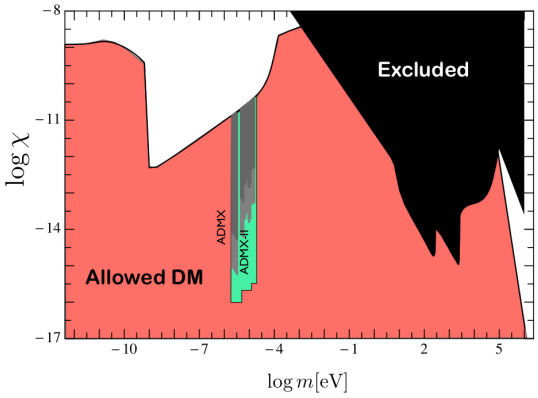

Figure 2: Parameter space for HPs where they can account for the cold DM of the Universe. Also shown are excluded regions and the forecasts of ADMX and IAXO.

The most promising range for such a setup is the mm-wavelength regime (meV mass). The unexplored allowed parameter range for HP DM starts at rather large couplings $\chi \sim 10^{-9}$ whilst for the ALP DM, available detector sensitivities are promising to tackle viable parameter range. However, good detectors in the millimeter range are costly and less sensitive than in the optical regime. Due to this fact, and due to the fact that the collaborators of this project are highly experienced in optical techniques, the dish/mirror Dark Matter search will be performed in the optical regime. With available equipment, eV photons down to $\chi \sim 10^{-12}$ should be accessible.

[1]For the HERA magnet at the magnet test-bench, the cavity option would profit from the fact that the beam-pipe was straightened for the future second ALPS setup [22].

For the search for ALPs, the mirror setup will be embedded in a magnetic field. The unprobed parameter range for ALPs in the optical regime is even harder to tackle than for HPs. However, running the envisaged setup also in a magnet environment (superconducting solenoids with large bore are in principle available at DESY) will yield insight in the experimental complications arising from this demand and eventually pave the way for a dedicated ALP DM search in the mm-wavelength regime.

In summary, there are many experimental options available to check the sub-eV range for Dark Matter – we look forward to see more such options realized and to eventual findings that could solve the Dark Matter puzzle.

5 Acknowledgments

The authors acknowledge the Helmholtz Alliance for Astroparticle Physics for funding the light-move workshop and all participants and co-organizers for contributing their ideas. We also thank the organizers of Patras 2013 for a stimulating workshop. JR acknowledges support from the Alexander von Humboldt Foundation and by the European Union through the Initial Training Network "Invisibles".

References

[1] J. Jaeckel and A. Ringwald, Ann. Rev. Nucl. Part. Sci. **60** (2010) 405 [arXiv:1002.0329 [hep-ph]].

[2] P. Arias, D. Cadamuro, M. Goodsell, J. Jaeckel, J. Redondo and A. Ringwald, JCAP **1206** (2012) 013 .

[3] O. Baker, M. Betz, F. Caspers, J. Jaeckel, A. Lindner, A. Ringwald *et al*, Phys. Rev. D **85** (2012) 035018.

[4] P. W. Graham and S. Rajendran, Phys. Rev. D **88** (2013) 035023.

[5] D. Budker, P. W. Graham, M. Ledbetter, S. Rajendran and A. Sushkov, arXiv:1306.6089 [hep-ph].

[6] D. Horns *et al*, JCAP **1304**, 016 (2013) [arXiv:1212.2970].

[7] J. Jaeckel and J. Redondo, arXiv:1308.1103 [hep-ph] and arXiv:1307.7181 [hep-ph].

[8] `https://indico.desy.de/conferenceDisplay.py?confId=7975`

[9] A. Ringwald, Phys. Dark Univ. **1** (2012) 116 [arXiv:1210.5081 [hep-ph]].

[10] J. Jaeckel, Frascati Phys. Ser. **56** (2012) 172 [arXiv:1303.1821 [hep-ph]].

[11] D. Cadamuro and J. Redondo, JCAP **1202** (2012) 032 [arXiv:1110.2895 [hep-ph]].

[12] S. Folkerts, C. Germani and J. Redondo, arXiv:1304.7270 [hep-ph].

[13] O. Erken, P. Sikivie, H. Tam and Q. Yang, Phys. Rev. D **85** (2012) 063520 [arXiv:1111.1157 [astro-ph.CO]].

[14] P. Sikivie, Phys. Lett. B **695** (2011) 22 [arXiv:1003.2426 [astro-ph.GA]].

[15] N. Banik and P. Sikivie, arXiv:1307.3547 [astro-ph.GA].

[16] R. Bradley *et al*, Rev. Mod. Phys. **75**, 777 (2003).

[17] S. J. Asztalos *et al.* [ADMX Collaboration], Phys. Rev. Lett. **104**, 041301 (2010)

[18] P. Sikivie, Phys. Rev. Lett. **51** (1983) 1415 [Erratum-ibid. **52** (1984) 695].

[19] IAXO LOI `http://cds.cern.ch/record/1567109` & I. G. Irastorza *et al.* J. Phys. Conf. Ser. **460**, 012002.

[20] D. Horns, A. Lindner, A. Lobanov and A. Ringwald, arXiv:1309.4170 [physics.ins-det].

[21] M. Betz, F. Caspers, M. Gasior and M. Thumm, arXiv:1309.7373 [physics.ins-det].

[22] R. Bähre *et al.* JINST **8**, T09001 (2013) [arXiv:1302.5647 [physics.ins-det]].

Search for Axionic Dark Matter

D.B. Tanner, for the ADMX collaboration

Department of Physics, University of Florida, Gainesville, FL 32611, USA

DOI: http://dx.doi.org/10.3204/DESY-PROC-2013-04/tanner_david

The Axion Dark Matter eXperiment (ADMX) searches for axions as part of the halo of our galaxy. These axions have a mass in the range 1–10 μeV and convert to photons in a microwave cavity permeated by a strong magnetic field. ADMX recently incorporated low-noise SQUID amplifiers into the experiment and at present is being upgraded with a dilution refrigerator, permitting operation with noise temperatures of 100–200 mK.

Our understanding of the energy and matter composition of the universe has undergone a revolution in recent years.[1–3] The picture has evolved from a universe dominated by protons, neutrons, and electrons to one where dark matter and dark energy dominate the mass-energy budget. The dark matter is convincingly constrained to be non-baryonic and cold. There are three widely discussed candidates for the dark matter: sterile neutrinos, weakly interacting massive particles (WIMPs), and axions. This paper describes the results and plans for a search for axions: the Axion Dark-Matter eXperiment (ADMX).

A discovery of the axion, or placing unambiguous limits on its existence, would have profound implications for the dark matter problem. Either result would also impact a second important problem in contemporary physics: the origin of parity P and the product of charge conjugation with parity CP symmetry in the strong interactions.[4, 5] The axion is thus motivated by and has the potential to solve two rather important issues in particle physics and astrophysics. Moreover, the fact that the LHC has not produced evidence for supersymmetric particles[6] makes the case for WIMP dark matter more difficult to muster.[7] In contrast, the case for axions remains as strong as ever.[8, 9] The most plausible mass for the axion is in the 1-1000 μeV range. At the low end of this window axions provide the dark matter.[10–14]

ADMX searches for axions that constitute the dark-matter halo of our galaxy. Many observations imply the existence of large halos of non-luminous matter surrounding galaxies.[15, 16] ADMX exploits the fact that axions may be stimulated to convert into microwave photons in a high Q cavity permeated by a large magnetic field. This detection method was proposed thirty years ago[17] and was developed during pilot experiments [18, 19] ADMX was initially located at the Lawrence Livermore National Laboratory (LLNL) but recently relocated to the University of Washington, Seattle. This axion detector,[8, 20, 21] which improved the sensitivity over the pilot detectors by at least a factor of 400, consists of a large superconducting magnet containing one or more microwave cavities. Axions which overlap the high-field region will be stimulated to decay into microwave photons when the resonant frequency of the cavity equals the mass of the axion. An ultra-sensitive microwave receiver, using superconducting electronics in its front end,[21] amplifies the cavity signal to a point where spectral analysis can search for signatures of axion–photon emission. Over the past few years, the detector has scanned the 1.9–3.6 μeV axion mass range with a sensitivity capable of a detection if the axion-photon coupling is near the upper end of theoretical predictions.

In 2003, the DOE approved Phase I of an upgrade to ADMX to give an additional improvement to the sensitivity: incorporation of SQUID amplifiers into the front end of the receiver. This upgrade is based on a remarkable breakthrough in making DC SQUIDs operate as high-gain, low-noise amplifiers up to GHz frequencies.[22] Phase I retrofitted the experiment to operate with SQUID amplifiers at a physical temperature of $T \sim 1.5$ K. In this case the system background temperature is dominated by the physical temperature, $T_s \sim 2$ K. The Phase I construction and commissioning ended in 2008 and was followed by a year-long science data run using the SQUID amplifiers.[23]

Phase II has recently begun as a second-generation dark matter detector. Our incremental approach will continue with the installation of a ^{3}He refrigerator (to cool to 400 mK) and a science run at a sensitivity required to detect weakly-coupled axions. Next, a high-circulation-rate dilution refrigerator will be added to the detector, reducing the physical temperature to $T \sim 100$ mK. The system noise temperature is then expected to be below 200 mK. The upgrade will improve system noise performance to such an extent that ADMX will be sensitive to—or be able to rule out—axions as a component of the halo of our galaxy with *all* plausible coupling strengths over the same mass range as the original detector ($\sim 1 - -10$ μeV) and at the same time to be able to scan the mass range 2–3 times more rapidly than in the past.

The axion arises in particle theory from a mechanism introduced by Peccei and Quinn (PQ)[4] to ensure that the strong interactions conserve P and CP in spite of the fact that the standard model as a whole violates those symmetries. No violation has been observed; the upper limit on the neutron electric dipole moment requires fine tuning to 1 part in 10^9, resulting in the "strong CP problem." The light, pseudo-scalar particle which necessarily results from the PQ mechanism is the axion.[5] Particle theory leaves the value of the axion mass, m_a, arbitrary. All of the couplings of the axion are proportional to m_a, so that a very light axion is also very weakly coupled to other particles and fields.[24, 25] However, astrophysical/cosmological considerations and laboratory searches do constrain these quantities. The constraints from SN1987a[13] and from searches for the axion in high-energy and nuclear physics experiments[26] rule out $m_a > 10^{-2}$ eV. In addition, cosmology places a *lower limit* on m_a of order 10^{-6} eV by requiring that axions do not overclose the universe.[10–12]

Axions are non-relativistic from the moment of their production during the QCD phase transition, making them cold dark matter (CDM). Studies of the cosmic microwave background anisotropy and of large-scale structure formation strongly imply that the dominant fraction of the energy density of the universe is in cold dark matter. There is good reason to believe also that CDM (either axions or WIMPs) is the constituent matter of galactic halos.[27]

There are large uncertainties in the relationship between Ω_a and m_a. Assuming standard concordance cosmology and that inflation happens before the PQ phase transition, the most likely value of the axion mass for which $\Omega_a = 0.23$ is 1.5×10^{-5} eV. This estimate includes the contributions from vacuum realignment, string decay, and wall decay. If inflation happens after the PQ phase transition, the most likely value of the axion mass for which $\Omega_a = 0.23$ is $m_a \sim 3 \times 10^{-6}$ eV. In this case there is no contribution from string or wall decay, but only a vacuum realignment contribution.

Superstring theories generally predict the existence of axion-like particles, one of which would be the QCD axion discussed here. Many superstring theories prefer lighter axions, in the neV range or smaller, although Witten and Svrcek[28] have shown that in some superstring theories the axion mass can be larger than this.

A number of years ago, Ipser and Sikivie[29] discussed the extent to which the phase-space distribution of cold dark matter particles is thermalized in a galactic halo and concluded that

many dark matter particles are in distinct flows, with each of these flows producing a peak in the local velocity distribution. Figure 1 shows a cartoon of infalling dark matter. The cold dark matter particles fall from the surrounding space into the galaxy. Those falling into the galaxy for the first time reach the detector with a specific velocity vector and give a narrow peak in the detector response. Other peaks that would be observed are due to particles falling out of the galaxy for the first time, particles falling into the galaxy for the second time, etc. The peaks due to particles that have fallen in and out of the galaxy a large number of times in the past are washed out because of scattering in the gravitational wells of stars, globular clusters and large molecular clouds. But the peaks due to particles which have fallen in and out of the galaxy only a small number of times in the past are not washed out.

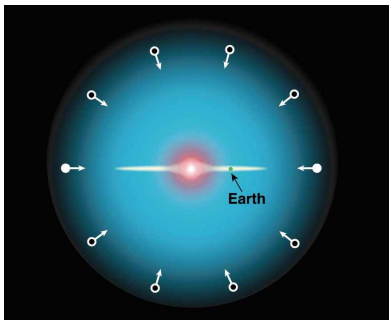

Figure 1: Infall of dark matter into the galaxy. Particles falling in for the first time arrive at the Earth with a well-defined velocity.

If the fraction of the local dark matter density which is in these velocity peaks is sufficiently large, a direct dark matter search may be made more sensitive by having it look specifically for sharp peaks in the energy spectrum. Moreover, it has been pointed out[30] that one or more peaks may be further enhanced because the sun lies close to a caustic ring in the dark matter distribution. In a fit[31] of caustic rings to the galactic rotation curve, it is found that the local density is dominated by a single flow, called the "Big Flow." ADMX has incorporated a high-resolution spectrometer to search for such fine structure in the energy spectrum of axion dark matter.

It was shown recently[32] that cold dark-matter axions must form a Bose-Einstein condensate as a result of their gravitational self-interactions when the photon temperature is of order 500 eV. This result has produced an argument that at least part of the dark matter is axions. The argument has three steps. First, axions behave differently from other dark-matter candidates because a rethermalizing axion BEC tracks the lowest-energy available state. Second, there is a tool to distinguish a BEC from other forms of dark matter on the band of observation, namely the study of the axion caustics of galactic halos. Third, the observational evidence for caustic rings of dark matter is consistent in every aspect with axion BEC, but not with other forms of dark matter.[33]

The ADMX detector is meter-scale cylindrical electromagnetic cavity permeated by a ~ 8 T static magnetic field $\vec{B}_0$. On resonance halo axions can convert to quanta of excitation (photons) of that cavity mode. Only the $\mathrm{TM}_{n\ell 0}$ modes couple in the limit where the cavity is much smaller than the de Broglie wavelength. The signal is proportional to g_γ, the coupling strength of the axion to two photons. The value $g_\gamma = 0.36$ is predicted by the Dine-Fischler-Srednicki-

Zhitnitskii (DFSZ) model.[24] In all other models that have been put forth, the magnitude of g_γ is predicted to be larger than 0.36. For example, $g_\gamma = -0.97$ in the Kim-Shifman-Vainshtein-Zakharov (KSVZ) model.[25]

Modes that can be used for the search are those with form factors $C_{n\ell 0} \neq 0$, those for which the integral of $\vec{E} \cdot \vec{B}_0$ is finite. $C_{n\ell 0}$ is 0.69 for the lowest (TM_{010}) mode and 0.12 for the next (TM_{020}) mode. This decrease in form factor is partially offset by the higher power emitted at the 2.3× higher frequency of the TM_{020} mode, making the ratio of signal powers $P_{020}/P_{010} = 0.41$.

The signal to noise ratio (and search rate) is determined by a thermal and technical background, described by T_n, the sum of the physical temperature of the cavity plus the excess-noise temperature of the microwave receiver. The search rate goes $1/T_n^2$ and both background and technical noise are found[21, 23] to be linear in the physical temperature T, with $T_n \approx 2T$.

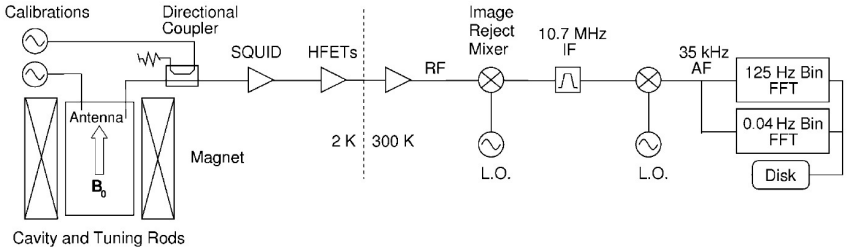

Figure 2: Schematic diagram of the axion detector.

The Axion Dark-Matter eXperiment (ADMX) experiment[20] has placed meaningful limits on axion couplings and densities.[34–39] Figure 2 is a schematic diagram of the axion detector in its present configuration.[21, 23] The magnet is a superconducting solenoid with 7.6 T central field. The cylindrical cavity (50 cm diameter, 100 cm length) has a resonant frequency tunable over 460–860 MHz. The cavity is tuned by moving metallic tuning rods, which run the full length of the cavity, between the wall and center. Initially, the first-stage preamplifiers in the receiver were balanced GaAs high electron mobility transistor (HEMT) with noise temperature $T_n \sim 2.5$ K. These have been replaced by SQUID amplifiers in the phase I upgrade of the experiment.

The preamplifiers are followed by additional amplification, after which the signal is converted to the 10.7 MHz intermediate frequency by an image-rejection mixer. An 8-pole crystal filter sets the 30 kHz measurement bandwidth and prevents image power from entering the second mixing stage. The signal is then mixed down a second time, in effect shifting the cavity resonant frequency to 35 kHz. A commercial FFT spectrum analyzer then generates the "medium-resolution" power spectrum, an average of 10^4 spectra at 125 Hz resolution. This resolution is well-matched to a search for the Maxwellian component of the halo, which should be about 6 channels wide.

The analog signal is also processed by a second "high resolution" data analysis channel. There is no averaging; instead, a commercial ADC/DSP PC board acquires and computes one 2,500,000 point, 0.04 Hz/point power spectrum. The resolution is well matched to a search for fine structure having fractional width $\sim 0(10^{-11})$ or less in the power spectrum.

The Phase I upgrade installed superconducting quantum interference device (SQUID) amplifiers[22] as the front end of the receiver. Phase I construction and commissioning took place

over 2004–2007, with first cooldown of the insert in fall 2007 and completion of commissioning in early 2008. The Phase I data run scanned the 3.3–3.5 μeV range.[23] It demonstrated that SQUID amplifiers can be produced which (with proper magnetic shielding) function in the high magnetic field environment of the experiment. In addition, the amplifiers can be coupled to the axion cavity, provide adequate gain so that the system noise is the physical noise from the cavity in series with the modest noise from the amplifiers themselves, and can deliver the signal to an automated data acquisition system.

Phase II has recently begun. It will upgrade the cryogenics with (first) a ^{3}He refrigerator (reducing the physical temperature to $\sim$ 400 mK) and then with a dilution refrigerator, (reaching $\sim$ 100 mK). We expect total background (system) noise temperatures to be 50–100% higher than the physical temperature. In addition to reducing the physical and noise temperatures, Phase II will add a receiver second channel to search the TM_{020} in parallel with the TM_{010} mode. Both modes tune in a similar way as the tuning rods are moved. Using metal tuning rods, the collaboration estimates that we will be able to search for axions in the 1.7–3.7 μeV (400–900 MHz) using the TM_{010} mode while *at the same time* scanning 3.7–8.7 μeV (900–2100 MHz) with the TM_{020} mode. The higher frequency search is expected to exceed the sensitivity required to detect DFSZ axions[24] by a small amount; the lower frequency search will exceed this limit by nearly an order of magnitude.

Figure 3 shows the axion couplings and masses excluded at the 90% confidence level by ADMX at the end of the Phase I data run.[23] The inset shows the results of earlier experiments.[34–37] The plot in the right panel shows the axion-to-photon coupling $g_{a\gamma\gamma}$ as a function of the axion mass $m_a = hf/c^2$. ADMX is the first experiment to exclude a realistic axion model: KSVZ axions of mass between 1.9 and 3.55 μeV. If a significant fraction of halo axions are distributed in a few narrow peaks, weaker axion two-photon couplings are excluded.[38–40] (left panel).

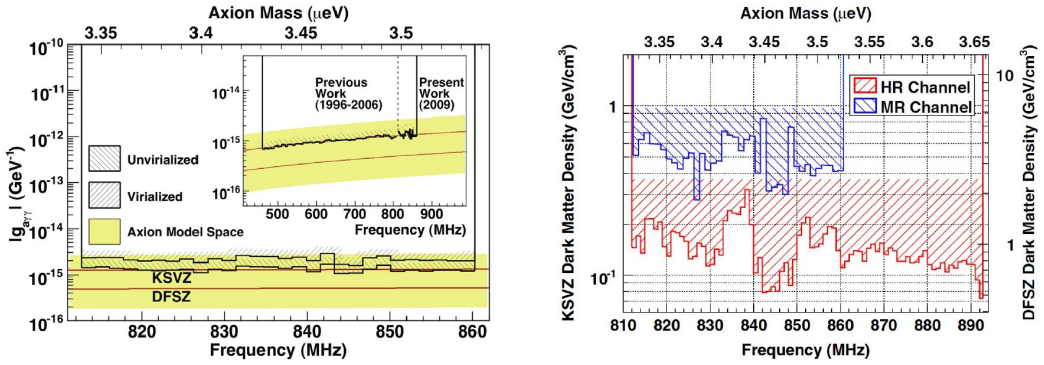

(a) (b)

Figure 3: a) Axion couplings and masses excluded at the 90% confidence level by the experiment. The R.F. frequency range is 460–860 MHz. (b) Axion density limits for axions with velocity dispersion less than $3 \times 10^{-6}c$ from 812 MHz to 892.8 MHz. The scale for predictions of the KSVZ and DFSZ models are shown on the left and right axes, respectively. The limit is below the KSVZ prediction. Density limits for the medium resolution channel (for axions with velocity dispersion less than $2 \times 10^{-4}c$) are also shown.

References

[1] S. Perlmutter *et al.*, Astrophys. J. **517**, 565 (1999).

[2] A.G. Riess *et al.*, Astron. J. **116**, 1009 (1998).

[3] E. Komatsu *et al.*, ApJS **192**, 18 (2011).

[4] R.D. Peccei and H. Quinn, Phys. Rev. Lett. **38**, 1440 (1977) and Phys. Rev. D **16**, 1791 (1977).

[5] S. Weinberg, Phys. Rev. Lett. **40**, 223 (1978); F. Wilczek, Phys. Rev. Lett. **40**, 279 (1978).

[6] G. Aad *et al.*(ATLAS Collaboration), Phys. Rev. Lett. **106**, 131802 (2011); S. Chatrchyan *et al.*(CMS Collaboration), Phys. Rev. Lett. **106**, 211802 (2011); S. Chatrchyan *et al.*(CMS Collaboration), Phys. Rev. Lett. **107**, 201804 (2011); G. Aad *et al.*(ATLAS Collaboration), Phys. Rev. Lett. **108**, 261804 (2012) (2012); S. A. Malik (for the CMS Collaboration), http://arXiv.org/abs/1206.0753 (2012); S. Lowette (for the ATLAS and CMS Collaborations), http://arXiv.org/abs/1205.4053 (2012).

[7] Alexander Merle and Tommy Ohlsson, Nat. Phys. **8**, 584 (2012).

[8] Richard Bradley *et al.*, Rev. Mod. Phys. **75**, 777 (2003).

[9] Jihn E. Kim and Gianpaolo Carosi, Rev. Mod. Phys. **82**, 557 (2010).

[10] L. Abbott and P. Sikivie, Phys. Lett. B**120**, 133 (1983).

[11] J. Preskill, M. Wise and F. Wilczek, Phys. Lett. B **120**, 127 (1983).

[12] M. Dine and W. Fischler, Phys. Lett. B **120**, 137 (1983).

[13] M.S. Turner, Phys. Rep. **197**, 67 (1990); G.G. Raffelt, Phys. Rep. **198**, 1 (1990).

[14] C. Amsler *et al.*, (Particle Data Group), Phys. Lett. B **667**, 1 (2008).

[15] K.G. Begeman *et al.*, Mon. Not. R. Astron. Soc. **249**, 523–537 (1991).

[16] D. Clowe *et al.*, Astrophys. J. **648**, L109 (2006).

[17] P. Sikivie, Phys. Rev. Lett. **51**, 1415 (1983).

[18] S. DePanfilis *et al.*, Phys. Rev. Lett. **59**, 839 (1987); W.U. Wuensch *et al.*, Phys. Rev. D **40**, 3153 (1989).

[19] C. Hagmann *et al.*, Phys. Rev. D **42**, 1297 (1990).

[20] H. Peng *et al.*, Nucl. Instrum. Methods A **444**, 569–583 (2000).

[21] S.J. Asztalos *et al.*, Nucl. Instrum. Methods A **656**, 39 (2011).

[22] M. Mück *et al.*, Appl. Phys. Lett. **72**, 2885 (1998); Appl. Phys. Lett. **75**, 3545 (1999); Appl. Phys. Lett. **75**, 698 (1999)

[23] S.J. Asztalos *et al.*, Phys. Rev. Lett. **104**, 041301/1–4 (2010).

[24] A. R. Zhitnitsky, Sov. J. Nucl. Phys. 31, 260, 1980; M. Dine, W. Fischler and M. Sredmicki, Phys. Lett. B **104**, 199 (1981).

[25] J.E. Kim, Phys. Rev. Lett. **43**, 103 (1979).; M.A. Shifman, A.I . Vainshtein and V.I. Zakharov, Nucl. Phys. B **166**, 493 (1980).

[26] For a review, see: J.E. Kim, Phys. Rep. **150**, 1 (1987); H.-Y. Cheng, Phys. Rep. **158**, 1 (1988); R.D. Peccei, in *CP-Violation*, edited by C. Jarlskog (World Scientific, 1989).

[27] J. Ipser and P. Sikivie, Phys. Rev. Lett. **50**, 925 (1983).

[28] See E. Witten's talk at Superstrings 2005: `http://www.fields.utoronto.ca/audio/05-06/strings/witten/`.

[29] P. Sikivie and J. Ipser, Phys. Lett. B **291**, 288 (1992).

[30] P. Sikivie, Phys. Lett. B **432**, 139 (1998).

[31] P. Sikivie, Phys. Lett. B **567**, 1 (2003).

[32] P. Sikivie and Q. Yang, Phys. Rev. Lett. **103**, 111301 (2009).

[33] P. Sikive, Phys. Lett. B **695**, 22 (2011).

[34] C.A. Hagmann *et al.*, **80**, 2043, (1998).

[35] S. Asztalos *et al.*, Phys. Rev. D **64**, 092003 (2001).

[36] S.J. Asztalos *et al.*, Astrophys. Jour. Lett. **571**, L27-L30 (2002).

[37] S.J. Asztalos *et al.*, Phys. Rev. D **69**, 011 101(R) (2004).

[38] L. Duffy *et al.*, Phys. Rev. Lett. **95**, 091304 (2005).

[39] L.D. Duffy *et al.*, Phys. Rev. D **74**, 012006 (2006).

[40] J. Hoskins *et al.*, Phys. Rev. D **84**, 121302(R) (2011).

Chapter 6

Dark Matter WIMPs

Results from DAMA/LIBRA and perspectives

R. Bernabei[1], *P. Belli*[1], *F. Cappella*[2], *V. Caracciolo*[3], *S. Castellano*[3], *R. Cerulli*[3], *C.J. Dai*[4], *A. d'Angelo*[2], *S. d'Angelo*[1], *A. Di Marco*[1], *H.L. He*[4], *A. Incicchitti*[2], *X.H. Ma*[4], *F. Montecchia*[1,5], *X.D. Sheng*[4], *R.G. Wang*[4], *Z.P. Ye*[4,6]

[1]Dip. di Fisica, Univ. "Tor Vergata" and INFN-Roma "Tor Vergata", I-00133 Rome, Italy
[2]Dip. di Fisica, Univ. di Roma "La Sapienza", and INFN-Roma, I-00185 Rome, Italy
[3]Laboratori Nazionali del Gran Sasso, I.N.F.N., Assergi, Italy
[4]IHEP, Chinese Academy, P.O. Box 918/3, Beijing 100039, China
[5]Dip. di Ingegneria Civile e Ingegneria Informatica, Univ. "Tor Vergata", I-00133 Rome, Italy
[6]University of Jing Gangshan, Jiangxi, China

DOI: http://dx.doi.org/10.3204/DESY-PROC-2013-04/cerulli_riccardo

The DAMA/LIBRA experiment (about 250 kg of highly radiopure NaI(Tl)) is in operation at the Gran Sasso National Laboratory of the INFN. The main aim of the experiment is to further investigate the Dark Matter (DM) particles in the Galactic halo by exploiting the model independent DM annual modulation signature. At the time of this Workshop, the DAMA/LIBRA experiment and the former DAMA/NaI one (the first generation experiment having an exposed mass of about 100 kg) have released results corresponding to a total exposure of 1.17 ton $\times$ yr over 13 annual cycles; they have provided a model independent evidence of the presence of DM particles in the galactic halo at 8.9 σ C.L.. The results of a further annual cycle, concluding the DAMA/LIBRA–phase1, have been released after this Workshop and are not included here. After the upgrade at fall 2010 when all the PMTs have been replaced with new ones having higher quantum efficiency, the feasibility to decrease the software energy threshold has been demonstrated and the set-up is running in this new configuration, named DAMA/LIBRA–phase2.

1 The DAMA/LIBRA results

The DAMA project develops and uses low background scintillators. It consists of the following experimental set-ups: i) DAMA/NaI ($\simeq$ 100 kg of highly radiopure NaI(Tl)) that took data for 7 annual cycles and completed its data taking on July 2002 [1, 2, 3, 4, 5, 6]; ii) DAMA/LXe, $\simeq$ 6.5 kg liquid Kr-free Xenon enriched either in ^{129}Xe or in ^{136}Xe [7]; iii) DAMA/R&D, a facility dedicated to tests on prototypes and to perform experiments developing and using various kinds of low background crystal scintillators in order to investigate various rare processes [8]; iv) DAMA/Ge, where sample measurements and measurements dedicated to the investigation of several rare processes are carried out as well as in the LNGS STELLA facility [9]; v) DAMA/CRYS, a new small set-up to test prototype detectors; vi) the second generation DAMA/LIBRA set-up, $\simeq$ 250 kg highly radiopure NaI(Tl)) [10, 11, 12, 13, 14, 15, 16, 17, 18]. Many rare processes have also been studied with these set-ups obtaining competitive results.

In particular, the DAMA/LIBRA set-up is mainly investigating the presence of DM particles in the galactic halo by exploiting the model independent DM annual modulation signature,

originally suggested in [19]. As a consequence of the annual revolution of the Earth around the Sun, moving in the Galaxy, our planet should be crossed by a larger flux of DM particles around $\sim$ June 2^{nd} (when the Earth orbital velocity has the same versus of the Sun velocity with respect to the Galaxy) and by a smaller one around $\sim$ December 2^{nd} (when the two velocities are opposite). Thus, this signature depends on the composition of the Earth and Sun velocitites and it is not correlated with seasons. This DM annual modulation signature is very distinctive since the effect induced by DM particles must simultaneously satisfy all the following requirements: (1) the rate must contain a component modulated according to a cosine function; (2) with one year period; (3) with a phase that peaks roughly around $\sim$ June 2^{nd}; (4) modulation must be present only in a well-defined low energy range, where DM particles can induce signals; (5) it must be present only in those events where just a single detector, among all the available ones in the used set-up, actually "fires" (*single-hit* events), since the probability that DM particles experience multiple interactions is negligible; (6) the modulation amplitude in the region of maximal sensitivity has to be less about 7% in case of usually adopted halo distributions, but it may be significantly larger in case of some particular scenarios. No systematic effects or side reactions able to simultaneously fulfil all the mentioned requirements have been found or suggested by anyone over more than a decade. At present status of technology it is the only model independent signature which can effectively be exploited by direct Dark Matter investigation. The ULB NaI(Tl) are suitable detectors to investigate this signature thanks to its very good sensitivity to many DM candidates and interaction types.

The description and the performances of the DAMA/LIBRA set-up are given in Ref. [10], where the procedures followed in the data taking are also described.

The DAMA/LIBRA data released at time of this Workshop correspond to six annual cycles for an exposure of 0.87 ton$\times$yr [10, 11, 12]. Considering these data together with those previously collected by DAMA/NaI over 7 annual cycles (0.29 ton$\times$yr), the total exposure collected over 13 annual cycles is 1.17 ton$\times$yr; this is orders of magnitude larger than the exposures typically collected in the field.

Several independent analyses on the model-independent DM annual modulation signature have been performed [11, 12]. In particular, Fig. 1 shows the time behaviour of the experimental residual rates of the *single-hit* scintillation events collected by DAMA/NaI and by DAMA/LIBRA in the (2–6) keV energy interval [11, 12]. The superimposed curve is the cosinusoidal function: $A\cos\omega(t-t_0)$ with a period $T=\frac{2\pi}{\omega}=1$ yr, with a phase $t_0=152.5$ day (June 2^{nd}), and modulation amplitude, A, obtained by best fit over the 13 annual cycles. The hypothesis of absence of modulation in the data can be discarded [11, 12] and, when the period and the phase are released in the fit, values well compatible with those expected for a DM particle induced effect are obtained [12]. In particular, in the cumulative (2–6) keV energy interval one gets: $A=(0.0116\pm0.0013)$ cpd/kg/keV, $T=(0.999\pm0.002)$ yr and $t_0=(146\pm7)$ day. Thus, the analysis of the *single-hit* residual rate favours the presence of a modulated cosine-like behaviour with proper features at 8.9 σ C.L.[12].

The same data of Fig. 1 have also been investigated by a Fourier analysis, obtaining a clear peak corresponding to a period of 1 year [12, 13]; this analysis in other energy regions shows only aliasing peaks instead. It is worth noting that for this analysis the original formulas in Ref. [20] have been slightly modified in order to take into account for the different time binning and the residuals errors (see e.g. Ref. [13]). In particular, DAMA has always shown the power spectrum up to the Nyquist frequency of the given residuals, which is $\simeq 3$ y^{-1}. Only recently [13] the power spectrum above 3 y^{-1} (up to 22 y^{-1}) has been shown in order to demonstrate that – as expected – no significant peak is present above the Nyquist frequency.

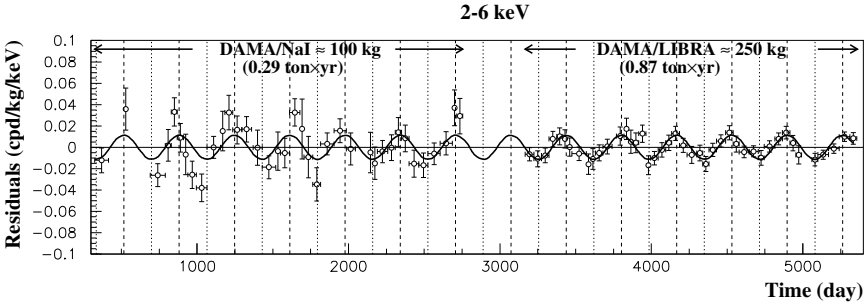

Figure 1: Experimental model-independent residual rate of the *single-hit* scintillation events, measured by DAMA/NaI over seven and by DAMA/LIBRA over six annual cycles in the (2 – 6) keV energy interval as a function of the time [5, 11, 12, 13]. The zero of the time scale is January 1^{st} of the first year of data taking. The experimental points present the errors as vertical bars and the associated time bin width as horizontal bars. The superimposed curve is $A\cos\omega(t-t_0)$ with period $T=\frac{2\pi}{\omega}=1$ yr, phase $t_0=152.5$ day (June 2^{nd}) and modulation amplitude, A, equal to the central value obtained by best fit over the whole data. The dashed vertical lines correspond to the maximum expected for the DM signal (June 2^{nd}), while the dotted vertical lines correspond to the minimum. See Ref. [11, 12, 13], references therein and text.

For completeness, we recall that long term modulation, with period higher than one year, has also been excluded by a different dedicated analysis reported e.g. in Refs. [13, 17].

In order to verify absence of annual modulation in other energy regions and, thus, to also verify the absence of any significant background modulation, the energy distribution in energy regions not of interest for DM detection has also been investigated. This has allowed the exclusion of a background modulation in the whole energy spectrum at a level much lower than the effect found in the lowest energy region for the *single-hit* scintillation events [12, 13].

A further relevant investigation has been performed by applying to the *multiple-hits* scintillation events (in which more than one detector "fires") the same hardware and software procedures used to acquire and to analyse the *single-hit* residual rate. In fact, since the probability that a DM particle interacts in more than one detector is negligible, a DM signal can be present just in the *single-hit* residual rate. Thus, this allows the study of the background behaviour in the same energy interval of the observed positive effect. A clear modulation is present in the *single-hit* scintillation events, while the fitted modulation amplitudes for the *multiple-hits* residual rate are well compatible with zero [12]. Similar results were previously obtained also for the DAMA/NaI case [5].

The annual modulation present at low energy has also been analyzed by depicting the differential modulation amplitudes, S_m, as a function of the energy [12]; in this case a maximum likelihood of the *single-hit* scintillation events is carried out considering $T=1$ yr and $t_0=152.5$ day. The measured S_m values as function of the energy are given in Fig. 2.

It can be inferred that a positive signal is present in the (2–6) keV energy interval, while S_m values compatible with zero are present just above. It has also been verified that the measured modulation amplitudes are statistically well distributed in all the crystals, in all the annual cycles and energy bins; these and other discussions can be found in Ref. [12, 13].

Many other analyses and discussions can be found in Refs. [11, 12, 13] and references therein. Both the data of DAMA/LIBRA and of DAMA/NaI fulfil all the requirements of the

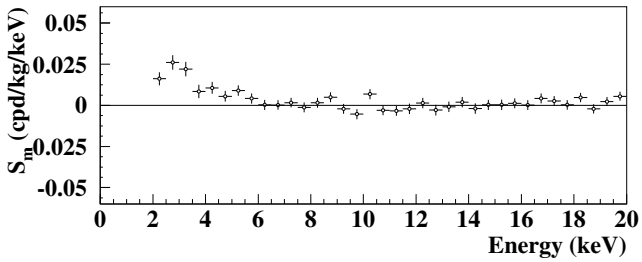

Figure 2: Energy distribution of the modulation amplitudes S_m for the total cumulative exposure 1.17 ton×yr. The energy bin is 0.5 keV. A clear modulation is present in the lowest energy region, while S_m values compatible with zero are present just above. In fact, the S_m values in the (6–20) keV energy interval have random fluctuations around zero with χ^2 equal to 27.5 for 28 degrees of freedom. See Ref. [11, 12, 13].

DM annual modulation signature.

Careful investigations on absence of any significant systematics or side reaction have been quantitatively carried out (see e.g. Ref. [5, 3, 10, 11, 12, 17, 13, 21, 22, 23, 24, 25, 26, 27], and references therein). No systematics or side reactions able to mimic the signature (that is, able to account for the measured modulation amplitude and simultaneously satisfy all the requirements of the signature) has been found or suggested by anyone over more than a decade.

In conclusion, the model-independent DAMA results have given evidence at 8.9 σ C.L. over 13 independent annual cycles for the presence of DM particles in the galactic halo.

The obtained DAMA model independent evidence is compatible with a wide set of scenarios regarding the nature of the DM candidate and related astrophysical, nuclear and particle Physics. For examples some given scenarios and parameters are discussed e.g. in Ref. [2, 3, 4, 5, 11, 13]. Further large literature is available on the topics (see for example in Ref [13]). Moreover, both the negative results and all the possible positive hints, achieved so-far in the field, are largely compatible with the DAMA model-independent DM annual modulation results in many scenarios considering also the existing experimental and theoretical uncertainties; the same holds for indirect approaches; see e.g. arguments in Ref. [13] and references therein.

We recall that a first upgrade of the DAMA/LIBRA set-up was performed in September 2008 when a broken PMT was replaced and a new DAQ with optical read-out and new Digitizers were also installed. The DAMA/LIBRA–phase1 concluded its data taking in this configuration on 2010; the results of the last (seventh) annual cycle of this phase1 have been released after this Workshop [28]. A further and more important upgrade has been performed at the end of 2010 when all the PMTs have been replaced with new ones having higher quantum efficiency; details on the developments and on the reached performances in the operative conditions are reported in Ref. [18]. Since then, the DAMA/LIBRA–phase2 is continuously running in order: (1) to increase the experimental sensitivity lowering the software energy threshold of the experiment; (2) to improve the corollary investigations on the nature of the DM particle and related astrophysical, nuclear and particle physics arguments; (3) to investigate other signal features. This requires long and heavy full time dedicated work for reliable collection and analysis of very large exposures, as DAMA collaboration has always done. Another upgrade at the end of 2012 was successfully concluded, while further improvements are planned. In the future DAMA/LIBRA will also continue its study on several other rare processes [14, 15, 16] as also the former DAMA/NaI apparatus also did [6].

References

[1] R. Bernabei et al., Il Nuovo Cim. A 112, 545 (1999).

[2] R. Bernabei et al., Phys. Lett. B 389, 757 (1996); Phys. Lett. B 424, 195 (1998); Phys. Lett. B 450, 448 (1999); Phys. Rev. D 61, 023512 (2000); Phys. Lett. B 480, 23 (2000); Phys. Lett. B 509, 197 (2001); Eur. Phys. J. C 23, 61 (2002); Phys. Rev. D 66, 043503 (2002); Int. J. Mod. Phys. A 21, 1445 (2006); Int. J. Mod. Phys. A 22, 3155 (2007); Eur. Phys. J. C 53, 205 (2008); Phys. Rev. D 77, 023506 (2008); Mod. Phys. Lett. A 23, 2125 (2008).

[3] R. Bernabei et al., Eur. Phys. J. C 18, 283 (2000).

[4] R. Bernabei et al., Eur. Phys. J. C 47, 263 (2006).

[5] R. Bernabei et al., La Rivista del Nuovo Cimento 26, n.1, 1 (2003); Int. J. Mod. Phys. D 13, 2127 (2004).

[6] See in the publication list in: http://people.roma2.infn.it/dama

[7] P. Belli et al., Astropart. Phys. 5, 217 (1996); Nuovo Cim. C 19, 537 (1996); Phys. Lett. B 387, 222 (1996); Phys. Lett. B 389, 783 (err.) (1996); R. Bernabei et al., Phys. Lett. B 436, 379 (1998); P. Belli et al., Phys. Lett. B 465, 315 (1999); Phys. Rev. D 61, 117301 (2000); R. Bernabei et al., New J. of Phys. 2, 15.1 (2000); Phys. Lett. B 493, 12 (2000); Nucl. Instr. Meth. A 482, 728 (2000); Eur. Phys. J. direct C 11, 1 (2001); Phys. Lett. B 527, 182 (2002); Phys. Lett. B 546, 23 (2002); Beyond the Desert 2003 (Berlin Springer), 365 (2003); Eur. Phys. J. A 27, s01 35 (2006).

[8] R. Bernabei et al., Astropart. Phys. 7, 73 (1997); Nuovo Cim. A 110, 189 (1997); P. Belli et al., Astropart. Phys. 10, 115 (1999); Nucl. Phys. B 563, 97 (1999); R. Bernabei et al., Nucl. Phys. A 705, 29 (2002); P. Belli et al., Nucl. Instr. Meth. A 498, 352 (2003); R. Cerulli et al., Nucl. Instr. Meth. A 525, 535 (2004); R. Bernabei et al., Nucl. Instr. Meth. A 555, 270 (2005); Ukr. J. Phys. 51, 1037 (2006); P. Belli et al., Nucl. Phys. A 789, 15 (2007); Phys. Rev. C 76, 064603 (2007); Phys. Lett. B 658, 193 (2008); Eur. Phys. J. A 36, 167 (2008); Nucl. Phys. A 826, 256 (2009); Nucl. Instr. Meth. A 615, 301 (2010); Nucl. Instr. Meth. A 626-627, 31 (2011); J. Phys. G: Nucl. Part. Phys. 38, 015103 (2011); J. Phys. G: Nucl. Part. Phys. 38, 015107 (2011); Phys. Rev. C 85, 044610 (2012); A.S. Barabash et al., J. Instr. 6, P08011 (2011).

[9] P. Belli et al., Nucl. Instr. Meth. A 572, 734 (2007); Nucl. Phys. A 806, 388 (2008); Nucl. Phys. A 824, 101 (2009); Proceed. of the Int. Conf. NPAE 2008 (ed. INR-Kiev, Kiev), p. 473 (2009); Eur. Phys. J. A 42, 171 (2009); Nucl. Phys. A 846, 143 (2010); Nucl. Phys. A 859, 126 (2011); Phys. Rev. C 83, 034603 (2011); Eur. Phys. J. A 47, 91 (2011); Nucl. Instr. Meth. A 670 (2012) 10; Phys. Lett. B 711 (2012) 41; Nucl. Instr. Meth. A 704 (2013) 40; Eur. Phys. J. A 49 (2013) 24; Phys. Rev. C 87 (2013) 034607.

[10] R. Bernabei et al., Nucl. Instr. Meth. A 592, 297 (2008).

[11] R. Bernabei et al., Eur. Phys. J. C 56, 333 (2008).

[12] R. Bernabei et al., Eur. Phys. J. C 67, 39 (2010).

[13] R. Bernabei et al., Int. J. Mod. Phys. A 28, 1330022 (2013).

[14] R. Bernabei et al., Eur. Phys. J. C 62, 327–332 (2009).

[15] R. Bernabei et al., Eur. Phys. J. C 72, 1920 (2012).

[16] R. Bernabei et al., Eur. Phys. J. A 49, 64 (2013).

[17] R. Bernabei et al., Eur. Phys. J. C 72, 2064 (2012).

[18] R. Bernabei et al., J. of Inst. 7, P03009 (2012).

[19] K.A. Drukier et al., Phys. Rev. D 33, 3495 (1986); K. Freese et al., Phys. Rev. D 37, 3388 (1988).

[20] J.D. Scargle, Ap.J. 263 (1982) 835; W.H. Press and G.B. Rybicki, Ap.J. 338 (1989) 277

[21] R. Bernabei et al., AIP Conf. Proceed. 1223 (2010) 50 [*arXiv:0912.0660*].

[22] R. Bernabei et al., J. Phys.: Conf. Ser. 203 (2010) 012040 [*arXiv:0912.4200*]; http://taup2009.lngs.infn.it/slides/jul3/nozzoli.pdf, talk given by F. Nozzoli.

[23] R. Bernabei et al., in the volume *Frontier Objects in Astrophysics and Particle Physics*, ed. S.I.F. (Vulcano, 2010), p. 157 [*arXiv:1007.0595*].

[24] R. Bernabei et al., Can. J. Phys. 89 (2011) 11.

[25] R. Bernabei et al., Physics Procedia 37 (2012) 1095.

[26] R. Bernabei et al., *arXiv:1210.6199*.

[27] R. Bernabei et al., *arXiv:1211.6346*.

[28] R. Bernabei et al., *arXiv:1308.5109*.

Annual modulation study of dark matter using CsI(Tl) crystals in KIMS experiment

J.H. Choi[1], *B.H. Kim*[1], *G.B. Kim*[1], *H.C. Bhang*[1], *H.J. Kim*[2], *H.S. Lee*[3], *I.S. Hahn*[3], *J.H. Lee*[1], *J.H. So*[2], *J.K. Lee*[1], *J. Li*[4], *J. Li*[1], *K.W. Kim*[1], *Q. Yue*[4], *S.C. Kim*[1], *S.H. Choi*[1], *S.K. Kim*[1], *S.L. Olsen*[1], *S.S. Myung*[1], *W.G. Kang*[5], *X.R. Li*[6], *Y.D. Kim*[5], *Y.J. Lie*[4]

[1]Seoul National University, Seoul, Korea
[2]Kyungpook National University, Daegu, Korea
[3]Ewha Womans University, Seoul, Korea
[4]Tsinghua University, Beijing, China
[5]Sejong University, Seoul, Korea
[6]Institute of High Energy Physics, Beijing, China

DOI: http://dx.doi.org/10.3204/DESY-PROC-2013-XX/choi_junghoon

The orbital motion of the Earth can result in annual modulation signatures of dark matter. The DAMA group reported a positive signal for an annual modulation with NaI(Tl) crystal detectors. The KIMS experiment uses a CsI(Tl) crystal detector array to search for dark matter and, if the DAMA result is in fact due to WIMP interactions, can be expected to see a similar annual modulation signal. This paper presents results of a search for a dark-matter-induced annual modulation of signals in CsI(Tl) detectors over a 2.5 year period.

1 Introduction

Common matter, so-called baryons, constitute only 4% of the energy density of the universe; the composition of the remaining 96% is unknown [1]. Today, we have various evidence that supports the existence of dark matter [2][3][4][5][6]. The Korea Invisible Mass Search (KIMS) group has carried out an experimental search for Weakly Interacting Massive Particles (WIMPs) using CsI(Tl) crystal detectors. This study used a 75.53-ton·day data-exposure that extended from Sep. 2009 to Feb. 2012, corresponding to 2.5 annual modulation cycles.

CsI(Tl) crystal pulse shapes can be used to discriminate nuclear recoil signals from gamma background, something that cannot be done with NaI(Tl) crystals. The KIMS experiment already reported lower limits than DAMA annual modulation signal in iodine using the pulse shape discrimination (PSD) method in 2007 [7] and 2012 [8]. However, DAMA argued that KIMS may lose some nuclear recoil events when PSD is used in crystal scintillators [9]. The annual modulation study of KIMS provides a more direct comparison compared to the non-PSD analysis.

2 Data analysis

2.1 Fitting Function

Because of the different characteristics of each CsI(Tl) detector module, this analysis is done separately for each detector and then the results are summed. Two-month-long time intervals are used for the study of the annual modulation as shown in Fig. 1.

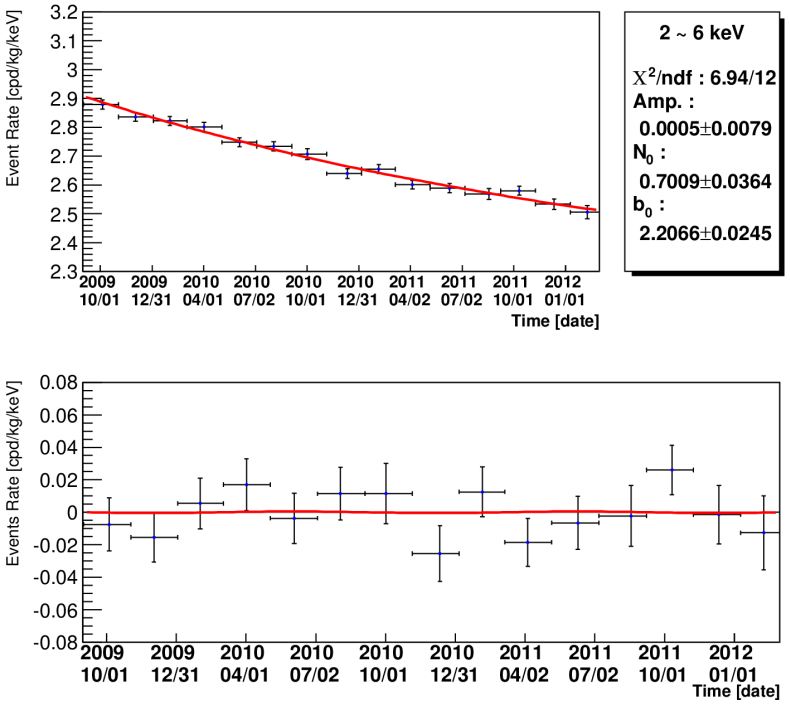

Figure 1: The preliminary result from the fit of an annual modulation function to the data. The fitted energy range is from 2 keV to 6 keV and the modulation phase is fixed to 2 June. The upper figure shows the best fit (red line) to the data. The lower figure shows the residuals, where the smooth background corresponding to the first and second terms of Eq. (1) are subtracted.

Equation (1) is used to fit the data. The first term is used to represent radioactive isotope decays, the second term is for the constant background level and the last term corresponds the annual modulation amplitude where the period is fixed at one year.

$$f(t) = A_{decay} e^{-\frac{t-t_0}{\tau}} + Bkg + A\cos\frac{2\pi}{T}(t-t_1)\,. \tag{1}$$

The decay constant of the first term is fixed at the ^{134}Cs lifetime of 2.065 y. Here, t_0 is fixed on the start time of data taking, and t_1 is 2 June and T is the cycle of the annual modulation. Equation (1) has three free parameters; A_{decay} (initial level of decay components), Bkg (constant background level) and A (annual modulation amplitude). The fitting result from each of the different detector modules are averaged to give the final value for each parameter.

2.2 Fitting results

The left panel of Fig. 2 shows the averaged parameters for each 1 keV energy interval. The amplitude at each energy is consistent with zero within 2 standard deviations. The right panel of Fig. 2 shows the phase shift of the annual modulation for each energy bin. All of phases are concentrated within 2 standard deviations of the origin, and the results do not show the significant shift toward the right side, which would indicate a summer's positive amplitude. The fitted values of A_{decay} and Bkg indicate a smooth background that is slightly less than

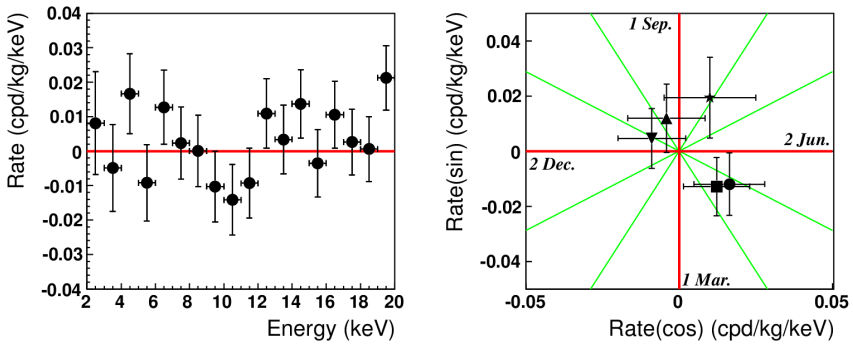

Figure 2: The preliminary result of the annual modulation amplitudes. The left spectrum of energy results in the fixed phase and the right shows the phase distribution of the annual modulation amplitude (Star-2 keV, Triangle-3 keV, Circle-4 keV, Inverted triangle-5 keV, Square-6 keV).

3 cpd/kg/keV. The fitted values of the annual modulation amplitude A are 0.0021±0.0062 cpd/kg/keV (2 keV-6 keV) and 0.0008±0.0068 cpd/kg/keV (3 keV-6keV). These amplitudes are consistent with a null signal within 1 standard deviation. The 90% confidence level (C.L.) upper limits of the annual modulation amplitudes are 0.0122 cpd/kg/keV for 2 keV-6 keV and 0.0119 cpd/kg/keV for 3 keV-6keV. This results can be compared with DAMA modulation signature, 0.0183±0.0082 cpd/kg/keV (2 keV-4 keV, 8.3σ). If the interaction is caused by the WIMP-iodine scattering, the 2 keV-4 keV energy range of NaI(Tl) should be compared with 3 keV-6 keV of CsI(Tl) to account for the slight difference in the quenching factors [13]. The 90% C.L. upper limit of this result is inconsistent with DAMA modulation signature.

2.3 Cross-section limits

The well-defined WIMP model, which gives the rate of the momentum transfers between WIMPs and detectors, and the Standard Halo Model (SHM) are used to convert from event rates to cross-sections. The SHM is well described in [10], [11] and [12]. The cross-sections are combined for both isotopes of ^{133}Cs and ^{126}I according to $1/\sigma = 1/\sigma_{Cs} + 1/\sigma_I$. Figure 3 shows the 90% C.L. upper limit of the cross-section for the cases of the spin-independent WIMP-nucleon, the spin-dependent WIMP-proton and the spin-dependent WIMP-neutron, respectively. The sensitivity becomes worse near 100 GeV/c^2 mass at the left panel of Fig. 3 because the positive (maximum in 2 June) and negative (maximum in 2 December) amplitudes

have zero amplitudes averaged over this range. Reference [10] briefly discusses the negative amplitude possibility. This broadens and shifts the limits toward higher WIMP masses in the spin-dependent case.

3 Conclusion

In this report, the spin-independent cross-section limits exclude a large part of DAMA's WIMP signal area for iodine. Furthermore, the spin-dependent cross-section limits rule out completely the iodine island that corresponds to the DAMA's annual modulation. Previous KIMS results ([7] and [8]) could not provide cross-section limits for very low mass WIMPs because the PSD technique requires a 3 keV threshold energy. In contrast, the annual modulation study does not use the PSD technique and, therefore, has a lower threshold of 2 keV. Because of this point, the spin-independent and spin-dependent limits can also exclude large parts of DAMA's sodium island.

References

[1] N. Jarosik *et al.*, Astrop. Phys. J. Suppl. **14**, 192 (2011).

[2] D. Tytler *et al.*, Astrono. J. **117**, 63 (1999).

[3] D.N. Spergel *et al.*, Astrop. Phys. J. Suppl. **148**, 175 (2003).

[4] M. Tegmark *et al.*, Phys. Rev. D. **66**, 103508 (2002).

[5] D. Clowe *et al.*, Astrop. Phys. J. **652**, 937 (2006).

[6] V. Trimble *et al.*, Annu. Rev. Astron. Astrophys. **25**, 425 (1987).

[7] H.S. Lee *et al.*, Phys. Rev. Lett. **99**, 091301 (2007).

[8] S.C. Kim *et al.*, Phys. Rev. Lett. **108**, 181301 (2012).

[9] R. Bernabei *et al.*, Eur. Phys. J. C. **53**, 205 (2008).

[10] J.D. Lewin and P.F. Smith, Astropart. Phys. **6**, 87 (1996).

[11] K. Freese *et al.*, (2013) [arXiv:1209.3339v3 [astro-ph.CO]].

[12] C. Savage *et al.*, J. Cosmol. Astropart. Phys. **04**, 010 (2009).

[13] H. Park *et al.*, Nucl. Instrum. Meth. A **491**, 460 (2002).

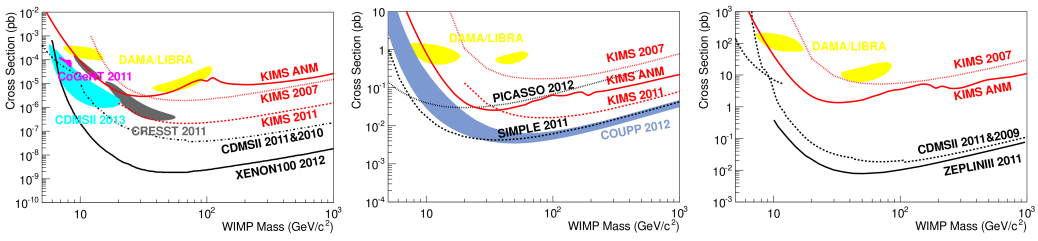

Figure 3: The preliminary results of the spin-independent (left), the spin-dependent WIMP-proton (middle) and the spin-dependent WIMP-neutron (right) cross-section limit.

Direct Dark Matter Search with XENON

T. Marrodán Undagoitia[1]
on behalf of the XENON collaboration

[1]Max-Planck-Institut für Kernphysik, Saupfercheckweg 1, 69117 Heidelberg, Germany

DOI: http://dx.doi.org/10.3204/DESY-PROC-2013-04/marrodan_undagoitia_teresa

Direct dark matter searches using liquid xenon have shown a great potential to detect WIMPs (Weakly Interacting Massive Particles) via elastic scattering off the target nuclei. XENON100 operates with an active volume of 62 kg liquid xenon and it is located at the Gran Sasso underground laboratory in Italy. So far the data released provides no evidence for dark matter. The resulting exclusion limits on the WIMP-nucleon cross section for spin-dependent and -independent interactions probe already significant regions of the cross section and WIMP mass parameter space. The XENON1T experiment currently under construction will improve the current sensitivity by two orders of magnitude.

1 Introduction

Cosmological and astronomical observations indicate that a large fraction of the matter in the universe is non baryonic. A common assumption states that dark matter consists of elemental particles which arise naturally in various theories beyond the standard model of particle physics [1]. Weakly Interacting Massive Particles (WIMPs) could interact elastically with target nuclei allowing to detect them directly. Such a measurement would provide information on the interaction probability of WIMPs with ordinary matter and on the WIMP mass. The detection is however challenging as the recoiling nucleus would deposit only a few keV energy and the predicted interaction rate is very low. Therefore, the required detectors need to have a low energy threshold, a large mass and a very low background. Among the various detector technologies currently in use, liquid xenon (LXe) combines a high WIMP sensitivity with an excellent self-shielding capability for background reduction. Its scintillation light at 178 nm can be detected directly with photomultipliers (PMTs) without wavelength-shifter. Furthermore, natural xenon contains almost 50% of non zero spin isotopes, ^{129}Xe and ^{131}Xe, providing sensitivity to spin-dependent WIMP interactions [2].

2 The XENON100 instrument

The XENON100 detector consist of a two-phase liquid xenon time projection chamber (TPC). If a charged particle deposits energy in the medium, not only excitation but also ionisation of the xenon atoms occur. This provides discrimination between signal and background events based on the simultaneous detection of the prompt scintillation light (S1) and the charge signal from electrons released. These electrons are drifted in an electric field and extracted into the gas

phase, where the charge is converted via proportional scintillation in the gas to an amplified secondary light signal (S2). Both signals are measured by two arrays of R8520 Hamamatsu PMTs placed on top and bottom of the TPC. The interaction vertices can be reconstructed with few mm precision based on the drift time (time difference between S1 and S2) and the PMT hit pattern of the S2 signal [3].

The detector is located at the Laboratori Nazionale del Gran Sasso in Italy. The total mass of liquid xenon is 161 kg of which 62 kg are contained inside the TPC. The remaining 99 kg of the xenon are used as an active veto surrounding the TPC. The whole system is placed inside a shield consisting of an inner copper layer, lead, polyethylene and an outer neutron shield. Due to a careful screening and selection of radio-pure detector materials, the experiment achieved an electronic recoil background of 5.3×10^{-3} events$\cdot$ kg$^{-1}\cdot$ keV^{-1} in the WIMP-search energy range for a 34 kg fiducial mass [4].

3 Dark matter searches with XENON100

During 2011 and 2012, a science run with a total of 225 life days was acquired [4]. Compared to the previous run, the krypton content was reduced to (19 ± 4) ppt $^{\mathrm{nat}}$Kr in xenon resulting in a subdominant ^{85}Kr contamination. Additionally, the ionisation threshold was lowered by using a new hardware trigger such that the efficiency was $> 99\%$ at 150 photoelectrons (PE) in S2.

The detector is calibrated with ^{137}Cs, ^{60}Co, ^{232}Th (gamma) and ^{241}AmBe (neutron) sources in order to characterize the detector performance, to determine the data selection criteria for dark matter searches and to define the signal and background regions. The region of interest for WIMP candidates was blinded to avoid bias during the analysis. The used science data were selected from periods of stable operating conditions. The criteria to select candidate events include data quality, energy range in S1 and S2, selection of single scatter events, consistency cuts and analysis volume [6]. The acceptance for these cuts was calculated using mainly nuclear recoils from calibration data. The nuclear recoil scale E_{nr} was calculated from the light signal (S1) using the equation $E_{nr} = (\mathrm{S1}/L_y)(1/L_{eff})(S_{ee}/S_{nr})$ where L_y is the light yield of a 122 keV gamma ray at zero applied drift field. The term L_{eff} accounts for all quenching effects of the nuclear recoil scale and it is parametrized using all existing measurements from neutron scattering experiments (see [5] and references therein). S_{ee} and S_{nr} are the electric field scintillation quenching factors for electronic recoils and nuclear recoils.

A profile likelihood method was use to test both the signal and the background-only hypothesis in the predefined energy range $(3 - 30)$ PE corresponding to $(6.6 - 43.3)$ keV$_{nr}$ recoil energy. The background prediction included electronic recoil leakage from the main background region and nuclear recoils from neutrons reaching the innermost 34 kg mass used for the analysis. After unblinding, the profile likelihood analysis yielded a $p-$value of $\leq 5\%$ for all WIMP masses indicating no signal over the predicted background.

This result was interpreted in terms of spin-independent [4] and -dependent [2] interactions of WIMPs. Figure 1 shows the expected sensitivity bands ($1\,\sigma$ in green and $2\,\sigma$ in yellow) together with the actual exclusion limits for spin-independent (left) and neutron coupling spin-dependent (right) WIMP-nucleon cross sections. The shaded gray regions represent theoretically favoured regions in this parameter space. The closed regions represent the $2\,\sigma$ signal indications from the DAMA, CoGeNT and CRESST-II experiments (see references in [4]) which are in tension with the result of XENON100.

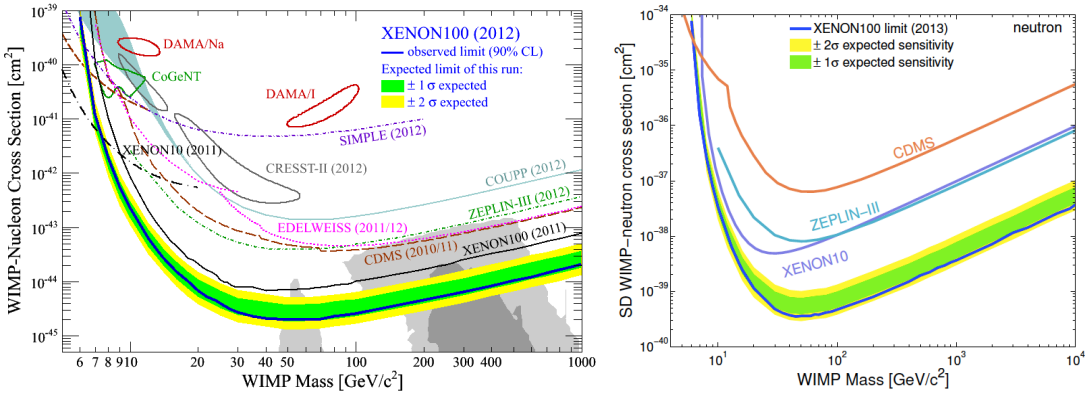

Figure 1: WIMP-nucleon cross section exclusion limits from 225 live days run of XENON100. (Left) Spin-independent. (Right) Spin-dependent (neutron coupling). Figures from [4] and [2], respectively.

3.1 Verification of nuclear recoil energy scale

A data/Monte Carlo comparison of the XENON100 nuclear recoil data acquired during the neutron source calibration with ^{241}AmBe has been performed [7] in order to verify the energy scale used for the results mentioned above. The response of the XENON100 experiment was modelled using a detailed geometry of the whole experiment including the shield and the generation of the two signals S1 and S2. The calculated acceptance for the data was also applied to the Monte Carlo generated events.

In a first step, the S2 Monte Carlo spectrum is fitted to the corresponding data. From this procedure, the number of free electrons per unit energy, charge yield Q_y, is extracted (see Figure 2, left). Best spectral matching was obtained for a neutron source rate of 159 n/s.

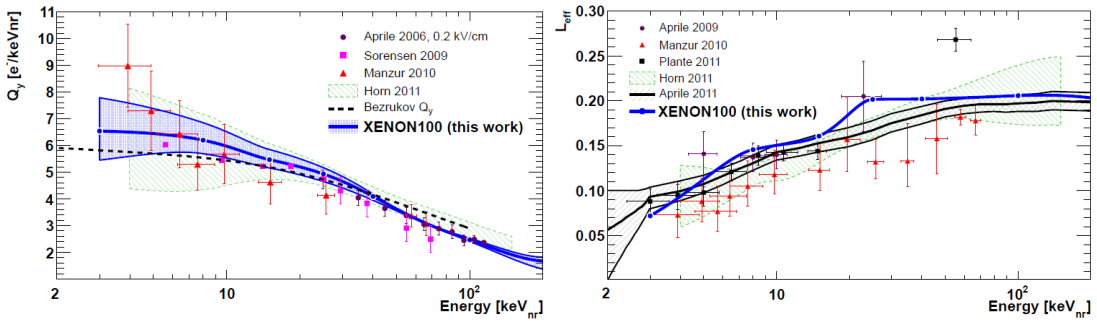

Figure 2: (Left) Q_y obtained from fitting data to the Monte Carlo generated S2 spectrum. (Right) L_{eff} obtained from the Monte Carlo/data matching of the S1 spectrum. Figures from [7].

This number is in agreement with an independent measurement of the rate which yielded (160 ± 4) n/s. Using the derived Q_y, the S1 spectrum of the ^{241}AmBe nuclear recoils is similarly fitted to the Monte Carlo data and the scintillation efficiency L_{eff} is calculated. As it can be

seen in Figure 2 (right), the best-fit curve is in agreement with the energy scale used in previous XENON100 analysis [4]. In both mentioned steps, a very good level of spectral shape matching is accomplished along with agreement in the 2-dimensional particle discrimination space (S2 versus S1). These results confirmed the validity of the calculated signal acceptance used by XENON100 for WIMP searches.

4 Determination of the LXe electronic recoil energy scale

In the sections above, the elastic scattering of WIMP particles off nuclei have been considered where the signal signature consists of a nuclear recoil. However, dark matter particle candidates such as axions or axion-like particles [8] would interact predominantly with shell electrons in the target. In order to study the sensitivity of XENON100 to electronic interactions, the response of liquid xenon down to $\sim$ keV electronic recoil energies needs to be measured.

Recently, laboratory experiments have shown [9][10] that at zero drift field, the light yield at 10 keV decreases below to 40% of its value at higher energies. These experiments use a strong gamma which interacts via Compton scattering in LXe and is then detected in an additional coincidence detector. Using an applied electric field of 450 V/cm [9] which is close to the field of 530 V/cm used in XENON100, the scintillation output is reduced to about 75% relative to the value at zero field. Figure 3 shows the energy dependence of the light yield at zero field (left) and the energy dependence of the field quenching at 450 V/cm. Despite of the light yield

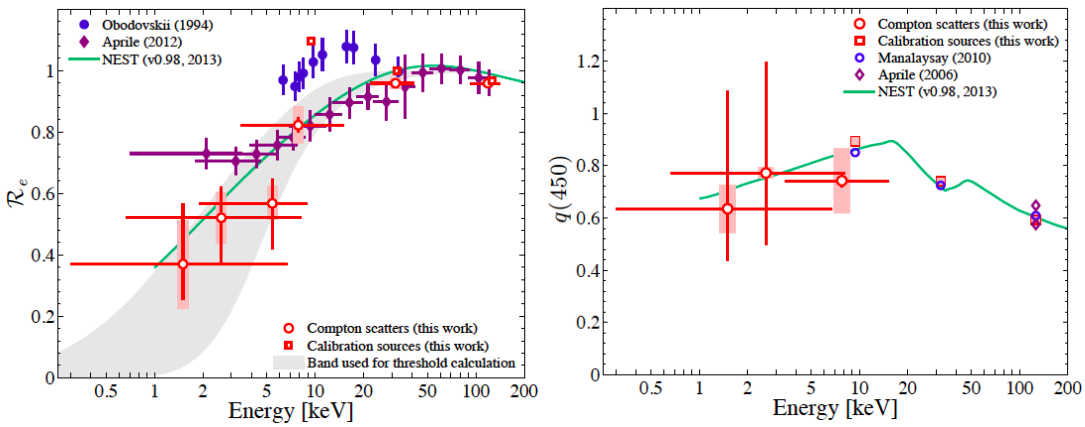

Figure 3: (Left) Energy dependence of the scintillation yield for electronic recoils. (Right) Field quenching at 450 V/cm for different energies. Figures from [9].

reduction mentioned above, liquid xenon shows scintillation at few keV energies in a presence of the tested drift field. Using the data of figure 3, the estimated electronic-recoil energy threshold for XENON100 has been calculated to be at about 2.3 keV.

5 Status of XENON1T

Currently, XENON100 continues being operational and is taking dark matter data. However, in order to increase the sensitivity significantly, the XENON collaboration proposed a next generation detector, XENON1T [11], consisting of about 3 tons of LXe. The design consists of a dual-phase TPC of about 1 m height and about 1 m in diameter. The goal is to reduce the background by a factor of ~ 100 compared to the one of XENON100 which is at the level of 5×10^{-3} events/(keV·kg·d) [4]. This is achieved by using an additional water muon-veto detector, an improved material screening and selection and by reducing the intrinsic contamination with ^{85}Kr and radon using dedicated devices. In addition, a 3 inch high quantum efficiency and low radioactive PMT (Hamamatsu R11410 [12]) will be use to further reduce the background.

XENON1T's goal is to probe spin-independent WIMP-nucleon cross sections down to 2×10^{-47} cm^2 for a 50 GeV/c^2 WIMP mass. Figure 4 shows the projected sensitivity using 2.2 ton-year exposure, 99.75% background rejection rejection in log(S2/S1) parameter space and 40% efficiency to detect nuclear recoils. The construction of the infrastructure for XENON1T has

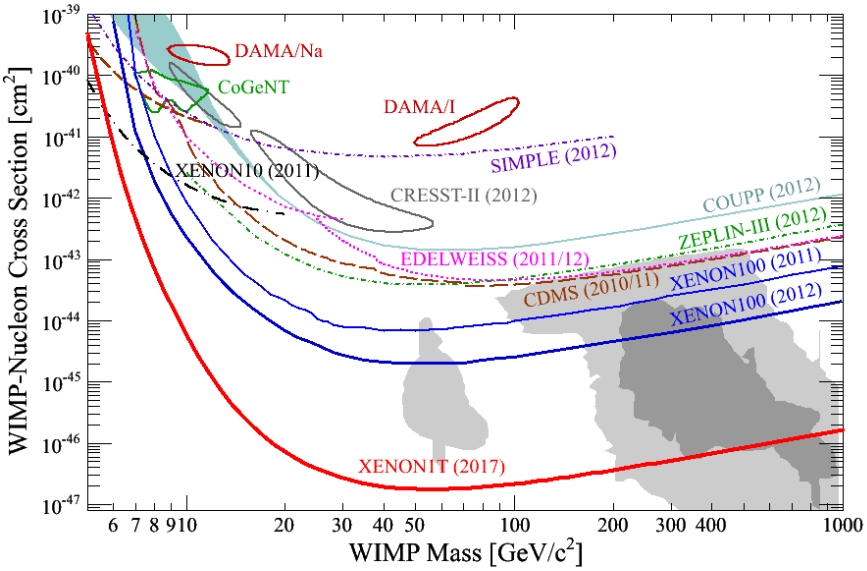

Figure 4: Projected sensitivity for spin independent WIMP-nucleon cross section with the XENON1T experiment.

started this summer at the Laboratori Nationale dell Gran Sasso in Italy and by the time of writing (September 2013) the upper part of the water tank is completed. The start of data taking is planned for 2015.

References

[1] G. Bertone, D. Hooper, and J. Silk, Phys. Rep. **405**, 279 (2005).

[2] E. Aprile *et al.* [XENON100 Collaboration], Phys. Rev. Lett. **111**, 021301 (2013) [arXiv:1301.6620].

[3] E. Aprile *et al.* [XENON100 Collaboration], Astropart. Phys. **35**, 573 (2012) [arXiv:1107.2155].

[4] E. Aprile *et al.* [XENON100 Collaboration], Phys. Rev. Lett. **109**, 181301 (2012) [arXiv:1207.5988].

[5] G. Plante, E. Aprile, R. Budnik, B. Choi, K. L. Giboni, L. W. Goetzke, R. F. Lang and K. E. Lim *et al.*, Phys. Rev. C **84**, 045805 (2011) [arXiv:1104.2587].

[6] E. Aprile *et al.* [XENON100 Collaboration], (2012) [arXiv:1207.3458].

[7] E. Aprile *et al.* [XENON100 Collaboration], Phys. Rev. D **88**, 012006 (2013) [arXiv:1304.1427].

[8] F. T. Avignone *et al.* Phys. Rev. D **35**, 27522757 (1987)

[9] L. Baudis, H. Dujmovic, C. Geis, A. James, A. Kish, A. Manalaysay, T. Marrodán Undagoitia and M. Schumann, Phys. Rev. D **87**, 115015 (2013) [arXiv:1303.6891].

[10] E. Aprile, R. Budnik, B. Choi, H. A. Contreras, K. L. Giboni, L. W. Goetzke, J. E. Koglin and R. F. Lang *et al.*, Phys. Rev. D **86**, 112004 (2012) [arXiv:1209.3658].

[11] E. Aprile *et al.* [XENON1T Collaboration], (2012) [arXiv:1206.6288].

[12] L. Baudis, A. Behrens, A. Ferella, A. Kish, T. Marrodán Undagoitia, D. Mayani and M. Schumann, JINST **8**, P04026 (2013) [arXiv:1303.0226].

The EDELWEISS Dark Matter search program

V. Kozlov[1] *on behalf of the EDELWEISS Collaboration*

[1]Karlsruhe Institute of Technology, Institut für Kernphysik, Postfach 3640, 76021 Karlsruhe, Germany

DOI: http://dx.doi.org/10.3204/DESY-PROC-2013-04/kozlov_valentin

The EDELWEISS experiment is a direct Dark Matter search experiment with a primary goal to detect Weakly Interacting Massive Particles (WIMPs). The setup is installed in the Modane underground laboratory (LSM, France) in French-Italian Alps. The second phase of the experiment was completed in 2011 and results are published setting new limits on the spin-independent WIMP-nucleon scattering cross-section and excluding most of the parameter space favored in some recent experimental hints. Currently the upgrades of the setup towards better sensitivity are being finalized and new detectors are being installed. The scientific goals of EDELWEISS-III program will be presented, including improvements of the background, data-acquisition and measurements with a subset of the forty 800-g detectors. Ongoing installation works of the EDELWEISS-III setup and further plans for a next generation experiment, EURECA, are discussed.

1 Dark Matter search with Edelweiss

The EDELWEISS experiment searches for the WIMP dark matter by means of germanium bolometers with an improved background rejection, thanks to an *interdigitized electrode design* (ID) [1]. Once these detectors are cooled to about 18 mK, one can simultaneously measure phonon and ionization signals after an energy deposit in the germanium crystal. The ratio of the two signals, called the Q-value or *ionization yield*, is different for nuclear and electron recoils with nuclear recoils having Q$\sim$0.3 when normalized to Q=1 for electron recoils. This separation in the ionization yield allows a powerful γ/β-background rejection. Additional rejection power arises from the special electrode arrangement (Fig. 1), called interdigitized electrode design, which provides rejection of *surface events* [1]. Aluminum electrodes evaporated onto the Ge crystal are used to collect electrons and holes. The temperature increase is measured by the use of neutron-transmutation-doped germanium (NTD) as a temperature sensor. The ID detectors used in the second phase of the experiment, EDELWEISS-II, had a mass of 400 g each with interleaved electrodes only on top and bottom surfaces, which limited the fiducial volume to about 40%, or 160 g per detector [2]. For the EDELWEISS-III phase the bigger detectors of 800 g with interleaved electrodes also on the lateral surface (Fig. 1) were developed, called *fully interdigitized* (FID) bolometers. This increased the fiducial volume to about 75%, or 600 g per detector. The experimental setup (Fig. 2) is located in the Laboratoire Souterrain de Modane (LSM), an underground lab in the Fréjus road tunnel in the French-Italian Alps. The laboratory profits from a shielding of 4850 m.w.e., which reduces the muon flux down to about 5 $\mu/\mathrm{m}^2/\mathrm{day}$. A general overview of the setup is shown in Fig. 2: The central part of the experiment is a dilution cryostat which can host up to 40 kg of detectors. A lead layer of 20 cm

shields the bolometers against an external γ/β-background while 50 cm of polyethylene is used to moderate neutrons. An additional layer of polyethylene is installed between the bolometers and the lead layer in the EDELWEISS-III setup to further reduce the neutron background. A muon veto system (>98% coverage) consisting of 100 m^2 of plastic scintillator to tag remaining cosmic muons completes the installation [3]. In addition, a continuous control of the Rn level is performed near the cryostat, and a ^{3}He-gas detector is installed inside the shields to monitor the thermal neutron flux. A neutron counter system based on 1 m^3 of Gd-loaded liquid scintillator [4] was used during year 2009-2012 to study the muon-induced neutron background. The EDELWEISS-II phase is now finished, and the upgrade to EDELWEISS-III is ongoing (Sec. 3). The scientific goal of EDELWEISS-III is to reach a sensitivity of a few 10^{-9} pb for the WIMP-nucleon spin-independent (SI) cross-section by 2014-2015.

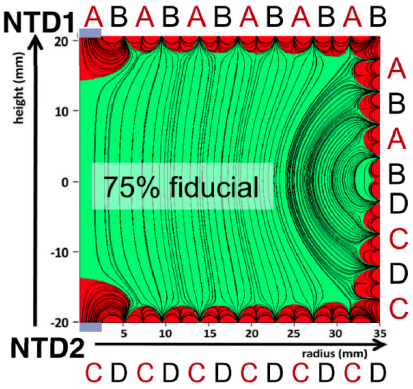

Figure 1: (color online) The electrode scheme of an FID detector (to be used in EDELWEISS-III). The detectors have a radius of 3.5 cm and a height of 4 cm (FID800). In this example, the top and bottom fiducial electrodes are B and D, while the surface veto electrodes are A and C.

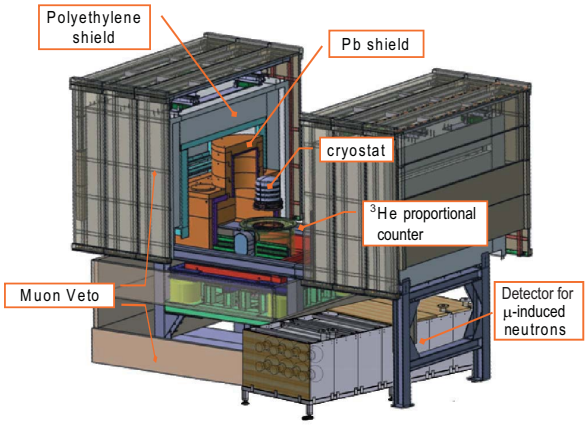

Figure 2: (color online) The EDELWEISS setup layout: in the center is the cryostat able to host up to 40 kg of detectors and surrounded by the passive and active (muon-veto) shields. Auxiliary detectors: ^{3}He proportional counter for thermal neutrons and liquid scintillator detector to measure muon-induced neutrons.

2 Results of the Edelweiss-II phase

In the second phase of the experiment the EDELWEISS collaboration successfully operated ten 400-g ID detectors over a period of 14 months from April 2009 to May 2010 and in addition two detectors during an initial run between July and November 2008. Here we summarize the main results of this measurement period.

2.1 WIMP search for $M_\chi > 50$ GeV

The analysis was optimized to maximize the exposure in a recoil energy range where the behavior of all of the ten detectors was homogeneous and well understood. It resulted in a 384 kg·day total effective exposure. Five nuclear recoil candidates were observed above *a priori* set threshold of 20 keV. In the background conditions of EDELWEISS-II (see Sec. 2.4), the result was interpreted in terms of limits on the cross-section of spin-independent interactions of WIMPs and nucleons. A cross-section of $4.4{\cdot}10^{-8}$ pb is excluded at 90% C.L. for a WIMP mass of 85 GeV (Fig. 4). New constraints were also set on models where the WIMP-nucleon scattering is inelastic [2]. As both EDELWEISS and CDMS experiments use the same target material, germanium, the two collaborations decided to combine their results. This allowed an increase of the total data set to 614 kg·day equivalent exposure and an improvement of the upper limit on the WIMP-nucleon spin-independent cross-section [5], e.g. a value of $3.3{\cdot}10^{-8}$ pb was excluded at 90% C.L. for a WIMP mass of 90 GeV where the combined analysis is most sensitive (Fig. 4). Chosen methods of combination and further details of the work can be found in Ref. [5].

2.2 Analysis for low-mass WIMPs

The direct detection of low-mass ($\sim$10 GeV or lower) WIMPs is challenging because the recoil energies generated by the elastic scattering on nuclei of such low-mass particles are close to the experimental thresholds of existing detectors; for WIMPs with a mass of about 10 GeV, the highest expected recoil energy is of the order of 10 keV. This is why in this analysis a restricted data set was used, selected on the basis of detector thresholds and backgrounds, for which a low-background sensitivity to nuclear recoils down to 5 keV could be achieved. The data quality cuts resulted in only four out of the ten detectors were used, and the total exposure reduced to 113 kg·day [6]. For WIMPs of 10 GeV mass, one event was observed in the WIMP search region, which lead to a 90% C.L. limit of $1.0{\cdot}10^{-5}$ pb on the spin-independent WIMP-nucleon scattering cross-section (Fig. 4) [6]. This extended the sensitivity of EDELWEISS-II down to WIMP masses below 20 GeV and constrained the parameter space associated with the findings reported by the CoGeNT, DAMA and CRESST experiments. Ref. [6] provides all details of this analysis.

2.3 Axion search

EDELWEISS is primarily a direct WIMP search experiment. However, the fact that germanium bolometers are also sensitive to low-energy electron recoils allows a search for such recoils potentially induced by solar or dark matter axions to be performed. The same data set was therefore analyzed to probe scenarios involving different hypotheses on the origin and couplings of axions. The extensive study has been presented at this conference [7]. Here we merely summarize that by combining all obtained results we exclude the mass range 0.91 eV $< \mathrm{m}_A <$ 80 keV for DFSZ (Dine-Fischler-Srednicki-Zhitnitskii) axions and 5.73 eV $< \mathrm{m}_A <$ 40 keV for KSVZ (Kim-Shifman-Vainstein-Zakharov) axions [7], which is a prominent result for a direct axion search from a single dataset.

2.4 Background studies

In order to interpret any result of a direct WIMP search, one has to properly evaluate all possible background components. We have carried out Monte-Carlo simulations based on Geant4 for

Background	EDELWEISS-II (event/kg·day)	EDELWEISS-III (event/kg·day)
Gamma rate	82	14 - 44
Ambient neutrons	$<8.1 \cdot 10^{-3}$	$(0.8 - 1.9) \cdot 10^{-4}$
Muon-induced neutrons	$<2 \cdot 10^{-3}$	$<4 \cdot 10^{-4}$

Table 1: Levels of background achieved in EDELWEISS-II and improvements expected for the EDELWEISS-III. When the limits are given, they at 90% C.L.

the complete EDELWEISS-II setup to study the gamma and neutron background coming from radioactive decays in the setup and shielding, and normalized the expected background rates to the measured material radiopurity (or upper limits) of all components [8]. The expected gamma-ray event rate in EDELWEISS-II at 20 - 200 keV agrees with the observed rate of 82 events/kg·day within the uncertainties in the measured concentrations. The neutron rate from radioactivity was estimated to be less than 3.1 event at 90% C.L. at 20 - 200 keV and for an effective exposure of 384 kg·days, or $< 8.1 \cdot 10^{-3}$ event/kg·day. The rate of muon-induced neutrons was deduced in the dedicated study [3] and resulted in < 0.72 events (90% C.L.) for the EDELWEISS-II total effective exposure, i.e. less than $2 \cdot 10^{-3}$ event/kg·day. However, the main contribution was dominated by a short period of malfunctioning muon veto. The contribution of misidentified gammas, taking into account the gamma-rejection power of the ID detectors deduced in ^{133}Ba calibrations, was estimated to be less than 0.9 events, while the surface event contribution is less than 0.3 for EDELWEISS-II effective exposure of 384 kg·days. The overall background was calculated to be less than 5.02 event and does not contradict the five observed events in nuclear recoil band.

The simulation framework was extended to the EDELWEISS-III configuration with 800-g crystals, better cryostat material purity and additional neutron shielding inside the cryostat. The results of the background studies showed that it is possible to upgrade the existing setup to further reduce the expected rate of background events (Tab. 1) and improve the sensitivity of the experiment by another order of magnitude. These results also helped to select higher purity components and improve shielding of the experiment.

3 Status and goals of Edelweiss-III

Since it was realized that it is possible to upgrade the setup in order to significantly improve the EDELWEISS sensitivity, the EDELWEISS-III phase of the experiment was started. The actual changes concern all aspects of the experiment. New copper thermal screens were produced out of higher radiopurity copper, which reduces the intrinsic gamma background. A new polyethylene shield was installed inside the cryostat between the detectors and the lead castle (Fig. 2) to protect against neutrons. There were installed additional modules of the muon veto, and further optimization of its operation is ongoing in order to improve its efficiency. The analog front-end electronics has been upgraded such that DAC-controlled mechanical relays are used instead of feedback resistors of charge sensitive preamplifiers [9]. The use of relays is expected to avoid Johnson noise contributions from resistances and thus improve the low frequency noise level. It also allows the electronics to be moved further away, and thus reduce its radioactive influence on the detectors. A new DAQ has been implemented to read up to 60 bolometers and includes the readout of the muon veto timing. The new design reduces the continuous data flow processed by acquisition computers for triggering and data storage. This is a highly scalable system

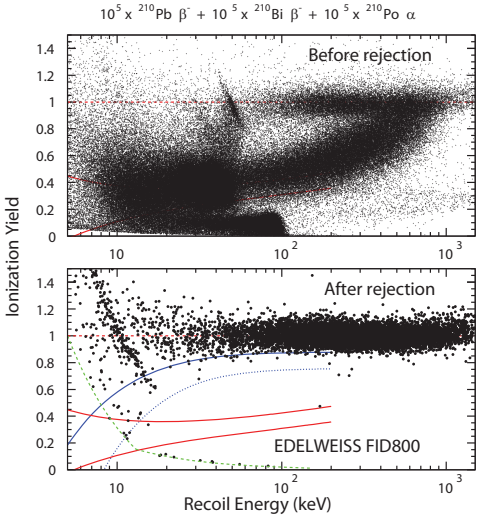

Figure 3: (color online) *Top*: Ionization yield versus energy for two 800-g FID detectors for an exposure to 10^5 ^{210}Pb decays. *Bottom*: same data after rejection of events which had sufficient signals on the veto electrodes (A,C on Fig. 1) and non-equal signals on fiducial electrodes (B,D on Fig. 1), so-called *fiducial cut*. Solid red lines represent the nuclear recoil band (90% region), while the full and dashed blue lines indicate the 90% and 99.99% regions for electron recoils, respectively. Only one event remains in the nuclear recoil band above 15 keV threshold on the recoil energy.

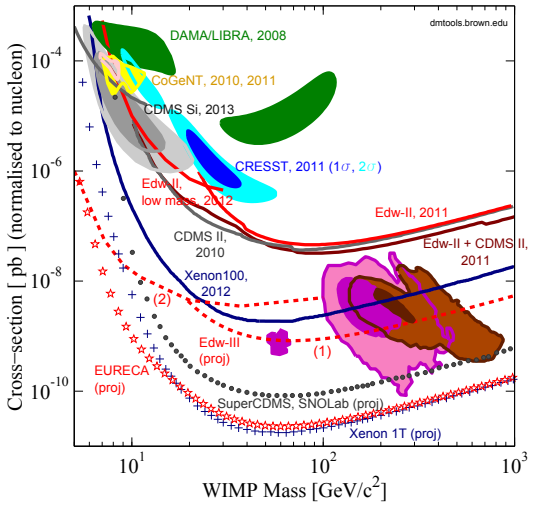

Figure 4: (color online) The upper limits on the WIMP-nucleon spin-independent cross-section as a function of WIMP mass. The EDELWEISS-II only data are marked with thick solid red lines and correspond to Refs. [2, 6]. Combined data of the EDELWEISS-II and CDMS-II experiments [5] are indicated as "Edw-II + CDMS II". As dashed red lines are shown EDELWEISS-III projections for two cases: (1) - the standard WIMP, 12000 kg·day, and (2) - low-mass WIMP analysis, 1200 kg·day, HEMT-based front-end electronics. The EURECA projection is shown as red stars. The magenta and brown shaded areas correspond to theoretical SUSY predictions.

and allows an inclusion of even more detectors in the future. Additionally, an increase in the sampling rate on the ionization channel from 10 kSamples to 40 MSamples has been studied. The higher resolution on timing of the ionization signal would improve further the discrimination power between fiducial and surface events [1]. Ongoing R&D on the HEMT-based front-end readout should allow us to lower the recoil energy threshold down to 3 keV and thus improve the low-mass WIMP search (Fig. 4). In order to handle a significantly increased data flow, a multi-tiered data structure, analysis toolkit and data processing management system has been constructed [10]. Finally, new FID detectors with twice the mass (800 g) and increased fiducial volume (∼600 g) have been developed (Fig. 1). These detectors are confirmed to have a better rejection of γ-events comparing to the previous ID400 detectors, e.g. out of $4{\cdot}10^5$ γ-events recorded in ^{133}Ba calibration, none leaked into the region-of-interest, i.e. nuclear recoil band

between 20 keV and 200 keV. Recently two of these detectors were also tested for rejection of surface events (Fig. 3) and showed a slightly better rejection power of $4{\cdot}10^{-5}$ above 15 keV recoil energy (90% C.L.) compared to that previously measured for ID bolometers of $6{\cdot}10^{-5}$ above 20 keV.

The plan of the fully funded EDELWEISS-III project is to acquire an exposure of 3000 kg·day within a half year of operation and to reach in 2014 a WIMP-nucleon scattering cross-section sensitivity of a few 10^{-9} pb. It is foreseen to continue further to achieve larger exposure and better sensitivity in case of no background (Fig. 4). The ongoing research builds a good ground for the EURECA project [11], a next generation dark matter experiment with a multi-nuclei target of up to 1000 kg mass. EURECA is supported by different European dark matter groups and a closer collaboration with the SuperCDMS experiment is foreseen. EURECA will probe in its 1-tonne phase a WIMP-nucleon SI interaction down to 10^{-11} pb (Fig. 4).

4 Acknowledgments

The help of the technical staff of the Laboratoire Souterrain de Modane and the participant laboratories is gratefully acknowledged. The EDELWEISS project is supported in part by the German ministry of science and education (BMBF Verbundforschung ATP Proj.-Nr. 05A11VK2), by the Helmholtz Alliance for Astroparticle Phyics (HAP) funded by the Initiative and Networking Fund of the Helmholtz Association, by the French Agence Nationale pour la Recherche, by Science and Technology Facilities Council (UK) and the Russian Foundation for Basic Research (grant No. 07-02-00355-a).

5 Bibliography

References

[1] A. Broniatowski *et al.*, Phys. Lett. B **681**, 305 (2009) [arXiv:0905.0753 [astro-ph.IM]].

[2] E. Armengaud *et al.*, Phys. Lett. B **702**, 329 (2011) [arXiv:1103.4070 [astro-ph.CO]].

[3] B. Schmidt *et al.*, Astropart. Phys. **44**, 28 (2013) [arXiv:1302.7112 [astro-ph.CO]].

[4] V. Yu. Kozlov *et al.*, Astropart. Phys. **34**, 97 (2010) [arXiv:1006 [astro-ph.IM]]; and in AIP Conf. Proc. **1549**, 231 (2013).

[5] Z. Ahmed *et al.*, Phys. Rev. D **84**, 011102 (2011) [arXiv:1105.3377 [astro-ph.CO]].

[6] E. Armengaud *et al.* [EDELWEISS Collaboration], Phys. Rev. D **86**, 051701(R) (2012) [arXiv:1207.1815 [astro-ph.CO]].

[7] E. Armengaud *et al.* [EDELWEISS Collaboration], arXiv:1307.1488 [astro-ph.CO]; and C. Nones *et al.* in these proceedings, *Patras 2013*.

[8] E. Armengaud *et al.*, Astropart. Phys. **47**, 1 (2013) [arXiv:1305.3628 [physics.ins-det]].

[9] B. Censier *et al.*, J. Low Temp. Phys. **167**, 645 (2012).

[10] G. A. Cox *et al.*, Nucl. Instr. and Meth. A **684**, 63 (2012).

[11] H. Kraus *et al.*, Nucl. Phys. B, (Proc. Suppl.) **173**, 168 (2007).

Recent Results from CDMS II, Status and Future of the SuperCDMS Experiment

S. Scorza[1] *for the SuperCDMS Collaboration*

[1]Department of Physics, Southern Methodist University, Dallas, TX, US

DOI: http://dx.doi.org/10.3204/DESY-PROC-2013-04/scorza_silvia

The CDMS II collaboration operated an experiment consisting of cryogenic Ge and Si detectors designed for the direct detection of Weakly Interacting Massive Particle (WIMPs) dark matter from 2003 - 2008. Currently the SuperCDMS collaboration is operating 9 kg of advanced iZIP germanium detectors with larger mass and improved background discrimination in the CDMS II cryostat. In this talk I will discuss the latest results from the CDMS II experiment and present the current status and plans of the new SuperCDMS experiment.

1 Introduction

There are substantial evidences that dark matter is present at all scales in the universe and also a compelling motivations to believe that it consist mainly of non-baryonic objects [1] . The latest Planck results are pointing out that dark matter is contributing for about 27% of the total Universe amount [2]. The most promising dark matter particle candidate is a WIMPs: stable particles which arise in several extensions of the Standard Model of electroweak interactions [3]. Typically they are presumed to have masses between few tens and few hundreds of GeV/c^2 and a scattering cross section with a nucleon below 10^{-42} cm^2.

The Cryogenic Dark Matter Search (CDMS) Collaboration has pioneered the use of low temperature phonon-mediated detectors to detect the rare scattering of WIMPs on nuclei and distinguish them from backgrounds. With this powerful technology, operating deep underground in the Soudan mine in Minnesota, CDMS II has provided the most sensitive WIMP search in the world, and this technology has the greatest discovery potential because it has achieved nearly background free performance. The SuperCDMS program includes a scaling up of the CDMS detector technology in several phases. For each phase of SuperCDMS, not only does the target exposure need to increase but also, to maintain maximum improvement in sensitivity as a function of exposure time, we desire a zero background experiment for each phase.

The direct detection principle consists in the measurement of the energy released by nuclear recoils produced in an ordinary matter target by the elastic collision of a WIMP from the Galactic halo. The main challenge is the expected extremely low event rate (<1 evt/kg/year) due to the very small interaction cross section of WIMPs with ordinary matter. Another constraint is the relatively small deposited energy (<100 keV). The dominant background for direct dark matter search experiment are electronic recoils induced by gamma, alpha and beta

particles. In addition, since the WIMP signal that we want to detect has the same proprieties of a nuclear recoil, neutrons and muon induced neutrons are the irreducible background.

In order to measure low energy recoils, cryogenic detectors - high purity Ge and Si crystals for CDMS II and high purity Ge crystals only for SuperCDMS - are employed. The simultaneous measurements of phonon and ionization signal allows an event by event discrimination between the electronic recoils which represent the main background and the nuclear recoils produced by neutrons and WIMPs. The ionization signal, corresponding to the collection on electrodes of electron-hole pairs created by the energy loss process, depends on the particle type whereas the phonon signal reflects the total energy deposit.

2 CDMS II: silicon detector results

During 2003-2008 the collaboration operated CDMS II, an array of Ge and Si detectors located at the Soudan Underground Laboratory [4] Results from data recorded between July 2007 and September 2008 in the silicon detectors will be discussed, whereas the results from Ge detectors for the same data set have been described in previous publications [5], [6].

The advantage of Si material as target is its low atomic mass: in searches for WIMPs of relatively low mass due to more favorable scattering kinematics, a WIMP of mass of 40 GeV/c2 will transfer more recoil energy to a Si nucleus than a Ge nucleus on average.

The CDMS II installation consist of 11 Si detectors. Three of them were excluded from the WIMP-search analysis: two due to wiring failures that led to incomplete collection of the ionization signal and one due to unstable response on one of its four phonon channels. The data recorded by the 8 Si detectors represent a total raw exposure of 140.2 kg-days. Background estimate, likelihood analysis and post unblinding checks are detailed in [7].

Left panel of Fig. 1 illustrates the data recorded with (bottom) and without (top) the phonon timing criteria which, providing z-position information for each event, allows to discriminate nuclear recoils form surface events which can leak into the signal region. Three WIMP-candidate events were observed with recoil energies of 8.2, 9.5, and 12.3 keV. The events were well separated in time and were in the middle of their respective tower stacks. After unblinding, extensive checks of the three candidate events revealed no analysis issues that would invalidate them as WIMP candidates.

The interpretation of these three WIMP-candidate event in terms of upper limits on the spin-independent WIMP-nucleon scattering cross section at the 90% confidence level (C.L.) is shown in the right panel of Fig. 1. The present data set an upper limit of 2.4 $\times 10^{?41}$ cm^2 for a WIMP of mass 10 GeV/c^2.

A likelihood analysis that includes the measured recoil energies of the three events favors by 3 sigma the WIMP hypothesis over that of an accidental fluctuations of known background. The resulting best-fit region from this analysis (68% and 90% confidence level contours) on the WIMP-nucleon cross-section is shown in the right panel of Fig. 1. While the results does not rise to the level of discovery it does warrant further investigations.

The CDMS collaboration is currently probing this region of WIMP nucleon cross section versus WIMP mass more completely out with our operating germanium detectors in the SuperCDMS experiment in the same Soudan underground environment with higher mass and better discrimination power.

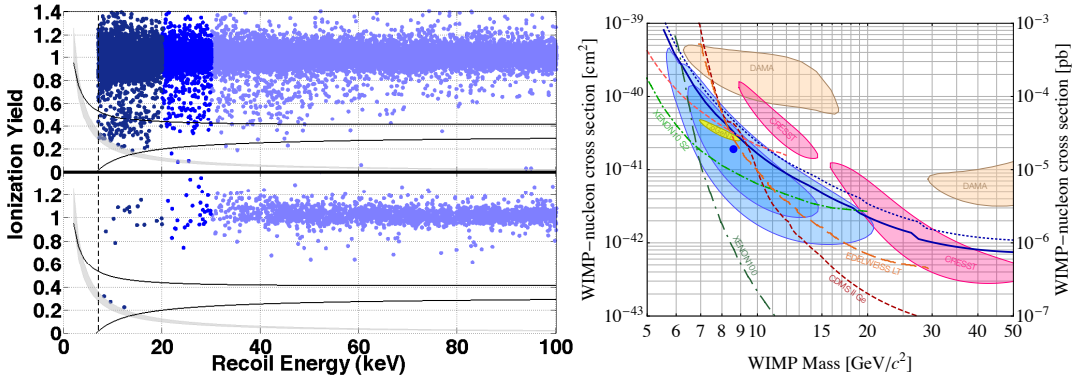

Figure 1: Left panel shows the ionization yield versus recoil energy in all detectors included in this analysis for events passing all signal criteria except (top) and including (bottom) the phonon timing criterion. The curved black lines indicate the signal region (-1.8σ and +1.2σ from the mean nuclear recoil yield) between 7 and 100 keV recoil energies. The gray band shows the range of ionization energy thresholds. Blue shades of colors refer to different recoil energy ranges of 720, 2030, and 30100 keV (dark to light). Right panel shows the experimental upper limits (90% confidence level) for the WIMP-nucleon spin-independent cross section as a function of WIMP mass.

3 The SuperCDMS Soudan experiment

SuperCDMS aims to reach a sensitivity in the WIMP-nucleus interaction detection better than 0.003 counts/kg·d for recoil energy above 8 keV. To reach this goal, background rejection and discrimination are necessary. SuperCDMS backgrounds includes gamma particles, beta particles and neutrons from cosmic rays and natural radioactivity. Thanks to simultaneous measurements of charge and phonon signals iZIP detectors can discriminate gammas from WIMPs at high efficiency, because WIMPs interact with nuclei and gammas with electrons. The iZIP detector consists of a 3-inch diameter x 1-inch thick Ge substrate (7.6 x 10^{10} cm^{-3} purity). Detector features are detailed in previous publications [8], [9].

The main limiting background of the experiment comes from interactions occurring just underneath the collecting electrodes: essentially low energy β-rays due to ^{210}Pb contamination (^{222}Rn daughter)of the detector surface and/or in the vicinity of the detectors. The incomplete charge collection of these events can mimic nuclear recoils.

Evidences of a ^{210}Pb contamination in CDMS detectors have been shown in previous data [5]: ^{222}Rn decays to ^{210}Bi, emitting X-rays conversion electrons with energies below 60 keV falling precisely within the energy range of interest for WIMP searches. ^{210}Bi decays to ^{210}Po with emission of a beta with an end-point at 1.1 MeV. Finally, ^{210}Po decays to ^{210}Pb via a 5.3 MeV alpha with a range of 20 μm, accompanied back-to-back by the recoil of the ^{210}Pb nucleus (40 nm) with a kinetic energy of 103 keV.

With the iZIP detector technology, surface events are tagged by the presence of charge on only one side charge electrode of the detector. For events occurring in the bulk of the crystal, the iZIP measures the number of electrons that travel across the detector to one charge electrode

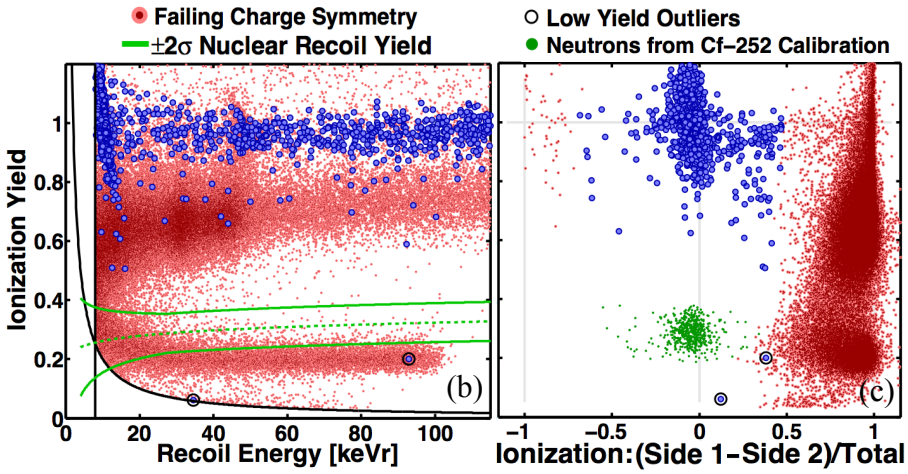

Figure 2: Left and right panels show the same data from ∼900 live hours of detector T3Z1 with the ^{210}Pb source facing side 1. The symmetric charge events are represent as the large blue dots and occurs in the interior of the crystal. The events which fail the symmetric charge cut (small red dots) include surface events from betas, gammas and lead nuclei incident on side 1 from the source. The two blue dots with circles around them are outliers that show a very low charge yield and just satisfy the symmetry requirement. Left panel shows the projection in the (Y, E) plane of the data recorded and the right panel shows, in addition to those data, the nuclear recoils from neutrons from a ^{252}Cf source (green, low yield).

while at the same time measuring the number of holes traveling in the other direction to the electrode on the opposite side of the crystal. The two charge signals are therefore symmetric. Then, iZIP detector have the ability to reject surface events from bulk ones just performing a cut based on charge signal: *symmetric cut* means that the charge signal is equally shared on both sides of the detector. Three separate populations: bulk electron recoil, bulk nuclear recoil (taking advantage of different yield value between electronic and nuclear recoil) and surface electron recoil were defined using the the charge symmetric cut.

In order to verify and quantify the surface event power rejection capabilities of the iZIP detectors two detectors have been equipped with a ^{210}Pb implanted Si wafer with an activity of 1000 Pb decays per day. Left panel of Fig. 2 shows the ionization yield (ratio of ionization signal to phonon signal normalized to electron recoil events from the gamma source) as a function energy of events recorded for detectors equipped with Pb source. It consist of 37.6 live time days. Green lines represent the $\pm$ 2 σ ionization yield range of neutrons. The hyperbolic black line is the 2 keVee ionization threshold whereas the vertical black line is the recoil energy threshold (8 keVr). Electrons from ^{210}Pb (below 60 keVr) and 210Bi (mostly above 60 keVr) are distinctly separated from ^{206}Pb recoils (low yield, below 110 keVr).

In addition to the data in left panel of Fig. 2, the right panel also shows nuclear recoils from neutrons from a ^{252}Cf source (green, low yield). Nuclear recoils as bulk events show a symmetric ionization response between sides like the bulk electron recoils at higher yield. They are thus nicely discriminated from the surface events via the symmetric charge cut.

In 37.6 live time days (from March to July 2012), no events are leaking into the signal region into 50% fiducial volume in the energy range 8-115 keVnr This result limits surface

events leakage to 1.7 x $10^{-}5$ @90% C.L., [10].

As with the standard CDMS detectors described in detail in [5], the phonon measurement provides z-position information for each event via the timing difference between rising edges of the phonon pulses. Phonon timing rejection capabilities of the iZIP detector have been tested and demonstrated to be preserved from the standard ZIP detector [11].

3.1 The SuperCDMS SNOLAB experiment

The SuperCDMS Soudan projected sensitivity will reach nearly an order of magnitude more sensitive than the CDMS II result. Extending the sensitivity by another order of magnitude will require a new, cleaner facility located farther underground, to reduce the neutron background that may ultimately limit our Soudan experiment. It will also require a substantial increase in Ge detector mass. This future SuperCDMS SNOLAB project will construct a new experimental apparatus, in the SNOLAB laboratory in Sudbury, Ontario, Canada.

One effective way to mitigate the challenge posed by nuclear recoils induced by neutrons in dark matter experiments is to employ active neutron vetoes. Such a strategy would improve the sensitivity of an experiment which would otherwise be limited by neutron backgrounds by vetoing a large fraction of the neutron induced recoils. In addition, it would provide sensitive in situ measurements of the true neutron environment in which the detectors are operating. This direct assay capability would allow experiments to convincingly demonstrate that low neutron backgrounds have been achieved. A neutron veto system with a very high detection efficiency can be produced by surrounding a dark matter detector with a layer of liquid scintillator. SuperCDMS collaboration is proposing to build active neutron veto shielding at SNOLAB underground laboratory.

Ongoing studies are assessing the necessity and feasibility of including a neutron veto in the SuperCDMS SNOLAB design.

SuperCDMS SNOLAB will extend the sensitivity by over an order of magnitude with an increased target mass of 200 kg and suppression of backgrounds through better shielding design, materials selection, and materials handling as well as the added depth to suppress backgrounds from cosmic-ray showers.

References

[1] G. Bertone, D. Hooper, J. Silk, Phys. Rept.**405** (2005), 279-390, arXiv:hep-ph/0404175 [hep-ph].

[2] P.A.R. Ade and others [Planck Collaboration], Astronomy & Astrophysics (2013) [arXiv:1303.5062 [astro-ph]].

[3] J. Hellis, J.S. Hagelin, D.V. Nanopoulos, K. Olive, and M. Srednicki, Nucl. Phys.**B238** (1984), 453.

[4] D. Akerib et al. (CDMS Collaboration), Phys.Rev., **D72**, 052009 (2005), arXiv:astro-ph/0507190 [astro-ph].

[5] Z. Ahmed et al. (CDMS), Science, **327**, 1619 (2010).

[6] Z. Ahmed et al. (CDMS), Phys.Rev.Lett. **106**, 131302 (2011).

[7] R.Agnese et al. (CDMS), CDMS Collaboration, arXiv:1304.4279 [astro-ph].

[8] P.L. Brink, et al, *Nucl. Instrum. Methods Phys. Res.* **A559**, 414-416 (2006).

[9] M. Pyle, et al, *AIP Conference Proceedings* **#1185**, 223-226 (2009).

[10] R.Agnese et al. (SuperCDMS) , arXiv: 1305.2405" [astro-ph].

[11] M. Pyle and others, LTD13 Conference Proceedings, **1185** (2009), 223.

Dark Matter Searches with sub-keV Germanium Detector

H.B. Li, H.T. Wong

(on behalf of TEXONO collaboration)
Institute of Physics, Academia Sinica, Taipei 11529, Taiwan.

DOI: http://dx.doi.org/10.3204/DESY-PROC-2013-04/li_hau-bin

We report new limits on spin-independent WIMP-nucleon interaction cross-section using 39.5 kg-days of data taken with a p-type point-contact germanium detector of 840 g fiucial mass at the Kuo-Sheng Reactor Neutrino Laboratory. Crucial to this study is the understanding of the selection procedures and, in particular, the bulk-surface events diffentiation at the sub-keV range. The signal-retaining and background-rejecting efficiencies were measured with calibration gamma sources and a novel n-type point-contact germanium detector. Part of the parameter space in cross-section versus WIMP-mass implied by various experiments is probed and excluded.

A kg-scale p-type point-contact germanium detectors (pGe) is sensitive to probe the "low-mass" WIMPs with $m_\chi < 10$ GeV.

We report new results with a pGe of 39.5 kg-days of data at Kuo-Sheng Reactor Neutrino Laboratory (KSNL).

The detector was enclosed by an NaI(Tl) anti-Compton (AC) detector and copper passive shieldings inside a plastic bag purged by nitrogen gas. This set-up was further shielded by, from inside out, 5 cm of copper, 25 cm of boron-loaded polyethylene, 5 cm of steel and 15 cm of lead. This structure was surrounded by cosmic-ray (CR) veto panels made of plastic scintillators read out by photomultipliers. Both AC and CR detectors serve as vetos to reject background and as tags to identify samples for efficiency measurements [1].

Signals from the point-contact is distributed to a fast-timing amplifier which keeps the rise-time information, and to amplifiers at both 6 s and 12 s shaping time which provide energy information. The trigger efficiency was 100% above 300 eVee.

Energy calibration was achieved by the internal X-ray peaks and the zero-energy was defined with the pedestals provided by the random events. The electronics noise-edge is at 400 eVee. A cut-based analysis was adopted. There are three categories of selection criteria: (i) PN cuts diffentiate physics signals from spurious electronic noise; (ii) the AC and CR cuts identify events with activities only at the pGe target; and (iii) the "bulk versus surface events" (BS) cut selects events at the interior. In addition, the efficiencies and suppression factors (ϵ_X,λ_X) for every selection (X=PN,AC,CR,BS) are measured. The physics samples selected these cuts are categorized by "$AC^{-(+)}\otimes CR^{-(+)}\otimes B(S)$", where $AC^{-(+)}$ and $CR^{-(+)}$ represent AC and CR signals in anti-coincidence(coincidence), respectively, while B(S) denote the bulk(surface) samples. The χN candidates would therefore manifest as $AC^-\otimes CR^-\otimes B$ events [1].

The *in situ* doubly-tagged $AC^+\otimes CR^+$ events serve as the physics reference samples, with which the ϵ_{PN} shown in Figure 2 are measured. The majority of the electronics-induced events

above noise-edge are identified($\lambda\sim1$).

The efficiencies for AC and CR selections are measured by the random events to be, respectively, $\epsilon_{\rm AC} > 0.99$ and $\epsilon_{\rm CR} = 0.93$. The suppressions $\lambda_{\rm AC} = 1.0$ above the NaI(Tl) threshold of 20 keVee, $\lambda_{\rm CR} = 0.92$, measured by reference cosmic samples in which the energy depositions at NaI(Tl) are above 20 MeVee.

The surface-electrode of *p*Ge is a lithium-diffused n^+ layer of mm-scale thickness. Partial charge collection in the surface layer gives rise to reduced measureable energy and slower rise-time (τ) in its fast-timing output. The thickness of the S layer was derived to be (1.16±0.09) mm, via the comparison of simulated and observed intensity ratios of γ-peaks from a ^{133}Ba source. This gives rise to a fiducial mass of 840 g.

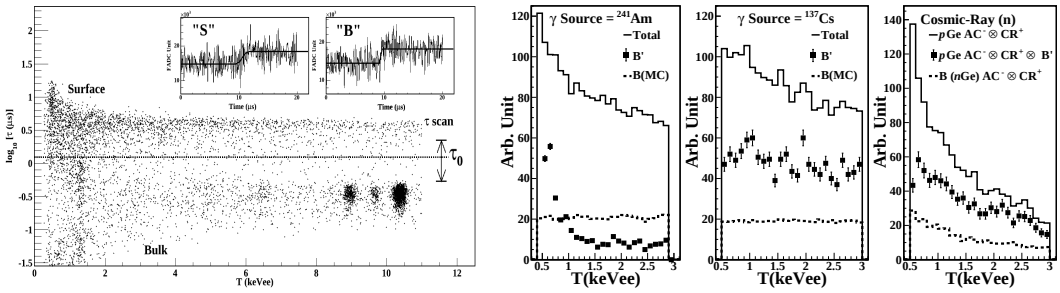

Figure 1: (**left**) log10[τ] versus energy, with τ-scan indicating the range of cut-stability test. Typical B′(S′) pulses at $T\sim700$ eVee are shown. (**right**) The measured Total and B′ spectra from *p*Ge with the surface-rich γ-ray (^{241}Am,^{137}Cs) and bulk-rich cosmic-ray induced neutrons. They are compared to reference B-spectra from simulation and *n*Ge AC$^-\otimes$CR$^+$.

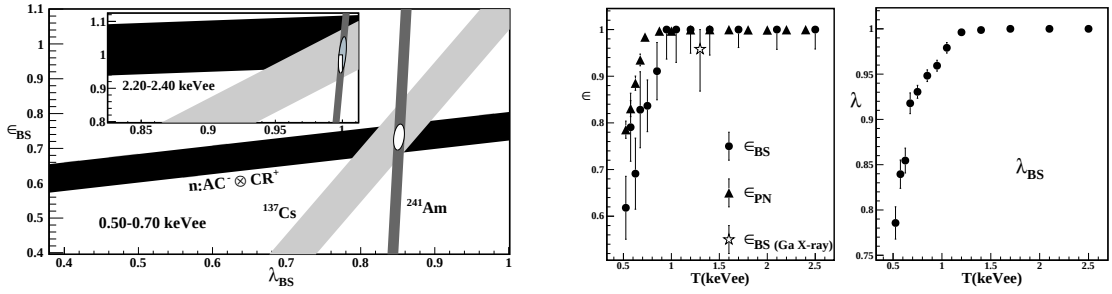

Figure 2: (**left**) Allowed bands at threshold and at a high energy band. (**right**) The measured ($\epsilon_{\rm BS}$,$\lambda_{\rm BS}$) and $\epsilon_{\rm PN}$ as functions of energy. Independent measurement on $\epsilon_{\rm BS}$ with Ga-L X-rays is included.

The $\log_{10}[\tau]$ versus measured energy(T) scatter plot is displayed in Figure 1. Events with τ less(larger) than τ_0 are categorized as B′(S′). The actual bulk(surface) rate are denoted B(S). At T>2.7 keVee where the τ-resolution is better than the separation between the two bands, the conditions B=B′ and S=S′ are justified. At lower energy, (B′,S′) and (B,S) are related by the coupled equations:

$$\mathrm{B}' = \epsilon_{\rm BS}\cdot\mathrm{B} + (1-\lambda_{\rm BS})\cdot\mathrm{S}, \quad \mathrm{S}' = (1-\epsilon_{\rm BS})\cdot\mathrm{B} + \lambda_{\rm BS}\cdot\mathrm{S}, \quad \mathrm{B}+\mathrm{S} = \mathrm{B}'+\mathrm{S}'.$$

The calibration of (ϵ_{BS},λ_{BS}) involves at least two measurements of (B′,S′) where (B,S) are independently known. Three complementary data samples were adopted:

(I) Surface-rich events with γ-ray sources – Calibrations with both low and high energy-sources (^{241}Am at 60 keVee and ^{137}Cs at 662 keVee, respectively) were performed. As displayed in Figure 1, the measured B′- spectra are compared to the reference B derived from simulation.

(II) Bulk-rich events with cosmic-ray induced fast neutrons – A 523 g n-type point-contact germanium (nGe) detector was constructed. The components and dimensions are identical to those of pGe. The surface of nGe is a p+ boron implanted electrode of sub-micron thickness. There are no anomalous surface effects. Data were taken under identical shielding configurations at KSNL. The trigger efficiency was 100% above T=500 eVee, and energy calibration was obtained from the standard internal X-ray lines. The AC$^-\otimes$CR$^+$ condition selects cosmic-ray induced fast neutron events without associated γ-activities, which manifest mostly(85%) as bulk events. Accordingly, the AC$^-\otimes$CR$^+$ spectrum in nGe is taken as the B-reference and compared with those of AC$^-\otimes$CR$^+\otimes$B′ in pGe.

Using calibration data (I) and (II), (ϵ_{BS},λ_{BS}) are measured by solving the coupled equations above. Uncertainties were derived from errors in (B,B′,S′). A consistent ϵ_{BS} is independently measured from Ga-L X-ray peak at 1.3 keVee. As shown in Figure 2.

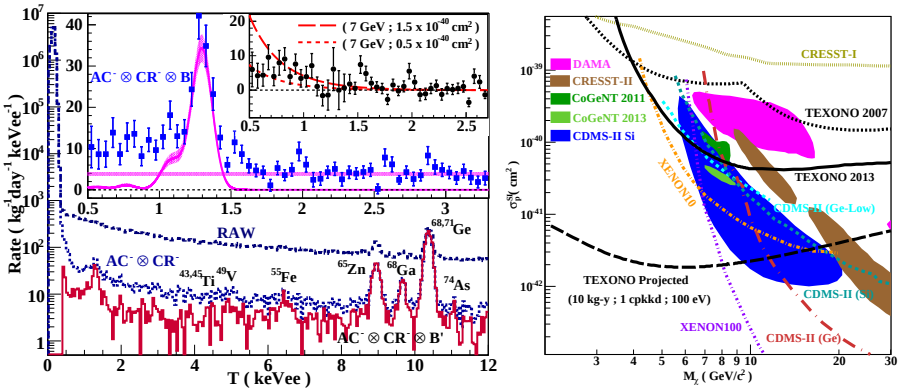

Figure 3: (**left**) Measured energy spectra, showing the raw data and those with AC$^-\otimes$CR$^-$($\otimes$B′) selections. The large inset shows the (ϵ_{BS},λ_{BS})-corrected AC$^-\otimes$CR$^-\otimes$B, with a flat background and L-shell X-ray peaks overlaid. The small inset depicts the residual spectrum superimposed with that due to an allowed (excluded) cross-section at m$_\chi$=7 GeV. (**right**) Exclusion plot of spin-independent χN coupling at 90% confidence level, superimposed with the results from other benchmark experiments.

The raw spectrum as well as those of AC$^-\otimes$CR$^-\otimes$(B′) are depicted in Figure 3. The peaks correspond to known K-shell X-rays from the cosmogenically-activated isotopes. Errors above $T\sim$800 eVee are dominated by statistical uncertainties, while those below have additional contributions due to the BS calibration errors of Figure 2, which increase as (ϵ_{BS},λ_{BS}) deviate from unity at low energy. The analysis threshold is placed at 500 eVee. The stability of B is studied over changes of τ_0 within the τ-scan range of Figure 1. Measurements of B are stable and independent of τ_0. High energy γ-rays from ambient radioactivity produce at electron-recoil background at low energy. This, together with the L-shell X-ray lines predicted by the higher energy K-peaks, are subtracted from AC$^-\otimes$CR$^-\otimes$B.

Constraints on $\sigma^{\rm SI}_{\chi \rm N}$ are derived via the "binned Poisson" method [2] with conventional astrophysical models [3] (local density of 0.3 GeV/cc and Maxwellian velocity distribution with υ_0=220 km/s and υ_{esc}=544 km/s). The quenching function in Ge is derived with the TRIM software.

Exclusion plot of $\sigma^{\rm SI}_{\chi \rm N}$ versus $\rm m_\chi$ at 90% confidence level is displayed in Figure 3. Bounds from other benchmark experiments are superimposeds [4, 5, 6, 7].

We note that an excess remains in the sub-keV region not yet accounted for in this analysis, the understanding of which is the theme of our on-going investigations.

References

[1] H.T. Wong, Mod. Phys. Lett. **A 23**, 1431 (2008). S.T. Lin *et al.*, Phys. Rev. **D 79**, 061101(R) (2009) H.B. Li *et al.*, Phys. Rev. Lett. **90**, 131802 (2003); H.T. Wong *et al.*, Phys. Rev. **D 75**, 012001 (2007); M. Deniz *et al.*, Phys. Rev. **D 81**, 072001 (2010).

[2] C. Savage et al., JCAP **04**, 010 (2009).

[3] M. Drees and G. Gerbier, Review of Particle Physics Phys. Rev. **D 86**, 289 (2012), and references therein.

[4] C.E. Aalseth *et al.*, Phys. Rev. Lett. **101**, 251301 (2008); C.E. Aalseth *et al.*, Phys. Rev. Lett. **106**, 131301 (2011); C.E. Aalseth *et al.*, Phys. Rev. Lett. **107**, 141301 (2011); C.E. Aalseth *et al.*, Phys. Rev. **D 88**, 012002 (2013).

[5] D.S. Akerib *et al.*, Phys. Rev. **D 82**, 122004 (2010); Z. Ahmed *et al.*, Phys. Rev. Lett. **106**, 131302 (2011); J. Angle *et al.*, Phys. Rev. Lett. **107**, 051301 (2011); E. Aprile *et al.*, Phys. Rev. Lett. **109**, 181301 (2012); Z. Ahmed *et al.*, [arXiv:1203.1309 [astro-ph.CO]]

[6] R. Bernabei *et al.*, Eur. Phys. J. **C 67**, 39 (2010); M. Felizardo *et al.*, Phys. Rev. Lett. **108**, 201302 (2012); G. Angloher *et al.*, Eur. Phys. J. **C 72**, 1971 (2012); S. Archambault *et al.*, Phys. Lett. **B 711**, 153 (2012).

[7] D. Hooper, Phys. Dark Univ. **1**, 1 (2012); C. Kelso, D. Hooper, and M.R. Buckley, Phys. Rev. **D 85**, 043515 (2012).

Dark matter directional detection with MIMAC

J. Lamblin[1], *G. Bosson*[1], *O. Bourrion*[1], *O. Guillaudin*[1], *F. Mayet*[1], *J.-F. Muraz*[1], *J.-P. Richer*[1], *Q. Riffard*[1], *D. Santos*[1], *J. Busto*[2], *J. Brunner*[2], *D. Fouchez*[2], *L. Lebreton*[3] , *D. Maire*[3]

[1]LPSC, Universite Joseph Fourier, CNRS/IN2P3, INPG, Grenoble, France
[2]CPPM, Aix-Marseille Universite, CNRS/IN2P3, Marseille, France
[3]LMDN, IRSN Cadarache, Saint-Paul-Lez-Durance, France
E-mail: jacob.lamblin@lpsc.in2p3.fr

DOI: http://dx.doi.org/10.3204/DESY-PROC-2013-04/lamblin_jacob

The MIMAC project aims at the directional detection of dark matter using a gaseous Time Projection Chamber (TPC) which enables the measurement of the energy and the track of low energy nuclear recoils. A 5-liter prototype has been developed and operated during several months. In this paper, after a description of the detector and the calibration procedure, we report the first results of the background studies.

1 Introduction

The dark matter directional detection firstly proposed by Spergel [1] consists in measuring the direction of the nuclear recoil induced by the WIMP-nucleus elastic scattering. Given the earth motion in the galaxy, the WIMPs of the galactic halo are expected to originate from a preferred direction, which corrresponds roughly to the Cygnus constellation. Since the background is supposed to be isotropic in galactic restframe, an anisotropy in the nuclear recoil direction distribution would provide a non-ambiguous signature of WIMP interactions [2]. Phenomenological studies have shown that a $50\,m^3$ detector filled with 10 kg of CF_4 at 50 mbar and operating during 3 years could reach a better sensitivity than the current limits in the spin-dependent interaction parameter space [3]. In case of a positive signal, the measurement of the nuclear recoil direction would also allow to constrain the galactic dark matter properties [4]. The MIMAC project [5] is one of the current R&D projects investigating the feasibility of the directional detection [6]. The proposed detector would be a matrix of TPC allowing the measurement of the 3D tracks and the energy of nuclear recoils down to 20 keV. A first 5-liter prototype has been developped and operated during several months to study the detector performance. In this paper, we first describe the current prototype. Then, we detail the calibration procedure. Finally, we report preliminary results of the background studies.

2 The MIMAC detector

The current MIMAC prototype (see fig. 1) is composed of two TPCs sharing one common cathode. Each TPC is 25 cm long and equipped with a pixelized micromegas detector ($10 \times 10\,cm^2$). Anode pixels are interconnected to constitute 512 X-Y strips with a pitch of $424\,\mu m$. Ionization electrons created by nuclear recoils drift toward the micromegas under an electric field of

$\sim 200\,\mathrm{V/cm}$. The electron avalanche in the micromegas thin gap ($256\,\mu\mathrm{m}$) induces a current on the strips. Every 20 ns, the fired X-Y strips (*i.e.* with a signal higher than a given threshold) are stored, providing two 2D images (X(t) and Y(t)). 3D tracks are obtained by combining these two images. In addition, the current collected on the micromegas grid is also sampled at 50 MHz. The total energy deposited in the detector can be measured by integrating this signal.

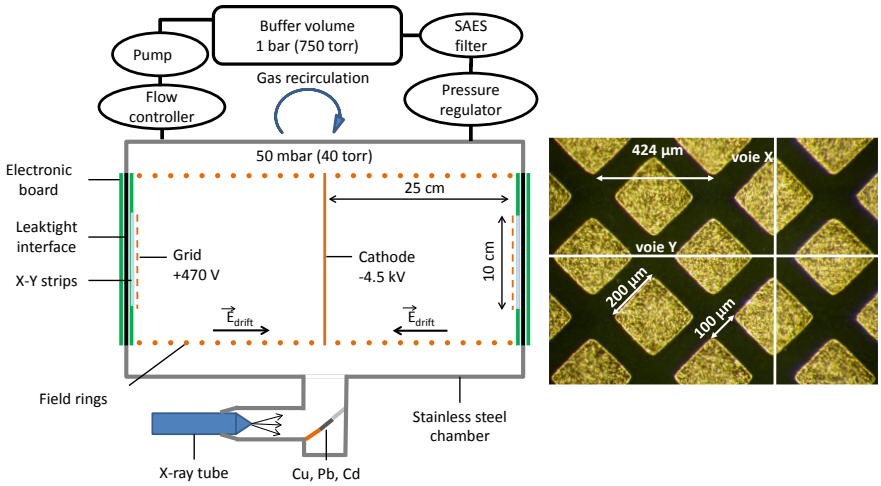

Figure 1: (left) Design of the 5-liter prototype which is composed of two TPC sharing one common cathode. (right) Picture of a portion of the pixelized anode.

The MIMAC detector is filled with a mixture of CF_4 (70 %), CHF_3 (28 %) and C_4H_{10} (2 %). To measure the nuclear recoil directions at very low energy (few tens of keV), the pressure inside the detector has to be as low as 50 mbar. CF_4 has been chosen for its qualities as a detection medium and because fluorine is an excellent target for the WIMP-nucleus spin-dependent interaction. CHF_3 is added to slow down the drift of ionization electrons, which allows for a better track sampling. Finally, C_4H_{10} is used as a quencher to improve the avalanche process in the micromegas gap. To ensure a good charge collection, the gas is permanently recirculated through a SAES filter which removes impurities, mainly H_2O and O_2 molecules.

3 Detector calibration

The detector is calibrated using electronic recoils induced by X-rays. A X-ray tube operated at 20 kV generates X-rays, with a continuous energy spectrum, towards copper, lead and cadmium foils. Secondary X-rays are emitted by fluorescence at several known energies and can interact inside the detector. The orientation of the X-ray tube is chosen in such a way that primary X-rays cannot enter the detector volume. An example of a measured spectrum is shown in figure 2. The spectrum is fitted very well with a sum of six Gaussian functions corresponding to the main expected X-rays, including the ones emitted by the cobalt and iron atoms of the stainless steel chamber. The detector resolution inferred from the Gaussian widths is about 8 % (σ) at 8 keV. The right plot demonstrates the excellent linearity between 3 and 12 keV. The relative size of lead peaks reveals that the detector becomes transparent above 10 keV due to the low pressure. Consequently, it is not possible to use this method at higher energy.

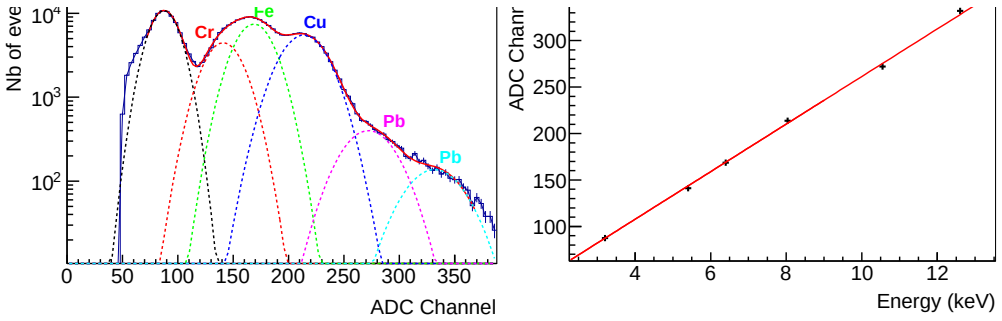

Figure 2: (left) Energy spectrum measured with the X-ray tube and fitted with a sum of 6 Gaussians corresponding to X-ray emitted by fluorescence. (right) Linearity of the detector.

To calibrate the detector at higher energy and in nuclear recoil energy, a new device is under development. This device, which includes an ECR source, is able to generate electrons and ions between 5 keV and 50 keV. These particles are injected inside the detector via a micro hole. This device will be also very useful to characterize all the aspects related to the energy and track measurements (efficiencies, angular resolution, drift dependences, etc.).

4 Background studies

To reach a competitive sensitivity on the WIMP-nucleus spin dependent interaction, a very low background is needed. In summer 2012, the detector has been installed at the Laboratoire Souterrain de Modane (LSM) to identify the main background sources. Thanks to the gas recirculation system, the detector could be operated remotely during several months. A weekly calibration showed that the detector gain was very stable.

The background studies are based on event discrimination using the track and the grid signal. There are several kinds of events. First, electronic recoils due to gamma interactions or beta decays are the dominant background. Most of them can be rejected because they do not have any track or only few-pixel tracks due to their low ionization density. Second, alpha events are easily identified with their very long straight track and their large energy. Remaining events are nuclear recoils. The length of their short tracks is correlated with energy. Nuclear recoils below 100 keV are the most problematic background since they correspond to the WIMP interaction signature. In this paper, only basic and preliminar cuts are used together with a conservative threshold of 20 keV while the trigger threshold is at the keV scale.

The rates of alpha events and nuclear recoil events are presented in figure 3. In normal operation with gas recirculation, the rates are stable: about 200 alphas and 10 nuclear recoils per hour are observed. When the recirculation is switched off, the rates decrease exponentially with a time constant compatible with 3.8 days, the [^{222}Rn] half-life. This demonstrates that the background is dominated by radon decay, and its progeny, coming from outside (probably due to a small leak in the pump). The corresponding contamination of the gas has been estimated to be few 10 mBq/g. Nuclear recoils that are detected correspond to the recoil of daughter nuclei when the alpha decay happens on the edge of the TPC (anode or cathode) and when the alpha is emitted outward from the detector. Daughter nuclei being positively charged, they are expected to drift and to stick on the cathode. The two peaks of the nuclear recoil energy spectrum (see fig. 3) would therefore correspond to the recoils of ^{210}Pb and ^{214}Pb after the

alpha decays of ^{214}Po and ^{218}Po. Given the theoretical recoil energies (112 keV and 146 keV), the mean energies of the peaks (32 keVee and 45 keVee) result in a quenching factor of $\sim 30\,\%$, which is a reasonable value for heavy nuclei. The constant background at higher energies could be explained with alpha events that escape from the detector leaving only a small part of their energy in the detector. The different components of the spectrum can be better separated using more sophisticated cuts, on the track shapes in particular. More details will be given in an upcoming paper.

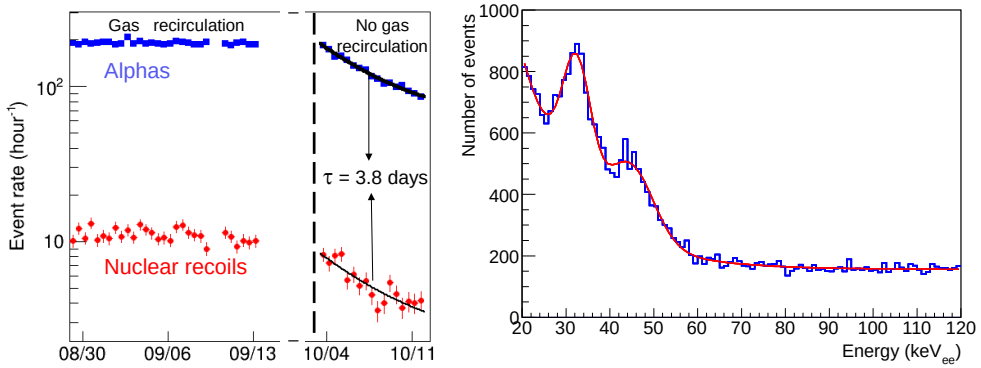

Figure 3: (left) Rate evolution of the alpha and nuclear recoil events. (right) Energy spectrum of the nuclear recoil background.

To reduce the nuclear recoil background, a new recirculation pump with a better leakage rate has been installed. The cathode has been also replaced with a thinner one (12 μm). Together with a time synchronization of both TPC, it will help to reject nuclear recoils emitted from the cathode since alphas should be detected in coincidence. New underground data taking is ongoing to validate these upgrades.

5 Conclusion and Outlook

The 5-liter bi-chamber prototype, which has been developed to investigate the feasibility of a dark matter directional detector, allows to measure the energy and the track of low energy nuclear recoils. The detector calibration using X-ray fluorescence has demonstrated the excellent linearity of the energy scale. The resolution is about 8 % at 8 keV. The first underground data taking in summer 2012 have shown that the dominant source of background is radon and its progeny. Several upgrades have been performed and they are currently tested underground. If the new level of background is low enough, the next step will be to build a detector at the cubic meter scale.

References

[1] D.N. Spergel, Phys. Rev. D **37**, 1353 (1988).
[2] J. Billard *et al.*, Phys. Lett. B **691**, 156 (2010).
[3] J. Billard *et al.*, Phys. Rev. D **85**, 035006 (2012).
[4] J. Billard *et al.*, Phys. Rev. D, **83**, 075002 (2011).
[5] D. Santos *et al.*, EAS Publications Series 53 (2012).
[6] S. Ahlen *et al.*, Int. J. Mod. Phys. A25, 1-51 (2010).

ULB-TH/13-11

Fermi-LAT and the Gamma-Ray Line Search

M. Gustafsson (for the Fermi LAT collaboration)

Service de Physique Théorique, Université Libre de Bruxelles, B-1050 Bruxelles, Belgium

DOI: http://dx.doi.org/10.3204/DESY-PROC-2013-04/gustafsson_michael

A distinct signature for dark matter in the form of weakly interacting massive particles (WIMPs) would be the detection of a monochromatic spectral line in the gamma-ray sky. The Fermi-LAT collaboration has searched for such a line in the energy range from 5 to 300 GeV in five sky regions around the Galactic centre. No globally significant line is detected, and 95% CL upper limits on monochromatic-line strengths are presented. The smallest search region reveals a line-like structure at 133 GeV with a local significance of $2.9\,\sigma$ after 4.4 years of data, which translates to less than 1σ global significance from a trial factor of around 200.

1 Introduction

Today, 80 years after Fritz Zwicky's first observation of a large content of invisible matter in galaxy clusters, the nature of dark matter (DM) still remains a mystery. By multiple observational probes it is by now well established that within the standard cosmological model about 27% of the total energy density of the Universe is in the form of non-baryonic DM [1]. From its presence at the time of the last scattering surface of the cosmic microwave background photons, DM continued to cluster and virialize into extended halos and subhalos that now host galaxy clusters and individual galaxies in their centers. The most well-studied class of models to explain the DM nature is that of weakly interacting massive particles (WIMPs). The WIMPs' interaction with standard model particles put them in thermal and chemical equilibrium in the early Universe. As the Universe expanded and cooled down their interactions stopped, WIMPs were basically no longer diluted by pairwise annihilations, and they 'froze-out', leaving a relic abundance of stable WIMPs that now constitute (cold) DM. The required effective annihilation cross-section for WIMPs to produce the observed DM density turns out to be of the same[1] size that can be probed by the sensitivity of current cosmic-ray telescopes. An instrument such as the Fermi Large Area Telescope (LAT) would indirectly see these WIMPs, if their mass and annihilation channels are favorable, as they pair annihilate in high-densities of DM halos today.

One of the main challenges of detecting signals from WIMPs is that any such signal needs to be discriminated against backgrounds. A smoking-gun signature like a monochromatic line in the cosmic gamma-ray energy-spectrum, caused by annihilation of WIMPs directly into two photons, could become the cornerstone for an unambiguous discovery of a DM particle signal. Recent claims ranging from tentative [2, 3] to strong evidence [4] for a gamma-ray line emission around the Galactic centre in the Fermi-LAT data have already received hundreds of citations. The publication of a careful gamma-ray line search by the Fermi-LAT collaboration [5] has therefore been anticipated.

[1] Notable exceptions where the WIMP annihilation strength today and at freeze-out are different are *e.g.* when cross sections are dominated by p-wave, resonance, threshold, Sommerfeld or coannihilation processes.

2 Analysis chain

2.1 The instrument

The LAT, on board the Fermi gamma-ray space telescope, is primarily a gamma-ray particle detector for energies 20 MeV to above 300 GeV [6]. Incoming photons at these energies have a cross section entirely dominated by pair conversion into e^+e^- due to quantum electrodynamical (QED) interaction with the nucleon fields in atoms. The LAT has therefore been constructed with three detector systems to measure the cosmic gamma-ray flux: a converter/tracker system that promotes the e^+e^- pair conversion and measures the charged particle tracks, a calorimeter composed of CsI(Tl) scintillation crystal layers adding up to 8.6 radiation length to absorb events' energy and provide an energy resolution of $\sim$10% around 100 GeV, and finally an anticoincidence system consisting of plastic scintillator tiles that surrounds the whole tracker to reveal and reject charged cosmic-ray backgrounds that enter the detector with up to 10^6 larger rates than gamma-ray events.

2.2 Event selection

LAT gamma-ray event reconstruction and classification algorithms have received several upgrades before and after the launch [7]. Upgrades are grouped into '`Passes`', and each such pass version includes various event '`Classes`'. These classes, like '`Transient`' or '`Clean`' , are designed to be optimal for different types of analysis, and are sub-samples of events with varying degrees of gamma-ray purity; *i.e.* more efficient cosmic-ray rejection can be provided at the price of degrading the effective area. In the years 2012 and 2013 all collected data were reprocessed using updated calibrations in the instruments reconstruction algorithms, which resulted in the pass `P7REP` data set [7]. In order to prevent cosmic-ray contamination to dominate at high Galactic latitudes, the more selective `Clean` class events were used for the line search. Additional standard quality cuts were performed [5], and only data in the energy range 2.61-541 GeV taken from August 4, 2008 to April 4, 2012 were used for the line limit analysis and data up to December 12, 2012 in the investigation of a line-like feature around 133 GeV. It is worth noticing that the use of this reprocessed `P7REP_CLEAN` (version `v10`, to be precise) data set differs from earlier published line-search studies.

2.3 Regions of interest

Gamma-ray data from five different (but nested) sky regions of interests (ROIs) were used in the WIMP line search. These ROIs are circular regions of radius $R_{\rm GC}$ around the Galactic centre with a rectangular region along the Galactic plane ($|b| < 5^\circ$ and $|l| > 6^\circ$) and with known point sources [8] (except for the smallest ROI) masked out. These sky regions are set up to optimize the signal-to-noise ratio for different assumed DM density profiles with the signal from annihilating or decaying DM on top of a background set by the LAT team's standard model for Galactic and isotropic gamma-ray diffuse emission[2]. The DM distributions considered are a contracted-NFW (inner slope $\gamma = 1.3$), Einasto, NFW, and Isothermal density profiles (as described in [5]). These profiles define the ROIs: R3, R16, R41 and R90 with $R_{\rm GC}$= 3°, 16°, 41° and 90°, respectively, for annihilating DM, and the full sky-region R180 for decaying DM.

[2]Specifically, gal_2yearp7v6 v0.fits and iso p7v6clean.txt, available at http://fermi.gsfc.nasa.gov/ssc/data/access/lat/BackgroundModels.html

2.4 Model of the energy dispersion

WIMPs in our Galaxy are primarily non-relativistic (with velocities $\lesssim 10^{-3}c$), therefore annihilations or decays into monochromatic photons in the center-of-mass frame become negligibly Doppler shifted and would thus be detected as a perfect spectral line by the LAT (as its energy resolution is ∼5-15% $\gg 10^{-3}$). The LAT deploys two separate energy reconstruction algorithms, and a classification-tree scheme is employed to determine event-by-event which algorithm gave the best energy measurement.

A notable analysis improvement (∼15% in sensitivity) compared to previous line searches [9] is achieved by employing a dispersion, or energy probability distribution, model on an event-by-event basis. Each event is assigned a dispersion function $D_{\rm eff}(E')$ based on its reconstruction quality $P_{\rm E}$ (an event quality quantifier arising from the event reconstruction algorithms [7]). The $D_{\rm eff}$ can for each E and P_E be well parametrized by a triple Gaussian function:

$$D_{\rm eff}(E';E,P_{\rm E}) = \sum_{k=1}^{3} -\frac{a_k}{\sigma_k\sqrt{2\pi}} e^{-((E'/E)-(1+\mu_k))^2/2\sigma_k^2}\,, \tag{1}$$

with the 9 parameters a_k and μ_k (constrained by $a_1+a_2+a_3=1$) determined from GEANT4/GLEAM [10] based detector simulations. This 2-dimensional approach (2D as it is a function of both energy E and P_E) is particularly good when the number of signal events are low, as it provides a better description of expected energy dispersion of the actually observed events.

2.5 Fitting method

For the line search, the null hypothesis for the energy spectrum is a single power law, with exponent $\Gamma_{\rm bkg}$ and flux normalization n_{bkg} as free parameters, whereas the signal hypothesis adds a monochromatic line signal with free normalization $n_{\rm sig}$. An exposure correction $\eta(E')$ must be applied to the energy-extended background before it is fitted against observed counts data, while this is already accounted for in the effective dispersion of the line signal. The model, including a line at energy E_γ, is given by

$$C(E',P_{\rm E}|\vec{\alpha}) = n_{\rm sig}D_{\rm eff}(E';E_\gamma,P_{\rm E})w_{\rm sig}(P_{\rm E}) + n_{\rm bkg}\left(\frac{E'}{E_0}\right)^{-\Gamma_{\rm bkg}}\eta(E')w_{\rm bkg}(P_{\rm E})\,, \tag{2}$$

where $\vec{\alpha}$ represent the model parameters E_γ, $\Gamma_{\rm bkg}$ $n_{\rm sig}$ and $n_{\rm bkg}$. The 2D dispersion model turns out to effectively absorb the otherwise significant variation in $D_{\rm eff}$ depending on photons' incident-angles to the LAT. This, when taken together with LAT's fairly uniform exposure of various pointing angles of the full sky and a narrow energy band for each line fit (see below), means that the expected probability distributions $\omega(P_E)$ of P_E for signal and background could be factored out and taken to be approximately equal. Moreover, with $w_{\rm sig}(P_{\rm E}) = w_{\rm bkg}(P_{\rm E}) = w^{\rm ROI}(P_{\rm E})$ the otherwise subtle 'Punzi effect' [11] becomes absent.

A sliding energy-window technique is then used, where each line fit is performed in separate energy bands of $\pm 6\sigma_{\rm E}$ around E_γ (where $\sigma_{\rm E}$ is the energy resolution[3]). The background model of a single power-law is a good approximation in such narrow energy windows. In fact, the use of narrow windows is a way to trade systematic uncertainty in the background model for larger statistical uncertainties. Energy steps of $0.5\sigma_E$ are taken to scan over all E_γ values.

[3] σ_E is defined as the half-width of the ±34% containment about the peak value at E_γ of the energy dispersion for on-axis events.

For a given E_γ, the best-fit values of $\Gamma_{\rm bkg}$, $n_{\rm sig}$ and $n_{\rm bkg}$ (with the restriction of $n_{\rm sig} \geq 0$) are given by maximising the following extended likelihood function for n unbinned events

$$\mathcal{L} = \frac{e^{-C_{\rm tot}}}{n!} \prod_i^n C(E'_i, P_{E_i}), \tag{3}$$

where $C_{\rm tot}$ is the total number of γ rays predicted by the model. In practice, binned fits are performed for $E_\gamma < 25$ GeV to speed up calculations.[4]

2.6 Statistic interpretation

The test statistic is constructed by the maximum likelihood ratio,

$$TS = 2\ln\frac{\mathcal{L}(n_{\rm sig} = n_{\rm sig,best})}{\mathcal{L}(n_{\rm sig} = 0)}. \tag{4}$$

The application of Chernoff's theorem [12] predicts that the TS distribution is $\frac{1}{2}\delta(TS) + \frac{1}{2}\chi^2(TS)$, with χ^2 of one degree of freedom. The local significance, in units of standard deviations (σ), is then defined[5] as the square-root of TS:

$$s_{\rm local} = \sqrt{TS}. \tag{5}$$

A line is fitted at 88 different E_γ values in R16, R41, R90 and R180, and 44 in R3[6], giving a total of 396 trial fits. These trials are not independent, as ROIs are nested and energy steps not fully separated. The effective number of trials is (*cf.* trial factor $\equiv p_{\rm global}/p_{\rm local}$)

$$n_t(s_x) \equiv \frac{\log(1 - p_{\rm global})}{\log(1 - p_{\rm local})}, \tag{6}$$

defined from the two p-values $p_{\rm global}$ and $p_{\rm local}$ that are, respectively, the probability of a *local* trial to have a $\sqrt{TS}$ larger than some value s_x, and the *global* (*i.e.* post all trials) probability that the maximal $\sqrt{TS}$ is larger than s_x. Empirically, from performing pseudo experiments on 1000 Monte Carlo generated background simulations, it was found that an effective number of trials $n_t \simeq 198 \pm 6$ gives a very good description for conversion from local to global significance.

3 Results

The local significances, defined in Eq. (5), for all tested energies and the five ROIs are shown in the left panels of Fig. 1. The largest significances are found at 135 GeV in R3 and at 6.3 GeV in R180; with significances $s_{\rm local}$=3.2σ and 3.1σ, respectively. A finer grid scan ($0.1\sigma_E$ steps) revealed that the best-fit is at 133 GeV, with $s_{\rm local} = 3.3\sigma$ and signal-to-background ratio $f_{\rm R3} = 0.61 \pm 0.19$. However, taking into account that the effective number of trials is about 200 (or about 300 for the finer $0.1\sigma_E$ steps) in the search for a spectral line in the data, their global statistical significances are less than 2σ.

[4] By the use of 60 bins, which is much narrower than the energy resolution, the information loss is negligible.
[5] Significance, expressed as N standard deviations, will be defined by $\frac{1}{2}\int_{N^2}^{\infty}\chi^2(x)\,{\rm d}x = p$-value.
[6] Energies were restricted to above 30 GeV in R3 to avoid complication due to a comparably large LAT point-spread-function and the many known point sources at the lowest energies in this ROI.

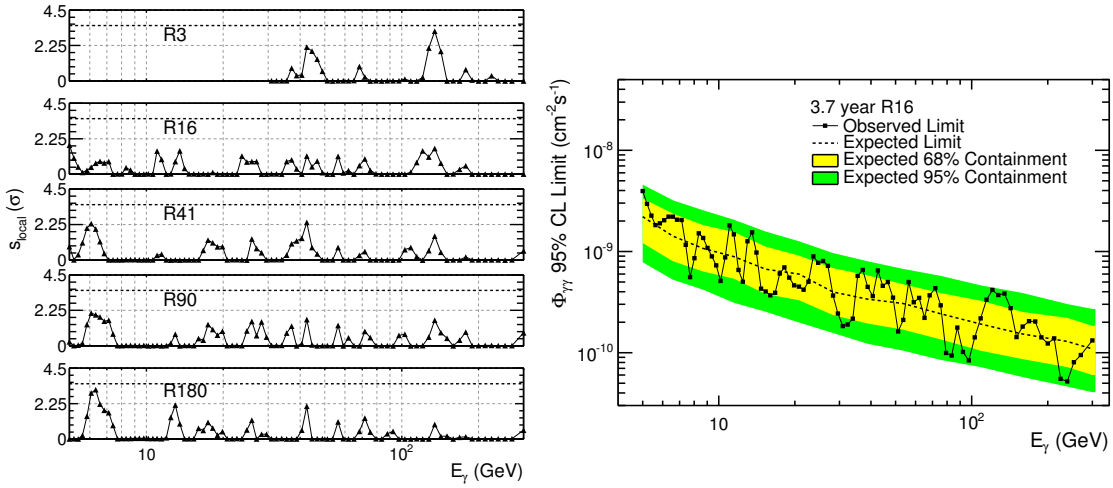

Figure 1: LEFT PANEL: Local fit significance vs. line energy in all five ROIs. The dashed line at the top of the plot indicates the local significance corresponding to 1.7σ global significance[5] derived with $n_t = 198$ in Eq. (6). RIGHT PANEL: 95% CL $\Phi_{\gamma\gamma}$ in the R16 ROI (black). Yellow (green) bands show the 68% (95%) expected containment derived from 1000 single-power law (no DM) MC simulations. The dashed lines show the median expected limits from those simulations.

An upper limit on $n_{\rm sig}(E_\gamma)$ is set at the point when the logarithm of the likelihood in Eq. (3) is decreased by factor 1.36 compared to its maximal value. This corresponds to a 95% confidence-level (CL) upper limit on $n_{\rm sig}$ (bounded to be positive). A limit on $n_{\rm sig}$ can then be directly converted to a 95% CL upper limit on the line flux by

$$\Phi_{\gamma\gamma}(E_\gamma) = \frac{n_{\rm sig}(E_\gamma)}{\mathcal{E}_{ROI}(E_\gamma)}, \tag{7}$$

where $\mathcal{E}_{ROI}$ is the LAT average exposure for the relevant ROI. The upper limits on line fluxes in region R16 are shown in the right panel of Fig. 1.

To translate a flux limit into a velocity averaged annihilation cross section ($\langle\sigma v\rangle$) or decay life-time (τ) limit requires the integrated signal contribution along the line-of-sight (s) and solid angle (Ω) spanned by the ROI. The differential γ-ray flux from annihilation of self-conjugated WIMPs is:

$$\frac{d\Phi_{\gamma\gamma}}{dE} = \frac{1}{8\pi}\frac{\langle\sigma v\rangle}{m_\chi^n}\frac{dN_\gamma}{dE}J, \quad \text{with} \quad J = \int \rho_{\rm DM}^n ds d\Omega, \tag{8}$$

where m_χ is the WIMP mass, and $n = 2$ in the exponent of the DM density ($\rho_{\rm DM}$) in the 'J-factor'. Prompt annihilation into two photons yields $dN_\gamma/dE = 2\delta(E_\gamma - E)$ with $E_\gamma = m_\chi$. Integration over the energy E is trivial, and a bound on $\Phi_{\gamma\gamma}$ directly translates to a $\langle\sigma v\rangle$ bound for a given J value. Figure 2 shows the limits from the contracted NFW profile and the Einato profile; with $J_{\rm R3} = 13.9 \cdot 10^{22}$ GeV^{2}cm^{-5} and $J_{\rm R16} = 8.48 \cdot 10^{22}$ GeV^{2}cm^{-5} in their optimized ROI. In the case of decaying DM into *one* monochromatic photon, perform the following replacements $\langle\sigma v\rangle \to 1/\tau$, $n \to 1$, $m_\chi \to m_\chi/2$, and $dN_\gamma/dE = \delta(m_\chi/2 - E)$ to calculate $\Phi_{\gamma\gamma}$.

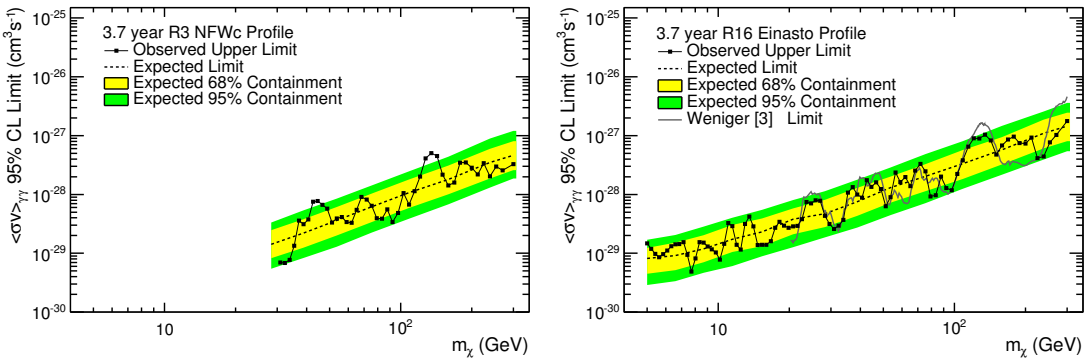

Figure 2: 95% CL $\langle\sigma v\rangle_{\gamma\gamma}$ upper limits for our contracted NFW and Einasto DM profile in ROI R3 and R16, respectively. Colored bands and lines are defined as in Fig. 1. The solid gray line shows the limits derived in [3] for a comparable ROI and identical DM density profile.

3.1 Systematic uncertainties

Systematic uncertainties are not included in the presented limits, therefore it is important to investigate how much this could alter the results. Table 1 summaries the potential size of such effects, where uncertainties have been split into three classes [5]:

1. Those that would induce a false signal or mask a true signal δf; from *e.g.* unmodeled variation in the effective area, imperfect background model and cosmic-ray contamination.
2. Those that would scale the fit estimates of the number of signal counts $\delta n_{\rm sig}$; from *e.g.* imperfect line dispersion model and E_γ grid spacing.
3. Signal to flux conversion uncertainties $\delta\mathcal{E}$; from exposure and effective area uncertainties.

Quantity	Energy	R3/R16	R180
δf	5 GeV	±0.020	±0.008
δf	50 GeV	±0.024	±0.015
δf	300 GeV	±0.032	±0.035
$\delta n_{\rm sig}/n_{\rm sig}$	All	$^{+0.07}_{-0.12}$	$^{+0.07}_{-0.12}$
$\delta\mathcal{E}/\mathcal{E}$	5 GeV	±0.10	±0.14
$\delta\mathcal{E}/\mathcal{E}$	300 GeV	±0.10	±0.16

Table 1: Magnitude of systematic effects, by ROI and Energy, where all contributing uncertainties have been added in quadrature.

One can now see that the systematic uncertainty δf in R180 at low energies is of the order 1%, which therefore could be an explanation for the 3.1σ signal significance seen at 6.3 GeV that had $f = 0.010 \pm 0.002$. The signal fraction for the 135 GeV feature is, on the other hand, $f = 0.58 \pm 0.18$ in R3 and thus much larger than known systematic effects. Notably, a spectral structure at 133 GeV with a significance of 2.0σ is also found in Earth albedo/limb data, which is used as a (DM free) bright gamma-ray control-region. This could indicate an instrumental issue at 133 GeV, but due to its much smaller signal-to-background fraction $f = 0.14 \pm 0.07$ and no line-like structure detected in a second control region, the Galactic plane, the line-like signal around the Galactic center cannot unambiguously be attributed to any instrumental effect.

3.2 Line-like feature at 133 GeV

The most significant fit from the line search was at E_γ=135 GeV in the R3 search region. Several steps in investigating the significance and properties of this spectral structure have been made.

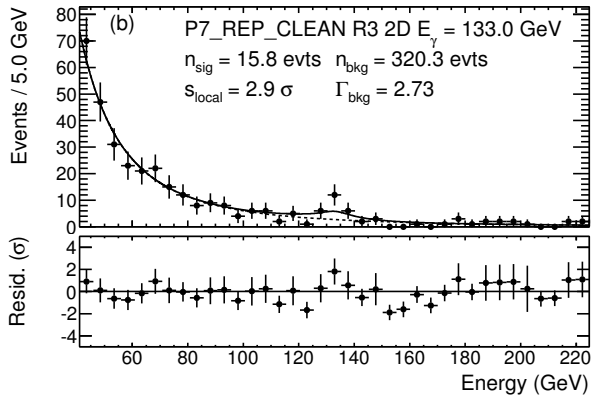

Figure 3: Fit for a line-signal signal at 133 GeV in R3 using a 4.4 year `P7REP_CLEAN` dataset with the 2D energy dispersion model. The solid curve shows the average model weighted using the P_E distribution of the fitted events. The data binning is only for visualization purposes.

The impact of various changes in datasets and modeling the signal can be summarized as:

- 3.7 years `P7_CLEAN` (un-reprocessed) data with a 1D dispersion (no use of P_E) line fit gives: $s_{\rm local} = 4.5\sigma$ at 130 GeV.
- 3.7 years `P7REP_CLEAN` (reprocessed) data with a 1D dispersion (no use of P_E) line fit gives: $s_{\rm local} = 4.1\sigma$ at 133 GeV.
- 3.7 years `P7REP_CLEAN` (reprocessed) data with a 2D dispersion (including P_E) line fit gives: $s_{\rm local} = 3.3\sigma$ at 133 GeV.
- 4.4 years `P7REP_CLEAN` (reprocessed) data with a 2D dispersion (including P_E) line fit gives: $s_{\rm local} = 2.9\sigma$ at 133 GeV.

The first point allows a good comparison to previous works and, even if *e.g.* our ROI differ somewhat from others works [3], it is clear that a local significance of above 4σ can be reached with this setup. In the next point, when reprocessed data is analyzed, the significance becomes about 10% smaller. Gamma-ray events might switch `classes` [13] due to reprocessed data, and it is only about 70-80% overlap of events in `P7_CLEAN` and `P7REP_CLEAN`. The shift of E_γ of 130 to 133 GeV is due to the correction of a known $\sim$1% per year degrading in light yield efficiency in the calorimeter crystals. The next point incorporates the switch to the 2D dispersion model given in Eq. (1), which decreases the significance by around 20%. The actual events around 133 GeV have lower P_E on average than expected, which cause the dispersion function to broaden and lower the likelihood value for events close to 133 GeV. In Fig. 3 it is clearly visible how the line-like feature seems narrower than the expected LAT energy dispersion. To quantify this, a rescaled energy width of our 2D dispersion was tested. The best-fit result was to rescale the width by a factor $s_\sigma = 0.32^{+0.11}_{-0.07}$, which also increased TS by 9.4. Pre-launch beam tests show however that the width is known within 10% up to 280 GeV, and this $\sim$0.32 times narrower dispersion functions is thus inconsistent with the pre-measured shape at the 2-3σ level. Finally, the last point includes more data (extending from 3.7 to 4.4 years) which further reduces the significance by about 10%, to a local significance of 2.9σ.

It is worth mentioning that the actual amount of change in significance depends on the specific ROI. For example, for Weniger's analysis in his Region 3 [3], the impact of going from

P7_CLEAN to P7REP_CLEAN dilutes the original significance of 4.3σ to 2.8σ, and then by utilizing a 2D dispersion model to 2.4σ, and finally by also extending to 4.4 years of data diminishes the local significance furter to 2.0σ [14]. All these additional tests around E_γ=133 GeV are outside the original line search, so their contribution to the trials factor is difficult to estimate precisely. It is however clear that taking the 2D dispersion model, applied to the 4.4 years reprocessed data-set, gives a 2.9σ local significance, which is less than a 1σ global significance when a trail factor of $\sim$200 is applied.

4 Summary and outlook

The hint of a line signal around 130 GeV towards the Galactic centre has resulted in enormous interest, as it could be a long-sought WIMP DM signal. The Fermi-LAT Collaboration has searched for spectral lines from 5-300 GeV in five ROIs without finding any globally significant lines. A line-like feature at 133 GeV with a signal-to-noise fraction larger than known systematic effects is present. However, with reprocessed P7REP_CLEAN data, improved 2D line dispersion model and including 4.4 years of data the local significance is 2.9σ, which translate to a global significance below 1σ. A statistical fluctuation is therefore a possible explanation. It will be very interesting to re-perform a line search with Fermi-LAT's upcoming Pass 8 data set [15], which will provide a larger effective area and the benefit of having almost all event reconstruction algorithms rewritten. The Fermi users' group has also already endorsed a recommendation that the Fermi mission undertake a new observing strategy that emphasizes coverage of the Galactic center region from December 2013 – which would lead to, on average, a doubled exposure rate of the region around the Galactic centre compared with the currently used survey mode.

M.G. is supported by the Belgian Science Policy (IAP VII/37), the IISN and the ARC project.The *Fermi* LAT Collaboration acknowledges support from a number of agencies and institutes. These include NASA and DOE in the United States, CEA/Irfu and IN2P3/CNRS in France, ASI and INFN in Italy, MEXT, KEK, and JAXA in Japan, and the K. A. Wallenberg Foundation, the Swedish Research Council and the National Space Board in Sweden. Additional support from INAF in Italy and CNES in France for science analysis during the operations phase is also gratefully acknowledged.

References

[1] P. A. R. Ade *et al.* [Planck Collaboration], arXiv:1303.5076 [astro-ph.CO].
[2] T. Bringmann, X. Huang, A. Ibarra, S. Vogl and C. Weniger, JCAP **1207**, 054 (2012) [arXiv:1203.1312].
[3] C. Weniger, JCAP **1208**, 007 (2012) [arXiv:1204.2797].
[4] M. Su and D. P. Finkbeiner, arXiv:1206.1616 [astro-ph.HE].
[5] M. Ackermann *et al.* [Fermi-LAT Collaboration], arXiv:1305.5597 [astro-ph.HE]. Accepted in PRD.
[6] W. B. Atwood *et al.* [Fermi-LAT Collaboration], Astrophys. J. **697**, 1071 (2009) [arXiv:0902.1089].
[7] M. Ackermann *et al.* [Fermi-LAT Collaboration], Astrophys. J. Suppl. **203**, 4 (2012) [arXiv:1206.1896].
[8] P. L. Nolan *et al.* [Fermi-LAT Collaboration], Astrophys. J. Suppl. **199**, 31 (2012) [arXiv:1108.1435].
[9] M. Ackermann *et al.* [LAT Collaboration], Phys. Rev. D **86**, 022002 (2012) [arXiv:1205.2739].
[10] S. Agostinelli *et al.* [GEANT4 Collaboration], Nucl. Instrum. Meth. A **506**, 250 (2003).
[11] G. Punzi, eConf C **030908**, WELT002 (2003) [physics/0401045].
[12] H. Chernoff, Annals Math. Statist. **25**, 573 (1938)
[13] J. Bregeon *et al.* [Fermi-LAT Collaboration], arXiv:1304.5456 [astro-ph.HE].
[14] Private communication with Christoph Weniger.
[15] W. Atwood *et al.* [Fermi-LAT Collaboration], arXiv:1303.3514 [astro-ph.IM].

Cosmic-ray research with AMS-02 on the International Space Station

H. Gast for the AMS Collaboration

I. Physikalisches Institut B, RWTH Aachen University

DOI: http://dx.doi.org/10.3204/DESY-PROC-2013-04/gast_henning

Henning Gast gave a talk on new results of the AMS-02 detector onboard the ISS. Three weeks after the Patras Workshop in Mainz, updated AMS results were presented at the 33rd International Cosmic Ray Conference (ICRC) and are described in the corresponding proceedings in detail.
For convenience of the Patras participants, the editors collected the following links to the respective AMS publications in addition to the slides that are available on the conference website.

References

[1] S. Haino et al., "Precision measurement of the proton flux with AMS," https://143.107.180.38/indico/contributionDisplay.py?sessionId=3&contribId=1265&confId=0.

[2] V. Choutko et al., "Precision measurement of the helium flux with AMS," https://143.107.180.38/indico/contributionDisplay.py?sessionId=3&contribId=1262&confId=0.

[3] A. Kounine et al., "Precision measurement of the positron fraction with AMS," https://143.107.180.38/indico/contributionDisplay.py?sessionId=3&contribId=1264&confId=0.

[4] S. Schael et al., "Precision measurements of the electron spectrum and the positron spectrum with AMS," https://143.107.180.38/indico/contributionDisplay.py?sessionId=3&contribId=1257&confId=0.

[5] B. Bertucci et al., "Precision measurement of the electron plus positron spectrum with AMS," https://143.107.180.38/indico/contributionDisplay.py?sessionId=3&contribId=1267&confId=0.

[6] A. Oliva et al., "Precision measurement of the boron to carbon ratio and nuclei with AMS," https://143.107.180.38/indico/contributionDisplay.py?sessionId=3&contribId=1266&confId=0.

[7] J. Casaus et al., "Determination of anisotropy with AMS," https://143.107.180.38/indico/contributionDisplay.py?contribId=1261&confId=0&sessionId=3.

Chapter 7

WISP Theory

Extended Axion Electrodynamics, relic Axions and Dark Matter Fingerprints in the terrestrial electromagnetic Field

A. Balakin

Kazan Federal University, Kazan, Russia

DOI: http://dx.doi.org/10.3204/DESY-PROC-2013-04/balakin_alexander

We consider extended versions of the Einstein-Maxwell-axion model based on the Lagrangian, which is linear in the pseudoscalar (axion) field, linear or quadratic in the gradient four-vector of the axion field, linear in the Riemann tensor, and includes the four-vector of macroscopic velocity of the system. We discuss applications to four problems, which are connected with axion-photon-graviton coupling in the anisotropic Bianchi-I cosmology, optical activity in the isotropic Friedmann-type universe, non-minimal effects in the plane gravitational waves background, and evolution of terrestrial magnetic and electric fields in the axion dark matter environment.

1 Introduction

Fundamentals of the theory of axions, massive particles, which were predicted by Peccei and Quinn [1] and introduced into the high-energy physics as new light pseudo-bosons by Weinberg [2] and Wilczek [3], are well-described (see, e.g., [4]-[6]). We are interested in extension of the theory of coupling between electromagnetic and pseudoscalar fields based on axion electrodynamics [7]-[10]. Why do we think that the extension of the axion-photon coupling theory is necessary? The main argument is that natural and artificial electromagnetic waves propagate (hypothetically) in the axionic dark matter environment, which has to be considered as a quasi-medium. This axionic quasi-medium has to be chiral, since the axion-photon interactions are predicted to induce the effect of polarization rotation. This axionic quasi-medium has to be non-stationary because of cosmological (accelerated) expansion. Also, it should be spatially non-homogeneous and anisotropic, since the density of the dark matter depends on the distance to the Galactic center. But, if we deal with an axionic quasi-medium, we have to describe the axion-photon coupling in terms of axion electrodynamics of continuous media rather than in terms of vacuum electrodynamics. This means that the theory of axion-photon coupling has to involve into consideration the velocity four-vector of the system as a whole, U^i, and its covariant derivative $\nabla_i U_k$, thus predicting, respectively, the existence of dynamic and dynamo-optic phenomena in the electromagnetic system. Besides, in addition to the pseudoscalar field itself, ϕ, this theory has to include the gradient four-vector of the pseudoscalar field, $\nabla_i \phi$. The quantity $\dot{\phi} = U^i \nabla_i \phi$ is responsible for the non-stationarity of the effect of axionically induced optical activity; the spatial part of this gradient, describing inhomogeneity and anisotropy of the system, can be the reason of axionically induced birefringence.

2 On the scheme of the theory extension

The standard Einstein-Maxwell-axion theory is based on the Lagrangian

$$S = \frac{\hbar}{c}\int d^4x\sqrt{-g}\left\{\frac{1}{2\kappa}\left[R{+}2\Lambda\right] + \frac{1}{4}\left[F_{mn}F^{mn}{+}\phi F^{*}_{mn}F^{mn}\right] - \frac{1}{2}\Psi_0^2\left[\nabla_m\phi\nabla^m\phi{-}V(\phi^2)\right]\right\}.$$

The extension of the electromagnetic part of this Lagrangian can be made by the replacement

$$\frac{1}{4}\left[F_{mn}F^{mn}{+}\phi F^{*}_{mn}F^{mn}\right] \;\;\Rightarrow\;\; \frac{1}{4}F_{pq}F_{mn}\cdot C^{pqmn}\left[g^{ik}, U^i, \nabla_i U_k, \phi, \nabla_i\phi, R_{ikmn}\right],$$

where the linear response tensor C^{pqmn} depends now not only on the metric g_{ik}, and on the pseudoscalar field ϕ, but also on the macroscopic velocity U^i, its covariant derivative $\nabla_i U_k$, on the gradient four-vector $\nabla_i\phi$, and finally, on the Riemann tensor R_{ikmn} and its convolutions. Similarly, the axionic part of the Lagrangian can be extended as follows:

$$\frac{1}{2}\Psi_0^2\nabla_m\phi\nabla^m\phi \;\;\Rightarrow\;\; \frac{1}{2}\Psi_0^2\nabla_m\phi\nabla_n\phi\cdot\mathcal{C}^{mn}\left[g^{ik}, U^i, \nabla_i U_k, F_{pq}, R_{ikmn}\right].$$

The tensor $\mathcal{C}^{mn}$ in principle can be a linear function of the Maxwell tensor F_{pq}. Let us consider three simplest examples in order to illustrate the idea of the model extensions.

2.1 The model linear in the axion field and its gradient four-vector

The simplest model is linear in the pseudoscalar field ϕ and its gradient four-vector, $\nabla_i\phi$. As it was proved in [11], all possible variants of this type can be reduced to the model with the linear response tensor of the form

$$C^{ikmn} = \frac{1}{2}\left(g^{im}g^{kn}{-}g^{in}g^{km}\right){+}\frac{1}{2}\epsilon^{ikmn}\left(\phi + \nu\; U^i\nabla_i\phi\right)$$

with one new coupling constant ν introduced phenomenologically (here ϵ^{ikmn} is the absolutely skew-symmetric Levi-Civita tensor). In this model only the structure of the tensor of magneto-electric cross-effect, $\nu_p{}^m$, is changed:

$$\nu_p{}^m = \epsilon_{ikpq}U^q C^{ikmn}U_n = -\Delta_p^m\left(\phi + \nu\dot{\phi}\right), \qquad \Delta_p^m = \delta_p^m - U_pU^m,$$

and the new term $\nu\dot{\phi}$ describes a non-stationarity in the polarization rotation effect induced by the axionic dark matter [11].

2.2 The model quadratic in the gradient four-vector of the axion field

This model is the two-parameter one [12], and it is described by the linear response tensor

$$C^{ikmn} = \frac{1}{2}\left(g^{im}g^{kn}{-}g^{in}g^{km}\right)\left(1{+}\lambda_1\nabla_p\phi\nabla^p\phi\right){+}\frac{1}{2}\phi\epsilon^{ikmn}{+}\frac{\lambda_2}{2}\left(g^{i[m}\nabla^{n]}\phi\nabla^k\phi{+}g^{k[n}\nabla^{m]}\phi\nabla^i\phi\right).$$

The corresponding dielectric permittivity tensor

$$\varepsilon^{im} = \Delta^{im}\left[1 + \lambda_1\overset{\perp}{\nabla}_q\phi\overset{\perp}{\nabla}{}^q\phi + \left(\lambda_1 + \frac{1}{2}\lambda_2\right)\dot{\phi}^2\right] + \frac{1}{2}\lambda_2\overset{\perp}{\nabla}{}^i\phi\overset{\perp}{\nabla}{}^m\phi,$$

and the tensor of magnetic impermeability

$$\left(\mu^{-1}\right)_{im} = \Delta_{im}\left[1+\lambda_1\dot{\phi}^2+\left(\lambda_1+\frac{1}{2}\lambda_2\right)\overset{\perp}{\nabla}_q\phi\overset{\perp}{\nabla}^q\phi\right]-\frac{1}{2}\lambda_2\overset{\perp}{\nabla}_i\phi\overset{\perp}{\nabla}_m\phi$$

become anisotropic, when the spatial part of the gradient four-vector $\overset{\perp}{\nabla}_i\phi = \Delta_i^k\nabla_k\phi$ is non-vanishing. This means that axionic dark matter is (in general case) a birefringent quasi-medium. As for the tensor of magneto-electric cross-effects

$$\nu^{pm} = -\phi\Delta^{pm}+\frac{1}{2}\lambda_2\dot{\phi}\,\epsilon^{pmkq}U_q\,\overset{\perp}{\nabla}_k\phi\,,$$

it demonstrates the possibility of a new type of optical activity, which can be realized, when the axionic dark matter is non-stationary and non-homogeneous simultaneously.

When we consider the applications to homogeneous cosmological models (anisotropic model of the Bianchi-I type with magnetic field, or isotropic model of the Friedmann type, see [12, 11]), we obtain the following expressions for the permittivity scalars and refraction index, respectively:

$$\varepsilon(t) = 1+\left(\lambda_1+\frac{1}{2}\lambda_2\right)\dot{\phi}^2\,,\quad \frac{1}{\mu(t)} = 1+\lambda_1\dot{\phi}^2\,,\quad n^2(t) = \varepsilon(t)\mu(t) = \frac{1+\left(\lambda_1+\frac{1}{2}\lambda_2\right)\dot{\phi}^2}{1+\lambda_1\dot{\phi}^2}\,.$$

Keeping in mind that the quantity $\dot{\phi}^2$ can be expressed using the mass density of the axionic cold dark matter $\rho_{(\mathrm{DM})}$ as $\dot{\phi}^2 = c^2\Psi_0^{-2}\rho_{(\mathrm{DM})}$ (see [12]), we obtain useful phenomenological formulas for the refraction index of the axionic dark matter as a function of cosmological time, and of the phase velocity $v_{\mathrm{ph}}=\frac{c}{n(t)}$ of the electromagnetic waves, which propagate in the axionic dark matter quasi-medium. The obtained function $n^2(t)$ can be (in principle) negative during some epoch, and because of axion-photon coupling in this (unlighted) epoch the electromagnetic waves do not propagate in the Universe, do not scan its internal structure and can not bring information to observers (see [13] for details).

One of the most important consequences of the gradient-type model of the axion-photon coupling is the following. Backreaction of the electromagnetic field on the pseudoscalar field evolution is shown to produce inflationary-type growth of the number of axions in the early Universe, and these axions become relic at present time and form now the axionic dark matter.

2.3 Non-minimal models

Non-minimal Einstein-Maxwell-axion models can be obtained, if the linear response tensor

$$\mathcal{C}^{ikmn} = \frac{1}{2}\left(g^{im}g^{kn}-g^{in}g^{km}\right)+\frac{1}{2}\phi\epsilon^{ikmn}+\mathcal{R}^{ikmn}+\frac{1}{2}\phi\left[\chi_{(\mathrm{A})}^{*ikmn}+^{*}\chi_{(\mathrm{A})}^{ikmn}\right]$$

is equipped by the terms $\mathcal{R}^{ikmn}$ and $\chi_{(\mathrm{A})}^{*ikmn}$ linear in the Riemann tensor R_{ikmn}, Ricci tensor R_{ik} and Ricci scalar R (see [14, 15] for details). The analysis of such models in application to the problem of gravitational wave action on the axion-photon system shows, that when the axion field is constant $\phi = \phi(0)$, and thus is hidden from the electrodynamic point of view, the coupling to curvature removes the degeneracy with respect to hidden pseudoscalar field, providing visualization of the effects of birefringence and optical activity induced by axion-photon coupling.

3 Outlook

Analysis of the extended models of axion electrodynamics shows that there is a chance to verify experimentally the predictions of the model of interaction of terrestrial magnetic and electric fields with the relic axion background (see [16] for details). The idea, based on the corresponding exact solutions, is the following. Relic dark matter axions produce in the terrestrial electrodynamic system oscillations of a new type, which belong to the class of longitudinal magneto-electric clusters. These oscillations have the following specific feature: the electric and magnetic fields are parallel to one another and are coupled by axion field; in the absence of axions such oscillations decouple. Electric and magnetic fields of this type are correlated, and the oscillations are characterized by identical frequencies. Generally, there are two sets of hybrid frequencies of longitudinal oscillations, which belong to the range $\nu_{\rm A} \simeq 10^{-3} - 10^{-5}$Hz. Optimistic estimations of the dimensionless parameter ξ, which characterizes the ratio between the amplitude of axionically induced electromagnetic oscillations and amplitude of their (electric or magnetic) sources, give the value of the order $\xi \simeq 10^{-7}$ for the mass density of the dark matter in the Solar system of the order $\rho_{\rm (DM)} \simeq 0.033\ M_{\rm (Sun)}{\rm pc}^{-3}$ and for the axion-photon coupling constant $g_{\rm A\gamma\gamma} \simeq 10^{-9}{\rm GeV}^{-1}$. We are waiting for the first results of the experiments with infra-low frequency variations of the terrestrial electric and magnetic fields, which are organized in the Vladimir University (Russia), and hope to find fingerprints of relic axions in the correlated components of the signals of longitudinal electric and magnetic field variations.

Acknowledgments

The work was partially supported by the Russian Foundation for Basic Research (Grants Nos. 11-02-01162 and 11-05-97518), and by the Russian Federal Targeted Program N14.T37.21.0668.

References

[1] R.D. Peccei, H.R. Quinn, Phys. Rev. Lett. **38**, 1440 (1977).

[2] S. Weinberg, Phys. Rev. Lett. **40**, 223 (1978).

[3] F. Wilczek, Phys. Rev. Lett. **40**, 279 (1978).

[4] R.D. Peccei, Lect. Notes Phys. **741**, 3 (2008).

[5] P. Sikivie, Lect. Notes Phys. **741**, 19 (2008).

[6] R. Battesti *et al.*, Lect. Notes Phys. **741**, 199 (2008).

[7] W.-T. Ni, Phys. Rev. Lett. **38**, 301 (1977).

[8] P. Sikivie, Phys. Rev. Lett. **51**, 1415 (1983).

[9] F. Wilczek, Phys. Rev. Lett. **58**, 1799 (1987).

[10] S.M. Carroll, G.B. Field, R. Jackiw, Phys. Rev. **D 41**, 1231 (1990).

[11] A.B. Balakin, N.O. Tarasova, Gravitation and Cosmology **18**, 54 (2012) [arXiv:1201.3010 [gr-qc]].

[12] A.B. Balakin, V.V. Bochkarev, N.O. Tarasova, EPJC, **72**, 1895 (2012) [arXiv:1201.3009 [gr-qc]].

[13] A.B. Balakin, V.V. Bochkarev, J.P.S. Lemos, Phys. Rev. D **85**, 064015 (2012) [arXiv:1201.2948 [gr-qc]].

[14] A.B. Balakin, W.-T. Ni, Class. Quantum Grav. **27**, 055003 (2010) [arXiv:0911.2940 [gr-qc]].

[15] W.-T. Ni, A.B. Balakin, H.-H. Mei, Proceedings of the Conference in Honour of Murray Gell-Mann's 80th birthday. World Scientific Publishing Co. 2011, pp. 526-535. [arXiv:1109.0581 [hep-ph]].

[16] A.B. Balakin, L.V. Grunskaya, Rep. Math. Phys. **71**, 45 (2013) [arXiv:1209.6261 [gr-qc]].

Solution to the Isotropy Problem for Cosmological Hidden Vector Models

J.A.R. Cembranos, A.L. Maroto and S.J. Núñez Jareño

Departamento de Física Teórica I, Universidad Complutense de Madrid, E-28040 Madrid, Spain

DOI: http://dx.doi.org/10.3204/DESY-PROC-2013-04/cembranos_jose

Gauge bosons associated to new gauge symmetries under which the standard model particles are not charged are predicted in many extensions of the standard model of particles and interactions. We show that under very general conditions, the average energy-momentum tensor of these rapidly oscillating vector fields is isotropic for any locally inertial observer. This result has a fundamental importance in order to consider coherent vector fields as a viable alternative to support models of dark matter, dark energy or inflation.

1 Introduction

Despite the large improvement in our knowledge about cosmology in the last decades, there are various puzzles associated with basic features of the history of the universe. For instance, observational data favour the existence of inflation in the early universe, or the existence of dark matter and dark energy at later times. However, the intimate nature of these components remains undetermined. A possible solution to these questions has been formulated in terms of coherent rapid oscillations of bosonic fields. In this context, scalar models have been traditionally proposed for inflation [1]. Scalar massive particles, such as axions [2], or other massive scalar [3] or pseudoscalar particles [4] have been considered standard candidates as non-thermal relics. Oscillating scalar fields have also been studied as dark energy models [5].

2 Hidden vector models in cosmology

The same approach to these open questions is offered by vector fields. Indeed, a large number of vector models have been studied in relation with cosmology [6]. For instance, inflationary models can be supported by vectors [7, 8, 9, 10, 11, 12]. Isotropic and homogeneous triad configurations of non-abelian vector gauge bosons have been recently considered as a viable model that can be supported even by the standard QCD action [13] (read [14] however).

Vector modes have been also studied as the origin of metric perturbations in the so called curvaton scenario [15]. Coherent oscillations of massive vector fields have been analyzed as non-thermal dark matter candidates in [16] and its phenomenology merges within general hidden photons models [17, 18, 19]. There are also a rich variety of vector dark energy models, with potential terms [20] or without them [21].

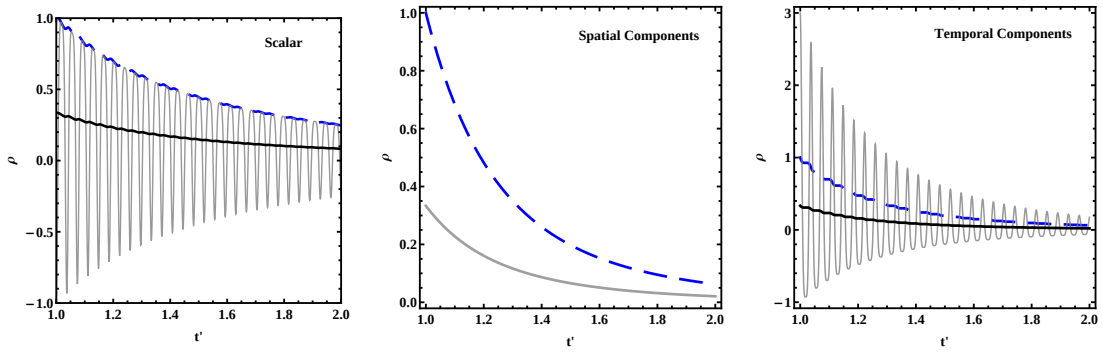

Figure 1: Graphical representation of different energy components of a scalar field (left), spatial components of a vector field (center) and its temporal component (right) for a quartic potential. In particular, one can observe the evolution of the average pressure along the three spatial directions p (grey line), energy density (blue dashed line) and average pressure $\langle p \rangle = \langle \rho \rangle / 3$ (black line). The evolution is compute in a radiation dominated-universe, the y-axis is normalized to the initial value $\rho(t'_0)$ and time, t', is in H_0^{-1} units. For this concrete case, the spatial components of a vector field verify $\langle p \rangle = p$ [26].

3 The isotropy problem

However, there is a generic problem associated to cosmological vector models. The dynamics of a homogenous vector field is necessarily anisotropic and these models are generically excluded by anisotropy constraints imposed by CMB observations. In any case, there have been several proposals in the literature to solve this isotropy problem. As we have already commented in the previous section, the presence of several vector modes can compensate their intrinsic anisotropy by tuning their global structure. In particular, triad configurations corresponding to SU(2) gauge groups have been extensively studied [22, 23, 24, 25, 13].

A simpler solution arises if only the temporal components of the vector fields are allowed to evolve [21]. On the other hand, the isotropy violation of vector models can be alleviated by increasing the number of vector modes. A large number N of randomly oriented vector fields reduce the amount of anisotropy by a factor $1/\sqrt{N}$ [8].

4 Averaged isotropy of rapid evolutions

Another possibility was analyzed in Ref. [15], where it was shown that a homogenous linear polarized Abelian coherent vector mode, oscillating with a quadratic potential, has associated an isotropic averaged energy-momentum tensor.

This idea has been recently extended to any kind of polarization and potential by means of the *isotropy theorem* [26]. In fact, it has also been shown to be independent of the Abelian character of the vector field. The theorem guarantees the isotropy of the averaged energy-momentum tensor for any type of initial configuration provided that the vector evolution is bounded and rapid compared to the metric evolution. A paradigmatic case is provided by massive vector fields with masses larger than the Hubble parameter in a Robertson-Walker geometry, but there is a large number of possibilities (see Fig. 1 for a different example).

5 Conclusions

Coherent homogeneous vector fields can be the origin of the unidentified cosmological constituents, such as the inflaton, the dark matter or the dark energy. This possibility is thought to suffer important constraints on anisotropies imposed by different astrophysical observations. However, a general isotropy theorem for vector fields have proved that this is not the case for models based on bounded rapid vector evolutions.

Acknowledgments

This work has been supported by MICINN (Spain) project numbers FIS 2008-01323, FIS2011-23000, FPA2011-27853-01 and Consolider-Ingenio MULTIDARK CSD2009-00064.

References

[1] T. Damour and V. F. Mukhanov, Phys. Rev. Lett. **80** (1998) 3440; A. R. Liddle and A. Mazumdar, Phys. Rev. D **58** (1998) 083508.

[2] R.D. Peccei, H.R. Quinn, Phys. Rev. Lett. **38** (1977) 1440; Phys. Rev. **D16** (1977) 1791 ; S. Weinberg, Phys. Rev. Lett. **40** (1978) 223; F. Wilczek, Phys. Rev. Lett. **40** (1978) 279.

[3] B. de Carlos, J. A. Casas, F. Quevedo and E. Roulet, Phys. Lett. B **318**, 447 (1993); J. A. R. Cembranos, Phys. Rev. Lett. **102**, 141301 (2009); J. Phys. Conf. Ser. **315**, 012004 (2011).

[4] A. Dobado and A. L. Maroto, Nucl. Phys. B **592**, 203 (2001); J. Alcaraz *et al.*, Phys. Rev.**D67**, 075010 (2003); J. A. R. Cembranos, A. Dobado and A. L. Maroto, Phys. Rev. **D65** 026005 (2002); Phys. Rev. Lett. **90**, 241301 (2003); A. L. Maroto, Phys. Rev. D **69**, 043509 (2004); Phys. Rev. D **69**, 101304 (2004).

[5] A. R. Liddle and R. J. Scherrer, Phys. Rev. D **59** (1999) 023509; S. Dutta and R. J. Scherrer, Phys. Rev. D **78**, 083512 (2008).

[6] JCAP **0902**, 025 (2009); J. Beltran Jimenez, R. Lazkoz and A. L. Maroto, Phys. Rev. D **80**, 023004 (2009); J. Beltran Jimenez and A. L. Maroto, Phys. Rev. D **80**, 063512 (2009);Int. J. Mod. Phys. D **18**, 2243 (2009); J. Beltran Jimenez, T. S. Koivisto, A. L. Maroto and D. F. Mota, JCAP **0910**, 029 (2009); J. Beltran Jimenez and A. L. Maroto, JCAP **1012**, 025 (2010);Phys. Rev. D **83**, 023514 (2011);J. Beltran Jimenez and A. L. Maroto, Mod. Phys. Lett. A **26**, 3025 (2011);E. Carlesi, A. Knebe, G. Yepes, S. Gottloeber, J. Beltran Jimenez and A. L. Maroto, arXiv:1205.1695 [astro-ph.CO]; J. Beltran Jimenez, A. L. Delvas Froes and D. F. Mota, Phys. Lett. B **725**, 212 (2013); J. Beltran Jimenez, R. Durrer, L. Heisenberg and M. Thorsrud, arXiv:1308.1867 [hep-th].

[7] L. H. Ford, Phys. Rev. D **40** (1989) 967.

[8] A. Golovnev, V. Mukhanov and V. Vanchurin, JCAP **0806** (2008) 009.

[9] A. Maleknejad, M. M. Sheikh-Jabbari and J. Soda, Phys. Rept. **528**, 161 (2013).

[10] K. Yamamoto, M. -a. Watanabe and J. Soda, Class. Quant. Grav. **29**, 145008 (2012); M. -a. Watanabe, S. Kanno and J. Soda, Phys. Rev. Lett. **102**, 191302 (2009); K. Murata and J. Soda, JCAP **1106**, 037 (2011); A. Maleknejad, M. M. Sheikh-Jabbari, Phys. Rev. D 85, 123508 (2012).

[11] T. Koivisto and D. F. Mota, JCAP **0808**, 021 (2008); K. Bamba, S. 'i. Nojiri and S. D. Odintsov, Phys. Rev. D **77**, 123532 (2008).

[12] B. Himmetoglu, C. R. Contaldi and M. Peloso, Phys. Rev. Lett. **102**, 111301 (2009); A. E. Gumrukcuoglu, B. Himmetoglu and M. Peloso, Phys. Rev. D **81**, 063528 (2010).

[13] A. Maleknejad and M. M. Sheikh-Jabbari, Phys. Lett. B **723**, 224 (2013); Phys. Rev. D **84**, 043515 (2011); P. Adshead and M. Wyman, Phys. Rev. Lett. **108**, 261302 (2012); Phys. Rev. D **86**, 043530 (2012); K. Yamamoto, Phys. Rev. D **85**, 123504 (2012); M. M. Sheikh-Jabbari, Phys. Lett. B **717**, 6 (2012); A. Ghalee, Phys. Lett. B **717**, 307 (2012); M. Noorbala and M. M. Sheikh-Jabbari, arXiv:1208.2807 [hep-ph]; K. -i. Maeda and K. Yamamoto, arXiv:1210.4054 [astro-ph.CO]; E. Dimastrogiovanni, M. Fasiello and A. J. Tolley, arXiv:1211.1396 [hep-th].

[14] E. Dimastrogiovanni and M. Peloso, Phys. Rev. D **87**, 103501 (2013); R. Namba, E. Dimastrogiovanni and M. Peloso, arXiv:1308.1366 [astro-ph.CO].

[15] K. Dimopoulos, Phys. Rev. D **74** (2006) 083502.

[16] A. E. Nelson and J. Scholtz, Phys. Rev. D **84** (2011) 103501.

[17] Raffelt GG., *Phys. Rev. D* 33, 897 (1986); Raffelt GG, Dearborn DSP., *Phys. Rev. D* 36, 2211 (1987); V. Popov and O.Vasil'ev, Europhys. Lett. **15**, 7 (1991); V. Popov, Turkish Journal of Physics **23**, 943 (1999); Schlattl H, Weiss A, Raffelt GG., *Astropart. Phys.* 10, 353 (1999); Gondolo P, Raffelt GG., arXiv:0807.2926 [astro-ph] Raffelt GG., *Lect. Notes Phys.* 741, 51 (2008); Redondo J., *JCAP* 0807:008 (2008); Redondo J, Postma M. *JCAP* 0902:005 (2009); Jaeckel J, et al., *Phys. Rev. D* 75:013004 (2007); M. Pospelov, A. Ritz, and M.B. Voloshin, Phys. Lett. B **662**, 53 (2008); B. Batell, M. Pospelov, and A. Ritz, Phys. Rev. D **80**, 095024 (2009); H. An, M. Pospelov and J. Pradler, Phys. Rev. Lett. 111, **041302** (2013).

[18] S. A. Abel, M. D. Goodsell, J. Jaeckel, V. V. Khoze, A. Ringwald, JHEP 0807, 124 (2008); JHEP 0911, 027 (2009); M. Cicoli, M. Goodsell, J. Jaeckel, A. Ringwald, J. Jaeckel and A. Ringwald, Ann. Rev. Nucl. Part. Sci. **60**, 405 (2010); M. Goodsell, A. Ringwald, Fortsch. Phys. 58, 716 (2010); J. Jaeckel and A. Ringwald, Ann. Rev. Nucl. Part. Sci. **60**, 405 (2010); M. Goodsell, J. Jaeckel, J. Redondo, A. Ringwald, JHEP 1107, 114 (2011); P. Arias, D. Cadamuro, M. Goodsell, J. Jaeckel, J. Redondo, A. Ringwald, JCAP 1206, 013 (2012); M. Goodsell, S. Ramos-Sanchez, A. Ringwald, JHEP 1201, 021 (2012); A. Ringwald, Phys. Dark Univ. **1**, 116 (2012).

[19] K. Baker, G. Cantatore, S. A. Cetin, M. Davenport, K. Desch, B. Dbrich, H. Gies and I. G. Irastorza *et al.*, Annalen Phys. **525**, A93 (2013); J. Jaeckel and J. Redondo, arXiv:1307.7181 [hep-ph]; arXiv:1308.1103 [hep-ph]; D. Horns, J. Jaeckel, A. Lindner, A. Lobanov, J. Redondo and A. Ringwald, JCAP **1304**, 016 (2013); J. Redondo and G. Raffelt, JCAP **1308**, 034 (2013).

[20] C. G. Boehmer and T. Harko, Eur. Phys. J. C **50** (2007) 423.

[21] J. Beltran Jimenez and A. L. Maroto, Phys. Rev. D **78** (2008) 063005; J. Beltran Jimenez and A. L. Maroto, JCAP **0903** (2009) 016; J. Beltran Jimenez and A. L. Maroto, Phys. Lett. B **686** (2010) 175; E. Carlesi, A. Knebe, G. Yepes, S. Gottloeber, J. Beltran Jimenez and A. L. Maroto, MNRAS **418** (2011) 2715, arXiv:1108.4173 [astro-ph.CO].

[22] J. Cervero and L. Jacobs, Phys. Lett. B 78, 427 (1978); M. Henneaux, J. Math. Phys. 23, 830 (1982); Y. Hosotani, Phys. Lett. B 147, 44 (1984).

[23] D. V. Galtsov and M. S. Volkov, Phys. Lett. B 256, 17 (1991) D. V. Gal'tsov, arXiv:0901.0115 [gr-qc].

[24] Y. Zhang, Phys. Lett. B340 (1994) 18; Class. Quan. Grav. 13 (1996) 2145; E. Elizalde, A. J. Lopez-Revelles, S. D. Odintsov and S. Y. Vernov, arXiv:1201.4302 [hep-th].

[25] C. Armendariz-Picon, JCAP **0407** (2004) 007.

[26] J. A. R. Cembranos, C. Hallabrin, A. L. Maroto and S. J. N. Jareno, Phys. Rev. D **86**, 021301 (2012); J. A. R. Cembranos, A. L. Maroto and S. J. N. Jareno, Phys. Rev. D 87, **043523** (2013).

Axion-like Particles from String Compactifications

M. Cicoli[1,2,3]

[1] Dipartimento di Fisica ed Astronomia, Università di Bologna, Bologna, Italy.
[2] INFN, Sezione di Bologna, Italy.
[3] Adbus Salam ICTP, Strada Costiera 11, Trieste 34014, Italy.

DOI: http://dx.doi.org/10.3204/DESY-PROC-2013-04/cicoli_michele

We review how axion-like particles (ALPs) naturally emerge in the low-energy effective field theory of string compactifications. We focus on the study of their mass spectrum and couplings, stressing that they depend on the mechanism used to fix the moduli. We present concrete examples where either open or closed string modes behave as QCD axions which do not overproduce cold dark matter. Relativistic ALPs can also be produced by the decay of the lightest modulus which drives reheating. These ALPs contribute to dark radiation and could be detected via axion-photon conversion in astrophysical magnetic fields.

1 Axions and strings

1.1 Axions as probes of high energy physics

The QCD axion $a_{\rm QCD}$ is the most plausible explanation of the strong CP problem. Its mass and couplings to ordinary particles are set by its decay constant $f_{a_{\rm QCD}}$ which must lie in the phenomenologically allowed window $10^9\,{\rm GeV} \lesssim f_{a_{\rm QCD}} \lesssim 10^{12}\,{\rm GeV}$, where the lower bound comes from the non-observation of cooling of stars due to axion emission, while the upper bound is due to the overproduction of axionic cold dark matter (DM).

Note that the upper bound is somewhat looser since it assumes a standard post-inflationary cosmological evolution which does not apply to cases where ordinary particles are diluted by the decay of new gravitationally coupled scalars. In particular, axionic DM can be diluted if this decay leads to a reheating temperate below the QCD phase transition, $T_{\rm rh} < \Lambda_{\rm QCD} \simeq 200$ MeV. The case of maximum dilution is obtained when $T_{\rm rh}$ is just above Big Bang Nucleosynthesis (BBN), $T_{\rm rh} \gtrsim T_{\rm BBN} \simeq 3$ MeV, which raises the upper bound to $f_{a_{\rm QCD}} \lesssim 10^{14}$ GeV [1]. Larger values of $f_{a_{\rm QCD}}$ require some tuning of the initial misalignment angle. Moreover, the transparency of the universe for TeV gamma-rays [2] and the anomalous cooling of white dwarfs [3] point together to a very light ALP with an intermediate scale decay constant.

All these constraints reveal that axions are associated with a very high energy scale. Hence, it is natural to search for them in beyond the Standard Model (BSM) theories like string theory. In fact, the low-energy limit of string compactifications yields an effective field theory (EFT) with promising QCD axion candidates [4, 5], or even an 'axiverse' containing a plethora of light ALPs with a logarithmically hierarchical mass spectrum [6]. The strongest constraint on the axiverse comes from the production of isocurvature fluctuations during inflation. Their fraction with respect to the total amplitude of adiabatic plus isocurvature fluctuations is $\beta_{\rm iso} < 0.039$ at 95% CL [7]. If all DM consists of axions, $\beta_{\rm iso}$ is set by the inflationary scale $H_{\rm inf}$, the axion

decay constants f_{a_i} and the initial misalignment angles θ_i: $\beta_{\rm iso} \simeq 4\cdot 10^7 \sum_i \left(\frac{H_{\rm inf}}{\theta_i f_{a_i}}\right)^2 \lesssim 4\cdot 10^{-2}$. Considering n_a axions with $f_{a_i} = f$ and $\theta_i = \theta\ \forall i = 1, ..., n_a$, the previous constraint becomes $f \gtrsim \sqrt{n_a}/\left(3\theta\right) 10^5\, H_{\rm inf}$. The inflationary scale sets also the amplitude of the tensor modes. In particular, a detection of gravitational waves by the Planck satellite would imply $H_{\rm inf} \simeq M_{\rm GUT} \simeq 10^{16}$ GeV, which, in turn, would rule out the axiverse since it would require $f \gtrsim 10^{21}$ GeV (for $n_a \sim \mathcal{O}(100)$ and $\theta \sim \mathcal{O}(\pi)$). Notice that such a high inflationary scale would be a problem also for cases with just one light axion, the QCD axion, if it contributes to DM and its initial misalignment angle is not tuned to small values.

Due to this interesting possibility to put stringy ideas to experimental test, it is crucial to give a solid answer to each of the following questions:

1. What kind of ALP masses and couplings should we expect from string compactifications? Is it generic to obtain an axiverse?

2. Can we build concrete examples of globally consistent semi-realistic chiral models with stabilised moduli and an explicit QCD axion candidate?

3. What can be the rôle played by additional ultra-light axions? How can we detect them?

This last question is particulary important since string theory naturally provides particles which can behave as the QCD axion, even if its presence might be considered as required only by the solution of the strong CP problem, and so as a feature of BSM theories which have no relation to string theory. On the other hand, ultra-light ALPs do not play any rôle in the solution of the strong CP problem. Hence, they can be considered as truly stringy predictions since their presence in BSM theories does not seem to be needed for any fundamental purpose.

1.2 Axions from string compactifications

The massless spectrum of any string theory contains antisymmetric forms whose Kaluza-Klein reduction gives rise to ALPs in the low-energy 4D theory. These axions are closed strings living in the bulk which come along with shift symmetries inherited from higher-dimensional gauge symmetries. They are the imaginary part a of a complex scalar field $T = \tau + {\rm i}a$, where τ is the 'saxion' field. This is a modulus whose vacuum expectation value (VEV) determines the size of the extra dimensions and key-features of the EFT like gauge and Yukawa couplings. The saxion τ, if long-lived, can cause a cosmological moduli problem (CMP). In fact, when $H \sim m_\tau$, τ starts oscillating around its minimum and stores energy. Given that it redshifts as matter, it quickly comes to dominate the energy density of the universe. When τ decays at $H \sim \Gamma \sim \epsilon^2 m_\tau$ where $\epsilon \equiv \frac{m_\tau}{M_P} \ll 1$, it reheats the universe to a temperature of order $T_{\rm rh} \sim \epsilon^{1/2} m_\tau$. Requiring $T_{\rm rh} > T_{\rm BBN}$, one obtains a strong lower bound on the modulus mass: $m_\tau \gtrsim \mathcal{O}(50)$ TeV.

The number n_a of these ALPs depends on the topology of the extra dimensions and for a generic Calabi-Yau (CY) one has $n_a \sim \mathcal{O}(100)$. In type II theories, some of these axions are removed from the low-energy spectrum by the orientifold projection which breaks the $\mathcal{N} = 2$ 4D theory down to a chiral $\mathcal{N} = 1$ theory. However, this operation does not significantly change the order of magnitude of the number of closed string axions left over.

Axions also arise as open strings living on space-time filling branes which wrap some of the extra dimensions and support visible or hidden gauge theories. These ALPs are phases ψ_a of matter fields $C = |C|\, e^{{\rm i}\psi_a}$ whose radial part breaks an effective global Peccei-Quinn $U(1)$ symmetry by getting a non-zero VEV via D-term stabilisation. The number of these open

string axions depends on the details of the brane set-up and it can also be rather large in cases with large numbers of branes (if allowed by tadpole cancellation).

The dynamics stabilising the moduli determines which of these axions can be kept light:

- *D-term stabilisation*: In the presence of an anomalous $U(1)$, one has a D-term scalar potential which schematically looks like (assuming just one charged open string mode C):

$$V_D \sim g^2 \left(|C|^2 - \xi\right)^2 , \tag{1}$$

  where ξ is the Fayet-Iliopoulos (FI) term that depends on the closed string modulus τ charged under the anomalous $U(1)$. Setting the D-terms to zero implies $|C|^2 = \xi(\tau)$. In turn, the gauge boson gets a Stückelberg mass by eating up the axion corresponding to the combination of $|C|$ and τ fixed by the D-term condition:

$$M_{U(1)}^2 \sim g^2 \left[(f_a^{\rm open})^2 + \left(f_a^{\rm closed}\right)^2\right] , \tag{2}$$

  where the open and closed string axion decay constants $f_a^{\rm open}$ and $f_a^{\rm closed}$ are given by:

$$(f_a^{\rm open})^2 = \langle |C|^2 \rangle = \xi \simeq \left|\frac{\partial K}{\partial \tau}\right| \qquad \text{and} \qquad \left(f_a^{\rm closed}\right)^2 \simeq \frac{\partial^2 K}{\partial \tau^2} . \tag{3}$$

  Here K is the Kähler potential of the 4D $\mathcal{N} = 1$ EFT. If $f_a^{\rm open} \gg f_a^{\rm closed}$, the combination of moduli fixed by D-terms is mostly $|C|$ and ψ_a is eaten by the anomalous $U(1)$. If instead $f_a^{\rm open} \ll f_a^{\rm closed}$, the modulus frozen by D-terms is τ and the axion eaten is a. Note that the $U(1)$ mass generated in this way is in general of order the string scale.

- *F-term stabilisation*: The axion a enjoys a shift symmetry $a \to a + \text{const}$ which is broken only by non-perturbative effects. On the contrary, the saxion τ is not protected by any symmetry, and so can develop a potential at both perturbative and non-perturbative level:

  1. If τ is fixed by perturbative effects, then a is exactly massless at this level and its direction is lifted only by subleading non-perturbative effects. In this case τ and a are stabilised by different effects, and so their masses can be different. In particular, τ can satisfy the cosmological bound $m_\tau \gtrsim \mathcal{O}(50)$ TeV with a almost massless.
  2. If perturbative effects are made negligible by tuning some parameters, both τ and a are fixed at non-perturbative level. Hence they get a mass of the same order of magnitude, rendering the axions too heavy: $m_a \sim m_\tau \gtrsim \mathcal{O}(50)$ TeV. These masses are generically of order the gravitino mass $m_{3/2}$, and so if m_a is lowered to smaller values relevant for phenomenology like $m_a \sim \mathcal{O}(\text{meV})$ (assuming a solution to the CMP), one would obtain a tiny scale of supersymmetry (SUSY) breaking.

  These considerations imply that very light axions can arise in the 4D EFT only when some moduli are fixed perturbatively. Moreover, stringy instantons or gaugino condensation should not develop a mass for the axions which is too large. In the case of the QCD axion, these non-perturbative effects should not be larger than QCD instantons.

1.3 Axions and chiral model building

In order to find a viable QCD axion from string theory, besides understanding how to keep the axions light, one should also embed QCD in CY compactifications. More generally, one should build consistent compact models with stabilised moduli and chiral non-Abelian gauge theories.

Type II theories seem to be a promising framework to achieve this goal because MSSM-like theories live on localised objects called D-branes. Chiral model building becomes therefore a *local* issue, and so decouples from moduli stabilisation which is a *global* issue. This allows a separate study of the two problems with the idea of combining the two independent solutions.

Focusing on type IIB compactifications, semi-realistic chiral models can be built using:

1. Intersecting fluxed D7-branes wrapping cycles in the geometric regime;
2. Fractional D3-branes at CY singularities obtained by shrinking some cycles to zero size.

The decoupling between chirality and moduli stabilisation is actually only a leading order effect since various tensions arise once chiral models are embedded in explicit CY constructions. A stabilisation scheme which avoids all these tensions is the LARGE Volume Scenario (LVS) [8] which allows the construction of globally consistent compact models where the visible sector can be either in the geometric [9] or in the singular [10] regime.

1.4 Axions and moduli stabilisation

In LVS models, the moduli are fixed by the interplay of all possible contributions to the scalar potential: tree-level background fluxes, D-terms, α' and g_s perturbative corrections, and non-perturbative effects. This allows us to illustrate the implications of any moduli fixing effect for the dynamics of the axion fields [5]. Let us summarise the LVS strategy to fix the moduli:

- The dilaton and complex structure moduli are fixed at semi-classical level by turning on background fluxes. The VEV of the flux-generated superpotential is naturally $W_0 \sim \mathcal{O}(1)$.
- The $h^{1,1}$ Kähler moduli $T_i = \tau_i + \mathrm{i}a_i$, where τ_i is the volume of the i-th internal 4-cycle and a_i the corresponding axion, are flat directions at tree-level due to the no-scale cancellation.
- The scalar potential for the T-moduli can be expanded in inverse powers of the CY volume $\mathcal{V}$. For $\mathcal{V} \gg 1$ (as required to trust the EFT), the dominant effect comes from D-terms.
- For vanishing open string VEVs, d combinations of T-moduli are fixed by the D-term potential, and so d axions get eaten by anomalous $U(1)$s. If $d = h^{1,1}$, the D-term conditions force the CY volume to collapse to zero size. Thus one has to choose a brane set-up and fluxes such that $d < h^{1,1}$. In this case, D-term fixing leaves $h^{1,1} - d \geq 1$ flat directions.
- $n_{\rm np}$ del Pezzo (dP) divisors generate single non-perturbative contributions to the superpotential whose existence is guaranteed by the rigidity of these cycles and the absence of any chiral intersection with the visible sector. Hence $n_{\rm np}$ Kähler moduli together with their corresponding axions develop a mass of order $m_{3/2}$ due to non-perturbative effects.
- The remaining $n_{\rm ax} = h^{1,1} - n_{\rm np} - d$ moduli tend to be fixed perturbatively by α' or g_s effects. Thus the corresponding axions remain massless and are good QCD axion candidates. The main example is given by the volume mode $\mathcal{V}$ which develops an exponentially large VEV due to α' corrections: $\mathcal{V} \sim W_0\, e^{\frac{2\pi}{N g_s}}$ where N is the rank of an $SU(N)$ theory

which undergoes gaugino condensation ($N = 1$ for D3-instantons). Another example is given by two intersecting local blow-up modes supporting the visible sector, with one combination fixed by D-terms and the other by string loop corrections [5].

- The $n_{\rm ax}$ massless axions are lifted by higher-order instanton effects. Given that for an arbitrary CY $h^{1,1} \sim \mathcal{O}(100)$, $n_{\rm ax}$ might turn out to be very large giving rise to an axiverse.

2 Axions in the LARGE Volume Scenario

2.1 Sequestered models

Type IIB LVS models are particularly interesting also because the moduli mass spectrum and couplings can be computed explicitly. Consequently, one can study the post-inflationary cosmological evolutions of these models in detail.

The volume mode ϕ turns out to be the lightest modulus with a mass of order:

$$m_\phi \simeq m_{3/2}\sqrt{\epsilon} \ll m_{3/2} \qquad \text{where} \qquad \epsilon \equiv \frac{m_{3/2}}{M_P} \simeq \frac{W_0}{\mathcal{V}} \simeq e^{-\frac{2\pi}{N g_s}} \ll 1\,. \tag{4}$$

Given that ϕ is lighter then the gravitino, there is automatically no cosmological problem associated with a possible decay of ϕ into gravitini. However, in gravity mediation one has in general $m_{3/2} \simeq \mathcal{O}(M_{\rm soft})$, and so the requirement of TeV-scale SUSY implies $m_\phi \simeq \mathcal{O}(1)$ MeV. Such a light modulus would definitely decay after BBN.

A viable solution to this cosmological problem relies on models with D3-branes at singularities. The simplest version of these models has a CY volume $\mathcal{V} = \tau_b^{3/2} - \tau_{\rm np}^{3/2} - \tau_{\rm vs}^{3/2}$, where τ_b is the 'big' cycle controlling the overall volume (ϕ is the corresponding canonically normalised field), $\tau_{\rm np}$ is a rigid divisor supporting non-perturbative effects and $\tau_{\rm vs}$ is the visible sector cycle. $\tau_{\rm vs}$ collapses to zero size due to D-terms without breaking SUSY. SUSY is instead broken by the T-moduli living in the bulk which develop a potential at α' and non-perturbative level:

$$V \sim \frac{\sqrt{\tau_{\rm np}}}{\mathcal{V}}\, e^{-\frac{4\pi\tau_{\rm np}}{N}} - W_0\,\frac{\tau_{\rm np}}{\mathcal{V}^2}\, e^{-\frac{2\pi\tau_{\rm np}}{N}} + \frac{W_0^2\xi}{g_s^{3/2}\mathcal{V}^3} \quad \Rightarrow \quad \langle\tau_{\rm np}\rangle \sim \frac{1}{g_s} > 1\,, \quad \langle\mathcal{V}\rangle \sim \frac{W_0}{\epsilon} \gg 1\,.$$

This set-up gives rise to *sequestered* models with suppressed soft-terms [11]:

$$M_{\rm soft} \simeq m_{3/2}\epsilon \ll m_\phi \simeq m_{3/2}\sqrt{\epsilon} \ll m_{3/2}\,. \tag{5}$$

For $\epsilon \simeq \mathcal{O}(10^{-7})$, one obtains the following mass hierarchy:

$$M_{\rm soft} \simeq \mathcal{O}(1)\,\text{TeV} \ll m_\phi \simeq \mathcal{O}(5\cdot 10^6)\,\text{GeV} \ll m_{3/2} \simeq \mathcal{O}(10^{11})\,\text{GeV}\,,$$

which avoids any CMP, leads to low-energy SUSY and allows a high string scale, $M_s \simeq M_P\sqrt{\epsilon} \simeq \mathcal{O}(10^{15})$ GeV, suitable for GUT and inflationary model building. The axion $a_{\rm np}$ acquires a mass of order $m_{3/2}$, the volume axion a_b remains in practice massless since $m_{a_b} \sim M_P\, e^{-2\pi\mathcal{V}^{2/3}} \sim 0$, while the local axion $a_{\rm vs}$ gets eaten up by an anomalous $U(1)$. This is always the case for arbitrary dP singularities where all local closed string axions get eaten up by anomalous $U(1)$s. However, some $a_{\rm vs}$ axions might remain light for more complicated singularities. On top of these closed string axions, there could also be some open string ones whose properties are more model-dependent. We shall discuss their rôle in Sec. 2.4.

2.2 Reheating

Reheating after the end of inflation is caused by the decay of the lightest modulus ϕ since it is the most long-lived. This decay injects entropy into the thermal bath diluting any previous matter-antimatter asymmetry, axionic DM (if $T_{\rm rh} < \Lambda_{\rm QCD}$), and standard thermal LSP DM (if $T_{\rm rh} < T_{\rm freeze-out} \simeq \frac{m_{\rm LSP}}{20}$). On the other hand, the decay of ϕ can recreate non-thermally baryon asymmetry [12] and LSP DM [13, 14], as well as relativistic particles which behave as dark radiation (DR) [15]. It is therefore crucial to study the decay of the volume mode ϕ which takes place when:

$$H \simeq \Gamma_\phi = \frac{c}{2\pi}\frac{m_\phi^3}{M_P^2} \qquad \Rightarrow \qquad T_{\rm rh} = c^{1/2}\left(\frac{m_\phi}{5\cdot 10^6\,{\rm GeV}}\right)^{3/2}\mathcal{O}(1)\,{\rm GeV}\,, \tag{6}$$

with c parameterising the contribution from different decay channels. The leading ones are [15]:

- **Higgses**: $c_{\phi\to H_u H_d} = Z^2/12$ where Z controls the Giudice-Masiero term $K \supset Z\,\frac{H_u H_d}{2\mathcal{V}^{2/3}}$;
- **Bulk closed string axions**: $c_{\phi\to a_b a_b} = 1/24$;
- **Local closed string axions** (if not eaten by $U(1)$s as in dP cases): $c_{\phi\to a_{\rm vs}a_{\rm vs}} = 9/384$.

The strength of the subleading decay channels is instead given by:

- **Gauge bosons**: $c_{\phi\to A^\mu A^\mu} = \lambda\,\alpha_{\rm vs}^2/(8\pi) \ll 1$;
- **Other visible sector fields**: $c_{\phi\to\psi\psi} \simeq \left(M_{\rm soft}/m_\phi\right)^2 \simeq 1/\mathcal{V} \ll 1$;
- **Local open string axions**: $c_{\phi\to a_b\psi_a} \simeq \left(M_s/M_P\right)^4\tau_{\rm vs}^2 \simeq \left(\tau_{\rm vs}/\mathcal{V}\right)^2 \ll 1$.

2.3 Dark radiation

As can be seen from the leading decay channels above, the branching ratio into light axions tends to be rather large. The relativistic axions produced in this way behave as DR since they contribute to the effective number of neutrino-like species $N_{\rm eff}$ defined as:

$$\rho_{\rm rad} = \rho_\gamma\left(1 + \frac{7}{8}\left(\frac{4}{11}\right)^{4/3}N_{\rm eff}\right), \tag{7}$$

where $\rho_{\rm rad}$ is the total radiation energy density whereas ρ_γ is the energy density of all the photons in the universe. $N_{\rm eff}$ is tightly constrained by observations, $N_{\rm eff} = 3.52^{+0.48}_{-0.45}$ at 95% CL [16], which seem to have a slight preference for an excess of DR at 2σ with respect to the SM value $N_{\rm eff,SM} = 3.046$: $\Delta N_{\rm eff} \equiv N_{\rm eff} - N_{\rm eff,SM} \simeq 0.5$.

In the presence of n_H Higgs doublets, 1 bulk (or volume) axion and n_a local closed string axions, sequestered LVS models give the following prediction for $\Delta N_{\rm eff}$:

$$\Delta N_{\rm eff} = \frac{3.48}{n_H Z^2}\left(1 + \frac{9n_a}{16}\right) \underset{n_a=0}{\longrightarrow} \frac{3.48}{n_H Z^2}\,. \tag{8}$$

Focusing on the case of dP singularities where $n_a = 0$, this prediction can give $\Delta N_{\rm eff} \simeq 0.5$ for $Z \simeq 2$ if $n_H = 2$ (as in the MSSM) or for $Z \simeq 1$ if $n_H = 6$ (as in some explicit left-right symmetric models [10]). Note however that in the case with a large number of closed string moduli, $n_a \sim \mathcal{O}(100)$ like in a typical axiverse scenario, this prediction yields definitely an overproduction of DR.

2.4 Axions in sequestered models

In LVS models the volume mode is fixed by perturbative α' effects. Thus the axion a_b remains light because of the shift symmetry. Moreover, a_b does not couple to QCD, and so cannot be the QCD axion [5]. This axion could still be eaten up by an anomalous $U(1)$ living on a bulk cycle. However, using (3) one has that the axions eaten up are the open string ones since:

$$K \supset -3\ln\tau_b \quad \Rightarrow \quad (f_a^{\rm open})^2 \simeq \left|\frac{\partial K}{\partial \tau_b}\right| = \frac{3}{\tau_b} \gg \left(f_a^{\rm closed}\right)^2 \simeq \frac{\partial^2 K}{\partial \tau_b^2} = \frac{3}{\tau_b^2} \quad \text{for} \quad \tau_b \sim \mathcal{V}^{2/3} \gg 1\,.$$

The final upshot is that ultra-light bulk closed string axions are a *model-independent* feature of LVS models, and so DR is a generic *prediction* of these string compactifications!

The relativistic axions produced from ϕ decay form a 'cosmic axion background' (CAB). They have initially an energy $E_a = m_\phi/2 \simeq T_{\rm rh}\sqrt{M_P/m_\phi} \simeq 10^6\, T_{\rm rh}$. Given that they redshift as photons (up to a small difference since the axions do not thermalise), this expression can be used to estimate the CAB energy by replacing $T_{\rm rh}$ with the present CMB temperature, giving an $\mathcal{O}(100)$ eV CAB [17]. These axions have the right energy to account for the observed soft X-ray excess in galaxy clusters due to their oscillation into photons in the cluster magnetic field [18]. In order to match the observations one needs and ALP $a_{\rm ALP}$ which is much lighter than the QCD axion $a_{\rm QCD}$ and has an intermediate scale decay constant.

Hence this CAB is populated by at least a_b and $a_{\rm QCD}$, and perhaps $a_{\rm ALP}$ if the observed soft X-ray excess is due to $a_{\rm ALP}$-γ conversion. However in the simplest sequestered models the only light axion is a_b. Which axions can then behave as $a_{\rm QCD}$ and $a_{\rm ALP}$? Here are two possibilities:

- **Open string QCD axion** ψ_a: In this case the axion is the phase of a matter field $C = |C|\, e^{{\rm i}\psi_a}$ charged under an anomalous $U(1)$. Given that the ϕ decay to local open string axions is subleading, ψ_a gives only a negligible contribution to $\Delta N_{\rm eff}$ without leading to DR overproduction. From (3) one has:

$$K \supset \frac{\tau_{\rm vs}^2}{\mathcal{V}} \quad \Rightarrow \quad (f_a^{\rm open})^2 \simeq \left|\frac{\partial K}{\partial \tau_{\rm vs}}\right| = \frac{2\langle\tau_{\rm vs}\rangle}{\mathcal{V}} \ll \left(f_a^{\rm closed}\right)^2 \simeq \frac{\partial^2 K}{\partial \tau_{\rm vs}^2} = \frac{2}{\mathcal{V}} \quad \text{for} \quad \langle\tau_{\rm vs}\rangle \ll 1\,,$$

  implying that the axions eaten up are the closed string ones contrary to geometric regime case where they are open string modes. Subleading F-terms fix $\langle\tau_{\rm vs}\rangle = 1/\mathcal{V} \ll 1$ in the singular regime, and so the open string axion decay constant becomes $f_a^{\rm open} \simeq M_s/\sqrt{\mathcal{V}} \simeq \mathcal{O}(10^{11-12})\,{\rm GeV}$. This is in the phenomenologically allowed window for the QCD axion, avoiding any axionic DM overproduction. In this scenario, DM might have two components: the QCD axion plus Wino/Higgsino non-thermal DM produced from ϕ decay [14].

  Sequestered models actually give rise to two light local open string axions since any dP singularity yields a gauge theory with two anomalous $U(1)$s. A combination of these two light axions could get massive due to QCD instantons and behave as $a_{\rm QCD}$, while the other combination would remain massless and play the rôle of $a_{\rm ALP}$. Both of these axions would have an intermediate decay constant. This scenario leads to interesting predictions:

  1. a_b could account for the observed excess of DR: $\Delta N_{\rm eff} \simeq 0.5$.
  2. The QCD axion $a_{\rm QCD}$ could be detected in microwave cavities and $a_{\rm ALP}$ in future light-shining-through-a-wall experiments [19].
  3. $a_{\rm ALP}$ could explain the transparency of the universe for TeV photons, the anomalous cooling of white dwarfs and the soft X-ray excess in galaxy clusters.

- **Closed string QCD axion** $a_{\rm vs}$: All local closed string axions are eaten by anomalous $U(1)$s in dP singularities but some of them could be left over for more complicated singularities. The axion decay constant would be set by the string scale $f_{a_{\rm vs}} \simeq M_s/\sqrt{4\pi} \simeq 10^{14}$ GeV, leading to axionic DM overproduction if $a_{\rm vs}$ is not diluted by ϕ decay. However, the reheating temperature in (6) can be rewritten as $T_{\rm rh} \simeq 0.3\, Z$ GeV for $m_\phi \simeq 5 \cdot 10^6$ GeV which leads to TeV-scale SUSY. In this case the ϕ decay to $a_{\rm vs}$ is a leading decay channel, and so this axion contributes to DR. The prediction for $\Delta N_{\rm eff}$ is given by (8) with $n_a = 1$: $\Delta N_{\rm eff} \simeq 2.72/Z^2$ (for $n_H = 2$). $\Delta N_{\rm eff} \simeq 0.5$ can be obtained for $Z \simeq 2.3$, implying $T_{\rm rh} \simeq \mathcal{O}(1)$ GeV which is above the QCD phase transition. Thus axionic DM cannot be diluted by the ϕ decay, and so one has to tune the initial misalignment angle. Consequently, this case looks less promising than the one with an open string QCD axion.

3 Acknowledgments

I would like to thank R. Allahverdi, J. Conlon, B. Dutta, M. Goodsell, S. Krippendorf, C. Mayrhofer, F. Quevedo, A. Ringwald, K. Sinha and R. Valandro for their collaboration on the topics covered in this review.

References

[1] P. Fox, A. Pierce and S. D. Thomas, hep-th/0409059.

[2] A. De Angelis, O. Mansutti, M. Roncadelli, Phys. Rev. **D76** (2007) 121301; M. Simet, D. Hooper, P. D. Serpico, Phys. Rev. **D77** (2008) 063001.

[3] J. Isern, L. Althaus, S. Catalan, A. Corsico, E. Garcia-Berro, M. Salaris and S. Torres, arXiv:1204.3565 [astro-ph.SR].

[4] E. Witten, Phys. Lett. B **149** (1984) 351; J. P. Conlon, JHEP **0605** (2006) 078; P. Svrcek and E. Witten, JHEP **0606** (2006) 051; K. -S. Choi, I. -W. Kim and J. E. Kim, JHEP **0703** (2007) 116.

[5] M. Cicoli, M. Goodsell and A. Ringwald, JHEP **1210** (2012) 146.

[6] A. Arvanitaki, S. Dimopoulos, S. Dubovsky, N. Kaloper and J. March-Russell, Phys. Rev. D **81** (2010) 123530.

[7] P. A. R. Ade *et al.* [Planck Collaboration], arXiv:1303.5082 [astro-ph.CO].

[8] V. Balasubramanian, P. Berglund, J. P. Conlon and F. Quevedo, JHEP **0503** (2005) 007.

[9] M. Cicoli, C. Mayrhofer and R. Valandro, JHEP **1202** (2012) 062.

[10] M. Cicoli, S. Krippendorf, C. Mayrhofer, F. Quevedo and R. Valandro, JHEP **1209** (2012) 019; M. Cicoli, S. Krippendorf, C. Mayrhofer, F. Quevedo and R. Valandro, arXiv:1304.0022 [hep-th].

[11] R. Blumenhagen, J. P. Conlon, S. Krippendorf, S. Moster and F. Quevedo, JHEP **0909** (2009) 007.

[12] R. Kitano, H. Murayama and M. Ratz, Phys. Lett. B **669** (2008) 145; R. Allahverdi, B. Dutta and K. Sinha, Phys. Rev. D **83** (2011) 083502.

[13] B. S. Acharya, P. Kumar, K. Bobkov, G. Kane, J. Shao and S. Watson, JHEP **0806**, 064 (2008); B. S. Acharya, G. Kane, S. Watson and P. Kumar, Phys. Rev. D **80** (2009) 083529; B. Dutta, L. Leblond and K. Sinha, Phys. Rev. D **80**, 035014 (2009).

[14] R. Allahverdi, M. Cicoli, B. Dutta and K. Sinha, arXiv:1307.5086 [hep-ph].

[15] M. Cicoli, J. P. Conlon and F. Quevedo, Phys. Rev. D **87** (2013) 4, 043520; T. Higaki and F. Takahashi, JHEP **1211** (2012) 125.

[16] P. A. R. Ade *et al.* [Planck Collaboration], arXiv:1303.5076 [astro-ph.CO].

[17] J. P. Conlon and M. C. D. Marsh, arXiv:1304.1804 [hep-ph].

[18] J. P. Conlon and M. C. D. Marsh, arXiv:1305.3603 [astro-ph.CO].

[19] K. Baker, G. Cantatore, S. A. Cetin, M. Davenport, K. Desch, B. Dbrich, H. Gies and I. G. Irastorza *et al.*, Annalen Phys. **525** (2013) A93.

Hidden Photons in Extra Dimensions

C. J. Wallace[1], *J. Jaeckel*[2], *S. Roy*[1]

[1]Institute for Particle Physics Phenomenology, Durham University, United Kingdom
[2]Institut für Theoretische Physik, Ruprecht-Karls-Universität Heidelberg, Germany

DOI: http://dx.doi.org/10.3204/DESY-PROC-2013-04/wallace_chris

Additional U(1) gauge symmetries and corresponding vector bosons, called hidden photons, interacting with the regular photon via kinetic mixing are well motivated in extensions of the Standard Model. Such extensions often exhibit extra spatial dimensions. In this note we investigate the effects of hidden photons living in extra dimensions. In four dimensions such a hidden photon is only detectable if it has a mass or if there exists additional matter charged under it. Here we point out that in extra dimensions suitable masses for hidden photons are automatically present in form of the Kaluza-Klein tower.

1 Motivation

Extra U(1) gauge groups are a well motivated and consequently well studied extension of the Standard Model (SM). The simplest way the corresponding gauge bosons can interact with the Standard Model is via kinetic mixing with the photon [1]. In absence of extra matter charged under this U(1) (and this is the case we are interested in here) this interaction is only observable if the hidden photon is massive. Usually one can consider a Higgs mechanism[1] or a Stueckelberg mechanism [3] (and references of [4]). If the hidden photon field extends into extra spatial dimensions an additional option presents itself in the form of a stack of massive Kaluza-Klein (KK) excitations. In this note we will consider this option, and discuss its phenomenology and constraints which present some novel features compared to the canonical 4-dimensional hidden photon limits (for a review, see [4]).

2 Toy Model

We consider a simple toy model with a low energy effective theory defined by the action,

$$S_D = \int \mathrm{d}^D x \sqrt{g} \Big(-\frac{1}{4} F^{\mu\nu} F_{\mu\nu} \delta^d(\vec{y}) - \frac{1}{4} X^{MN} X_{MN} - \frac{1}{2} \chi_{\mathrm{D}} F^{\mu\nu} X_{\mu\nu} \delta^d(\vec{y}) \Big),$$

which describes a D-dimensional bulk space (indices M, N) in which gravity and a U(1)$'$ gauge symmetry live. The standard model and its U(1) is localized to a 3-brane (indices μ, ν) within the bulk at $\vec{y} = 0$. Accordingly the kinetic mixing is also confined to the brane. For the sake of low energy (w.r.t. the extra dimensional Planck scale) phenomenology, the brane possesses

[1]The extra Higgs may lead to additional constraints [2].

no inherent dynamics of its own, being infinitesimally thin and infinitely heavy. We take the extra dimensions to be flat.

Since no direct evidence for extra spatial dimensions exists, the $d = D - 4$ additional dimensions have to be compactified. We choose the most straightforward compactification onto a d-dimensional torus $\mathcal{T}_d = \mathcal{S}_1 \times \mathcal{S}_1 \ldots \mathcal{S}_1$. Rough limits on the maximal size of the extra dimension are given in Table 1.

As a consequence of the hidden photon field being constrained onto a torus the fields must possess appropriate periodicity. This allows us to decompose them in a Fourier series. For example in the simplest 5-dimensional case this reads,

$$X_M(x^\mu, y^a) = \frac{1}{(\pi R)^{d/2}} \sum_{n>0} \left(X_M^{(n,+)}(x^\mu) \cos\left(\frac{ny}{R}\right) + X_M^{(n,-)}(x^\mu) \sin\left(\frac{ny}{R}\right)\right) + \frac{X_M^{(0)}}{(2\pi R)^{d/2}}. \quad (1)$$

Only the $X_M^+(x^\mu)$ modes interact with the SM photon. The X_M^- modes are associated with the sinusoidal part of the Fourier expansion and have zero amplitude for $y = 0$, where we have localized the SM 3-brane. The expansion quickly becomes unwieldy for higher numbers of extra dimensions, but the result generalizes easily - only the terms in the expansion where all modes are (+) (i.e. associated with the cosine) partake in kinetic mixing.

In the general case of d extra dimensions, inserting this Fourier series and choosing an appropriate gauge we have

$$S_{\text{eff}} = \int d^4x \left[-\frac{1}{4} F^{\mu\nu} F_{\mu\nu} - \frac{1}{4} X^{\mu\nu(0)} X^{(0)}_{\mu\nu} + \sum_{n>0,p} \left(\frac{1}{4} X^{\mu\nu(n,p)} X^{(n,p)}_{\mu\nu} + \frac{1}{2} \frac{n^2}{R^2} X^{(n,p)}_\mu X^{\mu\,(n,p)} \right) + \sum_{n>0} \left(\frac{1}{2} \chi F^{\mu\nu} X^{(n,+\ldots+)}_{\mu\nu} \right) + \ldots \right] \quad (2)$$

where the index p is d-dimensional and denotes the combination of + and − modes from the Fourier expansion.The index p is to be summed over, except in the case of the kinetic mixing term, which requires $p = +, \ldots, +$ (all plus). Our initially D-dimensional field is separated into a stack of 4-dimensional hidden photon fields $X_\mu^{(n,p)}$. The dots indicate d massless scalar fields originating from $X^0_{a=5\ldots D}$, $d-1$ of which have associated stacks of KK modes (the missing stack being "eaten" by the now massive 4-dimensional hidden photon fields). These scalars interact with the rest of the model only via gravity which we will neglect. Note also that the 4-dimensional kinetic mixing parameter is suppressed by a volume factor compared to the higher dimensional mixing, $\chi = \chi_{\text{D}}/(\pi R)^{d/2}$.

d	$1/R = m_0$	M^*
1	> 200 μeV	$\gtrsim 3 \times 10^5$ TeV
2	> 700 μeV	$\gtrsim 3$ TeV
3	> 100 eV	$\gtrsim 3$ TeV
4	> 50 keV	$\gtrsim 3$ TeV
5	> 2 MeV	$\gtrsim 3$ TeV
6	> 20 MeV	$\gtrsim 3$ TeV

Table 1: Limits on the size of extra dimensions from precision tests of gravity. For $d = 1$ the constraint arises from direct tests of the gravitational inverse square law [5]. For $d = 2-6$ the limits originate from constraints on the minimum value of the extra dimensional Planck scale M^* [6].

For our purposes the important consequence is that we now have a whole (infinite) tower of massive hidden photon fields with masses,

$$m^2_{\gamma'} = \frac{n^2}{R^2}(1 + \mathcal{O}(\chi^2)), \quad (3)$$

where n is the KK mode number. Each of these interacts with the ordinary photon via the same kinetic mixing χ. From the above we can see that we have observable massive hidden photons without the need to rely on an additional Higgs or Stueckelberg mechanism.

3 Experimental and Observational Constraints

For the simple 4-dimensional case a significant number of constraints already exists and have been discussed in the literature [4] (and references therein). Here, we will re-apply the same techniques to the case at hand. We will focus on three types of limits, stellar energy loss, fixed target experiments and precision measurements of $(g-2)$. A more detailed discussion with additional bounds will be presented in [7].

Stars lose energy when hidden photons are produced in the stellar interior and subsequently leave the star [8]. If this energy loss is too great (typically more than the Standard Model luminosity), this is in conflict with observation. In our extra-dimensional setup each KK mode constitutes a channel for energy loss, and the total energy loss is simply the sum over all channels. The resulting limits for $d = 1, 3, 5$ are shown in Fig. 1 as greyed out areas, with solid blue and purple lines corresponding to solar and horizontal branch star energy losses, respectively.

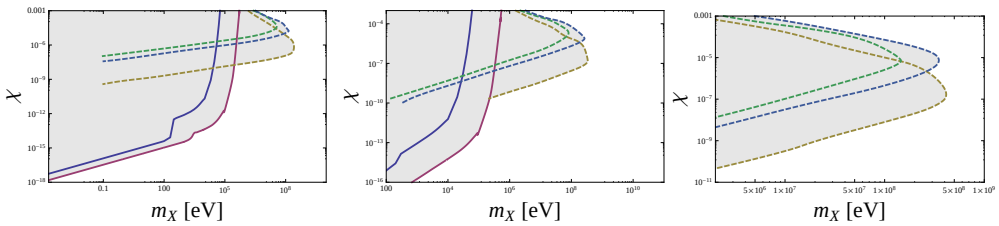

Figure 1: Limits on real processes for $n = 1, 3, 5$ extra dimensions.

At higher masses fixed target experiments provide superior limits. Important experiments of this type are the E137, E141 and E774 beam dumps at SLAC and Fermilab [9]. Essentially these experiments consist of an electron beam incident on a thick block of metal where hidden photons are produced via Bremsstrahlung. Then follows a region of thick shielding which stops all Standard Model particles but not the hidden photons. Finally we have a volume where the hidden photons can decay into electrons and which is instrumented to detect these electrons. Multiple hidden photon channels (KK modes) sum to give the total signal. The corresponding bounds are shown as dashed lines in Fig. 1.

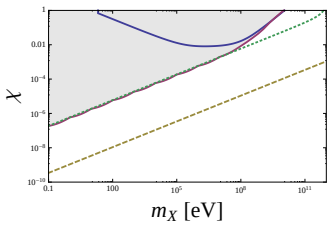

Figure 2: $(g-2)$ perturbativity limits.

Notice that the bounds have an interesting and generic feature that they become stronger as the mass of the lowest KK mode, m_0, decreases. In the general case, a small mass splitting gives a given experiment access to many modes to contribute to, say, energy loss.

An interesting issue arises when computing the constraints on our toy model from processes

where the hidden photon is produced off-shell. Taking the electron and muon $(g-2)$ constraint as an illustrative example, we soon encounter a problem with perturbativity.

The vertex correction responsible for the electron and muon anomalous magnetic moment is a 1-loop process. As such the 4-momentum in the loop is unconstrained and the whole, infinite, tower of KK modes of the hidden photon are accessible and contribute to the magnetic moment. Here we encounter the problem the non-renormalizabilty of higher dimensional gauge theories. To avoid this issue we impose a cutoff on the mass of the KK modes.

On top of that, a large number of KK modes contributing to the same quantity can invalidate our perturbative treatment. To be on the safe side we require,

$$\chi^2_{\text{pert.}} = \chi^2 \times \int_1^{\frac{\Lambda}{m_0}} d^d k = \chi^2 \times \int_1^{\frac{\Lambda}{m_0}} \frac{2\pi^{\frac{d}{2}}}{\Gamma(\frac{d}{2})} k^{d-1} dk \ll 1. \tag{4}$$

Each choice of cutoff then defines a region where our perturbative treatment is valid, providing a severe limitation on the range of validity for the $(g-2)$ constraints. This is illustrated for two different choices of the cutoff in Fig. 2 - $\Lambda \sim M_*$ (dotted line) and $\Lambda \sim 1$ TeV (dashed). The greyed out area would be excluded, but the whole grey region lies above the limit of a perturbativity for either choice of cutoff, and our perturbative treatment is insufficient.

4 Conclusions

Extensions of the Standard Model that contain extra hidden sector U(1) gauge bosons often also feature extra spatial dimensions. The hidden photon can then have its own KK tower and it can become observable even in absence of an additional mass generation via a Stueckelberg or Higgs mechanism. We have presented exclusion limits on such a setup and we find that the limits on the allowed kinetic mixing are generically stronger than in the 4-dimensional case.

Acknowledgements: *We are grateful to the organizers of Patras 2013 and CJW is indebted to the ITP in Heidelberg for generous hospitality while working on this project.*

References

[1] B. Holdom, Phys. Lett. B **166** (1986) 196; J. Polchinski and L. Susskind, Phys. Rev. D **26** (1982) 3661; K. R. Dienes, C. F. Kolda and J. March-Russell, Nucl. Phys. B **492** (1997) 104 [hep-ph/9610479]; S. A. Abel and B. W. Schofield, Nucl. Phys. B **685** (2004) 150 [hep-th/0311051]; S. A. Abel, *et al.*, Phys. Lett. B **666** (2008) 66 [hep-ph/0608248]; S. A. Abel, *et al.*, JHEP **0807** (2008) 124 [arXiv:0803.1449 [hep-ph]].

[2] M. Ahlers, *et al.*, Phys. Rev. D **78** (2008) 075005, [arXiv:0807.4143 [hep-ph]];

[3] H. Ruegg and M. Ruiz-Altaba, Int. J. Mod. Phys. A **19** (2004) 3265 [hep-th/0304245];

[4] J. Jaeckel and A. Ringwald, Ann. Rev. Nucl. Part. Sci. **60** (2010) 405 [arXiv:1002.0329 [hep-ph]]; J. Jaeckel, Frascati Phys. Ser. **56** 172 [arXiv:1303.1821 [hep-ph]].

[5] C. D. Hoyle, *et al.* Phys. Rev. D **70** (2004) 042004 [hep-ph/0405262];

[6] G. Aad *et al.* [ATLAS Collaboration], New J. Phys. **15** (2013) 043007 [arXiv:1210.8389 [hep-ex]]; S. Chatrchyan *et al.* [CMS Collaboration], JHEP **1209** (2012) 094 [arXiv:1206.5663 [hep-ex]].

[7] J. Jaeckel, S. Roy and C. J. Wallace, in preparation.

[8] J. A. Frieman, S. Dimopoulos and M. S. Turner, Phys. Rev. D **36** (1987) 2201; G. G. Raffelt and D. S. P. Dearborn, Phys. Rev. D **37** (1988) 549; J. Redondo, JCAP **0807** (2008) 008, [arXiv:0801.1527 [hep-ph]].

[9] J. D. Bjorken, R. Essig, P. Schuster, and N. Toro, Phys. Rev. **D80**, 075018 (2009), arXiv:0906.0580.

[10] S. Roy, Doctoral thesis, Durham University (2013)

Singlet portal extensions of the standard seesaw models to dark sector with local dark symmetry: An alternative to the new minimal standard model

S. Baek, P. Ko, W.-I. Park

School of Physics, KIAS, Seoul 130-722, Korea

DOI: http://dx.doi.org/10.3204/DESY-PROC-2013-04/ko_pyungwon

Assuming dark matter is absolutely stable due to unbroken dark gauge symmetry and singlet operators are portals to the dark sector, we present a simple extension of the standard seesaw model that can accommodate all the cosmological observations as well as terrestrial experiments available as of now, including leptogenesis, extra dark radiation of $\sim 8\%$ (resulting in $N_{\rm eff} = 3.130$ the effective number of neutrino species), Higgs inflation, small and large scale structure formation, and current relic density of scalar DM (X). The Higgs signal strength is equal to one as in the SM for unbroken $U(1)_X$ case with a scalar dark matter, but it could be less than one independent of decay channels if the dark matter is a dark sector fermion or if $U(1)_X$ is spontaneously broken, because of a mixing with a new neutral scalar boson in the models.

1 Introduction

The standard model (SM) based on $SU(3)_C \times SU(2)_L \times U(1)_Y$ is confirmed at quantum level with high accuracy, although there are a few places where the SM predictions do not reproduce the observations such as the muon $(g-2)$, top forward-backward asymmetry or ...

Still the SM has to be extended in order to accommodate the following observations: (i) neutrino masses and mixings, (ii) baryogenesis, (iii) nonbaryonic cold dark matter of the universe, and (iv) inflation and density perturbation.

For the 1st and the 2nd items, the most economic and aesthetically attractive idea is to introduce singlet right-handed neutrinos and the seesaw mechanism, and leptogenesis for baryon number asymmetry. For the 3rd item, there are many models for cold dark matter, from axion to lightest superparticles to hidden sector DMs, to name a few. For the 4th item the simplest inflation model without new inflaton fields would be R^2 inflation by Starobinsky [1] and Higgs inflation [2].

In nonsupersymmetric dark matter models, one often assumes ad hoc Z_2 symmetry in order to stabilize DM, without deeper understanding of its origin or asking if it is global or local discrete symmetry. If we assume that global symmetry is not protected by quantum gravity effects, this Z_2 symmetry would be broken by $1/M_{\rm Planck}$ suppressed nonrenormalizable operators [6]. Then the electroweak scale DM can not live long enough to be dark matter candidate of the universe. The simplest way to guarantee the stability of EW scale DM is to assume the DM carries its own gauge charge which is absolutely conserved. Then we are led

to local dark symmetry and dark gauge force. This would be a very natural route for the DM model building, since the unsurpassed successful SM is based on local gauge symmetry and its spontaneous breaking.

If weak scale DM carried nonzero SM gauge charges, it would be strongly constrained by direct detection cross section as well as electroweak precision observables and flavor physics. Therefore we assume the DM is neutral under the SM gauge interaction, and making a hidden sector. Hidden sector is quite common in many models beyond the SM, including SUSY models or superstring theories. For example, huge rank gauge group in the string theory would eventually break down to $G_{\rm SM} \times G_{\rm hidden}$, where $G_{\rm hidden}$ is nothing but the dark gauge symmetry acting on hidden sector dark matter. If $G_{\rm hidden}$ is unbroken, DM particles will be absolutely stable, like the electron is absolutely stable due to electric charge conservation. If dark gauge coupling is strong and dark gauge interaction is confining like ordinary QCD, the DM would be the lightest composite hadrons in the hidden sector. In this case it is possible to generate all the mass scales of the SM particles as well as the DM mass from dimensional transmutation in the hidden sector strong interaction [3]. If dark gauge coupling is weak, we can employ the standard perturbation method to analyze the problems, which we adopt in the model described in this talk.

Another guiding principle is renormalizability of the model. The present authors found that one would get erroneous results if the effective Lagrangian approach is used for singlet fermion or vector DM with Higgs portal [4, 5].

Finally we generalize the notion of Higgs portal to the singlet portal, assuming that the singlet operators in the standard seesaw model make portals to the dark sector. Note that there are only 3 singlet operators: $H^\dagger H, N_R$ and the kinetic mixing between $U(1)_X$ and $U(1)_Y$ field strength tensors.

In this talk, I present a simple renormalizable model where the dark matter lives in a dark (hidden) sector with its own dark gauge charge along with dark gauge force. We mainly discuss the unbroken $U(1)_X$ dark gauge symmetry, and briefly mention what happens if $U(1)_X$ is spontanesouly broken. This talk is based on Ref. [6], to which we invite the readers for more detailed discussions on the subjects described in this talk.

2 Model

As explained in Introduction, we assume that dark matter lives in a hidden sector, and it is stable due to unbroken local $U(1)_X$ dark gauge symmetry. All the SM fields are taken to be $U(1)_X$ singlets. Assuming that the RH neutrinos are portals to the hidden sector, we need both a scalar (X) and a Dirac fermion (ψ) with the same nonzero dark charge (see Table 1). Then the composite operator $\psi X^\dagger$ becomes a gauge singlet and thus can couple to the RH neutrinos N_{Ri}'s [1].

With these assumptions, we can write the most general renormalizable Lagrangian as follows:

$$\mathcal{L} = \mathcal{L}_{\rm SM} + \mathcal{L}_X + \mathcal{L}_\psi + \mathcal{L}_{\rm portal} + \mathcal{L}_{\rm inflation} \tag{1}$$

[1] If we did not assume that the RH neutrinos are portals to the dark sector, we did not have to introduce both ψ and X in the dark sector. This case is discussed in brief in Sec. 8.

where $\mathcal{L}_{\rm SM}$ is the standard model Lagrangian and

$$\mathcal{L}_X = \left|\left(\partial_\mu + ig_X q_X \hat{B}'_\mu\right) X\right|^2 - \frac{1}{4}\hat{B}'_{\mu\nu}\hat{X}^{\mu\nu} - m_X^2 X^\dagger X - \frac{1}{4}\lambda_X \left(X^\dagger X\right)^2 \quad (2)$$

$$\mathcal{L}_\psi = i\bar{\psi}\gamma^\mu \left(\partial_\mu + ig_X q_X \hat{B}'_\mu\right)\psi - m_\psi \bar{\psi}\psi \quad (3)$$

$$\mathcal{L}_{\rm kin-mix} = -\frac{1}{2}\sin\epsilon \hat{B}'_{\mu\nu}\hat{B}^{\mu\nu} - \frac{1}{2}\lambda_{HX} X^\dagger X H^\dagger H \quad (4)$$

$$- \frac{1}{2}M_i \overline{N_{Ri}^C} N_{Ri} + \left[Y_\nu^{ij}\overline{N_{Ri}}\ell_{Lj}H^\dagger + \lambda^i \overline{N_{Ri}}\psi X^\dagger + \text{H.c.}\right] \quad (5)$$

$$\mathcal{L}_{\rm inflation} = [\xi_H H^\dagger H + \xi_X X^\dagger X]R \quad (6)$$

g_X, q_X, $\hat{B}'_\mu$ and $\hat{B}'_{\mu\nu}$ are the gauge coupling, $U(1)_X$ charge, the gauge field and the field strength tensor of the dark $U(1)_X$, and R is the scalar curvature, respectively. $\hat{B}_{\mu\nu}$ is the gauge field strength of the SM $U(1)_Y$. We assume $m_X^2 > 0, \quad \lambda_X > 0, \quad \lambda_{HX} > 0$, so that the local $U(1)_X$ remains unbroken and the scalar potential is bounded from below at tree level.

This model has only 3 more fields compared to the standard seesaw models, and is based on local gauge principle related with absolutely stable DM. And unbroken dark symmetry implies massless dark photon which contributes to dark radiation of the universe, and Higgs

3 Implications on particle physics and cosmology

Our model is simple enough, but has sufficiently rich structures, so that it can accommodate various observations from cosmology and astrophysics related with (self-interacting) dark matter and dark radiation, and inflation with correct relic density of the DM.

- Dark scalar X can improve the stability of the electroweak vacuum up to Planck scale, unlike the SM. For the mass of SM-like Higgs, $m_h \sim 125\,\text{GeV}$ hinted by the recent data from LHC experiments, with $m_t = 173.2\,\text{GeV}$ and $\alpha_s = 0.118$, the problem of vacuum instability is cured if $\lambda_X > 0$ and $\lambda_{HX} \gtrsim 0.2$.

- Perturbativity of quartic couplings for scalar fields H and X up to Planck scale puts theoretical constraints on λ_X and λ_{HX} such that $\lambda_X \lesssim 0.2$ and $\lambda_{HX} \lesssim 0.6$.

- Massless dark photon mediates long range between dark matter, and can solve the small scale problem of DM subhalo while satisfying constraints from inner structure and kinematics of dark matter halos. This will constrain the dark gauge coupling strength to be $g_X \lesssim 2.5 \times 10^{-2}\,(m_X/300\,\text{GeV})^{3/4}$.

- If dark fermion ψ were lighter than X and became DM, then its thermal relic density would be too large since it can annihilate only into a pair of dark photon ($\sigma_{\rm ann} v \propto g_X^4$). On the contrary the dark scalar X can be diluted efficiently even if g_X is very small, since there is a Higgs portal term which makes $XX^\dagger \leftrightarrow$ (SM particles).

- Direct detection experiments such as XENON100 and CDMS put strong bound on the combination of the gauge kinetic mixing $10^{-12} \lesssim \epsilon g_X \lesssim 10^{-5}$ for $6\,\text{GeV} \lesssim m_X \lesssim 1\,\text{TeV}$ when the upper bound on g_X is used.

- Massless dark photon would contribute to the number of effective neutrinos which can be measured accurately by Planck satellite and others. We find that dark photon contributes to dark radiation by ~ 0.08, which is in agreement with the recent measurement by Planck, $\Delta N_{\rm eff} = 3.30 \pm 0.27$ at 68% CL.
- The decay of right-handed(RH) neutrinos generate both matter and dark matter thanks to see-saw mechanism. However the asymmetric component of dark matter disappears as the heavy dark fermion ψ decays eventually. Interestingly, the late decay of ψ also generates visible sector lepton number asymmetry which can be large enough to match the observation.
- Higgs inflation can work in our model since the gauge singlet scalar coupled to SM Higgs field cures the instability of potential in Higgs-singlet system. Inflation along the SM Higgs direction does not pose any new constraint on the model parameters.
- In case $U(1)_X$ is unbroken, the Higgs signal strength should be equal to "1", independent of production and decay channels. If we consider other variations of the model with broken $U(1)_X$ or only dark scalar or dark fermion, the number of Higgs-like scalar bosons can be more than one, with universally reduced Higgs signal strength. See Table 1 for summary

In conclusion, we presented a simple extension of the standard seesaw model where dark matter physics is constructed with local dark gauge symmetry. It has only 2 or 3 more fields compared with the standard seesaw models, is very simple due to local gauge principle, but has rich enough structure for thermalization and self interaction of dark matter, dark radiation, stable EW vacuum, Higgs inflation etc.

Dark sector fields	$U(1)_X$	Messenger	DM	Extra DR	μ_i
$\hat{B}'_\mu, X, \psi$	Unbroken	$H^\dagger H, \hat{B}'_{\mu\nu}\hat{B}^{\mu\nu}, N_R$	X	~ 0.08	1 $(i=1)$
$\hat{B}'_\mu, X$	Unbroken	$H^\dagger H, \hat{B}'_{\mu\nu}\hat{B}^{\mu\nu}$	X	~ 0.08	1 $(i=1)$
$\hat{B}'_\mu, \psi$	Unbroken	$H^\dagger H, \hat{B}'_{\mu\nu}\hat{B}^{\mu\nu}, S$	ψ	~ 0.08	< 1 $(i=1,2)$
$\hat{B}'_\mu, X, \psi, \phi$	Broken	$H^\dagger H, \hat{B}'_{\mu\nu}\hat{B}^{\mu\nu}, N_R$	X or ψ	~ 0	< 1 $(i=1,2)$
$\hat{B}'_\mu, X, \phi$	Broken	$H^\dagger H, \hat{B}'_{\mu\nu}\hat{B}^{\mu\nu}$	X	~ 0	< 1 $(i=1,2)$
$\hat{B}'_\mu, \psi$	Broken	$H^\dagger H, \hat{B}'_{\mu\nu}\hat{B}^{\mu\nu}, S$	ψ	~ 0	< 1 $(i=1,2,3)$

Table 1: Dark fields in the hidden sector, messengers, dark matter (DM), the amount of dark radiation (DR), and the signal strength(s) of the i scalar boson(s) (μ_i) for unbroken or spontaneously broken (by $\langle\phi\rangle \neq 0$) $U(1)_X$ models considered in this work. The number of Higgs-like neutral scalar bosons could be 1,2 or 3, depending on the scenarios.

4 Acknowledgments

This work was supported in part by Basic Science Research Program through the National Research Foundation of Korea (NRF) Research Grant 2012R1A2A1A01006053, and by SRC program of NRF funded by MEST (20120001176) through Korea Neutrino Research Center at Seoul National University (PK).

References

[1] A. A. Starobinsky, Phys. Lett. B **91**, 99 (1980).

[2] F. L. Bezrukov and M. Shaposhnikov, Phys. Lett. B **659**, 703 (2008) [arXiv:0710.3755 [hep-th]].

[3] T. Hur and P. Ko, Phys. Rev. Lett. **106**, 141802 (2011) [arXiv:1103.2571 [hep-ph]].

[4] S. Baek, P. Ko and W. -I. Park, JHEP **1202**, 047 (2012) [arXiv:1112.1847 [hep-ph]].

[5] S. Baek, P. Ko, W. -I. Park and E. Senaha, JHEP **1305**, 036 (2013) [arXiv:1212.2131 [hep-ph]].

[6] S. Baek, P. Ko and W. -I. Park, JHEP **1307**, 013 (2013) [arXiv:1303.4280 [hep-ph]].

[7] H. Davoudiasl, R. Kitano, T. Li and H. Murayama, Phys. Lett. B **609**, 117 (2005) [hep-ph/0405097].

Chapter 8

Detector Technologies

Overview on Low-flux Detectors

J. E. von Seggern

Deutsches Elektronen-Synchrotron (DESY), Hamburg, Germany

DOI: http://dx.doi.org/10.3204/DESY-PROC-2013-04/seggern_jan_eike_von

Laboratory based searches for weakly-interacting slim particles (WISPs) of the light-shining-through-a-wall type (LSW) use visible or near-infrared (NIR) laser light. Low-noise and highly efficient detectors are necessary to improve over previous experiments. These requirements overlap with the requirements for single-photon detectors (SPDs) for quantum information (QI) experiments. In this contribution, the sensitivity of several QI SPDs is compared to photo-multiplier tubes (PMTs) and imaging charge-coupled devices (CCDs). It is found that only transition edge sensors (TESs) are viable alternatives to CCDs if the signal can be focussed to a few μm.

1 Introduction

LSW experiments search for WISPs via the process $\gamma \to \text{wisp} \to \gamma$ [1]. For a photon-counting detection scheme, the signal rate, $\dot{N}_{\text{sig}}$, is given by

$$\dot{N}_{\text{sig}} = \dot{N}_{\text{in}}\, \mathcal{P}(\gamma \to \text{wisp})\, \mathcal{P}(\text{wisp} \to \gamma)\, \eta,$$

where $\dot{N}_{\text{in}}$ is the rate of photons fed into the experiment, $\mathcal{P}(\gamma \to \text{wisp})$, η the efficiency of the detector and $\mathcal{P}(\text{wisp} \to \gamma)$ the probability for photon-WISP and WISP-photon conversion, respectively, which are both proportional to the square of the photon-WISP coupling, g. Hence, the sensitivity on the coupling, $S(g)$, i.e. the expected upper limit on g for the case that $g = 0$ is realized in Nature, scales with the detector parameters as

$$S(g) \propto (\dot{N}_{\text{ul}}/\eta)^{1/4},$$

with $\dot{N}_{\text{ul}}$ the count-rate sensitivity and η the quantum efficiency of the detector. The count rate sensitivity is typically roughly proportional to the square root of the dark count rate, $\dot{N}_{\text{ul}} \propto \sqrt{\dot{N}_{\text{dc}}}$. Hence, the sensitivity can be improved (i.e. lowered) by decreasing the dark count rate or increasing the quantum efficiency.

To compare different detectors, the figure of merit $\mu = \eta/\dot{N}_{\text{ul}}$, is used. Thus, larger values of μ identify better detectors. The count rate sensitivity is taken to be the average upper limit of unified confidence intervals and is estimated using toy Monte Carlo simulations [7].

Early LSW experiments used PMTs for photo-detection [2]. Recent LSW experiments used CCDs and lasers in the visible spectrum [3, 4]. Future LSW experiments will use NIR lasers [5] because optical elements are known to withstand high powers at these wavelengths. At NIR wavelengths, silicon based CCDs have a much reduced quantum efficiency compared to the visible spectrum. Therefore, other devices for photo-detection are sought. These detectors

should have a quantum efficiency that is similar to the quantum efficiency of CCDs in the optical and a dark count rate below that of CCDs. Additionally, it is desirable that these detectors can time-resolve single photons (SPD). A review of SPDs is given in Ref. [6].

In Sections 2 to 4 (electron-multiplying) CCDs, QI SPDs from Ref. [6] and PMTs are discussed, respectively, and the figures of merit are calculated. The results are compared in Section 5. To calculate the count rate sensitivity, $\dot{N}_{\mathrm{ul}}$, a confidence level of 95 % is assumed.

2 Imaging Charge-coupled Devices

CCDs are currently the prime choice for scientific visual imaging with a wide range of devices to choose from. The imaging area of CCDs is segmented into columns each consisting of a series of MIS[1] capacitors. During data taking, these capacitors are biased into deep-depletion. Incident photons are absorbed in the semiconductor material and produce free charges which are stored by the capacitors. These charges are integrated during an exposure. At the end of an exposure, the collected charges are transported to a read-out structure and digitized. Hence, a CCD cannot resolve single photons. In addition to the charges generated by incident photons, thermally generated free charges are produced and stored as well. These constitute the dark counts, which contributes to the overall noise. The process of read-out and digitization adds a second source of noise. Hence, the total noise is given by

$$\sigma_{\mathrm{tot}}^2 = \sigma_{\mathrm{ro}}^2 + t\,R_{\mathrm{dc}},$$

where σ_{ro} is the read-out noise, t the exposure time and R_{dc} the production rate of dark counts.

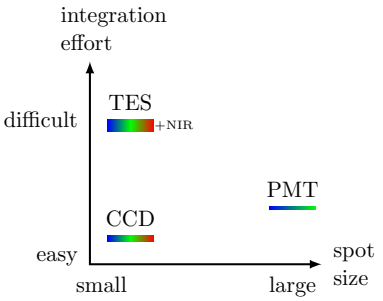

Figure 1: Schematic summary of findings. The discussed detectors are ordered by integration effort and possible spot sizes. The color scales indicate the spectral range. The colorbars' relative sizes indicate the quantum efficiency.

The LSW experiment ALPS at DESY used a commercially available, low noise CCD camera with $13 \times 13\,\mu\mathrm{m}^2$ sized pixels (PIXIS CCD) [3, 8]. A dark count rate below $8 \times 10^{-4}\,\mathrm{e}/(\mathrm{px\,s})$ was achieved by liquid cooling of the CCD chip and the camera was equipped with low-noise read-out electronics ($\sigma_{\mathrm{ro}} = 4.3\,\mathrm{e}$) [9]. Thus, the read-out noise is the larger contribution to the total noise for exposures shorter than 1.5 h. If the signal can be focussed to a single pixel, a data set of 20 one hour exposures yields a figure of merit $\mu = 1667\,\mathrm{s/photon}$ for a quantum efficiency of 80 % which is typical in the visible spectrum.

Electron multiplying CCDs (EMCCDs) amplify the charge signal before read-out in an avalanche multiplication register [10]. This allows to neglect the read-out noise and, hence, short exposure times are possible. But at the same time, the quantum efficiency is effectively reduced by a factor of two due to the additional noise from the multiplication process [11]. The original quantum efficiency, i.e. without charge multiplication in an avalanche register, can be recovered by interpreting the read-out values in a binary fashion, i.e. photon detected yes/no [12], where a photon is counted if the digitized signal is above a threshold, $k\,\sigma$. Hence, the analysis can be reduced to that of a counting experiment.

[1] metal-insulator-semiconductor structure

If contamination by noise and loss of signal due to the threshold can be neglected, this yields $\mu = 3307\,\mathrm{s/photon}$ assuming the same values as above ($\eta = 80\,\%$, $R_{\mathrm{dc}} = 8 \times 10^{-4}\,\mathrm{e/(px\,s)}$ and 20 h of data).

For NIR wavelengths, the PIXIS CCD was found to have a reduced quantum efficiency of 1.2 % [9]. The figure of merit is reduced accordingly for the PIXIS CCD ($\mu = 24\,\mathrm{s/photon}$) and EMCCD ($\mu = 50\,\mathrm{s/photon}$). InGaAs based CCDs exist, which have a much smaller band gap than silicon and, therefore, a much higher quantum efficiency ($\sim 85\,\%$) than the silicon-based PIXIS CCD. But these devices also have a dark count rate, which is six orders of magnitude above that of the PIXIS CCD [13]. Therefore, these specialized CCDs are of no help when improving the detector part of LSW experiments.

3 Quantum Information Photo-detectors

To maintain a low dark count rate and achieve a high quantum efficiency at NIR wavelengths at the same time, sensors operated at cryogenic temperatures can be used. Most of the devices listed in Ref. [6] (cryogenic or not) have however dark count rates much above that of the PIXIS CCD. Only transition edge sensors (TES) were found to have low dark count rates below that of the PIXIS CCD [14]. TES are bolometric sensors which are operated at $\mathcal{O}(50\,\mathrm{mK})$. Combined with a proper coating, high quantum efficiencies of 95 % can be reached [15]. The dark count rate and quantum efficiency expected for ALPS-II ($\eta = 75\,\%$ $\dot{N}_{\mathrm{dc}} = 10^{-5}\,\mathrm{s}^{-1}$) are assumed here as benchmark parameters [5]. The corresponding figure of merit for 20 hours of data is $\mu = 14045\,\mathrm{s/photon}$.

4 Photo-multiplier Tubes

The sensitive area of TES detectors and the pixels of a CCD are both of order $\mathcal{O}(10 \times 10\,\mu\mathrm{m}^2)$. If the signal cannot be focussed on such a small area, the pixels of a CCD can be binned. But, as discussed above, the integrated dark count rate increases at the same rate as the area of interest. Accordingly, the figure of merit and the sensitivity on the coupling may worsen significantly. In this case, PMTs are a very good alternative although they have a limited quantum efficiency ($\eta \lesssim 30\,\%$) and a limited spectral range ($300\,\mathrm{nm} \leq \lambda \leq 850\,\mathrm{nm}$) [16]. The sensitive area of a PMT consists of a photo-sensitive material with a low work function. Incident photons produce free electrons which are directed to an electron multiplier by a focussing electrode. The high gain of the electron multiplier allows single photon detection. Cooling the sensitive area reduces the dark count rate. For example, the SHIPS helioscope uses a PMT with an active area of $2.5\,\mathrm{cm}^2$, which has a peak quantum efficiency of 25 % and a dark count rate of $0.5\,\mathrm{cnt/s}$ when cooled to $-21°\mathrm{C}$ [18]. This corresponds to $\mu = 39\,\mathrm{s/photon}$.

Detector	η [%]	$\dot{N}_{\mathrm{dc}}$ [s^{-1}]	μ [s/photon]
CCD (visible)	80	8×10^{-4}	1667
EMCCD (visible)	80	8×10^{-4}	3307
CCD (NIR)	1.2	8×10^{-4}	24
EMCCD (NIR)	1.2	8×10^{-4}	51
TES	75	10^{-5}	14045
PMT	25	0.5	39

Table 1: Comparison of different detectors. The table lists the typical quantum efficiency, η, and dark count rate, $\dot{N}_{\mathrm{dc}}$, together with the figure of merit, μ, for silicon CCD/EMCCD, TES and PMT as discussed in the text.

5 Conclusion

Surprisingly, of all SPDs used in QI experiments, only TES detectors have a sufficiently low dark count rate to improve significantly over conventional CCDs. The figures of merit of the detectors mentioned in the above sections are summarized in Tab. 1. Of the presented alternatives, a TES is the best option. Especially in the NIR, a TES is superior to a CCD because its quantum efficiency does not deteriorate for these wavelengths. In the visible regime, CCDs remain a viable option when only few resources are available for detector development. From the values listed in Tab. 1, it seems that PMTs are the worst option. Their figure of merit is two orders of magnitude below that of CCDs (visible), which is caused mainly by their high dark count rate. However, considering their large sensitive area, PMTs are the detector of choice if the signal cannot be focussed very well. These findings are schematically summarized in Fig. 1.

Acknowledgments

The study of the PIXIS CCD was kindly supported by G. Wiedemann (Hamburger Sternwarte).

References

[1] J. Redondo and A. Ringwald, Contemp. Phys. **52**, 211 (2011) [arXiv:1011.3741 [hep-ph]].

[2] G. Ruoso, R. Cameron, G. Cantatore, A. C. Melissinos, Y. Semertzidis, H. J. Halama, D. M. Lazarus and A. G. Prodell *et al.*, Z. Phys. C **56**, 505 (1992).

[3] K. Ehret, M. Frede, S. Ghazaryan, M. Hildebrandt, E.-A. Knabbe, D. Kracht, A. Lindner and J. List *et al.*, Phys. Lett. B **689**, 149 (2010) [arXiv:1004.1313 [hep-ex]].

[4] P. Pugnat *et al.* [OSQAR Collaboration], arXiv:1306.0443 [hep-ex].
M. Sulc [OSQAR Collaboration], *contribution to this workshop.*

[5] R. Bähre, B. Döbrich, J. Dreyling-Eschweiler, S. Ghazaryan, R. Hodajerdi, D. Horns, F. Januschek and E. -A. Knabbe *et al.*, JINST **8**, T09001 (2013) [arXiv:1302.5647 [physics.ins-det]].
B. Döbrich [for the ALPS-II Collaboration], *contribution to this workshop* [arXiv:1309.3965 [physics.ins-det]].

[6] M. D. Eisaman, J. Fan, A. Migdall and S. V. Polyakov, Rev. Sci. Instrum. **82**, 7 (2011) [doi:10.1063/1.3610677].

[7] G. J. Feldman and R. D. Cousins, Phys. Rev. D **57**, 3873 (1998) [physics/9711021 [physics.data-an]].

[8] Princeton Instruments, `http://www.princetoninstruments.com/Uploads/Princeton/Documents/Datasheets/PIXIS/Princeton_Instruments_PIXIS_1024_eXcelon_rev_N3_8.21.2012.pdf`

[9] J. E. v. Seggern, PhD thesis, in preparation.

[10] S. Madan, B. Bhaumik and J. Vasi, IEEE TED **30**, 694 (1983) [doi:10.1109/T-ED.1983.21191].

[11] M. Stanford and B. Hadwen, IEEE TED **50** 1227 (2003) [doi:10.1109/TED.2003.813462].

[12] O. Daigle, C. Carignan, J.-L. Gach, C. Guillaume S. Lessard C.-A. Fortin, S. Blais-Ouellette, Publ. Astron. Soc. Pac. **121** 866 (2009).

[13] Princeton Instruments, `http://www.princetoninstruments.com/Uploads/Princeton/Documents/TechNotes/InGaAs_Tech_Note_Princeton_InstrumentsrevB0.pdf`

[14] G. Cantatore, *contribution to this workshop.*
J. Dreyling-Eschweiler and D. Horns, *contribution to this workshop*, [arXiv:1309.5024 [physics.ins-det]].

[15] A. Lita, A. Miller, and S. Nam, Opt. Express **16** 3032 (2008).

[16] Hamamatsu, "Photomultiplier tubes", edition 3a (2007).

[17] ET Enterprises, 9215B, `http://my.et-enterprises.com/pdf/9215B.pdf`.

[18] M. Schwarz, *contribution to this workshop.*

Detecting an infrared Photon within an Hour – Transition-Edge Detector at ALPS-II

J. Dreyling-Eschweiler[1,2] *and D. Horns*[2]*, for the ALPS-II collaboration*

[1]Deutsches Elektronen-Synchrotron (DESY), Hamburg, Germany
[2]University of Hamburg, Hamburg, Germany

DOI: http://dx.doi.org/10.3204/DESY-PROC-2013-04/dreyling-eschweiler_jan

An essential design requirement of the ALPS-II experiment is the efficient detection of single photons with a very low instrumental background of 10 μHz. In 2011 the ALPS collaboration started to set up a TES detector (Transition-Edge Sensor) for ALPS-II, the second phase of the experiment. Since mid of 2013 the setup is ready for characterization in the ALPS laboratory: an ADR cryostat (Adiabatic Demagnetization Refrigerator) as millikelvin environment, a low noise SQUID (Superconducting Quantum Interference Device) with electronics for read-out and a fiber-coupled high-efficient TES for near-infrared photons as sensor. First measurements have shown a good discrimination between noise and 1064 nm signals.

1 Photon detection at ALPS-I and ALPS-II

The ALPS-I experiment has provided the most constraining limits for photon-ALP coupling for a light-shining-through-a-wall experiment [1]. The detector was a CCD camera (Charged-coupled Device) with a quantum efficiency >90 % for the ALPS-I wavelength of 532 nm and a dark current of about 0.0008 e s^{-1} per pixel. Data acquisition was done with 1 h data respectively dark frames being in the linear noise regime where the dark current dominates the read-out noise, but limited by charged particle background like cosmics or decay products. For 1 h frames the overall detector noise is about 0.0018 s^{-1} including the read-out noise of the CCD and a beam focus on 3x3 pixel [2].

In the second phase, ALPS-II, the overall sensitivity of the experiment will mainly be improved by higher laser power, a regeneration cavity behind the wall and a length up to 200 m [2, 3]. But by switching to a laser wavelength of 1064 nm the quantum efficiency of the CCD drops below 1.5 % [4] because of the Si band gap. So in parallel the ALPS collaboration is looking for an alternative detector. A promising candidate is a TES having no dark counts intrinsically [5] and providing an energy and time resolution in addition compared to a CCD. A quantum efficiency for near-infrared photons near unity has been realized [6].

2 TES detectors: working principle and realizations

A TES is operating as a microcalorimeter: The sensor consists of a film that is biased by an electrical current into the superconducting phase transition. If energy is deposited e.g. by a

photon, the TES heats up fast and cools down slowly because the TES is weakly linked to the cold bath and relaxing to its working point [7]. The change of temperature results in a change of resistance and, in a voltage-biased circuit, in a change of current which can be measured by an inductive-coupled and impedance-matched SQUID and read out as a voltage change with proper electronics. In the linear description of these electro-thermal system the integral of the pulse is proportional to the energy input.

The realized TES detectors reached a big bandwidth in the last 20 years: They cover the electromagnetic spectrum from gamma rays, over X-rays and the optical/infrared regime, through millimeter range. Applications are found in spectroscopy, astronomy or direct Dark Matter searches for example. For ALPS there is an overlap with the field of quantum information, which uses TES detectors as single-photon counter at the telecommunication wavelength 1330/1550 nm. The research and development of fiber-coupled high-efficient TES for detection of near-infrared photons is actively carried out at NIST (National Institute of Standards and Technology) in the U.S. and AIST (National Institute of Advanced Industrial Science and Technology) in Japan. Both metrology institutes reached a near unity efficiency for detecting single infrared photons [6, 8] fitting to ALPS detection requirements. For these devices time resolution is up to $\sim$1 μs and energy resolution $\sim$0.1 eV. The superconducting transition of the sensor material is about $\sim$140 mK for the W-based TESs of NIST and about $\sim$300 mK for the Ti/Au-based TESs of AIST.

3 Realization for ALPS-II: history, croyostat and sensors

The ALPS collaboration set to work on TESs, SQUIDs and mK-cryogenics in the end of 2010. The primary goal has been to operate and characterize a TES. A focus has been on the background. Only upper limits have been set by previous studies [9, 10]. In early 2011 we had the opportunity to see the operation of SQUIDs coupled to NIST TES assembled in a DR (Dilution Refrigerator) at the PTB (Physikalisch-Technische Bundesanstalt) in Berlin. We tried to establish a TES setup at the University of Camerino, Italy, during two measurement periods in 2011, which were limited due the evaporating liquid Helium as pre-cooling technique [11]: In a dip-in DR we assembled a low-efficiency TES chip from INRIM (L'Istituto Nazionale di Ricerca Metrologica) coupled to a SQUID from the company Magnicon, Germany. The optical fiber fed in the cryostat wasn't directly coupled to the TES but its end pointed to the sensor area. We succesfully achieved single photon detection with this first setup [12]. Since the end of 2012 we operate and characterize an ADR cryostat from the company Entropy, Germany. First time we operated it at PTB, Berlin, for a good knowledge transfer. There we used a sensor module equipped with PTB SQUIDs and NIST TESs as proof of principle. After moving the cryostat to Hamburg in the end of 2012, in early 2013 we started operating sensor modules within the ADR in the ALPS laboratory.

The ADR is a no-liquid-cryogens cryostat with a closed pre-cooling He cycle: integrated is a two-stage pulse-tube cooler with which the 4 K stage is established, see Fig. 1. Attached to that is a superconducting magnet[1] which surrounds a double-stage salt pill unit which can be coupled/decoupled to the 4 K stage by a piezo-driven motor. An adiabatic demagnetization cycle reaches 30 mK as lowest temperature after >90 min. By regulating the magnet a constant bath temperature for sensors is achieved: For example the hold time for 80 mK $\pm$ 25 μK (rms)

[1] With 40 A current a magnetic field of 6 T is realized.

is about 24 h. The remnant magnetic field for regulating is screened by a cryoperm layer around the magnet passively and doesn't affect the operation of the sensors.

ALPS has two sensor modules, each with two channels and with optimized TESs for 1064 nm: One with TESs from AIST, where the single mode fiber is glued to the sensitive area [8], a second with TESs from NIST, where the single mode fiber is connected with the standard way of FC connectors [13], see Fig. 2. Both sensor modules are connected to PTB dc 2-stage SQUIDs, which were developed for low-noise TES readout. With a readout electronic (XXF-1) from the company Magnicon the SQUID and TES sensors are set to the working point. For the first measurements the data acquisition was done with an oscilloscope (DPO700c from Tektronix).

4 First results

We successfully set up the cryogenic mK-environment with an ADR cryostat in the ALPS laboratory. In several cool downs we operate the sensor modules as a single photon detector for the ALPS-II wavelength.

As a first important result for ALPS-II, signal and noise (electronic, Johnson and thermal noise) are distinguishable, see fig. 3. In this measurement we set the sensor module in an arbitrarily chosen working point and realized a single photon rate with an attenuated laser (1066.7 nm) as a signal. The relative energy resolution is $\Delta E/E = 7.7\,\%$.

Further measurements for optimization of the working point and long time measurements for background analysis are on the way [14]. Thermal photons of 300 K were found to be one main component for background events [10].

Acknowledgments

The ALPS collaboration wants to thank everybody who helped along the way to setup this TES detector. Special thanks go to Joern Beyer (PTB), Daiji Fukuda (AIST) and Sae Woo Nam (NIST) for supplying the superconducting devices.

References

[1] K. Ehret *et al.*, "New ALPS Results on Hidden-Sector Lightweights", Phys. Lett. B **689**, 149 (2010) [arXiv:1004.1313 [hep-ex]].

[2] R. Bähre *et al.*, "Any Light Particle Search II – Technical Design Report", JINST **1309**, T09001 (2013) [arXiv:1302.5647 [physics.ins-det]].

[3] B. Döbrich for the ALPS-II collaboration, these proceedings.

[4] J. E. von Seggern, PhD thesis in preparation, University of Hamburg.

[5] B. Cabrera *et al.*, "Detection of single infrared, optical, and ultraviolet photons using superconducting transition edge sensors", Appl. Phys. Lett. **73**, 735 (1998).

[6] A. E. Lita *et al.*, "Superconducting transition-edge sensors optimized for high-efficiency photon-number resolving detectors", SPIE Conf. Ser. **7681** (2010).

[7] K. D. Irwin, G. C. Hilton, "Transition-Edge Sensors", in Cryogenic Particle Detection (Springer, 2005).

[8] D. Fukuda *et al.*, "Titanium-based transition-edge photon number resolving detector with 98% detection efficiency with index-matched small-gap fiber coupling" Opt. Express **19**(2), 870 (2011).

[9] A. Miller *et al.*, "Demonstration of a low-noise near-infrared photon counter with multiphoton discrimination" Appl. Phys. Lett. **83** 791 (2003).

[10] A. J. Miller *et al.*, "Superconducting photon number resolving detectors: Performance and promise" in Proceedings of the 8th international conference on quantum communication, measurement and computing (NICT Press, 2007).

[11] G. Cantatore, contribution to PATRAS 2011.

[12] G. Cantatore, contribution to PATRAS 2013.

[13] A. J. Miller *et al.*, "Compact cryogenic self-aligning fiber-to-detector coupling with losses below one percent" Opt. Express **19**(10) (2012).

[14] J. Dreyling-Eschweiler, PhD thesis in preparation, University of Hamburg.

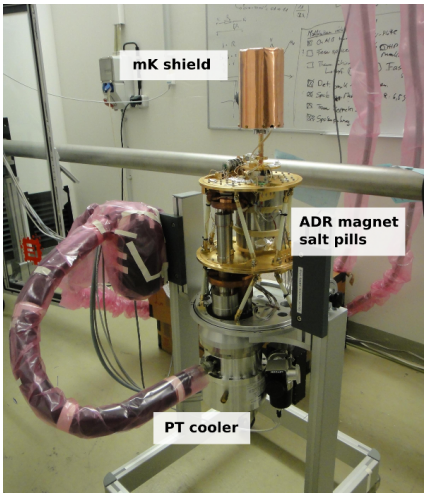

Figure 1: Open ADR cryostat (upside down) with different cooling stages in the ALPS-IIa lab: Here at the top a mK copper shield is connected to the cold finger where the sensors are located inside.

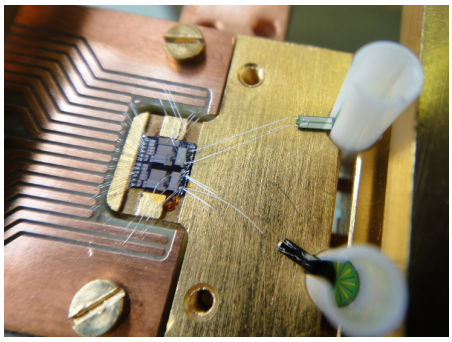

Figure 2: NIST module with two channels: Left at the end of the PCB the SQUID chip is located. Bondwires connect the TES, which has a shape similiar to a table-tennis bat. Around the chip is a ceramic split sleeve to connect a fiber with a ferrule end of a common FC connector. The sensitive area of doped tungsten (W) is about 25x25 μm.

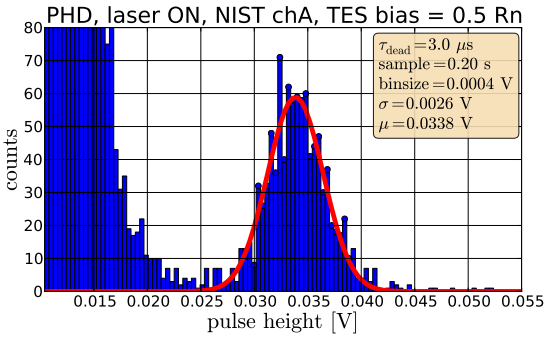

Figure 3: Pulse height distribution with a signal peak (red Gauss shape) of 1066.7 nm photons. Noise counts are below $\sim$ 25 mV.

Optomechanics and astroparticle physics; an (im)possible union

M. Karuza

University of Rijeka, Rijeka, Croatia and INFN Trieste, Trieste, Italy

DOI: http://dx.doi.org/10.3204/DESY-PROC-2013-04/karuza_marin

In recent year with the advent of optomechanics, physics has gained a new powerful tool for small displacement and small forces sensing. It is based on two key ingredients, a resonant optical cavity and a micro-fabricated mechanical resonator. By coupling the two by radiation pressure a powerful tool, capable of sensing extremely small signals at sensitivity limit imposed by Heisenberg uncertainty principle, can be constructed. Here we will try to exploit it's extraordinary sensitivity for detection of radiation pressure exerted by hypothetical particles that could be produced in the Sun's interior.

1 Introduction

In recent years, with development of micro-fabricating techniques a new field in physics has started its rapid growth. The field is cavity optomechanics. It offers a plethora of possibilities due to coupling of mechanical resonator to the light by radiation pressure. The mechanical degree of freedom can be provided by variety of designs as nanomechanical beam, silica toroidal micro-cavities, silicon nitride membranes etc, and the other ingredient, the resonating cavity can be either inside the mechanical element, or outside as in the case of Fabry - Perot cavity. The properties of mechanical and optical degrees of freedom can be relatively simply controlled and modified accordingly to the requests posed in front of them. A notable example is light by light control that can be achieved by tailoring the interaction of light with mechanical resonances. It is an optomechanical analogue of the electromagnetically induced transparency (EIT) [3], a well know effect that has been first observed in atomic systems. The optomechanical analogue is known as optomechanically induced transparency (OMIT) and has been demonstrated both in optical [4] and microwave domain [5]. In EIT, and by analogy also in the case of OMIT an intense control beam (pump) modifies the optical response of an opaque medium making it transparent in a narrow bandwidth. Concomitant with the transparency window there is also a variation of the refractive index that induces a significant slow down of the group velocity of the probe beam which can be used to delay, stop, store and retrieve both classical and quantum information. In OMIT the internal resonance of the atom is replaced by the interaction of optical and mechanical degrees of freedom which occurs when the control beam is tuned to the lower motional sideband of the cavity resonance. It can be exploited in a variety of technical applications with obvious advantages over atomic systems since its properties can be tailored at will, and due to lower resonance frequencies longer delay times can be achieved. Besides controlling light by light, also the properties of mechanical system could be controlled by the laser beam. The mechanical response of the vibrational mode is modified by its interaction

with light [6]. Both the mechanical frequency and the susceptibility are modified and the selected resonance mode becomes less sensitive to a thermal noise. This effect is known also as (resolved) sideband cooling. The exceptional tailoring possibilities and sensitive readout make these systems extraordinary sensors for small forces and displacement sensing limited only by Heisenberg uncertainty principle, making them interesting for various applications. One of the fields where it can find its place is, surprisingly, astroparticle physics.

One of the best known, and most studied, celestial bodies is the Sun, but nevertheless some of the questions related to the processes that happen inside still remain unanswered. This leaves a window for production of yet experimentally not observed Weakly Interacting Slim Particles (WISPs). Some types of these particles as for example axions are Dark Matter candidates, and the others, as Chameleons [7], could be an answer to the Dark Energy problem. The Chameleons due to their peculiar interaction with matter that is proportional to the density of matter offer a possibility of using kinetic detection together with an appropriate sensor. The kinetic detection exploits the fact that the Chameleons are reflected from a solid surface, thus changing their momentum which is compensated by momentum conservation law by the change in the momentum of the surface itself. A good sensor for the kinetic detection could be a thin membrane, with a readout sensitive to small displacements, caused, in this case, by the radiation pressure of solar Chameleons. If a thin silicon nitride membrane is placed inside a Fabry-Perot optical cavity, a setup sensible to movements caused by radiation pressure is obtained, thus making the detection of Chameleon flux possible. In the following section the experimental setup and the measuring technique will be presented.

2 Experimental setup

The experimental setup is based on the so called membrane in the middle setup 1, where a thin semitransparent silicon nitride membrane is placed in the middle between two high reflectivity mirrors that form a resonant Fabry-Perot cavity. If the membrane is tilted with

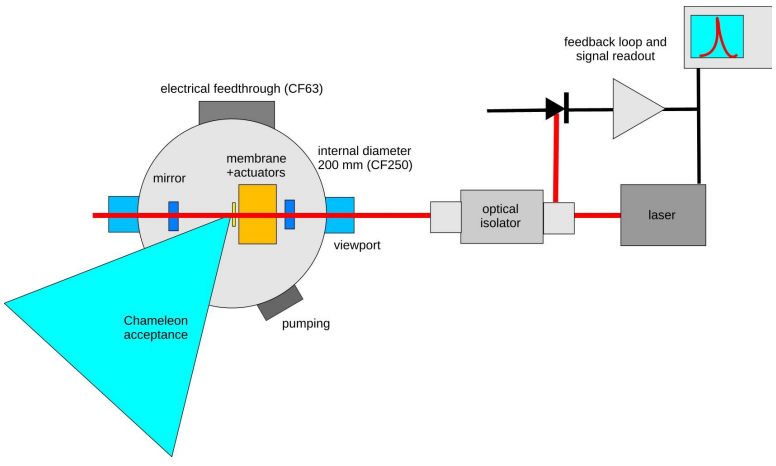

Figure 1: The simplest version of the membrane in the middle setup. The displacement readout is obtained directly from the feedback loop.

respect to the optical axis, the cavity modes become distorted and degenerate modes are split, avoided crossings are created, and the new cavity modes are superposition of the standard TEM_{mn} modes [2]. The new structure of the modes is shown in the following picture 2, where the cavity resonant frequency strongly depends on the linear position of the membrane

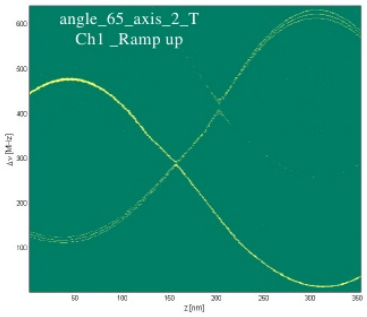

Figure 2: Cavity modes modified by a presence of a thin membrane. Avoided crossings and degenerate mode splitting can be seen.

along the optical axis. By positioning it where the derivative with respect to the position is highest, highest sensitivity is obtained. Once appropriately positioned the laser is locked to the cavity instantaneous resonant frequency, and a buildup of optical power in the cavity is obtained. It is sufficient to observe the Pound Drever Hall feedback signal, and an information on the movement of the membrane in the cavity can be extracted. The origin of the observed movement could be the radiation pressure of the solar Chameleons hitting the membrane [8]. This so called DC mode of detection is only one of the possibilities, otherwise in the AC mode height of the mechanical resonance peak can be observed since the height is proportional to the displacement. The sensitivity in the latter case can be enhanced by cooling the mechanical modes of the membrane either by placing it in a low temperature environment or by cooling it optically with resolved sideband cooling technique. The two modes can be also combined to reach mechanical resonance's ground state.

If this sensor is successfully applied an upper limit to the solar Chameleon flux could be inferred. An estimate could be obtained starting from the sensitivity of an setup constructed in the Camerino Quantum Optics Laboratory [1]. There a displacement sensitivity of $10^{-15}\frac{m}{\sqrt{HZ}}$ has been obtained. By using the cited displacement sensitivity together with an active surface of $25mm^2$, that is the maximum area of the membrane that is commercially available, a force sensitivity $s_F = 10^{-13}\frac{N}{\sqrt{Hz}}$ can be inferred. This corresponds to an solar Chameleon flux equal to $10^{-2}\frac{W}{m^2}$.

3 Conclusion

This measurement would be the first of its kind and would place a bound on the solar Chameleon flux. Furthermore, it could be improved by placing the sensor in front of an X-ray telescope that would focus the Chameleon flux on the membrane. If some of the cooling schemes are applied the sensibility can have a further improvement and by placing a chopper in the Chameleon

beam, and having a Chameleon reflector other improvement factors can be expected.

4 Acknowledgments

I would like to thank quantum optics group of David Vitali at Physics Department of School of Sciences and Technologies at University of Camerino where the results with the membrane in the middle setup have been obtained and Heinrich Brauniger, Giovanni Cantatore, Klaus Desch, Dieter Hoffmann, Jochen Kaminski, Axel Lindner, Stefan Neff and Konstantin Zioutas who made its extension and application in the field of astroparticle physics possible.

5 Bibliography

References

[1] M. Karuza *et al.* , "Optomechanical sideband cooling of a thin membrane within a cavity," New. Journal. of Physics **14**, 181301 (2012) [arXiv:1206.0614 [quant-ph]].

[2] M. Karuza *et al.*, "Tunable linear and quadratic optomechanical coupling for a tilted membrane within an optical cavity: theory and experiment," Journal of Optics **15**, 025704 (2013) [arXiv:1112.6002 [quant-ph]].

[3] M. Fleischhauer *et al.*, "Electromagnetically induced transparency: Optics in coherent media," Rev. Mod. Phys. , **77**, 633 (2005)

[4] S. Weis *et al.*, "Optomechanically Induced Transparency," Science, **330**, 1520 (2010)

[5] J.D. Teufel *et al.*, "Optomechanically Induced Transparency," Nature(London), **471**, 204 (2011)

[6] C. Biancofiore *et al.* , "Quantum dynamics of an optical cavity coupled to a thin semitransparent membrane: Effect of membrane absorption," Phys. Rev. A **84**, 033814 (2011)

[7] Ph. Brax *et al.* , "A Chameleon Primer," [arXiv:0706.1024v2 [astro-ph]].

[8] O.K. Baker *et al.* , "Detection of radiation pressure from solar chameleons," [arXiv:1201.6508v1 [astro-ph.IM]].

MainzTPC: A Time Projection Chamber for the Study of Liquid Xenon Light & Charge Response

P. Sissol, B. Beskers, M. Scheibelhut, C. Grignon, R. Othegraven, U. Oberlack

Institute of Physics & PRISMA Cluster of Excellence, Johannes Gutenberg University, Mainz, Germany

DOI: http://dx.doi.org/10.3204/DESY-PROC-2013-04/sissol_pierre

This proceeding is an overview on the development and construction of a dual-phase liquid xenon time projection chamber in Mainz. It will be used for the measurement of the scintillation and ionization yield of electronic and nuclear recoils off xenon nuclei in a scattering experiment across a wide range of energies. In addition, we aim at measuring the pulse shape of the scintillation light with high bandwidth and study its suitability as a discrimination method for background events.

1 Introduction

One of the most promising generic candidates for Dark Matter is the Weakly Interacting Massive Particle (WIMP). A recent review on direct WIMP Dark Matter detection can be found in [1]. Direct detection experiments seek to measure the recoil of WIMPs scattering off target nuclei in the detector. The currently most sensitive class of such experiments consists of dual-phase xenon time projection chambers (TPCs) such as XENON100, shown schematically in Fig. 1. The latest results of XENON100 can be retrieved from [2].

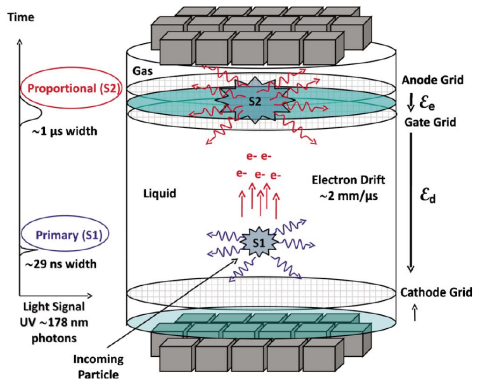

Figure 1: 1: Principle of a dual-phase LXe TPC [6].

The energy deposited in the target material in such an interaction is in the keV range, therefore high sensitivity and a good understanding of the background are crucial for the measurement.
If a particle (e.g. a WIMP) scatters in the liquid xenon (LXe), the deposited scattering energy leads to excited and ionized xenon atoms, resulting in a prompt scintillation signal and free electrons. While the scintillation light is detected as S1 signal by the photomultiplier tubes (PMTs) on top and bottom of the TPC, the electrons are forced to drift upwards in an applied electric field. For this three thin meshes are used to apply the high voltage, a cathode mesh at the bottom, an anode mesh at the top and a gate mesh just a bit below the anode mesh. The phase transition from liquid to gaseous xenon (GXe) is sited in the middle between gate and anode. The electrons encounter a

higher electric field between gate and anode and are extracted to $\approx 100\,\%$ into the gas phase, where they are accelerated additionally. This leads to a proportional scintillation called S2 signal which is primarily seen by the upper PMT array.
Using the time difference between S1 and S2 and the electron drift velocity, the z-coordinate of the interaction point can be determinated. Furthermore, the x-y-position of the interaction can be read out by the illumination pattern of the S2 signal on the top PMT array. This provides a 3D position reconstruction, allowing the definition of a fiducialized volume inside the LXe and discrimination of single vs. multiple site events. This volume is chosen to reject interactions in regions near the edges of the TPC where influences of electronics, electric field inhomogeneities and other background sources are most likely. Further information on the working principle of Dark Matter searches with xenon TPCs can be found in [6].

2 Liquid xenon low-energy response and scintillation pulse shape

Background discrimination is a crucial factor in Dark Matter search experiments. Therefore a well-founded knowledge of the possible background is necessary. One distinguishes between electronic recoils, caused by gamma-rays or electrons, and nuclear recoils, which result from neutron or WIMP scattering. The Mainz TPC is designed to examine two different approaches for discrimination.
After the scattering of a particle in LXe, the xenon atoms form excimers and dimers, respectively, and eventually deexcite, recombine and decay to ordinary xenon atoms. By dimer deexcitation, scintillation light is produced. Different types of recoil lead to different population of singlett states (with decay time $\tau_\mathrm{S} = 2.2\,\mathrm{ns}$) and triplett states ($\tau_\mathrm{T} = 27\,\mathrm{ns}$) of the xenon excimer, hence the shape of the primary scintillation signal S1 depends on the interaction type. Therefore the scintillation light will be measured with fast electronics to investigate pulse shape as discrimination criterion.
Furthermore, the ratio between prompt scintillation light S1 and free electrons, leading to the proportional scintillation signal S2, is dependend on the scattering process; for electronic recoils S2 is much larger than S1 while for nuclear recoils less electrons are produced and therefore S2 is reduced. This is already used for background discrimination in e.g. XENON100. The best approach to measure energy and discriminate between nuclear and electronic recoils consists of a 2D analysis in S1 and S2 simultaneously. This, however, requires precise knowledge of scintillation and charge yield at low energies, where measurements so far are incomplete or imprecise. The Mainz TPC will be used to probe low-energy recoils down to $\approx 2\,\mathrm{keV}$ with high precision.

3 TPC design

The TPC design is optimized for a Compton scatter experiment. This means especially that the active volume is relatively small with only 52 mm in diameter and 50 mm in height to reduce multiple scattering. Due to this small dimensions it is impossible to have an array of PMTs on top and bottom, hence just one cylindric 2 inch-diameter PMT is used on top and bottom each. This has additionally the advantage that there are no gaps between different PMTs resulting in a higher light yield of the TPC. To achieve x-y-position resolution by measuring the S2

signal, which is not possible using just one PMT, we added an array of 8 large area avalanche photodiodes (APDs) surrounding the liquid gas interface looking inwards. The active volume is surrounded by a PTFE cylinder, as PTFE is highly reflective for VUV wavelength. Besides this, the construction design was chosen to have the least amount of passive materials possible.

3.1 Electric field

The electric field is produced by meshes with a wire-width of only 14 μm and a pitch of 268 μm. Four meshes are implemented: A shield mesh above the bottom PMT to avoid influences of the electric field on the readout, the cathode mesh at the lower end of the active volume, at the upper end the gate mesh below the liquid gas interface, and the anode mesh just above. A mesh shielding the top PMT was not implemented, since we will use negative high voltage on the cathode and ground potential on the anode so that there is no field influence on the top PMT.
The uniformity of the electric drift field is crucial to get clean data sets. Nonuniformities would require corrections to the reconstructed interaction position in z and r for some parts of the active volume and might also require to decrease the size of the fiducial volume to avoid edge effects. To make the electric field as uniform as possible, a flexible printed circuit board with parallel conduction lines is used as electric field cage (brown cylinder in Fig. 3). The geometrical properties for the meshes as well as for the field cage were examined in finite element simulations. According to these the meshes and PCB were designed/chosen and we can achieve a very uniform drift field with deviations of the field in the outermost corners of the active volume of less than $\approx$ 5 % for very low drift fields (0.1 kV/cm). For stronger drift fields (3 kV/cm) the deviation is below 1%.

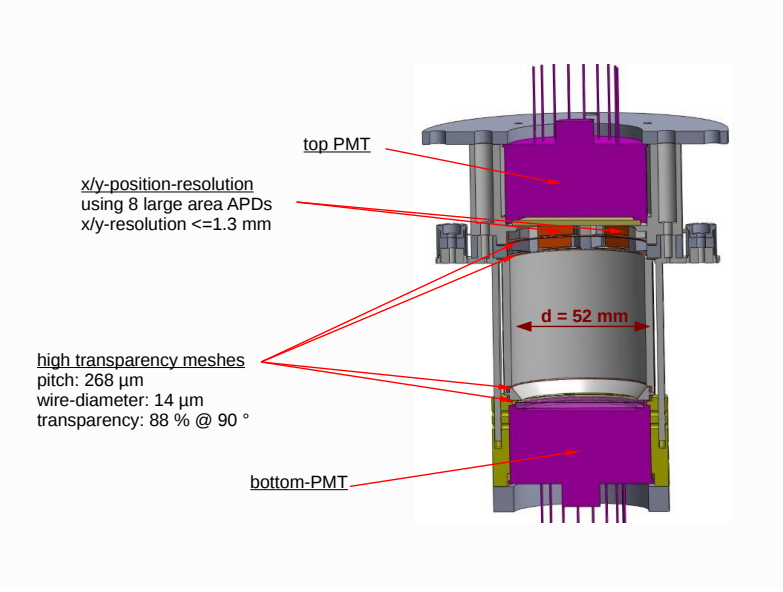

Figure 2: CAD section drawing of the TPC design.

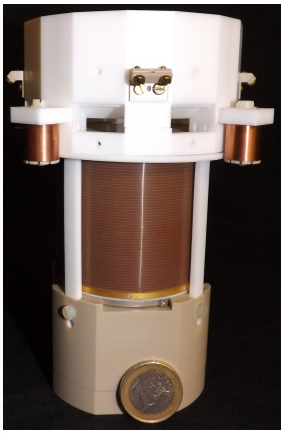

Figure 3: Photograph of the assembled TPC without photosensors.

3.2 Light readout

The PMTs have been chosen for their compact design, their fast response and their high quantum efficiency ($> 30\%$, stated by manufacturer [4]) in the VUV wavelength regime.
As mentioned before the PMTs in our TPC cannot be used for x-y-position resolution and therefore the APDs are introduced. Avalanche photodiodes provide relatively high internal gains ($\sim 10^3$), small housing and only little passive material while providing suitably large active areas ($>1\,\mathrm{cm}^2$) [5]. The APD model we use has been measured to achieve QE of $> 30\,\%$ at 178 nm in [7] and gains up to several 1000.
Both PMTs and APDs have to be characterized since their performance strongly depends on bias voltage and temperature and also because each device has slightly different properties which have to be taken into account for high precision.

3.3 Simulations

The classical Compton scatter experiment uses the scattering angle to determine the energy deposit in the scattering target (in this case the active volume of the xenon TPC) by using the Compton formula. Experimentally this is done using a scintillation detector (e.g. NaI) to measure the scattering angle. However, especially for low energy deposits (small angles) this method leads to large uncertainties due to the fact that the Compton formula only applies for electrons at rest. Bound electrons in an atomic potential have a certain momentum which has to be taken into account and results in a statistical smearing of the deposited energy for fixed angles.
This effect, called the Doppler effect, has been examined in a Geant4 simulation (see Fig.: 4). The plot shows the relative energy resolution for the deposited energy in the active volume, the red curve being the smeared resolution obtained by the angle measurement, in black the Doppler broadened resolution for a perfect angle measurement and in blue the resolution with a germanium detector which measures the scattered energy directly. As can be seen, the energy resolution for the direct energy measurement with the Ge detector is far better than for measuring the scattering angle. Therefore a Ge detector is implemented in the Mainz TPC setup as an improvement compared to some of the previous work by other groups.
Another simulation carried out was the study of the x-y-resolution for the 3D position reconstruction using the above mentioned APDs. In a Geant4 simulation we compared different numbers of APDs and different sizes. The simulations, based on code developed and tested for XENON100 [8], showed for a configuration of eight 13x13 mm^2 APDs a reconstruction error of less than 1.3 mm in the whole TPC (see also Fig.: 5). The z-position resolution was not simulated, as we expect it to be at least as good as in XENON100.

3.4 Electronics

As one of the main goals of our TPC is to measure the S1 pulseshape, we require very fast response of the photosensors and need accordingly very fast digitizers. That is the reason why we decided to use a 5GS/s 10bit FADC to digitize the PMTs signals. This will allow us to precisely measure the fast and slow decay time constant.
To make use of the good energy resolution of the Ge-detector it is necessary to use a digitizer with low noise and large dynamic range. Therefore a 16bit FADC will be used.

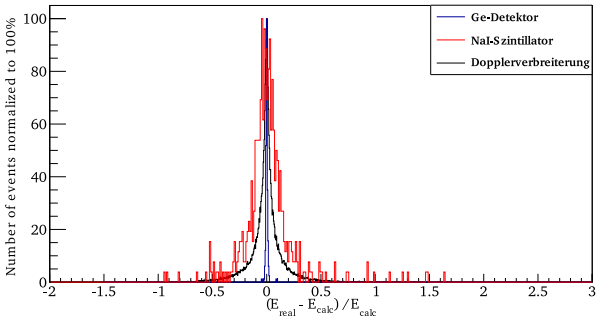

Figure 4: Comparison of simulated energy resolution with germanium (blue) or NaI (red) as secondary detector. [9]

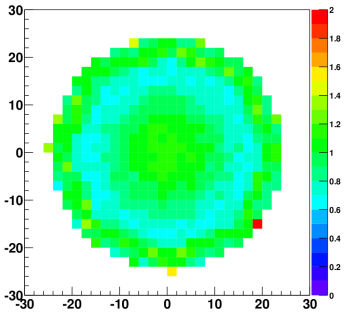

Figure 5: Position reconstruction error.

4 Summary & Outlook

The MainzTPC is designed to measure the liquid xenon light and charge response of low-energy electronic and nuclear recoils, including the pulse shape of the primary scintillation light. These measurements aim to improve our understanding of interaction signatures in direct Dark Matter searches with xenon, as well as to better discriminate backgrounds. The design of the TPC and the measurement setup for the Compton scatter experiment have been optimized with Monte Carlo and finite element simulations. Much of the hardware is already in place, while some components are still being worked on. First tests with the MainzTPC are planned for early 2014, and we hope to report on first measurements at the PATRAS 2014 meeting!

Acknowledgements This project is supported by the Helmholtz Alliance of Astroparticle Physics (HAP), the PRISMA Cluster of Excellence, and the state of Rhineland Palatinate through the EMG research center.

References

[1] L. Baudis, "Direct dark matter detection: The next decade", "Physics of the Dark Universe", Volume **1**, Issues 1-2, 94-108 (2012).

[2] The XENON100 Collaboration, "Dark Matter Results from 225 Live Days of XENON100 Data", Phys. Rev. Lett. **109**, 181301 (2012), [arXiv:1207.5988v2 [astro-ph.CO]].

[3] The XENON100 Collaboration, "The XENON100 dark matter experiment", Astroparticle Physics **35**, 573 (2012), [arXiv:1107.2155]

[4] Hamamatsu, Photomultiplier tube (PMT) Model R6041, `http://http://www.hamamatsu.com/`.

[5] Radiation Monitoring Devices, Inc. Avalanche Photodiode (APD) Model S1315, `http://rmdinc.com/`.

[6] E. Aprile and T. Doke, "Liquid Xenon Detectors for Particle Physics and Astrophysics", Rev. Mod. Phys. **82**, 2053-2097 (2010), [arXiv: 0910.4956 [physics.ins-det]].

[7] P. Shagin et al., "Avalanche Photodiode for liquid xenon scintillation: quantum efficiency and gain", JINST **4** P01005 (2009), [doi:10.1088/1748-0221/4/01/P01005].

[8] Y. Mei, "Direct Dark Matter Search with the XENON100 Experiment", PhD thesis, Dept. of Physics and Astronomy, Rice University, Houston, TX, USA (2011).

[9] P. Sissol, "Monte-Carlo-Simulationen eines Compton-Streuexperiments zur Messung der Szintillations- und Ionisationseigenschaften von flüssigem Xenon mit einer Zwei-Phasen-Xenon-Zeitprojektionskammer", Diploma thesis, Mainz (2012).

Chapter 9

Cosmology and Other Topics

Chameleon Fields Near and Far

A. Weltman

Astrophysics, Cosmology and Gravity Centre,
Department of Mathematics and Applied Mathematics, University of Cape Town, Private Bag, Rondebosch, 7700, South Africa

DOI: http://dx.doi.org/10.3204/DESY-PROC-2013-04/weltman_amanda

It was six men of Indostan
To learning much inclined,
Who went to see the Elephant
(Though all of them were blind),
That each by observation
Might satisfy his mind.
.....
And so these men of Indostan
Disputed loud and long,
Each in his own opinion
Exceeding stiff and strong,
Though each was partly in the right,
And all were in the wrong!

So, oft in theologic wars
The disputants, I ween,
Rail on in utter ignorance
Of what each other mean,
And prate about an Elephant
Not one of them has seen! **John Godfrey Saxe (1816 - 1887)**

In this presentation we contemplate the problem of dark energy and advocate for a multi-faceted approach to studying its solution. Indeed it may be that, like the philosophers described above, we too cannot understand the nature of our beast by only touching one side of the problem. In particular we will study chameleon fields as a candidate for driving the observed acceleration of the universe and we will look how to test this theory through a varied approach as advocated here .

1 Introduction

Remarkably, everything we see and experience on all human scales makes up less than 5% of the total matter in the universe. The ingredients of the planets and stars and oceans and cars is tiny compared to the vast amount of the universe that is dark; literally - not observed electromagnetically. At around 70% of the total matter budget, Dark Energy makes up the lion's share of the universe and yet it is the least well understood. What we do believe we know

is that Dark Energy drives the universe to expand ever faster with time leaving the universe ultimately a cold and empty place. This observed acceleration, awarded the Nobel Prize in 2011, remarkably is not convincingly explained. Einstein's cosmological constant has survived as the most phenomenologically simple solution while offering even greater puzzles as to why the value it assumes physically is 10^{123} times smaller than expected by theoretical computations of the vacuum energy. Ultimately, what we have here is a fundamentally ultraviolet problem. A problem of high energies and possibly quantum gravity, that plays out cosmologically on the largest scales and appears as an infrared effect. In this presentation we consider an approach that mirrors the problem. In particular, we will study chameleon fields [1, 2] which are a novel and compelling Dark Energy candidate [3, 4]. While, providing an exciting explanation of the observed acceleration of the universe with very testable consequences, these theories lack a full ultraviolet completion. Complementary to the fundamental framework we are working to build, we will also discuss a broad array of tests of this theory at the infrared level, from the laboratory to space tests to astrophysical observations.

2 Chameleon Fields

A cosmological constant is an allowed, if perhaps unnatural solution to the dark energy problem. A more compelling alternative of a scalar field driven acceleration is not without its own challenges. If a scalar field is driving the observed acceleration it would need to be very light $m \sim H_0$ and evolving today. A priori such fields should couple to all forms of matter with gravitational strength and thus cause an as yet unobserved fifth force. In fact these effects should be observable in a broad array of known physics settings, from the early universe through big bang nucleosynthesis, structure formation and in all tests of gravity done today. Thus, we are left with a puzzle as to how a scalar field can both be observable as dark energy and yet not be observed to date in all other experiments and observations.

A solution to this puzzle was presented in [1, 2, 3] with so-called chameleon fields. Chameleon fields couple to all Standard Model particles without violating any known laws or experiments of physics. They are nonetheless testable in ways entirely complementary to the standard observational cosmology techniques, and thus provide a new window into dark energy through an array of possible laboratory and astrophysical tests and space tests of gravity.

It is the self interaction of the scalar field, in conjunction with a matter coupling that gives the scalar field a large effective mass in regions of high matter density [1, 2]. A scalar field that is massive locally mediates a short-range fifth force that is difficult to detect, earning it the name "chameleon field." Furthermore, the massive chameleon field is sourced only by the thin shell of matter on the outer surface of a dense extended object. These nonlinear effects serve to screen fifth forces, making them more difficult to detect in certain environments.

Chameleon dark energy is currently treated as an effective field theory [3, 5] describing new particles and forces that might be seen in upcoming experiments, and whose detection would point the way to a more fundamental theory. The ultraviolet (UV) behavior of such theories and their connection to fundamental physics are not yet understood, although progress is being made [6, 7, 8, 9]. The role of quantum corrections to chameleon fields in the early universe is a hot topic, currently under development [10].

2.1 Chameleon Action

Chameleon fields coupled to matter and photons have an action of the form [3]

$$S = \int d^4x\sqrt{-g}\left(\frac{1}{2M_{pl}^2}R - \partial_\mu\phi\partial^\mu\phi - V(\phi)\right) - \frac{e^{\phi/M_\gamma}}{4}F^{\mu\nu}F_{\mu\nu} + S_m(e^{2\phi/M_m^i}g_{\mu\nu}, \psi_m^i)\ , \quad (1)$$

where S_m is the matter action, $V(\phi)$ is the chameleon self interaction and the chameleon field, ϕ can couple differently with coupling β_i, to different matter types ψ_i. Here we will consider a universal coupling to matter defined by $\beta_m = M_{\rm Pl}/M_m$ while allowing for a different coupling to electromagnetism, $\beta_\gamma = M_{\rm Pl}/M_\gamma$, through the electromagnetic field strength tensor $F_{\mu\nu}$.

Crucially, this coupling induces an effective potential

$$V_{\rm eff}(\phi, \vec{x}) = V(\phi) + e^{\beta_m\phi/M_{\rm Pl}}\rho_m(\vec{x}) + e^{\beta_\gamma\phi/M_{\rm Pl}}\rho_\gamma(\vec{x}), \quad (2)$$

where we have defined the effective electromagnetic field density $\rho_\gamma = \frac{1}{2}(|\vec{B}^2 - |\vec{E}|^2)$. An essential insight of chameleon models is noticing that the presence of matter and electromagnetic fields induces a minimum $\phi_{\rm min}$ in $V_{\rm eff}$ where V can be a monotonic function. The dependence of this minimum on the background matter and electromagnetic fields causes the effective mass of the chameleon field to change in response to its environment. In turn we find varied chameleon phenomenology depending on the experimental setup and hence the environment.

We can see explicitly that for an exponential potential, the effective mass of the field ϕ is dependent on the local density of matter and electromagnetic fields,

$$V(\phi) = \Lambda^4\exp\left(\frac{\Lambda^n}{\phi^n}\right), \quad \phi_{\rm min} \approx \left(\frac{nM_{\rm Pl}\Lambda^{n+4}}{\beta_{\rm m}\rho_m + \beta_\gamma\rho_g}\right)^{\frac{1}{n+1}} \text{ and } m_\phi^2 \approx \frac{(n+1)}{(n\Lambda^{n+4})^{\frac{1}{n+1}}}\left(\beta_m\rho_m + \beta_\gamma\rho_\gamma\right)^{\frac{n+2}{n+1}}$$

where the next to leading order terms are suppressed by factors of $\beta_i\phi/M_{\rm Pl} \ll 1$.

3 Chameleons Near

The chameleon dark energy parameter space is considerably more complicated than that of axions, but constraints can be provided under some assumptions. With the caveat that all matter couplings are the same but not equal to the photon coupling, and the assumption of a specific chameleon potential, $V(\phi) = M_\Lambda^4(1 + M_\Lambda^n/\phi^n)$ in which we set the scale $M_\Lambda = 2.4\times10^{-3}$ eV to the observed dark energy density and, for concreteness, $n = 1$, constraints and forecasts are provided by Figure 1. Current constraints (solid regions) and forecasts (curves) are discussed below.

Existing laboratory constraints on chameleon dark energy come from two different types of experiments: fifth force searches, and photon conversion experiments, both of which are shown as shaded regions in Figure 1. Gravitation-strength fifth forces can be measured directly between two macroscopic objects, such as the source and test masses in a torsion pendulum. Currently the shortest-range torsion pendulum constraints on gravitation-strength forces come from the Eöt-Wash experiment [11]. Another type of fifth force experiment uses an ultracold

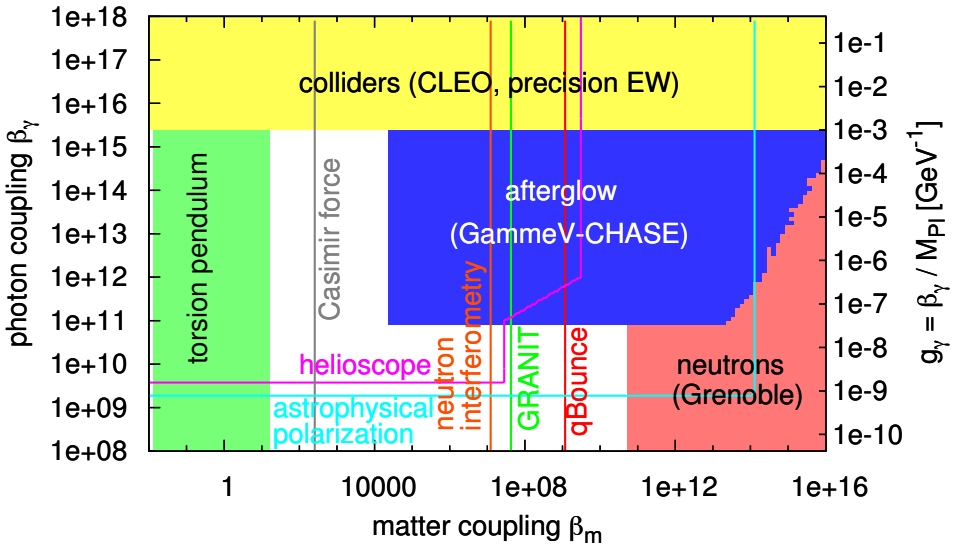

Figure 1: Constraints on the matter and photons couplings for a chameleon dark energy model with $V(\phi) = M_\Lambda^4(1 + M_\Lambda/\phi)$. Current constraints are shown as shaded regions, while forecasts are shown as solid lines.

gas of neutrons whose bouncing states in the gravitational field of the Earth are quantized, with energy splittings ~ 1 peV [12]. If the neutrons feel a fifth force from the experimental apparatus comparable to the gravitational force of the Earth, then the energy splittings will be altered. The Grenoble experiment measures these energy splittings at the $\sim 10\%$ level, excluding very strong matter couplings $\beta_m \gtrsim 10^{11}$.

Quantum corrections generate a photon coupling about three orders of magnitude smaller than the matter coupling [13], although classically this coupling is not required. The lowest order chameleon-photon interaction couples the chameleon field to the square of the photon field strength tensor, implying that photons oscillate into chameleon particles in a background electromagnetic field, The resultant chameleon field mass will be environmentally dependent on both the background energy density and the electromagnetic field strength. This allows for a broad array of different tests for these fields on Earth, in space, and through astrophysical observations.

This electromagnetic coupling would allow photons propagating through a magnetic field to oscillate into particles of dark energy, which can then be trapped inside a chamber if the dark energy effective mass becomes large in the chamber walls. An "afterglow experiment" produces dark energy particles through oscillation and then switches off the photon source, allowing the population of trapped dark energy particles to regenerate photons which may emerge from the chamber as an afterglow. Current afterglow constraints from the CHASE experiment exclude photon couplings $10^{11} \lesssim \beta_\gamma \lesssim 10^{16}$ for $\beta_m \gtrsim 10^4$, as shown in Fig. 1 for an inverse-power-law chameleon potential [14, 15, 16]. At yet higher photon couplings the trapped dark energy parti-

Experiment	Type	Couplings excluded
Eöt-Wash	torsion pendulum	$0.01 \lesssim \beta_m \lesssim 10$
Lamoreaux	Casimir	$\beta_m \gtrsim 10^5$ (ϕ^4)
Grenoble	bouncing neutron	$\beta_m \gtrsim 10^{11}$
GRANIT	bouncing neutron	forecast: $\beta_m \gtrsim 10^8$
NIST	neutron interferometry	forecast: $\beta_m \gtrsim 10^7$
CHASE	afterglow	$10^{11} \lesssim \beta_\gamma \lesssim 10^{16}$ subject to $10^4 \lesssim \beta_m \lesssim 10^{13}$,
ADMX	microwave cavity	$m_{\rm eff} = 1.952\ \mu$eV, $10^9 \lesssim \beta_\gamma \lesssim 10^{15}$
CAST	helioscope	forecast: $\beta_m \lesssim 10^9$, $\beta_\gamma > 10^{10}$

Table 1: Laboratory tests of dark energy. Approximate constraints on chameleon models with potential $V(\phi) = M_\Lambda^4(1 + M_\Lambda/\phi)$ and $M_\Lambda = 2.4 \times 10^{-3}$ eV (unless otherwise noted).

cles regenerate photons too quickly for CHASE to detect them. However, collider experiments can exclude such models, by constraining chameleon loop corrections to precision electroweak observables [17].

4 Chameleons Far

Chameleon fields are also testable in space tests of gravity as well as through astrophysical and astronomical effects. In fact several astrophysical puzzles could be explained by chameleons including a matter coupling, *e.g.*, [18]. In particular [18] shows that small galaxies are expected to have a higher peculiar velocity than large ones (independent of the velocity bias) and voids defined by small galaxies would appear larger than those expected by large galaxies. Even comparing the motions of galaxies and clouds in the same environment may reveal the chameleon mechanism at work.

Comparing lensing and dynamical masses of galaxies and clusters can point to a discrepancy as the deflection law for photons that leads to various gravitational lensing effects is the same with or without chameleons. However the acceleration of galaxies, which move at non-relativistic speeds, is altered as the Newtonian potential is different from that in GR: it receives additional contributions from the Chameleon fields. And while the gravitational lensing signature is identical to the signature predicted in general relativity, the Shapiro time delay can be strongly different for a large region of parameter space of chameleon coupling β. A dedicated catalog of gravitational lensing observations and time delay measurements should be able to constrain a wide range of chameleon models. Because photons travel on geodesics defined in the Jordan frame, constraints on the chameleon-matter coupling may be placed, independent of the necessity for a chameleon-photon coupling [20].

The approaches to detecting the effects listed above and distinguishing them from astrophysical sources have been discussed in the literature cited above. One key element to a convincing detection is to be able to compare to a controlled environment where the primary sources of astrophysical uncertainty can be ruled out. Ideal is to be able to compare between a screened and unscreened environment. There are many distinct chameleon signatures observable in the

astrophysical arena. We have discussed a few here. For a more extensive discussion - the reader is referred to the recent review [21].

5 Acknowledgments

I would like to sincerely thank my many chameleon collaborators for their insights, discussions and patience on this body of work over the last decade. My thanks to the organisers of the Patras series of workshops for bringing together theorists and experimentalists and allowing us to cross-fertilise our fields through this excellent discussion forum. This material is based upon work supported financially by the National Research Foundation. Any opinion, findings and conclusions or recommendations expressed in this material are those of the authors and therefore the NRF does not accept any liability in regard thereto. This work was supported by an Elsevier Young Scientist Award for which I am most grateful.

6 Bibliography

References

[1] J. Khoury and A. Weltman. *Phys. Rev. Lett.*, 93, 2004. 171104.

[2] J. Khoury and A. Weltman. *Phys. Rev. D*, 69, 2004. 044026.

[3] P Brax, C. van de Bruck , A. C. Davis, J. Khoury, A. Weltman, Aug 2004. 31pp. Published in Phys.Rev.D70:123518,2004. e-Print: astro-ph/0408415

[4] P. Brax, C. van de Bruck, A. C. Davis, J. Khoury and A. Weltman, AIP Conf. Proc. **736**, 105 (2005) [astro-ph/0410103].

P. J. E. Peebles and B. Ratra. *Ap. J. Lett.*, 325:17, 1988.

B. Ratra and P. J. E. Peebles. *Phys. Rev. D*, 37(12):3406, 1988.

[5] L. Hui and A. Nicolis. *Phys. Rev. Lett.*, 105, 2010. 231101.

[6] K. Hinterbichler, J. Khoury, and H. Nastase. *JHEP*, 1103(61), 2011.

[7] K. Hinterbichler, J. Khoury, H. Nastase and R. Rosenfeld [arXiv:1301:6756 [hep-th]].

[8] H. Nastase and A. Weltman [arXiv:1301:7120[hep-th]].

[9] H. Nastase and A. Weltman [arXiv:1302:1748 [hep-th]].

[10] A. L. Erickcek, N. Barnaby, C. Burrage and Z. Huang, arXiv:1304.0009 [astro-ph.CO].

[11] D. J. Kapner, T. S. Cook, E. G. Adelberger, J. H. Gundlach, B. R. Heckel, C. D. Hoyle, and H. E. Swanson. *Phys. Rev. Lett.*, 98:021101, 2007. e-Print arXiv:hep-ph/0611184.

[12] P. Brax and G. Pignol. *Phys. Rev. Lett.*, 107:111301, 2011.

[13] P. Brax, C. Burrage, A.-C. Davis, D. Seery, and A. Weltman. *Phys. Rev. D*, 81:103524, 2010. e-Print arXiv:0911.1267.

[14] J. H. Steffen et al. *Phys. Rev. Lett.*, 105:261803, 2010. ePrint: arXiv:1010.0988.

[15] A. Upadhye, J. H. Steffen, and A. Weltman. *Phys. Rev. D*, 81:015013, 2010.

[16] A. Upadhye, J. H. Steffen, and A. S. Chou. *Phys. Rev. D*, 86:035006, 2012.

[17] P. Brax, C. Burrage, A.-C. Davis, D. Seery, and A. Weltman. *JHEP*, 0909:128, 2009. e-print arXiv:0904.3002.

[18] L. Hui, A. Nicolis and C. Stubbs, Phys. Rev. D **80** (2009) 104002 [arXiv:0905.2966 [astro-ph.CO]].

[19] E. G. Adelberger et al. *Phys. Rev. Lett.*, 98:131104, 2007. e-Print arXiv:hep-ph/0611223.

[20] B. Poltis, A. Weltman and D. Mota To appear 2013.

[21] B. Jain, A. Joyce, R. Thompson, A. Upadhye, J. Battat, P. Brax, A. -C. Davis and C. de Rham *et al.*, arXiv:1309.5389 [astro-ph.CO].

Mirror Matter, the cosmological Lithium Problem and Dark Matter

A. Coc[1], *J.-P. Uzan*[2,3], *E. Vangioni*[2,3]

[1]Centre de Sciences Nucléaires et de Sciences de la Matière (CSNSM), CNRS/IN2P3, Université Paris Sud 11, UMR 8609, Bâtiment 104, 91405 Orsay Campus (France)
[2]Institut d'Astrophysique de Paris, UMR-7095 du CNRS, Université Pierre et Marie Curie, 98 bis bd Arago, 75014 Paris (France)
[3]Sorbonne Universités, Institut Lagrange de Paris, 98 bis bd Arago, 75014 Paris (France)

DOI: http://dx.doi.org/10.3204/DESY-PROC-2013-04/coc_alain

The abundance of lithium-7 confronts cosmology with a long lasting problem between the predictions of standard Big Bang Nucleosynthesis and the baryonic density determined from the Cosmic Microwave Background observations. We investigated the influence of the existence of a mirror world, focusing on models in which miror neutrons can oscillate into ordinary neutrons. Such a mechanism allows for an effective late time neutron injection, which induces an increase of the destruction of beryllium-7 but for mirror baryonic densities much lower than $\Omega_{\rm DM}$.

1 Introduction

The abundances of the light elements produced during the primordial nucleosynthesis (BBN) in the early hot phase of the Universe is one of the historical pillar of the big-bang model. When using for the baryon over photon number ratio (η), the value determined by the cosmic microwave observations, the BBN predictions for ^{4}He, D and ^{3}He are in very good agreement with those deduced from observations. However, there remains, a yet unexplained, discrepancy of a factor $\approx$3, between the calculated and observed ^{7}Li abundances [1, 2], that has not been reduced, neither by recent nuclear physics experiments, nor by new observations. One of the solutions to this problem would be to inject neutrons during the late stages of BBN [3]: that would increase ^{7}Be destruction (the BBN progenitor of ^{7}Li), due to a more efficient neutron capture, leading to a lower ^{7}Li final abundance. Injecting neutrons is indeed not something easily performed without including physics beyond the standard model of particle physics. Such an idea can be realized by introducing a mirror sector, constructed by assuming that the gauge group G of the matter sector is doubled to the product $G \times G'$. The Lagrangian of the two sectors, ordinary and mirror, are identical so that they have the same particles content such that ordinary (resp. mirror, noted with a prime) matter fields belonging to G (resp. G') are singlets of G' (resp. G). They also have the same fundamental constants so that the microphysics (and in particular the nuclear sector) is identical. However, the temperature evolutions and the baryonic densities can be different in both worlds [4]. In particular, if the temperatures in both worlds were identical, then the effect of the mirror world would be equivalent to an effective number of neutrino families, $\delta N_{\rm eff} = 6.14$, too large a number to be compatible with observations.

Such a sector was initially proposed by Li and Yang [5] in an attempt to restore global parity symmetry and was then widely investigated [4] (see also Refs. in [6]). As shown in Ref. [7], any *neutral* ordinary particle, fundamental or composite, can be coupled to its mirror partner hence leading to the possibility of, back and forth, oscillation between ordinary and mirror particles, in particular between neutrons (n) and mirror neutrons (n'). This has motivated experimental searches for nn'-oscillations which provided the constraint on the oscillation time scale: $\tau_{\rm osc} > 448\,{\rm s}$ (90% C.L) [8]. From a cosmological point of view, mirror particles have been advocated as a dark matter candidate (see e.g. Ref. [9]). In particular, mirror baryons do not interact with photons and have the same mass as ordinary baryons. From our world they can thus be considered as stable, self-interacting dark matter particles.

2 Model

The Friedmann equation contains both the ordinary and mirror matter and is dominated by the radiation energy density during BBN. The additional term corresponding to the contribution of the mirror sector is calculated as in the ordinary sector, including all relativistic particles, but with a difference in the temperature evolutions. The BBN computations depend on 4 parameters. The standard parameter is the number of ordinary baryons per photon (η) given by the CMB analysis [10, 11]. It has to be complemented by its mirror counterpart (η'), the ratio $x \equiv T'/T$ of mirror/ordinary photon temperatures (a constant except during the electron–positron annihilation period), and the the oscillation time scale ($\tau_{\rm osc}$). Since the physics in the two sectors is identical, the reaction rates are the same in both worlds and are those used in our previous BBN works [1]. However, BBN is different because of the different temperatures and baryonic densities. The network includes 16 isotopes and 27 reactions. These are the usual 8 isotopes and their mirror partners, the 13 main BBN reactions and their mirror counterparts plus the $n \leftrightarrow n'$ oscillation term. None of the previous investigations on mirror BBN [12] have considered the effect of neutron oscillations between the two worlds so that in this first study we use a few approximations. We assume that, during free mirror neutron decay, the mirror neutron abundance evolves as in vacuum, i.e. as $e^{-t/\tau}\cos^2(t/\tau_{\rm osc})$ [13], with τ the usual neutron beta-decay lifetime, i.e. that n' decay to n at a rate of $\lambda_{\rm n'\to n} = \frac{2}{\tau_{\rm osc}}\tan\left(\frac{t}{\tau_{\rm osc}}\right)$. In standard BBN, the weak interaction maintains the thermal equilibrium between neutrons and protons until their rates become slower than the Hubble expansion rate at a typical temperature of $T \approx 3.3$ GK. This freeze-out of the weak interaction is followed by neutron free decay until $T \approx 0.9$ GK when nucleosynthesis begins. This is during this phase of free decay that we assume that neutron oscillation occurs between the two worlds. We neglect $\lambda_{\rm n\to n'}$ inverse process because with our choice of parameters, relevant to the ^{7}Li problem, when the n abundance is initially dominant $\lambda_{\rm n\to n'}$ is suppressed by the factor $\tan(t/\tau_{\rm osc})$. Later, when this factor is no longer negligible, it is the n abundance that becomes negligible. In a subsequent study, we will consider the effect of interactions of mirror neutrons with other mirror/ordinary particles that could modify the $n \leftrightarrow n'$ oscillation rate.

3 Results

For a wide range of parameters, we obtain a reduction of the ^{7}Be+^{7}Li final abundance compatible with observations (at the expense of a moderate D overproduction) providing a possible

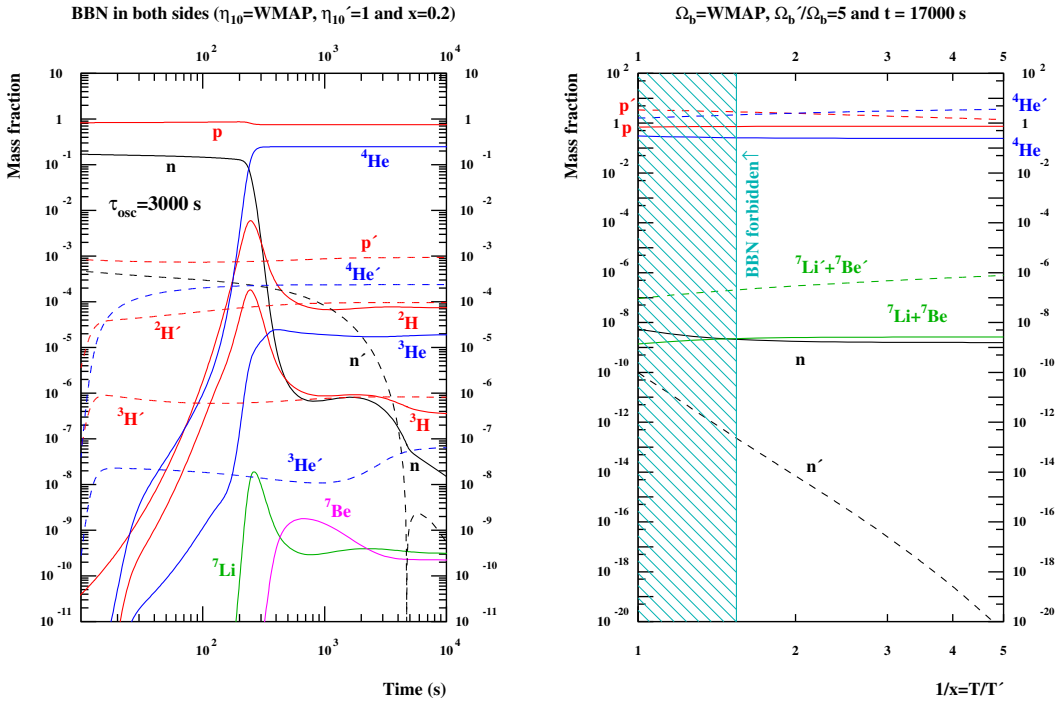

Figure 1: Left panel: abundances (mass fractions) in the ordinary (solid lines) and mirror (dashed lines) worlds as a function of time in the presence of $n' \leftrightarrow n$ oscillations. Right panel: final mass fractions as a function of T/T' (without oscillations) assuming $\Omega'_{\rm b} = \Omega_{\rm DM}$.

solution to the lithium problem [6]. Figure 1 (left) shows the result of a BBN calculation in both worlds with typical values of the parameters: $\eta = \eta_{\rm WMAP}$ [10], $\eta' = 10^{-10}$, $x = 0.2$ and $\tau_{\rm osc} = 3 \times 10^3$ s. (Mirror isotopes up to ^{4}He' are displayed for completeness but are not needed for the discussion.) Initially, because of the difference in baryonic densities, the neutron abundance is much higher in our world but, during standard BBN the neutron abundance decreases very rapidly compared to mirror BBN because of the higher temperature and density. It can be seen that after a time of order 300 s, the abundance of the mirror neutrons, n', is much higher than the normal neutron abundance. This is due to the fact that, for this choice of parameters (T' and $\rho'_{\rm b}$), mirror BBN is limited to n' decay while normal BBN is in its full development. Then, when the n abundance dropped below the n' one, n injection from oscillating n', at the time of ^{7}Be formation, leads to its destruction due to a more efficient neutron capture. On the contrary, the abundance of D increases: we obtain a reduction of the ^{7}Li + ^{7}Be abundance at the expense of a moderate higher deuterium abundance.

Obviously, it would be desirable to both solve the lithium problem and provide a candidate for dark matter with the observed density i.e. $\Omega'_{\rm b}/\Omega_{\rm b} \approx 5$ [10, 11]. Unfortunately, this is not the case as shown in Fig. 1 (right), corresponding to BBN final abundances as a function of x, assuming this ratio of baryonic densities. The hatched area on the left is excluded by BBN as for $T'/T \equiv x \gtrsim 0.6$ the increase in the effective number of neutrino families, $\delta N_{\rm eff} \approx 7x^4$ exceeds the

limits provided by ^{4}He observations. Within the x allowed range, the mirror neutron abundance is smaller than its ordinary counterpart by several orders of magnitude. This is easily explained by the higher mirror baryonic density that makes nucleosynthesis more efficient in the mirror sector than in the ordinary one. Neutron oscillations were switched off in these calculations, but it is obvious that they cannot provide a sufficient ordinary neutron source to significantly affect ^{7}Be production. Note that for $x \lesssim 0.5$, ^{4}He' is more abundant than p' (H') resulting in exotic stellar evolutions.

4 Conclusions

We investigated the possibility of a mirror sector in which mirror-ordinary neutrons oscillations could provide a solution to the primordial lithium problem We have shown [6] that as soon as $x \lesssim 0.6$ the helium-4 abundance is in agreement with the observations while the agreement for both the deuterium and helium-4 abundances can be obtained within a large domain of the parameter space. Unfortunately, the observed dark matter density is outside of this domain. Besides, being self-interacting and dissipative, mirror matter is not a good dark matter candidate.

5 Acknowledgments

This work made in the ILP LABEX (under reference ANR-10-LABX-63) was supported by French state funds managed by the ANR within the Investissements d'Avenir programme under reference ANR-11-IDEX-0004-02. This work was sponsored by the French Agence Nationale pour la Recherche (ANR) via the grant VACOUL (ANR-2010-BLAN-0510-01) and JPU acknowledges partial support from the ANR via the grant THALES (ANR-10-BLAN-0507-01-02).

References

[1] A. Coc & E. Vangioni, *Journal of Physics Conference Series* **202**, 012001 (2010).

[2] B. D. Fields, Annual Review of Nuclear and Particle Science **61**, 47 (2011) [arXiv:1203.3551 [astro-ph.CO]].

[3] K. Jedamzik, Phys. Rev. D **70**, 063524 (2004).

[4] P. Ciarcelluti, Int. J. Mod. Phys. D **19**, 2151 (2010); R. Foot, Int. J. Mod. Phys. A **19**, 3807 (2004).

[5] T.D. Lee and C.-N. Yang, Phys. Rev. **104**, 254 (1956).

[6] A. Coc, J.-P. Uzan, & E. Vangioni, Phys. Rev. D **87**, 123530 (2013) [arXiv:1303.1935 [astro-ph.CO]].

[7] R. Foot, and R.R. Volkas, Phys. Rev. D **52**, 6595 (1995); Z. Berezhiani, and R.N. Mohapatra, Phys. Rev. D **52**, 6607 (1995).

[8] A.P. Serebrov, E.B. Aleksandrov, N.A. Dovator, S.P. Dmitriev *et al.*, Nuclear Instruments and Methods in Physics Research A **611**, 137 (2009).

[9] Z. Berezhiani *et al.*, Int. J. Mod. Phys. D **14**, 107 (2005).

[10] E. Komatsu *et al.* [WMAP Collaboration], Astrophys. J. Supp. **192**, 18 (2011).

[11] P. A. R. Ade, N. Aghanim *et al.* [Planck Collaboration], [arXiv:1303.5076 [astro-ph.CO]].

[12] Z. Berezhiani, D. Comelli, and F.L. Villante, Phys. Lett. B **503**, 362 (2001).

[13] R.N. Mohapatra and R.E. Marshak, Phys. Rev. Lett. B **94**, 183 (1980).

The GERDA Experiment for the Search of Neutrinoless Double Beta Decay

M. Walter for the GERDA *collaboration*

Physik-Institut, Universität Zürich, 8057 Zürich, Switzerland

DOI: http://dx.doi.org/10.3204/DESY-PROC-2013-04/walter_manuel

The GERDA experiment, situated at Laboratori Nazionali del Gran Sasso is designed to search for the neutrinoless double β decay. Bare high purity Ge-diodes enriched to 86 % in ^{76}Ge are directly immersed into liquid Ar. Phase I operated from November 2011 till May 2013 yielding an exposure of 21.6 kg·yr, with a mean background near the Q-value of $2{\cdot}10^{-2}$ cts/(keV·kg·yr). A half-life of $1.84^{-0.10}_{+0.14} \cdot 10^{21}$ yr was recently published for the two-neutrino double β decay. For Phase II, additional 20 kg of broad-energy Ge detectors will be installed to reach an exposure of 100 kg·yr with one order of magnitude less background, exploring half-lifes up to $1.5{\cdot}10^{26}$ yr. This will be achieved by liquid Ar instrumentation as an active veto, pulse shape analysis and a refined selection of radio-pure materials.

1 Introduction

For some even-even nuclei single β-decay is energetically forbidden, but the neutrino accompanied double β decay ($2\nu\beta\beta$) is allowed. This standard model process has been observed for ^{48}Ca, ^{76}Ge, ^{82}Se, ^{96}Zr, ^{100}Mo, ^{116}Cd, ^{128}Te, ^{130}Te, ^{150}Nd, ^{238}U, ^{130}Ba and ^{136}Xe with a half-life between $7{\cdot}10^{18}$ yr and $2.5{\cdot}10^{24}$ yr. For ^{76}Ge it has been measure in GERDA to be $1.84^{+0.14}_{-0.10} \cdot 10^{21}$ yr [1].

The neutrinoless double β decay ($0\nu\beta\beta$) is not allowed in the standard model, it is however predicted by several extensions of the standard model. The most likely mechanism is by the exchange of light neutrinos. The existence of this decay in ^{76}Ge has been claimed by a subgroup of the Heidelberg-Moscow-Experiment [2].

The double β decay is detected by the summed energy of the two emitted electrons. In the neutrino accompanied decay, part of the energy is carried away by the neutrinos resulting in a continuous spectrum. For the neutrinoless case the energy is carried by the electrons only, resulting in a peak at the Q-value of the decay ($Q_{\beta\beta} = 2039$ keV for ^{76}Ge). In GERDA, Ge is used as both the decay source and the detection device. Ge detectors have a very high energy resolution, around 0.14 % at 2 MeV, which is important as a higher resolution results in a larger signal-to-background ratio.

2 The Low Background Experiment GERDA

GERDA is running in two phases. Phase I started in November 2011 and finished in May 2013 with 18 kg of enriched Ge diodes. Phase II is planned to start end of 2013 with additional 20 kg of enriched Ge and a background reduced by a factor of 10 compared to Phase I.

In GERDA bare Ge diodes enriched to 86% of ^{76}Ge are directly immersed into a 5.5 m high cryostat containing 64 m^3 of liquid Ar. The Ar serves as a coolant at 89 K and shielding. The cryostat is surrounded by a high purity water tank acting as additional shielding. It is equipped with photomultiplier tubes to veto muon induced events by their Cherenkov light emitted when passing through the water. Muons flying through the neck of the cryostat are detected by plastic scintillator panels installed above the water tank. For a detailed description of the GERDA experiment see [3].

2.1 Phase I

One non-enriched and eight refurbished enriched coaxial detectors from the past IGEX and Heidelberg-Moscow experiments were installed in Phase I. The latter are the same as used for the claimed observation. Two of the enriched detectors quickly developed high leakage currents and could not be used for the analysis. Additionally, five Phase II type Broad Energy Germanium (BEGe) detectors were installed in July 2012 of which one showed drifts in the energy calibration and was not used.

Coaxial and BEGe detectors differ by their geometry. Both types have the n-doped electrode on their outer surface shown in black in Fig. 1. The p-doped readout electrode is a pad on one face for the BEGe type detectors and a hole in the center for coaxial type detectors. For more details see section 2.2.1.

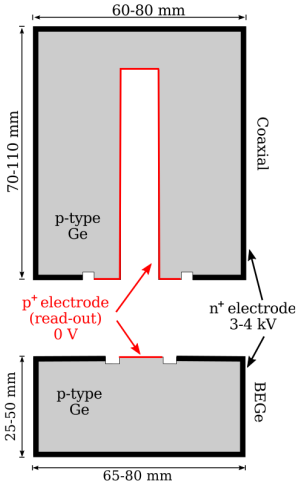

Figure 1: Cut through the rotation symmetry axis of coaxial and BEGe type detectors. Figure from [5].

2.1.1 Data Taking and Detector Stability

A total exposure of enriched Ge detectors of 21.6 kg·yr was reached during Phase I [4]. The data was taken with a blinded energy window of $Q_{\beta\beta} \pm 20$ keV. The open part of the data was used to develop analysis methods and background models. The unblinding was performed in two steps, first the blinding window was reduced to $Q_{\beta\beta} \pm 5$ keV for coaxial and $Q_{\beta\beta} \pm 4$ keV for BEGe detectors. The now unblind "side bands" were used to test the background models. Then the full energy range was unblinded and the unchanged analysis methods were applied.

For energy calibration of the Ge detectors about 10 peaks from a ^{228}Th source were used. The number of peaks used depends on the statistics in the individual peaks for each detector and calibration measurement. The FWHM at 2614.5 keV was between 4.2 and 5.8 keV for coaxial and between 2.6 and 4.0 keV for BEGe detectors. The maximum shift of this peak between two consecutive calibration measurements was about 2 keV [5].

2.1.2 Description of Background Sources

Several sources contributing to the background near $Q_{\beta\beta}$ are known and illustrated in Fig. 2. To understand those it is essential to know that the outer most, so called dead layer of the detector is not active. Interactions in this region will result in no signal. This layer is about 2 mm at the n+ contact and about 0.3 μm for the p+ contact. Electrons from β decays can penetrate either layer whereas α particles are able to penetrate only the p+ dead layer. There is a transition layer with incomplete charge collection between the active and dead volume.

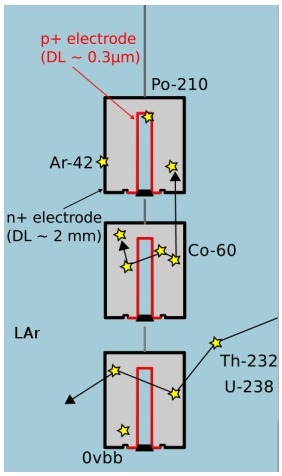

Figure 2: Illustration of typical interaction patterns for different background sources. Figure from [6].

High energy β decays contributing to the background in GERDA near $Q_{\beta\beta}$ originate primarily from ^{42}K in liquid Ar close to the detector surface and ^{214}Bi on the p+ contact. ^{42}K is the daughter of ^{42}Ar, traces of which are naturally contained in Ar. The background from ^{42}K is approximately a factor of 10 higher than expected. ^{214}Bi originates from ^{226}Ra present on the detector surface. Cosmogenically produced ^{60}Co is an internal β emitter occurring in coincidence with the emission of γ rays. α events originate from ^{210}Po and ^{226}Ra, including its daughter nuclei, on the p+ surface. ^{222}Rn is also present in liquid Ar near by [5].

Many materials and hence various set-up components contain elements from the ^{238}U and ^{232}Th decay chains. Among those the isotopes ^{208}Tl and ^{214}Bi emit γ rays which contribute to the background at $Q_{\beta\beta}$ by Compton scattering. This is also the case for cosmogenic ^{60}Co. These type of events can have several interaction locations inside the active volume, in which case they are called multi site events. Events with only one interaction location, like most double β decay events, are called single site events. The number of multi site events is reduced by cutting on detector coincidences and using pulse shape analysis. The latter is described in [7]. The number of surface β events were reduced using thin copper cylinders, so called mini-shrouds, preventing ^{42}K ions from drifting to the detector surface. A larger copper cylinder called radon shroud is installed with the goal to prevent Rn emanated from the cryostat from reaching the detector assembly.

2.1.3 Background Analysis

The coaxial detectors account for the largest fraction of the total Phase I exposure. For this reason the description of the background is focused on those detectors.

In a first step the spectral shape of each individual background source was simulated. A source is a sub decay chain expected to be in equilibrium and in a specific location in GERDA, e.g. the detector holders, p+ contact, etc.. A minimum number of well motivated sources resulting in a good fit of the measured spectrum are contained in the so called minimum model. These are all sources described in chapter 2.1.2 plus the $2\nu\beta\beta$ decay and ^{40}K. The measured spectrum, the model fit and the contributions of its individual components are shown in Fig. 3.

Alpha events clearly dominate the high energy region having a long tail on the low energy side. The tail of α events originates from different track length inside the dead- and transition layer as well as in liquid Ar, which means different amounts of not detected energy deposition.

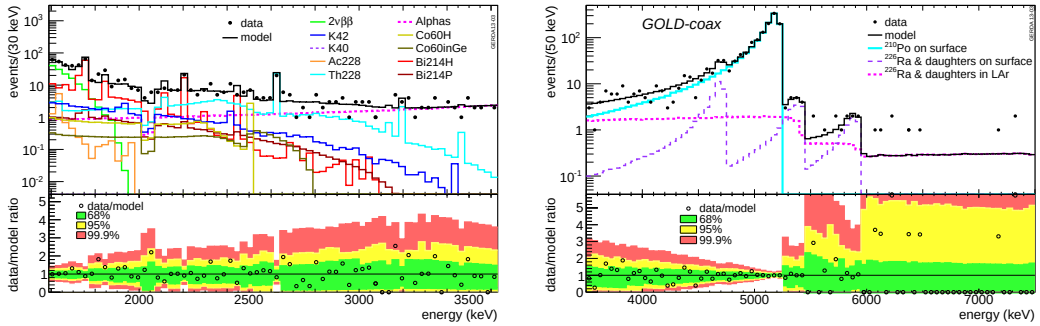

Figure 3: Fit of the minimal model to the measured spectrum in the enriched coaxial detectors and the individual components. Bottom part: Data divided by model with 68% (green), 95% (yellow) and 99.9% (red) probability intervals obtained from the model. Figure from [5].

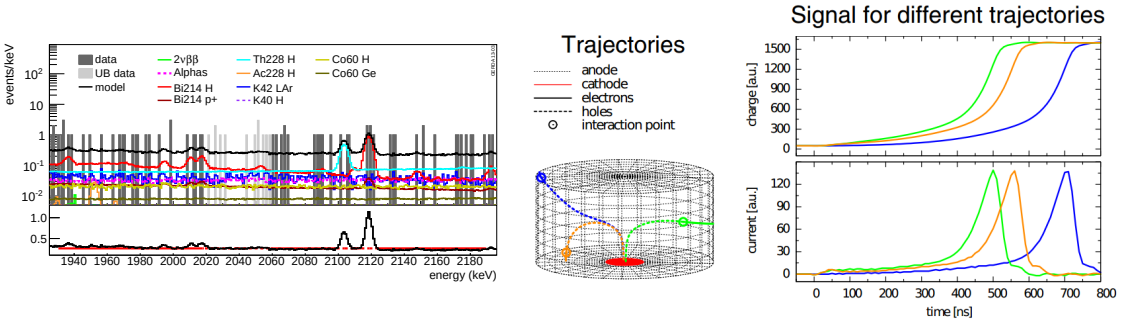

Figure 4: Left: Zoom into the energy region near $Q_{\beta\beta}$ together with the observed events, the minimum model and its individual components. A comparison of a constant fit and the model is shown in the lower half. A BEGe detector is shown in the center with three interactions (circles) and the resulting drift paths of the excited electrons and holes. Right and center from [8].

The contribution due to α events is extending down to energies below $Q_{\beta\beta}$. A zoom to the energy region around $Q_{\beta\beta}$ is shown in Fig. 4 on the left side. The main contributions at $Q_{\beta\beta}$ are in descending order ^{214}Bi and ^{228}Th from detector holders or other close objects, ^{42}K in liquid Ar and α decays close to the p+ surface.

Additionally to the sources in the minimum model, ^{42}K on the p+ and n+ surfaces of the detectors, ^{228}Th on the radon shroud and on the heat exchanger, ^{228}Ac and ^{214}Bi on the radon shroud and ^{214}Bi in liquid Ar close to p+ surface of the detectors are contained in a maximum model. The main difference is a higher contribution from surface and close to surface events compared to the minimum model.

From both models we do not expect a background peak at $Q_{\beta\beta}$. A constant fit to the background excluding the blinded region and ± 5 keV around the γ lines at 2104 keV (^{208}Tl single escape line) and 2119 keV (^{214}Bi) describes the background at $Q_{\beta\beta}$ well. This is shown at the bottom left part in Fig. 4. The predicted background from the two models is between $1.76{\cdot}10^{-2}$ and $2.38{\cdot}10^{-2}$cts/(keV·kg·yr). This is consistent with an extrapolation from a constant back-

ground. Shown in gray are the events in the unblinded sidebands which have not been used in the fits. They match well with the expectations from both models.

In the energy range above the endpoint of ^{39}Ar at 565 keV till about 1650 keV the $2\nu\beta\beta$ decay is dominating the spectrum. Both background models provide a half-life for this decay consistent with our previously published value of $1.84^{+0.14}_{-0.10} \cdot 10^{21}$ yr [1]. For more details about the background in GERDA see [5].

2.2 Phase II

In Phase II the mass of enriched Ge will be increased by 20 kg and the background will be reduced by a factor of 10. The latter will be achieved primarily by an active liquid Ar veto system and enhanced pulse shape discrimination properties of the BEGe type Phase II detectors.

2.2.1 Broad Energy Ge Detectors

The specific geometry of BEGe detectors, as described in chapter 2.1 results in well separated current peaks for different interaction locations of γ rays inside the detector [8]. Three interaction points (circles) together with the trajectories of the corresponding excited electrons (solid lines) and holes (dashed lines) are shown in the center of Fig. 4. On the right the corresponding charge and current pulses are shown (for a normalized energy deposition at each interaction point). A current signal from a single site, $\beta\beta$ like event has only one maximum, whereas a multi site, background like event is the sum of several current signals resulting in two or more maxima. This provides the possibility to effectively reject multi site events.

Events with an energy deposition in the transition layer have a different rise time compared to bulk events. This gives the possibility to reject α and β particles penetrating the dead layer.

An other advantage of BEGe type detectors is their low capacitance compared to coaxial detectors which results in a typical energy resolution of 2.7 keV instead of 4.5 keV FWHM at $Q_{\beta\beta}$.

2.2.2 Liquid Argon Veto

Many background events at $Q_{\beta\beta}$ occur in coincidence with an energy deposition in liquid Ar. Ar is a scintillator and hence can be used to efficiently suppress these background events. Suppression factors of a liquid Ar veto system have been measured in a test set-up for different sources. For close sources like impurities in holders, pre-amplifiers and other close objects suppression factors are approximately 1180 for ^{208}Tl in the ^{228}Th chain and approximately 4.6 for ^{214}Bi. The large suppression factor of the former originates from coincident γ decays.

Ar scintillation light has a wavelength of 128 nm and needs to be converted to longer wavelength before detection. In GERDA the conversion is performed by tetraphenyl butadiene coated Tetratex® reflector foils and wavelength shifting fibers. The design of the veto system is shown in Fig. 5. It consists of three cylinders which are called shrouds and a PMT array

Figure 5: Schematic view of the liquid Ar veto system. Figure by courtesy of M. Heisel, MPI-K.

at the top and bottom. The middle shroud, surrounding the Ge-detector strings consists of a close array of approximately 1000 m of fibers with Si photomultipliers at the end. This allows light from outside the shroud to be detected. The upper and lower shroud is made of Cu covered from the inside by the coated Tetratex® reflector.

3 Conclusions

Phase I of the GERDA experiment has successfully finished with an exposure of 21.6 kg·yr and a background of about $2 \cdot 10^{-2}$ cts/(keV·kg·yr). A detailed analysis shows that no peak from the background is expected at $Q_{\beta\beta}$. The results of Phase I have been published [4] soon after the Patras 2013 workshop. The transition to Phase II with a design sensitivity improvement by a factor of 10 has started.

4 Acknowledgments

The GERDA experiment is supported financially by the German Federal Ministry for Education and Research (BMBF), the German Research Foundation (DFG) via the Excellence Cluster Universe, the Italian Istituto Nazionale di Fisica Nucleare (INFN), the Max Planck Society (MPG), the Polish National Science Centre (NCN), the Foundation for Polish Science (MPD programme), the Russian Foundation for Basic Research (RFBR 12- 02-12135-ofi-M), and the Swiss National Science Foundation (SNF). The institutions acknowledge also internal financial support.

The GERDA collaboration thanks the directors and the staff of the LNGS for their continuous strong support of the GERDA experiment.

5 Bibliography

References

[1] GERDA collaboration, "Measurement of the half-life of the two-neutrino double beta decay of Ge-76 with the GERDA experiment", J. Phys. G: Nucl. Part. Phys. **40** (2013) 035110 [arXiv:1212.3210 [nucl-ex]]

[2] H.V. Klapdor-Kleingrothaus, I.V. Krivosheina, A. Dietz, O. Chkvorets, "Search for neutrinoless double beta decay with enriched 76Ge in Gran Sasso 1990–2003", Phys. Lett. **B586**, 198 (2004) [arXiv:hep-ph/0404088]

[3] GERDA collaboration, "The GERDA experiment for the search of $0\nu\beta\beta$ decay in ^{76}Ge", Eur. Phys. J. C **73** (2013) 2330 [arXiv:1212.4067 [physics.ins-det]]

[4] GERDA collaboration, "Results on neutrinoless double beta decay of 76Ge from GERDA Phase I", Phys. Rev. Lett. **111**, 122503 (2013), [arXiv:1307.4720 [nucl-ex]]

[5] GERDA collaboration, "The background in the $0\nu\beta\beta$ experiment GERDA", submitted to Eur. Phys. J. C [arXiv:1306.5084v1 [physics.ins-det]]

[6] M. Agostini, "The GERDA experiment for the search of neutrinoless double beta decay: status and perspectives" talk at 25th Rencontres de Blois, May 26-31, 2013

[7] GERDA collaboration, "Pulse shape discrimination for GERDA Phase I data", submitted to Eur. Phys. J. C [arXiv:1307.2610v1 [physics.ins-det]]

[8] M. Agostini, C. A. Ur, D. Budjas, E. Bellotti, R. Brugnera, C. M. Cattadori, A. di Vacri, A Garfagnini, L. Pandola and S. Schönert, "Signal modeling of high-purity Ge detectors with a small read-out electrode and application to neutrinoless double beta decay search in Ge-76" J. of Instrumentation (JINST), **6** (2011) P03005 [arXiv:1012.4300 [physics.ins-det]]

List of Authors

List of Participants

Anastassopoulos, Vassilis – University of Patras
Andreas, Sarah – DESY
Arias, Paola – PUC
Avignone, Frank – University of South Carolina
Baehre, Robin – Albert-Einstein-Institute Hannover
Baker, Keith – Yale University
Balakin, Alexander – Kazan Federal University
Balazs, Csaba – Monash University
Bauermeister, Boris – University of Mainz
Beranek, Tobias – University of Mainz
Betz, Michael – CERN
Büchner, Jörg – Max-Planck-Institut für Sonnensystemforschung
Cantatore, Giovanni – University and INFN Trieste
Caspers, Fritz – CERN
Cembranos, Jose – Universidad Complutense de Madrid
Cerulli, Riccardo – INFN-LNGS
Choi, JungHoon – Seoul National University
Cicoli, Michele – ICTP, Trieste and Bologna University
Coc, Alain – CSNSM (Orsay)
Couchot, Francois – CNRS-LAL
Davenport, Martyn – CERN
Davidek, Tomas – Charles University, IPNP
Denig, Achim – University of Mainz
Derbin, Alexander – St. Petersburg Nuclear Physics Institute
Dbrich, Babette – DESY
Dreyling-Eschweiler, Jan – DESY
Espriu, Domenec – University of Barcelona
Flambaum, Victor – University of New South Wales, Frankfurt Institute for Advanced Studies
Galan, Javier – University of Zaragoza
Gan, Liping – University of North Carolina Wilmington
Gasparian, Ashot – North Carolina A&T State University
Gburek, Szymon – Space Research Center, Solar Physics Division, Polish Academy of Sciences
Giannotti, Maurizio – Barry University
Gondolo, Paolo – University of Utah
Gradl, Wolfgang – University of Mainz
Gustafsson, Michael – ULB, Brussels
Heil, Werner – University of Mainz
Holtrop, Maurik – University of New Hampshire
Horns, Dieter – University of Hamburg
Huang, Feng – Xiamen Unversity
Inada, Toshiaki – University of Tokyo
Inoue, Yoshizumi – ICEPP, University of Tokyo
Jäckel, Jörg – Institut für theoretische Physik, Heidelberg
Jaegle, Igal – University of Hawaii
Jeong, Kwang Sik – Tohoku University

Kalliokoski, Matti – Lancaster University, Cockcroft Institute
Karuza, Marin – University of Rijeka
Ko, Pyungwon – Korea Institute for Advanced Study (KIAS)
Kozlov, Valentin – Karlsruhe Institute of Technology
Kunc, tpn – Technical University of Liberec
Lakic, Biljana – Rudjer Boskovic Institute, Zagreb
Lamblin, Jacob – LPSC Grenoble
Lebedev, Oleg – DESY
Li, Hau-Bin – Academia Sinica, Taipei
Lindner, Axel – DESY
Lindner, Manfred – Max Planck Institut fuer Kernphysik, Heidelberg
Lobanov, Andrei – MPIfR Bonn, University of Hamburg
Malagon, Ana – Yale University
Marrodn Undagoitia, Teresa – MPI Heidelberg
Marsh, M.C. David – University of Oxford
Masso, Eduard – Universidad Autonoma Barcelona
Muratova, Valentina – St. Petersburg Nuclear Physics Institute
Ni, Kaixuan – Shanghai Jiao Tong University
Nones, Claudia – CEA/DSM/IRFU/SPP
Oberlack, Uwe – University of Mainz
Parker, Stephen – University of Western Australia
Payez, Alexandre – University of Lige
Pospelov, Maxim – Perimeter Institute
Pradler, Josef – Johns Hopkins University
Redondo, Javier – MPP and LMU Munich
Reinhold, Bernd – University of Hawaii, Manoa
Ringwald, Andreas – DESY
Roncadelli, Marco – INFN, Pavia
Schael, Stefan – RWTH Aachen
Scheibelhut, Melanie – University of Mainz
Schumann, Marc – AEC - University of Bern
Schwarz, Matthias – University of Hamburg
Scorza, Silvia – Southern Methodist University
Sikivie, Pierre – University of Florida
Sissol, Pierre – University of Mainz
Sulc, Miroslav – Technical University of Liberec
Tullney, Kathlynne – University of Mainz
van de Ven, Glenn – Max Planck Institute for Astronomy (MPIA), Heidelberg
Viaux, Nicols – Pontificia Universidad Catolica de Chile
Vogel, Hendrik – Max Planck Institute for Physics
von Seggern, Jan Eike – DESY
Wallace, Chris – Institute for Particle Physics Phenomenology, Durham
Walter, Manuel – University of Zurich
Wayand, Stefan – Karlsruhe Institute of Technology
Weltman, Amanda – University of Cape Town
Wester, William – Fermi National Accelerator Laboratory
Woollett, Nathan – Lancaster University, Cockcroft Institute
Wouters, Denis – CEA, Irfu
Zioutas, Konstantin – University of Patras

92 participants

9th Patras Workshop
on Axions, WIMPs and WISPs

23-28 June 2013
Johannes Gutenberg
University Mainz
Schloss Waldthausen, Germany

Organizing committee:
Vassilis Anastassopoulos (University of Patras)
Laura Baudis (University of Zurich)
Joerg Jaeckel (University of Heidelberg)
Axel Lindner (DESY)
Uwe Oberlack (University of Mainz, chair)
Andreas Ringwald (DESY)
Marc Schumann (University of Bern)
Konstantin Zioutas (University of Patras)

The physics case for WIMPS, Axions, WISPs
Searches for Hidden Sector Photons
Direct and indirect searches for Dark Matter
Direct and indirect searches for Axions and WISPs
Signals from astrophysical sources
Review of collider experiments
New theoretical developments
Scalar Dark Energy, theory and experiment

http://axion-wimp.desy.de